Novel design concepts for visible-light-active semiconductor photocatalysts

Dissertation

zur Erlangung des akademischen Grades
„Doktor der Naturwissenschaften (Dr. rer. nat)“
im Promotionsfach Chemie
des Fachbereichs Chemie, Pharmazie und Geowissenschaften
der Johannes Gutenberg-Universität Mainz

vorgelegt von

Niklas Huber

geboren in Breisach am Rhein

Mainz, Mai 2021

Die vorliegende Arbeit wurde im Zeitraum von März 2018 bis März 2021 am Max-Planck-Institut für Polymerforschung im Arbeitskreis von [redacted] unter der Betreuung von [redacted] angefertigt.

Erklärung

Hiermit versichere ich, die vorliegende Arbeit selbstständig und ohne Benutzung anderer als der angegebenen Hilfsmittel angefertigt zu haben. Alle Stellen, die wörtlich oder sinngemäß aus Veröffentlichungen oder anderen Quellen entnommen sind, wurden als solche eindeutig kenntlich gemacht. Diese Arbeit ist in gleicher oder ähnlicher Form noch nicht veröffentlicht und auch keiner anderen Prüfungsbehörde vorgelegt worden.

Niklas Huber

Mainz, Mai 2021

Prüfungsdatum 05.07.2021

Danksagung

Abstract

The photocatalytic use of visible light represents a sustainable and promising approach for transforming organic synthesis in the 21st century. Inspired by natural systems, various materials have recently been investigated to perform chemical reactions with light. However, the step into the widespread and large-scale application of these materials has not been achieved so far due to versatile reasons. The relevance and value of the reactions performed, the nanostructuring of the materials, the precise control of catalyst properties, the catalyst price, and green solvent compatibility are critical challenges. This work aims to develop new semiconducting materials for efficient heterogeneous photocatalysis of organic redox reactions with visible light. Novel catalyst concepts have been developed that address critical challenges for large-scale and future practical applications.

First, the realization of high-value reactions is addressed. Three thiophene-based CTFs with variable-length phenyl linkers could be used for the photocatalytic oxidation of toluene to benzaldehyde with atmospheric oxygen. The performance of selective sp^3-C-H activations is a step towards atom-economical and technically useful photocatalytic reactions.

Second, the effects of nanoscaling and molecular fine-tuning through copolymerization on photocatalysts are investigated. CTF nanoparticles are obtained for the first time using a size-controllable confinement synthesis. Together with the admixture of electron-accepting comonomers, significant efficiency gains can be achieved in the investigated [3+2] cycloaddition benchmark reaction. The project highlights the importance of morphological synthesis control and points a way towards dispersible and highly active applied photocatalysts.

Third, the significance of controlling electro-optical properties in photocatalytic systems is highlighted. Controlling the thickness of CdSe nanoplatelets at the atomic level allows tuning of the bandgap and photocatalytic efficiency to reduce nitrobenzene to azoxybenzene. In a further project, porous aromatic frameworks are established as a versatile and highly porous platform for photocatalysis. Precise control of the conjugation length within the polymers allows the selective adjustment of frontier orbital potentials. The role of HOMO and LUMO redox potentials in oxidation and reduction strength in C-

H activations is emphasized. Precise control of electro-optical and structural properties is critical to tailor photocatalytic materials to target applications.

Fourth, the reduction of catalyst complexity, as well as synthetic effort and cost, is focused. Copolymerization of a photoactive monomer with MMA provides an efficient heterogeneous photocatalyst for [4+2] visible-light cycloadditions. The system combines the photoactive small molecule's photocatalytic properties with the robustness and chemical constitution of PMMA. The project highlights the importance of creating low-cost and straightforward catalyst platforms that can be easily applied.

Fifth, the high relevance of compatibility with green solvents is emphasized. Based on the PMMA platform and variable proportions of a sulfonic acid comonomer, water-compatible photocatalytic polymers to remove pollutants from an aqueous medium could be obtained. Thus, the project represents a step towards biological & environmental applications and promotes sustainable solvents in synthetic practice.

Overall, this work is intended to facilitate the broader application of heterogeneous photocatalytic materials and visible-light photocatalysis through its findings.

Zusammenfassung

Die photokatalytische Nutzung von sichtbarem Licht stellt einen nachhaltigen und vielversprechenden Ansatz für die Transformation der organischen Synthese im 21. Jahrhundert dar. Inspiriert von natürlichen Systemen wurden in letzter Zeit verschiedene Materialien untersucht, um chemische Reaktionen mit Licht durchzuführen. Der Schritt in die weit verbreitete und großflächige Anwendung dieser Materialien wurde bisher aus vielfältigen Gründen nicht erreicht. Die Relevanz und die Qualität der durchgeführten Reaktionen, die Nanostrukturierung der Materialien, die präzise Kontrolle der Katalysatoreigenschaften, der Katalysatorpreis und die Verträglichkeit mit grünen Lösungsmitteln sind entscheidende Herausforderungen. Ziel dieser Arbeit ist die Entwicklung neuer halbleitender Materialien für die effiziente heterogene Photokatalyse von organischen Redoxreaktionen mit sichtbarem Licht. Es wurden neuartige Katalysatorkonzepte entwickelt, die kritische Herausforderungen für großtechnische und zukünftige praktische Anwendungen adressieren.

Zunächst wird die Realisierung von hochwertigen Reaktionen adressiert. Drei Thiophen-basierte CTFs mit längenvariablen Phenyl-Linkern konnten für die photokatalytische Oxidation von Toluol zu Benzaldehyd mit Luftsauerstoff eingesetzt werden. Die Durchführung selektiver sp^3-C-H-Aktivierungen ist ein Schritt in Richtung atomökonomischer und technisch nutzbarer photokatalytischer Reaktionen.

Zweitens werden die Auswirkungen von Nanoskalierung und molekularem Feintuning durch Copolymerization auf Photokatalysatoren untersucht. CTF-Nanopartikel werden erstmalig durch eine größenkontrollierbare Confinement-Synthese erhalten. Zusammen mit der Beimischung von elektronenakzeptierenden Comonomeren können signifikante Effizienzgewinne in der untersuchten [3+2]-Cycloaddition-Benchmark-Reaktion erzielt werden. Das Projekt unterstreicht die Bedeutung der morphologischen Synthesekontrolle und weist einen Weg zu dispergierbaren und hochaktiven angewandten Photokatalysatoren.

Drittens wird die Bedeutung der Kontrolle elektrooptischer Eigenschaften in photokatalytischen Systemen hervorgehoben. Die Kontrolle der Dicke von CdSe-Nanoplättchen auf atomarer Ebene ermöglicht die Abstimmung der Bandlücke und der photokatalytischen Effizienz bei der Reduktion von Nitrobenzol zu Azoxybenzol. In einem weiteren Projekt werden poröse aromatische Gerüste (*porous aromatic frameworks)* als

eine vielseitige und hochporöse Plattform für die Photokatalyse etabliert. Die präzise Kontrolle der Konjugationslänge innerhalb der Polymere erlaubt die selektive Einstellung der Grenzorbitalpotentiale. Die Rolle der HOMO- und LUMO-Redoxpotentiale für die Oxidations- und Reduktionsstärke bei C-H-Aktivierungen wird hervorgehoben. Die präzise Kontrolle der elektrooptischen und strukturellen Eigenschaften ist entscheidend, um photokatalytische Materialien auf Zielanwendungen zuzuschneiden.

Viertens steht die Reduzierung der Komplexität des Katalysators sowie des synthetischen Aufwands und der Kosten im Vordergrund. Die Copolymerization eines photoaktiven Monomers mit MMA liefert einen effizienten heterogenen Photokatalysator für [4+2] Cycloadditionen mit sichtbarem Licht. Das System kombiniert die photokatalytischen Eigenschaften des photoaktiven kleinen Moleküls mit der Robustheit und chemischen Beschaffenheit von PMMA. Das Projekt zeigt, wie wichtig es ist, kostengünstige und einfach anzuwendende Katalysatorplattformen zu schaffen.

Fünftens wird die hohe Relevanz der Kompatibilität mit grünen Lösungsmitteln hervorgehoben. Basierend auf der PMMA-Plattform und variablen Anteilen eines Sulfonsäure-Comonomers konnten wasserverträgliche photokatalytische Polymere für die Entfernung von Schadstoffen aus einem wässrigen Medium erhalten werden. Das Projekt stellt einen Schritt in Richtung biologischer & ökologischer Anwendungen dar und fördert die Verwendung nachhaltiger Lösungsmittel in der synthetischen Praxis.

Insgesamt soll diese Arbeit durch ihre Erkenntnisse die breitere Anwendung von heterogenen photokatalytischen Materialien und der Photokatalyse mit sichtbarem Licht ermöglichen.

Table of Contents

1 Introduction 10
  1.1 Motivation and aim of work 10
  1.2 Theoretical background 14
  1.3 Characterization techniques 38
2 Results and discussion 44
  2.1 Visible-light-driven selective oxidation of hydrocarbons under ambient conditions over covalent triazine frameworks* 46
  2.2 Covalent triazine framework nanoparticles *via* size-controllable confinement synthesis for enhanced visible-light photoredox catalysis 74
  2.3 Semiconductor nanoplatelets with tunable photocatalytic activity for selective synthesis of azoxy aromatics 104
  2.4 Porous aromatic frameworks with precisely controllable conjugation lengths for visible-light-driven photocatalytic selective C-H activation reactions 126
  2.5 A PMMA-based heterogeneous photocatalyst for visible-light-promoted [4+2] cycloaddition 156
  2.6 A water-compatible PMMA-based polymer for photocatalytic pollutant remediation in aqueous media 192
3 Supporting information 216
  3.1 Visible-light-driven selective oxidation of hydrocarbons under ambient conditions over covalent triazine frameworks 216
  3.2 Covalent triazine framework nanoparticles via size-controllable confinement synthesis for enhanced visible-light photoredox catalysis 228
  3.3 Semiconductor nanoplatelets with tunable photocatalytic activity for selective synthesis of azoxy aromatics 240
  3.4 Porous aromatic frameworks with precisely controllable conjugation lengths for visible-light-driven photocatalytic selective C-H activation reactions 246
  3.5 A PMMA-based heterogeneous photocatalyst for visible-light-promoted [4+2] cycloaddition 264
  3.6 A water-compatible PMMA-based polymer for photocatalytic pollutant remediation in aqueous media 280
4 Summary and outlook 282
Appendix 286
  A.1 References 286
  A.2 List of Figures 302
  A.3 List of Tables 312
  A.4 List of publications 314
  A.5 Curriculum Vitae 316

1 Introduction

1.1 Motivation and aim of work

The UN forecasts a world population growth to 10 billion people by 2050.[1] Indicators such as global gross domestic product, literacy rates, mortality rates, and the global hunger index show a long-term improvement in global living conditions.[2-3] However, steadily growing populations and rising living standards worldwide lead to increased global energy demand. From 2000 to 2019, global primary energy consumption increased from 395 EJ to 584 EJ, a total of 48%.[4] This trend is expected to continue steadily in the future.

As a significant energy consumer, the chemical industry is facing innovation pressure. To date, chemical synthesis on a commercial scale is primarily based on fossil resources as energy carriers (directly for thermal energy generation or as part of the electricity mix) and as organic feedstock. In 2020, the chemical sector accounted for 15% of total oil and 9% of total gas primary demand, leading to all industries.[5] These resources are in limited supply on earth and exacerbate ongoing climate change through their extraction and consumption. Other organic carbon sources such as biomass and recycled materials are being investigated.[6] However, replacing fossil fuels for their energetic purposes is difficult due to their high energy density. The focus is often on technical process improvements to increase resource and cost-efficiency. A completely different approach to this challenge is using light energy to carry out chemical reactions with photocatalysis.

Solar energy is an environmentally friendly, sustainable, and unlimited available energy source. Its potential is immense: in 2h, energy of approx. 640 EJ reaches the earth's surface through sunlight, which exceeds the annual, worldwide primary energy consumption.[7] Photocatalytic systems use light to catalyze chemical reactions. Inspired by natural systems, a wide variety of materials have recently been investigated for performing chemical transformations with light. The most prominent and widely used examples are transition metal complexes, inorganic semiconductors, and conjugated polymers.

Although traditional photocatalytic systems, for example, transition metal complexes such as *fac*-Ir(ppy)$_3$ or Ru(bpy)$_3$ can achieve high photocatalytic efficiencies due to their strong absorption, long-lived excited states, and good distribution in the reaction medium, there are some drawbacks associated with these systems. In particular, the metals' toxicity, limited availability, and the difficulty of recovering the homogeneous catalysts after the reaction have limited their applicability. Many of these inherent disadvantages can be circumvented using heterogeneous systems such as inorganic semiconductors or conjugated polymers. Among the most widely used organic photocatalysts are, for example, graphitic carbon nitride, conjugated microporous polymers, and covalent triazine frameworks. However, various detrimental aspects of these materials, such as poor synthetic control of catalyst morphology, high synthesis cost due to catalyst complexity, highly varying and arbitrary conjugation lengths, and lack of solvent compatibility due to strongly aromatic character, have barely been addressed so far. Further progress is imperatively needed on the materials side to make photocatalytic systems relevant for practical applications.

This work aims to develop new materials for efficient heterogeneous photocatalysis of organic redox reactions with visible light. Novel catalyst concepts were developed that address critical challenges for large-scale and future practical applications. Specifically, the developed systems are based on covalent triazine frameworks (CTFs), semiconducting CdSe platelets, porous aromatic frameworks (PAFs), and photocatalytic classical copolymers.

1. High-value reactions: The ideal synthesis is atom-economical, uses inexpensively available building blocks, and yields valuable products in high yields under mild conditions. The photocatalytic realization of such so-called dream reactions offers enormous potential, as they save considerable effort (e.g., multiple steps, toxic by-products, waste). In chapter 1, the photocatalytic oxidation of toluene to benzaldehyde is carried out with atmospheric oxygen. This and other selective sp^3-C-H activations are achieved with thiophene-based CTFs.
2. Nanostructuring: Dispersion and increased surface-to-volume ratio are critical for high selectivity, activity, and turnover values of catalysts in large-scale applications. Achieving precise morphological control is a central but troublesome challenge in photocatalyst syntheses. In chapter 2, the synthesis of CTF nanoparticles and the effect of nanostructuring and doping on photocatalytic efficiency in [3+2] cycloadditions are investigated.
3. Precise property control: The bandgap and the frontier orbitals' redox potentials are crucial for the light absorption and the oxidation or reduction strength of a

photocatalyst. By controlling and tuning these properties, a material's photocatalytic properties can be tailored to a target application. In chapter 3, CdSe nanoplatelets with atomic thickness control to a few monolayers are synthesized. The elaborated synthesis allows direct control of the bandgap. They are employed for the high-value photocatalytic conversion of nitrobenzene to azoxybenzene. In chapter 4, PAFs are established as a versatile and highly porous platform for photocatalysis. In the study, the conjugation length, frontier orbital potentials, and photocatalytic activity of the materials could be precisely controlled.

4. Cost efficiency: The introduction of a technology is critically dependent on its economic viability. Many catalyst systems are several orders of magnitude away from a cost-competitive price due to their synthetic complexity or the use of expensive starting materials and noble metals. In chapter 5, a classical polymer, i.e. PMMA-based, low-cost, and easily synthesizable heterogeneous photocatalyst for visible-light-promoted [4+2] cycloaddition is presented.
5. Solvent compatibility: Occupational workers' safety, process safety, and environmental and regulatory considerations make the use of green solvents in upscaled processes essential. Conventional photocatalysts are often unsuitable for applications in water due to their highly aromatic nature. In chapter 6, the water compatibility of a PMMA-based photocatalyst series is systematically investigated and used to remediate contaminants in the aqueous medium.

The projects are put into context with an introductory theory and literature section and an explanation of the applied characterization methods. The thesis concludes with a summary and a brief outlook on future research goals.

1.2 Theoretical background

1.2.1 Catalysis

A catalyst increases the rate of a chemical reaction by lowering the activation energy without affecting the overall standard Gibbs energy change.[8]

In a reaction potential diagram, where the x-axis represents the reaction coordinate and the y-axis represents the potential energy, a simple monomolecular exothermic reaction A → P can be shown (**Figure 1**). In the absence of a catalyst, activation energy E_A must be added to molecule A to pass the highest energy transition state (TS) and form product molecule P. The reaction rate can be derived from the Arrhenius equation. At high E_A, the reaction proceeds slowly and can only be carried out by expending considerable amounts of thermal energy, for example. In the presence of a catalyst, reactant A forms a reactive intermediate. After conversion to an intermediate PC and detachment of the catalyst, the formation of the product P occurs. The energy barrier to be crossed (E'_A) is lower and the new transition state (TS') is energetically stabilized. The catalyst is not chemically converted in the process and is available for further reaction cycles.[9]

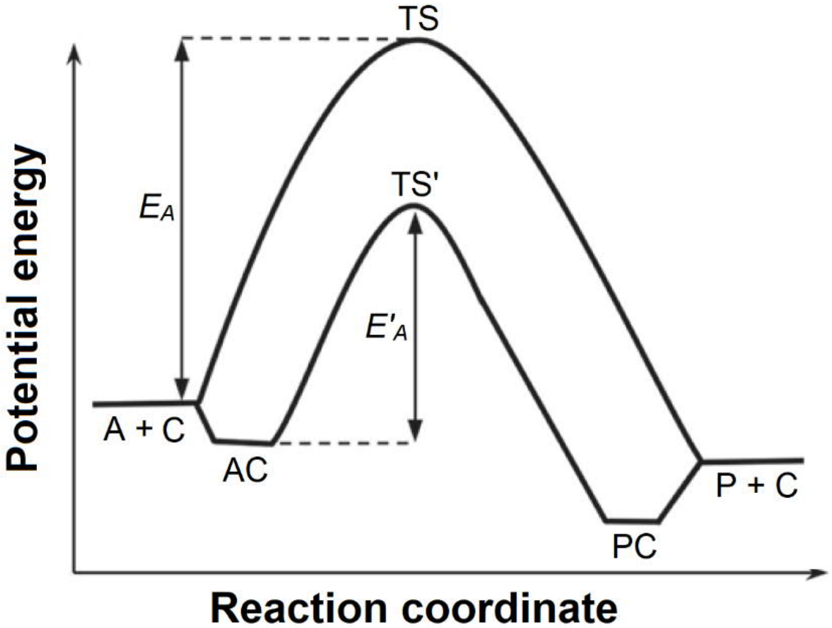

Figure 1. Simplified energy diagram of a monomolecular exothermic reaction with and without the use of a catalyst.[9]

In sum, favorable interactions of molecules with catalysts can lead to considerable reductions in the activation energies of reactions. This results in drastic increases in the reaction rate and enables, for example, the steering of a reaction in an initially kinetically unfavored but thermodynamically possible direction.

In a homogeneously catalyzed process, catalyst and reactants are used in a uniform phase. In a heterogeneously catalyzed process, the catalyst and reactants are used in different phases of the system. Typically, a catalyst in the solid state and reactants in solution, the liquid, or gaseous state are involved in the reaction. The catalytic reaction takes place at the phase interface.

More than 90% of all products in the chemical industry require catalytic processes at some point in the value chain.[10] The majority of these use heterogeneous systems (**Table 1**). Easy separability and regeneration of aged catalysts are decisive advantages in technical applications.

Table 1. Selected large-scale industrial processes using heterogeneous catalysts.

Industrial process	Product(s)	Catalyst
Contact process	H_2SO_4	V_2O_5
Fluid catalytic cracking	Propylene, short-chain hydrocarbons	Zeolites
Ziegler-Natta polymerization	Polyethylene, Polypropylene	$TiCl_x$ / $MgCl_x$
Haber-Bosch process	NH_3	Fe / Fe_3O_4 / FeO
Steam reforming	Syngas (CO/H_2)	Ni
Methanol production	Methanol	Cu / ZnO
Ethylene epoxidation	Ethylene oxide	Ag

A particular form of catalysis is photocatalysis, in which chemical reactions are carried out by using irradiated light.

1.2.2 Photocatalysis

The International Union of Pure and Applied Chemistry (IUPAC) defines photocatalysis as *"change in the rate of a chemical reaction or its initiation under the action of ultraviolet, visible or infrared radiation in the presence of a substance - the photocatalyst - that absorbs light and is involved in the chemical transformation of the reaction partners."* [11]

Although the term photocatalysis was first used in the 1910s and the utilization of light energy for chemical reactions was considered early on, it took until the late 1980s for the number of scientific publications on the subject to increase noticeably.[12-15] The key achievement was splitting water with photocatalytic semiconductors.[16] In 1972, the pioneers Fujishima and Honda constructed an electrochemical cell with a TiO_2 electrode that photocatalytically converted water into oxygen and hydrogen.[17]

A typical photocatalytic process in a semiconducting material consists of three elemental steps (**Figure 2**)

1) Absorption and excitation: When a semiconductor is irradiated, photons whose energy hv is equal to or greater than that of the bandgap (E_g) are absorbed. As a result, an electron is excited from the fully occupied valence band (VB) into the unoccupied conduction band (CB). The resulting hole remains in the conduction band. Photons whose energy is not sufficient to overcome the bandgap are transmitted. A significant proportion of the irradiated photons is also reflected.

2) Charge separation and transport: Diffusion and transport processes enable the mobility and dynamic behavior of the electron-hole pair. Depending on the binding energy, the electron-hole pair acts as bound exciton or as separate charge carriers. The excited-state lifetime depends on recombinant and dissipative processes. For example, electron and hole can recombine radiatively upon emission of a photon.

3) Electron transfer: The catalyst can reduce the target substrate if the potential of the excited electron exceeds the reduction potential of the molecule. The catalyst can oxidize the target substrate if the hole's potential exceeds the oxidation potential of the molecule. Depending on the reaction chosen, both electron transfers occur either at the target molecule or the target molecule and a sacrificial agent.

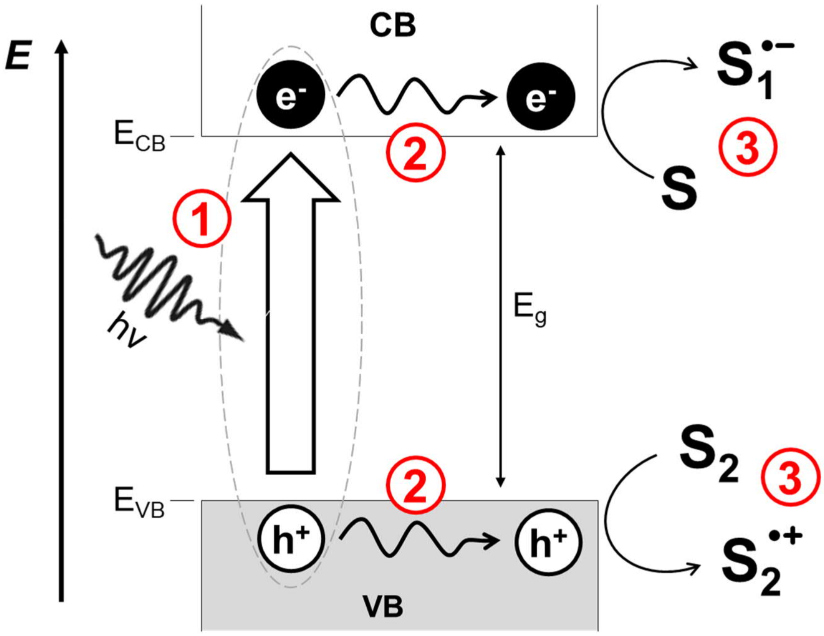

Figure 2. Photocatalytic reaction using semiconducting materials as photocatalysts. The process can be divided into light absorption and excitation (1), charge separation and transport (2), electron transfer between photocatalyst and substrates (3).

Actual band structures are far more complex than indicated in the schematic diagram. Whether a momentum change is required to excite an electron from the VB to the CB with the lowest possible energy distinguishes direct from indirect semiconductors. Direct semiconductors do not require a phononic momentum shift; indirect semiconductors do.

A key advantage of photocatalytic reactions is the use of light as an abundant and sustainable energy source. Conventional energy sources such as coal, oil, and natural gas face limited availability on our planet and produce exceptionally harmful effects on the environment through consumption or the by-products generated during conversion processes. The sun provides the earth with an enormous amount of energy in the form of electromagnetic radiation. The irradiated solar energy on the entire globe within two hours corresponds to the worldwide energy consumption within an entire year.[7]

Incident light is quantized into photons, of which those with wavelengths between 390 and 760 nm are perceptible to the human eye. The energy distribution of solar irradiation is not arbitrary. The large diameter and non-reflectance of the sun as a radiating object result in an absorption coefficient close to unity. The sun can be treated as a blackbody with a temperature of 5800 K and a maximum intensity at λ_{max} = 500 nm to a first approximation. Characteristic photospheric absorption (Fraunhofer lines), as well as atmospheric absorption (e.g., H_2O, CO_2, O_2, O_3) and reflection (e.g., dust, particulate matter), result in a spectrum of solar irradiance at sea level deviating from the ideal blackbody (**Figure 3**). Of the total solar energy, 3% is in the ultraviolet, 40% in the visible, and 57% in the spectrum's infrared part.

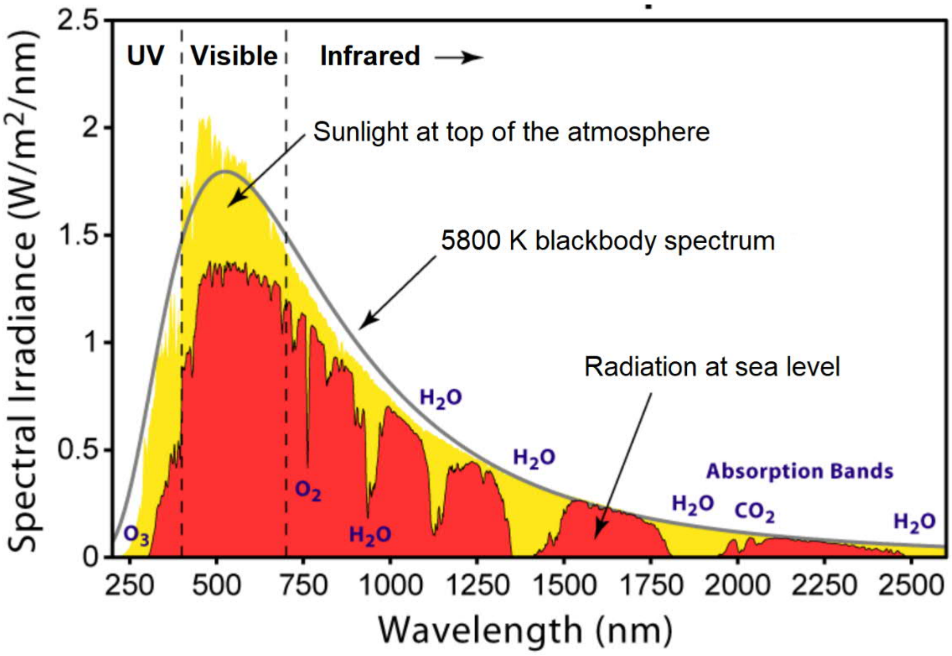

Figure 3. The solar spectrum at the top of the atmosphere and sea level compared to an ideal 5800 K emitter. The data is based on the American Society for Testing and Materials (ASTM) terrestrial reference spectra.[18-19]

Inorganic semiconductors such as TiO_2, ZrO_2, and ZnO have been crucial in establishing photocatalytic research and continue to be key contributors.[20-25] The photocatalysts employed with ultraviolet light have large bandgaps, enabling the generation of charge carriers with high oxidative or reductive potential. Inert molecules can be activated using the overpotential and challenging reactions can be carried out. However, the use of visible-light photocatalytic systems has decisive advantages. Visible-light excitations are lower in energy (1.6-3.2 eV) compared to ultraviolet irradiation. The resulting charge carriers available for catalysis are still sufficient in potential for the majority of chemically feasible redox reactions. Unnecessarily high overvoltages are avoided allowing milder and more selective photocatalysis.

Moreover, most solar energy is within the spectrum's visible region, so visible-light photocatalysis points a path to sustainable and solar-powered future synthetic chemistry. From a practical point of view, visible-light illumination setups are simple to implement on a laboratory scale and do not require special reaction tubes and photoreactors.

1.2.3 Homogeneous visible-light photocatalysis

When a photocatalyst and the reacted substrate are in a common phase, the process is called homogeneous photocatalysis. In terms of catalyst design, two basic models have proven successful.

Transition metal complex photocatalysts consist of a Lewis acidic central metal and Lewis basic ligands linked by coordinative bonds. The choice of ligands and central metals is variable and provides latitude to achieve and modify desired properties of the catalyst. Upon light irradiation, electrons are typically excited from metal-centered to ligand-centered orbitals and undergo a metal-to-ligand charge transfer (MLCT). In the subsequent intersystem crossing (ISC), an electron transitions from the singlet excited state to the triplet excited state and is available for electron transfer and catalyzing the substrate reaction (**Figure 4**). The most popular photocatalysts in this class are ruthenium and iridium pyridine complexes such as $\mathrm{Ru(bpy)_3^{2+}}$, *fac*-$\mathrm{Ir(ppy)_3^{2+}}$, and $\mathrm{Ru(bpz)_3^{2+}}$ (**Figure 4**).[26-29] The catalysis of dehalogenations,[30] C-C bond formations,[31] cycloadditions,[32-33] and asymmetric aldehyde alkylations[34] using transition metal complexes should be emphasized.

Organic dyes are being used as efficient metal-free homogeneous photocatalysts. They are mostly small-molecule heterocycles with planar extended π-systems based on phenothiazine, xanthene, pyrylium, quinolinium, and acridinium backbones.[35] The energy gap between the highest occupied molecular orbital (HOMO) and the lowest unoccupied molecular orbital (LUMO) allows visible-light excitation. Charge separation often takes place between electron-accepting and donating moieties of the molecules. Like transition metal complexes, a transfer from the singlet to the triplet excited state can occur and substrate reactions *via* single electron transfers (SET) follow. Among the most studied organic small molecules are eosin Y, rhodamine B, and methylene blue (**Figure**

4).[35-36] The realization of C-H activations [37-39] and C-C bond formations [40] with photocatalytic dyes have attracted particular attention.

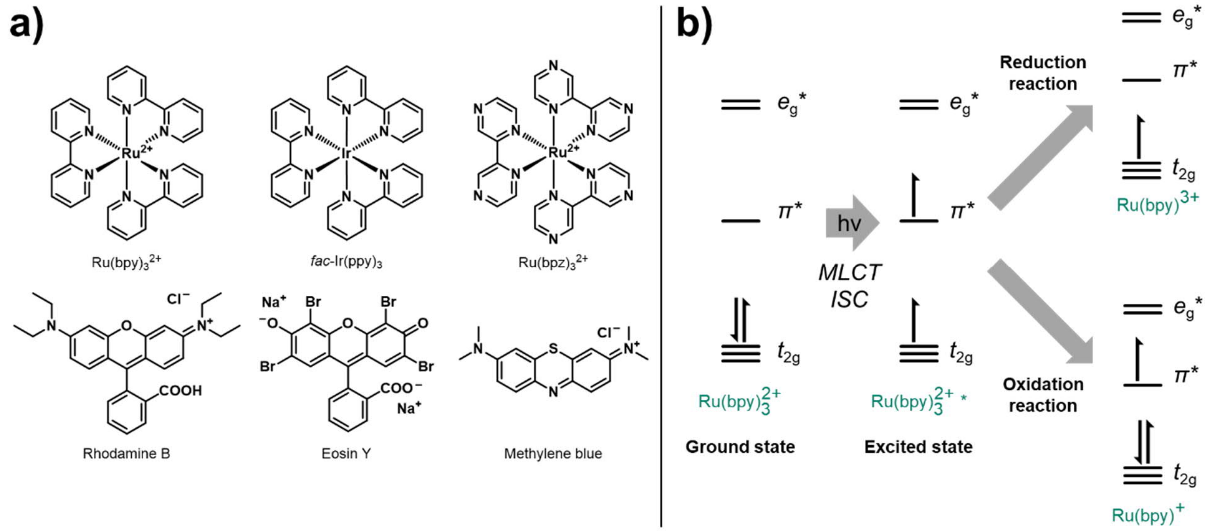

Figure 4. Selection of important photocatalytic transition metal complexes and small-molecular organic dyes (a). Simplified orbital illustration of the functional principle of Ru(bpy)$_3^{2+}$ photocatalysis (b).

Homogeneous photocatalytic systems combine decisive advantages. The molecules' optophysical properties are ideal for photocatalytic applications due to strong absorption and long-lived excited states. Besides, the ideal distribution in the reaction medium means that there are no diffusion restrictions. High efficiencies can be achieved with even the smallest amounts of catalyst. Further, the design, structure, and physical properties of homogeneous photocatalysts have been investigated in detail for many years. The recourse to known systems with distinct properties greatly facilitates the search for feasible reactions and estimating the expectable performance in photocatalytic applications. From a technical point of view, homogeneous catalysts enable upscaled chemical transformations in continuous reactors.

1.2.4 Heterogeneous visible-light photocatalysis

When a photocatalyst and the reacting substrate are in different phases, the process is called heterogeneous photocatalysis. The catalytic material can be separated and recovered from the remaining reactants and products in the process. In principle, heterogeneous photocatalysis with visible light divides into metal-containing and metal-free systems.

Of the metal-containing photocatalysts, chalcogenides (oxides, sulfides, selenides, tellurides) were studied in particular. Since the elemental composition of semiconductors limits the chemical design scope, various methods are used to optimize materials for photocatalytic applications. The central focus of many works is nanostructured morphologies,[41-42] constructing heterojunctions with other semiconducting materials,[43] or the decoration of the catalyst surface with noble metals to enhance the photocatalytic performance.[44-45]

Among oxidic materials, TiO_2, ZnO, and Nb_2O_5 are the best-known photocatalytic systems.[46-48] The bandgaps usually require light from the more energetic violet region of the visible spectrum for excitation or allow activation only with ultraviolet radiation. In the case of regular anatase and rutile titanium dioxide, the bandgap is about 3.2 eV (413 nm) and 3.0 eV (387 nm), respectively.[49] The optical bandgap could be reduced using dye sensitization,[50-54] doping,[44, 55-57], and partial hydrogenation strategies.[58-60] Zhang and coworkers were able to evolve NH_3 from N_2 up to 700nm by tuning oxygen vacancies in ultrathin TiO_2 nanosheets.[61] Exemplary applications of visible-light catalysis with Nb_2O_5 include the selective oxidation of amines[62] and alcohols.[63] Zinc oxide is mainly used in the degradation of organic contaminants in water.[64-66]

Various metal sulfides have found their way into photocatalytic research, with cadmium selenide being the most prominent example. Xu and coworkers have succeeded in selectively oxidizing saturated primary C-H bonds with CdS.[67] Li and Zhang's research groups have constructed CdS-based heterostructures to evolve hydrogen from water efficiently.[68-69] CdS quantum dots have shown promising results in the photocatalytic reduction of carbon dioxide.[70-71] Layered 2D structures of MoS_2 and WS_2 on, e.g., graphene, recently showed high efficiencies in photocatalytic applications.[72-74] Among the semiconducting selenide compounds, CdSe stands out as a particularly efficient photocatalytic material. Nanostructured CdSe platelets allowed the photocatalytic deuteration of halogenated compounds.[75] CdSe quantum dots were used for a wide variety of C-C bond formations.[76] The established CdSe synthesis protocols allow the fabrication of nanostructures with atomic precision. The structures allow isolated analyses of the interrelationships of optophysical and photocatalytic properties. For this reason, defined CdSe nanoplatelets are part of more detailed consideration in the results section of this work.

An often-used method to improve metal-containing semiconducting materials' photocatalytic capabilities is the deposition of noble metal nanoparticles on the surface.[77-78] When light of a specific wavelength is irradiated onto noble metal nanoparticles, its alternating electromagnetic field can induce collective oscillations of the electronic charges against the positively charged nuclei. When light and plasmon oscillations within the nanoparticle are in resonance, this effect is referred to as localized surface plasmon resonance (LSPR). Locally strongly enhanced electric fields in close proximity around the particles result, generating beneficial interactions with photocatalytic materials in heterojunction structures (**Figure 5**).

In the first mode of action, the incident light can be scattered by the plasmonic nanoparticles and coupled into the semiconductor. As a result, the electric near field has an additional amplifying effect and the photon flux into the semiconductor is enormously increased. Second, strong dipoles can be generated in plasmonically-excited metal nanoparticles. Through dipole-dipole interactions, energy can be non-radiatively transferred to the semiconductor (plasmon-induced resonance energy transfer, PIRET) and cause charge separations. Third, *via* Landau damping, a plasmon's energy can dissipate non-radiatively and produce hot quantum charge carriers (QHC) of exceptionally high energy. They can overcome the potential barrier at the nanoparticle-semiconductor interface and inject directly into the semiconductor's conduction band. Interestingly, QHCs injected can also occupy energy levels significantly below the valence band or above the conduction band level. In a fourth variant, plasmonic energy can dissipate by inelastic scattering from phonons and lead to locally elevated temperatures. The first three effects mentioned increase the number of charge carriers available for photocatalysis in the semiconductor and increase the material's photocatalytic performance.

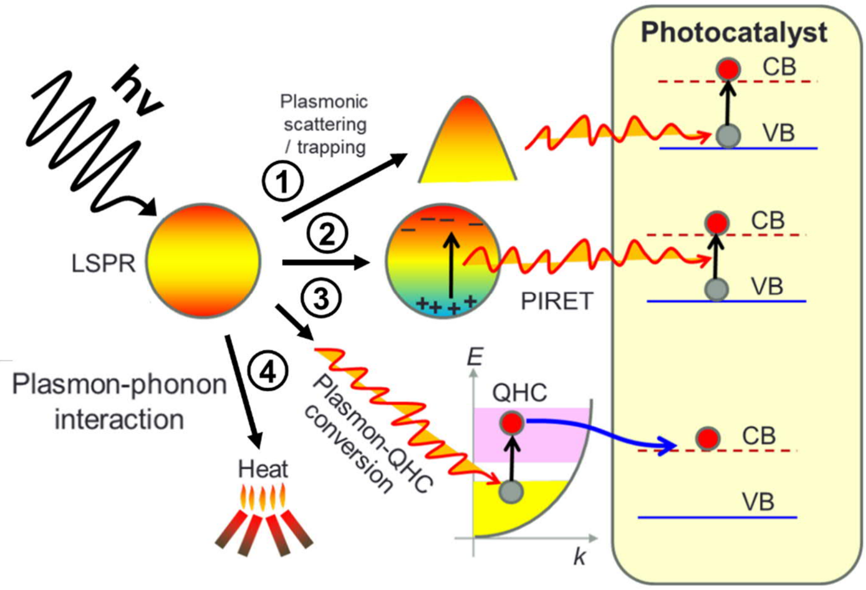

Figure 5. Types of energy transfers in plasmonic photocatalysts with 1) Plasmonic light scattering, 2) PIRET, 3) hot electron injection, and 4) thermal energy dissipation.[79-80]

The metals with pronounced localized SPR effect are especially Ag, Au, and Cu. The resonance wavelengths are size- and support-dependent at about 400, 530, and 580 nm. Halas and coworkers were able to dissociate hydrogen by depositing Au nanoparticles on TiO_2 photocatalytically.[81] The same group recently designed a plasmonic system using aluminum and other earth-abundant materials to reduce carbon dioxide efficiently.[82] Several groups have been working on plasmonic photocatalysis of water splitting and organic redox reactions.[46, 77] Through the deposition of Au nanoparticles on CeO_2, a material for, e.g., the selective oxidation of alcohols into the corresponding aldehydes, could be established.[83-84]

In the second class of heterogeneous visible-light photocatalysts, polymer-based photocatalytic systems do not use noble or toxic metals. In addition to the general recoverability and robustness of heterogeneous photocatalysts, polymeric systems offer further decisive advantages. Polymers provide enormous structural and morphological diversity as a platform and can be easily varied synthetically through monomer modifications. Direct structure-property relationships enable targeted adaptation to specific photocatalytic applications.

Typical polymer systems that have been crucial to the development of polymer photocatalysis and those used in this work are discussed in more detail below.

1.2.5 Conjugated polymers for photocatalysis

Fully conjugated polymers with delocalized π-electron systems along the polymer backbone were synthesized and explored starting in the 1950s.[85-86] However, conductivity in organic polymers was not discovered until 1977 by Shirakawa, Heeger, and MacDiarmid.[87-88] They found that a dramatic increase in electrical conductivity in polyacetylene can be achieved by oxidizing the material with halogen vapors or AsF_5. The measured conductivity was comparable to that of metals and metallic semiconductors in the solid state. The discovery of this new polymer class was of such high relevance that it was honored with the Nobel Prize in 2000.[89]

Conjugated polymers have several intrinsic advantages that have accelerated research into photocatalytic use since their discovery, as shown below.[90-92]

1) Optical absorption: Organic semiconducting polymers typically have optical bandgaps in the range of 1.5 to 3 eV, making them capable of interacting with light. They can be excited upon irradiation, and charges can separate.
2) Conductivity: To efficiently separate charge carriers from each other and prevent recombination, charges must be mobile along the polymer chain.
3) Modifiability: Monomer properties translate into polymer properties, so polymer properties can be tuned by modifying their monomer building units. These changes can, but do not have to, affect the conjugated π-system. For example, light absorption properties, redox potentials, polarity and solubility, morphology, and processability can be directly controlled.
4) Robustness: Macromolecules with high molecular weights are usually more mechanically, chemically, and thermally resilient than molecular analogs. This simplifies their reuse as heterogeneous photocatalysts.

The first group to use conjugated polymers for photocatalysis was Yanagida and coworkers.[93] They irradiated poly(p-phenylene) with medium-wave UV light in the presence of triethyl- or diethylamine in water and were able to catalyze the evolution of hydrogen.

Graphitic carbon nitride (*g*-C_3N_4)

The cornerstone for the application of polymer-based photocatalytic systems was the use of semiconducting graphitic carbon nitride for water splitting by Wang and Antonietti.[94] *g*-C_3N_4 consists of ordered graphite-like layers of tri-s-triazine units linked by planar tertiary amino groups. The degree of condensation is variable and depends on the synthesis conditions and precursors used.[95] The material has a high molecular weight and is fully conjugated in two dimensions.

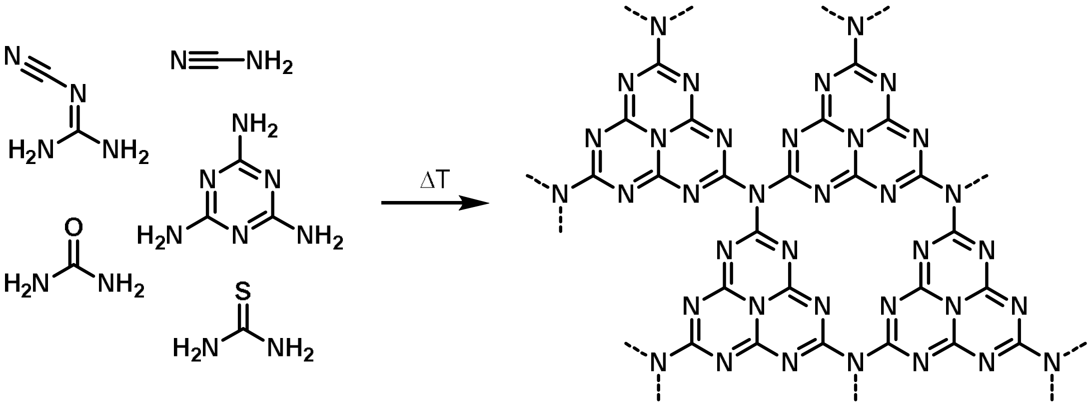

Figure 6. Thermal synthesis of graphitic carbon nitride *g*-C_3N_4 and selected precursors cyanamide, dicyanamide, melamine, urea, and thiourea.[96-97] The structure shown represents the thermodynamically most stable tri-s-triazine phase.

Strategies to improve properties for the photocatalytic application included varying starting materials[98] and adding comonomers,[99] targeted modifications of the morphology,[100-102] doping,[103-104] post-polymerization modifications,[105-107], and the combination with other materials to form composite systems.[108-110] The material has found widespread application in hydrogen evolution, CO_2 reduction, and organic redox reactions.[95, 97]

Conjugated microporous polymers (CMPs)

In recent years, conjugated microporous polymers (CMPs) have emerged prominently among photocatalytic polymers.[91, 111-112] CMPs are characterized by three-dimensional linkage of building units to rigid microporous polymer networks with extended π-electron systems. They combine the properties of porous materials and conjugated polymers. While their pore size is smaller than two nanometers, CMPs have low long-range order and are considered amorphous networks.

The conjugation of CMPs and the resulting electronic properties make them very interesting for photocatalytic application. Further, the high porosity and small pore size maximize the active catalyst surface available for substrate interactions. Substrate molecules can diffuse into the network and remain in the vicinity of the photocatalyst for extended periods. The textured surface can scatter light and improve light absorption properties.[91, 111]

In 2007, the first CMP was synthesized in Cooper's group.[113] Sonogashira-Hagihara coupling of organic di-/triethynyl compounds and di-/trihalides yielded microporous poly(aryleneethynylene) with surface areas up to 834 m^2 g^{-1}. The first CMP for photocatalytic applications was prepared by cross-coupling 4,7-dibromobenzo[c]-1,2,5-thiadiazole and 1,3,5-triethynylbenzene.[114] Silica nanoparticle templates allowed the porosity to be varied in a series from 270 to 660 m^2 g^{-1}. The obtained catalysts were able to activate oxygen and convert α-terpinene to ascaridole upon irradiation with blue light. Further noteworthy early developments included the synthesis of benzodifuran-containing CMPs for photocatalytic amine conversions[115] and the development of CMPs from high internal phase emulsion polymerizations (polyHIPE).[116] Zhang and coworkers were able to fine-tune CMP bandgaps through copolymerization.[117] The preparation of dye-embedded CMPs gave high efficiencies in photocatalytic aza-Henry reactions[118-119] and selective oxidations of thioanisoles.[120]

To date, CMPs have found wide application in additional research fields. These include gas storage and separation,[121-123] chemical encapsulation,[124-125] heterogeneous catalysis,[126-129] light emission,[130-132] chemosensing,[133-135] energy storage,[136-139] and biological applications.[140-142]

Covalent triazine frameworks (CTFs)

Another class of conjugated polymers highly relevant to photocatalysis is covalent triazine frameworks (CTFs). Although aromatic nitrile polymerization was reported early,[143-145] CTFs were not established as a new material class until several decades later.[146] CTFs consist of s-triazine units connected *via* aromatic linkers, together spanning an extended π-conjugated network. The triazine rings provide the polymers with a strong covalent character and high robustness. Furthermore, the nitrogen-rich units are strong electron acceptors and very well suited for donor-acceptor systems, repeatedly applied as a design concept in photovoltaics, optoelectronics, and photocatalysis.[147-149]

The surface area, porosity, crystallinity, and optoelectronic properties of CTFs are strongly dependent on the synthesis process. CTFs can be obtained by high-temperature ionothermal syntheses or superacid-catalyzed from aromatic nitriles. More recently, polycondensations of amidine derivatives have found increased application in CTF preparation. Other, less used methods use Friedel-Crafts alkylation of aromatics with cyanuric chloride or P_2O_5-catalyzed conversion of aromatic primary amides.[150]

The first CTFs were prepared *via* ionothermal synthesis by Kuhn *et al.* (**Figure 7**).[146] For this purpose, dinitriles and $ZnCl_2$ were heated to 400°C for 48h in vacuo. In the melt, the terminal nitriles trimerize to triazine rings. The resulting CTFs were black monolithic materials with an amorphous to semi-crystalline structure. In subsequent work, the synthetic procedure was optimized and amorphous to semi-crystalline solids with very high surface areas were obtained.[151-153] However, the high reaction temperature and harsh reaction conditions of ionothermal syntheses can cause uncontrolled side reactions to take place, carbonize the materials, cleave nitrile groups, create pore defects and damage the structure.[154-155]

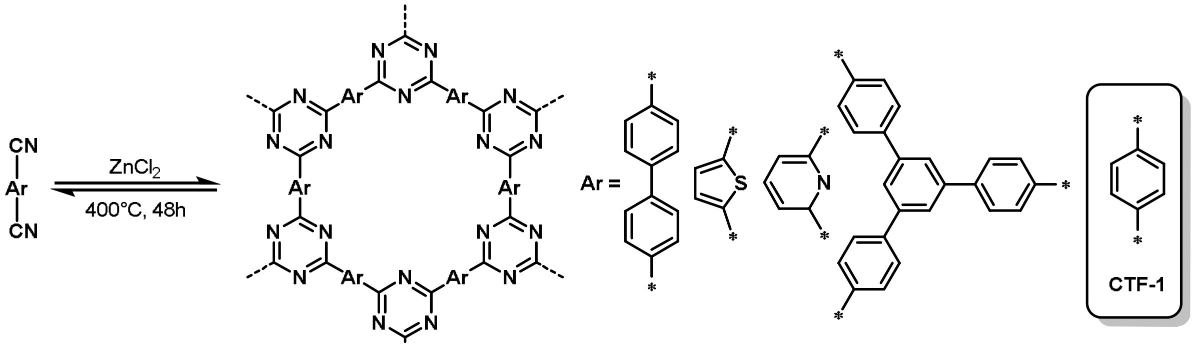

Figure 7. Exemplary ionothermal synthesis of a covalent triazine framework by Kuhn *et al.*[146]

Another synthesis variant is the Brønsted superacid-catalyzed preparation. In 2012, Cooper's group succeeded for the first time in converting aromatic dinitriles with trifluoromethanesulfonic acid (TfOH) to CTFs.[156] The synthesis was carried out either at room temperature with the solvent chloroform or in the microwave in pure superacid. The significantly milder conditions avoid carbonization of the polymers and distinct photophysical properties resulted. The polymers show optical absorption in the blue spectral range and pronounced photoluminescence (**Figure 8a**). The polarity and volatility of TfOH enabled novel and compelling synthetic procedures that provided access to sophisticated CTF morphologies. Dai and coworkers synthesized fluorescent CTF membranes with intrinsic porosity from 4,4'-biphenyldicarbonitrile (**Figure 8b**).[157] Xu and colleagues succeeded in preparing crystalline few-layer CTFs by interfacial polymerization (**Figure 8c**).[158-159] Huang *et al.* synthesized nanoporous structures by TfOH vapor-assisted polymerization in the solid-state from various dinitrile monomers (**Figure 8d**).[160-161] Overall, TfOH-catalyzed CTF synthesis offers significant advantages for preparing photocatalytic materials and was used throughout this work. However, the synthesis is not trivial in handling due to the highly corrosive properties of the TfOH superacid. The challenging and low-yielding synthetic accessibility of aromatic dinitrile monomers currently complicates rapid advances.

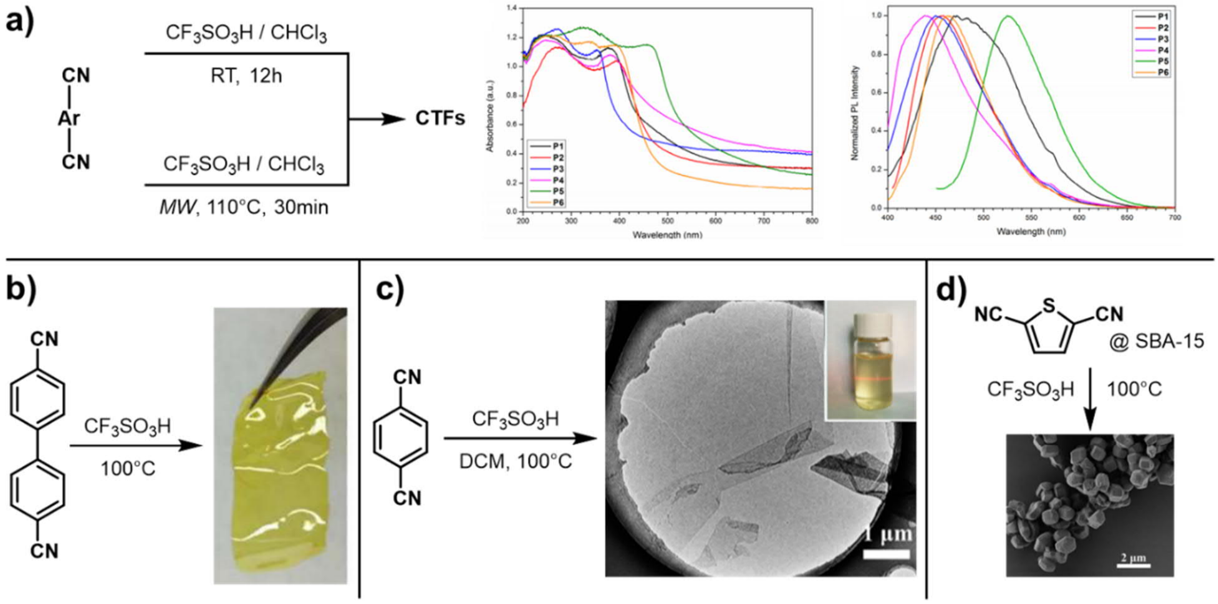

Dai et al., 2012, JACS

Xu et al., 2017, JACS

Huang et al., 2017, ACS Catal.

Figure 8. Selected literature examples of superacid-catalyzed CTF syntheses. First TfOH-based CTF preparation (a),[156] CTF membrane (b),[157] few-layer CTF through interfacial polymerization (c),[158] and nanoporous thiophene-based CTF through SBA-15 templating (d).[160]

In 2017, Tan and coworkers developed a method for preparing CTFs based on the condensation of bifunctional aldehydes and amidine dihydrochlorides.[162] In the synthesis, a Schiff base is formed first. Employing Michael addition, the ring closure to the triazine follows (**Figure 9a**). The synthesis takes place in solution at 120°C reaction temperature with Cs_2CO_3 as base and DMSO as solvent. Similar to the TfOH-catalyzed route, the mild reaction conditions prevent the carbonization of the polymers and favorable optoelectronic properties can be observed. In follow-up works of the authors, they succeeded in improving the synthesis process.[163-164] Both in situ oxidation of primary alcohols to aldehydes and controlled feeding of aldehydes resulted in a slowing of triazine formation kinetics (**Figure 9b**). Crystalline CTFs were formed for the first time. Compared to more amorphous structures, the long-range order had positive effects on electronic transport and light absorption. In recent work, Jin and Tan's group prepared hollow CTF nanospheres using the amidine route.[165] The so far limited synthetic accessibility of aromatic amidine and aldehyde derivatives makes further progress in this field challenging.

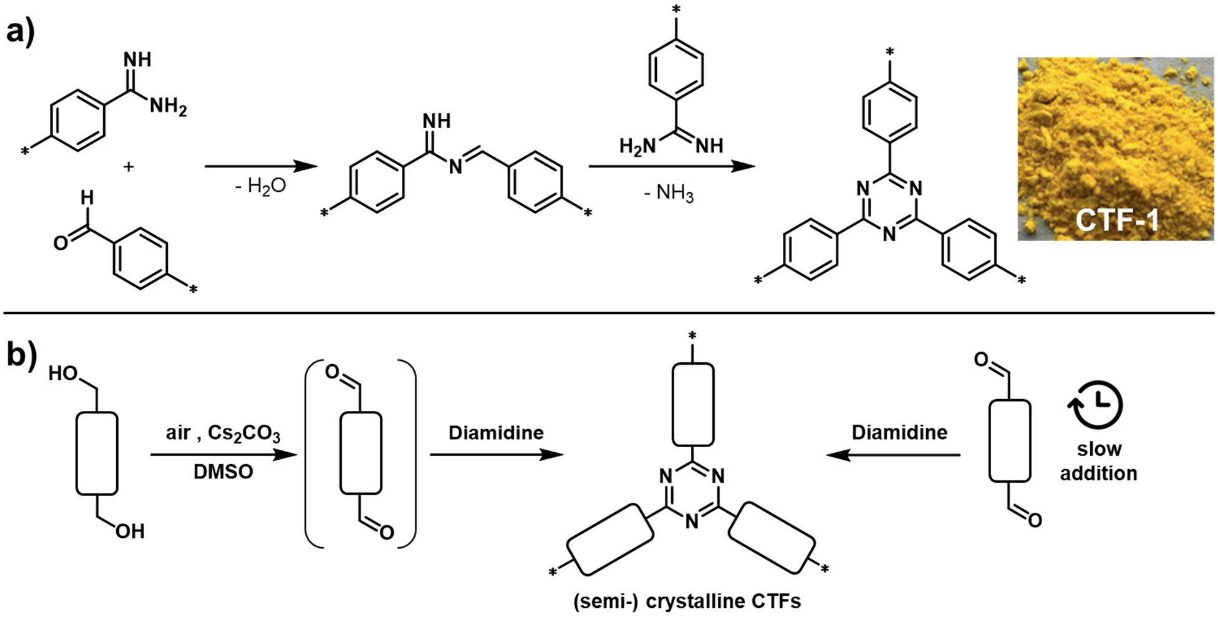

Figure 9. Exemplary amidine-based syntheses of covalent triazine frameworks. Mechanism of the triazine ring formation[162] (a) and slowdown synthesis strategies (b).[163-164]

The choice and modifiability of monomers open enormous variability of CTFs as a polymer platform. CTFs have found wide application in gas storage and separation,[166-168] pollutant removal,[169-170] catalysis,[171-174] as well as energy storage and conversion.[175-177] In photocatalytic applications, the most notable uses are in water splitting,[178-181] CO_2 reduction,[182-183] and organic redox reactions.[160, 184] In this work, the variability of the CTF platform was used to introduce novel morphological and photocatalytic properties. Two works will be presented in the results subchapter of this thesis.

1.2.6 Non-fully conjugated polymers for photocatalysis

Although fully conjugated systems show remarkable properties, some characteristics could only be tailored through considerable synthetic or postsynthetic effort. Adjustments in polymer rigidity, polarity, or conjugation length for photocatalytic applications are inherently difficult to implement.

- Rigidity: Polymerization in multiple spatial directions leads to high rigidity and stability of the networks. This is essential for conjugated systems since fully extended π-conjugation can only be preserved by limiting rotational and vibrational degrees of freedom. Inflexibility hinders solvent interaction, e.g., by swelling, and limits substrate diffusion to the porosity achieved in the synthesis step.

- Polarity: Conjugated macromolecules have strongly aromatic and often only moderately polar character. Polar groups such as sulfones and sulfoxides integrated into the polymer backbone or solution-mediating groups postsynthetically attached *via* side chains can provide a solution. The realization of solvent compatibility, e.g., with water, is challenging.
- Conjugation length: Most photocatalytic conjugated polymers are structurally amorphous or have low crystallinity. The lack of long-range order limits the conjugation to a few units. Accurate predictions of electronic and optical properties from monomer properties or theoretical calculations are challenging since each system behaves differently.

Two platforms that can address these aspects are porous aromatic frameworks and classical polymers.

Porous aromatic frameworks (PAFs)

A family of materials closely related to CMPs are porous aromatic frameworks (PAFs). PAFs are porous 3D polymer networks of tetrahedral building blocks linked *via* metal-catalyzed polymerizations. In the rigid frameworks, aromatic subunits are typically separated by quaternary tetrel central atoms. Accordingly, there is no extended π-system but sectional conjugation. Exceptionally high surface areas characterize the materials.

Ben and coworkers synthesized the first PAF in 2009.[185] Using nickel(0)-catalyzed Yamamoto-like Ullmann coupling of tetrakis(4-bromophenyl)methane, a microporous network with a diamond-like structure was obtained (**Figure 10**). The polymer exhibited an unprecedented BET surface area of 5600 m^2 g^{-1}. The framework revealed high uptake capacities of hydrogen, carbon dioxide, as well as benzene and toluene vapors. Zhou's group exchanged the quaternary carbon atom for other quadricovalent centers such as silicon, germanium, and adamantane.[186] With the Si-analog, the researchers were able to synthesize the all-organic material with the highest BET surface area ever recorded (6461 m^2 g^{-1}).

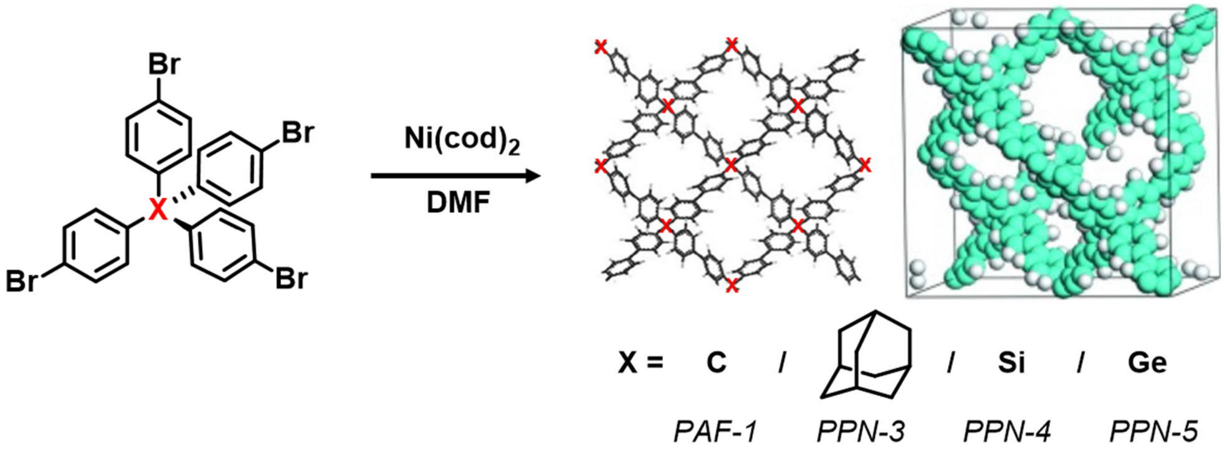

Figure 10. One-step Ullmann polycondensation of the tetrahedral precursors gave PAF-1 and PPN-3 to 5.[185-186]

Due to their surface area, porosity, physicochemical stability, and amenable structure, PAFs offer a wide range of applications. The main areas of application are gas storage, membrane separation, adsorption of hazardous organic molecules, and catalysis.[187-189] Lau and coworkers succeeded in separating hydrogen from an H_2/N_2 mixture by depositing ultraporous PAF nanoparticles on a microporous membrane.[190] Further noteworthy examples of applications are the efficient removal of mercury and uranium ions from aqueous solutions using postsynthetically modified PAFs.[191-192] The group of Zhu was able to mimic enzymatic hydrolase activity by post-polymerization modifying a porous aromatic framework.[193]

In general, PAFs provide a platform whose inherent properties make a metal-free photocatalytic application conceivable. The conjugation length is precisely defined and identical for each repeat unit. The structure could allow accurate predictions of structure-property relationships from monomer properties as well as theoretical calculations. The introduction of photocatalytic PAFs will be made in one of the results subchapters of this thesis.

Like CMPs, PAFs are polymerized *via* irreversible metal-catalyzed covalent bond formation. Apart from the Yamamoto synthesis of PAFs, there are examples where Suzuki or Sonogashira cross-couplings have been applied.[194-196] The two main cross-couplings used in this work, the Suzuki and Sonogashira reactions, will be briefly discussed in more detail.

In a Suzuki cross-coupling, aryl organoboron and halide compounds are reacted under palladium(0) catalysis to form a carbon-carbon bond (**Figure 11**). The reaction takes place in basic milieu. In 1979, the Japanese researchers Miyaura and Suzuki documented the reaction for the first time.[197-198]

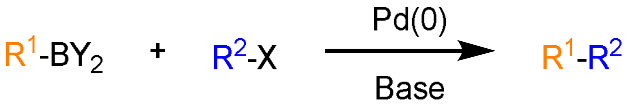

Figure 11. General scheme of the Suzuki-Miyaura cross-coupling reaction. Y is typically O-alkyl or OH, R^1 and R^2 are aryl residues, and X is an organohalide. Commonly used bases are carbonates. Further, more special cases are known from the literature.[199-200]

The catalytic mechanism has four consecutive steps (**Figure 13a**). Initially, oxidative addition of the organic halide to the active Pd(0) species takes place. In this process, the palladium inserts into the C-X bond and oxidizes to Pd(II). Subsequently, the base causes a ligand exchange at the catalytic center (metathesis). In the transmetallation step, the base-activated organoboron compound and the catalyst complex swap ligands. The Pd-center takes up a second organic residue. In the reductive elimination, a new carbon-carbon bond is formed, and the catalyst is regenerated to the Pd(0) oxidation state for the next cycle. The base acts in a dual function: it activates the organoboron compound by forming a trialkoxylboronate and enables transmetallation by converting the palladium-halogen complex to a palladium alkoxy complex. The mechanistic elucidation of the Suzuki reaction is still the subject of current research.[201-202]

Good commercial availability of boronic acids, wide tolerance to functional groups, low toxicity of chemicals, and mild reaction conditions have led to wide chemical application of the reaction.

The Sonogashira reaction is a palladium-catalyzed cross-coupling of terminal alkynes and aryl halides (**Figure 12**). A copper(I) salt and an amine base are required as co-catalysts. The reaction was established by the Japanese scientists Sonogashira and Hagihara.[203]

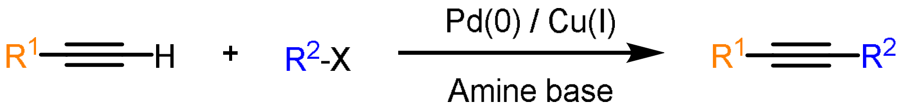

Figure 12. General scheme of the Sonogashira-Hagihara cross-coupling. R^1 and R^2 are typically aryl residues and X is an organohalide. A frequently used base is triethylamine. Further, more special cases are known from the literature.[204]

The mechanism of Sonogashira coupling also follows a sequence of oxidative addition, transmetallation, and reductive elimination (**Figure 13b**). As in Suzuki coupling, the Pd center inserts into the C-X bond by oxidative addition. The triple bond replaces the halogen atom on the catalyst complex with the corresponding organic residue in the transmetallation step. By reductive elimination, a new carbon-carbon bond is formed, the catalyst is reduced again to Pd(0), and the catalytic cycle is closed. Cu(I) present in the reaction solution takes on a special role: triple bonds are activated in a copper co-catalyzed cycle. It is suggested that copper first forms a pi-complex with a free terminal alkyne. Then a copper-acetylide complex can be formed by deprotonation with an amine base, which enters the actual catalytic Pd-cycle during transmetallation. Recent studies continue to clarify the coupling and have mechanistically elucidated Cu-free routes.[205-207]

Sonogashira coupling has found wide application in chemical research due to its high efficiency, mild reaction conditions, functional group tolerance, and simplicity of implementation.[204]

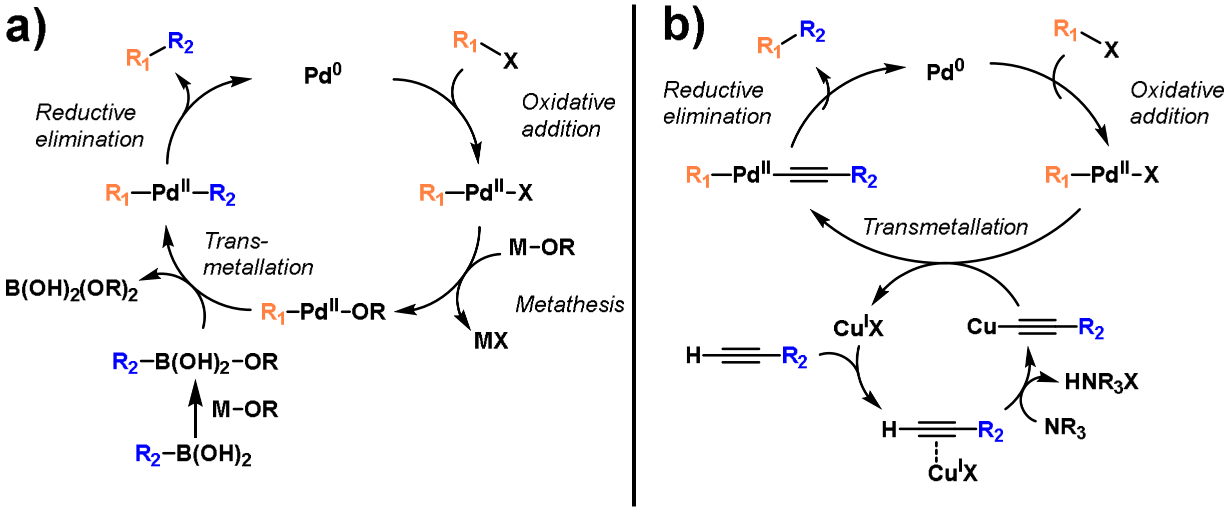

Figure 13. Reaction mechanisms for the Suzuki-type (a) and Sonogashira-type (b) cross-couplings.

Classical polymers

Since the discovery of polymers as macromolecules consisting of chains of repeating molecular units by Hermann Staudinger, they have proved to be a versatile class of materials.[208] Conventional polymers such as poly(methyl methacrylate), polyethylene, polystyrene, or poly(ethylene terephthalate) are used in millions of tons worldwide.[209] The classical polymer chemistry toolbox provides access to a wide variety of polymeric materials with variable solubility, biological compatibility, mechanical properties, thermal characteristics, or responsibility to external triggers.[210] However, the role of classical polymers as a platform for photocatalytic systems has barely been explored. In the limited literature available, two strategies have proven to be effective.

The first method works by postsynthetic covalent attachment of a photocatalytic moiety to a polymer support. Neckers and coworkers were the first to attach rhodamine B to a chloromethylated styrene-divinylbenzene copolymer and use it, e.g., for the photocatalytic cleavage of C-C double bonds.[211-213] In a subsequent work by Burguete *et al.*, it was possible to increase the systems' hydrophilicity and photocatalytic efficiency in polar media by modification with pyridine.[214] Yan and colleagues used click-chemistry to attach BODIPY to polyHIPEs and used the materials photocatalytic oxidation of thioanisole.[215] Similar steps have been taken in the attachment of photocatalytic transition metal complexes to polymers. The groups of Bergbreiter and Kappe have immobilized the $[Ru(bpy)_3]^{2+}$ complex on polyisobutylene and dendrimeric polyamidoamine.[216-217] Rackl *et al.* were able to modify polyisobutylene with *fac*-$Ir(ppy)_3$ for diiodination and cyclization photoredox reactions in flow.[218] The limitation of this strategy is that the quantitative functionalization of polymers is often challenging to perform. High-yielding grafting reactions are limited to few functional group combinations and further complicate the synthesis of precursor.

Another strategy to make classical polymers useful for photocatalytic applications is radical copolymerization with photocatalytic units. In the groups of Hisaeda, Kobayashi, and Chen, efficient photocatalysts were obtained by copolymerizing metal complexes carrying vinyl groups with commercially available monomers.[219-221] Among the metal-free copolymerized systems, there are only a few literature examples so far (**Figure 14**). Save and coworkers RAFT-polymerized a vinyl derivative of rhodamine B with n-butyl acrylate to form photocatalytic self-assembled particles.[222] Tobin *et al.* crosslinked styrene with a benzothiadiazole-based photoredox-active monomer to obtain gels, beads, and polyHIPE structures.[223] The group of Kai Zhang combined a benzotriazole unit with methyl methacrylate in a self-initiated copolymerization where the monomer acts as a photoinitiator. The polymer was able to catalyze a halobenzonitrile and a furan carbon-carbon coupling efficiently.[224] The copolymerization method has the advantage that the photocatalytic active moiety concentration can be precisely controlled through the monomer feed. Incorporation preserves the polymeric materials' properties and combines them with photocatalytic attributes of small redox-active molecules.

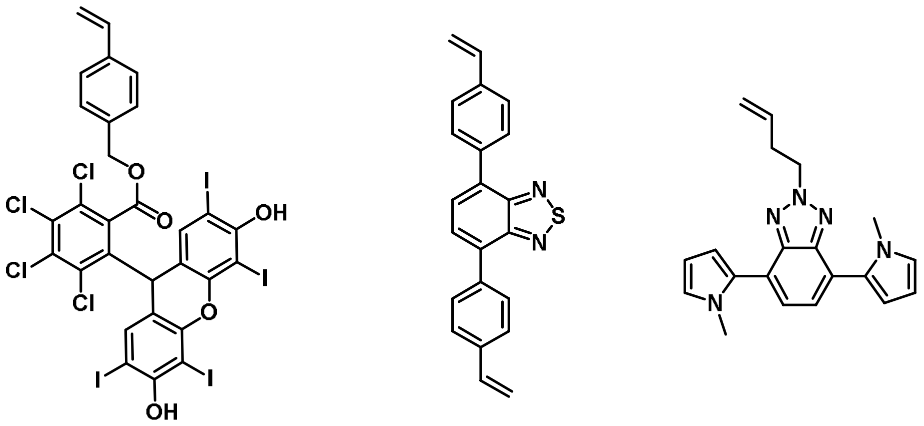

Save et al., 2019,
Macromol. Rapid Commun.

Vilela et al., 2017,
ACS Catal.

Zhang et al., 2018,
Adv. Synth. Catal.

Figure 14. Literature examples for photocatalytic units with vinyl groups for radical copolymerization to photoactive classical polymers.[222-224]

In general, the incorporation of photocatalytic properties into classical polymer networks *via* copolymerization of photoactive monomers could be an effective strategy towards a novel class of efficient, cheap, and metal-free photocatalysts. Two projects that use the classic polymer platform are presented in the results subsection of this thesis.

1.3 Characterization techniques

In the following, the most relevant characterization techniques used will be theoretically outlined. The focus is to emphasize the relation of the measurement techniques to the projects.

Fourier-transform infrared (FTIR) spectroscopy

Chemical bonds specifically absorb radiation in the infrared range through discrete molecular vibrations and rotations. Thus, the absorption behavior and the chemical constitution of a material can be studied using Fourier-transform infrared (FTIR) spectrometers. The FTIR spectrum of a substance is characteristic and can be used for unique identification and structure elucidation. In a spectrum, the relative transmittance is usually plotted against the wavenumber in reciprocal centimeters (~4000-700 cm^{-1}).[225]

In the present work, FTIR spectroscopy in an attenuated total reflection (ATR) setup was primarily used to detect specific functional groups in the polymer catalyst networks. As a sensitive, quantitative, and solid-state compatible method, it is very well suited for verifying, e.g., the degree of polymerization or the incorporation of comonomers.

Transmission electron microscopy (TEM) and scanning electron microscopy (SEM)

Transmission electron microscopy (TEM) is a technique in which an electron beam is passed through a sample, interacts by elastic scattering, and is detected by imaging after magnification. Corresponding amplitude and phase contrasts are formed by differences in the mass-thickness and the diffraction behavior of the specimen. The accelerating voltage is typically chosen between 60 kV and 300 kV. The resulting small de Broglie wavelength of the highly accelerated electrons allows several orders of magnitude higher resolution than conventional optical microscopy and other electron microscopy techniques. The strength of the TEM technique lies in resolving internal structures, where features down to a lateral size of about 0.1 nm can be resolved.[226]

Scanning electron microscopy (SEM) is based on a different working principle. The electron beam is scanned across the surface of the sample in a raster fashion. Inelastic scattering processes produce secondary and backscattered electrons of low energy that can be detected for imaging. The accelerating voltage is usually between 0.1 kV and 30 kV. In general, the SEM technique focuses on resolving surface features from 1 to several hundreds of nanometers.[227]

The two techniques have specific material requirements: Samples must be free of contaminants, non-volatile, and vacuum stable. The electron beam can damage organic samples. For TEM imaging, samples must be extremely thin (< 100 nm) to ensure transmission.

In this work, both techniques were employed to analyze the morphology (shape, size, topography, etc.) and internal organization of photocatalyst nanostructures. Energy-dispersive X-ray spectroscopy units provided further information about the elemental composition of the specimen.

Gas adsorption

In a typical gas adsorption measurement, nitrogen (adsorptive) is dosed onto the material under test (adsorbent). At a temperature of -196°C and a pressure below the saturated vapor pressure of the nitrogen sample gas, a pressure gauge can be used to determine the amount adsorbed with the increase in pressure. After the adsorption half cycle is completed, the pressure within the apparatus is reduced. Part of the adsorbed gas quantity is desorbed again. The adsorption-desorption isotherm obtained allows conclusions to be drawn about, among other parameters, the surface area, porosity, and pore size of the porous solid.[228]

Essential parts of the theoretical background were established by the trio S. Brunauer, P. H. Emmett, and E. Teller, who developed the method for calculating the specific surface area from experimental pressure data.[229] The BET model describes physisorptions with sufficient accuracy. Three types of pores can be distinguished based on their diameter: micropores (<2 nm), mesopores (2-50 nm), and macropores (>50 nm). According to IUPAC, gas adsorption isotherms can be divided into six types.[230] In this work, isotherms of type IV and mixed forms of types I to IV were most prevalent.

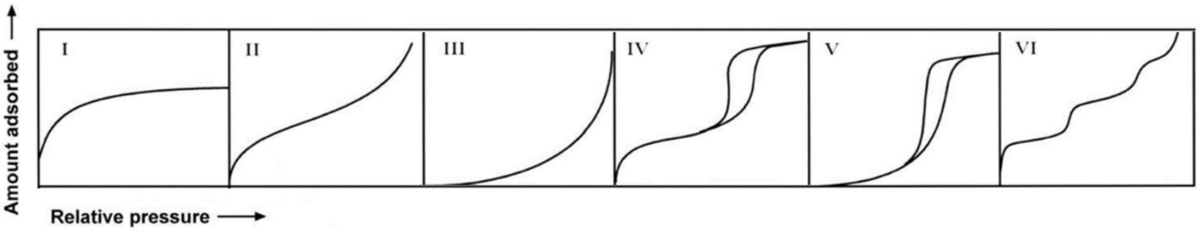

Figure 15. Types of physisorption isotherms.[231]

Type I isotherms result from microporous solids with relatively small external surface area. Type II isotherms are characteristic of non-porous or macroporous adsorbents. Type IV isotherms show a characteristic hysteresis loop resulting from capillary condensation and can be assigned to mesoporous materials. Type III and V isotherms are rare but may occur in samples with weak adsorbate-adsorbent interactions. Type VI isotherms correspond to stepwise adsorption in multilayers, as it can occur on uniform non-porous surfaces.

Catalytic reactions of substrates take place at the catalyst interface. Therefore, the available surface area, pore size distribution, and total pore volume play a major role in the efficiency of a heterogeneous photocatalytic system. These characteristics were analyzed in this work by gas adsorption measurements.

Nuclear magnetic resonance (NMR) spectroscopy

NMR spectroscopy is a crucial technology for the structural elucidation of chemical compounds. Many atomic nuclei have an intrinsic angular momentum (nuclear spin) and thus a magnetic moment (e.g., ^{1}H, ^{13}C, ^{19}F, ^{31}P). When a nucleus of this type is placed in an external magnetic field, only specific magnetic moment orientations are quantum-mechanically allowed. The interaction energy is quantized and can only assume certain values. During the irradiation of radio frequencies in an NMR experiment, transitions of the spin states of all nuclei of the investigated nuclear type are excited. The absorbed frequencies give direct information about the atoms' electronic environment and can be used to identify functional groups, their interconnectedness, and entire molecules.[225]

For NMR spectra, the signal intensity is plotted against the chemical shift in ppm. The latter is defined as the resonance frequency relative to the reference tetramethylsilane and is independent of the applied strength of the magnetic field.

In solid-state NMR spectroscopy, crystalline or amorphous solid samples can be characterized. The lack of molecular mobility leads to anisotropic interactions in NMR experiments and is corrected by additional measures such as spin rates in the kHz range and magic angle spinning (MAS).[232]

In this work, liquid ^{1}H and ^{13}C NMR spectroscopy were used to characterize monomers and photocatalysis products. Solid-state cross-polarization magic angle spinning ^{13}C NMR measurements were used for the structure verification of the polymeric catalysts since sufficient solubility was mostly not given owing to three-dimensional crosslinking.

Ultraviolet-visible (UV/Vis) and photoluminescence (PL) spectroscopy

UV/Vis spectroscopy is the primary analytical technique for studying optical absorption behavior in the ultraviolet and visible-light regions. In the spectrum, absorbance is plotted against wavelength in nanometers. In the special form of diffuse reflectance (DR) UV/Vis spectroscopy, solid samples can be characterized. Strong diffuse and specular reflectance on powder samples does not allow absorbance to be determined from the transmitted light. An integrating sphere setup is commonly used.[225]

In optically active, semiconducting polymers, electrons can be excited from valence bands into the conduction bands upon irradiation with light with energy at least equal to the bandgap. The recombination of the resulting electron-hole pair can be radiative and emit a photon. In a photoluminescence (PL) measurement, a sample is excited with light of a constant wavelength and the emitted radiation is detected. The excitation beam and detector are arranged at a 90° angle to avoid overlapping and indistinguishable signals. Compared to the absorption maximum, the emission maximum is usually red-shifted. This effect is described as Stokes shift and is caused by relaxation processes. The time decay of the emission maximum after pulsed light excitation can be studied in time-resolved photoluminescence (TRPL) measurements.[233]

The conjugated photocatalysts in the present work were analyzed *via* DR UV/Vis spectroscopy to determine optical bandgaps and derive band positions. In addition, PL and TRPL measurements were used to investigate and compare the behavior of the polymers upon light excitation and the dynamics of the charge carriers and the excited state.

Cyclic voltammetry (CV)

Cyclic voltammetry is an electrochemical method for studying oxidation and reduction processes. The setup consists of an electrochemical cell where a polished working electrode (e.g., glassy carbon, gold), a reference electrode (e.g., saturated Hg_2Cl_2 solution), and a counter electrode (e.g., Pt wire) are immersed in an electrolyte solution. The solvent choice is arbitrary but limits the potentials that can be investigated to the stable redox potentials of the chosen medium ("solvent window"). The electrolyte salt tetrabutylammonium hexafluorophosphate is usually added to the organic solvent to enable conductivity.[234]

In the measurement, a periodic triangular voltage is applied to the working electrode *via* a potentiostat. If redox-active substances are in solution or pre-applied to the electrode, they can be oxidized or reduced when sufficient potentials are reached. An increased current can be detected between the working and the counter electrode. The setup is sensitive, so water and atmospheric oxygen must be removed from the solution prior to the analysis. In a voltammogram, the current is shown as a function of the working electrode's potential, with oxidation processes shown as peaks pointing upward according to the IUPAC convention.[235]

Cyclovoltammetry was used to determine frontier orbital and band edge potentials of molecular reference molecules and conjugated polymer catalysts.

2 Results and discussion

The chapters align with the introductory chapter's development goals for the practical and larger-scale use of photocatalytic materials: High-quality reactions, nanostructuring, precise property control, cost efficiency, and solvent compatibility are essential for further photocatalytic material advancement. The results and discussion section is divided into six chapters. While the first two chapters are based on CTF materials, new systems are established in chapters 3 and 4. In the final two chapters, crosslinked linear polymers based on PMMA are used. Every chapter contains the summarized results and experimental details. Supplementary information can be found in the following section.

In chapter 2.1, three thiophene-based CTFs with variable phenyl-spacer linkers were synthesized and used for the photocatalytic oxidation of toluene to benzaldehyde with atmospheric oxygen. The realized selective sp^3-C-H activations are a step towards atom-economical and high-value photocatalytic reactions.

In chapter 2.2, the first literature-known synthetic procedure for CTF nanoparticles is presented. The size-controllable confinement synthesis allows the variation of electronic properties through doping. The effect of both nanostructuring and doping on photocatalytic efficiency is investigated in [3+2] cycloadditions. The work increases the morphological design scope and points a way towards dispersible and highly active applied photocatalysts.

In chapter 2.3, few-layer CdSe nanoplatelets are established as efficient photocatalytic materials. Controlling thickness at the atomic level allows the role of the bandgap and light absorption in the conversion of nitrobenzene to azoxybenzene to be studied in detail.

In chapter 2.4, porous aromatic frameworks are established as a versatile and highly porous platform for photocatalysis. Here, the role of the frontier orbitals' redox potentials for oxidation and reduction strength in photocatalysts is highlighted. Precise property control is crucial to tailor photocatalytic materials to target applications.

In chapter 2.5, a PMMA-based, low-cost, and easily synthesizable heterogeneous photocatalyst is presented. Although a particularly low loading of photocatalytically active comonomer was used, visible-light-promoted [4+2] cycloaddition could be catalyzed efficiently. The project emphasizes the importance of creating simple and cost-competitive catalyst platforms that can be easily applied.

In chapter 2.6, the water compatibility of a PMMA-based photocatalyst series is systematically investigated and used to remediate contaminants in the aqueous medium. Biological or environmental applications and the drive to use sustainable solvents in synthetic practice make compatibility with green media increasingly urgent.

2.1 Visible-light-driven selective oxidation of hydrocarbons under ambient conditions over covalent triazine frameworks*

The chapter is based on unpublished results. The manuscript is in preparation and will be submitted promptly. The project is a joint effort of Dr. Wei Huang, Prof. Katharina Landfester, Prof. Kai Zhang, and me. I carried out the project's experimental work with the following exceptions: Wei Huang performed parts of the photocatalytic substrate screening.

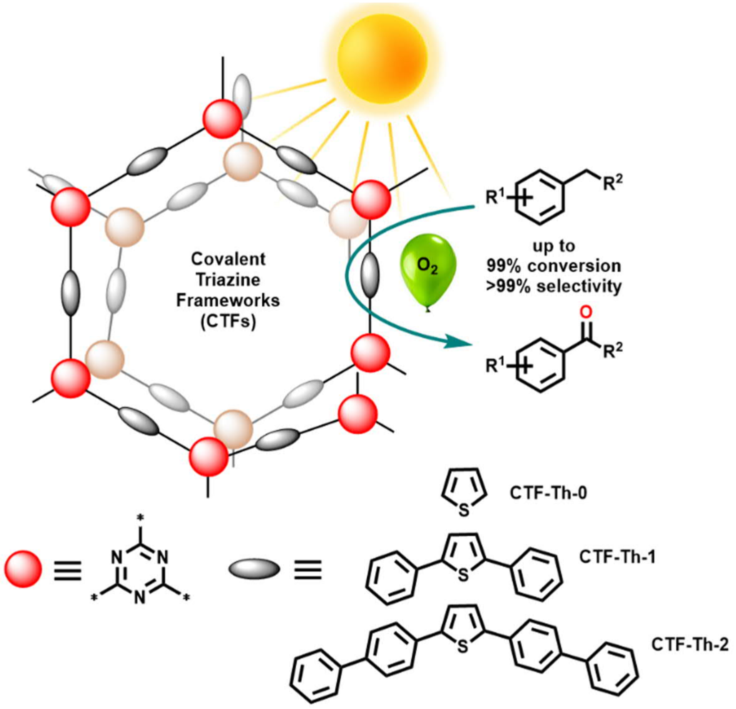

Selective oxidation of inert sp^3 C-H bonds in hydrocarbons under mild and sustainable conditions constitutes a challenging task in green chemistry. Typically, high temperature, pressure, and metal catalysts are required, which results in increased energy consumption, high cost, and unsatisfactory selectivity. Here, we report that covalent triazine frameworks (CTFs) can function as metal-free, visible-light-active heterogeneous catalysts for highly efficient and selective oxidation of a series of hydrocarbons (e.g., toluene) to aldehydes or ketones at room temperature, with molecular oxygen as a benign oxidant. Three donor-acceptor-based thiophene CTFs with different spacer lengths were compared to elucidate structure-property relationships. A precursor of the neurological drug AMG-579 was easily synthesized according to a photocatalytic protocol to emphasize the concept. This study showcases the promising potential of metal-free polymer photocatalysts for visible-light-driven, atom-economic C-H activations under aerobic ambient conditions.

2.1.1 Motivation

Selective oxidation of hydrocarbons to corresponding aldehydes or ketones are pivotal transformations in organic synthesis and chemical industry.[236-239] However, to activate inert C(sp^3)-H bonds, reactions with catalytic metals or highly corrosive oxidants at elevated process temperatures and pressures are typically required.[240-243] In addition to cost and environmental difficulties, these syntheses often offer immense potential for improvements in selectivity, atom economy, and resource efficiency.[244-245] Semiconductor-based heterogeneous photocatalytic activation of C-H bonds with molecular oxygen represents an attractive and promising alternative.[46, 246-247] It allows for the utilization of abundant oxygen as a clean and terminal oxidant and employs solar energy as a driving force, making the approach a green and sustainable process. Given the immense chemical stability of saturated sp^3 C-H bonds, the efficient photocatalytic aerobic oxidation of hydrocarbons under ambient conditions poses a substantial challenge. Despite enormous efforts, so far, only a few heterogeneous photocatalytic systems could be identified for such transformations, such as TiO_2,[248] CdS,[67, 249] V_2O_5,[250] alcohol grafted metal hydroxides,[251] Nb_2O_5,[252-253] and Bi_2WO_6.[254] Inherent drawbacks such as the use of high-energy ultraviolet light, insufficient photon absorption in the visible-light range, the use of toxic transition metals and extremely low photocatalytic efficiency strongly limit the practical applicability of many systems. The development of novel environmentally friendly and moderate photocatalytic systems for the efficient oxidative functionalization of hydrocarbons is highly desirable to solve these problems and advance atom-economic synthesis methods.

Organic polymer semiconductors have recently attracted growing attention in the field of visible-light-induced organic synthesis.[105, 114, 255] The materials display significant advantages concerning metal-free composition, structural robustness, broad visible-light absorption, and systematically tunable optoelectronic properties.[90, 112, 256] Given their synthetic and structural diversity, various efforts have been made to improve photocatalytic performance systematically: tailoring electron donor and acceptor monomers and their copolymerization ratio,[117, 224, 255, 257-259] elemental doping,[260-261] morphologically controlled synthesis[262-264] as well as optimizing the structural conformation[265-268] are prominent examples. However, few examples have dealt with the controlled variation of the distance between donor and acceptor units by spacer molecules.[269-271] Hence, polymer semiconductors are a flexible material platform for the target-oriented design of visible-light photocatalysts with desired oxidation and reduction abilities. Using a pure organic heterogeneous photocatalyst for highly efficient aerobic oxidation of inert hydrocarbons with visible light and oxygen at ambient temperature and pressure remains an appealing but unachieved goal so far.

Covalent triazine frameworks (CTFs) are a class of nitrogen-rich conjugated polymers and have been demonstrated as promising candidates for solar energy conversion.[162, 269, 272-274] Here, we report CTFs as efficient visible-light photocatalysts for the mild and selective aerobic oxidation of inert hydrocarbons under ambient conditions for the first time (**Figure 16**). The challenging activation of terminal sp^3-C-H bonds was facilitated by a series of three thiophene-based CTFs with variable phenylene spacer length synthesized via TfOH-assisted polymerization. The effect of tuning the distance between electron-donating segments and electron-accepting triazine units could be investigated through detailed electrooptical and structural characterization. Kinetic studies of the photocatalytic oxidation of toluene to benzaldehyde showed that a minimum spacer length is favorable for catalyst performance and efficiency, which is supported by quantum chemical calculations. With the top-performing catalyst, a series of alkyl aromatics could be oxidized to the respective aldehydes and ketones with excellent conversion and selectivity. To illustrate the catalyst's reactivity and applicability, a precursor to the neurological drug AMG 579 was synthesized through direct oxidation of a benzimidazole derivative. Recycling experiments underlined the photocatalysts' robustness. Solvent-free oxidation of toluene points a future path towards green and scaled-up applications without wasteful solvent consumption.

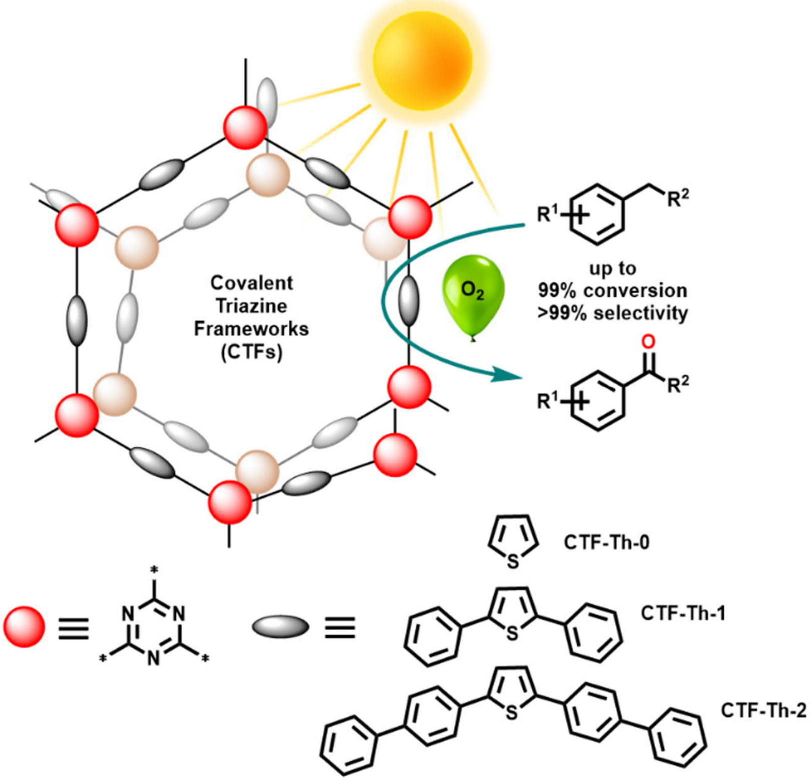

Figure 16. Schematic illustration of the CTF molecular design and their application for visible-light-driven selective aerobic oxidation of hydrocarbons

2.1.2 Synthesis and characterization

The CTFs were synthesized through a TfOH-assisted trimerization of aromatic nitriles, according to a previous report.[161] To investigate the spacer length effect on electrooptic and photocatalytic properties the three monomers 2,5-dicyanothiophene, 4,4'-(thiophene-2,5-diyl)dibenzonitrile, and 4',4'''-(thiophene-2,5-diyl)bis(([1,1'-biphenyl]-4-carbonitrile)) were used. The monomers were obtained in one to two steps with good yields and their syntheses were confirmed by liquid phase ^{1}H and ^{13}C NMR spectroscopy. The superacid-catalyzed polymerization takes place in the solid phase, where monomers are mixed with densely packed SiO_2 nanoparticles. The respective CTF materials obtained after NH_4HF_2

etching were denoted as CTF-Th-0, CTF-Th-1, and CTF-Th-2 according to the number of phenylene units between thiophene donor and triazine acceptor units. Details on synthetic procedures are provided in the supplementary information.

The scanning electron microscopy (SEM) images of the CTFs samples exhibited hollow structures (**Figure 17a-c**). The porous systems are partly interconnected and show diameters of ca. 300 nm. This corresponds to the diameter of the silica nanoparticles as confirmed by dynamic light scattering (DLS) and SEM (**Figure 17d-f**).

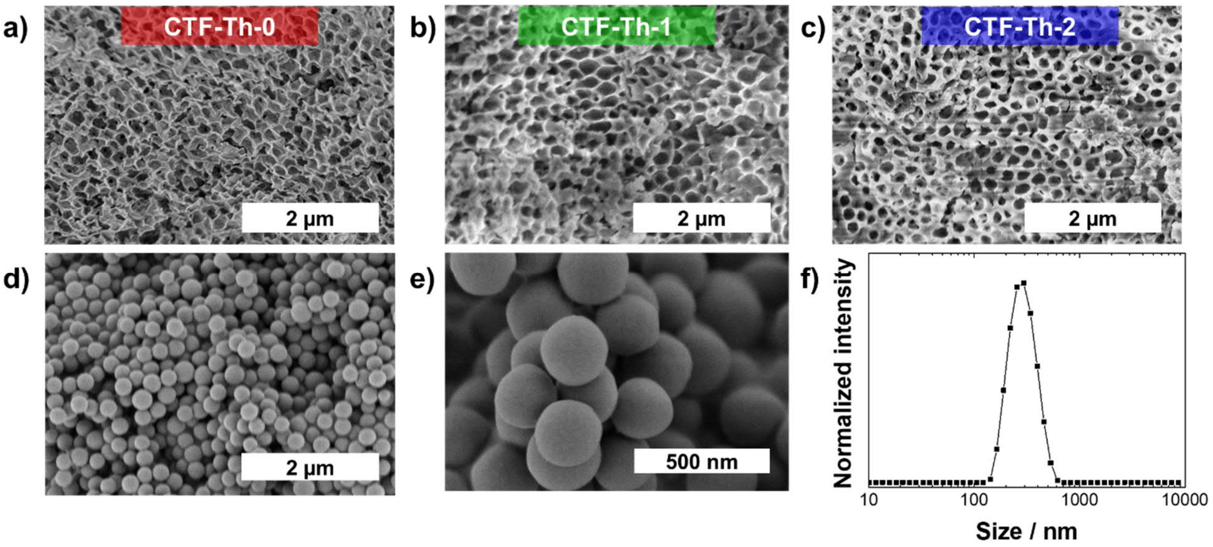

Figure 17. SEM imaging of CTFs (a-c) and synthesized silica nanoparticles (d-e). Dynamic light scattering (DLS) data on SiNPs.

Fourier-transformed infrared spectroscopy (FTIR) confirmed the successful formation of triazine frameworks. Two characteristic intensive peaks from triazine units at ca. 1500 and 1360 cm^{-1} were observed in all CTFs. Around 2300 cm^{-1}, no distinct signal could be identified. The absence of terminal nitrile groups indicates a particularly high degree of polymerization (**Figure 18a**). A slight absorption shift for the 1360 cm^{-1} signal towards higher wavenumbers was observed in the CTF-Th-1 and CTF-Th-2 traces (**Figure 18b**). This could be attributed to weakening electron-withdrawing effects when separating thiophene from the triazine cores. In the CTF-Th-2 sample, the triazine signals are comparably less pronounced owing to the highly attenuated aromatic C-H bending vibration at 730 cm^{-1}.

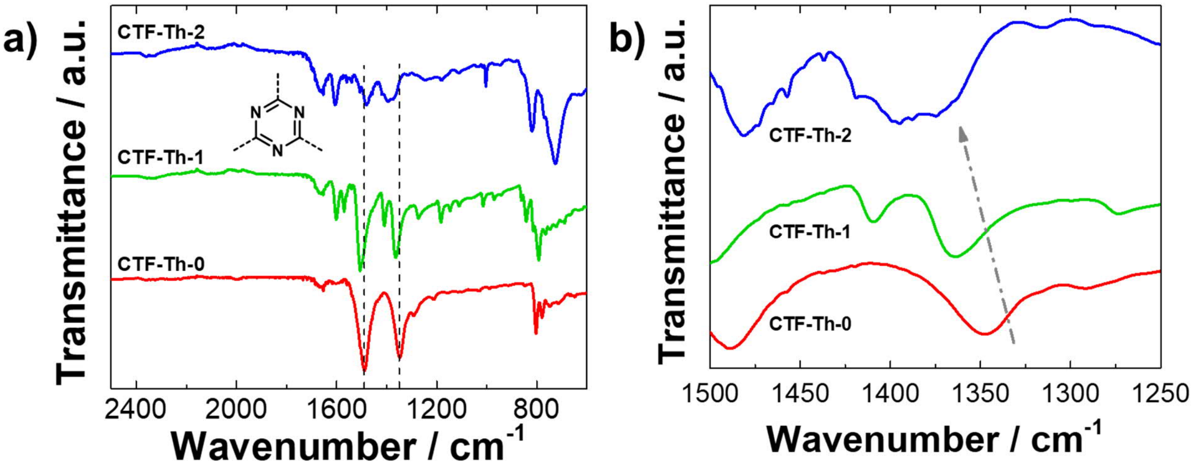

Figure 18. Regular (a) and magnified (b) FTIR spectra. The signals originating from triazine vibrations are highlighted.

Furthermore, solid-state ^{13}C cross-polarization magic-angle-spinning nuclear magnetic resonance (CP-MAS) NMR unambiguously revealed the presence of sp^2 carbons in the triazine rings at ca. 169 ppm (**Figure 19a**). Minimal signals from terminal nitriles are indicated at about 115 ppm. Nitrogen sorption experiments measured at 77 K gave Brunauer-Emmet-Teller (BET) surface areas of 48, 38, and 68 m^2 g^{-1} (**Figure 19b**). While ordered porosity is usually highly beneficial for molecular diffusion and charge carrier dynamics,[275] it seems that the inherent nonlinear angles in the five-membered thiophene heterocycles do not allow the formation of orderly structures. Similar results could be observed in previous reports.[161, 276] Powder X-ray diffraction (PXRD) confirmed their amorphous character lacking long-range ordered networks (**Figure 19c**). Thermogravimetric analysis (TGA) showed that the CTFs are thermally stable up to around 450°C in air without significant weight loss, comparable to CTFs in previous studies (**Figure 19d**).[160]

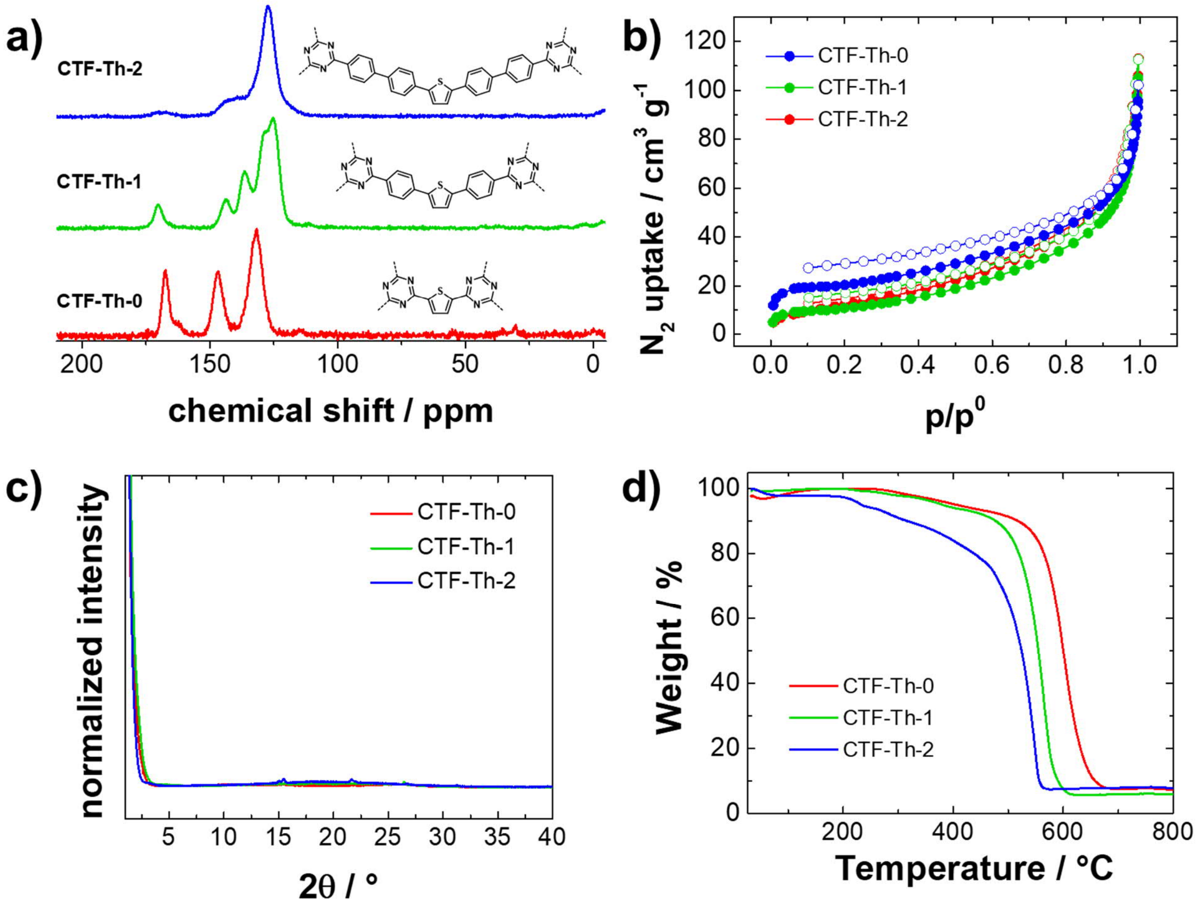

Figure 19. ^{13}C CP/MAS NMR spectra (a), nitrogen sorption isotherms (b), PXRD patterns (c), and thermogravimetric analysis (d, in air, 10 K/min) of CTF-Th-0, CTF-Th-1, and CTF-Th-2.

The optoelectronic properties of the CTFs were assessed by solid-state UV/Vis diffuse reflection (DR) measurements. All CTFs show similar visible-light absorption behavior from 550 nm to shorter wavelengths. A slight increase of the absorption onset wavelength can be observed from CTF-Th-0 to CTF-Th-2 (**Figure 20a**). Correspondingly, the bandgaps gradually decrease from 2.84 eV for CTF-Th-0 to 2.61 eV for CTF-Th-1 and 2.59 eV for CTF-Th-2, as shown in the Kubelka-Munk transformed reflectance spectra (**Figure 20b**). All powders are yellow in color, which matches the observations made above (**Figure 20c**).

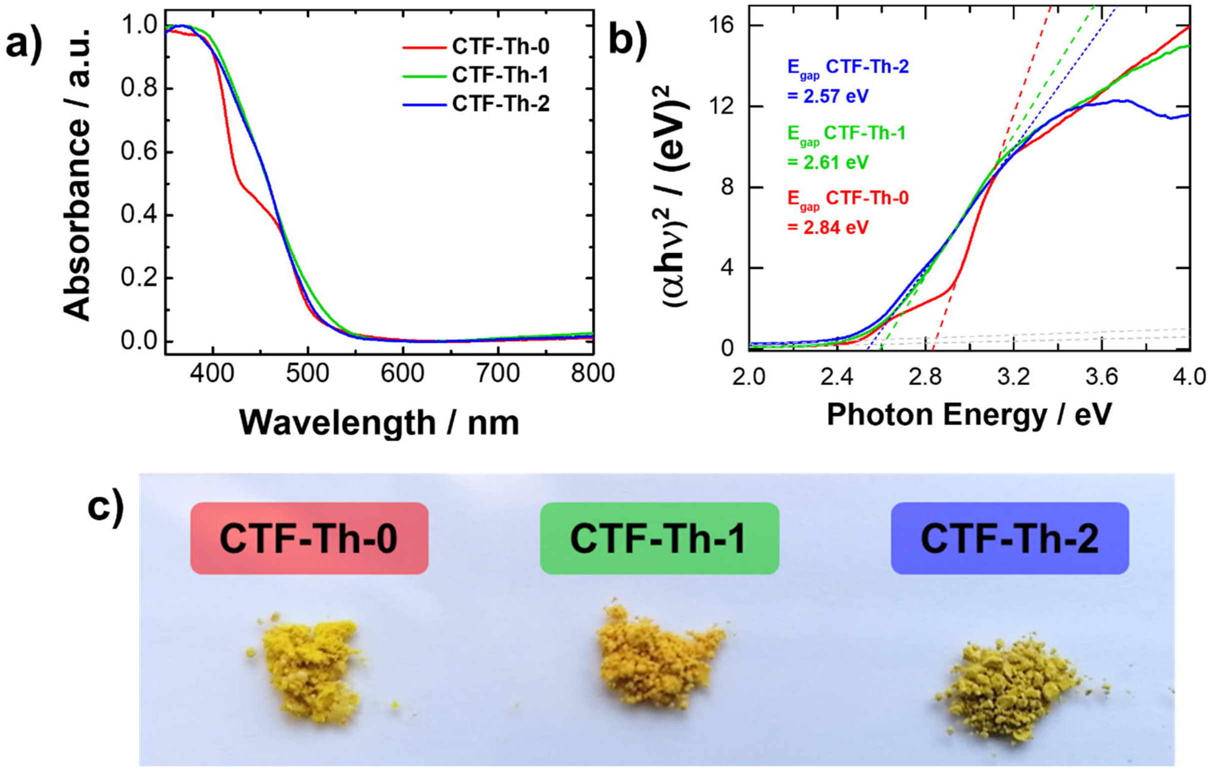

Figure 20. Regular (a) and Kubelka-Munk transformed UV/Vis reflectance spectra (b) of CTFs with different phenyl spacer lengths. Photograph of the CTFs (c).

Cyclic voltammetry measurements were conducted for each sample and determined the lowest unoccupied molecular orbital (LUMO) levels (vs. SCE) at -0.73 V for CTF-Th-0, -0.88 V for CTF-Th-1, and -0.81 V for CTF-Th-2 (**Figure 21a**). The highest occupied molecular orbital (HOMO) levels were obtained by combining LUMO potentials and the optical bandgaps (**Figure 21b)**. The determined band structures of the CTFs are consistent with the theoretical values calculated from model compounds (**Figure 21c)**.

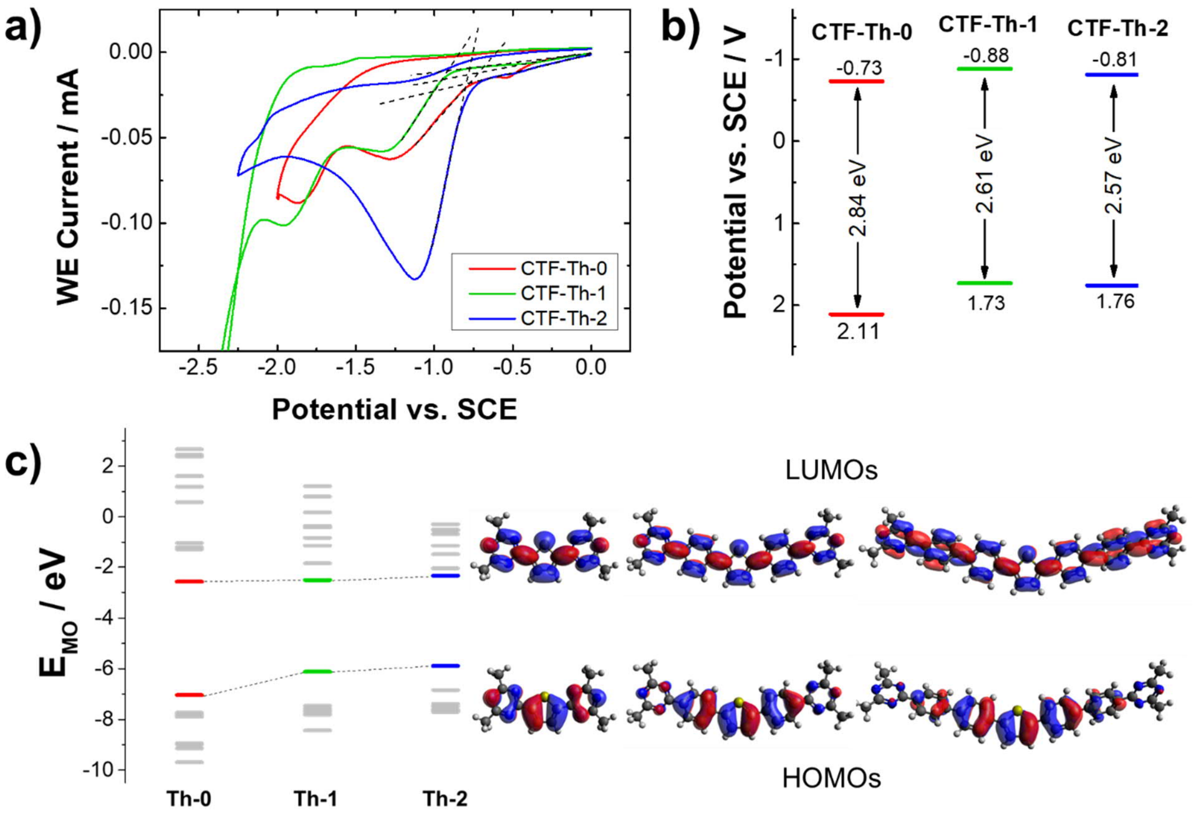

Figure 21. Cyclic voltammetry with a scan rate of 100 mV/s in CH3CN (a) and derived HOMO and LUMO potentials (b). DFT calculations on the PBE0 level using def2svp as a basis set for triazine structures analogous to the CTFs in this study (c). The systems were reduced to smaller units to limit the complexity of the theoretical calculations and were conducted to prove the general trend on frontier orbital energies upon spacer elongation.

A DFT analysis on the influence of insufficient conversion is displayed in **Figure 22**. The conversion effect was assessed at three different levels of complexity (**Figure 22a**). The DFT calculations showed that while both ground state frontier orbital potentials depend on the conversion (**Figure 22b**), small amounts of cyanides from unpolymerized monomers could be beneficial by lowering the HOMO and increase the oxidative power of the materials (**Figure 22c**).

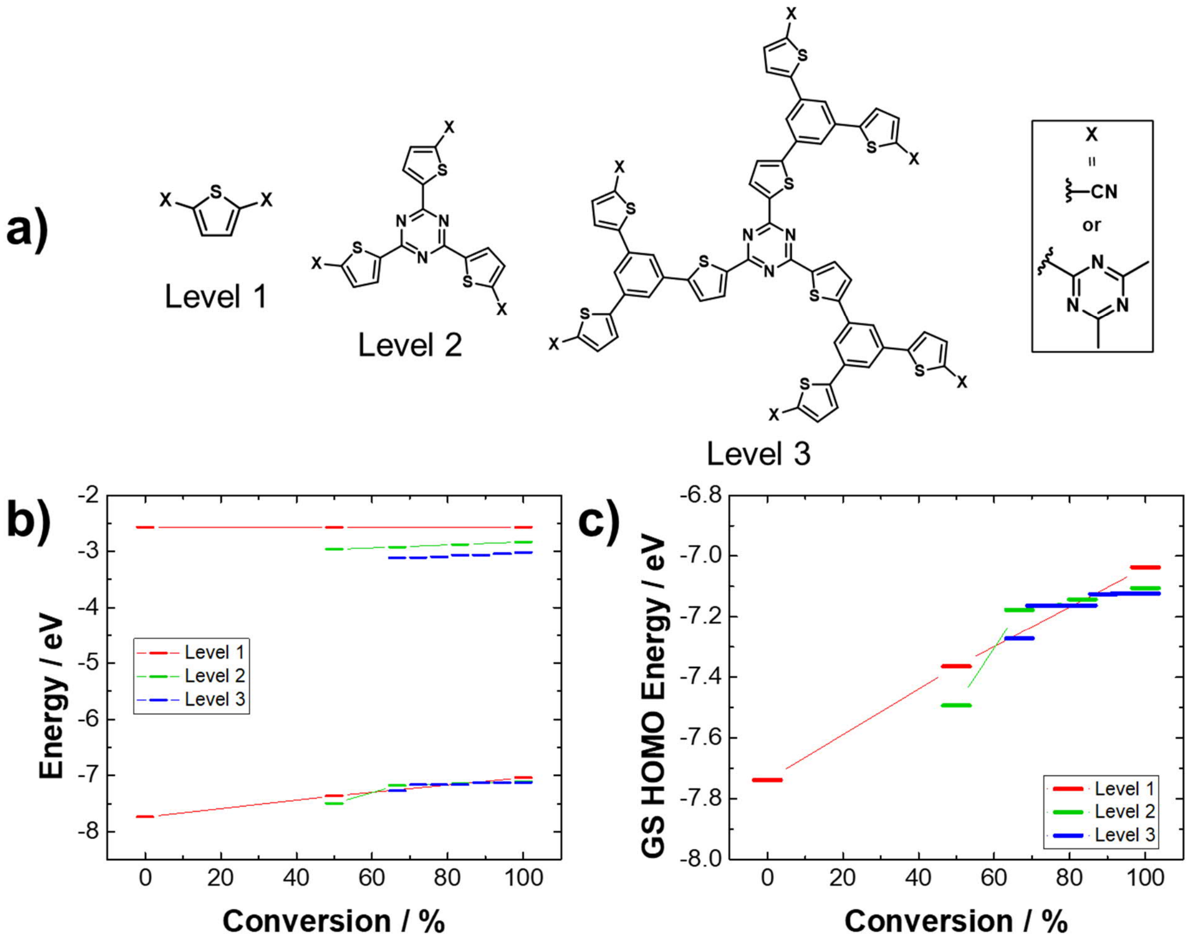

Figure 22. DFT calculations on the influence of conversion on the HOMO and LUMO potentials. The calculations were performed on three different levels of complexity to obtain representative trends (a). Cyanides or triazine rings were placed at position X depending on the conversion tested. At level 1, for example three conversions (0%, 50%, 100%) result. Ground state HOMO and LUMO potentials vs. vacuum (b) and the magnified HOMO potentials vs. vacuum (c).

Moreover, photoluminescence (PL) spectra with an excitation of 380 nm were recorded. The PL intensity increased with more phenylene spacer units and shifted to slightly longer wavelengths (**Figure 23a**). This could be due to an enhanced charge carrier separation in CTF-Th-0, which does not favor radiative pathways. The observed redshift in the catalysts' emission characteristics could be derived from the slightly changed UV/Vis absorption behavior. Time-resolved photoluminescence (TRPL) measurements show an increasing tendency of lifetimes with the size of the linker (**Figure 23b**). However, a slight increase in charge carrier lifetime from 0.53 ns for CTF-Th-0 to 0.61 ns for CTF-Th-1 and 0.70 ns for CTF-Th-2 could be noticed. Extended distribution of electron and hole density among the phenyl spacers could lead to slowed carrier recombination in the excited state. This is supported by time-dependent DFT calculations (**Figure 23c**).

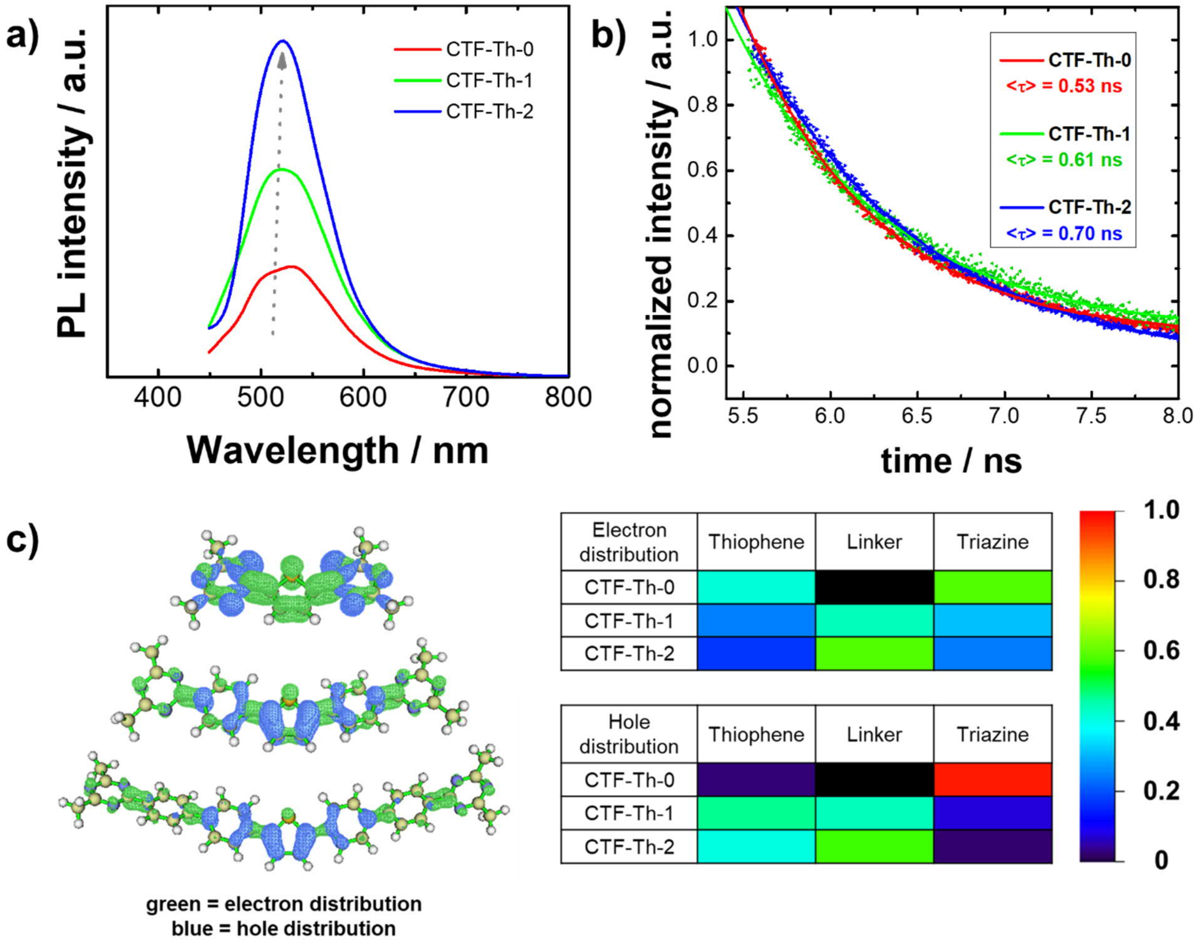

Electron distribution	Thiophene	Linker	Triazine
CTF-Th-0	🟦	⬛	🟩
CTF-Th-1	🟦	🟩	🟦
CTF-Th-2	🟦	🟩	🟦

Hole distribution	Thiophene	Linker	Triazine
CTF-Th-0	🟪	⬛	🟥
CTF-Th-1	🟩	🟦	🟦
CTF-Th-2	🟦	🟩	🟪

Figure 23. Steady-state photoluminescence spectra with λ_{exc} = 380 nm (a). Normalized PL lifetimes of CTFs with different spacer lengths (b). PL signals were read at the respective emission maximum. Lifetimes of the NPLs were fitted with an exponential function. The samples were excited with λ_{exc} = 380 nm. Excited state electron and hole distributions calculated on the PBE0 level using def2svp as basis set (c). The color code indicates the percentage distribution of electrons and holes (red = 100%, black = 0% localization on respective fragment). For the visualization, the multifunctional wave function analyzer Multiwfn was used.[277]

2.1.3 Photocatalysis

Next, we evaluated the photocatalytic activity of the CTFs in the selective oxidation of toluene to benzaldehyde under visible-light irradiation using molecular oxygen as terminal oxidant at room temperature. Benzaldehyde is the simplest aromatic aldehyde and is extensively used in pharmaceutical, food, and cosmetic products.[278] Its industrial production can be carried out by radical halogenation of toluene and subsequent hydrolysis of, e.g., benzal chloride or partial direct oxidation of toluene.[279-280] Both processes inherently face challenges regarding selectivity and turnovers. For the kinetic study, nitromethane was selected as solvent owing to its high polarity and ability to disperse the catalysts. In a typical experiment, the catalyst and toluene were dispersed in nitromethane and oxygen was passed through for 2min. The reactions were sampled after 1, 2, 3, 4, and 5h reaction time and analyzed by GCMS (**Figure 24**).

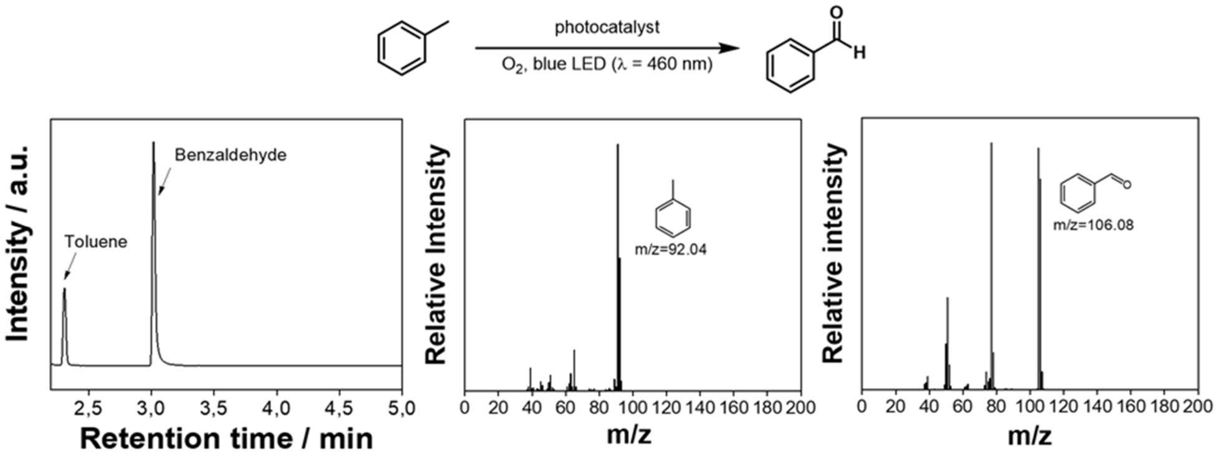

Figure 24. Representative GC trace and MS information for the photocatalytic oxidation of toluene to benzaldehyde with the used CTFs. The conditions of the experiment are listed in the experimental details.

CTF-Th-0 showed the highest photocatalytic efficiency with a conversion of 83%, followed by CTF-Th-1 with 47% and CTF-Th-2 with 28% (**Figure 25**). Several factors may cause the superior catalytic performance of CTF-Th-0. Mainly the extremely low HOMO level enables the reaction to be carried out efficiently. Other advantages include the localization of the DFT hole density on the triazine rings and the comparatively low radiative losses after excitation, as seen in the PL studies. The latter can also be considered to explain the superior performance of CTF-Th-1 over CTF-Th-2. Furthermore, the formation of low energy trap states by incomplete polymerization in CTF-Th-0 and CTF-Th-1 might benefit their photocatalytic performance.

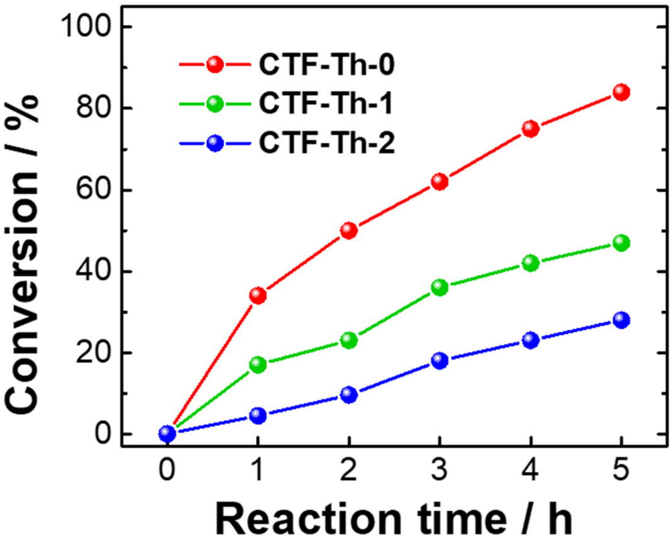

Figure 25. Visible-light-induced selective oxidation of toluene in different solvents performed with CTFs with different phenyl spacer lengths.

The turnover frequency (TOF) of the CTF-Th-0 photocatalyst was estimated to be 2.2 mmol $g^{-1}h^{-1}$, which outperforms the state-of-art catalysts reported (**Table 2**). To our knowledge and according to literature comparison, no metal-free systems have been used for this reaction so far. By doubling the reaction time of CTF-Th-0, full completion of the reaction to 99% conversion and 99% selectivity could be achieved.

Table 2. Benchmark of the present study to literature examples of photocatalytic oxidation of sp^3-hydrocarbons. [a] Under UV light (310 nm); [b] 4-chlorotoluene as the substrate

Photocatalysts	t (h)	Cat. concentration (mg/mL)	Oxidant	Conv. (%)	Sel. (%)	Ref.
CTF-Th-0	10	5	O_2	99	>99	this work
CTF-Th-0	5	5	O_2	83	>99	this work
VO@*g*-C_3N_4	8	12.5	H_2O_2	94 (yield)		[281]
Hollow TiO_2[a]	2	10	air	<22	<24	[248]
CdS	10	5.3	O_2	33	100	[67]
Graphene/CdS/TiO_2	10	5.3	O_2	70	80	[249]
BiOBr/TiO_2 (surface chlorinated)	4	20 (no solvent)	O_2 (0.1 MPa)	1	91	[282]

riboflavin tetraacetate (RFT); [Fe(TPA)(MeCN)$_2$] (ClO$_4$)$_2$	5	RFT (10 mol%), [Fe(TPA)(MeCN)$_2$](ClO$_4$)$_2$ (2 mol%)	air	60 (yield)$^{b)}$	[283]

In general, the reaction conversion and selectivity are highly dependent on the solvent choice (**Figure 26a**). In a screening experiment with CTF-Th-0, the reaction in nitromethane shows the highest conversion after 5h irradiation. The setups in 1,2,4-benzotrifluoride, acetonitrile, chloroform, and 1,2-dichloroethane feature lower conversions between 10 and 33%. To gain insight into the reaction mechanism in the photocatalytic selective oxidation of toluene over CTF-Th-0, we performed a series of control experiments (**Figure 26b**). Product formation in the absence of photocatalyst and light was negligible, confirming the photocatalytic nature of the process. Similarly, the oxidative transformation of toluene was almost terminated when the experiment was performed under N_2 atmosphere, confirming the primary role of oxygen in the mechanism. When $CuCl_2$ and benzoquinone (BQ) were added as electron scavenger and superoxide radical ($O_2^{\cdot-}$) scavenger, the conversion was significantly decreased to 23% and 29%, respectively. The addition of NaN_3 as the $^1O_2$ scavenger resulted in an extremely low conversion rate of 2%. The reaction was inhibited by adding the ammonia oxalate (AO) as a hole scavenger, indicating an active part of photogenerated holes. These observations unambiguously suggest the role of photogenerated electrons in activating molecular oxygen to reactive superoxide, which acts as an oxidant for the catalytic conversion of toluene. In addition, the primary function of singlet oxygen ($^1O_2$), which is frequently observed in photocatalytic oxidation reactions,[284-285] was demonstrated. The addition of *tert*-butyl alcohol (TBA), a hydroxyl radical scavenger (·OH), has a negligible effect on the toluene conversion. Due to the high reactivity and non-selectivity in organic reactions,[25] the diminished role of hydroxyl radicals in the current oxidation conversion is considered a rational reason for the excellent selectivity. Thus, a reaction pathway via hydroxyl radicals seems unlikely. When (2,2,6,6-tetramethylpiperidin-1-yl)oxyl (TEMPO) was added, the reaction was quenched, which implied a radical mechanism was involved. Carrying out the reaction in air reduces the catalytic activity but still results in 56% conversion and >99% selectivity after 5h visible-light irradiation.

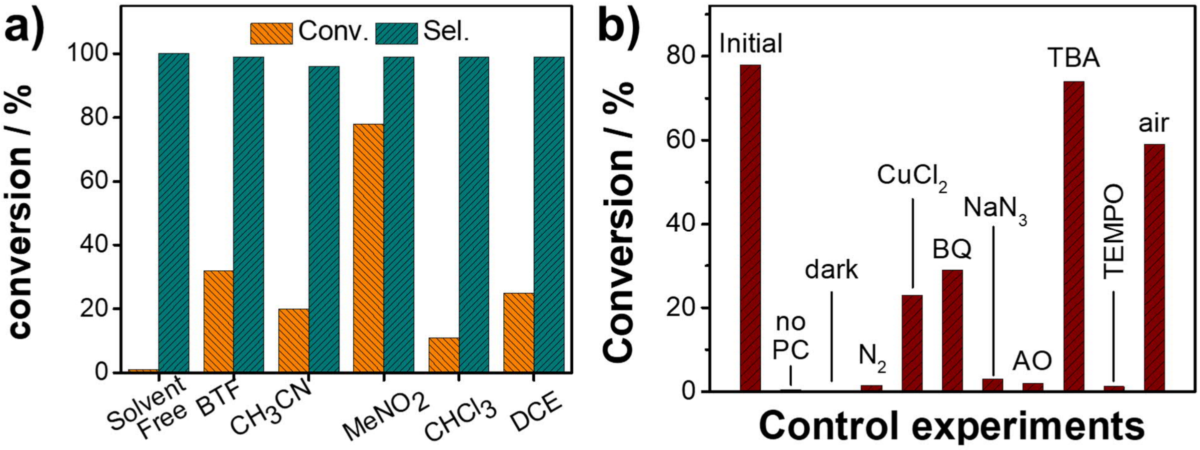

Figure 26. Solvent optimization (a) and control experiments (b) of the photocatalytic oxidation of toluene with CTF-Th-0.

The formation of the reactive oxygen species (e.g., $O_2^{\cdot-}$ and $^1O_2$) in this catalytic process was further confirmed by electron paramagnetic resonance (EPR) using 5,5-dimethyl-1-pyrroline N-oxide (DMPO) and 2,2,6,6-tetramethylpiperidine (TEMP) as trapping agents (**Figure 27a-b**). The EPR signals of $O_2^{\cdot-}$ and $^1O_2$ gradually increased with prolonged irradiation time, indicating ongoing activity of CTF-Th-0.

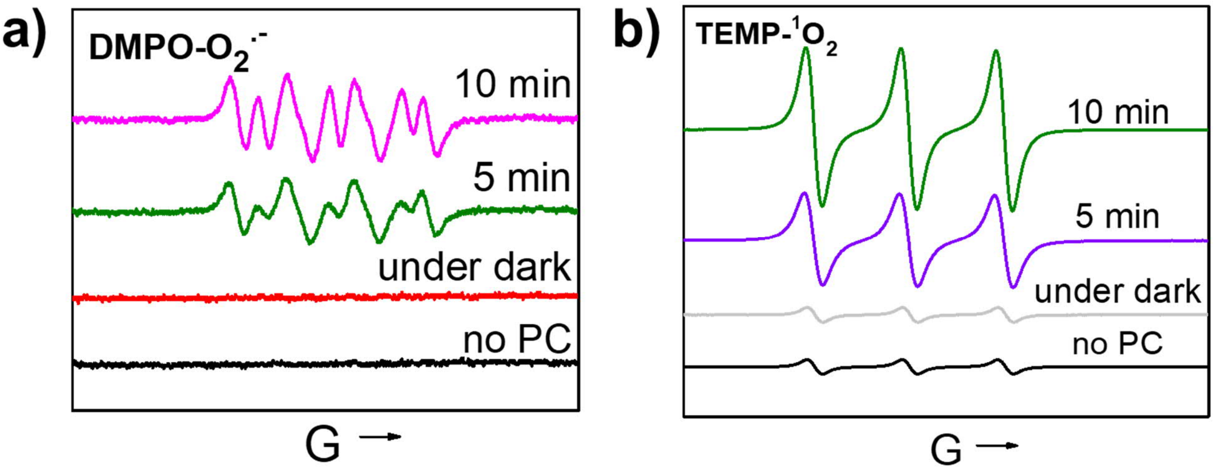

Figure 27. EPR spectra of superoxide radical (a) and singlet oxygen (b) trapping by DMPO and TEMP, respectively.

Based on the above observations, a reaction mechanism is proposed (**Figure 28**). Under visible-light irradiation, the excited photocatalyst activates oxygen on its surface to generate $O_2\cdot^-$ and $^1O_2$ through single electron transfer and energy transfer. Subsequently, the positive holes will oxidize toluene to the corresponding benzylic radical, which undergoes proton abstraction. The reactive intermediate then reacts with the activated oxygen species to give the target product. The mechanism and the drawn conclusions from our experiments are in alignment with previous reports.[286-287]

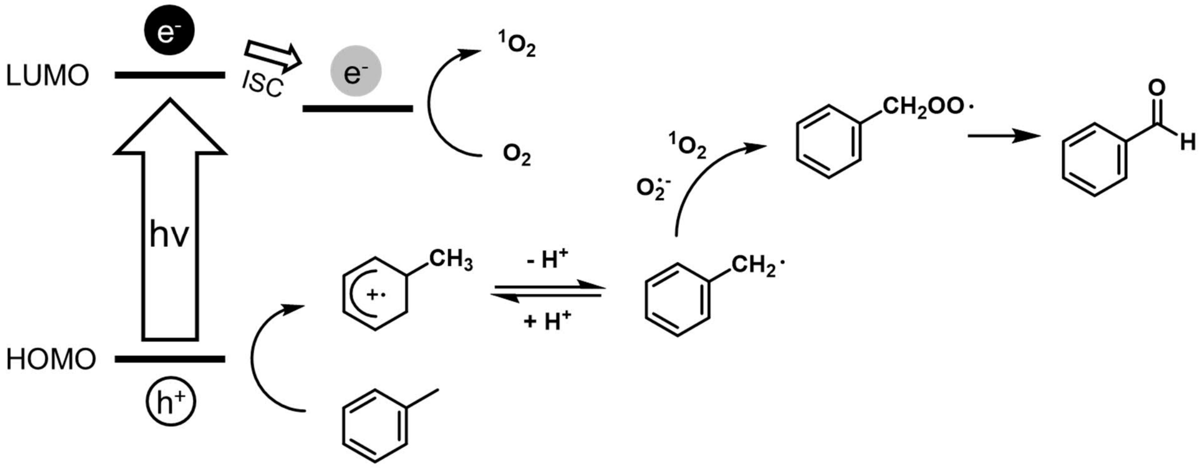

Figure 28. Proposed mechanism of the photocatalytic oxidation of toluene towards benzaldehyde.

Inspired by the high photocatalytic reactivity of CTF-Th-0 in the selective oxidation of toluene, we investigated the scope of the reaction (**Figure 29**). The generality of the catalytic scheme should be demonstrated by the conversion of substances with different substituents. As shown below, *o*-, *m*- and *p*-substituted toluene can be readily oxidized to the corresponding aldehydes. Notably, the substituent did not change the selectivity but significantly affected the conversion rate. In addition, compared to the *m*- and *p*-substituted toluene, the *o*-substituted toluene has a lower conversion, owing to increased steric hindrance. The series of *p*-substituted halogen compounds reveals that higher conversions can be achieved the more electron-withdrawing the substituent is. These observations clearly assert that both the electronic and steric effects of the substituents have an essential impact on the final photocatalytic efficiency. Besides the oxidation of primary C-H bonds, secondary C-H bonds could also be effectively oxidized to the corresponding ketones with good conversion and selectivity. The alkane cyclohexene can be oxidized to cyclohexanone with 10% conversion and >99% selectivity. It should be mentioned that this approach was also applicable to heteroatom-containing substrates with an intermediate conversion but high selectivity, making this photocatalytic protocol a potential application for the preparation of pharmaceutically relevant intermediates.

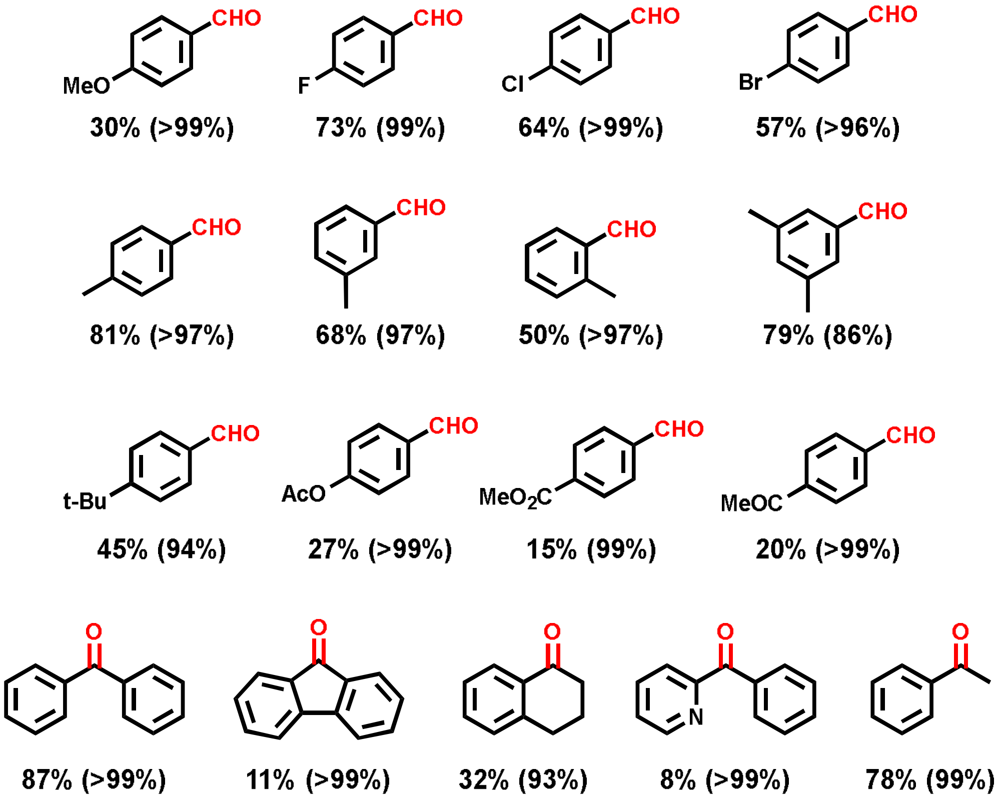

Figure 29. Substrate scope for visible-light-induced aerobic oxidation of C-H bonds in hydrocarbons. The values in the bracket represent the selectivity. Reaction conditions: substrate (0.1 mmol), photocatalyst (10 mg), nitromethane (1.5 mL), O_2 bubbling for 5min, blue LED irradiation (λ = 460 nm, 0.16 W/cm^2), 5h, room temperature. The conversion and selectivity were determined by GC-MS analysis.

As a proof of concept, a nitrogen-containing heterocycle ketone, an intermediate to the neurological drug AMG 579,[288] was synthesized via a facile two-step route from commercially available precursors (**Figure 30**). Compared to previously performed syntheses, the visible-light-driven selective oxidation approach offers an economical and more environmentally friendly way to obtain the value-added product.[289]

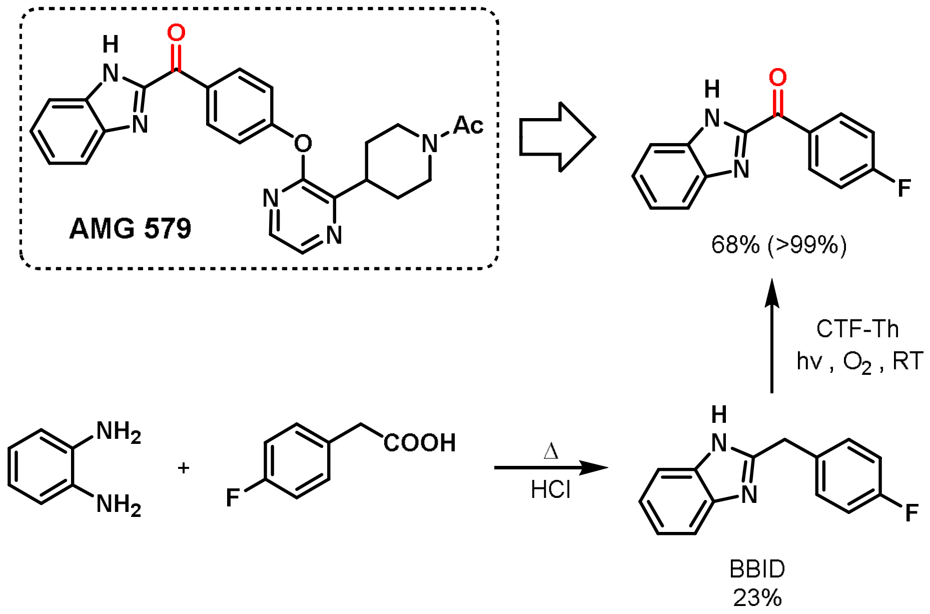

Figure 30. Possible retrosynthesis of AMG 549 (inhibitor of phosphodiesterase 10A for the treatment of schizophrenia) via a photocatalytic synthesized intermediate.

Recycling experiments confirmed the robustness of CTF-Th-0 in the photocatalytic process. It could retain a 64% conversion after reusing the material for three cycles without selectivity loss (**Figure 31a**). UV-Vis and FTIR spectra of CTF-Th-0 after cycling show little change, suggesting that the catalyst retains its chemical integrity (**Figure 31b-c)**.

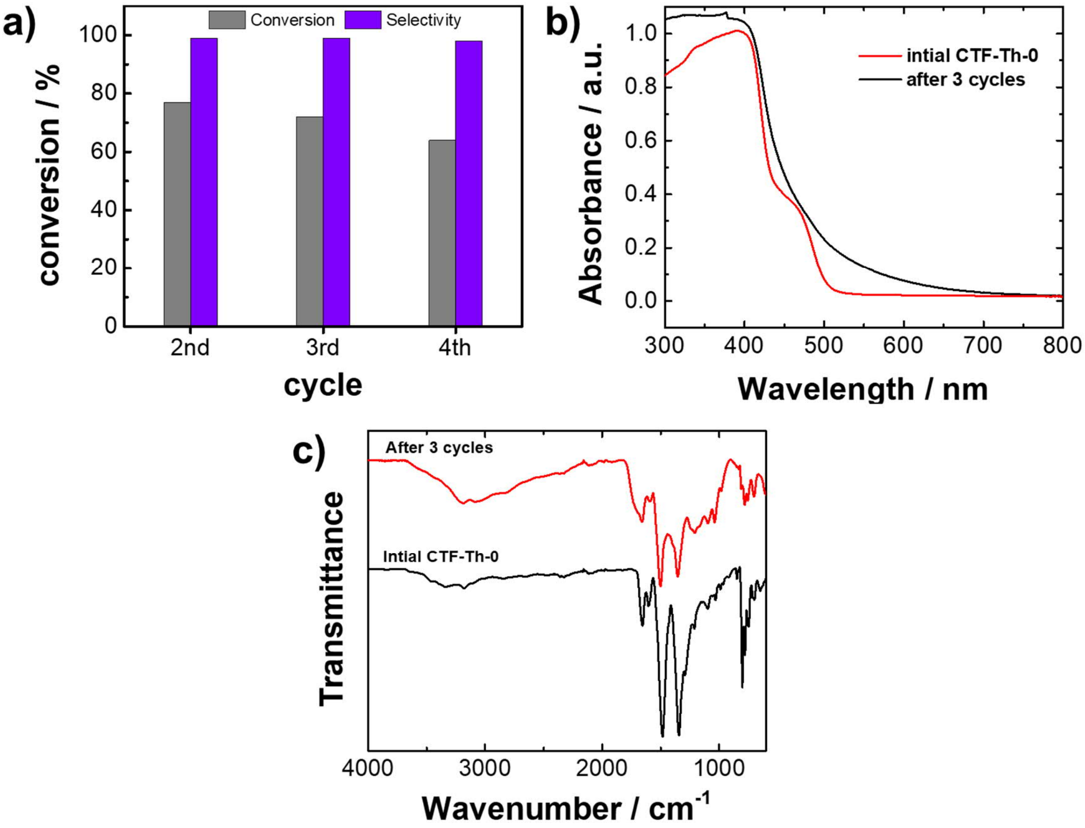

Figure 31. Bar diagram of conversion and selectivity after 5h of reaction using CTF-Th-0 in the benchmark reaction (a). UV/Vis and IR spectra before and after the application (b,c)

A solvent-free experiment with the catalyst in pure toluene achieved a conversion of 1.02% and a selectivity of >99% (**Figure 32**) in 24h of reaction time. This equals a TOF of 0.60 mmol $g^{-1}h^{-1}$. The experiment points a future path towards green and scaled-up applications without wasteful solvent consumption.

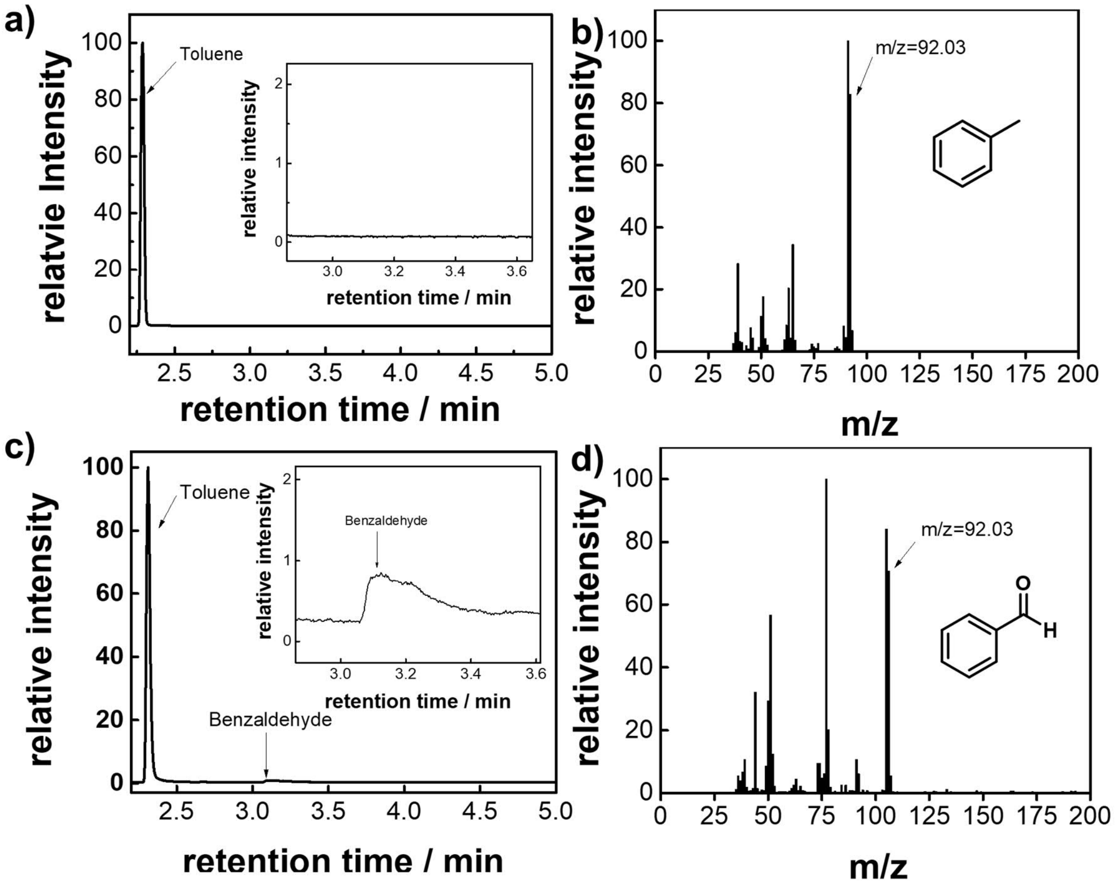

Figure 32. GCMS traces from the solvent-free experiment. The reaction setup is given in the experimental details.

2.1.4 Conclusion

In summary, we demonstrated that covalent triazine frameworks act as efficient and robust metal-free, heterogeneous visible-light photocatalysts for selective oxidation of sp^3 C-H bonds. Aldehydes or ketones could be obtained from a series of hydrocarbons under ambient reaction conditions with molecular oxygen as a clean and terminal oxidant. Importantly, their optoelectronic properties and photocatalytic performance could be readily tuned by varying the phenyl spacer length between thiophene and triazine units. The photocatalytic activity of CTF-Th-0 exceeds literature-documented state-of-the-art catalysts. Control and EPR experiments further elucidated the mechanism of the reaction. The synthesis of a precursor of an active pharmaceutical ingredient, recycling tests, and a solvent-free experiment underline the excellent applicability of the material and offer starting points for future studies. Considering the structural and synthetic diversity of CTF materials, they provide an ideal material platform for the target-oriented design of advanced metal-free photocatalysts. The realization of high-value and complex redox reactions represents an essential step towards a broader application of heterogeneous photocatalytic solar energy conversion.

2.1.5 Experimental details

Materials and methods

All chemicals were purchased from commercial sources and used as received unless otherwise noted. Technical solvents were used unless otherwise noted. Millipore quality (18.2 MΩ cm) water was used throughout.

Solid-state diffuse reflectance UV-Vis absorption and fluorescence spectra were recorded on a Perkin Elmer Lambda 100 spectrophotometer and a J&M TIDAS spectrofluorometer at ambient temperature. Liquid ^{1}H and ^{13}C NMR spectra for all compounds were measured using a Bruker Avance 300 MHz. FTIR measurements were conducted with a Varian 1000 FTIR spectrometer. Solid-state ^{13}C CP MAS NMR measurements were carried out using Bruker Avance II solid-state NMR spectrometer operating at 300 MHz Larmor frequency equipped with a standard 4 mm magic angle spinning (MAS) double resonance probe head. Scanning electron microscope (SEM) images were acquired on a LEO Gemini 1530 (Carl Zeiss AG). The thermal gravity analysis (TGA) measurement was conducted in a nitrogen atmosphere with increasing temperature from 25 °C to 800 °C at a rate of 10 °C/min. BET surface areas and pore size distributions were measured by nitrogen adsorption and desorption at 77 K using a Micromeritics Tristar II Plus. All samples were degassed at 120 °C for 12h under high vacuum before the analysis. The BET surface area calculation was based on data points obtained from $0<P/P_0<0.25$. The nonlinear density functional theory (NLDFT) equilibrium model was used for the BET model fitting. Pore size distributions and pore volumes were derived from the adsorption branches of the isotherms using Density Functional Theory (DFT, N_2, assuming carbon adsorbent with slit pores). X-ray diffraction (XRD) was conducted on a Philips PW 1820 diffractometer with monochromatic Cu Kα radiation. Cyclic voltammetry (CV) measurements were performed using an Autolab PGSTAT204 potentiostat/galvanostat (Metrohm) with a three-electrode setup: a glassy carbon electrode as the working electrode, a Hg/HgCl$_2$ electrode (stored in saturated KCl solution) as the reference electrode, and a platinum wire as the counter electrode. Bu$_4$NPF$_6$ (0.1 M in acetonitrile) was used as the electrolyte with a scan rate of 100 mV s^{-1} in the range of 0 eV to 2 eV. All DFT calculations were carried out with the Gaussian 09 package.[290] The structures were optimized and calculated at the PBE0 level of theory [291] with the basis set of def2svp.[292-293] The single-point calculations were performed together with the PCM (Polarizable Continuum Model) model by employing nitromethane as the solvent.[294-296] GC-MS measurements were performed on a Shimadzu GC-2010 plus gas chromatograph and QP2010 ultra mass spectrometer setup (fused silica column Phenomenex, Zebron 5-ms nonpolar, flame ionization detector). PL lifetime measurements were conducted with a FluoTime200 time-correlated single-photon counting setup. Samples were excited with a blue laser at 380 nm, which was controlled by PicoQuant PDL 800-D. The signal was detected using a micro-channel plate photomultiplier tube connected to the PicoHarp 300 time-correlated single-photon counting system. PL signals were read at their respective PL emission maxima.

Synthesis of monomers

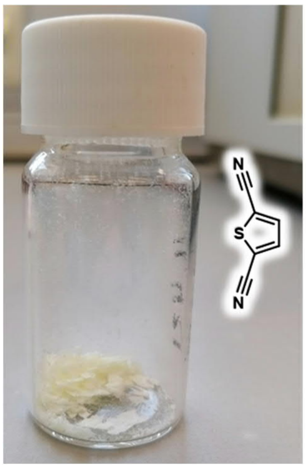

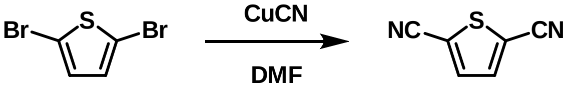

2,5-Dicyanothiophene: To a solution of 2,5-dibromothiophene (1.0 g, 4.1 mmol) in DMF (10 mL) was added CuCN (3.5 g, 39.1 mmol). The suspension was degassed with nitrogen for 10min followed by stepwise microwave heating (2h at 60 °C, 2h at 75 °C, 2h at 90 °C, 200 W, stirring, max. pressure 16 bar). The mixture was cooled to room temperature. Then the crude was transferred to an Erlenmeyer flask and stirred for 30min with water (100 mL), aqueous ammonia (28%, 20 mL), and DCM (200 mL). The mixture was separated with a separatory funnel and further extracted with DCM (3 x 30 mL). The combined organic phase was washed with Milli Q water and dried with anhydrous $MgSO_4$. The filtrate was concentrated under vacuum and purified through a silica column eluting with hexane/dichloromethane (gradient from 5:1 to 0:1) to give the titled product as white needles (250 mg, 45%). ^1H NMR (300 MHz, $CDCl_3$) δ 7.63 (s, 2H) ppm. ^{13}C NMR (75 MHz, $CDCl_3$) δ 137.01, 116.36, 112.01 ppm.

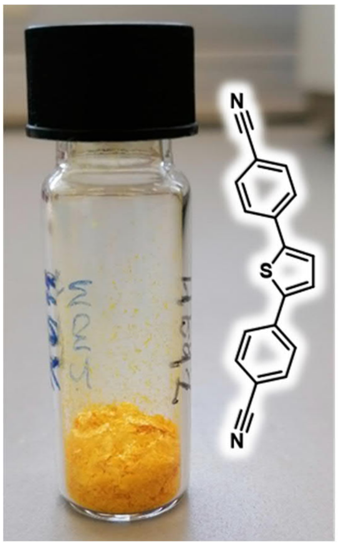

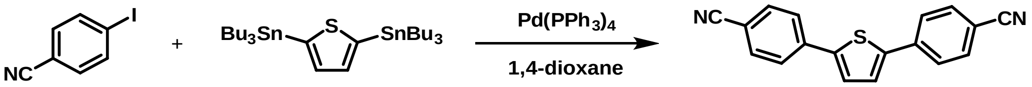

4,4'-(Thiophene-2,5-diyl)dibenzonitrile: 4-Iodobenzonitrile (229 mg, 1.0 mmol), 2,5-bis(tributylstannyl)thiophene (301 mg, 0.45 mmol) and dry dioxane (5 mL) were added to a previously dried Schlenk tube. The solution was degassed with argon for 15min, $Pd(PPh_3)_4$ (26 mg, 0.02 mmol) was added, and the mixture was heated to 110 °C for 24h under vigorous stirring. After cooling to room temperature, the resulting mixture was filtered. The obtained solid was recrystallized in 1,3,4-trichlorobenzene, washed with cold toluene, and dried under high vacuum. The product was obtained as orange platelets (110 mg, 85%). ^1H NMR (300 MHz, $CDCl_3$) δ 7.71 (dd, 8H), 7.44 (s, 2H) ppm. ^{13}C NMR (75 MHz, $CDCl_3$) δ 143.45, 138.05, 133.02, 126.51, 126.13, 118.78, 111.37 ppm.

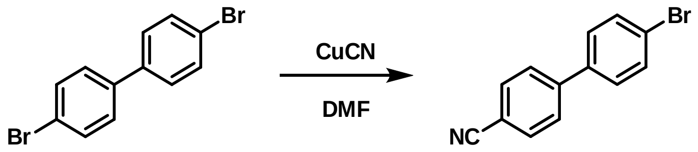

4'-Bromo-[1,1'-biphenyl]-4-carbonitrile: To a solution of 4,4’-dibromobiphenyl (800 mg, 2.56 mmol) in DMF (10 mL) was added CuCN (1.15 g, 12.8 mmol). The suspension was degassed with nitrogen for 10min followed by microwave heating (6h at 100 °C, 200 W, stirring, max. pressure 16 bar). The mixture was cooled to room temperature. Then the crude was transferred to an Erlenmeyer flask and stirred for 30min with water (200 mL), aqueous ammonia (28%, 30 mL), and DCM (150 mL). The mixture was separated with a separatory funnel and further extracted with DCM (3 x 40 mL). The combined organic phase was washed with Milli Q water and dried with anhydrous $MgSO_4$. The filtrate was concentrated under vacuum and purified through a silica column eluting with hexane/dichloromethane (gradient from 10:1 to 1:2) to give the titled product as a white powder (308 mg, 47%). ^{1}H NMR (300 MHz, $CDCl_3$) δ 7.73 (d, 2H), 7.64 (d, 2H), 7.61 (d, 2H), 7.45 (d, 2H) ppm. ^{13}C NMR (75 MHz, $CDCl_3$) δ 144.55, 138.19, 132.85, 132.42, 128.90, 127.67, 123.31, 118.87, 111.47 ppm

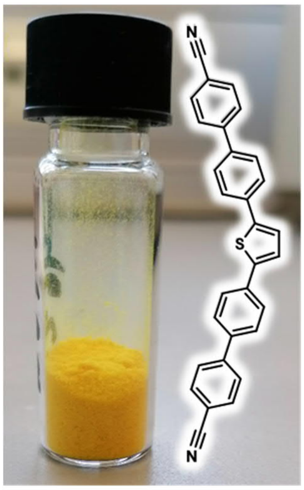

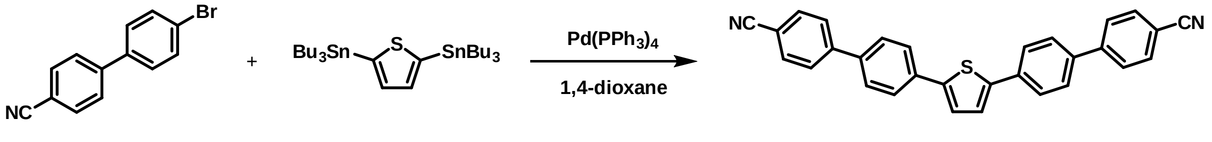

4',4'''-(Thiophene-2,5-diyl)bis(([1,1'-biphenyl]-4-carbonitrile)): 4'-Bromo-[1,1'-biphenyl]-4-carbonitrile (150 mg, 0.58 mmol), 2,5-bis(tributylstannyl)thiophene (187 mg, 0.28 mmol) and dry dioxane (5 mL) were added to a previously dried Schlenk tube. The solution was degassed with argon for 15min, $Pd(PPh_3)_4$ (16 mg, 0.01 mmol) was added, and the mixture was heated to 110°C for 24h under vigorous stirring. After cooling to room temperature, the resulting mixture was filtered. The obtained solid was recrystallized in 1,3,4-trichlorobenzene, washed with cold toluene, and dried under high vacuum. The product was obtained as a yellow powder (63 mg, 51%). ^{1}H NMR (500 MHz, d_6-DMSO, 373 K) δ 7.90 (dd, 8H), 7.83 (m, 8H), 7.61 (s, 2H) ppm. ^{13}C NMR (126 MHz, d_6-DMSO, 373 K) δ 143.43, 142.09, 137.04, 133.45, 132.15, 127.17, 126.78, 125.47, 125.03, 118.00, 109.82 ppm.

Synthesis of silica nanoparticles

The silica nanoparticles were synthesized according to the Stöber method.[297] TEOS (6.21 mL) was slowly added to a stirring mixture of ethanol (75.6 mL), H_2O (16.2 mL), and 28 wt% ammonia aqueous solution (2 mL) under vigorous stirring. Then, the mixture was then left stationary for 2h at room temperature. The precipitated silica was separated by centrifugation and washed with water and ethanol. The silica spheres were dried under high vacuum at room temperature overnight.

Synthesis of CTF materials

The CTF samples were prepared through a solid-state polymerization strategy using silica nanoparticles as templates.[160-161] For CTF-Th, vacuum-dried silica nanoparticles (300 mg) were dispersed in a solution of 2,5-dicyanothiophene (100 mg) and tetrahydrofuran (2 mL) by sonication. The mixture was then stirred for 2h under vacuum. The solvent was slowly removed by rotary evaporation. The solid monomer precursor and trifluomethanesulfonic acid (0.3 mL) were placed into two separate glass vials in a sealed Erlenmeyer flask (100 mL). The solid monomer was polymerized at 100 °C for 24h. After cooling down to room temperature, the product was immersed in water and aqueous ammonia (28%, five drops). The mixture was stirred for 2h. Then, the solids were separated by centrifugation and the silica was etched with 4M ammonium bifluoride

(NH_4HF_2) solution for 24h in a plastic bottle. The pure polymer was then washed carefully with Milli Q water and ethanol. The sample was dried under high vacuum overnight. CTF-Th(Ph)$_2$ and CTF-Th(Ph)$_4$ were synthesized with similar procedures except using the respective monomers.

General procedure for photocatalytic oxidation of hydrocarbons

Typically, photocatalyst (10 mg) was suspended in nitromethane (1.5 mL) in a 10 mL glass vial. The substrate was added (0.1 mmol) and oxygen was bubbled through the mixture for 5min using an oxygen balloon. The reaction vessel was then irradiated with a blue LED lamp (λ = 460 nm, Kessil) for 5h. Samples were taken at the given times and added to DCM. The conversion and selectivity were determined by GC-MS.

Recycling experiments

The general procedure was followed for setting up the reactions. The catalyst CTF-Th was used in the recycling study. After the completion of a reaction cycle after 5h, the conversion was analyzed by GCMS and the reaction mixture was centrifuged at 10,000 rpm for 1min. The supernatant was removed and fresh CH_3NO_2 (2 mL) was added for washing. The centrifugation was repeated and residual CH_3NO_2 was removed. The nanoparticles were then dried in a nitrogen stream for 30min and used for a new setup. Eventual weight loss was accounted for by adjusting the amount of toluene and solvent. After oxygen bubbling, the following reaction cycle was started by blue LED light irradiation.

Drug synthesis

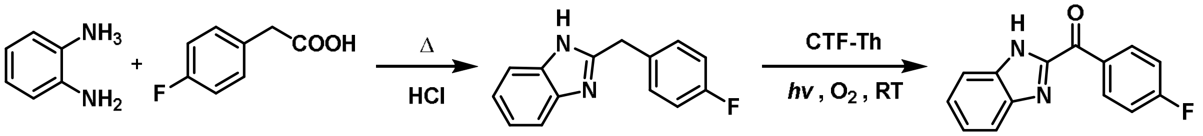

Step 1 (2-(4-fluorobenzyl)benzimidazole): A vial was charged with *o*-phenylene-diamine (220 mg, 2.05 mmol), 4-fluorophenylacetic acid (316 mg, 2.05 mmol) and 5 M HCl (7 mL). The solution was degassed with argon for 5min and heated to 100 °C for 18h. After cooling to room temperature, ice was added and the mixture was neutralized with a saturated solution of $NaHCO_3$ while stirring. Precipitated solids were collected through filtration followed by recrystallization in an ethanol/water mixture. After filtration and high-vacuum drying, the product was obtained as an off-white solid (107 mg, 23%). The data is consistent with the literature.[238] ^1H NMR (300 MHz, d_6-DMSO) δ 12.3 (s, 1H), 7.49-7.46 (m, 2 H), 7.39-7.34 (m, 2H), 7.18-7.10 (m, 4H), 4.16 (s, 2H) ppm. ^{13}C NMR (300 MHz, d_6-DMSO) δ 162.6, 159.4, 153.4, 133.75, 133.7, 130.66, 130.55, 121.3, 115.3, 114.99, 33.99 ppm.

Step 2 ((Benzimidazole-2-yl)(4-fluorophenyl)methanone): CTF-Th (20 mg) was suspended in nitromethane (3 mL) in a 10 mL glass vial. 2-(4-fluorobenzyl)benzimidazole (45 mg, 0.2 mmol), was added and oxygen was bubbled through the mixture for 5min using an oxygen balloon. The reaction vessel was then irradiated with a blue LED lamp (λ = 460 nm, Kessil) for 10h. All volatiles were removed by rotary evaporation and the crude mixture was directly absorbed onto silica. Column chromatography using DCM as solvent gave the desired product as a yellow powder (33 mg, 68%). ^1H NMR (300 MHz, d_6-DMSO) δ 13.6 (s, 1H), 8.74-8.69 (m, 2H), 7.90-7.88 (d, 1H), 7.64-7.61 (d, 1H), 7.50-7.32 (m, 4H) ppm. ^{13}C NMR (300 MHz, d_6-DMSO) δ 181.8, 167.0, 163.7, 143.1, 134,1, 133.9 (d), 132.2 (d), 125.8, 123.2, 121.3, 115.5 (d), 112.8 ppm.

Solvent-free photocatalytic oxidation of toluene

Toluene (0.5 mL) and photocatalyst CTF-Th (10 mg) were added to a glass vial. The suspension was bubbled with O_2 for 5min and irradiated with a blue lamp (λ = 460 nm, Kessil) for 24h while stirring. The conversion and selectivity were determined by GC-MS.

2.2 Covalent triazine framework nanoparticles *via* size-controllable confinement synthesis for enhanced visible-light photoredox catalysis

In the previous chapter, the performance of CTF materials in visible-light photocatalysis was underlined. The strong electron-withdrawing character of the triazine rings results in excellent optoelectronic properties. At least as essential for the photocatalytic performance is the morphology of the systems. The following project focuses on the combined innovative optimization of both areas morphology and optoelectronic characteristics. The chapter is based on the published article "Covalent triazine framework nanoparticles *via* size-controllable confinement synthesis for enhanced visible-light photoredox catalysis, *Angewandte Chemie International Edition* 2020, 59(42), 18368-18373."[276] The project is a joint effort of Dr. Wei Huang, Dr. Shuai Jiang, Prof. Katharina Landfester, Prof. Kai Zhang, and me. I carried out the project's experimental work with the following exceptions: Wei Huang performed parts of the photocatalysis kinetics. Shuai Jiang performed parts of the polymer synthesis as well as electron microscopy imaging.

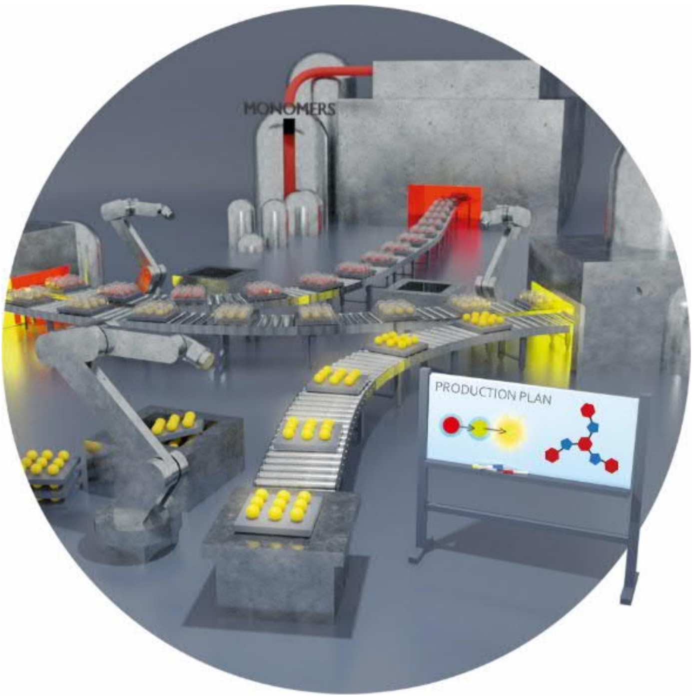

.

The construction of defined nanostructures is a key for enhancing the efficiency of heterogeneous catalytic materials. However, for metal-free, organic conjugated polymer-based photocatalysts, the synthesis of defined nanostructures is still highly challenging due to their mostly amorphous nature or specialized synthetic routes. Here, we report the formation of covalent triazine framework (CTF) nanoparticles *via* a size-controllable confined polymerization strategy. The uniform CTF nanoparticles exhibited significantly enhanced activity in the photocatalytic formation of dibenzofurans compared to the irregular bulk material. Moreover, the optoelectronic properties of the nanometer-sized CTFs could be easily tuned by copolymerizing small amounts of benzothiadiazole into the conjugated molecular network. This optimization of electronic properties led to a further increase in observed photocatalytic efficiency, resulting in an 18-fold enhancement compared to the bulk material. Full recyclability of the heterogeneous photocatalysts as well as catalytic activity in dehalogenation, hydroxylation, and benzimidazole formation reactions demonstrated the utility of the designed materials.

2.2.1 Motivation

Nanostructured materials have been vital to catalytic research in recent years.[298-300] By scaling a catalyst down to the nanoscale, the materials surface-to-volume ratio increases and the active interface is exposed to the reaction media. In most cases, the downscaling has beneficial effects on, for instance, activity, selectivity, or turnover of an applied catalyst.[301-303] For heterogeneous photocatalytic systems using light as a clean and highly sustainable energy source, efforts to synthesize nanometer-sized morphologies included nanoparticles,[304-305] nanowires[306-307] as well as hollow nanostructures.[308-311] Photocatalysts with improved performance in catalyzing hydrogen evolution from water,[106, 165] pollutant degradation,[312-313] or organic reactions[161, 314] compared to bulk materials have been reported. Precise morphological control over the material synthesis constitutes a major interest in producing defined and highly efficient heterogeneous photocatalysts. So far, a vast number of synthetic methods to form nanostructured photocatalysts have been mainly applied to inorganic materials. Due to their mostly amorphous nature or specific synthetic routes, for pure organic heterogeneous photocatalytic systems, synthesis for defined nanostructures is still highly challenging.

Among the organic photocatalytic systems being used, covalent triazine frameworks (CTFs) have emerged as promising heterogeneous polymer photocatalysts for visible-light-promoted chemical transformations.[146, 150, 179, 315-316] They have been employed as an efficient platform for visible-light photoredox reactions such as water splitting,[153, 178-179, 317] carbon dioxide reduction,[318] or organic reactions.[90, 184, 319] The CTF systems comprise various advantageous properties, such as high activity in photoredox reactions, low cost and non-toxicity, excellent recoverability, as well as stability in repeated applications. Moreover, CTFs have proven to be easily tuneable in their electronic, optical, and chemical properties.[168, 320-321] However, the main challenge within photocatalytic CTF systems remains in establishing mild synthetic procedures yielding morphologically defined structures. Conventional liquid-phase approaches in molten $ZnCl_2$ or trifluoromethanesulfonic acid (TfOH) solution are not suitable to give CTFs with regular morphologies and defined optical properties. Recently, as one of the few examples, our group reported on the use of silica templates to form hollow or mesoporous CTFs.[160-161] The group of Tan and Jin was able to synthesize hollow CTF nanospheres for photocatalytic hydrogen evolution.[165] The study emphasizes the benefits of nanoscale features for catalytic applications and the crucial role of morphology control in designing efficient photoactive CTF materials. Even though initial progress could be made, synthetic methods for self-standing covalent triazine framework nanoparticles with defined size for photocatalytic applications have not yet been documented.

In this work, we present a confinement synthesis for size-controllable covalent triazine framework nanoparticles, inspired by the baking techniques for fine-shaped cookies. A thiophene-derived dinitrile monomer can be encapsulated inside a temporarily formed silica shell using an emulsion approach. *Via* in-situ trifluoromethanesulfonic acid (TfOH)-catalyzed polymerization followed by silica shell removal, uniform CTF nanoparticles can be obtained. Variation of the emulsifying parameters led to feature sizes between 80 and 550 nm. Apart from controlling the morphology, the electronic and optical properties of the CTF photocatalysts can be further optimized through copolymerizing electron-withdrawing benzothiadiazole units into the CTF backbone and thereby boosting photogenerated charge separation. Kinetic studies of the photocatalytic dihydrobenzofuran synthesis proved that both nanoscaling and copolymerization significantly affected photocatalytic activity with an enhanced 18-fold efficiency compared to bulk CTF. Furthermore, recycling experiments underlined the photocatalysts' robustness. The versatility of the CTF nanoparticles was further investigated by conducting the dehalogenation of α-chloroacetophenone, the hydroxylation of 4-biphenylboronic acid, and the benzimidazole formation from *o*-phenylenediamine with excellent selectivity and efficiency.

2.2.2 Synthesis and characterization

The general synthetic route is outlined below (**Figure 33**) and precisely described in the experimental part (**Figure 51**). In detail, the liquid monomer 2,5-dicyano-3-hexylthiophene (DCHT) was specifically designed to ease the formation of a two-phase system with tetraorthosilicate (TEOS) in water. In aqueous media, DCHT and TEOS combine in a non-miscible oil phase and can, upon ultrasonication, or a surfactant-stabilized miniemulsion. When stirred at room temperature, TEOS in the droplets slowly hydrolyses at the oil-water interphase and forms the silica shell as confinement around the monomer DCHT. The silica encapsulation of liquid monomers in a miniemulsion process was reported in previous studies.[322-323] After freeze-drying, the resulting particles are exposed to trifluoromethanesulfonic acid (TfOH) vapor, leading to the formation of the corresponding CTF inside the silica capsule. To obtain pure CTF nanoparticles, the silica shell is removed by etching with an NH_4HF_2 solution.

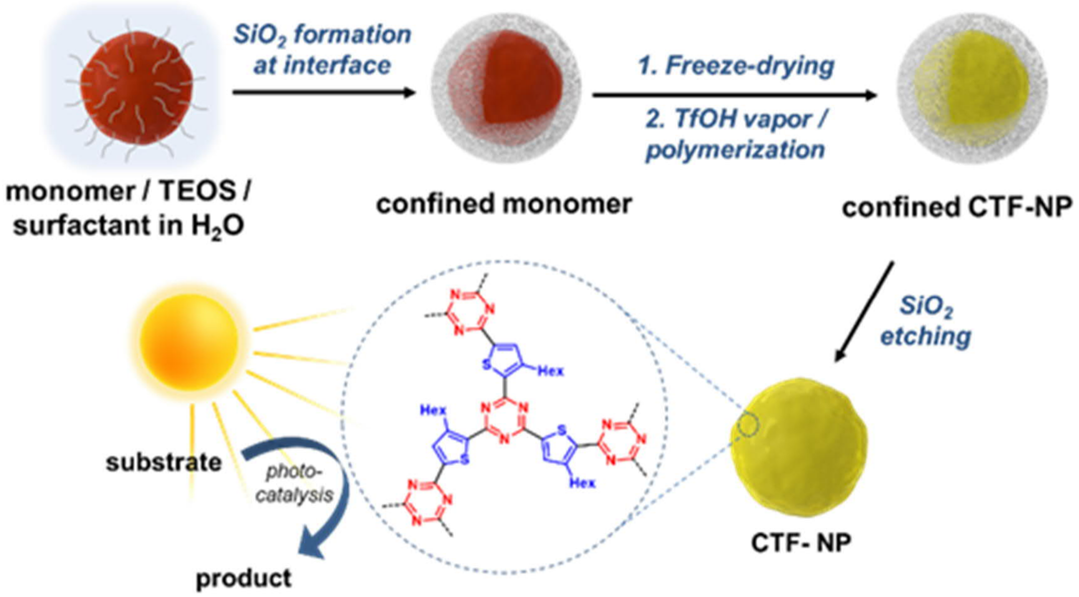

Figure 33. Synthetic route for covalent triazine framework nanoparticles in confinement. In a combined sol-gel emulsion and TfOH vapor-assisted polymerization approach, CTF nanoparticles

are formed. The resulting material can be used for visible-light-promoted organic redox photocatalysis.

In order to shed light on the formation of the nanoparticles, transmission electron microscopy (TEM) and scanning electron microscopy (SEM) studies were conducted. As shown in **Figure 34a**, TEM imaging indicated the successful confinement of DCHT in the formed silica capsules. The core-shell structure was retained after the TfOH-assisted polymerization step, as shown in **Figure 34b**. Energy-dispersive X-ray spectroscopy (EDX) mapping on the encapsulated CTF-NPs showed a high prevalence of silicon and oxygen in the shell area, whereas carbon and sulfur could be detected exclusively in the core of the nanoparticles (**Figure 34c**).

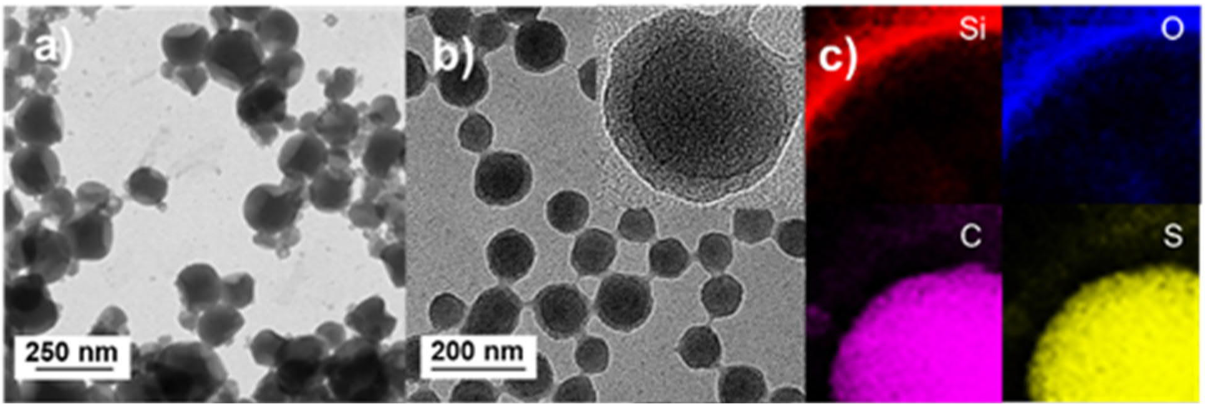

Figure 34. TEM image of monomer (a) and CTF-NPs (b) confined in silica capsules. Elemental mapping shows enriched contents of silicon and oxygen in the shell and carbon and sulfur in the core (c).

After the silica shell removal, CTF NPs with different diameters ranging from circa 80 to 550 nm (CTF_{80}, CTF_{180}, CTF_{550}) on average were obtained (**Figure 35**), depending on the volume ratio between dispersed phase and water phase in the miniemulsion synthesis. Light scattering on the colloidal particles in a diluted THF suspension (insert **Figure 35d**), known as the Tyndall effect, further underlined the successful synthesis of the uniform covalent triazine framework nanoparticles.

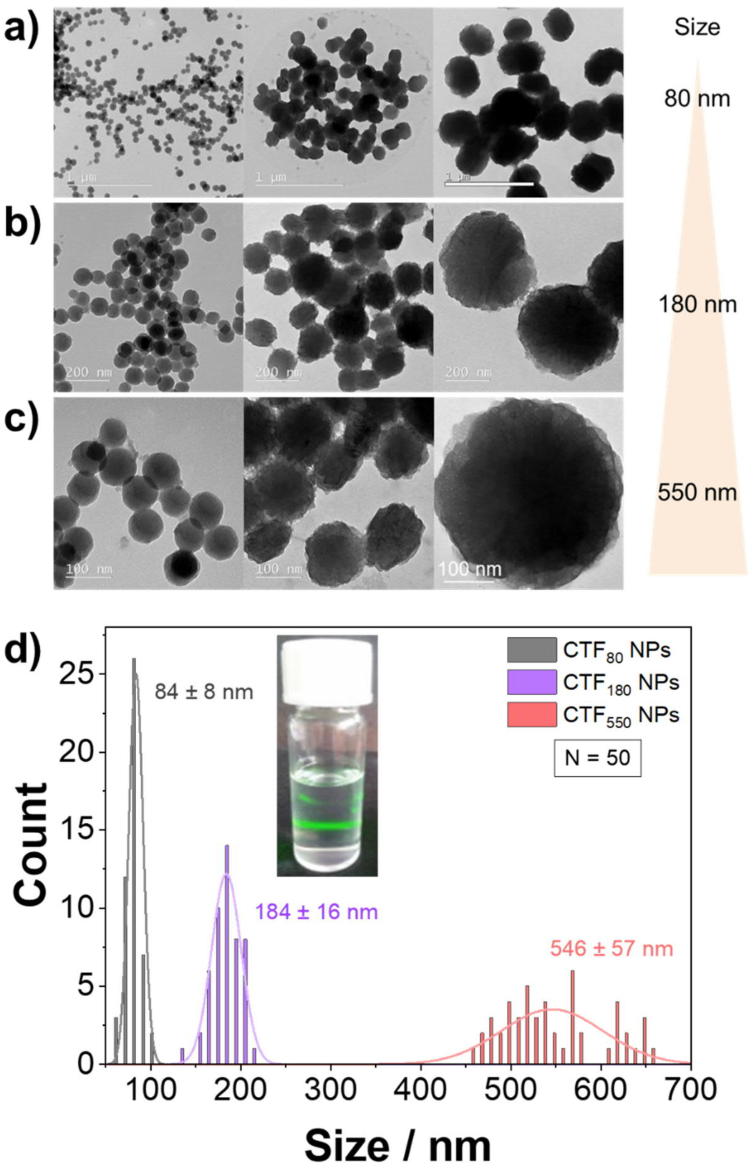

Figure 35. Different CTF-NP sizes of 80, 180, and 550 nm on average could be obtained (a-c). Size histogram of counted nanoparticles (N=50 each) from transmission electron microscopy images (d). The inset in (d) shows the Tyndall effect of CTF_{80} in THF (0.01 mg/mL).

A control experiment in which the premier synthesis step was conducted with chloroform instead of DCHT yielded collapsed silica capsules after the evaporation of hexane during the freeze-drying step (**Figure 36**).

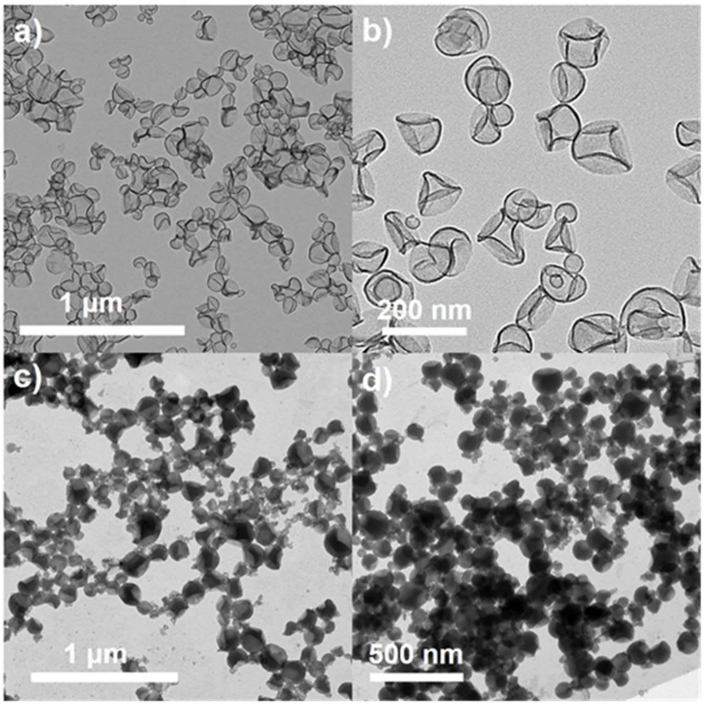

Figure 36. TEM images of silica capsules synthesized without DCHT (a, b) and silica capsules with DCHT (c, d).

Further characterization was conducted using CTF_{80} (denoted as CTF NPs) if not stated otherwise. The Fourier-transformed infrared (FTIR) spectra of the obtained nanoparticles exhibited three characteristic signals of the triazine group at 1482, 1385, and 824 cm^{-1}. A comparably low-intensity signal at 2225 cm^{-1} hints at the presence of terminal nitriles and indicates the effective formation of triazine networks with a high degree of polymerization (**Figure 37a**). Similar conclusions could be drawn from the corresponding solid-state ^{13}C cross-polarization magic-angle-spinning (CP-MAS) NMR spectrum. A pronounced signal at ca. 168 ppm verified the presence of sp^2 triazine carbons (-C=N), whereas the terminal nitrile signal around 112 ppm vanishes into the baseline signal. All signals could be matched with the assumed structure, confirming the CTF synthesis from DCHT (**Figure 37b**). Powder X-ray diffraction (PXRD) patterns) show a broad peak at 13.0° for all materials, which becomes more prominent with increasing BT content (**Figure 37c**). Thermogravimetric analysis (TGA) showed that the CTF NPs stay intact up to 400°C, comparable to CTFs from previous studies, and prove good thermal stability (**Figure 37d**).[160]

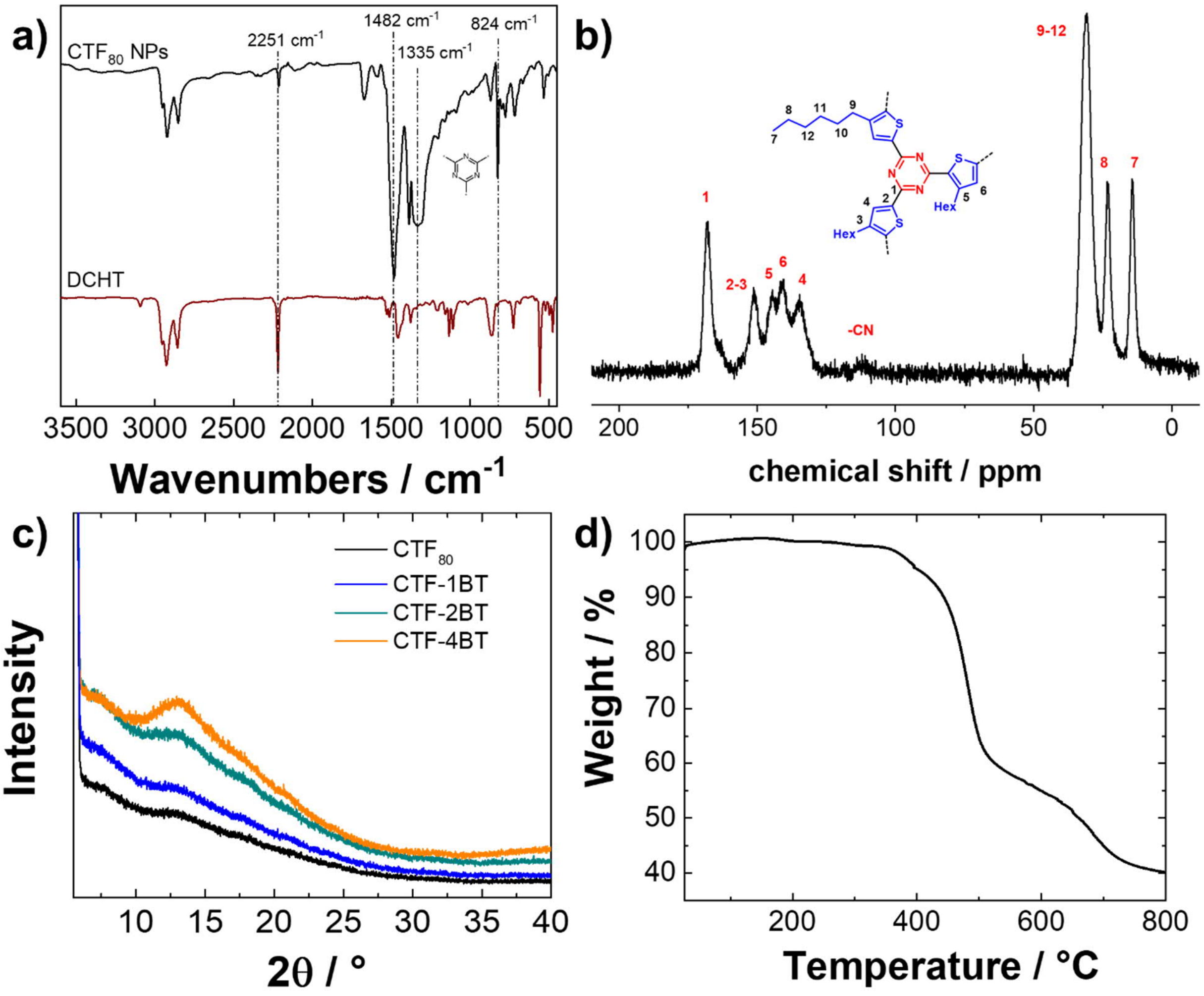

Figure 37. Comparison of Fourier-transform infrared (FTIR) spectra of CTF$_{80}$ NPs with the monomer 2,5-dibromo-3-hexylhiophene (a). 13C CP-MAS NMR spectrum of CTF$_{80}$ NPs (b). Powder XRD pattern comparison of CTF$_{80}$, CTF-1BT, CTF-2BT and CTF-4BT (c). TGA of CTF$_{80}$ NPs under N$_2$ with temperature increasing from room temperature to 800°C at a rate of 10 K/min (d).

To further optimize the optoelectronic properties of the as-synthesized CTF NPs, copolymerizations of DCHT with 1, 2, and 4 mol% of dicyanobenzothiadiazole (DCBT) were carried out. The aim was to incorporate the benzothiadiazole as an additional electron acceptor into the CTF backbone structure and improve the photogenerated charge separation. The resulting CTF NPs were denoted as CTF-xBT NPs with x = 1, 2, or 4 depending on the benzothiadiazole (BT) unit content. The experimental approach for the nanoparticle synthesis remained unchanged; for experimental details, see the experimental details. The morphological nanoparticle formation was confirmed by TEM imaging (**Figure 38**). Higher amounts of BT seem to yield less uniform particles after silica removal.

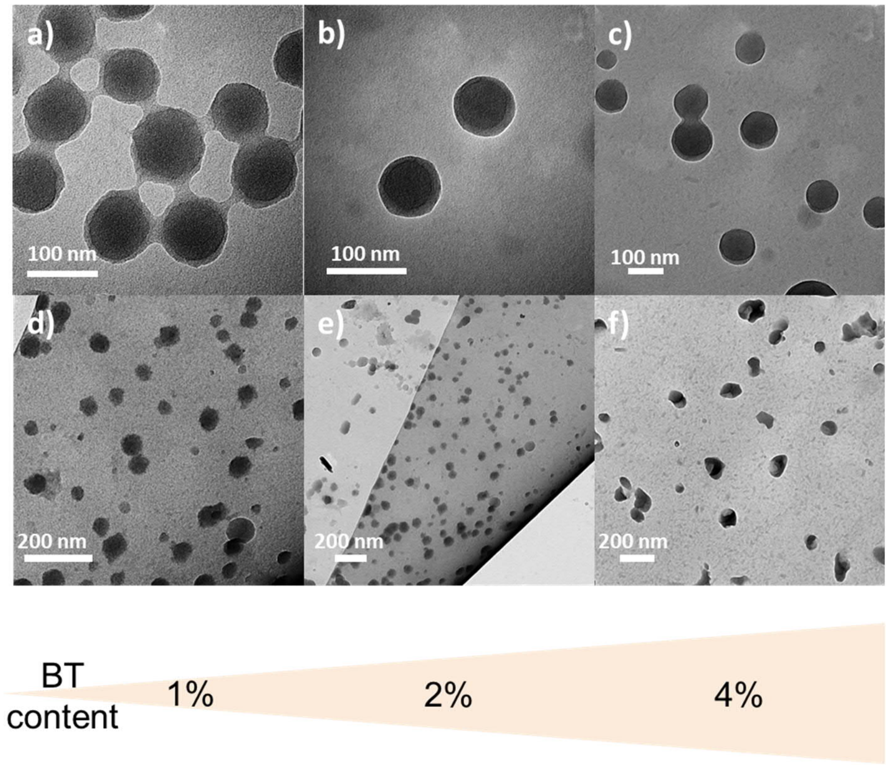

Figure 38. Transmission electron microscopy of CTF-NPs with different BT contents in silica capsules (a-c) and after removing silica (d-f).

FTIR spectra of the CTF-xBT samples resemble the spectrum of the CTF nanoparticles without BT, hinting at a retained chemical constitution and connectivity of the materials despite the introduction of BT units (**Figure 39a**). In the ^{13}C CP MAS NMR spectra of the CTF-xBT samples, a minor peak at ca. 155 ppm can be detected, which corresponds to the BT imine carbon following previous reports (**Figure 39b**).[161] These findings demonstrate the successful introduction of BT units into the conjugated molecular networks.

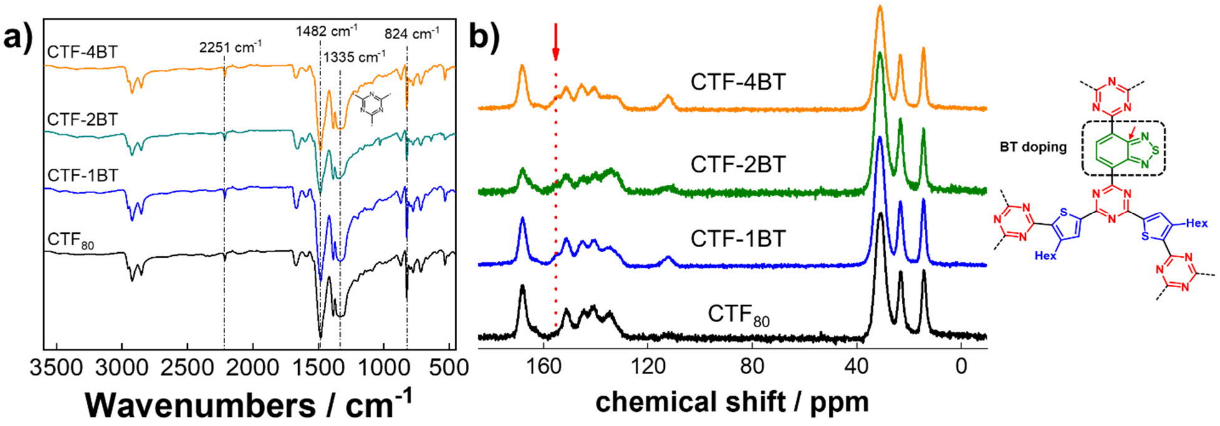

Figure 39. Comparison of FTIR spectra (a) and ^{13}C CP-MAS NMR spectra (b) of CTF-NPs with different BT content.

The optical properties of the CTF nanoparticles were then characterized by UV/Vis diffuse reflection (DR) measurements. As displayed in **Figure 40a**, the pristine CTF NPs exhibited visible-light absorption, which is considered characteristic of semiconductors. Interestingly, the absorption onset at around 550 nm shifts towards longer wavelengths when increasing the amounts of DCBT. This corresponds to bandgaps of 2.82 eV for the pristine CTF NPs, 2.79 eV for CTF-1BT, 2.76 eV for CTF-2BT and 2.66 eV for CTF-4BT, as derived from Kubelka-Munk-transformed reflectance spectra plots (**Figure 40b**). The color of the materials changes with increasing BT content from yellow to brownish orange (**Figure 40c**).

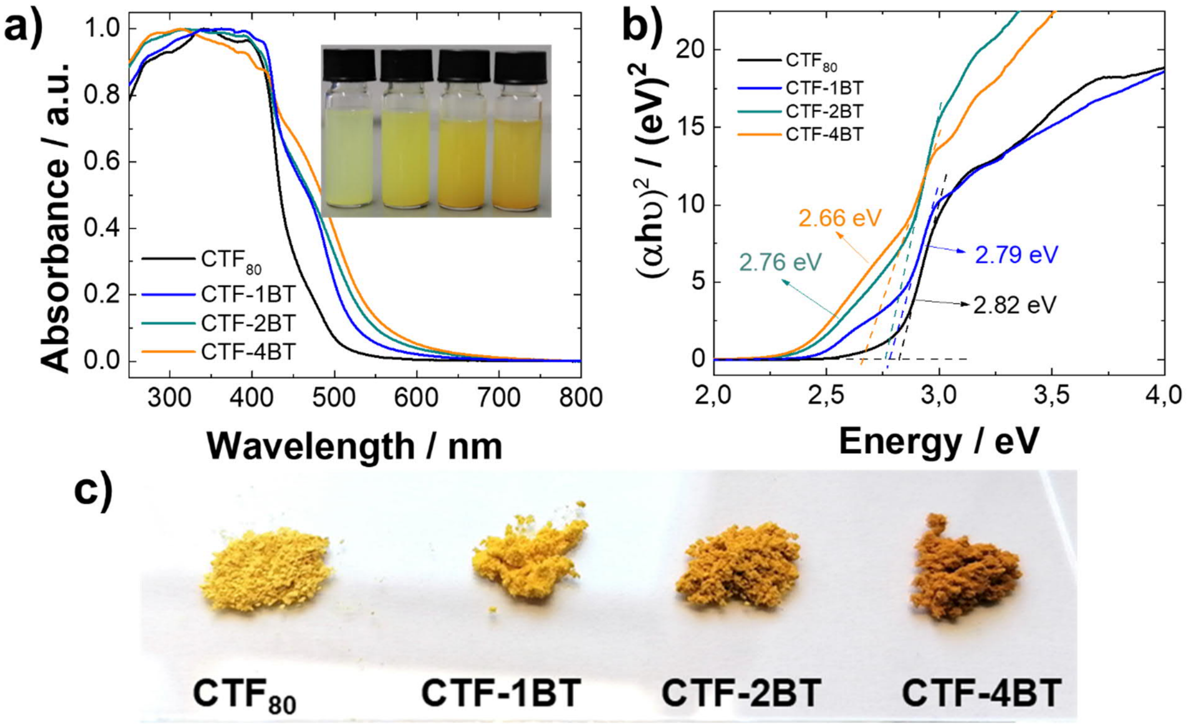

Figure 40. Diffuse reflectance spectra (a), Kubelka-Munk transformed UV/Vis spectra (b), and photograph (c) of CTF nanoparticles with different BT contents.

To assess the location of the lowest unoccupied molecular orbitals (LUMO) of the materials in this study, cyclic voltammetry (CV) measurements were conducted. As depicted in **Figure 41**, a higher BT content shifts the LUMO energy to more positive potentials versus the saturated calomel electrode standard.

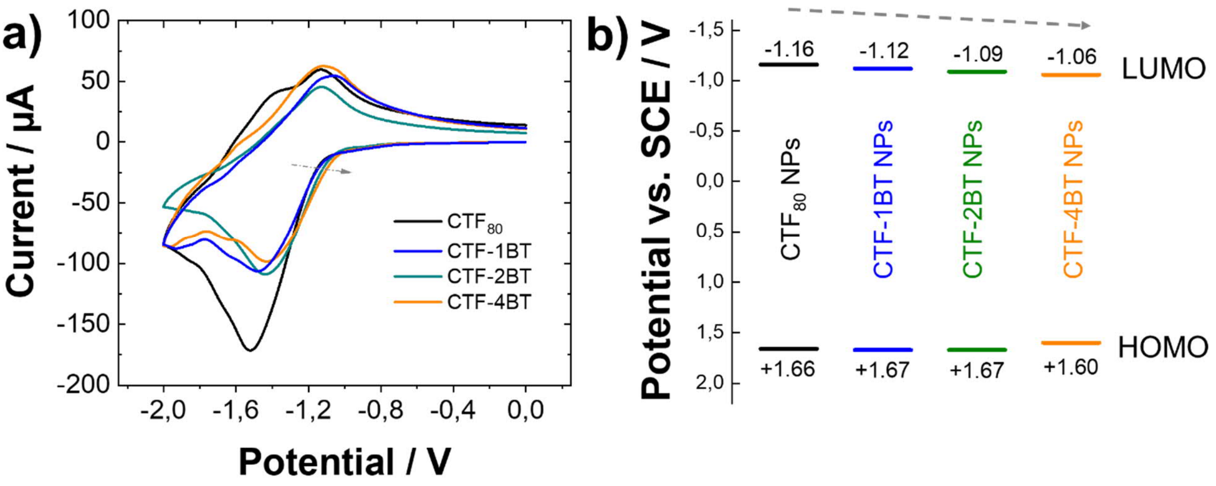

Figure 41. Cyclic voltammetry of CTF-NPs with different BT contents with a scan rate of 100 mV/s in CH_3CN (a) and CV HOMO/LUMO potentials vs. SCE (b). LUMO values result from the CV

onset potentials; HOMO levels are derived by combining CV values and bandgaps from the Kubelka-Munk-transformed diffuse reflectance UV/Vis spectra.

This trend is consistent with B3LYP/6-31G(d) density functional theory (DFT) calculations for triazine structures analogous to the CTFs in this study (**Figure 42**). By adding the strong electron acceptor 2,1,3-benzothiadiazole, D-A charge transfer and electron localization are further promoted.[324] The consequent LUMO energy decrease and the reduction of the HOMO/LUMO gap account for the observations made in the optoelectronic characterizations above.

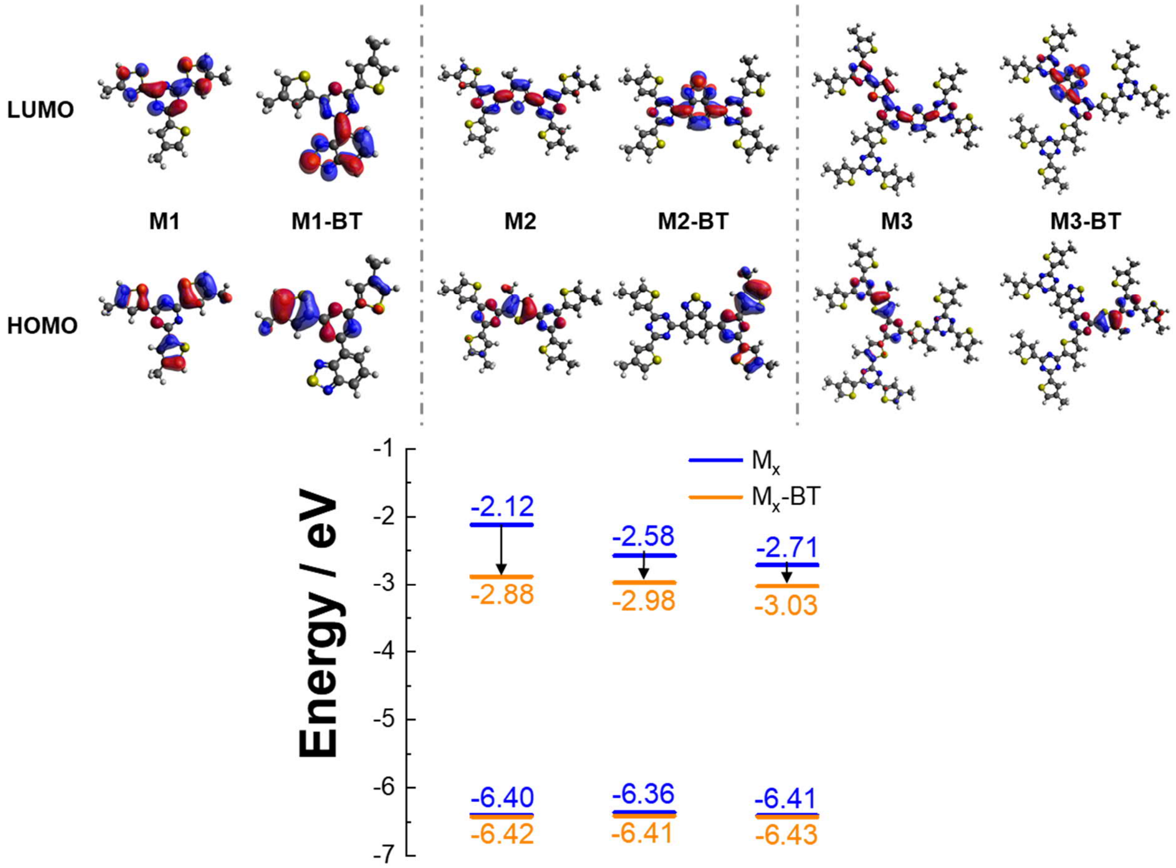

Figure 42. DFT Calculations on the B3LYP/6-31G(d) level for triazine structures analogous to the CTFs in this study. The structures were reduced to smaller units to limit the complexity of the theoretical calculations and were conducted to prove the general trend on frontier orbital energies upon benzothiadiazole incorporation.

Moreover, photoluminescence (PL) spectra with an excitation wavelength of 380 nm were recorded. The PL intensity of the CTF-xBT NPs significantly decreased with the emission maximum shifting to longer wavelengths compared to the pristine CTF NPs (**Figure 43a**).

This could be due to a promoted charge carrier separation in CTF-xBTs, leading to other non-radiative charge recombination pathways being favored. The observed redshift in the catalysts' emission characteristics could be derived from the changed UV/Vis absorption behavior. The LUMO lowering and bandgap shrinking leads to the CTF-xBT NPs emitting from an excited state with lower energy. To further investigate the photogenerated electron separation in CTF-xBT NPs, photocurrent measurements were conducted (**Figure 43b**). A significant increase of photocurrent for CTF-xBT NPs compared to pristine CTF NPs was observed, with CTF-2BT showing the highest photocurrent intensity. This indicates improved light-induced charge mobility within the copolymerized CTF.

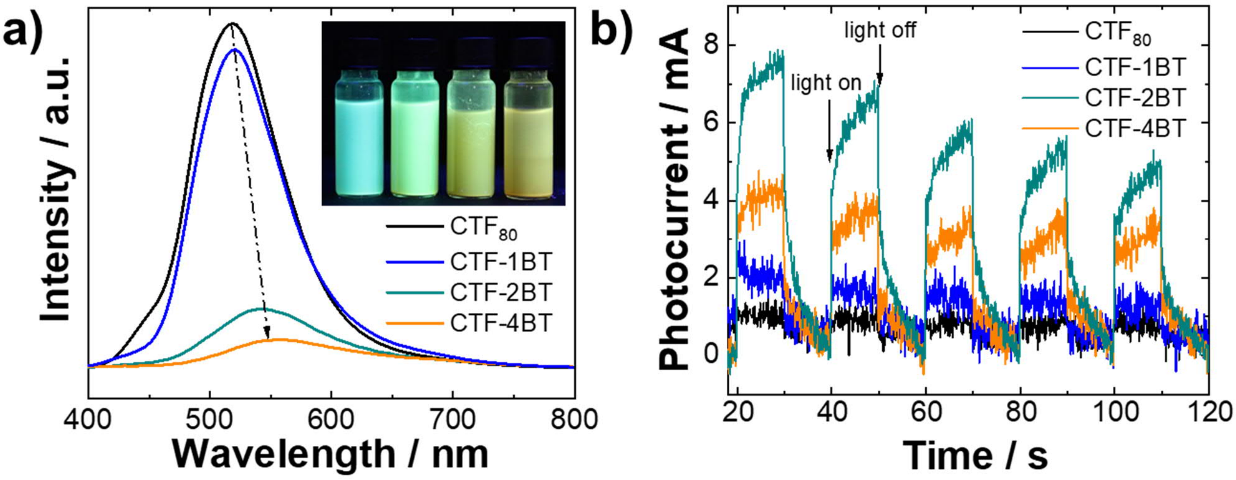

Figure 43. Steady state photoluminescence spectra with λ_{exc}=380 nm (a) and photocurrent measurement under visible-light irradiation for CTF-xBT NPs (b).

Furthermore, electron paramagnetic resonance (EPR) measurements were carried out. As shown in **Figure 44a**, a single Lorentzian line centered at a *g*-value of 2.0031 was observed for all CTF NPs. This signal originates from unpaired electrons in the π-conjugated system. Particularly, the EPR intensity of CTF-2BT showed considerable enhancement compared to the other CTF NPs under visible-light irradiation. This might confirm the finding of the photocurrent measurements, where CTF-2BT could offer more effective photogenerated electrons during the catalytic process.

Time-resolved photoluminescence (TRPL) spectroscopy at an excitation wavelength at 400 nm showed that by adding the strong electron acceptor unit (BT), the fluorescence lifetime decreased proportionally to the increasing BT content (**Figure 44b**). The lifetimes were 0.89 ns for CTF_{80}, 0.57 ns for CTF-1BT, 0.62 ns for CTF-2BT and 0.29 ns for CTF-

4BT, respectively. This indicates that among the BT-containing CTFs, CTF-2BT might possess the best balance of effective charge separation and delocalization (non-radiative recombination of the excitons) within the CTF-xBTs. The change in nanoparticle sizes does not lead to a change in the lifetime of the photoexcited species (**Figure 44c**). The lifetimes are 0.89 ns for CTF_{80}, 0.85 ns for CTF_{180} and 0.87 ns for CTF_{550}.

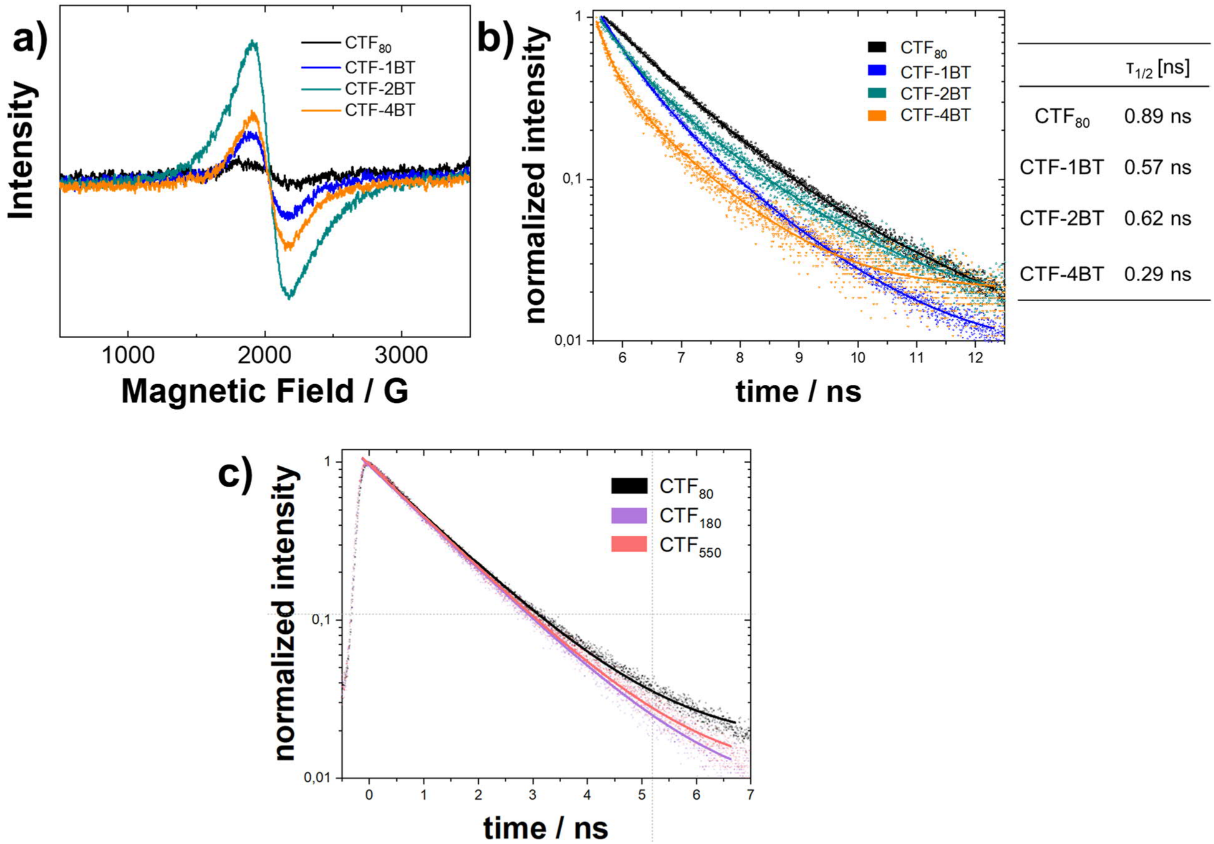

	$\tau_{1/2}$ [ns]
CTF_{80}	0.89 ns
CTF-1BT	0.57 ns
CTF-2BT	0.62 ns
CTF-4BT	0.29 ns

Figure 44. EPR spectra at room temperature with integrated blue light irradiation (a) Time-resolved photoluminescence (TRPL) spectra of the CTF-xBT NPs at an excitation wavelength of 400 nm (b). TRPL) spectra of the different sizes of pristine CTF NPs using the same excitation wavelength.

In summary, the CTF nanoparticles' systematic tunability of electronic and optic properties by benzothiadiazole copolymerization could be proven.

2.2.3 Photocatalysis

We then examined the photocatalytic activity of the CTF NPs in the photocatalytic synthesis of dibenzofuran derivatives. The photocatalytic oxidative [3+2] cycloaddition was first published by Yoon and coworkers, using ruthenium-based homogeneous photocatalysts.[325] The 2,3-dihydrobenzofuran core is a common motif in bioactive natural products and poses a complex photocatalytic synthesis target.[326-330] In a typical experiment, *trans*-anethole was reacted with mequinol in nitromethane using CTF NPs as photocatalyst under blue light irradiation (**Figure 45a**). Ammonium peroxodisulfate was added to act as a terminal oxidant. Pristine CTF_{80} NPs exhibited a highly enhanced photocatalytic activity compared to the bulk material (**Figure 45b-c**). After 10h of reaction time, for example, the reaction yield is increased 8-fold. This effect could be attributed to the decreased particle size and increased number of reactive sites having a positive impact on photocatalytic activity. CTF_{180} and CTF_{550} NPs showed slightly lower activity than CTF_{80}. Looking at the copolymerized nanoparticles, CTF-2BT showed the highest photocatalytic efficiency with a conversion of about 90% after 10h, which equals an 18- and a 2.3-fold increase compared to the bulk and pristine CTF_{80} NPs, respectively.

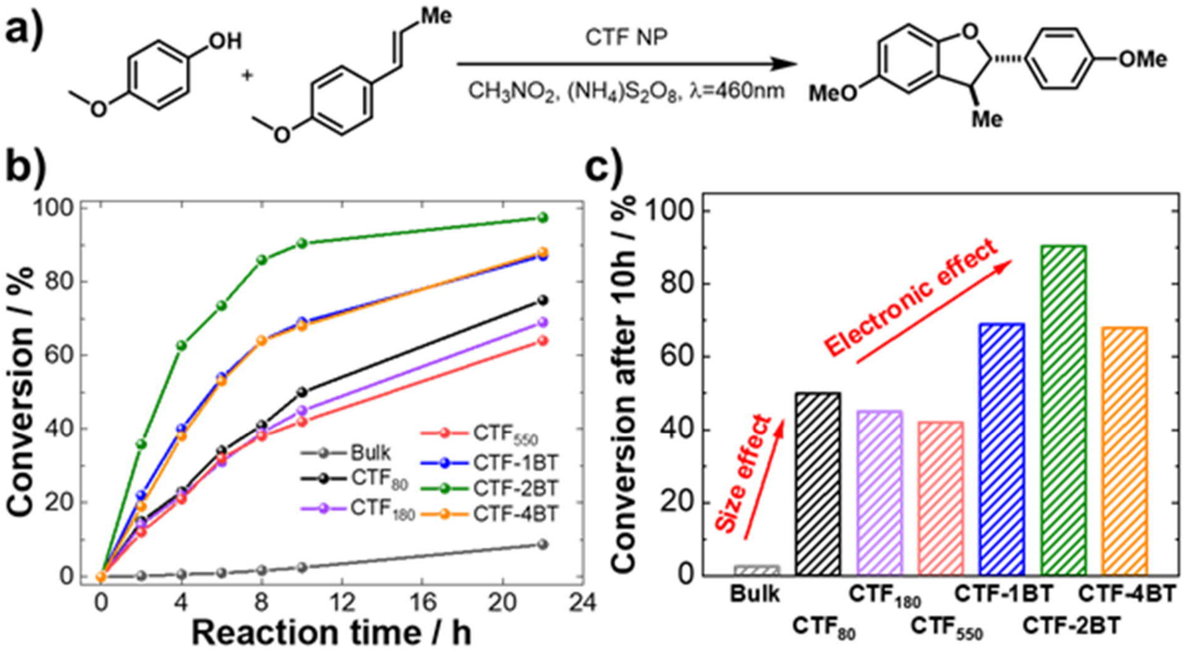

Figure 45. (a) Benchmark [3+2] cycloaddition reaction of *trans*-anethole and mequinol. (b) Kinetic study using different CTF nanoparticles as photocatalysts over the course of 24h and (c) at the specific time point of 10h reaction time.

Considering the similar BET surface area (**Figure 46**) and particle size of the CTF-xBT samples, the superior catalytic efficiency of CTF-2BT could be attributed to improved photoelectronic properties as indicated previously. The amount of copolymerized electron-accepting unit appears to have optimal beneficiary effects on photoelectronic properties at 2 mol% BT since CTF-1BT and CTF-4BT exhibit inferior photocatalytic efficiency in the benchmark reaction. Based on these observations, the nanoscaling (size effect) and the introduction of benzothiadiazole into the CTF backbone (electronic effect) synergistically contribute to a substantial improvement in photocatalytic performance.

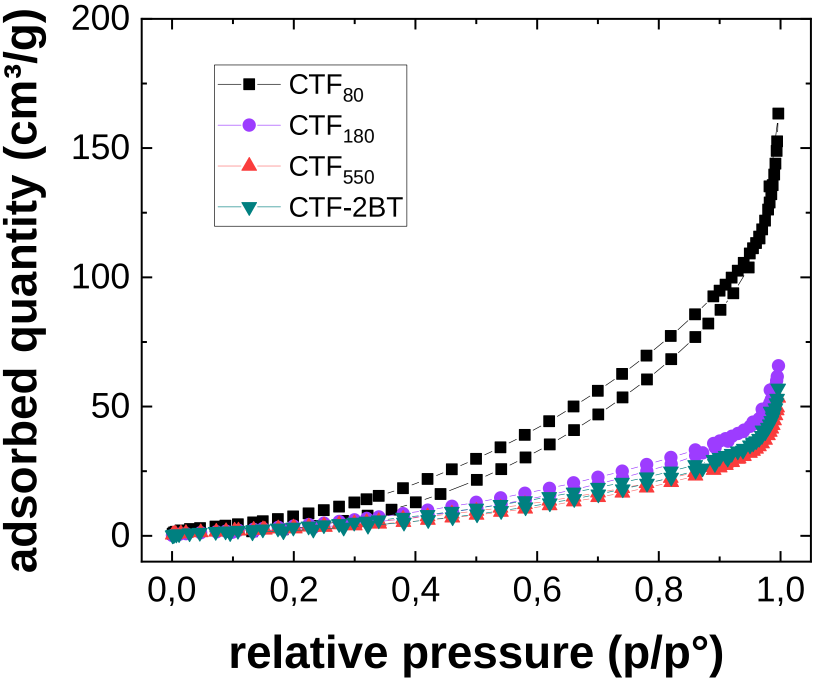

Figure 46. Nitrogen sorption isotherms for CTF NPs. The nitrogen sorption isotherms are typical for non-porous materials. It is supposed that porosity, if present, would not be detectable due to the long alkyl chains of DCHT blocking N_2 from accessing pores.

Control experiments conducted in the absence of light, photocatalyst, and $(NH_4)_2S_2O_8$ only gave trace amounts of product, indicating their indispensable roles in the current catalytic system (**Table 3**).

Table 3. Control reactions of the benchmark reaction. 4-Methoxyphenol (0.1 mmol), anethole (0.15 mmol), $(NH_4)_2S_2O_8$ (0.2 mmol) and photocatalyst (2 mg) were added into solvent (2 mL). The mixture was irradiated with a blue LED lamp (λ = 460 nm) for 22h. The yield was determined by GC-MS with trimethylsilican as an internal standard. ***** In reaction 1 with O_2 as oxidant, multiple products (>4) can be detected by GC-MS. The desired compound is among the products but could not be synthesized selectively.

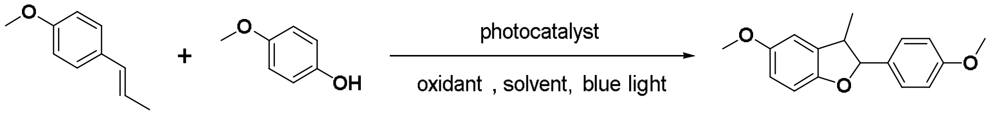

Entry	PC	Solvent	Oxidant	Time (h)	Conv. (%)
1	CTF_{80}	CH_3CN	Air (O_2)	22	40*
2	CTF_{80}	DMF	$(NH_4)_2S_2O_8$	22	<1
3	CTF_{80}	CH_3CN	$(NH_4)_2S_2O_8$	22	41
4	CTF_{80}	DMSO	$(NH_4)_2S_2O_8$	22	0
5	CTF_{80}	DCM	$(NH_4)_2S_2O_8$	22	51
6	CTF_{80}	DCE	$(NH_4)_2S_2O_8$	22	22
7	CTF_{80}	CH_3NO_2	$(NH_4)_2S_2O_8$	22	76
8	Bulk CTF	CH_3NO_2	$(NH_4)_2S_2O_8$	22	9
9	CTF - 1BT	CH_3NO_2	$(NH_4)_2S_2O_8$	22	87
10	CTF - 2BT	CH_3NO_2	$(NH_4)_2S_2O_8$	22	97
11	CTF - 4BT	CH_3NO_2	$(NH_4)_2S_2O_8$	22	89

Entry	PC	Light	Oxidant	Scavengers	Time (h)	Conv. (%)
1	-	+	+	-	22	3
2	+	-	+	-	22	<1
3	+	+	-		22	9
4	+	+	+	$CuCl_2$	22	95
5	+	+	+	KI	22	2

The catalytic mechanism is proposed in accordance with the literature (**Figure 47**) and was supported by scavenger experiments employing $CuCl_2$ as electron and KI as hole scavengers.[325] Upon visible-light irradiation, the excited photocatalyst oxidizes the phenol and generates a corresponding radical cation. Through hydrogen abstract transfer (HAT), the molecule is converted to a resonance-stabilized phenoxonium cation, which reacts with anethole to give the desired dibenzofuran. With its high oxidizing potential, $S_2O_8^{2-}$ quenches the generated excited electrons from the photocatalyst and closes the catalytic cycle.

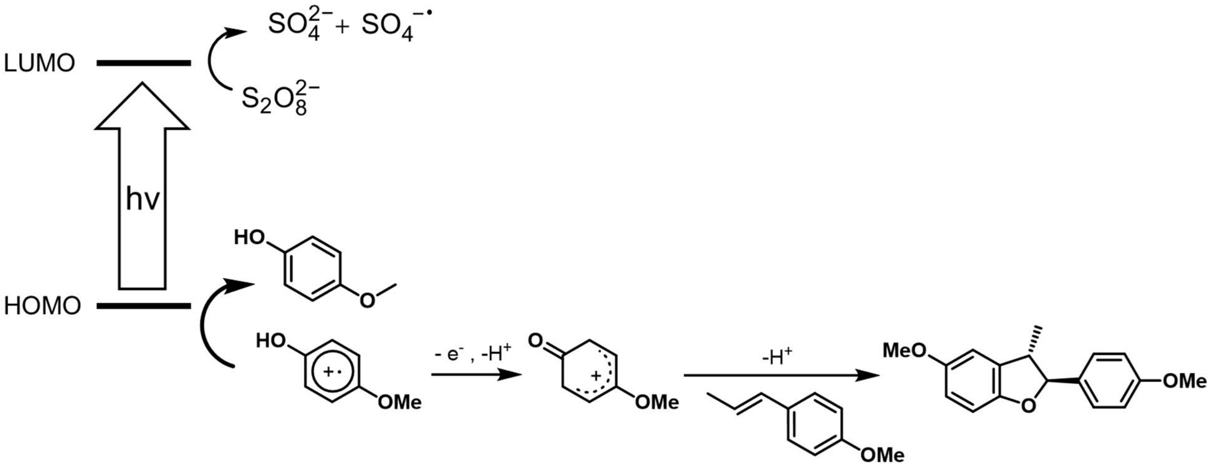

Figure 47. Proposed mechanism of the oxidative [3+2] cycloaddition on CTF NPs.

The apparent quantum yield (AQY) in the reaction is wavelength-dependent and shows a maximum of 1.89% (**Figure 48**) at 385 nm for CTF-2BT.

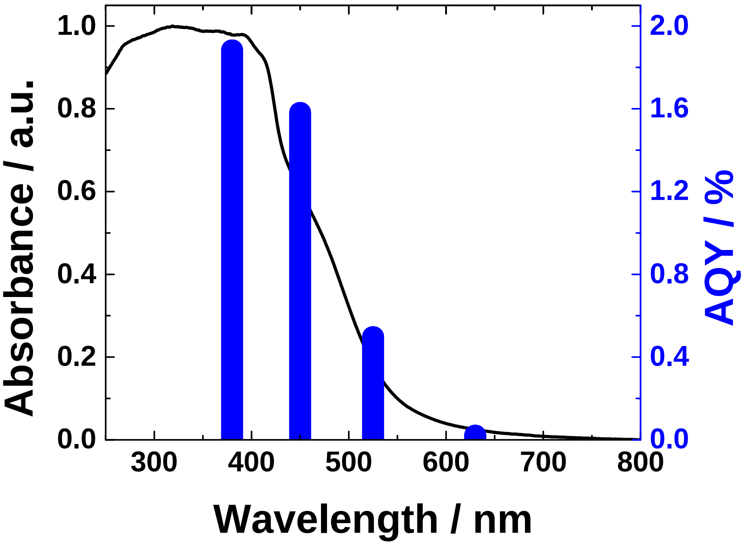

Figure 48. Apparent quantum yield (AQY) for CTF-2BT when irradiated at four different wavelengths.

Additionally, recycling experiments demonstrated that CTF-2BT could be used for five reaction cycles without apparent loss of its catalytic efficiency. No noticeable change in

FTIR, UV/Vis DR spectra, and morphology could be observed (**Figure 49**). The heterogeneous photocatalyst, therefore, reveals excellent stability and recyclability in its photocatalytic application.

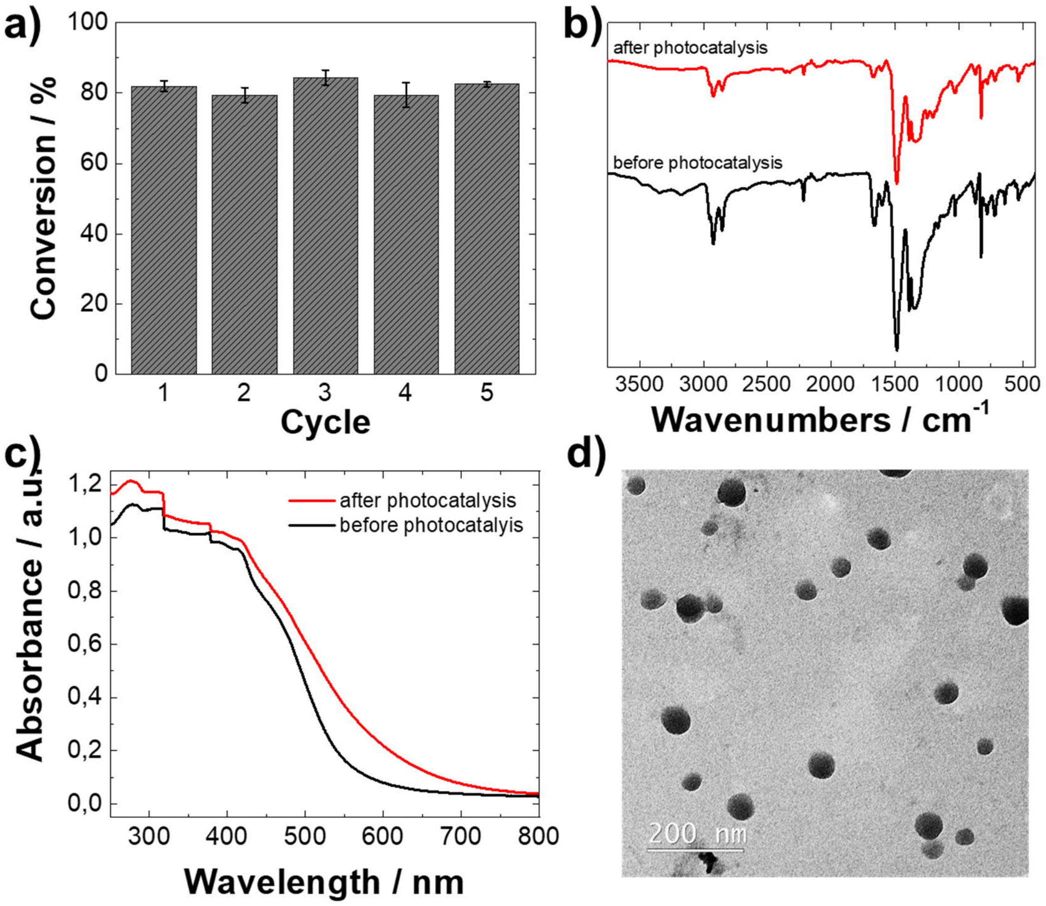

Figure 49. Bar diagram of yields after 24h of reaction using CTF_{80} as photocatalyst in the benchmark reaction. The error bar represents two independent measurements. UV/Vis and IR spectra before and after (b,c) and TEM image after the application (d).

The versatility of the photocatalytic material was investigated by employing different alkenes and phenols in the cycloaddition reaction (**Figure 50a**). Apart from depicted synthesis, further organic photoredox reactions could be catalyzed using the nanoparticle catalyst. Furthermore, as shown in **Figure 50b**, dehalogenation of α-chloroacetophenone, hydroxylation of 4-biphenylboronic acid, and benzimidazole formation from *o*-phenylenediamine as examples of photoredox reactions could be catalyzed with excellent yields of above 95%. This demonstrates the general applicability of the CTF nanoparticles in the application as photocatalysts for organic photoredox reactions.

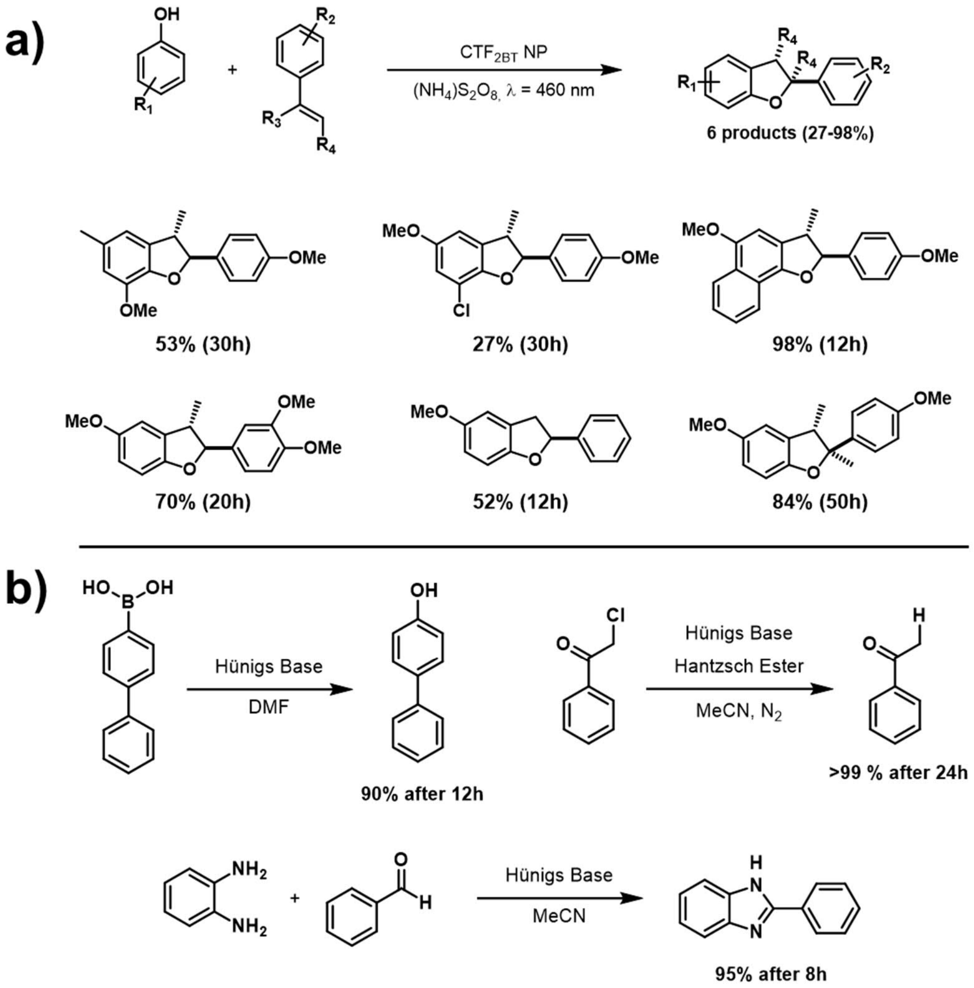

Figure 50. Overview of the substrate scope for different 2,3-dibenzofurans (a) and three further redox reactions (b) catalyzed using CTF-2BT NPs. Detail on synthetic procedures is given in the experimental subchapter.

2.2.4 Conclusion

In conclusion, we report the size-controlled confinement synthesis of covalent triazine framework nanoparticles and their application in organic photoredox catalysis. The CTF nanoparticles were obtained with uniform size distribution and could be varied in diameter between 80 and 550 nm. Additionally, the optoelectronic properties of the CTF NPs could easily be tuned by copolymerizing electron-withdrawing benzothiadiazole units. The photocatalytic activity of the CTF NPs was tested in the oxidative [3+2] cycloaddition of *trans*-anethole and mequinol as benchmark reaction. Both the decreased particle size and the modified photoelectronic properties through BT-introduction synergistically contributed to its superior photocatalytic efficiency compared to the bulk CTF material. Moreover, the CTF NPs could be employed as efficient photocatalyst in further dibenzofuran syntheses as well as dehalogenation, hydroxylation, and benzimidazole formation reactions. In summary, the materials depict a compelling example for the morphological, compositional, and electronic engineering of advanced polymer-based photocatalysts. We believe that this study could pave the way for defined nanometer-sized CTF materials in photocatalytic applications. Furthermore, the innovative and mild assembly route to obtain CTF nanoparticles could be adapted using various monomers and, therefore, be relevant for a broader application range.

2.2.5 Experimental details

Materials and methods

All chemicals and solvents were purchased from commercial sources and used as received unless otherwise noted. Millipore quality (18.2 MΩ cm) water was used throughout.

^{1}H and ^{13}C NMR spectra for all compounds were measured using a Bruker Avance 300 MHz. Solid-state ^{13}C CP MAS NMR measurements were carried out using Bruker Avance II solid-state NMR spectrometer operating at 300 MHz Larmor frequency equipped with a standard 4mm magic angle spinning (MAS) double resonance probe head. Solid-state diffuse reflectance UV-Vis absorption and fluorescence spectra were recorded on a Perkin Elmer Lambda 100 spectrophotometer and J&M TIDAS spectrofluorometer at ambient temperature, respectively. Gas sorption was measured using a Micromeritics Tristar II Plus with samples degassed for 12h at 120°C under vacuum before analysis. Morphology of nanocapsules was examined with a Gemini 1530 (Carl Zeiss AG, Oberkochem, Germany) scanning electron microscope (SEM) operating at 0.35 kV and a Jeol 1400 (Jeol Ltd, Tokyo, Japan) transmission electron microscope (TEM) operating at an accelerating voltage of 120 kV. SEM and TEM samples of nanocapsules were prepared by casting the diluted dispersion on silicon wafers and carbon layer-coated copper grids, respectively. X-Ray diffraction (XRD) was conducted on a Philips PW 1820 diffractometer with monochromatic Cu Kα radiation. PL lifetime measurements were conducted with a FluoTime200 time-correlated single-photon counting setup. Samples were excited with a blue laser at 380 nm, which was controlled by PicoQuant PDL 800-

D. The signal was detected using a micro-channel plate photomultiplier tube connected to the PicoHarp 300 time-correlated single-photon counting system. PL signals were read at their respective PL emission maxima. Cyclic voltammetry measurements were carried out on a Metrohm Autolab PGSTAT204 potentiostat/galvanostat with a three-electrode-cell system: glassy carbon electrode as the working electrode, $Hg/HgCl_2$ electrode as the reference electrode, platinum wire as the counter electrode, and Bu_4NPF_6 (0.1 M in acetonitrile) as supporting electrolyte with a scan rate of 100 mV s^{-1} in the range of 0 eV to 2 eV. All DFT calculations were carried out with the Gaussian 09 package.[290] The structures were optimized at the B3LYP level of theory[331] with the basis set of 6-31G*.[332-333] TD-DFT results were obtained from excited-state calculations at the same level of theory. Thermogravimetric analysis (TGA) was conducted in a nitrogen atmosphere with temperature increasing from room temperature to 800 °C at a rate of 10 K/min. FTIR measurements were conducted with a Varian 1000 FTIR spectrometer. EPR (Electron Paramagnetic Resonance) was measured on a Magnettech Miniscope MS200 spectrometer at room temperature. GC-MS measurements were performed on a Shimadzu GC-2010 plus gas chromatograph and QP2010 ultra mass spectrometer setup (fused silica column Phenomenex, Zebron 5-ms nonpolar, flame ionization detector).

Synthesis of monomers

2,5-Dicyano-3-hexylthiophene: $K_4[Fe(CN)_6] \cdot 3\ H_2O$ is dried under vacuum (ca. 0.01 mbar) at 60 °C for 1h. To a dry 25 mL Schlenk tube was added $K_4[Fe(CN)_6] \cdot 3\ H_2O$ (442 mg, 1.20 mmol, 0.40 eq.), CuI (114 mg, 0.60 mmol, 0.20 eq.), 2,5-dibromo-3-hexylthiophene (1.02 g, 3.00 mmol, 1.00 eq.) and 1-methylimidazole (5 mL). After degassing the solution by Ar bubbling for 20min, the tube was heated to 140 °C for 24h with an oil bath. After cooling to room temperature, the resulting mixture was extracted with dichloromethane (3 x 10 mL). The combined organic phases were washed with brine (30 mL) and dried over anhydrous Na_2SO_4. After filtration and rotary evaporation of solvents, the brown oil residue was purified by column chromatography on silica gel (petroleum ethyl acetate/petrol ether 0:1 to 1:10). A colorless oil (256 mg, 37%) resulted.

^{1}H NMR (300 MHz, $CDCl_3$) δ 7.46 (s, 1H), 2.80 (t, 2H), 1.65 (q, 2H), 1.31 (m, 6H) and 0.88 (t, 3H) ppm. ^{13}C NMR (75 MHz, $CDCl_3$) δ 154.59, 137.61, 115.17, 112.36, 112.12, 111.80, 31.45, 30.02, 29.93, 28.77, 22.57 and 14.09 ppm.

Benzo[*c*][1,2,5]thiadiazole-4,7-dicarbonitrile: To a solution of 4,7-dibromobenzothiadiazole (2.0 g, 6.8 mmol) in DMF (10 mL), CuCN (1.8 g, 20.4 mmol) was added. The suspension was degassed with nitrogen for 10min followed by heating to 145 °C for 20h. The mixture was allowed to cool to room temperature. Then $FeCl_3 \cdot 6H_2O$ (14 g) in 2 M HCl (32 mL) was added into the reaction solution. The resulting suspension was stirred for an hour. The mixture was extracted with DCM (100 mL × 3). The combined organic phase was washed with Milli Q water, dried with anhydrous $MgSO_4$. The filtrate was concentrated under vacuum and purified through a silica column eluting with hexane/dichloromethane (1:1) to give the titled product as a pale yellow powder (52%). ^1H NMR (300 MHz, $CDCl_3$) δ 8.14 (s, 1H) ppm. ^{13}C NMR (75 MHz, $CDCl_3$) δ 152.56, 134.58, 113.97 and 110.83 ppm.

Preparation of CTF nanoparticles

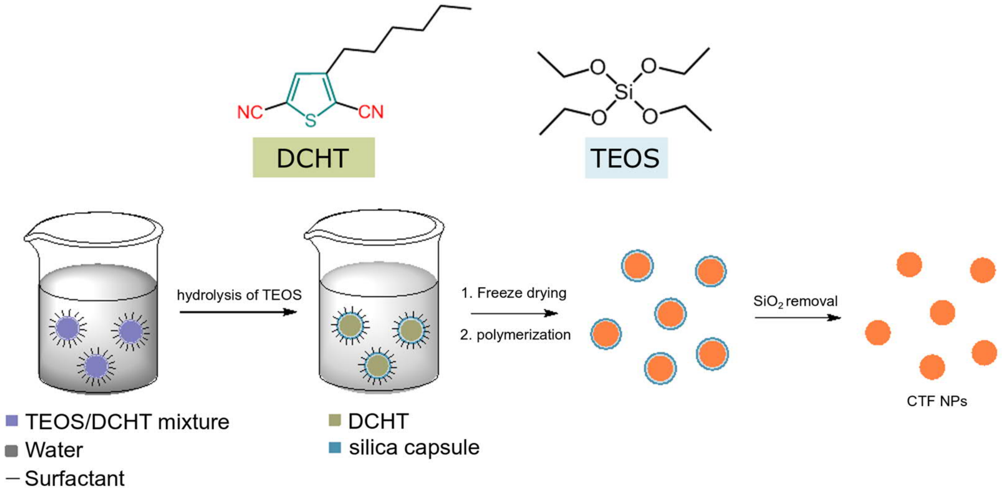

Figure 51. Synthetic route for covalent triazine framework nanoparticles in confinement.

Step 1: Tetraethoxylsilane (TEOS) (0.52 g, 2.5 mmol) and 2,5-dicyano-3-hexylthiophene (0.4 g, 1.83 mmol) were first mixed to form a homogeneous oil phase. Then an aqueous solution of cetyltrimethylammonium chloride (6.2 mg in 8 mL) was poured into the oil mixture under vigorous stirring. The obtained microemulsion was further sonicated for 3min using an ultrasonic tip (Branson 450 W, at 70% amplitude). The resulting miniemulsion was stirred at 1000 rpm for another 24h at room temperature. During this process, the silica capsule was formed by slow hydrolysis of TEOS at the oil-water interface.

Step 2: The freeze-dried particles were directly polymerized under trifluoromethane sulfonic acid (TfOH) at 100°C in a degassed sealed desiccator for 24h. The formed yellow solid was washed with water and diluted aqueous ammonia to remove the TfOH. Further purification was conducted by continuously washing the sample with DCM in a Soxhlet extractor.

Step 3: The resulting yellow powder was stirred with 4M NH_4HF_2, followed by careful washing with water and ethanol. After drying the material at 80 °C under vacuum overnight, CTF NPs were obtained as a yellow to orange powder.

Nanoparticles with larger sizes were synthesized by increasing the volume ratio between the dispersed phase and water phase of the emulsion to two and four times.

The copolymerization of benzo[*c*][1,2,5]thiadiazole-4,7-dicarbonitrile with 2,5-dicyano-3-hexylthiophene was conducted according to the same procedure. Correspondingly, 1, 2, or 4 mol% of the BT monomer was added when forming the homogeneous oil phase with TEOS. The synthesis was then continued as described above. The resulting nanoparticle samples are denoted as CTF-1BT, CTF-2BT, and CTF-4BT.

In a control experiment, chloroform (260 µL, 3.25 mmol) was used instead of DCHT as an oil phase. The above procedure was followed. After freeze-drying and evaporation of all solvents, TEM pictures (**Figure 37**) were taken.

Preparation of bulk CTF

A vial of 2,5-dicyano-3-hexylthiophene (100 mg) was placed into a conical flask, in which there was another vial with trifluoromethanesulfonic acid (0.3 mL). The conical flask was degassed with nitrogen and sealed, followed by heating to 100 °C in a sand bath for 24h. After cooling down to room temperature, the product was immersed in water and washed well with an ammonia solution (10%) and Milli Q water. The resultant material was further purified with Soxhlet extraction with DCM/MeOH (1:1). After drying under vacuum at 80 °C overnight, the polymer (48 mg, 48%) was obtained.

Photocatalytic dibenzofuran syntheses

General procedure: To a 20 mL vial with a magnetic stir bar was added nanoparticle photocatalyst (4 mg), alkene (1.30 eq.), phenol (1.0 eq.), $(NH_4)_2S_2O_8$, and nitromethane. Then the vial was capped, degassed for 5min with nitrogen, and placed under the irradiation of a blue LEDs lamp (λ = 460 nm, 0.061 W/cm^2). The reaction mixture was stirred at room temperature. The conversion and yield were determined by GC-MS with trimethylsilan as an internal standard. Afterward, the mixture was transferred to a separatory funnel containing DCM and H_2O (v/v, 1/1). The organic layers were separated and extracted thrice with DCM. The combined organic layers were washed with brine, dried over anhydrous Na_2SO_4, and concentrated by rotary evaporation. The crude product was purified *via* column chromatography on silica using EtOAc/hexane as elute to afford the pure compound.

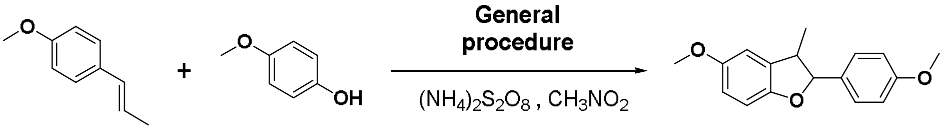

5-Methoxy-2-(4-methoxyphenyl)-3-methyl-2,3-dihydrobenzofuran: 4-Methoxyphenol (12.4 mg, 0.10 mmol), anethole (0.15 mmol, 22.2 mg), $(NH_4)_2S_2O_8$ (456 mg, 0.20 mmol) and photocatalyst (2 mg) were added into CH_3NO_2 (2 mL). The mixture was irradiated under N_2 for 22h. The crude product was purified by silica chromatography (EtOAc/Hex = 5:95) to afford the product as a colorless oil (26.2 mg, 97%). ^{1}H NMR (300 MHz, $CDCl_3$) δ 7.36 (d, 2H), 6.92 (d, 2H), 6.74 (m, 3H), 5.08 (d, 1H), 3.82 (s, 3H), 3.79 (s, 3H), 3.42 (m, 1h) and 1.38 (d, 3H). ^{13}C NMR (75 MHz, $CDCl_3$) δ 159.79, 154.56, 153.42, 133.26, 132.85, 127.78, 114.15, 113.02, 110.24, 109.48, 92.73, 56.19, 55.45, 45.81 and 17.73 ppm.

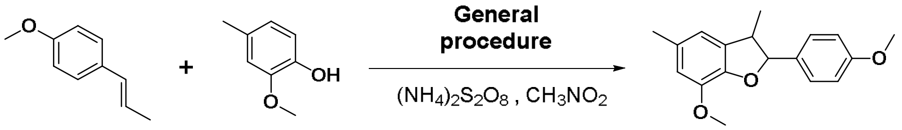

7-Methoxy-2-(4-methoxyphenyl)-3,5-dimethyl-2,3-dihydrobenzofuran: 2-methoxy-4-methyl-phenol (13.8 mg, 0.10 mmol), anethole (22.2 mg, 0.15 mmol), $(NH_4)_2S_2O_8$ (456 mg, 0.20 mmol) and photocatalyst (2 mg) were added into CH_3NO_2 (2 mL). The mixture was irradiated under N_2 for 30h. The crude product was purified by silica chromatography (EtOAc/Hex=10:90) to afford the titled product as a colorless oil (15.1 mg, 53%). ^{1}H NMR (300 MHz, $CDCl_3$) δ 7.40 (d, 2H), 6.93 (d, 2H), 6.64 (d, 2H), 5.15 (d, 1H), 3.91 (s, 3H), 3.84 (s, 3H), 3.47 (m, 1H), 2.33 (s, 3H) and 1.40 (d, 3H) ppm. ^{13}C NMR (75 MHz, $CDCl_3$) δ 159.61, 145.26, 143.86, 133.07, 132.63, 131.01, 127.87, 116.13, 113.87, 112.39, 93.13, 55.99, 55.28, 45.81, 21.31 and 17.79 ppm.

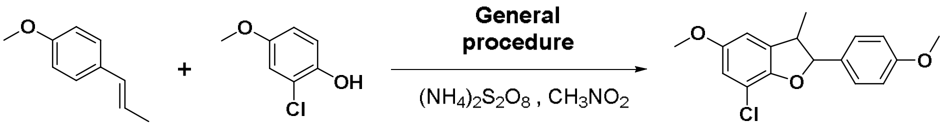

7-Chloro-5-methoxy-2-(4-methoxyphenyl)-3-methyl-2,3-dihydrobenzofuran: 2-chloro-4-methoxyphenol (34.5 mg, 0.20 mmol), anethole (44.4 mg, 0.30 mmol), $(NH_4)_2S_2O_8$ (912 mg, 0.40 mmol) and photocatalyst (3 mg) were added into CH_3NO_2 (3 mL). The mixture was irradiated under N_2 for 30h. The crude product was purified by silica chromatography (EtOAc/Hex=10:90) to afford the titled product as a colorless oil (16.4 mg, 27%). ^{1}H NMR (300 MHz, $CDCl_3$) δ 7.36 (d, 2H), 6.92 (d, 2H), 6.73 (d, 1H), 6.63 (d, 1H), 5.16 (d, 1H), 3.82 (s, 3H), 3.77 (s, 3H), 3.47 (m, 1H) and 1.38 (d, 3H) ppm. ^{13}C NMR (75 MHz, $CDCl_3$) δ 159.92, 154.81, 149.45, 134.52, 132.06, 127.88, 114.56, 114.16, 113.22, 109.24, 93.16, 56.30, 55.45, 46.52 and 17.75 ppm.

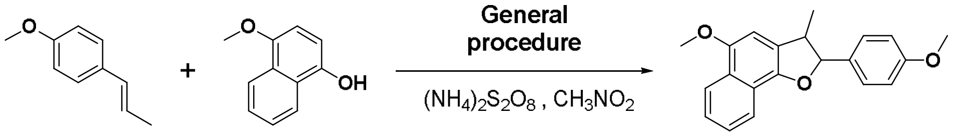

5-Methoxy-2-(4-methoxyphenyl)-3-methyl-2,3-dihydronaphtho[1,2-*b*]furan: 4-methoxynaph-thalen-1-ol (17.4 mg, 0.10 mmol), anethole (22.2 mg, 0.15 mmol), $(NH_4)_2S_2O_8$ (456 mg, 0.20 mmol) and photocatalyst (2 mg) were added into CH_3NO_2 (2 mL). The mixture was irradiated under N_2 for 12h. The crude product was purified by silica chromatography (EtOAc/Hex = 10:90) to afford the desired product as white solid (31.3 mg, 98%). ^{1}H NMR (300 MHz, $CDCl_3$) δ 8.22 (d, 1H), 7.96 (d, 1H), 7.46 (m, 2H), 7.41 (d, 2H), 6.93 (d, 2H), 6.67 (s, 1H), 5.29 (d, 1H), 3.99 (s, 3H), 3.82 (s, 3H), 3.60 (m, 1H) and 1.48 (d, 3H). ^{13}C NMR (75 MHz, $CDCl_3$) δ 159.72, 150.51, 148.05, 133.65, 127.70, 126.17, 125.66, 125.16, 123.62, 122.63, 121.52, 121.09, 114.17, 100.58, 92.65, 56.25, 55.48, 47.22 and 18.96 ppm.

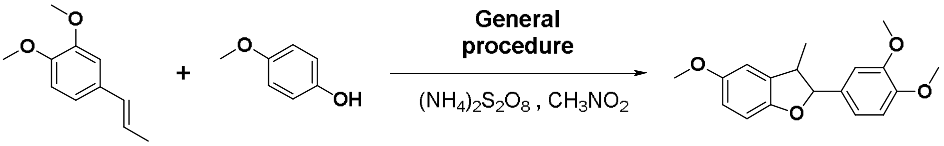

2-(3,4-Dimethoxyphenyl)-5-methoxy-3-methyl-2,3-dihydrobenzofuran: 4-Methoxyphenol (12.4 mg, 0.10 mmol), *trans*-methylisoeugenol (35.6 mg, 0.20 mmol), $(NH_4)_2S_2O_8$ (456 mg, 0.20 mmol) and photocatalyst (2 mg) were added into CH_3NO_2 (2 mL). The mixture was irradiated under N_2 for 12h. The crude product was purified by silica chromatography (EtOAc/Hex=10:90) to afford the desired product as colorless oil (21 mg, 70%). ^{1}H NMR (300 MHz, $CDCl_3$) δ 6.96 (d, 2H), 6.86 (d, 1H), 6.75 (m, 3H), 5.06 (d, 1H), 3.89 (s, 3H), 3.88 (s, 3H), 3.79 (s, 3H), 3.43 (m, 1H) aznd 1.39 (d, 3H) ppm. ^{13}C NMR (75 MHz, $CDCl_3$) δ 157.31, 153.37, 149.41, 149.26, 133.24, 133.16, 119.05, 113.03, 111.13, 110.24, 109.54, 109.35, 93.02, 56.20, 56.09, 56.06, 45.80 and 18.79 ppm.

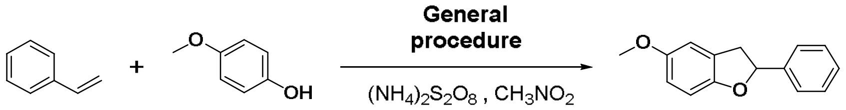

5-Methoxy-2-phenyl-2,3-dihydrobenzofuran: 4-Methoxyphenol (25.0 mg, 0.20 mmol), styrene (41.6 mg, 0.40 mmol), $(NH_4)_2S_2O_8$ (912 mg, 0.40 mmol) and photocatalyst (3 mg) were added into CH_3NO_2 (3 mL). The mixture was irradiated under N_2 for 12h. The crude product was purified by silica chromatography (EtOAc/Hex=5:95) to afford the desired product as colorless oil (23.5 mg, 52%). ^{1}H NMR (300 MHz, $CDCl_3$) δ 7.38 (m, 5H), 6.79 (m, 2H), 6.72 (m, 1H), 5.75 (t, 1H), 3.78 (s, 3H), 3.61 (m, 1H) and 3.21f (m, 1H) ppm. ^{13}C NMR (75 MHz, $CDCl_3$) δ 154.45, 153.93, 142.16, 128.76, 128.11, 127.63, 125.89, 113.16, 111.35, 109.33, 84.36, 56.17 and 39.01 ppm.

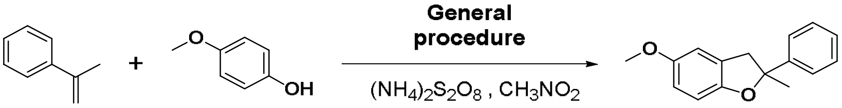

5-Methoxy-2-phenyl-2,3-dihydrobenzofuran: 4-Methoxyphenol (12.4 mg, 0.10 mmol), α-methylstyrene (23.6 mg, 0.20 mmol), $(NH_4)_2S_2O_8$ (456 mg, 0.20 mmol) and photocatalyst (2 mg) were added into CH_3NO_2 (2 mL). The mixture was irradiated under N_2 for 50h. The crude product was purified by silica chromatography (EtOAc/Hex=10:90) to afford the desired product as colorless oil (20.1 mg, 84%). ^{1}H NMR (300 MHz, $CDCl_3$) δ 7.48 (d, 2H), 7.36 (t, 2H), 7.27 (t, 1H), 6.81 (d, 1H), 6.72 (m, 2H), 3.76 (s, 3H), 3.39z (d, 2H) and 1.77 (s, 3H) ppm. ^{13}C NMR (75 MHz, $CDCl_3$) δ 154.30, 153.20, 147.03, 128.48, 127.60, 127.15, 124.67, 113.16, 111.51, 89.32, 56.16, 45.30 and 29.37 ppm.

Photocatalytic recycling experiments

The general procedure was followed for setting up the reactions. The catalyst in the recycling study was the regular CTF NP (70 nm) sample. After completing a reaction cycle after 24h, the conversion was analyzed by GCMS and the reaction mixture was centrifuged at 10 000 rpm for 1min. Then, the supernatant was removed and fresh CH_3NO_2 (2 mL) was added for washing. The centrifugation was repeated and residual CH_3NO_2 was removed. The nanoparticles were then dried in a nitrogen stream for 30min and weighed. Eventual weight loss was accounted for by adjusting the amounts of *trans*-anethole, mequinol, $(NH_4)_2S_2O_8$, and solvent. After degassing, the next reaction cycle was started by LED irradiation.

Photocatalytic dehalogenation

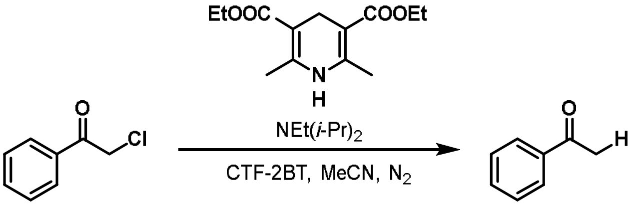

To a 20 mL vial with a magnetic stir bar was added nanoparticle photocatalyst CTF_{2BT} (4 mg), α-chloroacetophenone (77.3 mg, 0.50 mmol, 1.0 eq.), Hünig's base (71.1 mg, 0.55 mmol, 1.1 eq.), Hantzsch ester (253 mg, 1.0 mmol, 2.0 eq.) and acetonitrile (4 mL). Then the vial was capped, degassed by N_2 bubbling, and placed under a blue LEDs lamp (0.061

W/cm^2). The reaction mixture was stirred at room temperature for 8h. The GCMS conversion was found to be 99%. Afterward, the mixture was transferred to a separatory funnel containing DCM and H_2O (v/v, 1/1). The organic layers were separated and extracted thrice with DCM. The combined organic layers were washed with brine, dried over anhydrous $MgSO_4$, and concentrated by rotary evaporation. The crude product was purified *via* column chromatography (Petrol ether/ethyl acetate, 6:1) on silica to afford benzaldehyde (57 mg, 95%). ^{1}H NMR (300 MHz, $CDCl_3$) δ 10.02 (s, 1H), 7.88 (d, 2H), 7.64 (t, 2H), 7.53 (t, 2H) ppm. ^{13}C NMR (75 MHz, $CDCl_3$) δ 188.45, 136.92, 134.59, 129.87, 129.12 ppm.

Photocatalytic hydroxylation of boronic acids

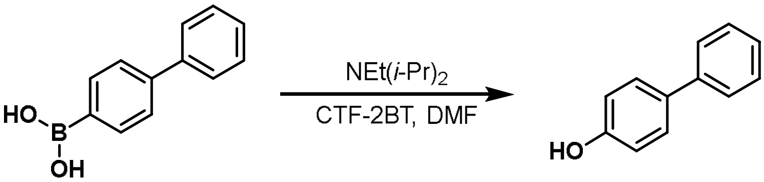

To a 20 mL vial with a magnetic stir bar was added nanoparticle photocatalyst CTF$_{2BT}$ (4 mg), 4-biphenylboronic acid (99.0 mg, 0.50 mmol, 1.0 eq.), Hünig's base (129 mg, 1.0 mmol, 2.0 eq.) and *N,N*-dimethylformamide (4 mL). Then the vial was capped and placed under the irradiation of a blue LEDs lamp (0.061 W/cm^2). The reaction mixture was stirred at room temperature for 12h. The GCMS conversion was found to be 90%. Afterward, the mixture was transferred to a separatory funnel containing DCM and H_2O (v/v, 1/1). The organic layers were separated and extracted thrice with DCM. The combined organic layers were washed with brine, dried over anhydrous $MgSO_4$, and concentrated by rotary evaporation. The crude product was purified *via* column chromatography (Petrol ether/ethyl acetate, 3:1) on silica to afford 4-phenylphenol (71 mg, 83%). ^{1}H NMR (300 MHz, $CDCl_3$) δ 7.55 (d, 2H, 7.49 (d, 2H), 7.42 (t, 2H), 7.31 (t, 1H), 6.91 (d, 2H), 4.92 (s, 1H) ppm. ^{13}C NMR (75 MHz, $CDCl_3$) δ 152.67, 140.89, 135.59, 128.87, 128.54, 127.36, 115.78 ppm.

Photocatalytic benzimidazole formation

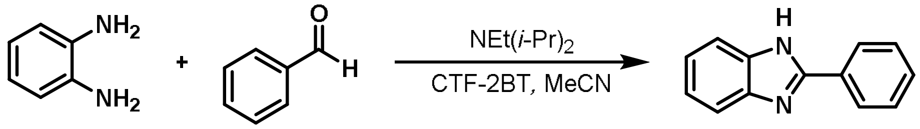

To a 20 mL vial with a magnetic stir bar was added nanoparticle photocatalyst CTF_{2BT} (4 mg), *o*-phenylenediamine (54.1 mg, 0.50 mmol, 1.0 eq.), benzaldehyde (53.1 mg, 0.50 mmol, 1.0 eq.), Hünig's base (129 mg, 1.0 mmol, 2.0 eq.) and acetonitrile (4 mL). Then the vial was capped, degassed by N_2 bubbling, and placed under a blue LEDs lamp (0.061 W/cm^2). The reaction mixture was stirred at room temperature for 15h. The GCMS conversion was found to be 95%. Afterward, the mixture was transferred to a separatory funnel containing DCM and H_2O (v/v, 1/1). The organic layers were separated and extracted thrice with DCM. The combined organic layers were washed with brine, dried over anhydrous $MgSO_4$, and concentrated by rotary evaporation. The crude product was purified *via* column chromatography (Petrol ether/Ethyl acetate, 1:1, 3% of acetic acid was added to the ethyl acetate used) on silica to afford 2-phenylbenzimidazole (71 mg, 73%). ^1H NMR (300 MHz, $CDCl_3$) δ 8.06 (m, 2H), 7.65 (m, 2H), 7.48 (m, 3H), 7.28 (m, 2H), 4.46 (br s, 1H) ppm. ^{13}C NMR (75 MHz, $CDCl_3$) δ 151.65, 139.09, 130.43, 129.81, 129.26, 126.71, 123.22, 115.36 ppm.

Quantum yield experiments

For determining the apparent quantum yield, CTF-2BT was used as a photocatalyst. The general procedure of the photocatalytic dibenzofuran benchmark synthesis was followed. The product formation was studied using four different LEDs (385 nm, 55 mW/cm^2; 450 nm, 50 mW/cm^2; 525 nm, 15 mW/cm^2; 620 nm, 60 mW/cm^2). An area of 1.44 cm^2 was illuminated for 4h. The apparent quantum yields were estimated using the following equation $\Phi_{\mathrm{AQY}} = \frac{\text{number of product molecules formed}}{\text{number of incident photons}} = \frac{n * N_A * h * c}{P * t * \lambda}$ with n = chemical amount, N_A = Avogadro number, h = Planck constant, c = speed of light, P = lamp power, t = irradiation time and λ = wavelength of used lamp.

2.3 Semiconductor nanoplatelets with tunable photocatalytic activity for selective synthesis of azoxy aromatics

In the previous chapter, it has been shown that precise fine-tuning of the electro-optical properties can lead to control and enhancement of photocatalytic activity. While polymeric systems make isolated observations difficult due to the superposition of effects, defined inorganic nanostructures can facilitate detailed investigations. In the following project, the focus is on studying the influence of bandgap and photon absorption on the catalytic performance of photocatalysts using CdSe nanoplatelets as an example. The chapter is based on unpublished results. The manuscript is in preparation and will be submitted promptly. The project is a joint effort of Dr. Henry Halim, Dr. Andreas Riedinger, Prof. Kai Zhang, and me. I carried out the projects' experimental part with the following exception: Henry Halim provided 3, 4, and 5 ML nanoplatelets and performed parts of the UV/Vis and PL characterization.

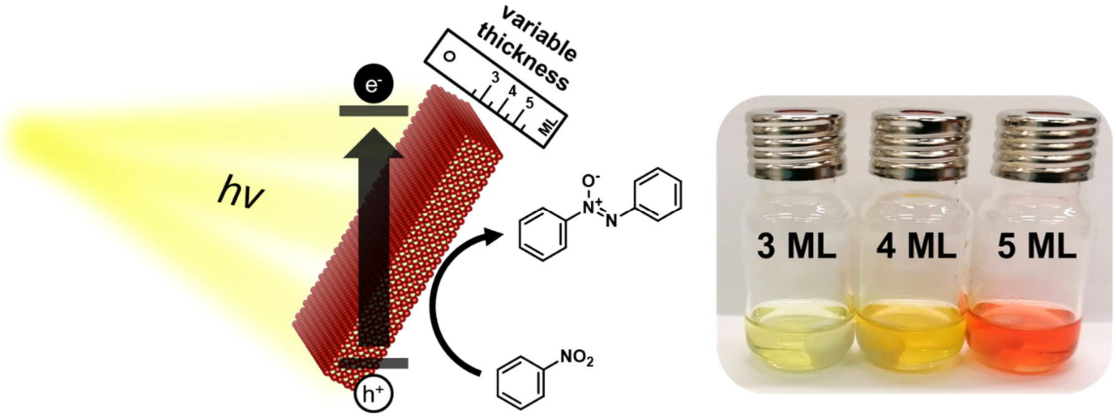

Heterogeneous semiconducting materials for organic photoredox transformations have recently moved into the focus of catalytic research. One of the central challenges is the multifactorial nature of photocatalytic performance, which simultaneously depends on light absorption, charge separation, transport, and transfer properties. The prevalence of irregular material morphologies often makes the derivation of clear conclusions considerably more difficult. Here, we introduce 2D cadmium selenide nanoplatelets (NPLs) with monolayer-precise thickness control as efficient heterogeneous photocatalysts. The materials have a defined morphology and tunable optical properties while exhibiting similar redox properties across all thicknesses. This allows an isolated analysis of the role of photon harvesting for photocatalytic performance in the controlled white-light photoreduction of nitrobenzene towards azoxybenzene. Recyclability and an expanded scope of reaction demonstrated the utility of the synthesized nanocrystal dispersions.

2.3.1 Motivation

Inorganic heterogeneous photocatalytic systems utilize light as a renewable, environmentally friendly, and abundant energy source for many photoreactions.[334-337] Among other factors, light absorption, charge separation and transport within the materials, and electron transfer from the catalyst to the substrate are crucial for photocatalytic efficiency.[338-343] Since fundamental synthetic changes in chemical composition are non-trivial for inorganic materials, the scope for fine-tuning such properties is limited. So far, heteroatom doping,[344-345] metal deposition,[346-349] and hybridization of different semiconductors[350-351] can be considered the most prevalent strategies to precisely tune and adapt inorganic systems to specific photocatalytic applications. Nanostructuring also plays an essential role in inorganic material design for photocatalysis.[352-354] Mostly, however, the focus is on enhancing catalytically active surface area, light-harvesting through scattering, or reducing charge transfer distance to increase efficiency. Only a few works deal with the targeted synthesis of nanostructures at the atomic level for selective control and modification of electrooptic and photocatalytic properties. Related research efforts offer great potential and could expand the scope of inorganic materials to challenging organic photoredox transformations.

Among low-dimensional cadmium chalcogenides, different morphologies have emerged as promising research targets in the field of inorganic functional materials.[355-357] In particular, CdSe nanoplatelets (NPLs) have attracted special interest due to their remarkable properties.[358-360] The colloidal semiconducting particles are of uniform rectangular shape and can be synthesized with precise thickness control at the atomic level. This defined 2D nanostructure results, for example, in spectrally pure fluorescence,[361] high absorption cross-sections,[362] increased energy transfer,[363] and enhanced optical gain.[364] Although structural characteristics, physicochemical properties, and formation mechanism[365] seem to be well understood, studies of potential applications like light-emitting devices,[366] field-effect transistors,[367] solar cells,[363] or lasers[364] are still in their infancy. One area of use that has hardly been considered so far is the photocatalytic utilization of nanoplatelets. While previous work on photocatalytic nanoplatelets focuses mainly on hybrid materials in combination with metallic nanoparticles for photocatalytic hydrogen evolution,[349, 368-369] free-standing nanoplatelets as photocatalysts for organic photoredox reactions are not yet known in the literature.

We present 2D cadmium selenide nanoplatelets as efficient and heterogeneous photocatalysts for visible-light-promoted photoredox transformations in this work. Based on facile and reproducible synthesis protocols, which do not require the use of precious metals, platelet dispersions with 3, 4, and 5 monolayers (ML) thickness can be obtained. Morphological and optophysical characterizations underline the excellent quality and uniformity of the prepared platelets. The precise synthetic control enables tunable optical and redox properties depending on the platelet thickness. The platelets' photocatalytic application could efficiently and selectively catalyze the highly challenging synthesis of azoxybenzene from nitrobenzene. Kinetic studies of the reaction show a direct correlation between the photocatalytic efficiencies and the number of catalyst MLs. Further connections between photocatalytic performance, bandgap, light absorption, as well as charge separation and generation within the platelets are indicated. All reactions are conducted with particularly low catalyst concentrations of about 5×10^{-8} M CdSe, hinting at the superior photocatalytic performance of CdSe NPLs. Control and scavenger experiments support mechanistic correlations. Multiple uses underlined the robustness and photostability of the photocatalysts in recycling experiments. No significant photobleaching effects were observed during the repeating experiments. The scope of the reaction was further investigated by analyzing more nitrobenzene derivatives.

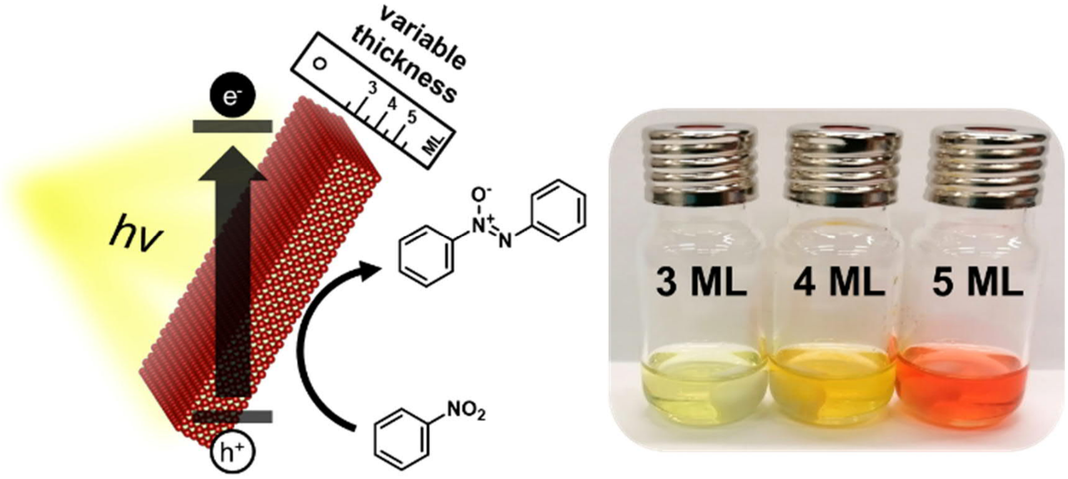

Figure 52. Illustration of the thickness variation concept of the CdSe nanoplatelets and their application in the photocatalytic azoxybenzene synthesis.

2.3.2 Synthesis and characterization

In this study, the nanoplatelets were synthesized *via* liquid-phase reaction in octadecene from cadmium myristate and bis(stearoyl)selenide. Platelet dispersions in hexane with 3, 4, and 5 monolayer thickness were obtained. The preparations could be performed reproducibly and in high yield. Details on synthetic procedures and characterization details are given in the supporting information in chapter 3.3.

The nanoplatelets' morphology was assessed by transmission electron microscopy (TEM) to confirm the successful synthesis. The images show lateral particle sizes in the range of 20 to 35 nm. The NPLs are rectangular with an average lateral area of 130 ± 10 nm^2, 190 ± 40 nm^2, 170 ± 20 nm^2 for 3, 4, and 5 ML NPLs. For the same NPL thickness, the lateral area of the NPLs increases the molar absorption cross-sections linearly.[362] The nanoplatelets mostly stack discontinuously in an edge-up configuration (**Figure 53**). Previous studies have shown that this configuration is thermodynamically favored and facilitated by slow solvent evaporation and high platelet concentrations.[370] In terms of thickness, the colloidal self-assembly gave exclusively the number of MLs intended.

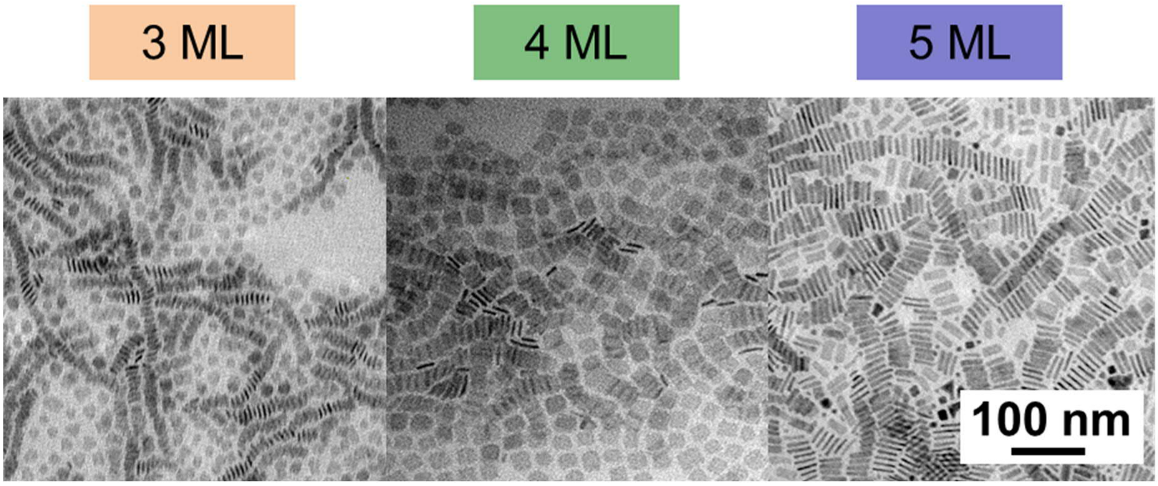

Figure 53. TEM imaging of 3, 4, and 5 ML CdSe nanoplatelets.

For the optical characterization of the NPLs, both UV/Vis spectra and photoluminescence (PL) data were acquired (**Figure 54b**). The light absorption shows a trend from 3 ML to 5 ML NPLs. While 3 ML NPLs absorb light up to about 466 nm, 5 ML NPLs reveal an onset absorption at about 555 nm. 4 ML NPLs lie in between with an absorption beginning at approximately 519 nm. The resulting optical bandgaps are 2.66 eV, 2.39 eV, and 2.24 eV, derived from the Kubelka-Munk transformed UV/Vis plots (**Figure 54b**). The photoluminescence spectra show the fluorescence with emission maxima from 464 nm over 515 nm to 550 nm when excited at the respective absorption maxima, with quantum yields of 0.27, 0.40, and 0.84, respectively. The values correspond to literature examples. The given distinctness of the PL emission is a clear indicator for sample purity, as indicated in literature examples. To ensure that the excited state of the NPLs live long enough for photocatalytic purposes, we measured the time-resolved photoluminescence (TRPL) of the NPLs (**Figure 54c**, **Table 5**). By fitting the decay curves with a double exponential fitting, we determined the effective lifetime of the NPLs to be in a range between 5.3 to 7.1 ns. There are no notable differences between the different ML thicknesses, suggesting that the electrons' recombination rate and holes in the NPLs are similar.

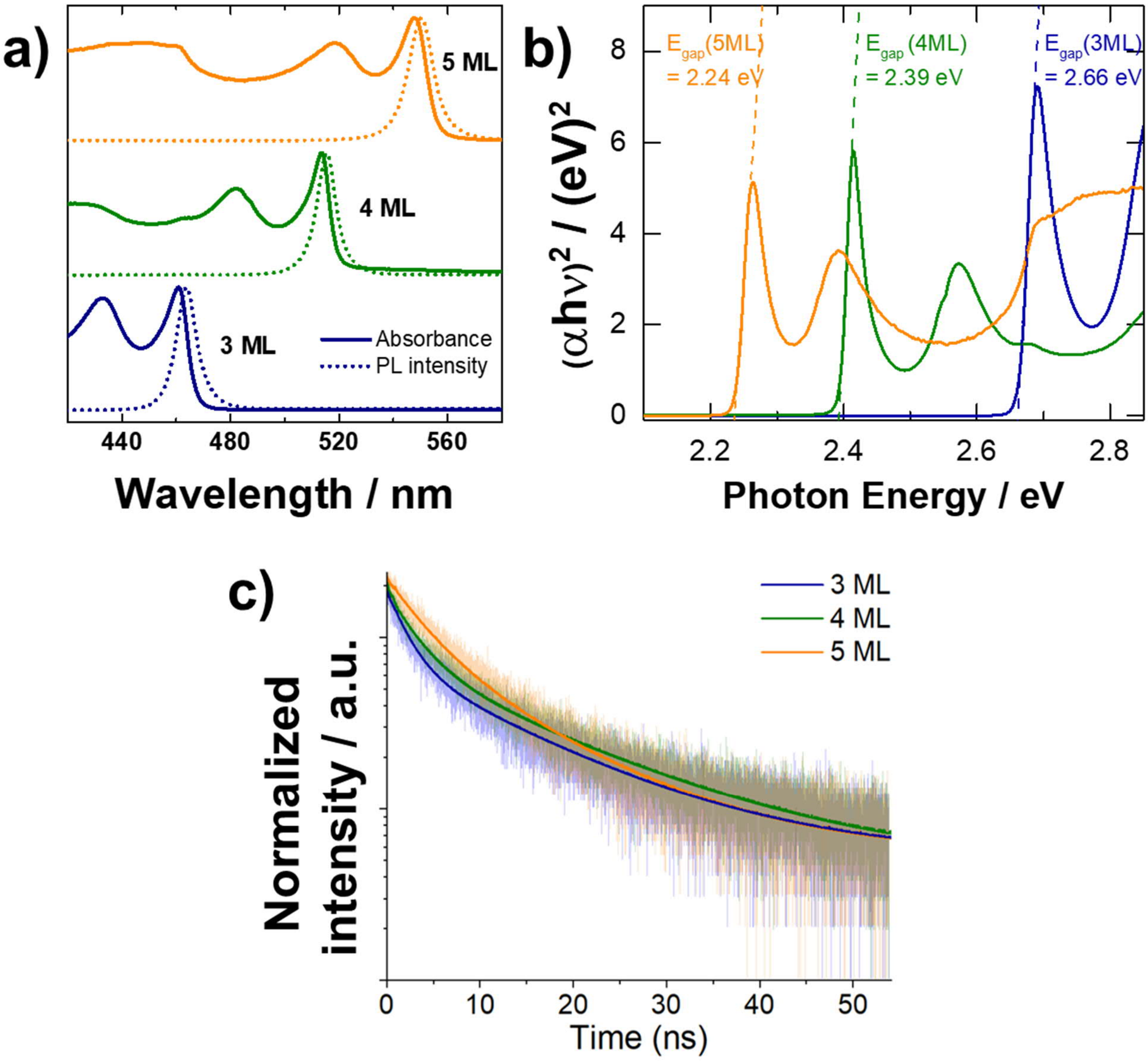

Figure 54. Combined UV/Vis absorption and PL (a) and Kubelka-Munk transformed UV/Vis spectra of nanoplatelets with different thicknesses in n-hexane (b). Normalized PL lifetimes of NPLs with different ML thicknesses. The signals were read at 462 nm, 510 nm, and 550 nm for 3ML, 4ML, and 5ML NPLs. Lifetimes of the NPLs were fitted with a double exponential function.

The electronic properties of the platelets were investigated by cyclovoltammetry (CV, **Figure 55a**). The NPLs were measured in the colloidal state with a saturated calomel reference electrode (SCE) and the conduction band (CB) positions could be determined directly at reducing potentials. 4 ML NPLs have the highest CB with -0.69 eV vs. SCE, followed by 3 ML NPLs and 5 ML NPLs with -0.67 eV and -0.61 eV vs. SCE, respectively. In combination with the bandgaps resulting from the UV/Vis measurement, the valence band (VB) positions can be determined empirically (**Figure 55b**) as 1.99 eV (3 MLs), 1.70

eV (4 MLs), and 1.63 eV (5 MLs). The results are consistent with band edge assessments in the literature. Interestingly, the CB position is hardly affected by the thickness variation. Inamdar *et al.*[371] and Kucur *et al*.[372] have previously measured similar quantum dot systems using cyclic voltammetry. In contrast, Spittel *et al*.[373] identified the band edge positions of CdSe quantum dots and NPLs with potential-modulated absorption spectroscopy (EMAS) – albeit the complications with the bleach model for the NPLs resulting in discrepancies. In general, the data shows that the thickness can precisely vary the NPLs electro-optical properties. The platelets' bandgap shows stepwise positioning over the visible-light range and lead, together with a constant CB edge, to exciting properties.

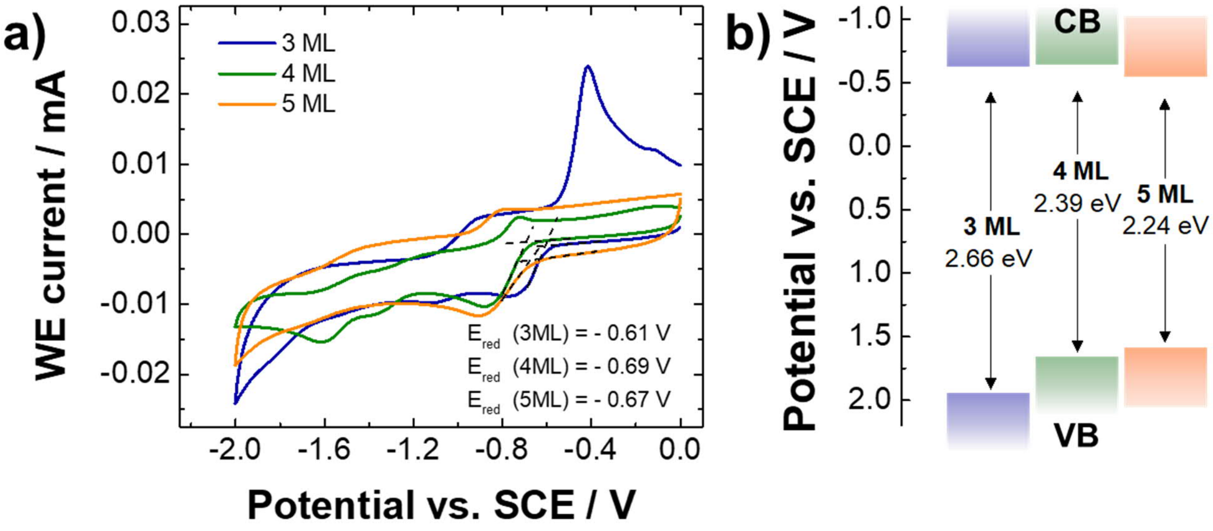

Figure 55. Cyclic voltammetry of nanoplatelets with different ML thickness with a scan rate of 100 mV/s in CH_3CN. CV conduction band potentials vs. SCE were deducted from the onset potential (a). CB and VB positioning derived from cyclovoltammetry and optical absorption (b).

The photocatalytic properties were investigated in detail in the following using the reduction reaction of nitrobenzene to azoxybenzene.

2.3.3 Photocatalysis

The highly challenging reduction of nitroarenes to azoxy aromatics was selected to demonstrate the platelet system's photocatalytic activity. Azoxy compounds are important feedstocks for dye-, electronic-, pigment-, and drug products.[374] The difficulty in the controlled reduction of nitrobenzene lies in the multitude of possible products. Besides azobenzene and azoxybenzene, a reductive pathway from nitrobenzene can also yield aniline, nitrosobenzene, or *N*-phenylhydroxylamine (**Figure 56a**).[375-376] The low-lying CBs and therefore mild reduction potentials of the nanoplatelets upon excitation prevent an over oxidation towards aniline and allow the chemical reaction to be carried out in the first place. While other literature examples have presented considerable success in selectively catalyzing this reaction,[376-377] our focus is on introducing CdSe NPLs as stand-alone photocatalytic materials and the isolated analysis of different photon harvesting abilities for photocatalytic performance.

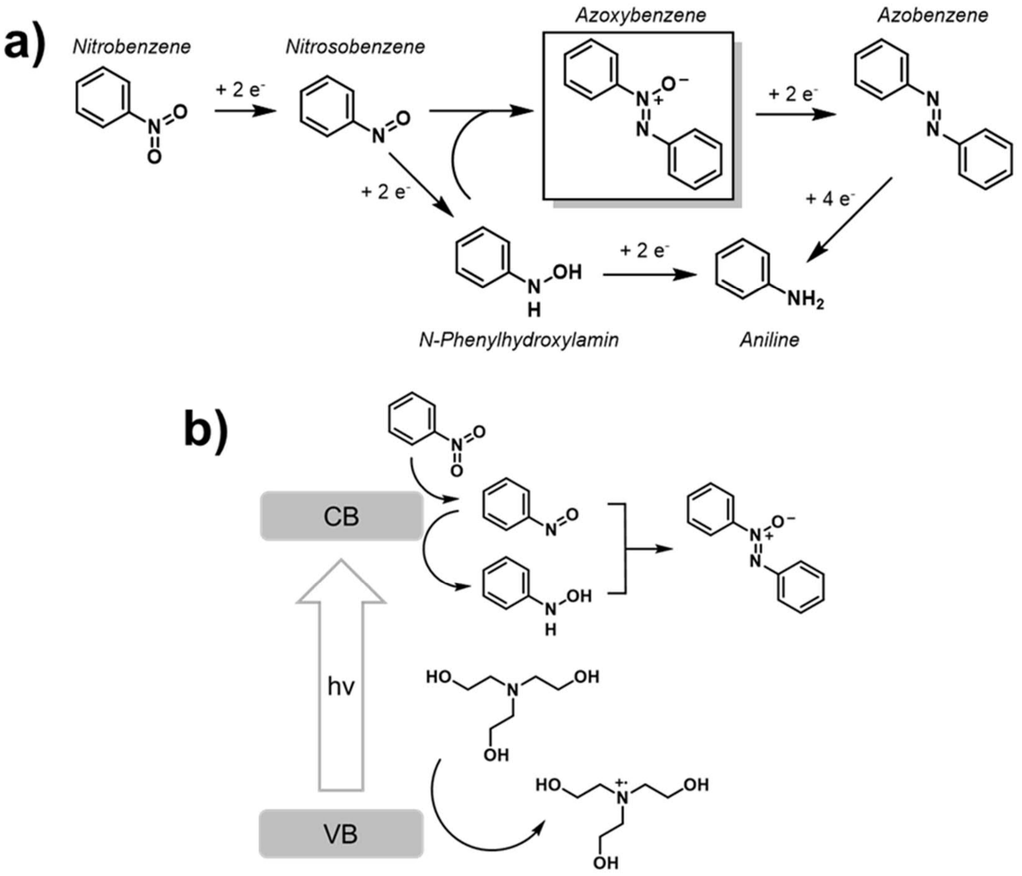

Figure 56. Proposed reaction mechanism and intermediate products of the photocatalytic reduction of nitrobenzene (a). Catalytic cycle involving conduction band and valence band of the photocatalytic CdSe nanoplatelets (b).

3 ML, 4 ML, and 5 ML nanoplates were compared in a kinetic study (**Figure 57**, **Table 6**) with samples taken after 1, 2, 3, 4, 6, 8, 12, and 24h for GC-MS analysis. 5 ML-NPLs yield the highest photocatalytic activity. After 24h, the conversion towards azoxybenzene is 98% with a selectivity of 73%. Selectivity is above 90% throughout the reaction but drops significantly for the last sample taken. This could be due to a further reduction of the azoxy product to the azo compound, which is clearly more prevalent than in the initial samples. While 3 ML and 4 ML NPLs are comparably selective, the conversion after 24h reaches only a maximum of 22% and 54%, respectively.

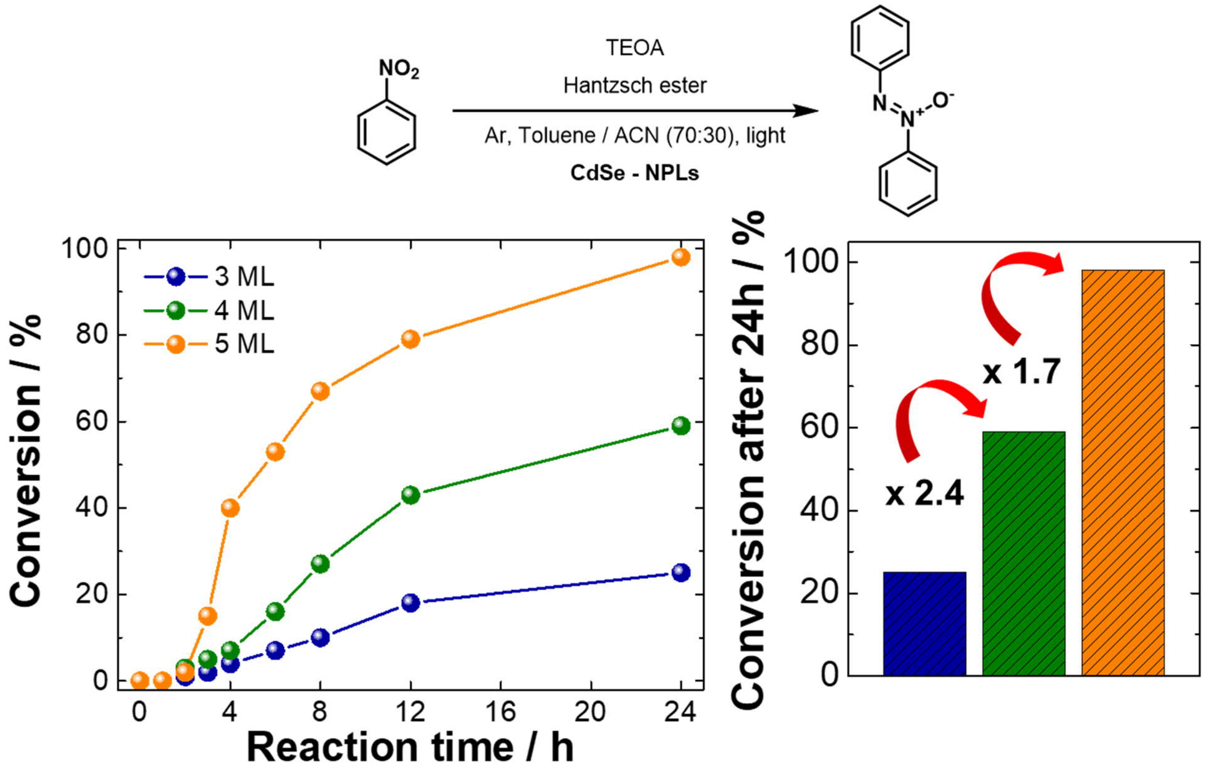

Figure 57. Conversion of nitrobenzene to azoxybenzene at different time points, using NPL photocatalyst of different ML thicknesses and white LED excitation. Reaction conditions: [Nitrobenzene] = 75 mM, [TEOA] = 100 mM, [Hantzsch ester] = 45 mM, toluene/acetonitrile 1.7 mL (70:30), [CdSe NPL] = 1 x 10^{-7} M, white LED lamp (0.16 W/cm^2), room temperature, Argon atmosphere. Conversion determined by GC-MS.

The variation in the product formation rate among the platelets can be attributed to their different absorption behavior. Given the used white light spectrum (**Figure 58**), the thicker 5 ML NPLs can harvest a 2.5-fold multiple of 4 ML NPLs and a 5.8-fold multiple of 3 ML NPLs.

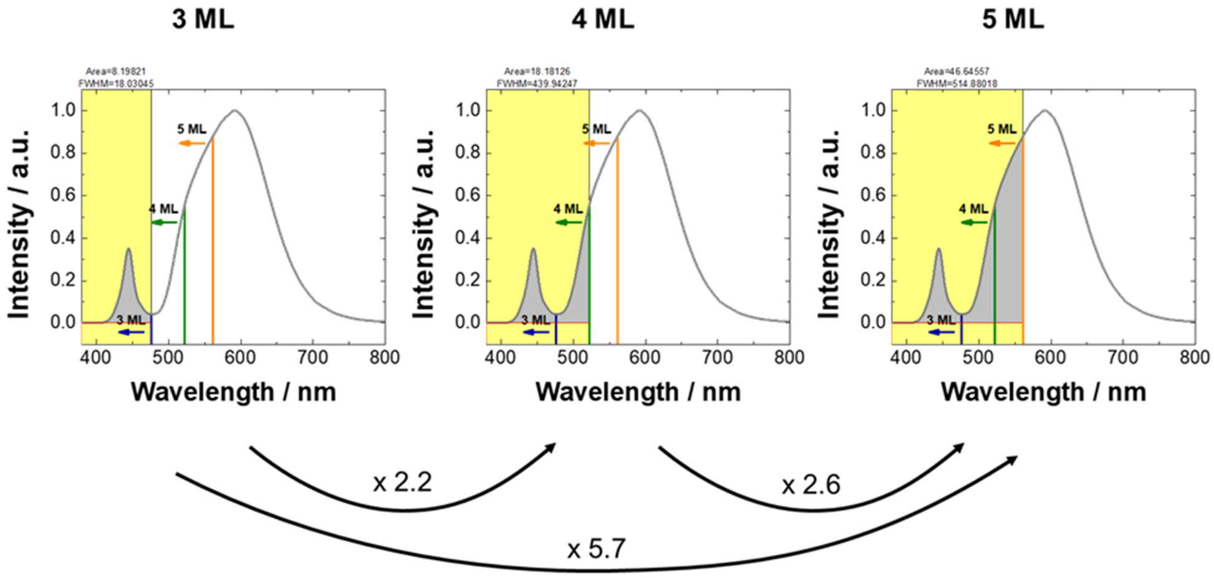

Figure 58. Relative integral covered from the white LED based on the absorption range of the NPLs.

This effect is amplified by the higher PL quantum yields of 5 ML NPLs, allowing more photoexcited charge carriers to catalyze the conversion over the same period. Note that this improved conversion cannot be explained by the increased PL quantum yields alone, as the increase in conversion is larger than the difference in quantum yield (e.g., 4ML vs. 3ML = ~2.5× conversion at 24h, but 1.5× PL quantum yield). The reduction potentials of the conduction bands are similar over all NPLs and cannot be used to clarify the differences in reactivity. All reactions have in common that the product formation rate only increases after a particular time. In the onset of 2 to 4h, no or little product can be detected by GCMS. Relevant increases in product formation only become apparent afterward.

To explain this phenomenon, we further investigated the mechanism of the conversion (**Figure 56b**). Azoxybenzene gradually forms through a two-step reduction reaction where nitrobenzene is converted to azoxybenzene and then reduced to azobenzene depending on the reaction conditions.[376] During the initial stage of this mechanism, there is likely a buildup of the intermediates nitrosobenzene, N-phenylhydroxylamine, and azoxybenzene, before further potential reduction to azobenzene. While we could not detect the first two intermediates in the regular reaction setup, both show up clearly in GC analysis in a concentrated reaction procedure (**Figure 59**).

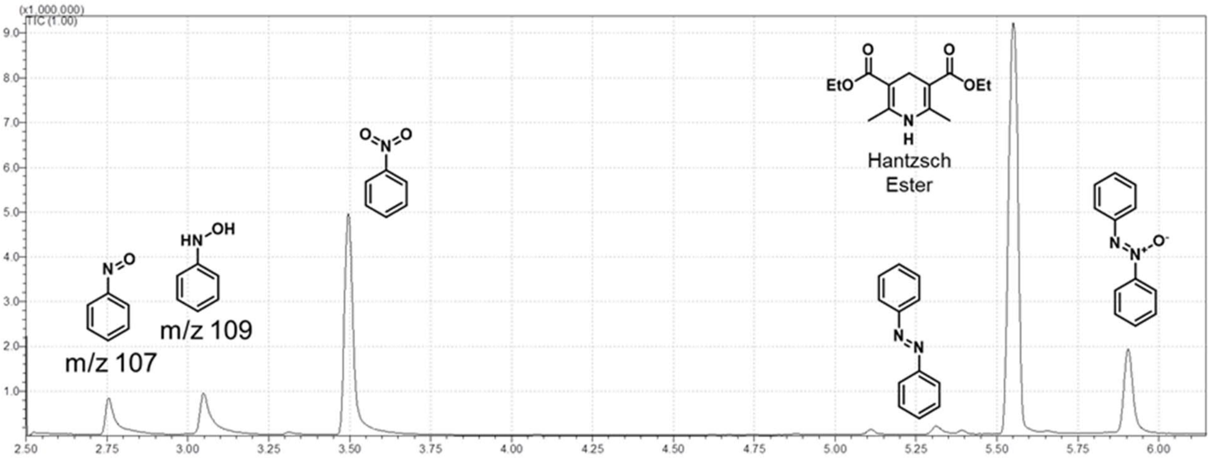

Figure 59. Intermediates nitrosobenzene and *N*-phenylhydroxylamine in the concentrated reaction setup.

To gain more precise mechanistic insights into the reaction and prove the photocatalytic nature of the conversion, control experiments of the model reaction were carried out with the best performing 5 ML photocatalyst (**Table 4**).

Table 4. Screening and control experiments of the photocatalytic reduction of nitrobenzene. [a] Reaction conditions: [Nitrobenzene] = 75 mM, [TEOA] = 100 mM, [Hantzsch ester] = 45 mM, toluene/acetonitrile 1.7 mL (70:30), [CdSe 5 ML NPL] = 5x 10^{-8} M (300µL stock solution), white LED lamp (0.16 W/cm^2), room temperature, Argon atmosphere. [b] Conversion determined by GC-MS. [c] [Aniline] = 75 mM, [d] [$CuCl_2$] = 200 mM [e] toluene 1.7 mL

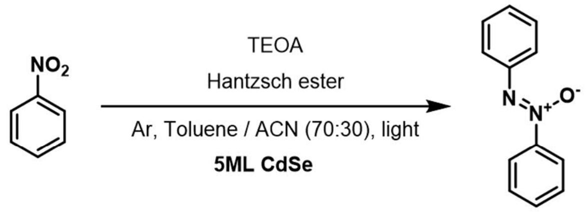

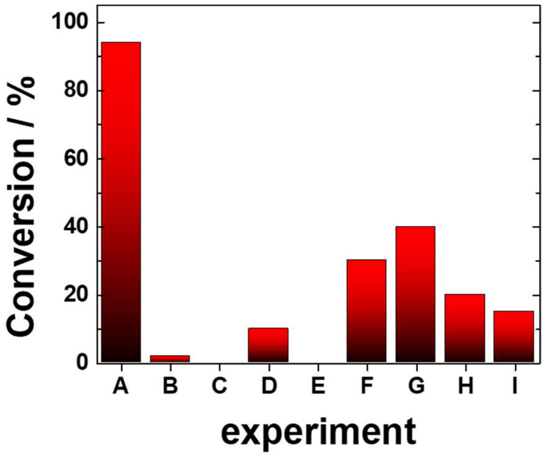

Entry	Reaction condition variations	Time	Conv. (%)[b]
A	standard condition	24h	94
B	no light	24h	2

C	no catalyst	24h	0
D	in air	24h	10
E[c]	with aniline as substrate	24h	0
F[d]	with $CuCl_2$	24h	30
G[e]	in toluene	24h	40
H	without Hantzsch ester	24h	20
I	without TEOA	24h	15

The reaction did not proceed without light irradiation (entry B), confirming the process's light-induced nature. Likewise, the catalyst is essential for the proceeding of the reaction (entry C). In the absence of an inert atmosphere, reduced product formation could be observed after 24h (entry D). Reverse pathways to azoxybenzene can be ruled out since carrying out the reaction with aniline as substrate yields no product (entry E). When using $CuCl_2$ as an electron scavenger, the conversion drops to 30%, indicating that the copper salt competes with nitrobenzene for reducing excited electrons (entry F). The importance of a polar solvent within the mixture, stabilizing highly polar transition states, is underlined by the experiment's conduction in pure toluene (entry G). The reaction conversion is reduced to 40%. The proportion of acetonitrile cannot be increased arbitrarily without risking colloidal destabilization and agglomeration. The removal of Hantzsch ester or TEOA from the reaction mixture leads to diminished product formation (entries H and I). While the ester is an essential proton transfer agent necessary in the mechanism, TEOA acts as a whole scavenger needed to complete the catalytic cycle. The benchmark reaction demonstrates the high efficiency of 5 ML NPLs in catalyzing organic reactions and the successful application of NPLs as a free-standing photocatalyst.

The recyclability of the 5 ML NPL photocatalysts for the reaction was further investigated. A series of four recycling experiments were conducted. After completing the reaction, the heterogeneous photocatalysts were separated from the reaction mixture by dialysis in a toluene/acetonitrile mixture. Then, the reaction was repeated with the recycled platelets by adding new reagents TEOA, Hantzsch ester, and nitrobenzene. No significant loss of photocatalytic performance could be demonstrated in the five cycles tested (**Figure 60**, **Figure 63-SI**).

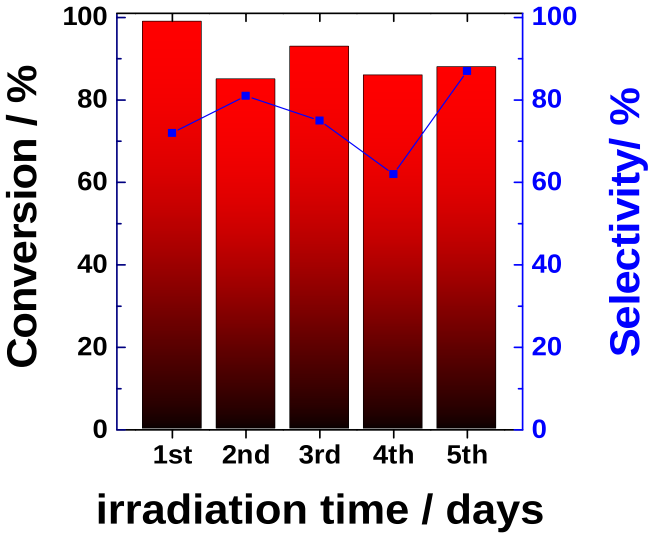

Figure 60. Photocatalytic conversions for recycling 5 ML NPLs in the reduction of nitrobenzene.

The versatility of the photocatalytic materials in the reduction of nitrobenzene was investigated (**Figure 61a**). The substrate scope could be extended by six products. Good reaction conversions were obtained. However, some reactions are not selective towards the azoxy product and yield considerable amounts of side products. We suspect that additional substituents significantly change the nitrobenzenes' electronic configuration shifting the selectivity towards other products in the reductive pathway. This is supported by a detailed DFT study on vertical electron affinities of the reaction intermediates and different substrates (**Figure 61b**).

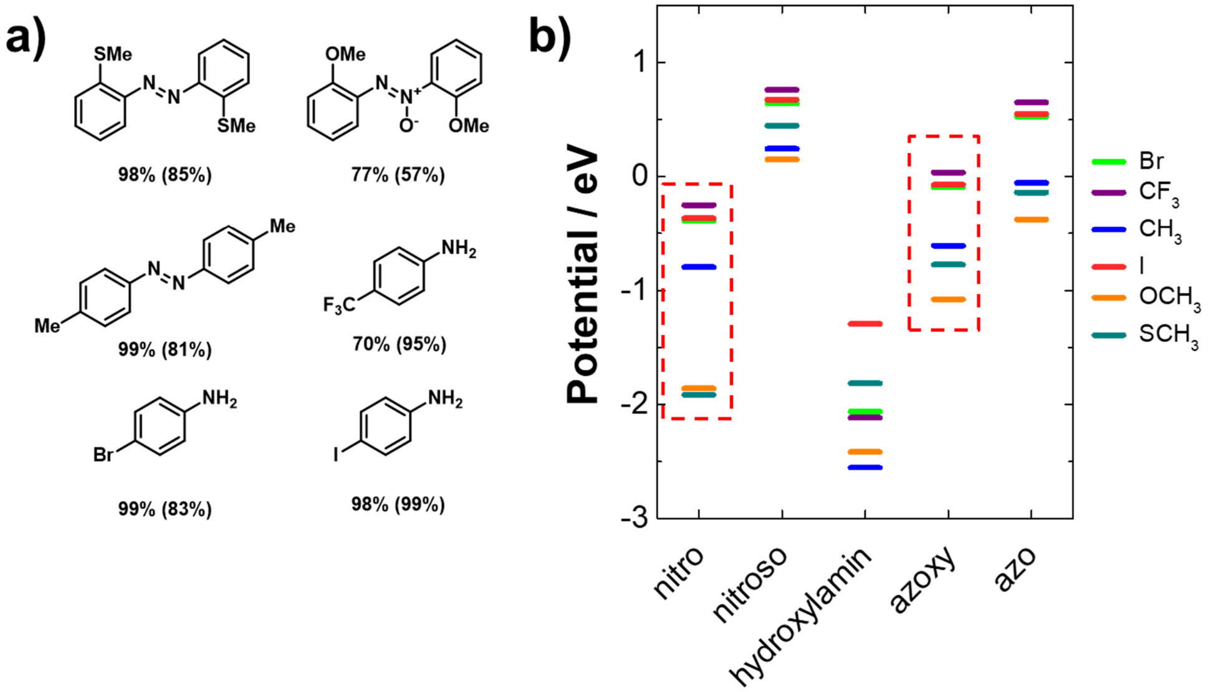

Figure 61. Scope of the photocatalytic reduction of nitrobenzene derivatives using 5 ML NPLs (a). The reactions were irradiated with a white LED lamp (0.16 W/cm^2). PBE0/def2svp DFT study on vertical electron affinities of the reaction intermediates (b). While the absolute values are prone to systematic errors, the general trend between intermediates and between substrates should suffice for analysis.

Regarding the nitro compound, the OCH_3 and the SCH_3 molecule seem to be most prone to reduction, followed by the CH_3 analog. The Br-, I-, and CF_3 nitrobenzene derivatives can be reduced easier. As expected for the radical and highly reactive nitroso species, a reduction can be carried out in a facile fashion for all analogs. The hurdle for the reduction of hydroxylamine compounds is comparatively high. This reveals an important aspect of the reaction cascade, making the non-reductive reaction to the azoxy compounds possible. For the azoxy compounds, the situation is similar to the reduction of the nitro compounds. The OCH_3 and the SCH_3 molecule seem to be most prone to reduction, followed by the CH_3 analog. The Br-, I-, and CF_3 nitrobenzene derivative can be reduced easily. Considering the DFT results, it is evident that the bromo, iodo, and trifluoromethyl compounds can be reduced through to the amine. For the methyl and methyl sulfide molecules, the azo compound can be found as the main product. The reduction from azoxy to azo product is least favorable for the methoxy compound, so the azoxy compound is mainly formed.

In general, the range of substrates and functional groups tolerated underlines the applicability of the NPLs as photocatalysts

2.3.4 Conclusion

In conclusion, we found that 2D CdSe nanoplatelets can be used as efficient heterogeneous photocatalysts. The materials can be produced quickly and reproducibly in the different thicknesses 3, 4, and 5 monolayers. The platelets' defined properties regarding UV/Vis absorption, photoluminescence, and band positions allow their use for photocatalytic studies. In their photocatalytic application, the platelets could be used to catalyze the controlled reduction of nitrobenzene to azoxybenzene. The photocatalytic activity increases with the number of monolayers. This was feasible due to increasing bandgaps and improved white light absorption with a rising number of monolayers while maintaining the same reduction potential in the conduction bands. Thicker NPLs also exhibited higher PL quantum yields, which may have further helped the efficient transfer of electrons to the nitrobenzene substrates. Additional control experiments, recycling, and a substrate scope expansion further demonstrate the applicability and showcase the potential of CdSe NPLs as a new class of effective photocatalysts.

2.3.5 Experimental details

Materials and methods

n-Hexane (95%), toluene, triethanolamine, and acetonitrile were purchased from Fischer scientific. Methyl acetate (99%) was purchased from Merck KGaA. 1-octadecene (ODE, 90%), cadmium acetate dihydrate (98%) were purchased from Acros Organics. Selenium powder (99.999%), methanol (100%), and Hantzsch ester were purchased from Alfa-Aesar. Toluene (99.8%) was purchased from VWR chemicals. Oleic acid (90%), cadmium nitrate tetrahydrate (98%), myristic acid (>98%), nitrobenzene and all nitrobenzene derivatives were purchased from Aldrich. All chemicals were used as received without further purification.

The absorption spectra were measured using an Agilent Cary 60 Spectrophotometer or Avantes spectrophotometer, consisting of Avantes AvaLight-DH-S-BAL as the UV-Vis light source passing through a neutral density filter (optical density = 2.0) and fibercoupled to an Avantes SensLine AvaSpec-HSC-TEC detector. Photoluminescence spectra were recorded using an Avantes SensLine AvaSpec-HSC-TEC spectrophotometer in 90° geometry. A Prizmatix Silver high power LED was used as the excitation source (emission peak 369 nm, FWHM ~ 10 nm). For TEM, samples were prepared by drop-casting a hexane dispersion of the NPLs onto a carbon-coated copper grid. The grid sat on filter paper during the drop-casting to assist the drying of solvent. TEM imaging was done using JEOL1400 TEM with an acceleration voltage of 120 kV. Cyclic voltammetry measurements were carried out on a Metrohm Autolab PGSTAT204 potentiostat/galvanostat with a three-electrode-cell system: glassy carbon electrode as the working electrode, $Hg/HgCl_2$ electrode as the reference electrode, platinum wire as the counter electrode, and Bu_4NPF_6 (0.1 M in acetonitrile) as supporting electrolyte with a scan rate of 100 mV s^{-1} in the range of 0 eV to 2 eV. All DFT calculations were carried out with the Gaussian 09 package.[290] The structures were optimized and calculated at the PBE0 level of theory[291] with the basis set of def2svp.[292-293] The single-point calculations were performed together with the PCM (Polarizable Continuum Model) model by employing toluene as the solvent.[294-296] Vertical electron affinities were computed as single-point energy difference between the neutral molecule and a negatively charged analog using the optimized structure of the neutral molecule.

GC-MS measurements were performed on a Shimadzu GC-2010 plus gas chromatograph and QP2010 ultra mass spectrometer setup (fused silica column Phenomenex, Zebron 5-ms nonpolar, flame ionization detector). Time-Resolved PL Spectroscopy/Time-Correlated Single-Photon Counting (TCSPC) measurements were conducted with a FluoTime200 time-correlated single-photon counting setup. Samples were excited with a laser at 380 nm, which was controlled by PicoQuant PDL 800-D. The signal was detected using a microchannel plate photomultiplier tube connected to a PicoHarp 300 time-correlated single-photon counting system. The instrument response function was measured using a dispersion of silica nanoparticles (LUDOX HS-40 colloidal silica) in water.

Synthesis of CdSe nanoplatelets

Cadmium myristate: Cadmium myristate was prepared from its nitrate salt using standard literature methods.[378-380] Cadmium nitrate (1.23 g) was dissolved in 10 mL of methanol. Sodium myristate (3.13 g) was dissolved in 100 mL of methanol. The solutions were stirred well separately for 10min until they are clear. Then, they were mixed and stirred for 30min at room temperature. The resulting white precipitate (Cd Myristate) was filtered, rinsed three times using cold methanol, and dried under vacuum overnight. The white powder was stored at room temperature in the dark.

Synthesis of Bis(stearoyl)selenide: Bis(stearoyl)selenide was prepared using LiAlHSeH as the selenating agent.[381] To prepare the LiAlHSeH, $LiAlH_4$ (0.76 g, 20 mmol) was added to a suspension of Se powder (1.92 g, 24 mmol) in 200 mL THF at -10 °C under argon atmosphere. The mixture was stirred for 30min. The LiAlHSeH was formed *in situ* as a grayish dispersion. 80 mmol (27.2 mL) of stearoyl chloride was slowly added to the dispersion of 20 mmol LiAlHSeH. The mixture was stirred at -10 ºC under a nitrogen atmosphere. After 2h, 5 mL of deionized water was added to quench unreacted reagents. The organic reaction mixture was diluted with 300 mL of diethyl ether and washed four times with 100 mL brine. Bis(stearoyl)selenide was crystallized at 20 °C (12h), filtered, and dried under high vacuum for 12h. The resulting white flakes were stored in a nitrogen-filled glove box.

3ML NPLs[382]: In a three-necked flask, 127.5 mg (0.225 mmol) of cadmium myristate and 17.3 mg (0.065 mmol) of $Cd(OAc)_2 \cdot 2\ H_2O$ were dispersed in 15 mL ODE. This mixture was heated up to 100 °C and degassed under vacuum for 15min. Afterward, the mixture was heated up to 140 °C under argon. At this temperature, a solution of 45.8 mg (0.075 mmol) of bis(stearoyl)selenide dissolved in 1 mL of anhydrous toluene was added with a syringe. One minute later, 52 mg (0.195 mmol) $Cd(OAc)_2 \cdot 2\ H_2O$ was added. The mixture was kept heated at 140 °C with an oil bath for five days. After five days, the mixture was cooled down to room temperature. Then 0.5 mL oleic acid was added. The reaction mixture was transferred to a centrifuge tube, the volume was filled up to 15 mL with hexane, and the mixture was centrifuged at 5000 rpm (2599 g) for 10min. The supernatant of this centrifugation was diluted with 15 mL of methyl acetate to induce agglomeration of the NPLs and centrifuged again at 8000 rpm (6654 g) for 10min. The precipitate of this centrifugation was re-dispersed in 5 mL hexane. The resulting solution was clear yellow and contained pure 3 ML NPLs.

4ML and 5ML NPLs: Our CdSe NPL synthesis was slightly modified from a protocol by Tessier *et al*.[383] Briefly, 170 mg (0.3 mmol) Cd(myristate)$_2$, 12 mg (0.15 mmol) Se powder, and 15 mL ODE were added to a 100 mL round-bottom flask and degassed under vacuum for 30min. Then, the mixture was heated up to 240 °C under N_2. At 200 °C, 80 mg (0.3 mmol) Cd(acetate)$_2$ dihydrate was added. The mixture was kept at 240 °C for 8min. Afterward, the reaction flask was cooled using an air gun to 150 °C. During this cooling step, 0.5 mL OA was added when the temperature reached 180 °C. Once at 150 °C, the flask was placed in a water bath and cooled to room temperature (RT), and then 5 mL hexane was added. The mixture was centrifuged at 7500 rpm (5849 g) at 25 °C for 10min. The precipitate was re-dispersed in 5 mL hexane and centrifuged at 7000 rpm (5095 g) for 8min. Unwanted 3-monolayer-thick NPLs were removed as the precipitate. The 4-monolayer or 5-monolayer thick NPLs in the supernatant were then stored in the dark under ambient conditions until needed.

Estimation of Cd atoms / NPL

Average sizes of NPLs were determined from the TEM images using ImageJ. The NPLs were modeled using VESTA, accounting for the zincblende crystal structure and the lattice parameters. The total number of atoms in an NPL was obtained from the model. The number of Cd was calculated by the total number of atoms times the number of Cd monolayers divided by the total number of monolayers). Cd atoms/NPL = 2950, 5470, 5750 Cd/NPL for 3, 4, 5ML NPLs respectively.

General procedure for the photocatalytic reduction of nitrobenzene

Nitrobenzene (15 µL, 18 mg, 0.15 mmol), TEOA (27 µL, 25 mg, 0.17 mmol), Hantzsch ester (25 mg, 0.10 mmol), 300 µL NPLs (stock concentration 3.4 x 10^{-7} M) and acetonitrile (510 µL) were added to toluene (1190 µL). The final catalyst concentration is 5.0 x 10^{-8} M, which equals 0.00007 mol%. The mixture was bubbled with argon for 5min, sealed, and stirred under white LED exposure for 24h. Aliquots were taken and assessed with GC-MS. The procedure was applied for both the kinetic study as well as the control experiments. For the scope experiments, nitrobenzene was replaced by the respective nitro compound (0.15 mmol).

Recycling experiments

The general procedure was followed for setting up the reactions. The 5 ML catalyst was used in the recycling study. After completing a reaction cycle after 24h, the conversion and selectivity were analyzed by GCMS. The reaction mixture was transferred to a small regenerated cellulose dialysis tubing and dialyzed for 8h in toluene/acetonitrile (70:30, 5 mL). The solvent was exchanged once. The dialyzed platelets were transferred to a new vial (4 mL) and used for a new setup. The eventual solvent loss was accounted for by adjusting the amount of new solvent. Nitrobenzene, Hantzsch ester, and TEOA were added. The absence of products from the previous cycle was confirmed by GCMS. After argon bubbling, the following reaction cycle was started by white LED light irradiation.

Procedure for the intermediate detection

Nitrobenzene (10 µL, 12 mg, 0.10 mmol), TEOA (35 µL, 32 mg, 0.22 mmol), Hantzsch ester (100 mg, 0.40 mmol), 300 µL NPLs and acetonitrile (150 µL) were added to toluene (350 µL). The mixture was bubbled with argon for 5min, sealed, and stirred under white LED exposure for 4h. An aliquot was taken and assessed with GC-MS.

Table 5. Lifetimes of the components obtained from double exponential fitting.

	A1	t1 / ns	A2	t2 / ns	Intensity weighted <τ> / ns	Amplitude weighted <τ> / ns
3 ML	75.6	14.1	207	2.1	10.6	5.3
4 ML	96.8	15.7	202	3.0	12.1	7.1
5 ML	54.2	12.9	260	3.7	7.6	5.3

$$I(t) = \int_{\infty}^{t} IRF\ (t') \sum_{i=1}^{2} A_i e^{-\frac{t-t'}{\tau_i}} dt'$$

with

IRF = Instrument response function

A_i = amplitude of the ith component, in counts

τ_i = lifetime of the ith component, in nanoseconds

Fit results gave X^2(reduced) of 1.0653, 1.0343, and 1.0570, which confirms a good fit to the data points.

Table 6. Conversion and selectivity overview of the kinetic study. Data points with low conversions do not have robust values for selectivity (*).

	time / h	conversion / %	Selectivity for azoxybenzene / %
3 ML	1	0.2	49,7%*
	2	1.1	83,8%
	3	2.3	83,4%
	4	4.7	92,9%
	6	6.9	87,6%
	8	9.7	89,5%
	12	18.2	92,6%
	24	25.1	96,8%
4 ML	1	0.1	34,0%*
	2	2.9	92,1%
	3	3.6	88,6%
	4	7.3	91,5%
	6	15.9	91,7%
	8	27.1	92,1%
	12	42.5	88,7%
	24	59.1	91,7%
5 ML	1	0.5	46,0%*
	2	1.7	80,7%
	3	14.8	89,2%
	4	40.3	93,1%
	6	53.3	94,9%
	8	66.8	93,5%
	12	76.8	91,2%
	24	97.7	72,5%

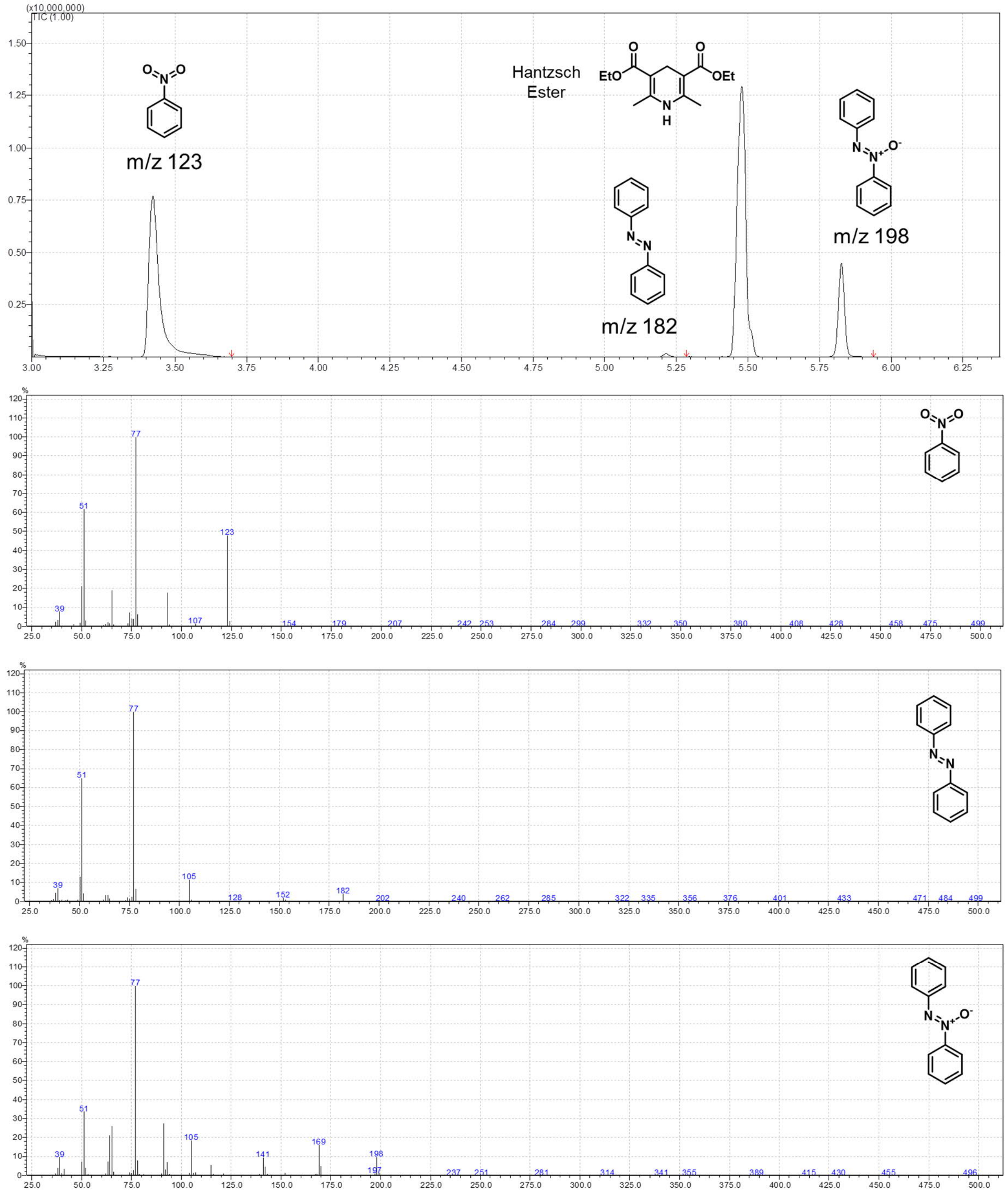

Figure 62. Exemplary GC trace and mass spectra at the peak maxima for the kinetic study obtained from the 3ML series after 24h. Depending on the amount injected, signals for TEOA and its interaction products with the column material appear for other samples.

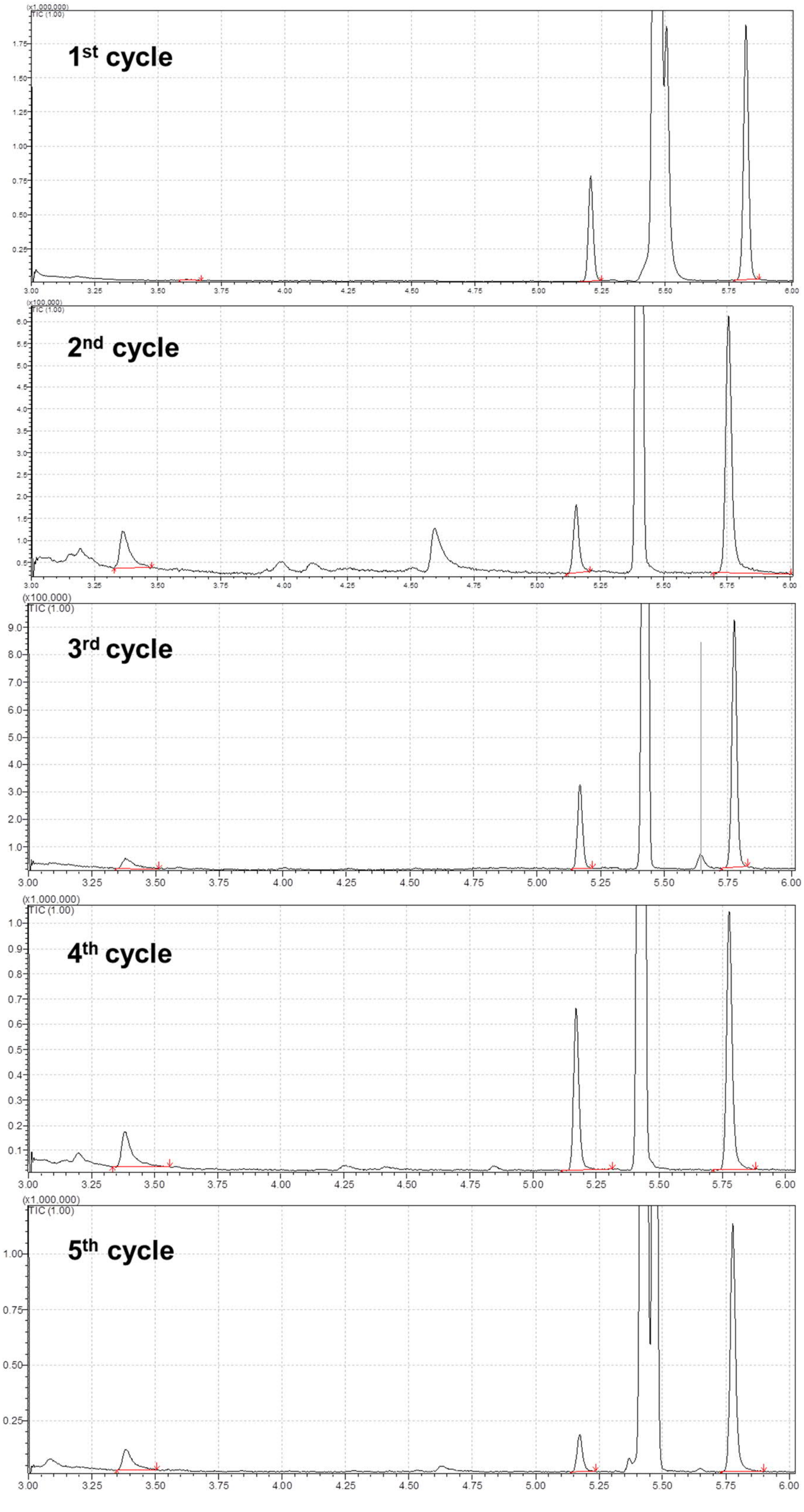

Figure 63. GCMS traces for recycling experiments. The signal around 3.3min elution time can be assigned to the starting material. Other signals include TEOA (4.6min), azobenzene (5.2min), Hantzsch ester (5.5min) and azoxybenzene (5.8min).

2.4 Porous aromatic frameworks with precisely controllable conjugation lengths for visible-light-driven photocatalytic selective C-H activation reactions

The previous chapter has emphasized the importance of bandgap and photon absorption as well as their fine-tuning for the progress of a photocatalytic reaction. A porous polymer class which, due to its defined conjugation lengths and rigidity, also allows for the isolated consideration of the influence of electrooptical on photocatalytic properties is presented in the following. Specifically, the variation of the frontier orbital potentials on the oxidative and reductive nature of photocatalysts is investigated. The chapter is based on the published article "Porous aromatic frameworks with precisely controllable conjugation lengths for visible-light-driven photocatalytic selective CH activation reactions, *European Polymer Journal* 2020, *140*, 110060."[384] The project is a joint effort of Prof. Kai Zhang and me. I carried out the project's experimental work.

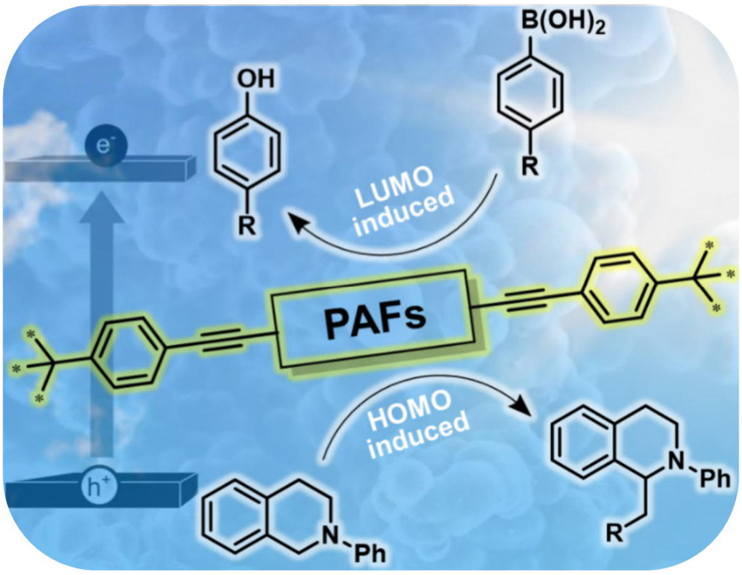

Organic visible-light-active porous polymers have been established as a novel and promising class of heterogeneous photocatalysts for various important photoredox reactions. However, given the usually fully conjugated nature of most polymer-based photocatalysts, precise control of the energy band structure and their redox potentials in photocatalytic reactions while retaining highly active surface area is a considerable challenge. Here, we design a series of porous aromatic frameworks (PAFs) with precise control of the conjugation length within the polymer architecture as efficient metal-free photocatalysts. The polymers exhibit high intrinsic surface areas of up to 1070 m^2/g and tunable optical and redox properties that allow applications in C-H activation reactions driven selectively either by the photogenerated electron or hole species. Furthermore, as an attractive example for high-value chemical conversions, the formation of dantrolene, an active pharmaceutical ingredient, was successfully catalyzed by the PAFs in the simple one-pot cascade synthesis.

2.4.1 Motivation

Using visible-light as a sustainable activation energy source, purely organic and macromolecular photocatalysts have recently demonstrated their high efficiency and broad application range in challenging photoredox reactions, such as water splitting,[94, 178-179, 385] CO_2 reduction,[318, 386] and organic redox reactions.[184, 387-388] The opportunity of structural designability down to the monomer level gave polymer photocatalysts the advantage of precise photophysical and electronic property control.[90, 389-390] The band positions, in particular the thermodynamic potentials of generated holes in the highest occupied molecular orbital (HOMO) and electrons in the highest occupied molecular orbital (LUMO), have to exceed the target substrate potentials to ensure electron transfer and therefore play a decisive role for photocatalytic activity.[391] Among the efforts to engineer a polymers' band positions and bandgap, tailoring electron donor and acceptor monomers and their copolymerization ratio,[117, 224, 257-259] elemental doping,[260-261] substitution of atoms and molecular groups[392-394] as well as optimizing the structural conformation[265-268] are most prominent. However, since the conjugation length in conventional polymer photocatalysts still varies from system to system and can hardly be controlled, many systems lack a clear correlation between molecular structure and observed characteristics. Consequently, the accurate prediction of electronic and photocatalytic properties of a photocatalyst remains a major challenge in the molecular and structural design of modern photocatalytic systems.

In 2009, Ben *et al.* introduced porous aromatic frameworks (PAFs) as a novel class of three-dimensional polymer networks with local diamond-like structures and extraordinary surface areas up to 7100 m^2/g.[185] The reported polymer PAF-1 was obtained through Yamamoto homo coupling of a tetrahedral precursor and, most importantly, did not require a template-assisted synthesis approach. Due to their exceptional morphology, the PAFs were highly suited and explored for gas and organic molecules storage and uptake applications.[188, 194, 395-398] A closer look at the structural build-up of the materials reveals the potential of PAFs as a platform for photocatalytic applications. By replacing the individual building units separated by sp^3-carbon atoms with photocatalytically active units, a new class of tunable photocatalysts with excellent control of conjugation length and morphology could result. With a suitable choice of monomers, direct control of band positions in the polymer system could be possible. So far, PAFs have only been vaguely or rather indirectly explored for photocatalytic purposes, either *via* the use of attached transition metals or only approximated the basic PAF design principle.[119, 399-400] This could lie at the synthetic challenge of constructing photoactive PAFs while maintaining the high surface area and porosity. In our view, the possible findings on substrate-catalyst electron transfer and photocatalytic performance merit the investigation of PAFs as a toolbox for a new class of macromolecular organic photocatalysts. Investigations of photocatalytic PAFs are highly needed.

In this work, we bottom-up designed three porous aromatic frameworks (PAFs) as efficient metal-free, heterogeneous and redox-active photocatalysts for visible-light-promoted chemical transformations (**Figure 64**). Based on 4,7-benzothiadiazole (BT), a stable electron acceptor, three photoactive molecules with phenyl- (Ph), thienyl- (Th), and 3,4-ethylenedioxythienyl (EDOT) moieties were incorporated into a PAF *via* Sonogashira coupling. The obtained polymers exhibited tunable optical and redox properties similar to the molecular analogs, indicating precise conjugation length control within the polymer architecture. The resulting networks showed high intrinsic porosity (surface area from 740 to 1070 m^2/g, pore diameter ~1.1 nm) and demonstrated advantageous chemical robustness and recyclability within their photocatalytic application. As applications, two C-H activation reactions, namely an *aza*-Henry reaction with tetrahydroisoquinoline derivatives and the direct arylation of heteroarenes with aryl diazonium salts, could be efficiently catalyzed by the designed PAFs, showing two different initiation pathways either by the photogenerated electron or hole species. Furthermore, a direct correlation of the photocatalytic efficiencies and the electronic band positions of the polymer photocatalysts could be proven. We were able to selectively control either electron- or hole-initiated reactions with the photocatalytic PAF series. The mechanistic correlations were supported by control and scavenger experiments. The polymer photocatalysts were readily recyclable and no photobleaching was observed during the repeating experiments. Additionally, the reactivity scope was expanded to a broader range of substrates and the vital drug molecule dantrolene was synthesized using the PAFs as photocatalysts as a real-life application example.

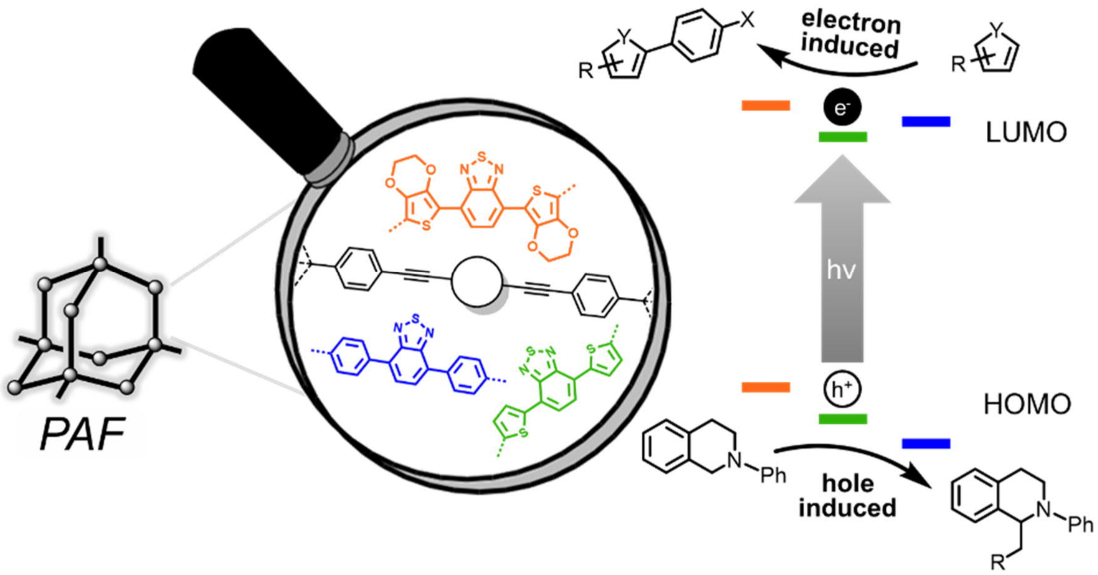

Figure 64. Illustration of the design concept of the PAF-based photocatalysts and their dual-functional application in the selective photocatalytic activation of C-H bonds either by the photogenerated electron on LUMO or hole on HOMO.

2.4.2 Synthesis and characterization

The photocatalytic PAFs in this study were synthesized *via* palladium-catalyzed Sonogashira cross-coupling reaction from tetra(4-ethynylphenyl)methane and 3 dibromo-monomers based on 4,7-diphenylbenzothiadiazole (BT(Ph)$_2$), 4,7-di(thiophen-2-yl)benzothiadiazole (BT(Th)$_2$) and 4,7-di(3,4-ethylenedioxythiophene-2-

yl)benzothiadiazole ($BT(EDOT)_2$) (**Figure 65**). All monomers were synthesized in two steps. Details on synthetic procedures and characterization details are given in the experimental section. The monomers were designed to encompass electron-rich (BT) and electron-poor building blocks (Ph, Th, EDOT) following a donor-acceptor-donor approach. The tetrahedral Sonogashira coupling was selected being an efficient and reliable polymerization method for highly porous polymer photocatalysts.[114-115, 401] Ordered PAFs based on this cross-coupling have been synthesized, e.g., by the groups of Zhu and Cooper.[195-196] The high conversion of the coupling is key to achieve high polymerization degrees and large surface areas.[189]

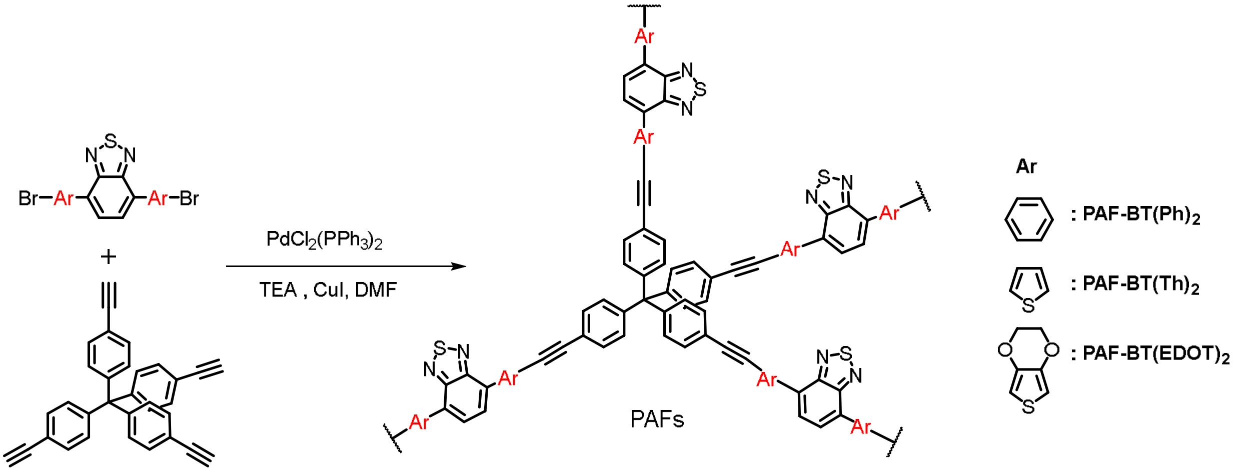

Figure 65. The synthetic route towards $PAF-BT(Ph)_2$, $PAF-BT(Th)_2$, and $PAF-BT(EDOT)_2$.

The PAF synthesis of $PAF-BT(Ph)_2$, $PAF-BT(Th)_2$, and $PAF-BT(EDOT)_2$ was evaluated by ^{13}C CPMAS solid-state NMR spectroscopy (**Figure 66a**). All spectra have a pronounced signal at ca. 65 ppm, which results from the quaternary carbon atoms confining individual conjugated units. No peaks of terminal alkynes could be found. All signals could be matched with the assumed structures, confirming the successful PAF syntheses from the respective monomers. FTIR spectra were used to support the chemical composition and structural elucidation of the synthesized materials (**Figure 66b**). The FTIR spectra showed typical signals, for example, at 820 cm^{-1}, which is characteristic of the stretching vibration of the quaternary carbon atom towards the surrounding benzyl rings. The absence of a pronounced signal at 3280 cm^{-1}, corresponding to alkyne stretching vibrations, indicates that no significant amounts of terminal triple bonds are present and that a high degree of polymerization could be achieved. The polymeric nature of the synthesized substances was further confirmed by thermogravimetric analysis (TGA, **Figure 66c**). The PAFs in this study show thermal stability up to about 400°C. It is noticeable that the decomposition of PAF-BT(EDOT)$_2$ takes place at significantly lower temperatures than with the other PAFs. It is assumed that the decomposition of the oxygen-containing side chain accelerates the degradation of the network.[402] In comparison, PAF materials known from literature show similar decomposition temperatures under thermal stress.[196, 399]

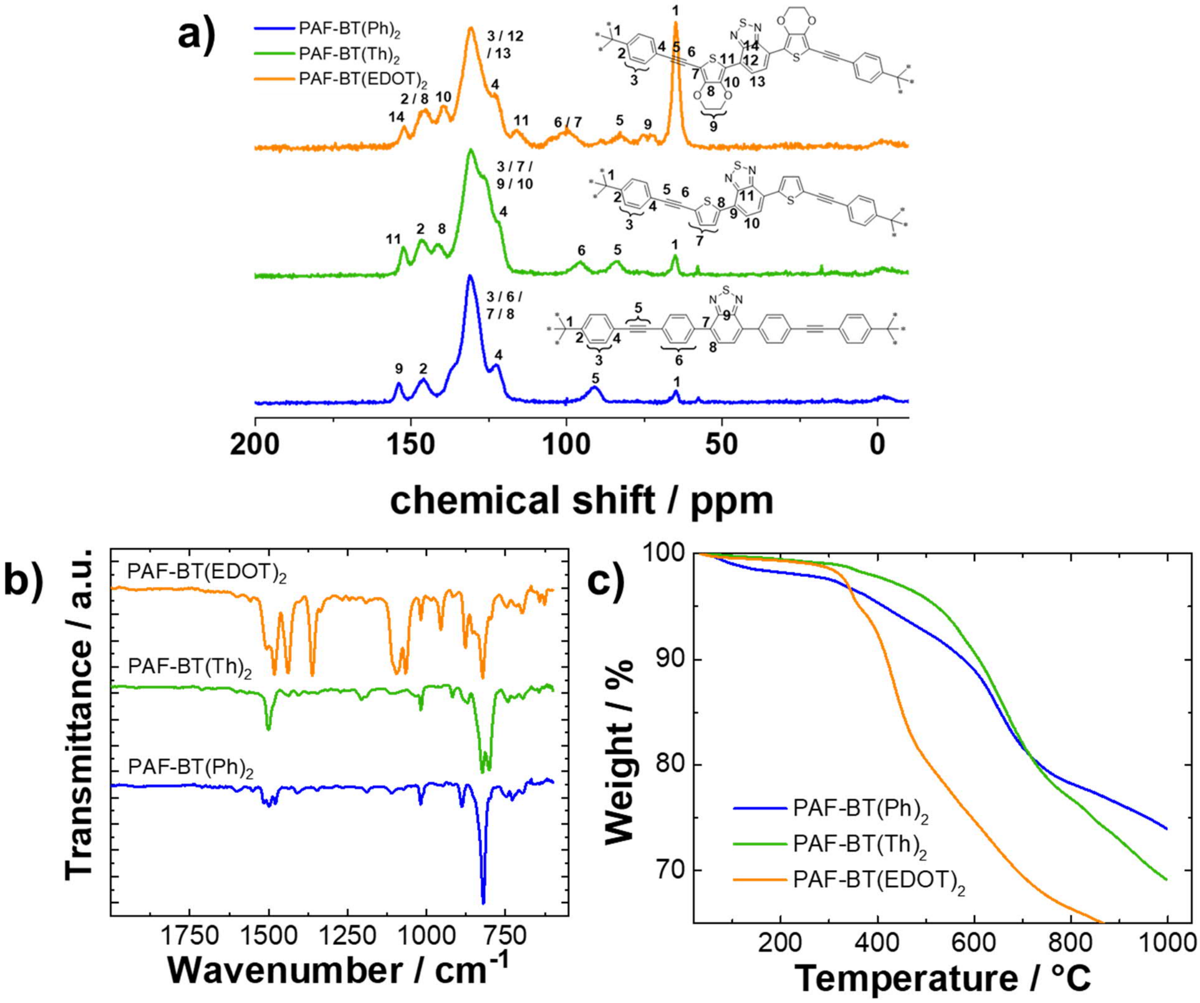

Figure 66. Comparison of ^{13}C solid-state NMR (a), Fourier-transformed infrared (FTIR) spectra (b) and thermogravimetric analysis from 25 to 1000°C (10 K/min) in N_2 atmosphere (c) for PAF-BT(Ph)$_2$, PAF-BT(Th)$_2$ and PAF-BT(EDOT)$_2$.

The porosity of the polymer networks was investigated using nitrogen sorption measurements at 77 K (**Figure 67a**). Adsorption and desorption isotherms of the PAFs are similar in appearance and can be described as type I sorption isotherms.[231] The isotherms show a steep nitrogen absorption at pressures below 0.1 p/p^0, which indicates microporosity of the materials. Non-local density functionality (NLDFT) calculations gave pore size distributions (PSD) with maxima around 1.0-1.1 nm (**Figure 67b**), confirming the presence of micropores in the networks. The application of Brunauer-Emmett-Teller (BET) theory yields specific surface areas of 1071 m^2 g^{-1} for PAF-BT(Ph)$_2$, 747 m^2 g^{-1} for PAF-BT(Th)$_2$, and 899 m^{2}g^{-1} for PAF-BT(EDOT)$_2$.

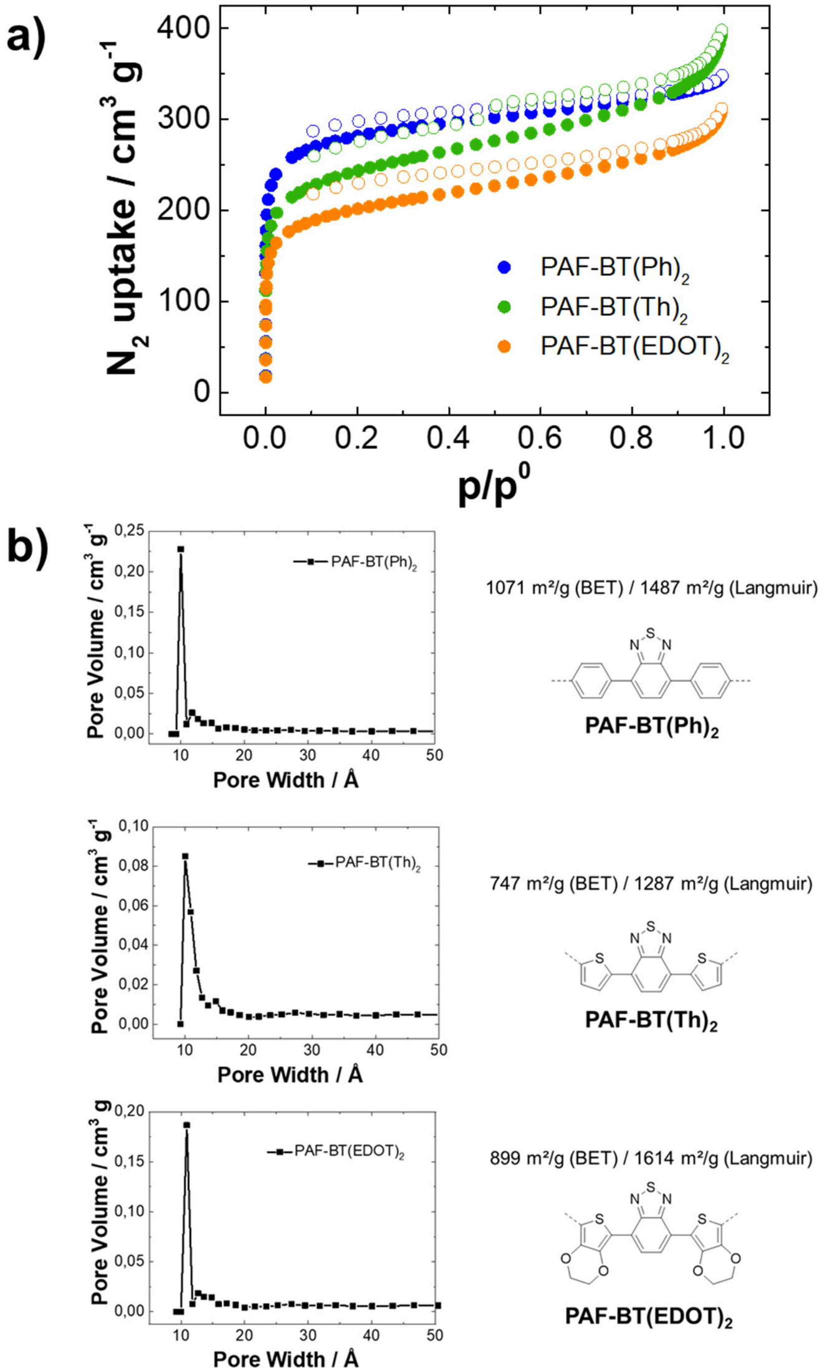

Figure 67. Nitrogen adsorption isotherms at 77K (a) and pore size distributions of PAF-BT(Ph)$_2$, PAF-BT(Th)$_2$, and PAF-BT(EDOT)$_2$ (b).

The morphological investigation of the catalysts was performed by scanning electron microscopy (SEM). The images show particles with a size in the order of a few micrometers and appear to be fused aggregates of much smaller particles with dimensions around 100 nm (**Figure 68**). This morphology is typical for conjugated microporous polymers and indicates comparatively amorphous structures.

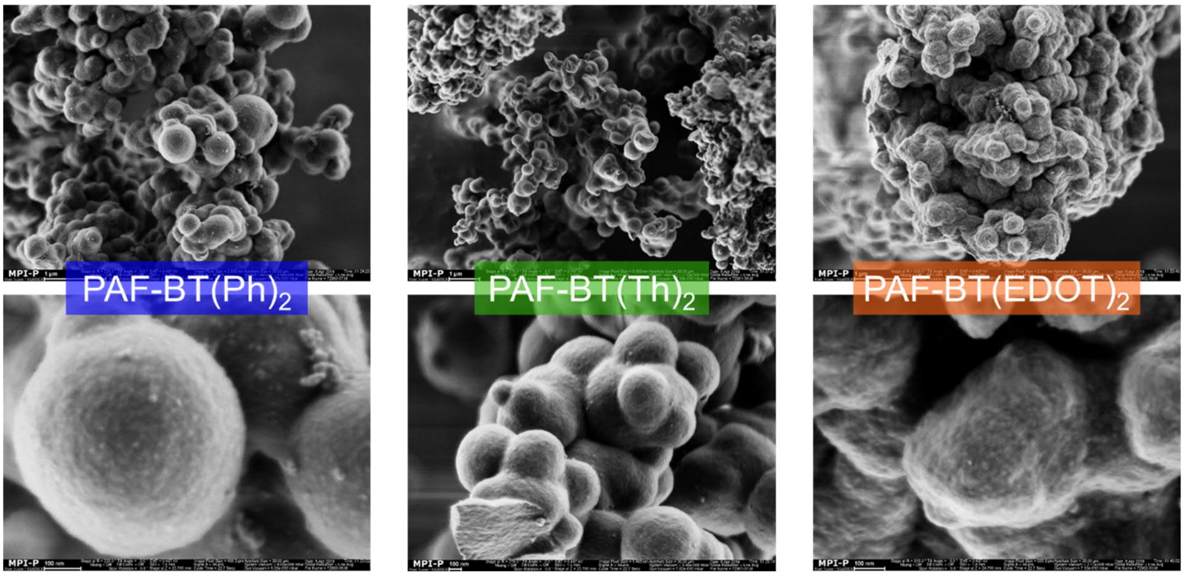

Figure 68. Scanning electron microscopy (SEM) images of PAF-BT(Ph)$_2$, PAF-BT(Th)$_2$, and PAF-BT(EDOT)$_2$.

For the optical characterization of the PAF polymers, both diffuse reflectance UV/Vis spectra (**Figure 69a**) and photoluminescence (PL) data were acquired (**Figure 69b**). The light absorption shows a trend from PAF-BT(Ph)$_2$ to PAF-BT(EDOT)$_2$. While PAF-BT(EDOT)$_2$ absorbs light up to about 730 nm, PAF-BT(Ph)$_2$ reveals an onset absorption at about 540 nm. PAF-BT(Th)$_2$ lies in between with an absorption beginning at approx. 650 nm. The resulting optical bandgaps are 1.85 eV, 1.99 eV, and 2.44 eV, derived from the Kubelka-Munk plots (**Figure 69c**). The photoluminescence spectra show the fluorescence with emission maxima from 540 to 725 nm when excited at the respective absorption maximum.

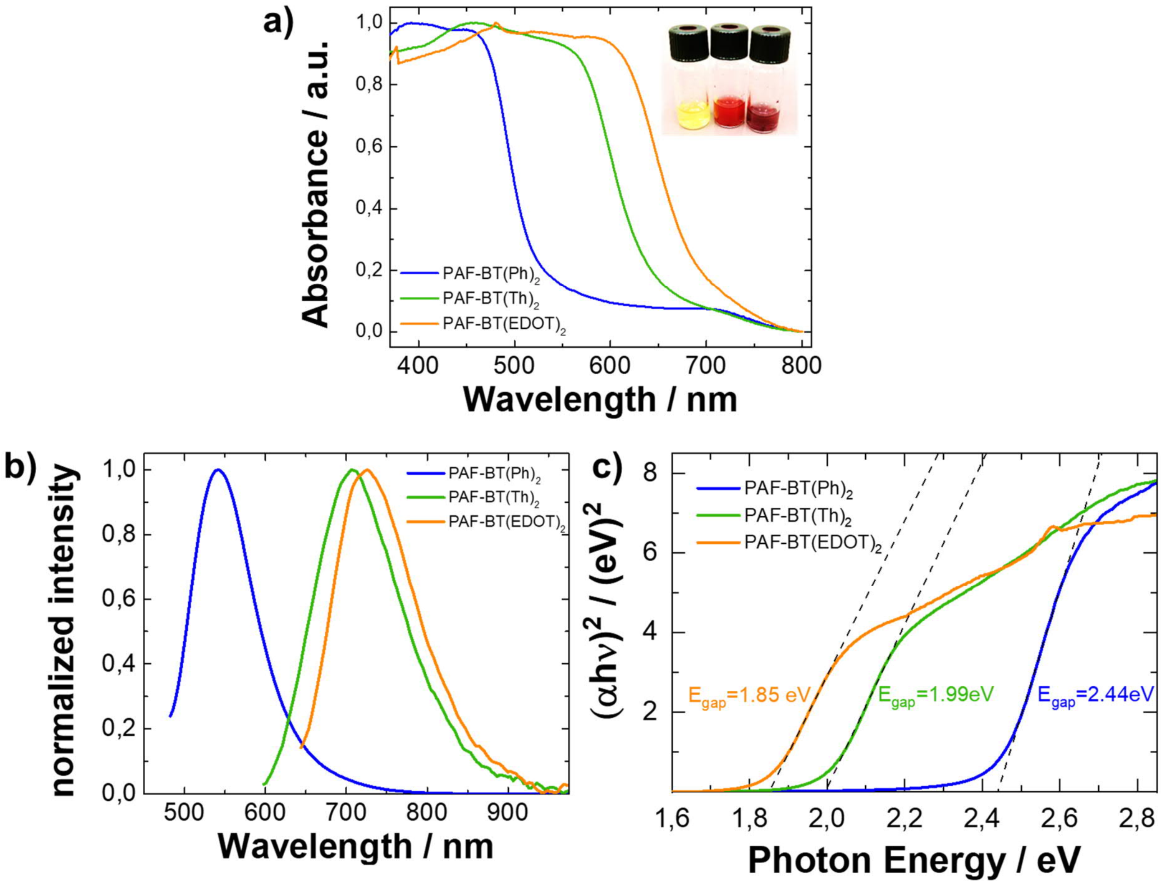

Figure 69. DR UV/Vis absorption (a) and photoluminescence spectra of PAF-BT(Ph)$_2$, PAF-BT(Th)$_2$, and PAF-BT(EDOT)$_2$ (b). The excitation wavelengths were 450 nm, 525 nm, and 575 nm, respectively. Kubelka-Munk transformed UV/Vis spectra for deduction of bandgap potentials (c).

The electronic properties of the polymers were investigated by cyclovoltammetry (CV, **Figure 70a**). The PAFs were measured in the solid state with a saturated calomel reference electrode (SCE) and the LUMO positions could be determined directly at reducing potentials. PAF-BT(EDOT)$_2$ has the highest LUMO with -1.37 eV vs. SCE, followed by PAF-BT(Ph)$_2$ and PAF-BT(Th)$_2$ with -0.97 eV and -0.91 eV vs. SCE, respectively. In combination with the bandgaps resulting from the UV/Vis measurement, the HOMO positions can be determined empirically (**Figure 70b**). The results are consistent with the predicted energy levels of the density functional theory (DFT) calculations at the B3LYP/6-31G(d) level (**Figure 78-SI**).

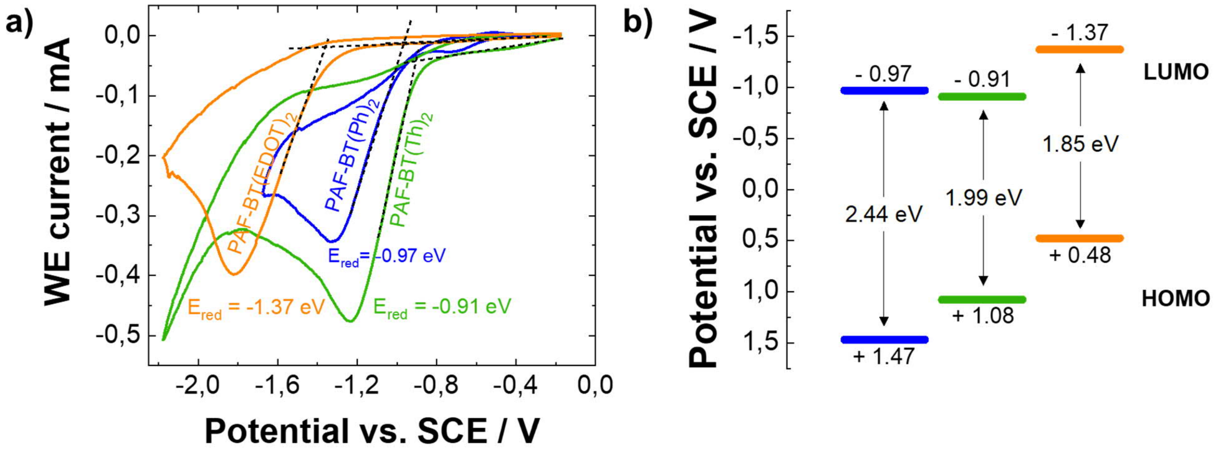

Figure 70. Cyclic voltammetry of the PAF photocatalysts at a scan rate of 100 mV/s. A Pt wire was used as the counter electrode; a saturated calomel electrode as the reference electrode. Bu4NPF6 (0.1 M in acetonitrile) was used as the electrolyte (a). HOMO and LUMO frontier orbital potentials derived from cyclovoltammetry and optical absorption (b).

If one compares the PAFs with the corresponding molecular analogs $BT(Ph)_2$, $BT(Th)_{2,}$ and $BT(EDOT)_{2,}$ it can be stated that the deviations of the frontier orbital positions are only minimal (**Figure 71** and **Figure 72**) This underlines the strength of the concept to enable the synthesis of a macromolecular photocatalyst with predictable electronic levels and reactivity. The fixed conjugation length allows direct *ex-ante* statements on electrooptical and photocatalytic properties even before catalyst preparation has been carried out.

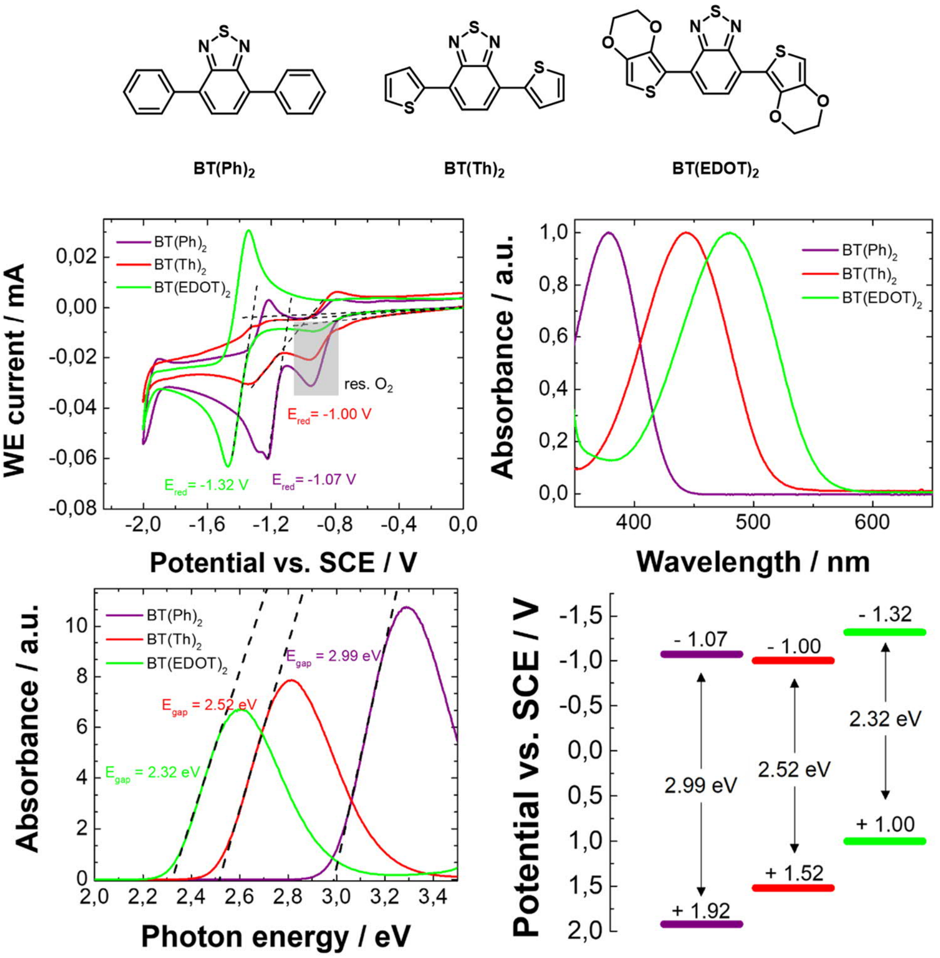

Figure 71. Determination of frontier orbital potentials for $BT(Ph)_2$, $BT(Th)_2$, and $BT(EDOT)_2$, from CV and UV/Vis studies.

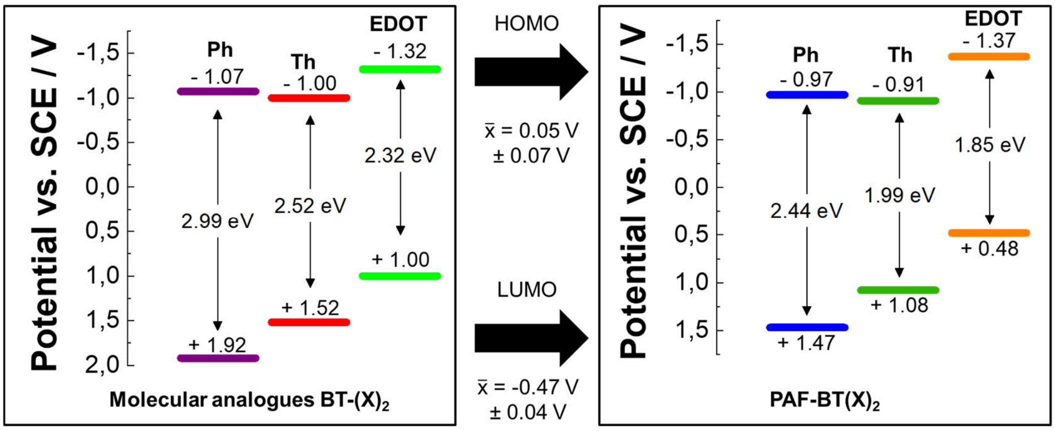

Figure 72. Frontier orbital comparison between the molecular analogs $BT(X)_2$ and the PAF photocatalysts in this study. In the center, the average of the deviations (both Ph systems compared, both Th systems compared, both EDOT systems compared) and the standard deviation of the value comparison are given.

In general, the data showed that the electro-optical properties of the PAFs could be varied *via* the strength of the electron-donating unit. Three PAFs with stepwise positioning of the boundary orbitals resulted. The influence on the photocatalytic properties was investigated in detail in the following through two C-H activation reactions.

2.4.3 Photocatalysis

Direct C-H bond activations represent a particularly difficult reaction class within organic synthesis and are of special interest.[403-404] While the classical approach usually requires coordinated transition metals based on, e.g., palladium or ruthenium at elevated temperatures, photocatalytic systems pose a promising alternative.[37, 405] To test the photocatalytic activity of the synthesized PAFs, we chose two specific C-H bond activation reactions. The direct arylation of heteroarenes with aryl-diazonium salts is based on a reductive, LUMO-induced partial step. The aza-Henry reaction is initiated by an oxidative HOMO-induced partial step. Both reactions are different in nature and were chosen to underline the dual applicability and versatility of the PAF platform. The couplings are known from literature and have already been investigated concerning photocatalytic feasibility.[37, 40] The synthesized PAFs are completely insoluble in all organic solvents used in this study, making them attractive targets for heterogeneous photocatalysis. The investigation of residual palladium content by inductively coupled plasma mass spectrometry (ICP-MS) revealed no significant Pd residues (<0.1 ppm) in the polymer networks. The excessive washing protocol has successfully removed transition metal traces which could interfere with the photocatalytic analysis.

Table 7. Control experiments of the photocatalytic aza-Henry reaction with *N*-phenyltetrahydroisoquinoline and nitromethane (left) and the direct arylation of thiophene and 4-bromobenzenediazonium tetrafluoroborate (right). Reaction conditions for the aza-Henry reaction: *N*-phenyltetrahydroisoquinoline (52 mg, 0.25 mmol), nitromethane (40µL, 0.75 mmol), DMF (2 mL), catalyst (2 mg), 23W lamp, room temperature, air. Reaction conditions direct arylation 4-bromobenzenediazonium tetrafluoroborate (40 mg, 0.15 mmol), thiophene (118 µL, 1.5 mmol), DMSO (2 mL), catalyst (2 mg), 23W lamp, room temperature, argon atmosphere. [a] Conversion determined by NMR. [b] Conversion determined by GC-MS.

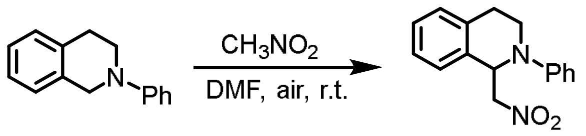

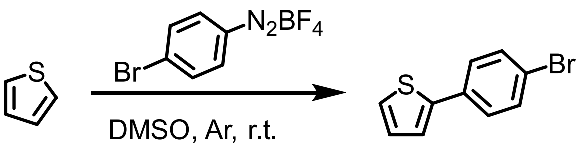

entry	catalyst	condition variation	conv. (%)[a]	entry	Catalyst	conditions variation	conv. (%)[b]
1	PAF-BT(Ph)$_2$	-	97	9	PAF-BT(Ph)$_2$	-	64
2	PAF-BT(Th)$_2$	-	65	10	PAF-BT(Th)$_2$	-	61
3	PAF-BT(EDOT)$_2$	-	<1	11	PAF-BT(EDOT)$_2$	-	93
4	-	-	3	12	-	-	2
5	PAF-BT(Ph)$_2$	no light	<1	13	PAF-BT(EDOT)$_2$	no light	<1
6	PAF-BT(Ph)$_2$	under nitrogen	8	14	PAF-BT(EDOT)$_2$	under air	32
7	PAF-BT(Ph)$_2$	with CuCl$_2$ / under nitrogen	81	15	PAF-BT(EDOT)$_2$	with CuCl$_2$ / under argon	15
8	PAF-BT(Ph)$_2$	with KI	5	16	PAF-BT(EDOT)$_2$	with KI	40

The catalytic reactions of PAFs in the photocatalytic aza-Henry reaction were performed with 2-phenyl-1,2,3,4-tetrahydroisoquinoline as substrate and nitromethane as solvent and reactant. The setups were stirred in air and irradiated with a commercial light bulb (23W) as the light source for 24h. After 1, 2, 4, 8, and 24h, samples were taken from the reaction solution and NMR spectroscopic kinetics of the reaction with different catalysts were obtained (**Figure 73a**). Among the catalysts tested, PAF-BT(Ph)$_2$ showed the best reactivity, catalyzing the benchmark reaction with a conversion of 97% in 24h. The catalyst outperforms PAF-BT(Th)$_2$, which converted 65% after the same reaction time. For catalysis with PAF-BT(EDOT)$_2$, no signals of the desired product could be found in the NMR spectra or mass spectrometric analysis after 24h. The kinetic analysis shows a first-order reaction where the catalysis activity of PAF-BT(Ph)$_2$ is highest (**Figure 79-SI**).

To gain more precise mechanistic insights into the reaction and prove the conversion's photocatalytic nature, control experiments were carried out with the best performing catalyst PAF-BT(Ph)$_2$ (**Table 7**). The reaction did not proceed without light irradiation or the use of catalyst. In the absence of oxygen, no product formation could be observed after 24h. From the control experiment using $CuCl_2$ as an electron scavenger under nitrogen atmosphere, a high reaction conversion (71%) was obtained, indicating that the copper salt can take the role of oxygen as catalyst regenerator. Addition of KI as a scavenger for photo-generated holes led only to traces of the desired product. The observations correspond to the derived band positions of the catalysts: while the oxidation potential of the Ph-type PAF is highest with its low-lying orbital, PAF-BT(EDOT)$_2$ is not capable of catalyzing the reaction. The oxidative potential of the catalyst is not sufficient to convert the tertiary isoquinoline. The photocatalytic performance of PAF-BT(Th)$_2$ is, following its HOMO level band position, in between the other catalysts. The potential of the LUMO level should not be of relevancy here since the oxygen present in the reaction solution scavenges the photogenerated electrons equally for all catalysts.

Similar relationships were investigated for the direct arylation of heteroarenes with diazonium salts. The reactions were conducted with 4-bromobenzenediazonium tetrafluoroborate and thiophene as substrates and DMSO as solvent. The reaction mixtures were degassed with argon and irradiated for 24h. Samples were taken after 1, 2, 4, 8, and 24h for GC-MS analysis using an internal standard. PAF-BT(EDOT)$_2$ was the best performing catalyst with a conversion of 93% after 24h, as shown in the kinetics study (**Figure 73b**). Both PAF-BT(Ph)$_2$ and PAF-BT(Th)$_2$ achieve lower photocatalytic activity during the same period. Also, in this kinetic analysis, a reaction order of one can be proved. In the series of control experiments, the presence of light and catalyst was identified as necessary for the successful progress of the reaction (**Table 7**). While the presence of oxygen or $CuCl_2$ drastically reduces the conversion achieved (15%), the addition of the hole scavenger KI has no effect. The present photocatalytic efficiency of the catalysts can be justified by the location of the LUMO energy levels. The reduction potential of PAF-BT(EDOT)$_2$ is highest because of its high LUMO and excited electrons can efficiently catalyze the activation. Although the reduction potential of PAF-BT(Ph)$_2$

and PAF-BT(Th)$_2$ is sufficient to photocatalytically activate the azo compound, lower photocatalytic efficiency can be achieved compared to the EDOT-type PAF. The potential difference of the LUMO level leads to the observed reaction difference.

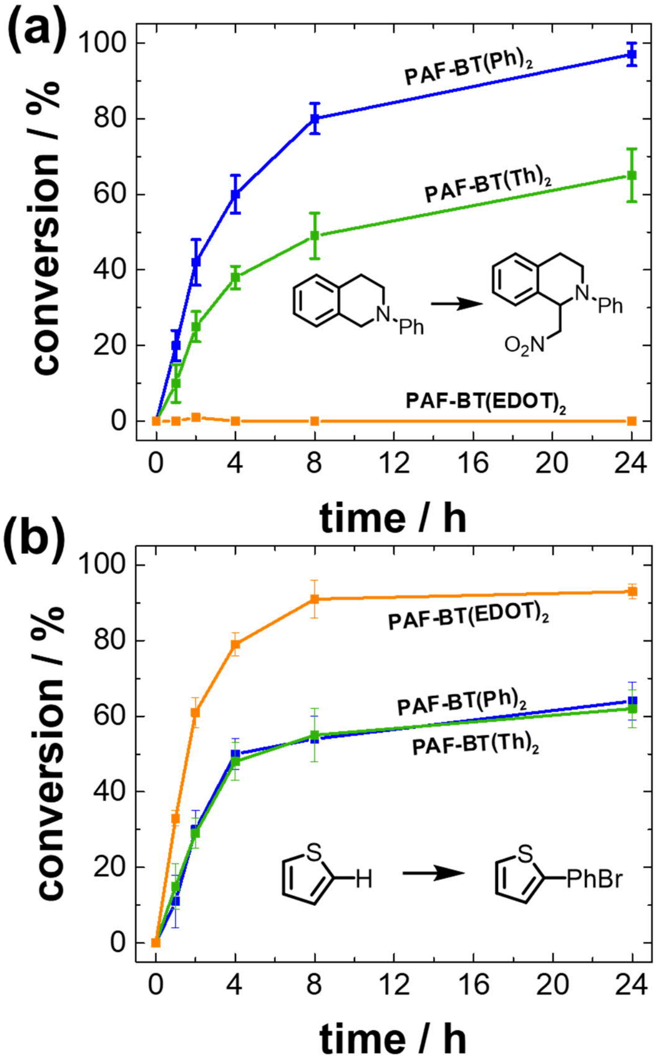

Figure 73. Kinetic study of the (a) aza-Henry reaction of 2-phenyl-1,2,3,4-tetrahydroisoquinoline and nitromethane, and (b) direct arylation of thiophene with 4-bromobenzenediazonium tetrafluoroborate using different PAFs as photocatalysts.

Based on the findings mentioned above by the control experiments, we propose reaction mechanisms *via* either electron- or hole-initiated reaction pathways similar to literature.[37, 40] As displayed in **Figure 74** (right), for the hole-initiated pathway, 2-phenyl-1,2,3,4-tetrahydroisoquinoline as a substrate is first oxidized by the photogenerated hole of the PAF, transforming into its cationic radical as intermediate. The electron at the LUMO level simultaneously activates molecular oxygen to form superoxide, which then removes a proton from the cationic radical intermediate to form the next cationic intermediate. The intermediate reacts with nitromethane to form the new C-C bond. After losing one more proton, the final product is formed.

For the electron-initiated pathway, as displayed in **Figure 74** (left), 4-bromobenzenediazonium tetrafluoroborate is first reduced by the photogenerated electron on LUMO into the aromatic radical, with N_2 and tetrafluoroborate anion as side products. The aromatic radical reacts with thiophene to form the radical intermediate, which is then oxidized by the hole at the HOMO and loses an electron. The formed cationic intermediate then loses one proton to form the final product with the new C-C bond.

In general, we could selectively control either electron- or hole-initiated reactions with the photocatalytic PAF series. A direct correlation between photocatalytic performance and electronic band positions could be found.

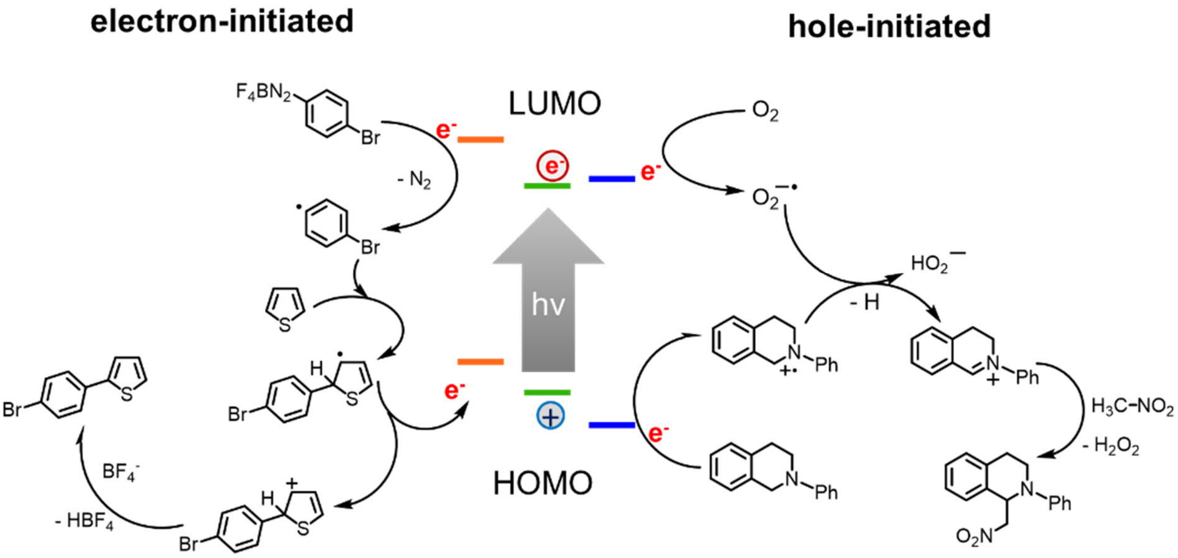

Figure 74. Proposed reaction mechanisms of the investigated electron- and hole-initiated reactions.

The recyclability of the heterogeneous photocatalysts PAF-BT(EDOT)$_2$ and PAF-BT(Ph)$_2$ for the respective reactions was further investigated. For both reactions, a series of five recycling experiments were conducted. After completing the reaction, the heterogeneous photocatalysts were separated from the reaction mixture by centrifugation, washed with little isopropanol, and dried overnight under high vacuum. In both cases, no loss of photocatalytic performance could be demonstrated in the five cycles tested (**Figure 75**).

The UV-Vis DR spectra acquired after recycling indicate that no significant photobleaching effects restrict the photocatalysts' use.

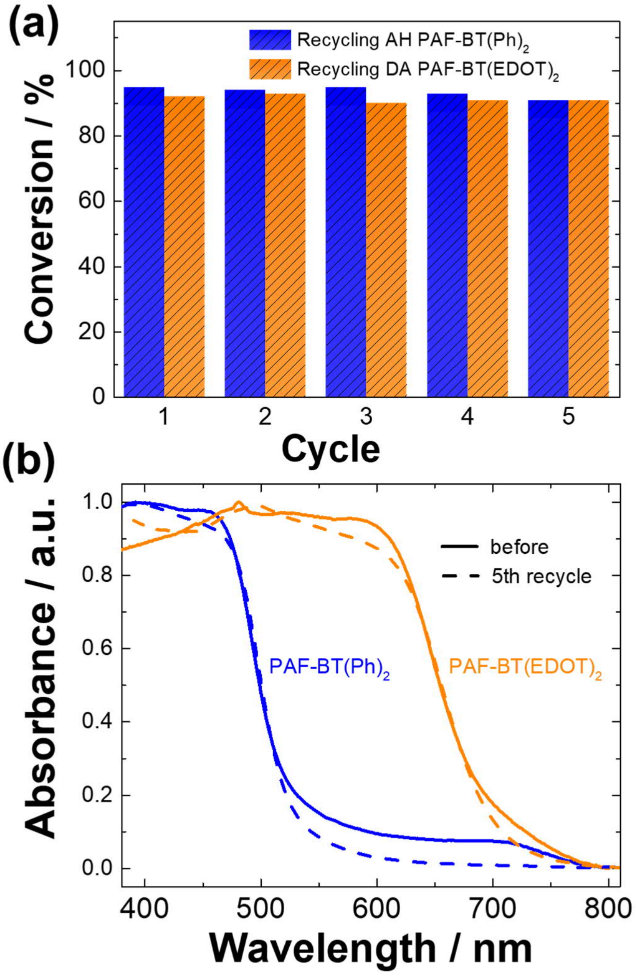

Figure 75. (a) Photocatalytic conversions for recycling PAF-BT(Ph)$_2$ in the aza-Henry reaction and PAF-BT(EDOT)$_2$ in the direct arylation. (b) UV/Vis DR spectra before and after recycling the catalysts five times.

The versatility of the photocatalytic materials in the aza-Henry reaction and the direct arylation was investigated (**Figure 76**). In both examples, the substrate scope could be extended by four products each. For the aza-Henry reaction, *N*-phenyltetrahydroisoquinoline was reacted with acetone, malononitrile, diethyl phosphite, and nitroethane. For the direct arylation, *N*-Boc-pyrrole, 3,4-dibromothiophene, 3,4-ethylenedioxythiophene, and furan were converted with 4-bromobenzenediazonium tetrafluoroborate. The conversions were found to be selective towards the desired products. Reaction conversions from 86 to 92% were obtained. The range of substrates and functional groups tolerated underlines the applicability of the PAF photocatalysts in the studied reactions.

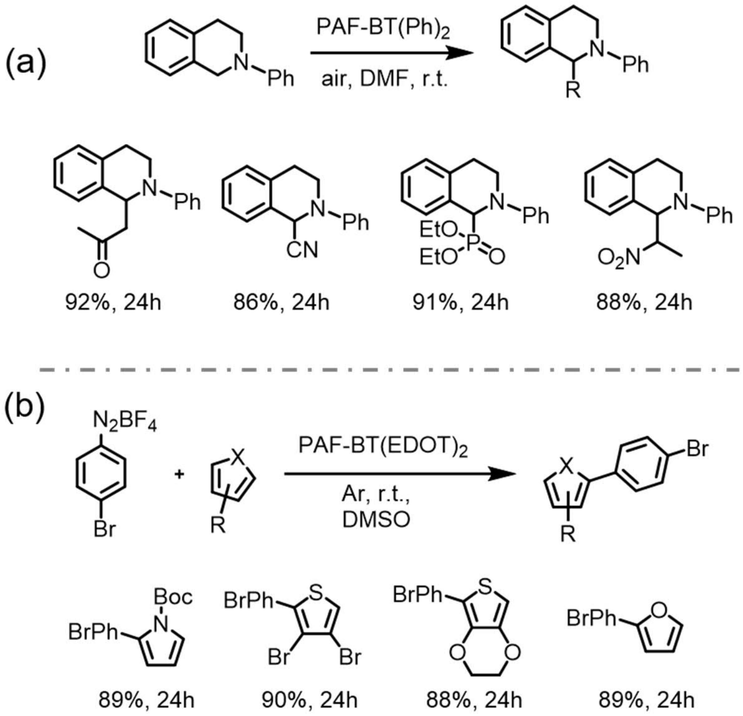

Figure 76. Reaction scopes for the reaction of 2-phenyl-1,2,3,4-tetrahydroisoquinoline (a) and 4-bromobenzenediazonium tetrafluoroborate (b) with different substrates. PAF-BT(Ph)$_2$ and PAF-BT(EDOT)$_2$ were used as photocatalysts.

The versatility of the catalysts was highlighted by an application example from pharmaceutical drug synthesis (**Figure 77**). The direct arylation of furfural with 4-nitrobenzenediazonium tetrafluoroborate and subsequent condensation with 1-aminohydantoin hydrochloride gave dantrolene in excellent yield. The muscle relaxant inhibits the release of calcium ions in muscle cells and is, therefore, a valuable drug to treat, e.g., malignant hyperthermia. The functionalization of the direct arylation product was conducted in one batch without intermediate purification.

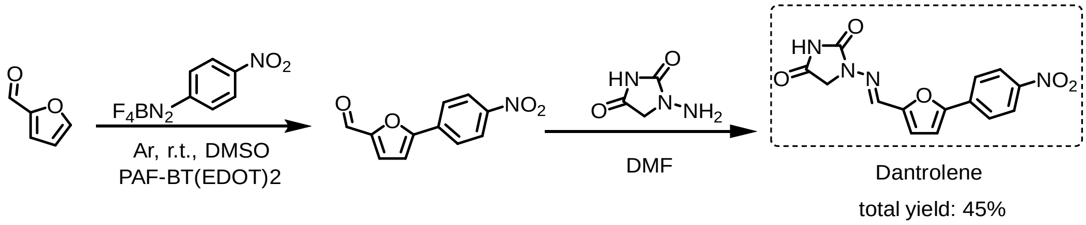

Figure 77. Synthesis of dantrolene in two steps and one batch as a practical example for applying the PAF-based photocatalysts.

2.4.4 Conclusion

In summary, we bottom-up designed three porous aromatic frameworks (PAFs) as efficient metal-free and redox-active photocatalysts for visible-light-promoted chemical transformations. The introduction of three photoactive molecules gave rise to optical and redox-tuneable properties that match the molecular analogs' characteristics. The PAF platform allows precise conjugation length control and the easy incorporation of photoactive dibromo-compounds into a high surface area and robust environment. The catalysts could efficiently catalyze two C-H activation reactions *via* either the photogenerated electron- or hole-initiated pathways, namely the aza-Henry reaction of tetrahydroisoquinoline derivatives and the direct arylation of heteroarenes with aryl diazonium salts. The PAFs allowed photocatalytic performance control in direct correlation with their respective band edge potentials. By expanding the scope of the reactions, broader applicability of the catalyst could be obtained. The vital muscle relaxant dantrolene was synthesized over two steps in a convenient one-batch approach applying a PAF photocatalyst. In general, we believe that the concept of introducing photocatalytic units into the porous aromatic frameworks provides a platform for a broad range of new versatile photocatalytic materials with improved recyclability and stability. The predictability of electro-optical and photocatalytic properties renders PAFs an exciting approach for photocatalytic material synthesis.

2.4.5 Experimental details

Materials and methods

All chemicals and solvents were purchased from commercial sources and used as received unless otherwise noted. ^{1}H and ^{13}C NMR spectra for all compounds were measured using a Bruker Avance 300 MHz. Solid-state ^{13}C CP MAS NMR measurements were carried out using a Bruker Avance II solid-state NMR spectrometer operating at 300 MHz Larmor frequency equipped with a standard 4mm magic angle spinning (MAS) double resonance probe head. Solid-state diffuse reflectance UV-Vis absorption and fluorescence spectra were recorded on a Perkin Elmer Lambda 100 spectrophotometer and J&M TIDAS spectrofluorometer at ambient temperature, respectively. Gas sorption was measured using a Micromeritics Tristar II Plus with samples degassed for 12h at 120 ^{o}C under vacuum prior to analysis. The BET surface area calculation was based on data points obtained from $0<P/P_0 \lesssim 0.15$, considering the Rouquerol criteria for microporous materials.[406] The nonlinear density functional theory (NLDFT) equilibrium model was used for the BET model fitting. Pore size distributions and pore volumes were derived from the adsorption branches of the isotherms using density functional theory (DFT, N_2, assuming a carbon substrate with slit pores). The morphology was examined with a Gemini 1530 (Carl Zeiss AG, Oberkochem, Germany) scanning electron microscope (SEM) operating at 0.35 kV. Cyclic voltammetry measurements were carried out on a Metrohm Autolab PGSTAT204 potentiostat/galvanostat with a three-electrode-cell system: glassy carbon electrode as the working electrode, $Hg/HgCl_2$ electrode as the reference electrode, platinum wire as the counter electrode, and Bu_4NPF_6 (0.1 M in acetonitrile) as supporting electrolyte with a scan rate of 100 mV s^{-1} in the range of 0 to -2 V. All DFT calculations were carried out with the Gaussian 09 package.[290] The structures were optimized at the B3LYP level of theory[331] with the basis set of 6-31G*.[332-333] Thermogravimetric analysis (TGA) was conducted in a nitrogen atmosphere with temperature increasing from room temperature to 800 °C at a rate of 10 K/min. FTIR measurements were conducted with a Varian 1000 FTIR spectrometer.

Monomer synthesis

Tetrakis(4-ethynylphenyl)methane:[407] In a dried Schlenk tube, tetra(4-bromophenyl)methane (597 mg, 0.94 mmol), CuI (7 mg, 0.04 mmol), PPh_3 (30 mg, 0.11 mmol), diisopropylamine (7.5 mL), trimethylsilylacetylene (641 µL, 4.51 mmol) and $PdCl_2(PPh_3)_2$ (40 mg, 0.06 mmol) were combined. The mixture was degassed with argon and heated to 90°C for 24h. After cooling to room temperature, all solvents were removed through rotary evaporation. DCM (50 mL) was added the solution was passed through a pad of Celite. The filtrate was washed with Na_2EDTA solution (0.5 M, 2 x 20 mL), H_2O (2 x 20 mL), and dried over $MgSO_4$. The solution was concentrated in vacuo. For the next step, DCM (2 mL) and NaOH (26 mg, 0.65 mmol) in EtOH (800 µL) were added to the intermediate. The reaction was stirred at room temperature overnight. Then, additional DCM (10 mL) was added. The organic phase was extracted with H_2O (2 x 10 mL) and brine (10mL). After drying over anhydrous $MgSO_4$, the solution was concentrated on the rotary evaporator until a saturated solution was obtained. With the addition of EtOH, the product could be precipitated and washed. Tetrakis(4-ethynylphenyl)methane resulted as a light yellowish powder (250 mg, 65%).^{1}H NMR (300 MHz, $CDCl_3$) δ 7.40 (d, 8H), 7.12 (d, 8H), 3.06 (s, 4H). ^{13}C NMR (75 MHz, $CDCl_3$) δ 146.35, 131.81, 130.90, 120.43, 83.32, 77.78, 64.95.

4,7-Bis(4-bromophenyl)benzo[c][1,2,5]thiadiazole:[408] A 250 mL three-necked flask was charged with 4,7-dibromobenzo[c][1,2,5]thiadiazole (1.47 g, 5 mmol), phenylboronic acid (2.68 g, 22 mmol) and toluene (25 mL). Then, a solution of potassium carbonate (2.76 g, 20 mmol) in H_2O (10 mL) was added to the flask. After degassing for 30min, $Pd(PPh_3)_4$ (0.047 g, 0.04 mmol) was added, and the reaction mixture was heated to 90 °C and reacted overnight under N_2 atmosphere. After cooling to room temperature, the mixture was poured into water and extracted with dichloromethane. The organic layer was washed with water and dried over anhydrous $MgSO_4$. After concentration with a rotary evaporator, the crude product was purified *via* column chromatography on silica with dichloromethane as eluent. For further purification, the crude product was recrystallized with methanol to afford $BTPh_2$ as yellow needles. Yield: 1.17 g (82%). ^{1}H NMR (300 MHz, $CDCl_3$) δ 7.97 (m, 4H), 7.79 (s, 2H), 7.56 (m, 4H), 7.47 (t, 2H). ^{13}C NMR (75 MHz, $CDCl_3$) δ 154.24, 137.56, 133.50, 129.39, 128.77, 128.51, 128.26. A solution of bromine (854 µL, 16.7 mmol) in chloroform (1 mL) was added to 4,7-diphenylbenzo[c][1,2,5]thiadiazole (200 mg, 0.69 mmol) and iodine (10.6 mg, 0.04 mmol) in chloroform (3 mL). The mixture was stirred at room temperature for 24h. DCM (30 mL) was added and the organic phase was washed with saturated $NaHSO_3$ (10 mL), H_2O (3 x 10 mL), and brine (10 mL). After drying over anhydrous $MgSO_4$, the solution was concentrated *via* rotary evaporation. The crude product was recrystallized in toluene to give 4,7-bis(4-bromophenyl)benzo[c][1,2,5]thiadiazole as yellow needles (275 mg, 89%).^{1}H NMR (300 MHz, d6-DMSO, 373K) δ 8.35 (m, 6H), 8.11 (d, 2H). ^{13}C NMR (75 MHz, d6-DMSO, 373K) δ 152.78, 135.48, 131.01, 130.95, 130.51, 127.75, 121.35.

4,7-Bis(5-bromothiophen-2-yl)benzo[c][1,2,5]thiadiazole:[409] 4,7-Dibromobenzo[c][1,2,5]-thiadiazole (1.15 g, 3.91 mmol), tributyl(thiophen-2-yl)stannane (2.73 mL, 8.61 mmol) were added to a previously dried Schlenk tube and dissolved in dry THF (40 mL). The solution was degassed with argon for 15min, $PdCl_2(PPh_3)_2$ (55 mg, 0.08 mmol) was added, and the mixture was heated to 70°C for 12h. After cooling to room temperature, THF was evaporated and the residue was taken up in DCM (50 mL). The organic phase was extracted with water (3 x 25 mL) and brine (25 mL). After drying with anhydrous

$MgSO_4$ and filtration, the resulting solution was concentrated by evaporation. The crude product was recrystallized in methanol followed by washing with cold hexanes (100 mL). 4,7-Di(thiophen-2-yl)benzo-2,1,3-thiadiazole was obtained as red needles (1.09 g, 85%). ^1H NMR (300 MHz, $CDCl_3$) δ 8.10 (d, 2H), 7.83 (s, 2H), 7.45 (d, 2H), 7.21 (t, 2H) ppm. ^{13}C NMR (75 MHz, $CDCl_3$) δ 152.72, 139.47, 128.13, 127.62, 126.92, 126.07, 125.86 ppm. To a solution of 4,7-di(thiophen-2-yl)benzo-2,1,3-thiadiazole (200 mg, 0.67 mmol) in chloroform (30 mL), NBS (710 mg, 4.00 mmol) was added and the mixture was stirred for 30h at room temperature. DCM (50 mL) was added and the organic phase was washed with saturated $NaHCO_3$ (50 mL), H_2O (2 x 10 mL), and brine (10 mL). After drying over anhydrous $MgSO_4$, the solution was concentrated *via* rotary evaporation. 4,7-bis(5-bromothiophen-2-yl)benzo[c][1,2,5]thiadiazole (290 mg, 95%) was obtained as red powder. ^1H NMR (300 MHz, d6-DMSO, 373K) δ 8.35 (m, 6H), 8.11 (d, 2H). ^{13}C NMR (75 MHz, d6-DMSO, 373K) δ 150.98, 139.59, 130.57, 127.18, 125.12, 124.11, 113.51.

4,7-Bis(5-bromo-3,4-ethylenedioxythiophene-2-yl)benzo[c][1,2,5]thiadiazole:[410] In a flame-dried Schlenk tube, 4,7-dibromobenzo[c][1,2,5]thiadiazole (400 mg, 1.36 mmol), 3,4-ethylenedioxythiophene (1.93 g, 13.6 mmol), potassium acetate (400 mg, 4.08 mmol) and dimethylacetamide (7 mL) were combined. After degassing with Ar for 15min, $Pd(OAc)_2$ (3 mg, 0.01 mmol) was added, and the reaction mixture was heated to 160 °C and reacted for 48h under Ar atmosphere. Ethyl acetate (200 mL) was added and the organic phase was extracted with H_2O (3 x 50 mL) and brine (1 x 30 mL). After drying with anhydrous $MgSO_4$, the crude product was purified by column chromatography (DCM / petrol ether 2:1 to 1:0). 4,7-Di(3,4-ethylenedioxythiophene-2-yl)benzo[c][1,2,5]-thiadiazole was obtained as purple powder (408 mg, 72%). ^1H NMR (300 MHz, DMSO) δ 8.41 (s, 2H), 6.87 (s, 2H), 4.43 (d, 4H), 4.31 (d, 4H). ^{13}C NMR (75 MHz, DMSO) δ 151.41, 141.56, 140.71, 125.90, 123.04, 112.11, 102.59, 65.08, 64.03. The previous compound (150 mg, 0.36 mmol) was dissolved in chloroform (160 mL) followed by the addition of NBS (320 mg, 1.80 mmol). The mixture was stirred over night at room temperature. The formed precipitate was filtered, washed with H_2O (3 x 75 mL) and DCM (2 x 10 mL). 4,7-bis(5-bromo-3,4-ethylenedioxythiophene-2-yl)benzo[c][1,2,5]thiadiazole was obtained as purple powder (196 mg, 95%). ^1H NMR (300 MHz, $CDCl_3$) δ 8.36 (s, 2H), 4.40 (s, 8H). 574.05 m/z [M+H]

Polymer synthesis

In a dried Schlenk tube, tetrakis(4-ethynylphenyl)methane (100 mg, 0.24 mmol), dibromo monomer (0.32 mmol), copper iodide (6 mg, 0.03 mmol), triethyl amine (7.5 mL), and anhydrous DMF (7.5 mL) were combined. The setup was degassed with Ar for 15min and $PdCl_2(PPh_3)_2$ (19mg) was added. The mixture was degassed for another 5min and heated to 90 °C for 48h. After cooling to room temperature, the mixture was filtered and washed with MeOH and THF. The resultant polymer was immersed in MeOH (10 mL) and sonicated for 1h to remove impurities. After centrifugation and collection of the solid, the purification step was repeated with THF and DCM. The polymers were dried under high vacuum for 24h (Ph 190 mg, 95%; Th 111 mg, 92%; EDOT 132 mg, 89%).

Photocatalytic aza-Henry & direct arylation reactions

General Procedure 1: In a 4 mL vial equipped with a magnetic stirring bar, the *N*-phenyltetrahydroisoquinoline derivative (1 eq.) was dissolved in DMF (2 mL). The respective reaction partner (1.5 eq.) and photocatalyst were added (2 mg). The resulting mixture was irradiated with a 23W commercial energy-saving light bulb for the time given. After the reaction was completed, the reaction mixture was filtered and the solvent was evaporated under reduced pressure. The residue was purified by flash chromatography on silica gel using petrol ether/ethyl acetate as eluent.

General Procedure 2: In a 4 mL vial equipped with a magnetic stirring bar, the diazonium salt (1 eq) was dissolved in DMSO (2 mL). The heterocyclic compound (10 eq.) and photocatalyst (2 mg) were added. The resulting mixture was degassed by passing Ar through the solution for 5min and subsequently irradiated with a 23W commercial light bulb for the time given. Afterward, the reaction mixture was filtered, DCM (10 mL) was added and the mixture was washed with brine (4 x 10 mL). Then, the solvent was evaporated under reduced pressure. The residue was purified by flash chromatography on silica gel using petrol ether/ethyl acetate as eluent.

Photocatalytic synthesis of dantrolene

In a 20 mL round-bottom flask equipped with a magnetic stirring bar, 4-nitrobenzenediazonium tetrafluoroborate (250 mg, 1.06 mmol) was dissolved in DMSO

(3 mL). Furfural (1.01 g, 10.55 mmol) and photocatalyst PAF-BT(EDOT)$_2$ (3 mg) were added. The resulting mixture was degassed by passing Ar through the solution for 5min and subsequently irradiated with a 23W commercial light bulb for 24h. All solvents were removed by high vacuum evaporation. DMF (5 mL) and 1-aminohydantoin (88 mg, 0.58 mmol) in an aqueous HCl solution (0.67 M, 2 mL) were added to the flask. The mixture was stirred at room temperature for 4h. After H_2O (20 mL) was added, the precipitate was filtered off, washed with water (2 x 10 mL), and dried under vacuum to give dantrolene (152 mg, 0.48 mmol, 45% over two steps).

Recycling experiments

The recycling experiments were conducted similar to the general procedures. After 24h hours of reaction, the conversion was determined through either GC-MS or NMR. The reaction mixture was centrifuged at 1000 rpm for 2min and the supernatant was removed. After the catalysts were washed with isopropanol (5 mL) and dried under high vacuum overnight, the reactions were repeated. The substrates (*N*-phenyltetrahydroisoquinoline/CH_3NO_2 and 4-bromobenzenediazonium tetrafluoroborate/thiophene) as well as the solvents DMF or DMSO were added into the mixture. The vial was further irradiated. The catalysts were recycled 5 times.

Photocatalytic products

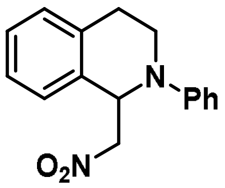

1-(Nitromethyl)-2-phenyl-1,2,3,4-tetrahydroisoquinoline (General procedure 1, 3 eq. Nitromethane, 24h, Yield: 90%, Column: PE / EA 10:1). ^1H NMR (300 MHz, $CDCl_3$) δ 7.32 (m, 5H), 7.21 (d, 1H), 7.06 (d, 2H), 6.93 (t, 1H), 5.63 (t, 1H), 4.95 (dd, 1H), 4.64 (dd, 1H), 3.72 (m, 2H), 3.16 (m, 1H), 2.87 (dt, 1H). ^{13}C NMR (75 MHz, $CDCl_3$) δ 148.57, 135.42, 133.07, 129.65, 129.33, 128.26, 127.14, 126.84, 119.58, 118.29, 115.25, 114.03, 78.93, 58.34, 42.22, 26.61.

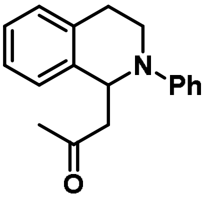

1-(2-Phenyl-1,2,3,4-tetrahydroisoquinolin-1-yl)propan-2-one (The reaction was conducted in acetone (1.5 mL) and MeOH (1.5 mL). L-Proline was added (0.2 eq.), 24h, Yield: 86%, Column: PE / EA 15:1). ^{1}H NMR (300 MHz, $CDCl_3$) δ 7.23 (t, 2H), 7.14 (s, 4H), 6.92 (d, 2H), 6.76 (t, 1H), 5.38 (t, 1H), 3.63 (m, 1H), 3.51 (m, 1H), 3.03 (m, 2H), 2.80 (m, 2H), 2.05 (m, 2H). ^{13}C NMR (75 MHz, $CDCl_3$) δ 207.40, 148.99, 138.40, 134.56, 129.47, 128.80, 126.98, 126.93, 126.40, 118.38, 114.89, 54.92, 50.34, 42.18, 31.23, 27.34.

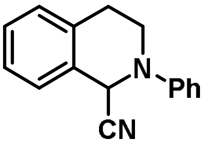

2-Phenyl-1,2,3,4-tetrahydroisoquinoline-1-carbonitrile (General procedure 1, Malononitrile, 24h, Yield: 82%, Column: PE / EA 10:1). ^{1}H NMR (300 MHz, $CDCl_3$) δ 7.30 (t, 2H), 7.20 (m, 4H), 7.02 (d, 2H), 6.95 (t, 1H), 3.72 (m, 1H), 3.43 (dt, 1H), 3.10 (m, 1H), 2.91 (d, 1H). ^{13}C NMR (75 MHz, $CDCl_3$) δ 148.53, 134.76, 129.72, 129.51, 128.91, 127.21, 127.01, 122.06, 117.88, 117.77, 53.40, 44.34.

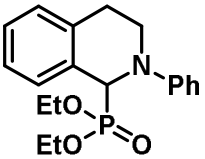

Diethyl (2-phenyl-1,2,3,4-tetrahydroisoquinolin-1-yl)phosphonate (General procedure 1, diethyl phosphite, 24h, yield: 83%, column: PE / EA 5:1). ^{1}H NMR (300 MHz, $CDCl_3$) δ 7.39 (d, 1H), 7.25 (t, 2H), 7.18 (m, 3H), 6.99 (d, 2H), 6.80 (t, 1H), 5.20 (d, 1H), 4.02 (m, 4H), 3.91 (m, 1H), 3.64 (m, 1H), 3.05 (m, 2H), 1.25 (t, 3H), 1.15 (t, 3H). ^{13}C NMR (75 MHz, $CDCl_3$) δ 149.50, 136.53, 130.77, 129.23, 128.84, 128.23, 127.52, 125.96, 118.54, 114.87, 63.34, 62.36, 59.97, 57.86, 43.58, 26.87, 16.52.

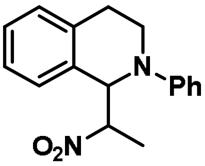

1-(1-Nitroethyl)-2-phenyl-1,2,3,4-tetrahydroisoquinoline (General procedure 1, Nitroethane, 24h, Yield: 81%, Column: PE / EA 5:1). ^{1}H NMR (300 MHz, $CDCl_3$) overlap δ 7.25, 7.19, 7.01, 6.83, 5.26, 3.07, 2.90. Major isomer δ 5.06, 3.59, 1.54. Minor isomer δ 4.90, 3.84, 1.70. ^{13}C NMR (75 MHz, $CDCl_3$) δ Major isomer 148.98, 135.72, 132.13, 129.41, 129.21, 128.45, 128.30, 126.23, 119.42, 115.52, 85.54, 62.85, 42.77, 26.49, 16.50. Minor isomer 149.26, 134.89, 133.92, 129.53, 129.21, 128.82, 127.35, 126.69, 118.88, 114.59, 89.05, 61.26, 43.65, 26.85, 17.53

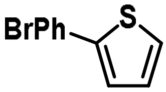

2-(4-Bromophenyl)thiophene (General procedure 2, Thiophene, 24h, Yield: 81%, Column: PE / DCM 5:1). ^{1}H NMR (300 MHz, $CDCl_3$) δ 7.49 (d, 4H) 7.30 (d, 2H), 7.08 (t, 1H). ^{13}C NMR (75 MHz, $CDCl_3$) δ 143.24, 133.51, 132.11, 128.31, 127.55, 125.40, 123.63, 121.41.

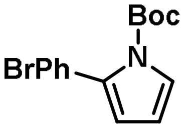

Tert-butyl 2-(4-bromophenyl)-1H-pyrrole-1-carboxylate (General procedure 2, *N*-Boc-pyrrole, 24h, Yield: 74%, Column: PE / DCM 8:1). ^{1}H NMR (300 MHz, $CDCl_3$) δ 7.47 (d, 2H), 7.34 (m, 1H), 7.22 (d, 2H), 6.20 (m, 2H). ^{13}C NMR (75 MHz, $CDCl_3$) δ 149.32, 133.93, 133.42, 130.93, 130.85, 123.03, 121.42, 114.94, 110.83, 84.05, 27.83.

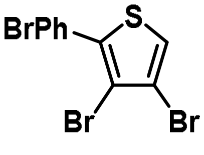

3,4-Dibromo-2-(4-bromophenyl)thiophene (General procedure 2, 3,4-Dibromothiophene, 24h, Yield: 81%, Column: PE / DCM 5:1). ^{1}H NMR (300 MHz, $CDCl_3$) δ 7.58 (d, 2H), 7.48

(d, 2H), 7.39 (s, 1H). ^{13}C NMR (75 MHz, $CDCl_3$) δ 138.30, 132.01, 131.92, 130.59, 123.34, 122.73, 115.16, 111.93.

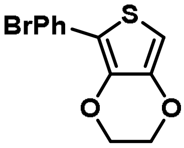

5-(4-Bromophenyl)-2,3-dihydrothieno[3,4-b][1,4]dioxine (General procedure 2, 3,4-Ethylenedi-oxythiophene, 24h, Yield: 79%, Column: PE / DCM 5:1). ^{1}H NMR (300 MHz, $CDCl_3$) δ 7.58 (d, 2H), 7.47 (d, 2H), 6.32 (s, 1H), 4.27 (dd, 4H). ^{13}C NMR (75 MHz, $CDCl_3$) δ 142.39, 138.60, 132.25, 131.73, 127.51, 120.23, 116.31, 98.10, 64.90, 64.51.

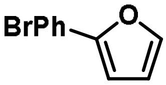

2-(4-Bromophenyl)furan (General procedure 2, Furan, 24h, Yield: 70%, Column: PE / DCM 6:1). ^{1}H NMR (300 MHz, $CDCl_3$) δ 7.60 (d, 2H), 7.47 (s, 1H), 7.35 (d, 2H), 6.64 (d, 1H), 6.47 (s, 1H). ^{13}C NMR (75 MHz, $CDCl_3$) δ 142.47, 138.04, 129.01, 128.50, 125.16, 118.31, 111.92, 105.56.

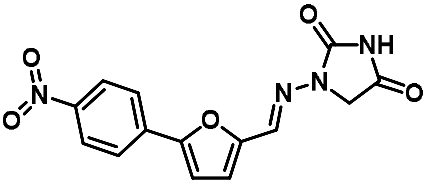

(E)-1-(((5-(4-nitrophenyl)furan-2-yl)methylene)amino)imidazolidine-2,4-dione, Dantrolene. ^{1}H NMR (300 MHz, DMSO) δ 11.33 (s, 1H), 8.31 (d, 2H), 8.01 (d, 2H), 7.76 (s, 1H), 7.46 (d, 1H), 7.04 (d, 1H), 4.36 (s, 2H). ^{13}C NMR (75 MHz, DMSO) δ 168.85, 153.27, 152.10, 151.08, 146.27, 135.20, 132.62, 124.57, 124.52, 115.56, 112.44, 48.99.

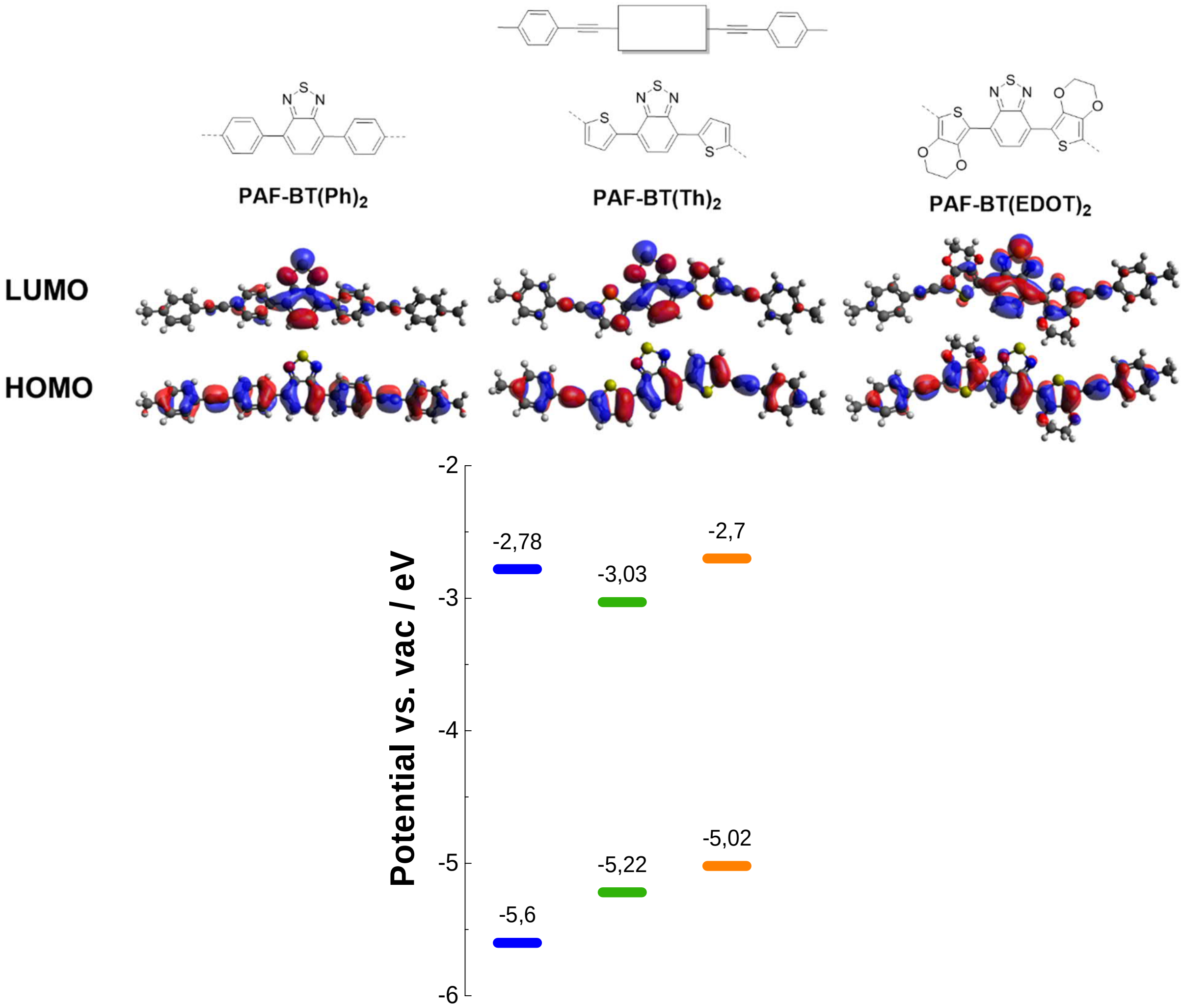

Figure 78. HOMO and LUMO levels of simplified PAF structures at the B3LYP/6-31G(d) level.

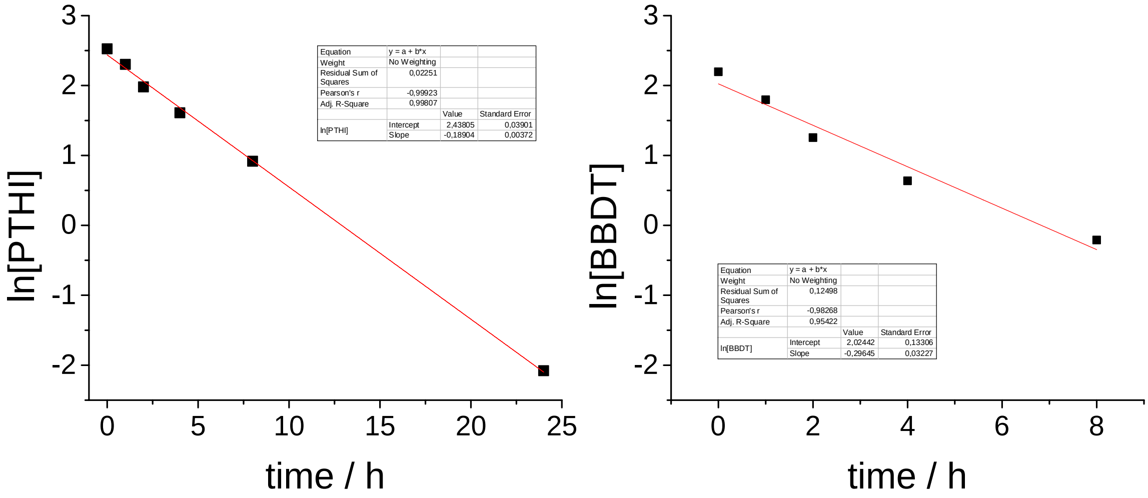

Equation	y = a + b*x		
Weight	No Weighting		
Residual Sum of Squares	0,02251		
Pearson's r	-0,99923		
Adj. R-Square	0,99807		
		Value	Standard Error
ln[PTHI]	Intercept	2,43805	0,03901
	Slope	-0,18904	0,00372

Equation	y = a + b*x		
Weight	No Weighting		
Residual Sum of Squares	0,12498		
Pearson's r	-0,98268		
Adj. R-Square	0,95422		
		Value	Standard Error
ln[BBDT]	Intercept	2,02442	0,13306
	Slope	-0,29645	0,03227

Figure 79. Logarithmic plot of the concentration of N-Phenyltetrahydroisoquinoline and 4-Bromobenzodiazonium tetrafluoroborate during the reaction with PAF-BT(Ph)$_2$ and PAF-BT(EDOT)$_2$, respectively. The initial concentrations were 0.125 M of PTHI and 0.09 M of BBDT.

2.5 A PMMA-based heterogeneous photocatalyst for visible-light-promoted [4+2] cycloaddition

The assembly of photocatalysts from functionalized building blocks in the previous chapter is an efficient and often used method for photocatalytic material synthesis. In platforms such as PAFs, various polymers can be built up with a few chemically similar monomers and the stepwise change of properties can be studied. A similar concept was leveraged in the following chapter. By copolymerizing small amounts of photoactive monomers with MMA to crosslinked polymers, cost-effective and powerful photocatalysts could be obtained in a simple way. The chapter is based on the published article "A PMMA-based heterogeneous photocatalyst for visible-light-promoted [4+ 2] cycloaddition, Catalysis Science & Technology 2020, 10(7), 2092-2099."[411] The project is a joint effort of Dr. Run Li, Dr. Calum Ferguson, Dr. Dominik Gehrig, Dr. Charusheela Ramanan, Prof. Paul Blom, Prof. Katharina Landfester, Prof. Kai Zhang, and me. I carried out the project's experimental work with the following exceptions: Run Li and Calum Ferguson performed parts of the photocatalytic screening and reaction optimization. Dominik Gehrig and Charusheela Ramanan performed time-resolved photoluminescence and transient adsorption characterization.

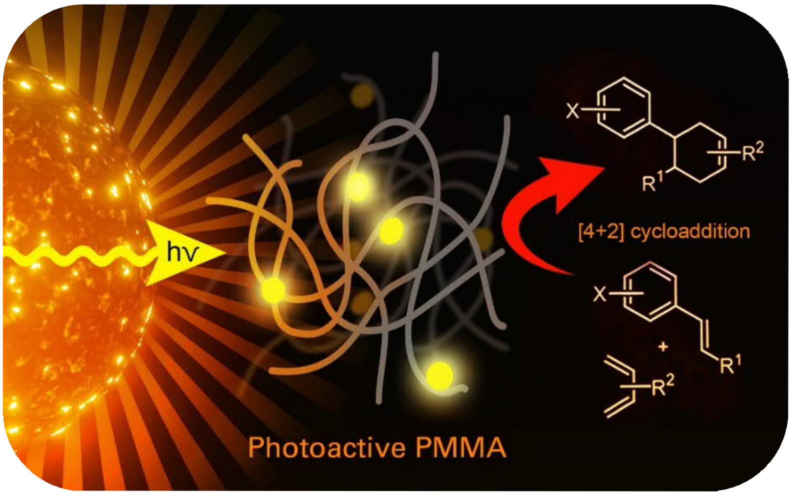

Macromolecular organic photocatalysts consisting of a completely conjugated network have broad and promising applications in visible-light-promoted photoredox catalysis. However, precise reproduction and control of exact conjugation length remain a fundamental challenge for fully conjugated and macromolecular photocatalysts. Here, we introduce a new photocatalytic material based on classical PMMA copolymerized with defined electron donor and acceptor units with precisely controllable redox potential and conjugation length, creating a promising class of metal-free, stable and low-cost heterogeneous photocatalysts. Furthermore, swelling of the PMMA copolymer matrix in organic solvents led to enhanced substrate diffusion and thereby increased catalytic efficiency. High efficiency and selectivity were achieved for photocatalytic [4+2] cycloaddition reactions in air with low effective photocatalyst loading. The photocatalytic efficiency of the PMMA photocatalyst was comparable with the state-of-art metal or non-metal catalysts while facilitating easy recyclability.

2.5.1 Motivation

Metal-free heterogeneous photocatalysts have attracted much attention empowering chemical synthesis under sustainable and environmentally benign reaction conditions.[94, 153, 160, 412-414] They have shown widescale use in catalyzing visible-light promoted photoredox reactions in many application fields, including energy for water splitting,[101, 389, 415-416] organic redox reactions,[116, 417-419] and environmental photocatalysis;[420-422] or in biological applications for photodynamic therapy[423-426] and enzyme regeneration.[427-429] Among fully conjugated systems being used, exact control of conjugation length and thereby electronic and optical properties within the polymer network is not easily obtainable. Moreover, the inflexible conjugated networks hinder swelling by solvents and, as a result, substrate diffusion. A key challenge is therefore to design a low-cost and flexible polymer-based photocatalyst with reproducible, well-defined optical and electronic properties.

The classical polymer chemistry toolbox provides access to tunable polymeric materials with variable solubility, biological compatibility, mechanical properties, and responsibility to external triggers. However, the role of classic polymers as a platform for photocatalytic systems has barely been explored, and studies are limited to attaching photoactive metal complexes [218-219] or organic dyes [222] to linear polymers. Recently, our group published temperature-responsive photocatalytic nanogels based on poly-N-isopropylacrylamide, demonstrating the versatility of combining photoactive units with well-known polymeric systems.[430] In general, the incorporation of photocatalytic properties into classical polymer networks *via* copolymerization of photoactive monomers could be an effective strategy towards a novel class of efficient, cheap, and metal-free photocatalysts. Moreover, this combination may yield photocatalytic materials with considerable advantages in terms of stability and long-term usage for visible-light-promoted redox catalysts.

In this work, we designed a crosslinked copolymer based on poly(methyl methacrylate) (PMMA) with integrated photocatalytic units consisting of 4,7-diphenylbenzothiadiazole (cPMMA-BTPh2). The resulting polymer is an efficient metal-free and redox-active heterogeneous photocatalyst for visible-light-promoted chemical transformations. This material must exhibit optical and redox properties similar to the molecular photocatalytic analog unit while demonstrating advantageous chemical robustness and recyclability attributed to polymer materials. [4+2] Cycloaddition reactions (the Diels-Alder reaction) could be efficiently catalyzed by the PMMA photocatalytic material upon low catalyst loading, in particular, 0.06 mol-% of the effective photocatalytic unit with respect to the substrate. The copolymer photocatalyst exhibited comparable photocatalytic efficiency and selectivity to the state-of-art molecular and transition metal-containing photocatalysts. Specifically, the photocatalytic copolymer material exhibited comparable efficiency when compared to its small molecule analog. No photo-bleaching effect of the polymer photocatalyst was observed, as confirmed by recycling experiments. Furthermore, a detailed mechanistic study employing advanced photophysical methods as time-resolved photoluminescence and transient absorption spectroscopy was conducted. Further to the detailed studies on the benchmark reaction, the scope of the reactivity of the copolymer photocatalyst was expanded to a broader range of substrates proving excellent efficiencies and functional group tolerance.

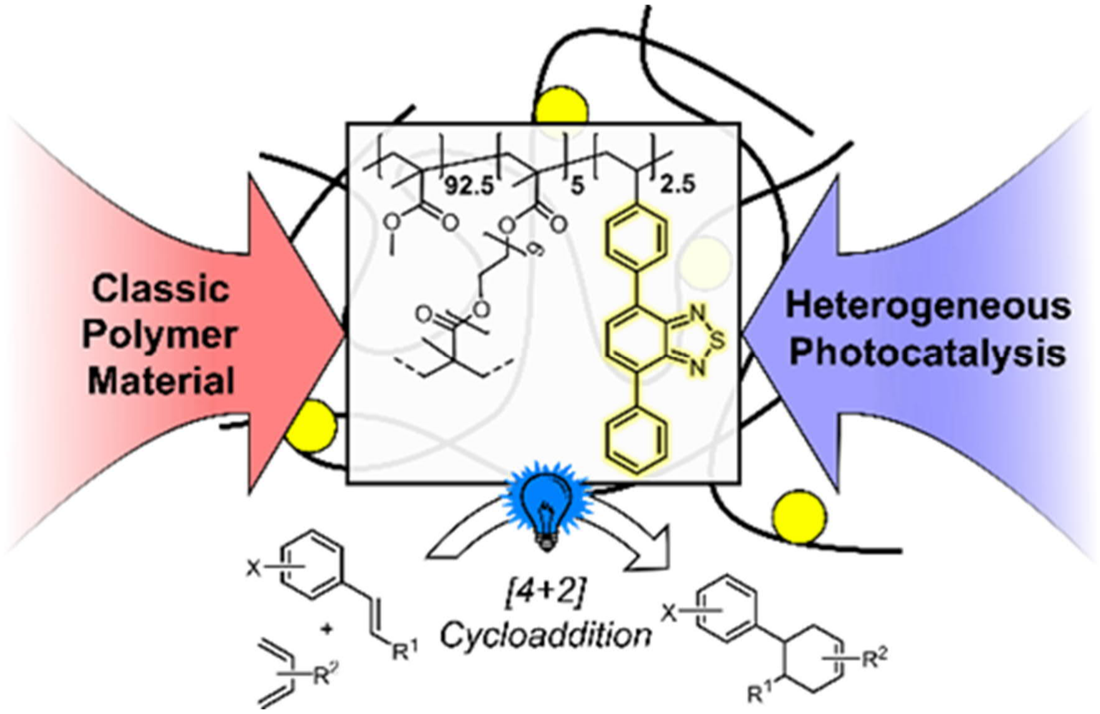

Figure 80. Illustration of the PMMA-based photocatalyst copolymer design concept and its application in the photocatalytic [4+2] cycloaddition.

2.5.2 Synthesis and characterization

The photocatalytic copolymer (cPMMA-BTPh$_2$) in this study was synthesized *via* free-radical polymerization from methyl methacrylate (MMA) as well as polyethylene glycol dimethacrylate (PEGDMA) and 4-phenyl-7-(4-vinylphenyl)benzothiadiazole (BTPh$_2$) in low concentrations. Details on synthetic procedures and characterization details are given in the Experimental Section and Electronic Supplementary Information (ESI).

In order to confirm the incorporation of the photoactive BTPh$_2$ unit into the crosslinked PMMA, solid-state nuclear magnetic resonance (ssNMR), UV/Vis, photoluminescence (PL), and cyclic voltammetry (CV) analyses were performed. The ssNMR comparison of cPMMA-BTPh$_2$ and a photoinactive cPMMA analog gives clear signals for the photoactive unit (**Figure 81**).

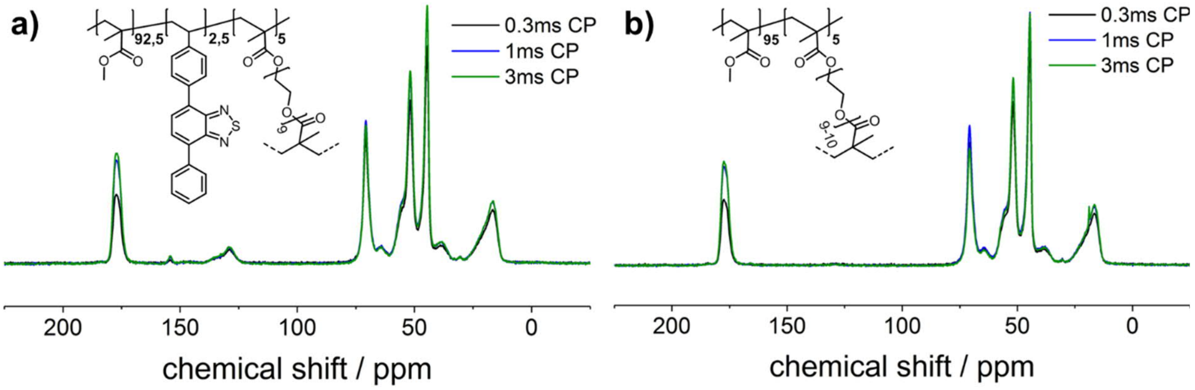

Figure 81. ^{13}C CP-MAS NMR spectra at different contact times (0.3 ms, 1 ms, 3 ms) of cPMMA-BTPh$_2$ (a) and cPMMA (b).

The UV/vis absorption spectrum of cPMMA-BTPh$_2$ showed an absorption range up to 475 nm with a maximum at 386 nm, while the emission area between 425 nm and 650 nm with a maximum at 512 nm was determined (**Figure 82**). The result is consistent with the optical properties of the corresponding small molecule BTPh$_2$ and previous reports.[431-432] The slight redshift of the cPMMA-BTPh$_2$ compared to BTPh$_2$ can be attributed to hyperconjugation effects of the photoactive unit in cPMMA-BTPh$_2$ which is one-sidedly attached to the polymer backbone. The optical properties of cPMMA-BTPh$_2$ in terms of emission and absorption behavior are similar to those of *fac*-[Ir(ppy)$_3$], a well-established transition metal photocatalyst.[433]

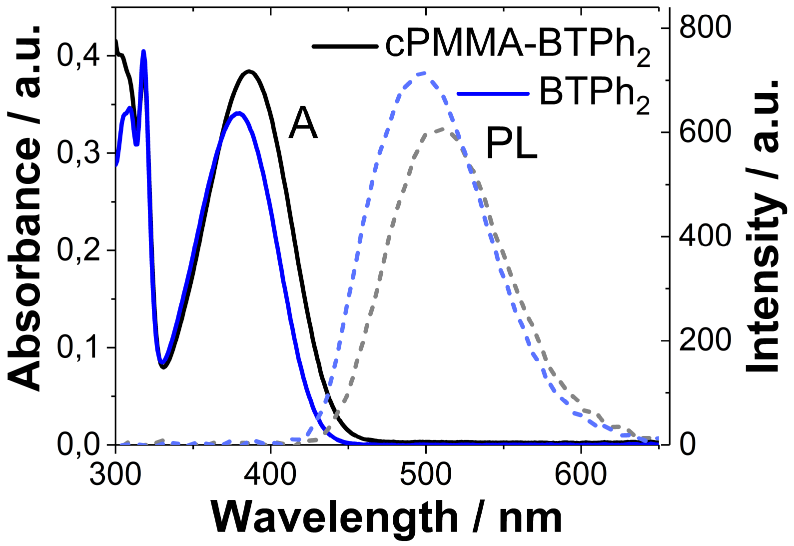

Figure 82. Photoluminescence and UV/Vis comparison of BTPh$_2$ units and the polymer cPMMA-BTPh$_2$ in the solid state.

Cyclic voltammetry (CV) measurements revealed the highest occupied molecular orbital (HOMO) and the lowest unoccupied molecular orbital (LUMO) of cPMMA-$BTPh_2$ at +1.62 eV and -1.33 eV *vs.* SCE (**Figure 83**), which matches the potentials of the analogous small molecular organic photocatalyst $BTPh_2$.

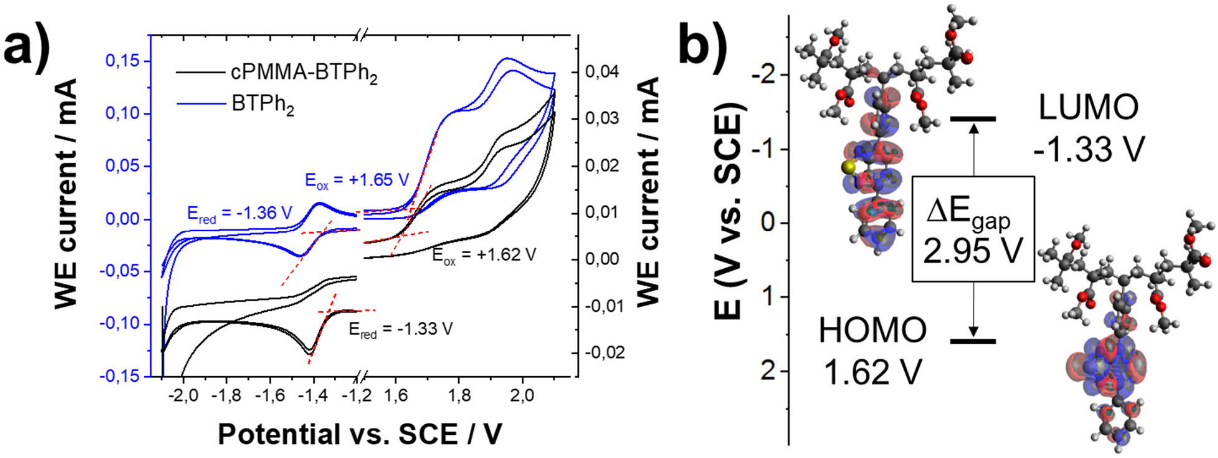

Figure 83. Cyclic voltammetry of cPMMA-$BTPh_2$ and $BTPh_2$ with a scan rate of 100 mV/s in CH_3CN (a). DFT/B3LYP 6-31G(d) calculated electronic structures for HOMO and LUMO of a simplified cPMMA-$BTPh_2$. Potentials result from the CV measurement on cPMMA-$BTPh_2$ (b).

Theoretical calculations of cPMMA-$BTPh_2$ using the density functional theory (DFT) at B3LYP/6-31G(d) level (**Table 8**) revealed that the electron densities of HOMO and LUMO are mainly located on the diphenylbenzothiadiazole unit. This indicates that the electronic structure is determined by the side-chain consisting of the D-A-type unit $BTPh_2$. The slight deviations in UV/Vis, PL, and CV between $BTPh_2$ and cPMMA-$BTPh_2$ were reproducible and we attribute them to hyperconjugation effects in cPMMA-$BTPh_2$.

Table 8. DFT and TDDFT-calculated electrooptical parameters of the catalysts (rB3LYP, 6-31+g(d)).

		HOMO *vs.* SCE	LUMO *vs.* SCE	Bandgap (electr.)	λ_{max} (calc.)	Bandgap (optic. calc. from λ_{max})
BTPh$_2$	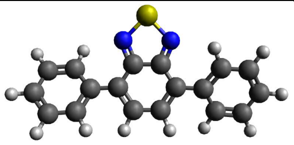	+1.64 V	-1.70 V	2.93 eV	480 nm	2.58 eV
cPMMA-BTPh$_2$ analog 1	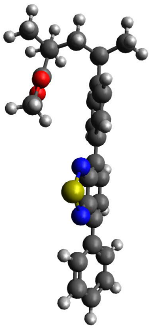	+1.36 V	-1.51 V	2.87 eV	496 nm	2.50 eV
cPMMA-BTPh$_2$ analog 2	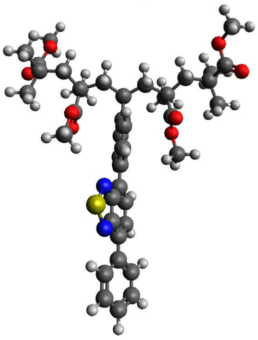	+1.40 V	-1.47 V	2.87 eV	496 nm	2.50 eV

The swelling behavior of cPMMA-BTPh$_2$ was investigated by live-imaging the photocatalytic material after exposure to CH_3NO_2 with a bright-field/fluorescence microscope (**Figure 84**). The photocatalytic gel was observed to swell to about four times its original size within 2s. The ability of the gel to swell is controlled by the crosslinking density and the crosslinker length. The long ethylene glycol chains in the crosslinker PEGDMA allow the gel to expand, enabling easy diffusion of substrates and products into and out of the photocatalytic material.

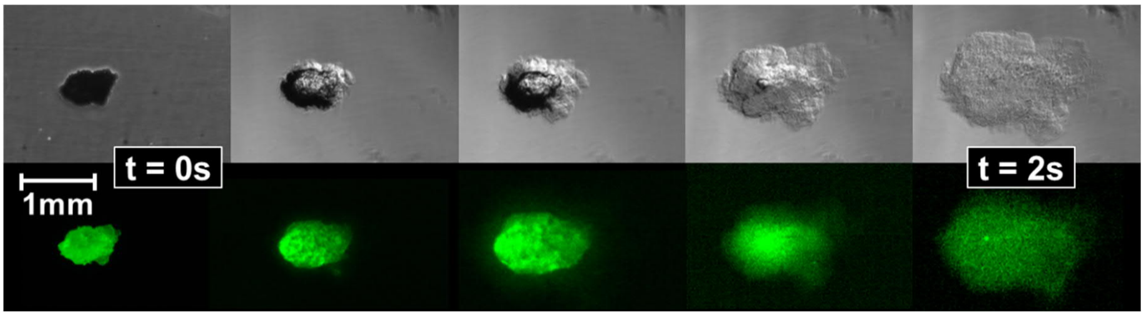

Figure 84. Optical microscopy images of cPMMA-$BTPh_2$ swelling after exposure to CH_3NO_2.

Fourier-transformed infrared (FTIR) spectroscopy and thermogravimetric analysis (TGA) characterization were performed with the cPMMA-$BTPh_2$ photocatalyst and compared to a non-photoactive cPMMA analog. The FTIR spectrum (**Figure 85a**) showed typical signals, for example, at 2950 cm^{-1}, which is characteristic of the C–H bond stretch vibrations of the $–CH_3$ and $–CH_2–$ groups, respectively. The signal at 1724 cm^{-1} indicates the presence of the acrylate carboxyl group. The broad signals at 1143 cm^{-1} can be assigned to the C–O–C stretching vibration. Interestingly, the influence of the photoactive unit on the FTIR spectrum is minimal (**Figure 85b**), showing that the chemical constitution and connectivity of the catalyst are mainly determined by the PMMA network. Thermogravimetric analysis (TGA) showed that the photocatalyst stayed intact up to 295°C under nitrogen, comparable to the cPMMA blank test (**Figure 85c**). FTIR and TGA measurements prove the robustness of the cPMMA-$BTPh_2$ photocatalyst, which shows that the properties of the crosslinked PMMA network were directly transferred to the polymeric cPMMA-$BTPh_2$ system.

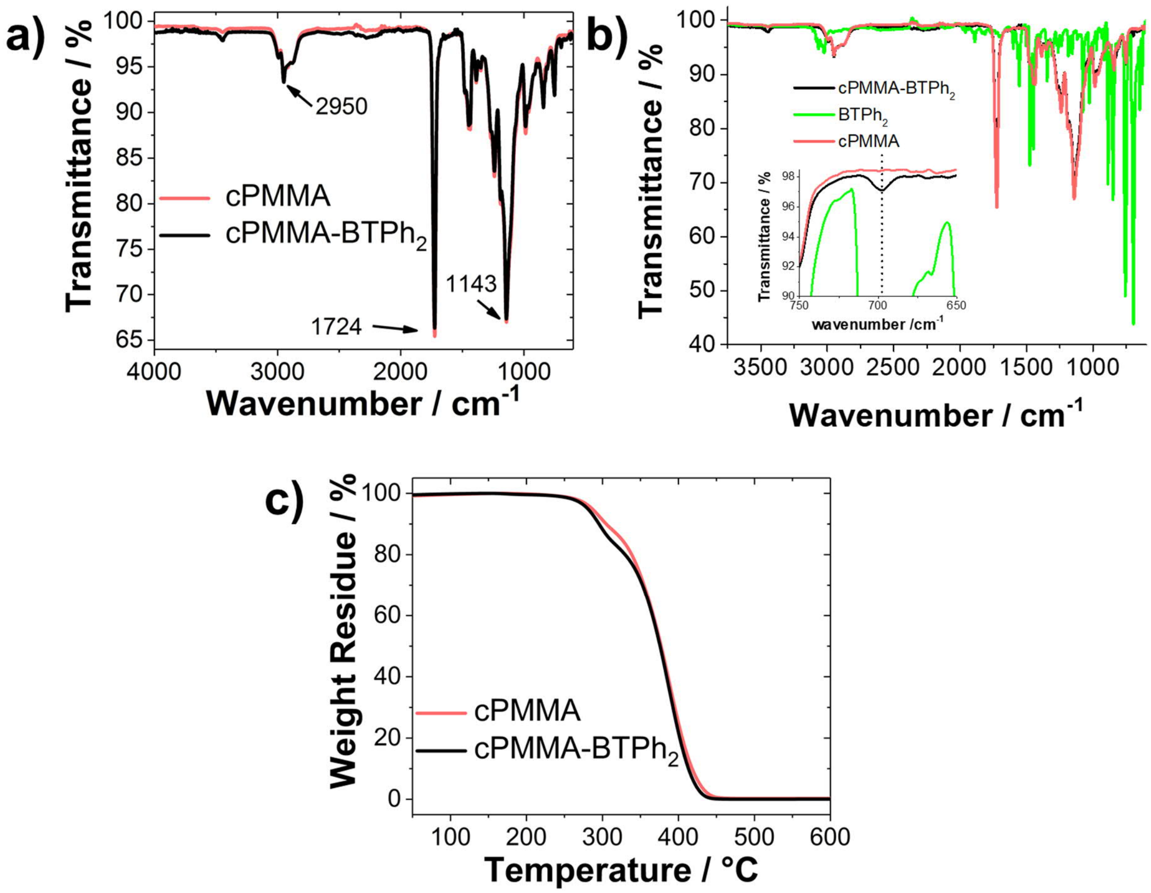

Figure 85. FTIR comparison of cPMMA-BTPh$_2$ and the blank cPMMA sample (a). Detailed FTIR comparison of cPMMA-BTPh$_2$, cPMMA and BTPh$_2$ (b). cPMMA and cPMMA-BTPh$_2$ differ only slightly at 696 cm^{-1}, the major resonance of BTPh$_2$. TGA comparison of cPMMA-BTPh$_2$ and the blank cPMMA sample (c).

A rough estimation of the material cost of the cPMMA-BTPh$_2$ photocatalyst gave a value of approximately 7€/g based on current commercial prices of chemicals used in the synthesis (**Figure 86**). The low photoactive unit loading in the catalyst and using PMMA as a commodity polymer gives the system a cost advantage.

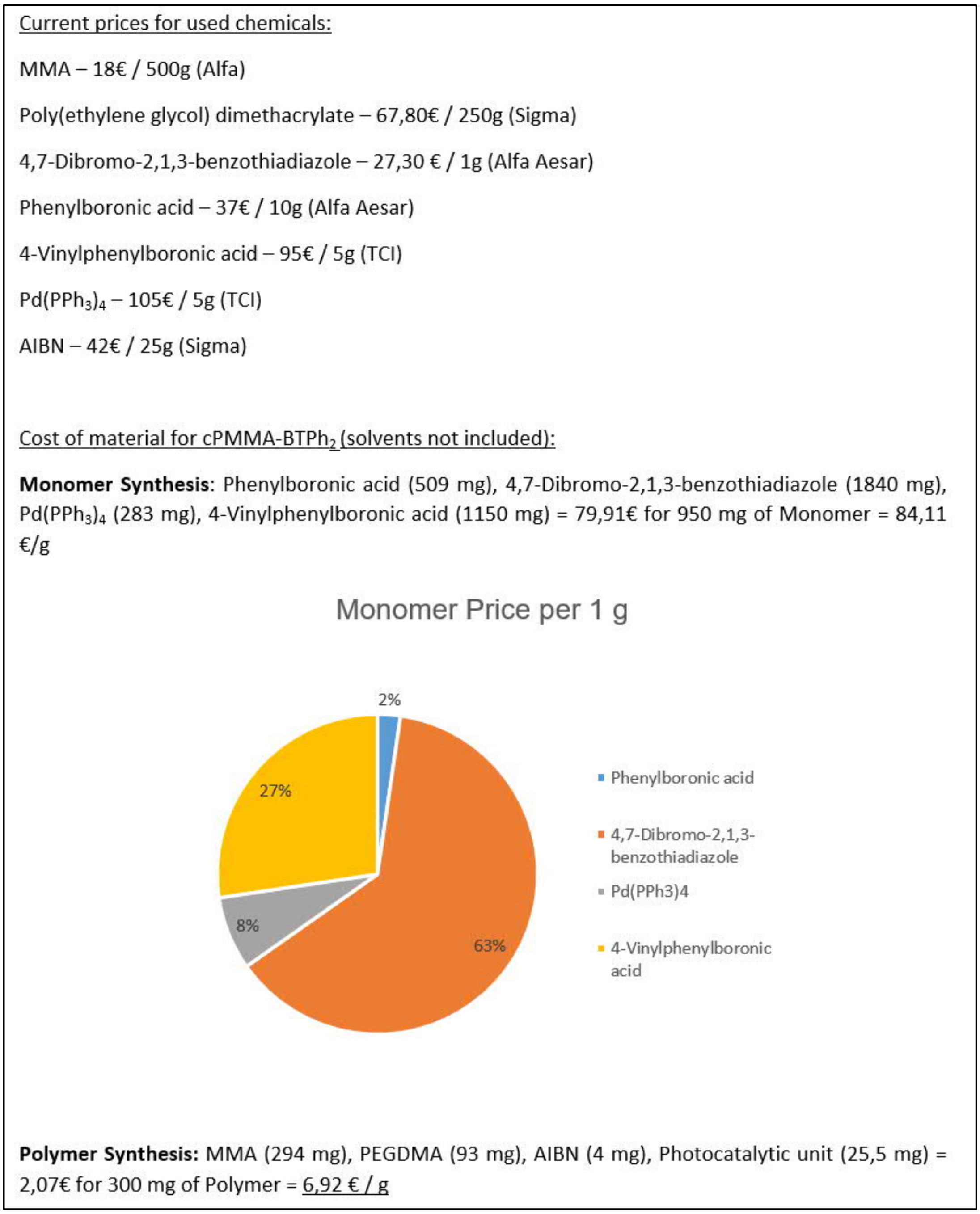

Current prices for used chemicals:

MMA – 18€ / 500g (Alfa)

Poly(ethylene glycol) dimethacrylate – 67,80€ / 250g (Sigma)

4,7-Dibromo-2,1,3-benzothiadiazole – 27,30 € / 1g (Alfa Aesar)

Phenylboronic acid – 37€ / 10g (Alfa Aesar)

4-Vinylphenylboronic acid – 95€ / 5g (TCI)

$Pd(PPh_3)_4$ – 105€ / 5g (TCI)

AIBN – 42€ / 25g (Sigma)

Cost of material for cPMMA-$BTPh_2$ (solvents not included):

Monomer Synthesis: Phenylboronic acid (509 mg), 4,7-Dibromo-2,1,3-benzothiadiazole (1840 mg), $Pd(PPh_3)_4$ (283 mg), 4-Vinylphenylboronic acid (1150 mg) = 79,91€ for 950 mg of Monomer = 84,11 €/g

Polymer Synthesis: MMA (294 mg), PEGDMA (93 mg), AIBN (4 mg), Photocatalytic unit (25,5 mg) = 2,07€ for 300 mg of Polymer = 6,92 € / g

Figure 86. Material cost estimation for the synthesis of 1g of cPMMA-$BTPh_2$.

2.5.3 Photocatalysis

To demonstrate the photocatalytic activity of the cPMMA-$BTPh_2$ system, the stereochemically highly challenging [4+2] reaction was selected. The [4+2]-cycloaddition of *trans*-anethole and isoprene was achieved with high selectivity (>99%) and quantitatively within 4 h at room temperature in air. An apparent quantum yield of 2.27% could be observed, with 0.6 µmol/mL photoactive unit present in the model reaction, making 0.06 mol% with respect to the substrate (**Figure 95-SI**). A first-order kinetic reaction was observed (**Figure 87**).

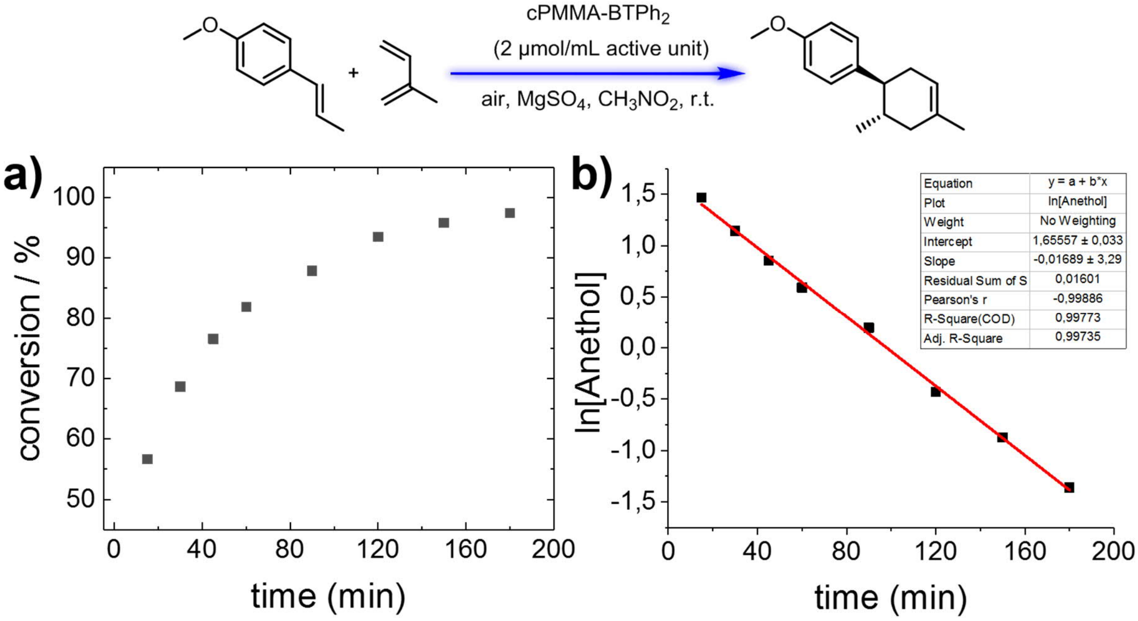

Figure 87. Monitoring experiment of the photocatalytic Diels-Alder reaction. Reaction conversion (a) and logarithmic plot of the concentration of *trans*-anethole during the reaction (b). The initial concentration of *trans*-anethole was 0.1 M.

A control experiment was conducted under light, then dark, and then light again yielded only a trace of product in the dark period. This indicated that the generated radical cation of *trans*-anethole was only active during light irradiation (**Figure 88**), suggesting a temporal and spatial limitation of the radical-based reaction.[434]

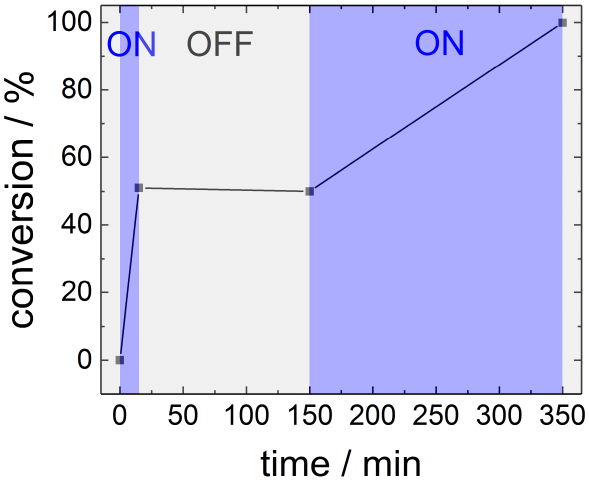

Figure 88. Reaction conversion change during the light-on-and-off experiment.

The screening and control experiments of the model reaction between *trans*-anethole and isoprene are listed in

Table 9. Nitromethane out-performed both acetonitrile and dichloromethane for the model reaction (entries 2 and 3). The reaction did not proceed without light irradiation or the use of cPMMA-$BTPh_2$ (entries 4 and 5). In the absence of oxygen, no product formation could be observed after 4h (entry 6). When using $CuCl_2$ as an electron scavenger under the nitrogen atmosphere, an increased reaction conversion (71%) was obtained, indicating that the copper salt can take the role of oxygen as catalyst regenerator (entry 7). The addition of KI as a photo-generated hole scavenger led only to traces of the desired product (entry 8). The small molecular photocatalyst $BTPh_2$ (applied in a similar loading) shows complete conversion to the [4+2] adduct within 2h of reaction time, demonstrating the efficiency of homogeneous catalysis. The benchmark reaction demonstrates the high efficiency of cPMMA-$BTPh_2$ in catalyzing organic reactions and the successful application of the concept. Incorporating photoactive units into the polymer network yields a catalyst, which works efficiently on a similar timescale as its homogeneous analog.

Table 9. Screening and control experiments of the photocatalytic [4+2] cycloaddition of *trans*-anethole and isoprene. Reaction conditions: [*trans*-anethole] = 0.1 M, [isoprene] = 1 M, nitromethane 1.5 mL, [cPMMA-$BTPh_2$] = 4 mg/mL (effective concentration of photocatalytic unit = 0.6 mM), blue LED lamp (460 nm, 0.16 W/cm^2), room temperature, air. [a] Conversion determined by GC-MS. [b] [$CuCl_2$] = 1.5 M, [c] [KI] = 1.5 M, [d] [$BTPh_2$] = 0.6 mM.

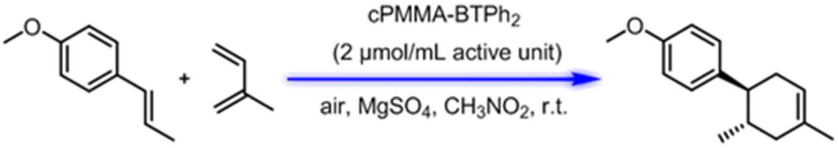

Entry	Reaction condition variations	time	Conv. (%)[a]
1	standard condition	4h	>99
2	CH_3CN as solvent	4h	91
3	DCM as solvent	4h	54
4	no cPMMA-$BTPh_2$	4h	<1
5	no light	4h	<1
6	under nitrogen	4h	<1
7[b]	with $CuCl_2$ / under nitrogen	4h	71
8[c]	with KI	4h	4
9[d]	$BTPh_2$ as catalyst	2h	>99

The cPMMA-$BTPh_2$ photocatalyst could be repeatedly used for several cycles without losing its photocatalytic efficiency (**Figure 89a**), outperforming the molecular analog $BTPh_2$ (**Figure 89b**). No photobleaching was observed in the UV/vis absorption spectra of cPMMA-$BTPh_2$ after the reaction (**Figure 89c**). Solubility tests with nitromethane, chloroform, and THF underlined the heterogeneity of the photocatalyst (**Figure 96-SI**). These findings demonstrate the robustness, high stability, and reusability of the photocatalytic material designed.

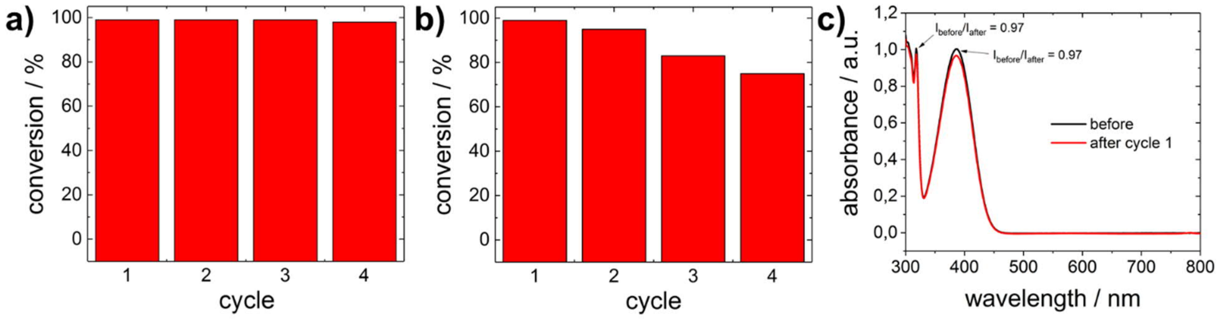

Figure 89. Repeating experiment of the photocatalytic Diels-Alder reaction with cPMMA-$BTPh_2$ (a) and with $BTPh_2$ (b). UV-Vis spectra of cPMMA-$BTPh_2$ before and after the photocatalytic Diels-Alder reaction (c). The maximum intensities on both peaks show a similar decrease indicating this to be a concentration-related effect.

We propose a reaction mechanism based on our observations and previous reports.[435-437] Three reaction pathways are possible, as illustrated in **Figure 90**. Proposed reaction mechanism of the photocatalytic [4+2] cycloaddition using cPMMA-$BTPh_2$ as photocatalyst. Under light irradiation, the substrate *trans*-anethole was oxidized by the photo-generated hole of cPMMA-$BTPh_2$ to its cationic radical intermediate, which reacts with isoprene to form the cyclic intermediate. The cyclic intermediate could be reduced by cPMMA-$BTPh_2$ formed *via* reductive quenching, regenerating the photocatalyst back to its ground state, and forming the final product to complete the catalytic cycle (pathway i). In addition, the final product may also be obtained either *via* oxidation of another neutral *trans*-anethole by cyclic intermediate, chain propagation characteristics (pathway iii), or oxidation of $O_2^{\bullet-}$,[160] generated by electron transfer from cPMMA-$BTPh_2$ to oxygen (pathway ii).

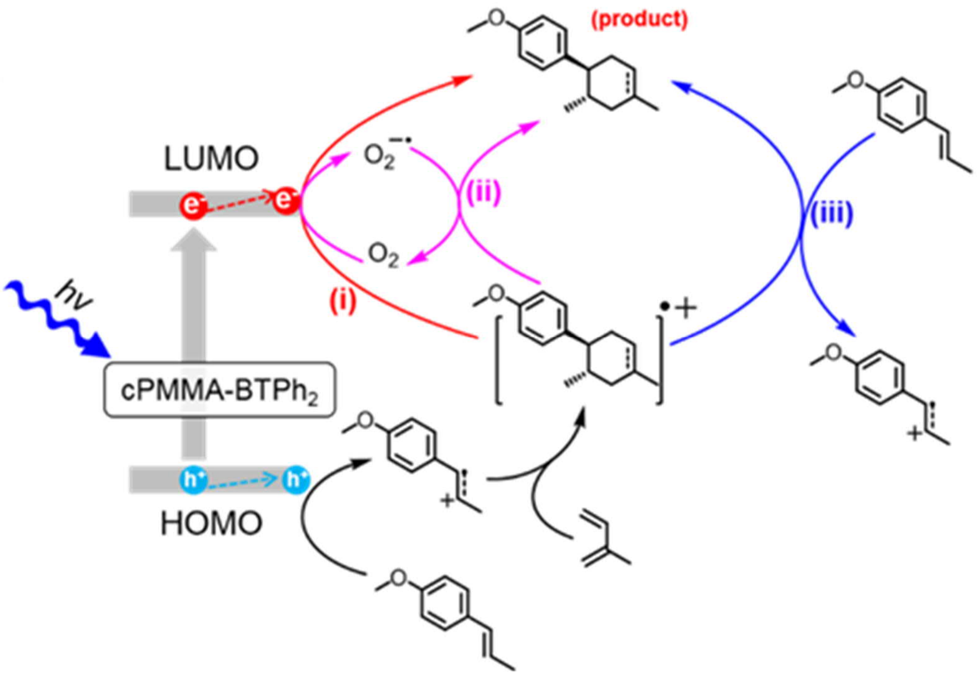

Figure 90. Proposed reaction mechanism of the photocatalytic [4+2] cycloaddition using cPMMA-$BTPh_2$ as photocatalyst.

The formation of the electron-activated superoxide radical ($O_2^{\bullet-}$) was confirmed by electron paramagnetic resonance (EPR) experiments. In a control experiment using 5,5-dimethyl-1-pyrroline N-oxide (DMPO) as a superoxide radical trapping agent, typical EPR patterns for DMPO-$O_2^{\bullet-}$ adducts resulted (**Figure 91a**).

Time-resolved photoluminescence (TRPL) was used to gain a deeper insight and elucidate the electron transfer between the $BTPh_2$ as photocatalytic unit and substrates. As shown in **Figure 91b**, the fluorescence lifetime of $BTPh_2$ in CH_3CN after purging with N_2 was determined to be 12.9 ns, which was comparable to the well-applied organic photocatalysts, such as Acr^+-Mes (15 ns)[39] and Eosin Y (6 ns).[438] In the presence of O_2, the excited state of $BTPh_2$ could be quenched to the decreased fluorescence lifetime of 10.7 ns. A similar phenomenon was observed when using *trans*-anethole as a quencher, leading to a reduced fluorescence lifetime of 11.5 ns. This indicated a hole filling process by electron transfer between $BTPh_2$ and *trans*-anethole.[160] By simulating the conditions of the model reaction with *trans*-anethole in air, a similar decayed lifetime of $BTPh_2$ of 11.2 ns was observed, further confirming that the [4+2] cycloaddition is hole initiated.

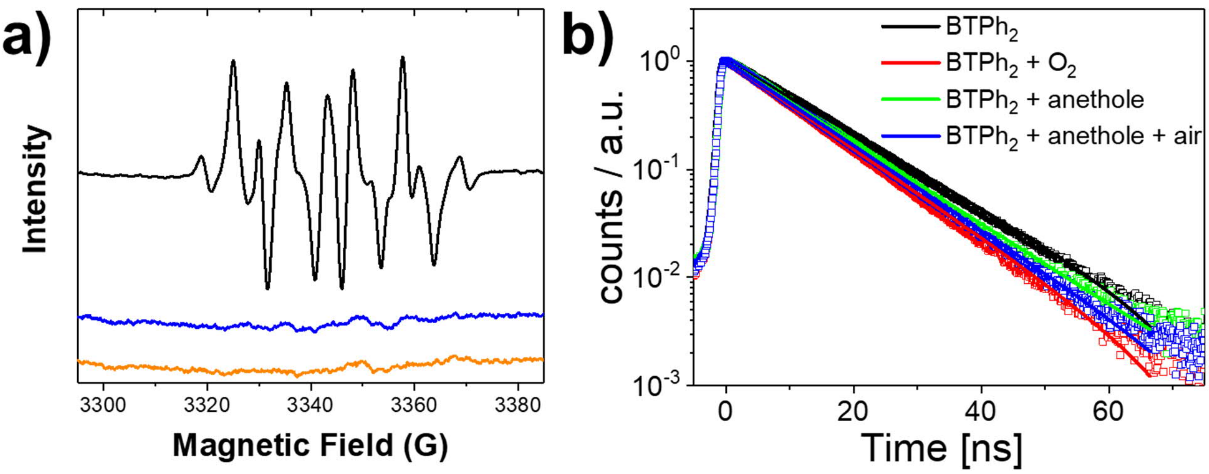

Figure 91. (a) EPR spectra of DMPO-$O_2^{\bullet-}$ adducts with cPMMA-BTPh$_2$ as photocatalyst in darkness or under blue light irradiation (λ = 460 nm, 1.2 W/cm^2). (b) Time-resolved photoluminescence spectra of BTPh$_2$ under N_2 (black), O_2 (red), with *trans*-anethole under N_2 (green) or in air (blue) with 20 mg/mL of BTPh$_2$ and 2 mM *trans*-anethole in acetonitrile.

Transient absorption (TA) spectra were recorded (**Figure 92**). Transient absorption spectra were recorded to investigate the concrete electron transfer process between the photocatalyst BTPh$_2$ and substrates in the Diels-Alder reaction. The signal peaking at 660 nm represents the photo-induced absorption (PIA) of BTPh$_2$ in its excited state (**Figure 92a**). The lifetime of the singlet excited state of BTPh$_2$ in an N_2-purged solution was determined to be 11.1 ns, which is consistent with that obtained from the time-resolved photoluminescence spectroscopy (TRPL). However, the addition of O_2 did not affect the PIA of BTPh$_2$ (**Figure 92b**). The possible reason might be that the phosphorescence signal for active oxygen species such as $^1O_2$, typically localized at 1270 nm, was beyond the detection limit of the transient absorption measurement. In comparison, the PIA curves of BTPh$_2$ with the addition of *trans*-anethole initially retain a similar shape to that of pure BTPh$_2$ within the initial period of 1 ns to 3.1 ns. Then, a new absorption peak at 610 nm appears after 9.9 ns pulse irradiation (**Figure 92c-d**). This observation indicates that the formation of the radical cation of *trans*-anethole began to occur after 9.9 ns, which is similar to a previous report,[439] thus supporting the proposed hole initiation mechanism. By increasing the concentration of *trans*-anethole, the absorption intensity of the mixture decayed faster, demonstrating the active electron transfer from the substrate to the photo-generated holes of the photocatalyst (**Figure 92e-f**).

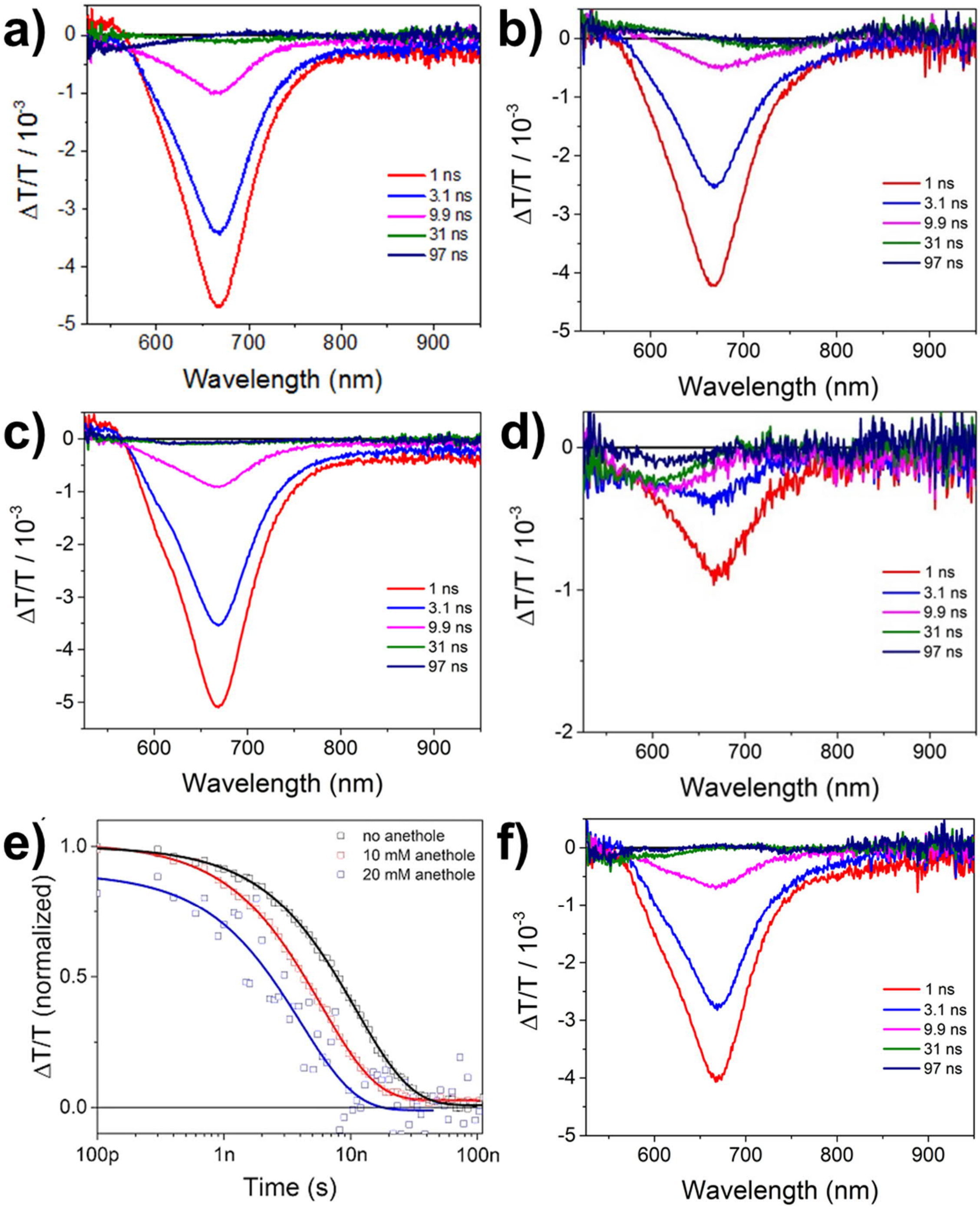

Figure 92. TA spectra of $BTPh_2$ (20 mg/L in CH_3CN) under N_2 at different times (a). TA spectra of $BTPh_2$ (20 mg/L in CH_3CN) under O_2 at different times (b). TA spectra of $BTPh_2$ (20 mg/L) and *trans*-anethole with lower concentration (2 mM, c) and higher concentration (20 mM, d) under N_2 atmosphere in CH_3CN at different times. Time profiles of the absorbance decay at 675 nm of $BTPh_2$ with 0, 10, and 20 mM *trans*-anethole in CH_3CN (e). Transient absorption spectra of $BTPh_2$ (20 mg/L) and *trans*-anethole (2 mM) under O_2 atmosphere in CH_3CN at different times (f). For all measurements, an excitation wavelength of 355 nm was used.

The decay profiles of the TA were consistent with the ones of the TRPL (**Figure 93** and **Table 10**).

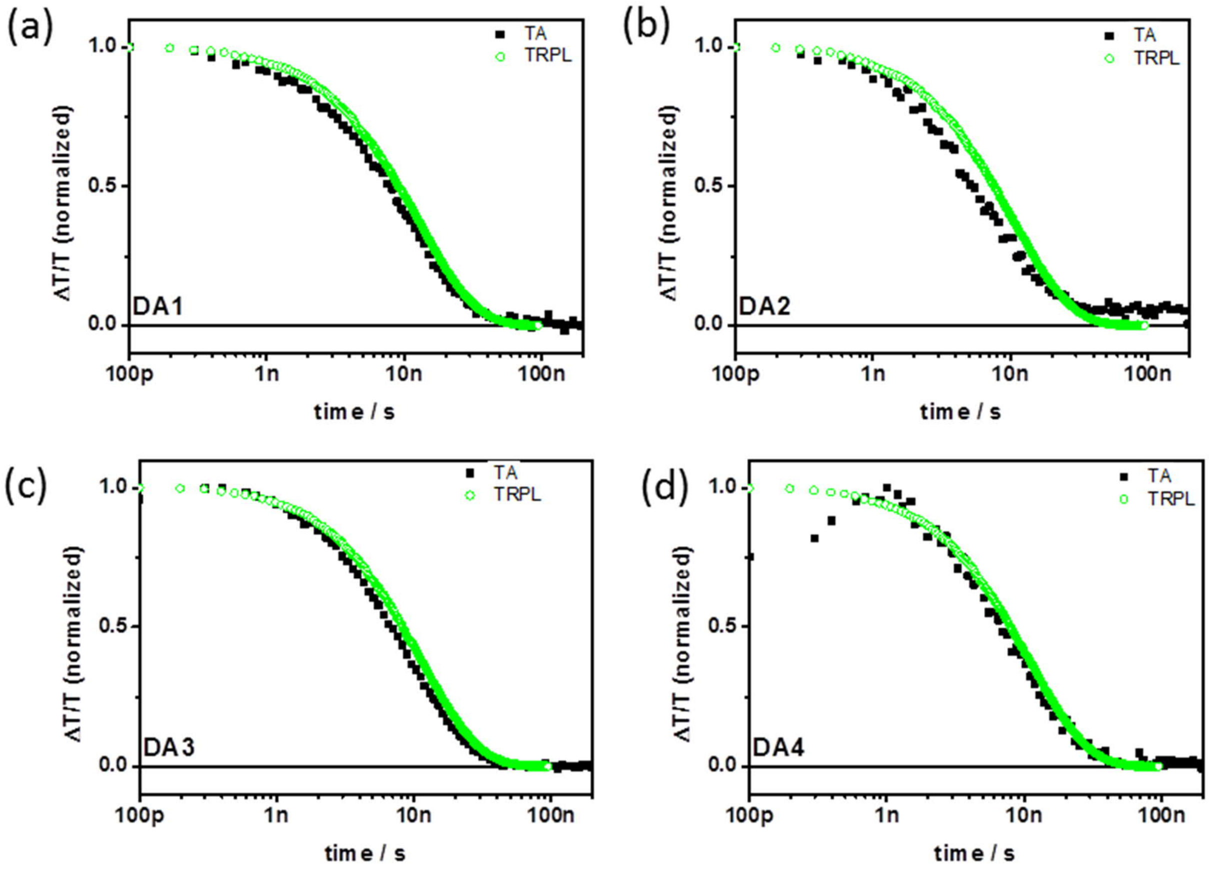

Figure 93. Comparison of decay profiles of transient absorption (TA) at 660 – 690 nm and time-resolved photoluminescence (TRPL) at 480-520 nm for the Diels-Alder reaction. Pure $BTPh_2$ (20 mg/L in CH_3CN) under N_2 (a), pure $BTPh_2$ (20 mg/L in CH_3CN) under O_2 (b), $BTPh_2$ (20 mg/L) and *trans*-anethole (2 mM) under N_2 atmosphere in CH_3CN (c), $BTPh_2$ (20 mg/L) and *trans*-anethole (2 mM) under O_2 atmosphere in CH_3CN (d).

Table 10. Excited-state lifetime of the measured mixtures.

Entry	Sample name	Fluorescence lifetime (ns)	Transient lifetime (ns)
1	$BTPh_2$ (CH_3CN)	12.9	11.1
2	$BTPh_2$ + O_2	10.7	7.5
3	$BTPh_2$ + anethole	11.5	9.1
4	$BTPh_2$ + anethole + O_2	11.2	9.4

The versatility of the photocatalytic material was investigated by employing different dienes and dienophiles in the [4+2] cycloaddition reaction (**Figure 94**). High reaction yields from 76 to 99% were obtained, confirming the general applicability of cPMMA-$BTPh_2$ for organic photoredox reactions. The conversions were found to be selective towards the [4+2] cycloaddition. The formation of (2+2) cycloaddition products could not be observed.

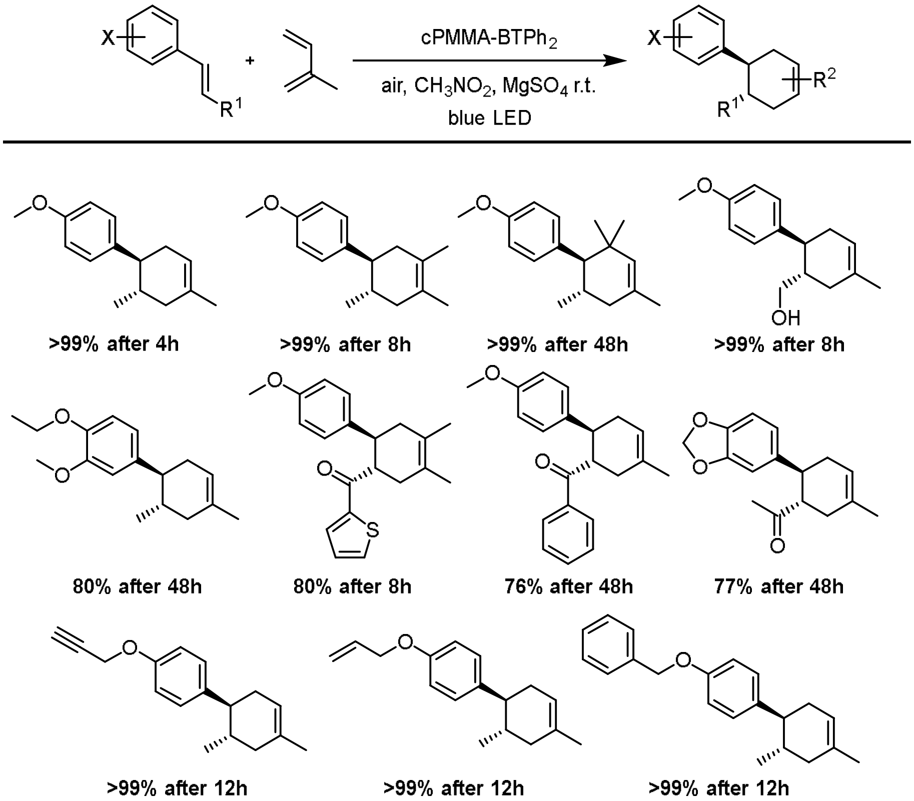

Figure 94. Scope of the photocatalytic Diels-Alder reaction using cPMMA-$BTPh_2$ as photocatalyst. The reactions were irradiated with a blue LED lamp (460 nm, 0.16 W/cm^2).

2.5.4 Conclusion

In summary, introducing photocatalytic units into classical polymeric materials gives a new class of metal-free, stable, and low-cost photocatalysts. Photoactive copolymer organogels based on PMMA show similar optical and redox properties compared to the molecular photocatalytic analog unit while retaining advantageous chemical robustness and recyclability attributed to its parent polymeric material. The PMMA photocatalyst could efficiently catalyze [4+2] cycloaddition reactions with an efficiency comparable to its homogeneous molecular counterpart. Furthermore, the PMMA photocatalyst demonstrated excellent stability and recoverability. A deeper mechanistic insight of the photocatalytic process was investigated using advanced photophysical studies. Electron transfer between the photocatalyst and substrates, involving the electron and hole migration during the catalytic processes, was observed. By expanding the scope of the reactions, broader applicability of the catalyst could be obtained. In general, we believe that the concept of introducing photocatalytic units into classical polymeric systems provides a platform for a broad range of new versatile photocatalytic materials. The approach elaborated in this study may open the door for future large-scale applications and photocatalytic materials with improved recyclability and stability.

2.5.5 Experimental details

Materials and methods

All chemicals and solvents were purchased from commercial sources and used as received unless otherwise noted. For the photocatalytic Diels-Alder reaction, all dienes and reaction solvents, i.e., nitromethane, were purified by elution through neutral aluminum oxide (50-200 um) and anhydrous $CaCl_2$ (w/w, 95/5). Column flash chromatography was conducted over silica 60 (0.063-0.2 mm). Reaction yields refer to the pure compound after being purified *via* column chromatography. Solid-state diffuse reflectance UV-Vis absorption and fluorescence spectra were recorded on a Perkin Elmer Lambda 100 spectrophotometer and J&M TIDAS spectrofluorometer at ambient temperature, respectively. EPR (Electron Paramagnetic Resonance) was measured on a Magnettech Miniscope MS200 spectrometer at room temperature. DMPO (0.1 M) and catalyst (1 mg/mL) in acetonitrile were used for the spin trap experiment. The irradiation was conducted with an integrated blue light source. Cyclic voltammetry measurement was carried out on a Metrohm Autolab PGSTAT204 potentiostat/galvanostat with a three-electrode-cell system: glassy carbon electrode as the working electrode, $Hg/HgCl_2$ electrode as the reference electrode, platinum wire as the counter electrode, and Bu_4NPF_6 (0.1 M in acetonitrile) as supporting electrolyte with a scan rate of 100 mV s^{-1} in the range of -2 eV to 2 eV. GC-MS measurement was performed on Shimadzu GC-2010 plus gas chromatography and QP2010 ultra mass spectrometer with fused silica column (Phenomenex, Zebron 5-ms nonpolar) and flame ionization detector. ^1H and ^{13}C NMR spectra for all compounds were measured using a Bruker Avance 300 MHz. Solid-state ^{13}C CP MAS NMR measurements were carried out using Bruker Avance II solid-state NMR spectrometer operating at 300 MHz Larmor frequency equipped with a standard 4mm magic angle spinning (MAS) double resonance probe head. FTIR measurements were conducted with a Bruker Tensor II FTIR spectrometer. Bright-field and fluorescence images were acquired on a Leica DMi8 inverted light microscope. The morphology was recorded by a scanning electron microscope (SEM) (LEO Gemini 1530, Germany) with an in-lens SE detector. Thermogravimetric analysis (TGA) was conducted in a nitrogen atmosphere with temperature increasing from room temperature to 1000 °C at a rate of 10 K/min. All DFT calculations were carried out with the Gaussian 09 package.[440] The structures were optimized at the B3LYP level of theory[331] with the basis set of 6-31G*.[332-333] TD-DFT results were obtained from excited-state calculations at the same level of theory. Time-resolved photoluminescence (TR-PL) spectra were taken with a C4742 Hamamatsu streak camera system in slow sweep mode. Excitation pulses at 400 nm were provided by frequency doubling the output of a commercial femtosecond amplifier laser system (Coherent LIBRA-HE).

Synthesis of $BTPh_2$

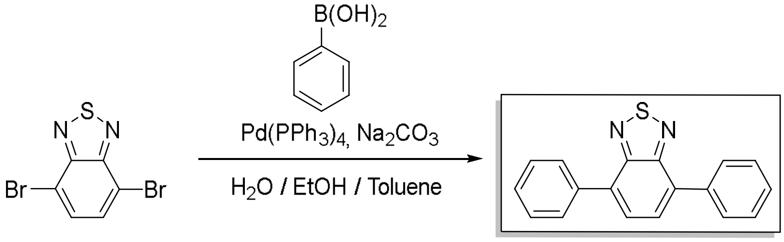

A 250 mL three-necked flask was charged with 4, 7-dibromo-2,1,3-benzothiadiazole (1.47 g 5 mmol), phenylboronic acid (2.68 g, 22 mmol) and toluene (25 mL). Then, a solution of potassium carbonate (2.76 g, 20 mmol) in H_2O (10 mL) was added to the flask. After degassing for 30min, $Pd(PPh_3)_4$ (0.047 g, 0.04 mmol) was added, and the reaction mixture was heated to 90 °C and reacted overnight under N_2 atmosphere. After cooling to room temperature, the mixture was poured into water and extracted with dichloromethane. The organic layer was washed with water and dried over anhydrous $MgSO_4$. After concentrated with a rotary evaporator, the crude product was purified *via* column chromatography on silica with dichloromethane as eluent. For further purification, the crude product was recrystallized with methanol to afford $BTPh_2$ as yellow needles. Yield: 1.17 g (82%).

^1H NMR (300 MHz, $CDCl_3$) δ 8.00 (m, 4H), 7.81 (s, 2H), 7.58 (m, 4H), 7.49 (t, 2H). ^{13}C NMR (75 MHz, $CDCl_3$) δ 128.13, 128.38, 128.63, 129.25, 133.39, 137.44, 154.11.

Synthesis of monomer

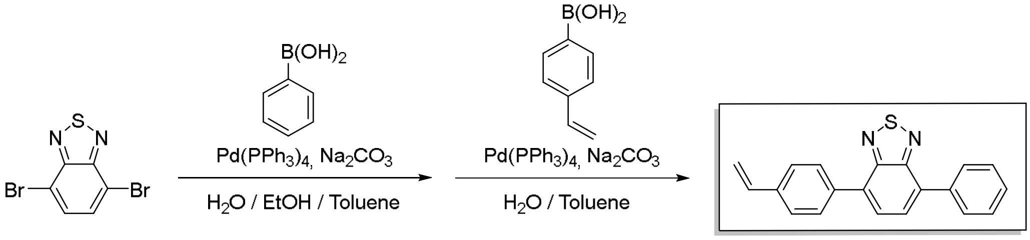

Step 1 (4-bromo-7-phenylbenzo[c][1,2,5]thiadiazole): Phenylboronic acid (509 mg, 4.18 mmol, 1.00 eq.), 4,7-dibromobenzo[c][1,2,5]thiadiazole (1.84 g, 6.26 mmol, 1.50 eq.), 17 mL of toluene, 7 mL of 2.0 M aqueous Na_2CO_3 solution and 7 mL of ethanol were placed in a 100 mL Schlenk flask. After degassing by Ar bubbling for 20min, $Pd(PPh_3)_4$ (144 mg, 125 µmol, 0.03 eq.) was added in an Ar counter stream. The solution was vigorously stirred at 90°C for 48h. After cooling to room temperature, the resulting mixture was extracted with dichloromethane (4 x 20 mL). The combined organic phases were washed with brine (50 mL) and dried over anhydrous $MgSO_4$. After filtration and rotary evaporation of solvents, the residue was purified by column chromatography on silica gel (petroleum ether/dichloromethane 3:1). The light green solid (1.75 g) was used as is in the next step.

Step 2 (4-phenyl-7-(4-vinylphenyl)benzo[c][1,2,5]thiadiazole): The crude product from step 1 (1.75 g), (4-vinylphenyl)boronic acid (1.15 g, 7.83 mmol, 1.3 eq.), 16 mL of toluene and 12 mL of a 2.0 M aqueous Na_2CO_3 were combined in a 100 mL Schlenk tube. After degassing by Ar bubbling for 20min, $Pd(PPh_3)_4$ (139 mg, 120 µmol, 0.02 eq.) was added in an Ar counter stream. The solution was vigorously stirred at 90°C for 48h. After cooling to room temperature, water was added (40 mL), and the resulting mixture was extracted with dichloromethane (4 x 20 mL). The combined organic phases were washed with 1 M NaOH (50 mL) and brine (50 mL). After drying over anhydrous $MgSO_4$ and filtration, rotary evaporation yielded the crude product. The residue was purified by column chromatography on silica gel (petroleum ether/ethyl acetate 20:1→0:1). After recrystallization in H_2O/MeCN (1:9), the product was obtained as bright yellow needles

(950 mg, 2.99 mmol, 72% over two steps).^{1}H NMR (300 MHz, $CDCl_3$) δ 7.97 (d, 4H), 7.79 (s, 2H), 7.58 (m, 4H), 7.48 (q, 1H), 6.82 (q, 1H), 5.86 (d, 1H), 5.34 (d, 1H). ^{13}C NMR (75 MHz, $CDCl_3$) δ 154.27, 154.21, 137.78, 137.56, 136.91, 136.53, 133.50, 133.05, 129.52, 129.38, 128.77, 128.52, 128.27, 127.99, 126.61, 114.67.

Synthesis of cPMMA-BTPh$_2$

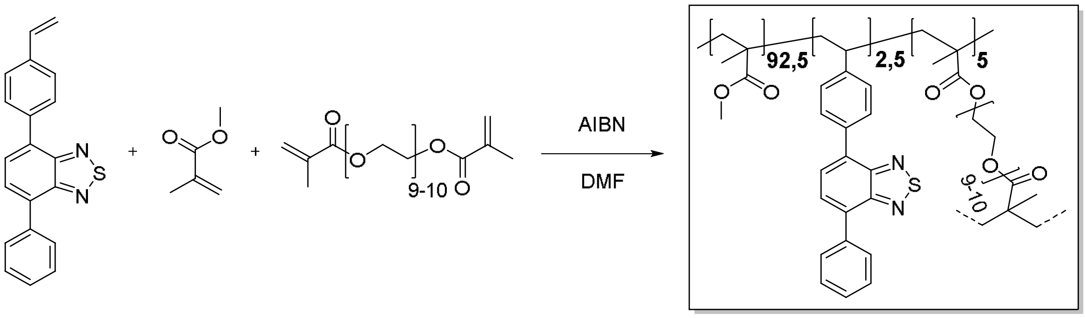

4-Phenyl-7-(4-vinylphenyl)benzo[c][1,2,5]thiadiazole (25.5 mg, 81.1 µmol, 0.025 eq.), methyl methacrylate (315 µL, 3.00 mmol, 0.93 eq.) and poly(ethylene glycol dimethacrylate) (93.0 mg, 55.3 µmol, 0.05 eq.) were charged in a 20 mL vial and dissolved in DMF (3.6 mL). Azobisisobutyronitrile (4.26 mg, 25.9 µmol, 0.80 eq.) was added. Then the vial was capped and the solution was purged with Ar under harsh stirring for 10min. After heating to 70 °C overnight, gel formation could be observed. The gel was transferred to an extraction thimble, purified by Soxhlet extraction with DCM/MeOH (1:1) for 12h, and dried under a nitrogen stream. After subsequent high vacuum drying, the polymer was obtained as bright yellow solid (300 mg).

Synthesis of cPMMA

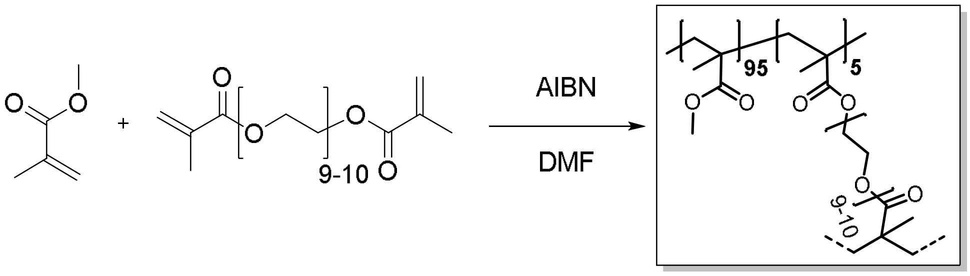

Methyl methacrylate (315 µL, 3.00 mmol, 0.95 eq.) and poly(ethylene glycol dimethacrylate) (101 mg, 60.0 µmol, 0.05 eq.) were charged in a 20 mL vial and dissolved in DMF (3.6 mL). Azobisisobutyronitrile (4.26 mg, 25.9 µmol, 0.80 eq.) was added. Then the vial was capped and the solution was purged with Ar under harsh stirring for 10min. After heating to 70 °C overnight, gel formation could be observed. The gel was transferred to an extraction thimble, purified by Soxhlet extraction with DCM/MeOH (1:1) for 12h, and dried under a nitrogen stream. After subsequent high vacuum drying, the polymer was obtained as bright yellow solid (321 mg).

Synthesis of Substrates

(*E*)-1-(4-hydroxyphenyl)propene was synthesized from *trans*-anethole according to a previously reported literature procedure.[441] Small impurities (*Z*)-1-(4-hydroxyphenyl)propene affected the purity of the following synthetic steps.

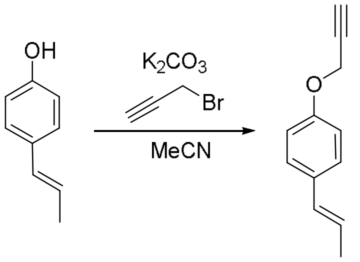

(*E*)-1-(prop-1-en-1-yl)-4-(prop-2-yn-1-yloxy)benzene: (*E*)-1-(4-hydroxyphenyl)propene (200 mg, 1.49 mmol, 1.00 eq.), potassium carbonate (206 mg, 1.49 mmol, 1.00 eq.) and acetonitrile (5 mL) were added to a 20 mL vial. Propargyl bromide (213 mg, 1.79 mmol, 1.20 eq.) was added slowly and the mixture was stirred overnight. The next day, the sample was extracted with ethyl acetate (4 x 20 mL). The combined organic phases were washed with brine (50 mL) and dried over anhydrous $MgSO_4$. After filtration and rotary evaporation of solvents, the residue was purified by column chromatography on silica gel (petroleum ether/ethyl acetate 1:0 → petroleum ether/ethyl acetate 3:1). Small amounts of the *Z* isomer could be detected in the NMR spectra originating from impurities in the starting materia. The resulting oil (234 mg, 91%) was used as a substrate in the photocatalytic reaction. ^1H NMR (300 MHz, $CDCl_3$) δ 7.28 (d, 2H), 6.92 (d, 2H), 6.36 (d, 1H), 6.12 (m, 1H), 4.69 (s, 2H), 2.53 (s, 1H), 1.87 (d, 3H). ^{13}C NMR (75 MHz, $CDCl_3$) δ 156.63, 131.84, 130.33, 126.98, 124.14, 115.06, 78.75, 75.58, 55.97, 18.55.

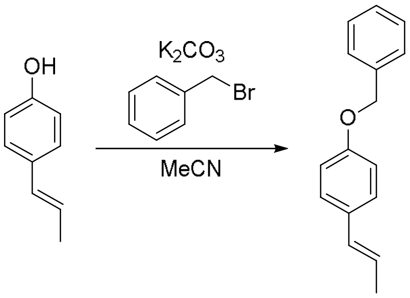

(*E*)-1-(Benzyloxy)-4-(prop-1-en-1-yl)benzene: (*E*)-1-(4-hydroxyphenyl)propene (201 mg, 1.50 mmol, 1.00 eq.), potassium carbonate (311 mg, 2.25 mmol, 1.50 eq.) and acetonitrile (4 mL) were added to a 20 mL vial. Benzyl bromide (308 mg, 1.80 mmol, 1.20 eq.) was added and the mixture was heated to 80 °C overnight. The next day, the sample was extracted with ethyl acetate (4 x 20 mL). The combined organic phases were washed with brine (50 mL) and dried over anhydrous $MgSO_4$. After filtration and rotary evaporation of solvents, the residue was purified by column chromatography on silica gel (petroleum ether/ethyl acetate 1:0 → petroleum ether/ethyl acetate 7:1). The resulting oil (320 mg, 95%) was used as a substrate in the photocatalytic reaction. ^1H NMR (300 MHz, $CDCl_3$) δ 7.32 (m, 5H), 7.20 (d, 2H), 6.85 (d, 2H), 6.28 (d, 1H), 6.02 (m, 1H), 4.99 (s, 2H), 1.80 (d, 3H). ^{13}C NMR (75 MHz, $CDCl_3$) δ 157.92, 137.20, 131.21, 130.45, 128.70, 128.06, 127.59, 127.02, 123.76, 115.01, 70.16, 18.56.

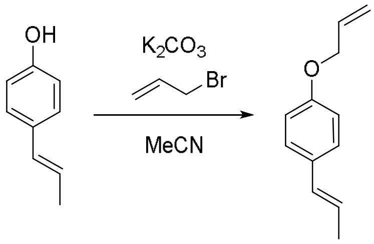

(*E*)-1-(Allyloxy)-4-(prop-1-en-1-yl)benzene: (*E*)-1-(4-Hydroxyphenyl)propene (200 mg, 1.49 mmol, 1.00 eq.), potassium carbonate (206 mg, 1.49 mmol, 1.00 eq.) and acetonitrile (5 mL) were added to a 20 mL vial. Allyl bromide (216 mg, 1.79 mmol, 1.20 eq.) was added and the mixture stirred overnight. The next day, the sample was extracted with ethyl acetate (4 x 20 mL). The combined organic phases were washed with brine (50 mL) and dried over anhydrous $MgSO_4$. After filtration and rotary evaporation of solvents, the residue was purified by column chromatography on silica gel (petroleum ether/ethyl acetate 1:0 → petroleum ether/ethyl acetate 7:1). The resulting oil (244 mg, 94%) was used as a substrate in the photocatalytic reaction. ^1H NMR (300 MHz, $CDCl_3$) δ 7.28 (d, 2H), 6.88 (d, 2H), 6.37 (d, 1H), 6.10 (m, 2H), 5.45 (d, 2H), 5.31 (d, 2H), 4.56 (d, 2H), 1.89 (d, 3H). ^{13}C NMR (75 MHz, $CDCl_3$) δ 157.71, 133.47, 131.09, 130.45, 126.97, 123.67, 117.72, 114.87, 68.95, 18.54.

General procedure of photocatalysis

A 20 mL vial with a magnetic stir bar was added with cPMMA-$BTPh_2$, alkene (1.0 eq.), diene (10 eq.), and nitromethane. Then the vial was capped and placed under the irradiation of a blue LEDs lamp (0.061 W/cm^2). The reaction mixture was stirred at room temperature until completion was confirmed by GC-MS. Afterward, the mixture was transferred to a separatory funnel containing DCM and H_2O (v/v, 1/1). The organic layers were separated and extracted thrice with DCM. The combined organic layers were washed with brine, dried over anhydrous $MgSO_4$, and concentrated by rotary evaporation. The crude product was purified *via* column chromatography on silica to afford the pure compound.

Recycling

The recycling experiment was conducted similar to the general procedure. Specifically, a dried vial with a magnetic stir bar was charged with *trans*-anethole (35.6 mg, 0.24 mmol), isoprene (240 µL, 2.4 mmol), cPMMA-$BTPh_2$ (2.4 mg), and nitromethane (2.4 mL). After 4h of reaction, the conversion was analyzed by GC-MS. The reaction mixture was centrifuged at 1000 rpm for 2min and the supernatant was replaced by CH_3NO_2. Then, another equivalent of *trans*-anethole (35.6 mg, 0.24 mmol) and isoprene (24 µL, 0.24 mmol) were added into the mixture and the solution was further irradiated under blue light. The catalyst was recycled four times.

In the same way, $BTPh_2$ was tested. Without purification process, another equivalent of *trans*-anethole (35.6 mg, 0.24 mmol) and isoprene (24 µL, 0.24 mmol) were added into the mixture and the solution was further irradiated under blue light. The catalyst was recycled four times.

Solubility testing

To prove the heterogeneity of the cPMMA-$BTPh_2$ photocatalyst, the catalyst was irradiated with blue light while being stirred in CH_3NO_2 (I), $CDCl_3$ (II), and *d₈*-THF (III), respectively. For sample I, the mixture was filtered through a syringe filter after 4h. The solution was centrifuged for 10min at 10000 rpm and the supernatant was evaporated to dryness on the rotary evaporator. $CDCl_3$ was added to the round-bottom flask and taken for ^{1}H-NMR analysis. The mixture was filtered through a syringe filter for setups II and III, centrifuged as above, and the supernatant was directly taken for ^{1}H-NMR.

Compounds

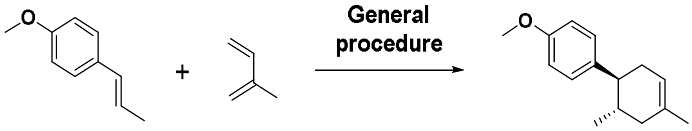

(1S,2S)-4'-Methoxy-2,4-dimethyl-1,2,3,6-tetrahydro-1,1'-biphenyl: According to the general procedure, a dried vial with a magnetic stir bar was charged with *trans*-anethole (35.6 mg, 0.24 mmol), isoprene (240 µL, 2.4 mmol), catalyst (2.4 mg), $MgSO_4$ (15mg) and nitromethane (2.4 mL). After the reaction was finished, the mixture was worked up according to the protocol and purified by chromatography on silica with hexane/ethyl acetate (12/1) as the elution to afford the pure cycloadduct as a clear oil. R_f (hexane/ethyl acetate 12/1): 0.76. ^{1}H NMR ($CDCl_3$, 300 MHz): δ 6.99 (d, J=9 Hz, 2H), 6.75 (d, J=9 Hz, 2H), 5.36 (bs, 1H), 3.71 (s, 3H), 2.21 (m, 1H), 2.11 (m, 1H), 2.04 (m, 1H), 1.98 (m, 1H), 1.81 (m, 1H), 1.71 (m, 1H), 1.61 (s, 3H), 0.62 (d, J=6 Hz, 3H). ^{13}C NMR ($CDCl_3$, 75 MHz): δ 157.8, 138.2, 133.8, 128.5, 120.9, 113.7, 55.2, 47.0, 39.9, 35.3, 34.0, 23.4, 20.2.

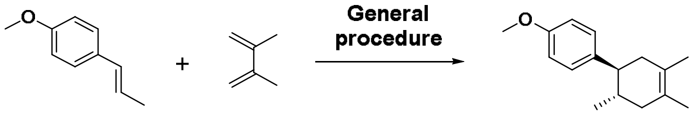

(1S,2S)-4'-methoxy-2,4,5-trimethyl-1,2,3,6-tetrahydro-1,1'-biphenyl: According to the general procedure, a dried vial with a magnetic stir bar was charged with *trans*-anethole (35.6 mg, 0.24 mmol), 2,3-dimethylbuta-1,3-diene (81.5 µL, 0.72 mmol), catalyst (2.4 mg), $MgSO_4$ (15mg) and nitromethane (2.4 mL). After the reaction was finished, the mixture was worked up according to the protocol and purified by chromatography on silica with hexane/dichloromethane (1/1) as the elution to afford the pure cycloadduct as a clear oil. R_f (hexane/dichloromethane 1/1): 0.81. ^{1}H NMR ($CDCl_3$, 300 MHz): δ 7.02 (d, J=9 Hz, 2H), 6.78 (d, J=12 Hz, 2H), 3.71 (s, 3H), 2.33 (td, J=6, 12 Hz, 1H), 2.07 (m, 1H), 1.98 (m, 2H), 1.77 (m, 2H), 1.56 (s, 3H), 1.54 (s, 3H), 0.63 (d, J=9 Hz, 3H). ^{13}C NMR ($CDCl_3$, 75 MHz): δ 157.6, 138.2, 128.5, 125.5, 125.4, 113.7, 55.2, 47.8, 41.9, 41.7, 34.3, 20.1, 18.8, 18.7.

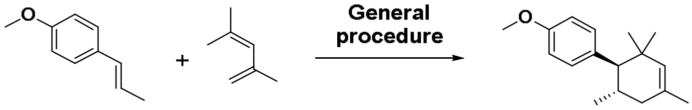

(1R,2S)-4'-methoxy-2,4,6,6-tetramethyl-1,2,3,6-tetrahydro-1,1'-biphenyl: According to the general procedure, a dried vial with a magnetic stir bar was charged with *trans*-anethole (35.6 mg, 0.24 mmol), 2,4-dimethylpenta-1,3-diene (93.1 µL, 0.72 mmol), catalyst (2.4 mg), $MgSO_4$ (15mg) and nitromethane (2.4 mL). After the reaction was finished, the mixture was worked up according to the protocol and purified by chromatography on silica with hexane/ethyl acetate (25/1) as the elution to afford the pure cycloadduct as a clear oil. R_f (hexane/ethyl acetate 25/1): 0.61. ^{1}H NMR ($CDCl_3$, 300

MHz): δ 6.97 (dd, J=6, 18 Hz, 2H), 6.76 (dd, J=9, 18 Hz, 2H), 5.12 (s, 1H), 3.72 (s, 3H), 2.11 (d, 9 Hz, 1H), 2.05 (m, 1H), 1.98 (m, 1H), 1.70 (m, 1H), 1.59 (s, 3H), 0.75 (s, 3H), 0.70 (s, 3H), 0.64 (d, J=6 Hz, 3H). ^{13}C NMR ($CDCl_3$, 75 MHz): δ 157.7, 133.3, 130.3, 129.3, 113.2, 112.2, 57.4, 56.1, 40.5, 36.3, 30.0, 28.8, 24.6, 23.3, 20.8.

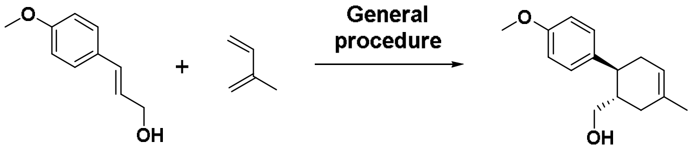

((1S,2S)-4'-methoxy-4-methyl-1,2,3,6-tetrahydro-[1,1'-biphenyl]-2-yl)methanol: According to the general procedure, a dried vial with a magnetic stir bar was charged with (E)-3-(4-methoxyphenyl)prop-2-en-1-ol (39.4 mg, 0.24 mmol), isoprene (240 µL, 2.4 mmol), catalyst (2.4 mg), $MgSO_4$ (15mg) and nitromethane (2.4 mL). After the reaction was finished, the mixture was worked up according to the protocol and purified by chromatography on silica with hexane/ethyl acetate (4/1) as the elution to afford the pure cycloadduct as a clear oil. R_f (hexane/ethyl acetate 4/1): 0.56. ^{1}H NMR ($CDCl_3$, 300 MHz): δ 7.06 (d, J=9 Hz, 2H), 6.78 (d, J=9 Hz, 2H), 5.37 (bs, 1H), 3.70 (s, 3H), 3.33 (dd, J=3, 9 Hz, 1H), 3.22 (dd, 6, 12 Hz, 1H), 2.45 (m, 1H), 2.14 (m, 1H), 2.12 (m, 1H), 2.03 (t, J=12 Hz, 1H), 1.93 (m, 1H), 1.90 (m, 1H), 1.64 (s, 3H). ^{13}C NMR ($CDCl_3$, 75 MHz): δ 158.1, 137.0, 133.4, 128.4, 120.6, 114.1, 65.9, 55.2, 42.2, 41.5, 34.7, 33.9, 23.5.

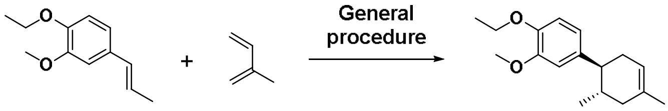

(1S,2S)-4'-ethoxy-3'-methoxy-2,4-dimethyl-1,2,3,6-tetrahydro-1,1'-biphenyl: According to the general procedure, a dried vial with a magnetic stir bar was charged with (E)-1-ethoxy-2-methoxy-4-(prop-1-en-1-yl)benzene (48.1 mg, 0.25 mmol), isoprene (250 µL, 2.5 mmol), catalyst (2.4 mg), $MgSO_4$ (15mg) and nitromethane (2.4 mL). After the reaction was finished, the mixture was worked up according to the protocol and purified by chromatography on silica with hexane/ethyl acetate (12/1) as the elution to afford the pure cycloadduct as a clear oil. R_f (hexane/ethyl acetate 12/1): 0.46. ^{1}H NMR ($CDCl_3$, 300 MHz): δ 6.71 (m, 1H), 6.63 (m, 2H), 5.37 (bs, 1H), 4.02 (m, 2H), 3.78 (s, 3H), 2.21 (m, 1H), 2.14 (m, 1H), 2.09 (m, 1H), 1.99 (m, 1H), 1.83 (m, 1H), 1.72 (m, 1H), 1.62 (s, 3H), 1.38 (t, J=6 Hz, 3H), 0.66 (d, J=6 Hz, 3H). ^{13}C NMR ($CDCl_3$, 75 MHz): δ 149.1, 146.4, 138.8, 133.8, 120.8, 119.6, 112.6, 111.0, 64.3, 55.9, 47.4, 39.8, 35.2, 34.0, 23.4, 20.2, 14.9.

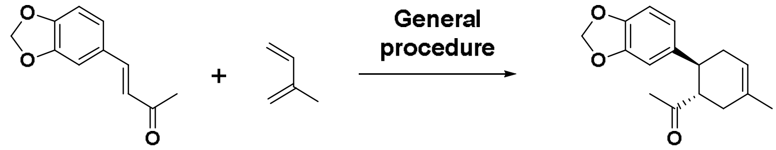

1-((1S,6S)-6-(benzo[d][1,3]dioxol-5-yl)-3-methylcyclohex-3-en-1-yl)ethan-1-one: According to the general procedure, a dried vial with a magnetic stir bar was charged with (E)-4-(benzo[d][1,3]dioxol-5-yl)but-3-en-2-one (45.6 mg, 0.24 mmol), isoprene (240 µL, 2.4 mmol), catalyst (2.4 mg), $MgSO_4$ (15mg) and nitromethane (2.4 mL). After the reaction was finished, the mixture was worked up according to the protocol and purified by chromatography on silica with hexane/ethyl acetate (10/1) as the elution to afford the pure cycloadduct as a clear oil. R_f (hexane/ethyl acetate 10/1): 0.36. ^{1}H NMR ($CDCl_3$, 300 MHz): δ 6.72 (d, J=9 Hz, 1H), 6.70 (d, J=1.6 Hz, 1H), 6.67 (dd, J= 3, 9 Hz, 1H), 5.93 (s, 2H), 5.48 (m, 1H), 2.99 (dt, J=5.3, 10.3 Hz, 1H), 2.87 (dt, J=5.4, 11 Hz, 1H), 2.31 (m, 1H), 2.26 (m, 1H), 2.17 (m, 1H), 2.07 (m, 1H), 1.90 (s, 3H), 1.73 (s, 3H). ^{13}C NMR ($CDCl_3$, 75 MHz): δ 212.0, 147.7, 146.1, 138.0, 132.1, 120.6, 120.5, 108.3, 107.7, 100.9, 53.7, 42.5, 34.2, 33.3, 29.8, 23.2.

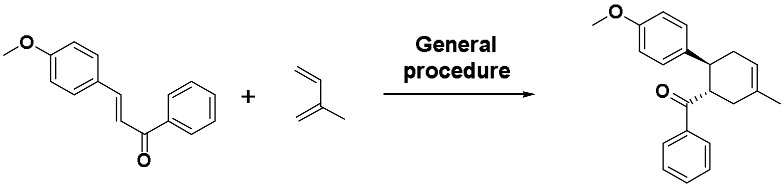

((1S,2S)-4'-methoxy-4-methyl-1,2,3,6-tetrahydro-[1,1'-biphenyl]-2-yl)(phenyl)methanone: According to the general procedure, a dried vial with a magnetic stir bar was charged with (E)-3-(4-methoxyphenyl)-1-phenylprop-2-en-1-one (57.2 mg, 0.24 mmol), isoprene (240 µL, 2.4 mmol), catalyst (2.4 mg), $MgSO_4$ (15mg) and nitromethane (2.4 mL). After the reaction was finished, the mixture was worked up according to the protocol and purified by chromatography on silica with hexane/dichloromethane (1/1) as the elution to afford the pure cycloadduct as a clear oil.

R_f (hexane/dichloromethane 1/1): 0.28. ^{1}H NMR ($CDCl_3$, 300 MHz): δ 7.84 (d, J=7.4 Hz, 2H), 7.50 (t, J=6.8 Hz, 1H), 7.39 (t, J=7.5 Hz, 2H), 7.13 (d, J=8.5 Hz, 2H), 6.72 (d, J=8.4 Hz, 2H), 5.56 (bs, 1H), 3.98 (m, 1H), 3.71(s, 3H), 3.22 (m, 1H), 2.34 (m, 4H), 1.74 (s, 3H). ^{13}C NMR ($CDCl_3$, 75 MHz): δ 203.8, 157.8, 137.4, 136.5, 132.7, 132.5, 128.41, 128.38, 128.0, 121.0, 113.7, 55.1, 47.4, 41.6, 35.2, 34.2, 23.2.

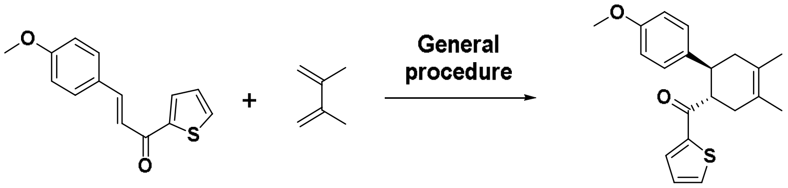

((1S,2S)-4'-methoxy-4,5-dimethyl-1,2,3,6-tetrahydro-[1,1'-biphenyl]-2-yl)(thiophen-2-yl)methanone: According to the general procedure, a dried vial with a magnetic stir bar was charged with (E)-3-(4-methoxyphenyl)-1-(thiophen-2-yl)prop-2-en-1-one (58.6 mg, 0.24 mmol), 2,3-dimethylbuta-1,3-diene (271.6 µL, 2.4 mmol), catalyst (2.4 mg), $MgSO_4$ (15mg) and nitromethane (2.4 mL). After the reaction was finished, the mixture was worked up according to the protocol and purified by chromatography on silica with hexane/ethyl acetate (4/1) as the elution to afford the pure cycloadduct as a clear oil. R_f (hexane/ethyl acetate 4/1): 0.61. ^{1}H NMR ($CDCl_3$, 300 MHz): δ 7.54 (d, J=4.1 Hz, 2H), 7.10 (d, J=8.2 Hz, 2H), 7.00 (t, J=4.1 Hz, 1H), 6.79 (d, J=8.5 Hz, 2H), 4.77 (d, J=15 Hz, 2H), 3.92 (m, 2H), 3.72 (s, 3H), 2.41 (t, J=9.7 Hz 1H), 2.02 (t, J=10 Hz, 1H), 1.65 (s, 3H), 1.07 (s, 3H). ^{13}C NMR ($CDCl_3$, 75 MHz): δ 193.4, 158.2, 152.5, 143.8, 133.6, 131.9, 131.7, 129.3, 128.1, 113.5, 108.7, 55.2, 48.7, 45.0, 42.0, 35.0, 21.9, 18.8.

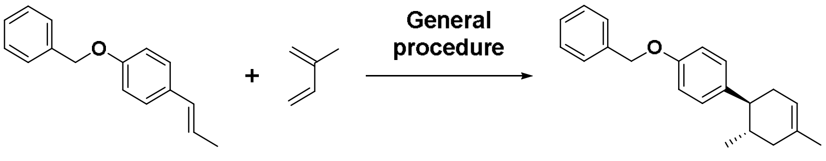

(1S,2S)-4'-(benzyloxy)-2,4-dimethyl-1,2,3,6-tetrahydro-1,1'-biphenyl: According to the general procedure, a dried vial with a magnetic stir bar was charged with (E)-1-(benzyloxy)-4-(prop-1-en-1-yl)benzene (53.8 mg, 0.24 mmol), isoprene (240 µL, 2.4 mmol), catalyst (2.4 mg), $MgSO_4$ (15mg) and nitromethane (2.4 mL). After the reaction was finished, the mixture was worked up according to the protocol and purified by chromatography on silica with hexane/ethyl acetate (8/1) as the elution to afford the pure cycloadduct as a clear oil. R_f (hexane/ethyl acetate 8/1): 0.37. ^{1}H NMR ($CDCl_3$, 300 MHz) δ 7.42 (m, 5H), 7.13 (d, 2H), 6.96 (d, 2H), 5.49 (s, 1H), 5.08 (s, 2H), 2.34 (m, 1H), 2.23 (m, 2H), 2.13 (m, 1H), 1.94 (m, 1H), 1.86 (m, 1H), 1.74 (s, 3H), 0.76 (d, 3H). ^{13}C NMR ($CDCl_3$, 75 MHz) δ 157.18, 138.56, 137.39, 133.87, 128.63, 127.97, 127.62, 121.01, 114.73, 70.12, 47.07, 39.94, 35.36, 34.04, 30.99, 23.50, 20.37.

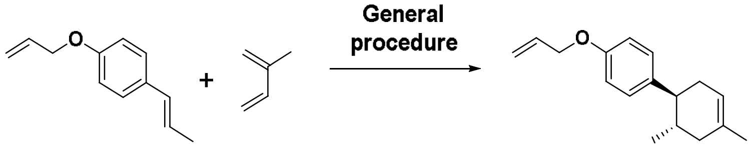

(1S,2S)-4'-(allyloxy)-2,4-dimethyl-1,2,3,6-tetrahydro-1,1'-biphenyl: According to the general procedure, a dried vial with a magnetic stir bar was charged with (E)-1-(allyloxy)-4-(prop-1-en-1-yl)benzene (41.8 mg, 0.24 mmol), isoprene (240 µL, 2.4 mmol), catalyst (2.4 mg), $MgSO_4$ (15mg) and nitromethane (2.4 mL). After the reaction was finished, the mixture was worked up according to the protocol and purified by chromatography on silica with hexane/ethyl acetate (8/1) as the elution to afford the pure cycloadduct as a clear oil. R_f (hexane/ethyl acetate 8/1): 0.32. ^{1}H NMR ($CDCl_3$, 300 MHz) δ 7.11 (d, 2H), 6.89 (d, 2H), 6.10 (m, 1H), 5.44 (d, 2H), 5.30 (d, 2H), 4.55 (d, 2H), 2.33 (m, 1H), 2.22 (m, 2H), 2.12 (m, 1H), 1.91 (m, 1H), 1.85 (m, 1H), 1.73 (s, 3H), 0.74 (d, 3H). ^{13}C NMR ($CDCl_3$, 75 MHz) δ 156.88, 138.37, 133.64, 128.51, 120.96, 117.45, 114.56, 68.85, 47.00, 39.89, 35.29, 34.00, 30.91, 23.43, 20.28.

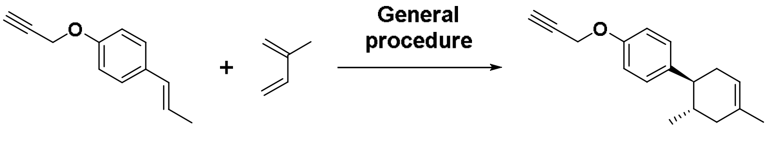

(1S,2S)-2,4-dimethyl-4'-(prop-2-yn-1-yloxy)-1,2,3,6-tetrahydro-1,1'-biphenyl: According to the general procedure, a dried vial with a magnetic stir bar was charged with (E)-1-(prop-1-en-1-yl)-4-(prop-2-yn-1-yloxy)benzene (41.3 mg, 0.24 mmol), isoprene (240 µL, 2.4 mmol), catalyst (2.4 mg), $MgSO_4$ (15mg) and nitromethane (2.4 mL). After the reaction was finished, the mixture was worked up according to the protocol and purified by chromatography on silica with hexane/ethyl acetate (8/1) as the elution to afford the pure cycloadduct as a clear oil. R_f (hexane/ethyl acetate 8/1): 0.30. ^{1}H NMR ($CDCl_3$, 300 MHz) δ 7.10 (d, 2H), 6.92 (d, 2H), 5.45 (s, 1H), 4.68 (d, 2H), 2.52 (s, 1H), 2.31 (m, 1H), 2.20 (m, 2H), 2.10 (m, 1H), 1.91 (m, 1H), 1.82 (m, 1H), 1.70 (s, 3H), 0.72 (d, 3H). ^{13}C NMR ($CDCl_3$, 75 MHz) δ 155.95, 139.28, 133.93, 128.65, 120.98, 114.81, 79.01, 75.44, 55.99, 47.10, 39.93, 35.33, 34.05, 23.51, 20.37.

$$\Phi_{AQY} = \frac{\text{number of product molecules formed}}{\text{number of incident photons}}$$

$$= \frac{N_e}{N_p}$$

$$= \frac{n * N_A}{\left(\frac{P * t}{\frac{h * c}{\lambda}}\right)}$$

$$= \frac{n * N_A * h * c}{P * t * \lambda}$$

$$= \frac{0.125 * 10^{-3}\text{mol} * 6.023 * 10^{23}\text{mol}^{-1} * 6.63 * 10^{-34}\,\frac{\text{m}^2\text{kg}}{\text{s}} \times 3 * 10^{8}\,\frac{\text{m}}{\text{s}}}{\left(0.8\text{cm} * 2.3 * 0.065\,\frac{\text{W}}{\text{cm}^2}\right) \times 240 * 60\text{s} \times 460 * 10^{-9}\ \text{m}}$$

$$= 0.0227 = 2.27\%$$

Figure 95. Apparent quantum yield calculation.

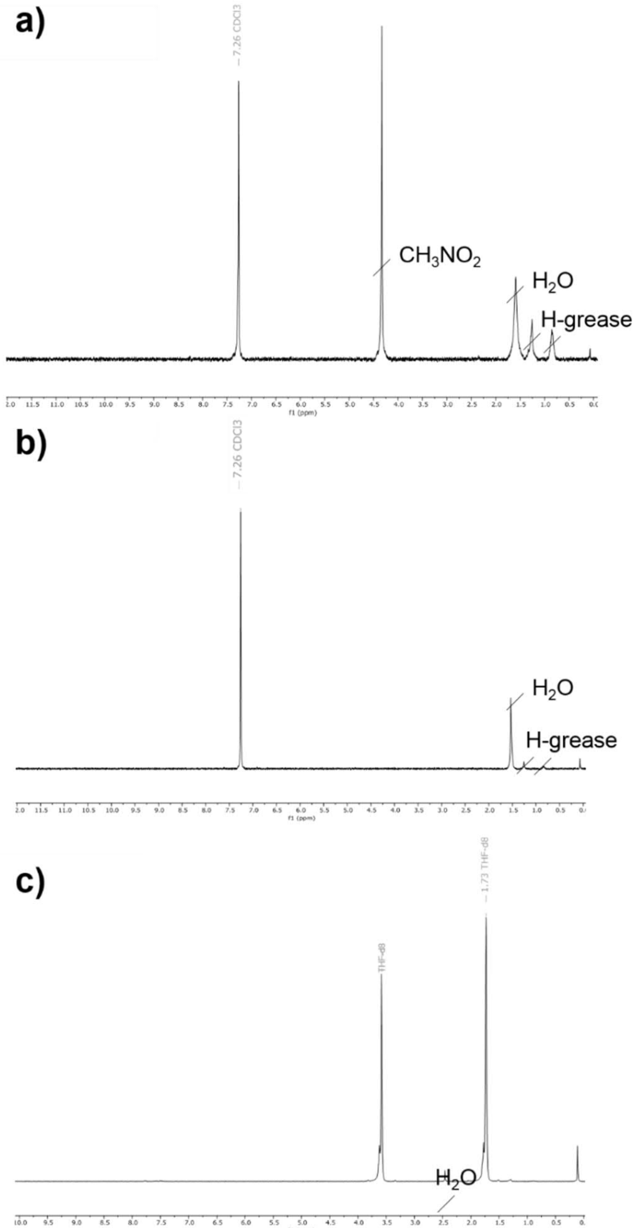

Figure 96. ^{1}H-NMR spectra of a) experiment I (CH_3NO_2), b) experiment II ($CDCl_3$), and c) experiment III (d_8-THF).

2.6 A water-compatible PMMA-based polymer for photocatalytic pollutant remediation in aqueous media

With the establishment of the novel PMMA photocatalyst platform in the previous chapter, a proof-of-concept was presented and new options for photocatalytic material design were created. New options are urgently needed, especially in the increasingly important field of compatibility and application of photocatalysts in green solvents. The basis created was used to synthesize and systematically investigate water-compatible PMMA-based polymers in the following chapter. The chapter is based on unpublished results. The manuscript is in preparation and will be submitted promptly. The project is a joint effort of Masis Sirim, Prof. Katharina Landfester, Prof. Kai Zhang, and me. I carried out the project's experimental work with the following exception: Masis Sirim assisted on monomer and polymer synthesis.

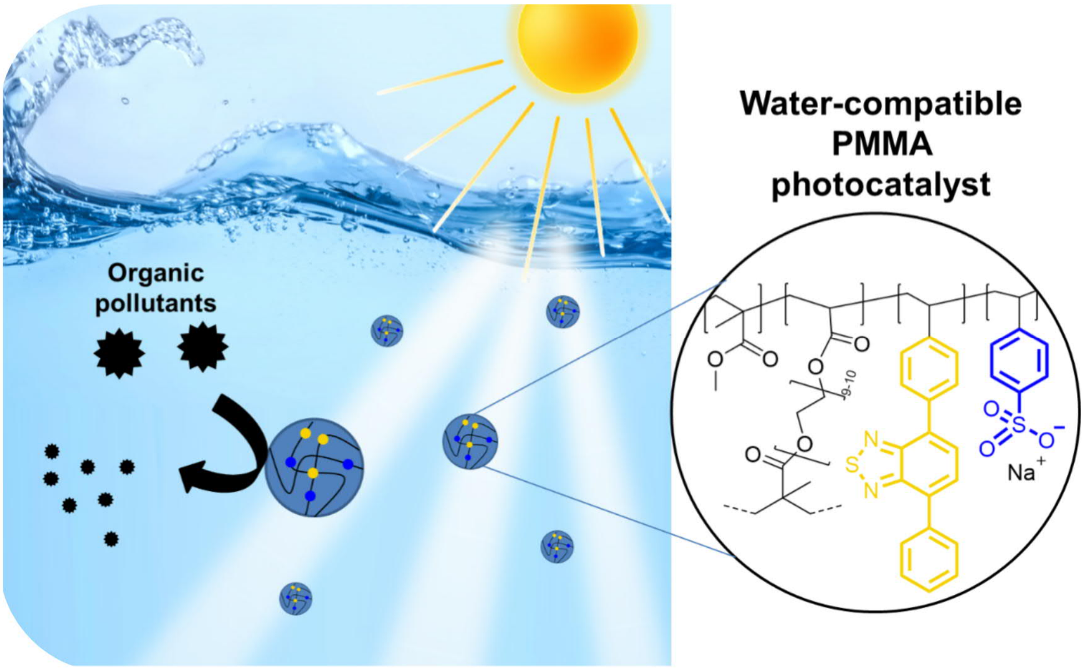

Heterogeneous polymeric photocatalysts are capable of using natural light for chemical transformations. However, numerous promising photocatalytic applications, such as water splitting, reactions with pharmaceutical or biological relevance, or wastewater treatment, are tied to being carried out in an aqueous medium. Typical photocatalytic polymers show little water tolerance due to their aromatic nature and high molecular network architecture. In this work, we developed a novel concept for designing PMMA-based and highly water-compatible photocatalysts by charged monomer copolymerization. By varying the amount of photoactive unit and water-mediating monomers, structure-property relationships for the precise tuning of crucial structural, electrooptical, and photocatalytic properties could be identified. Kinetic studies of the 2,4-dichlorophenol degradation in water showed a polymer composition and solubility optimum for the photocatalytic reactivity. The catalysts were further applied in the efficient photocatalytic remediation of different organic pollutants in water.

2.6.1 Motivation

The use of visible light for the reactive conversion of organic substances is an environmentally friendly alternative to conventional chemical reaction conduction.[442-443] Among the materials commonly used for heterogeneous photocatalytic processes are semiconductors,[46-48] conjugated microporous polymers,[91, 111-112] or covalent triazine networks.[146, 162] A scarcely studied class of substances is photoactive classical polymers.[219-222, 224] They combine polymeric materials and photoactive small molecules' properties by incorporating the latter as repeating units in a polymer backbone. Their advantages include precise control of conjugation lengths, cost-effectiveness, chemical robustness, and variability of properties through facile synthesis and direct access to the toolbox of classical polymer chemistry.[210, 411, 430] The few studies undertaken to date show great potential in synthesis and photocatalytic applications but do not include systematic investigations of structure-property relationships.[222-224] In particular, the effect of monomer composition remains unclear. However, such insights are essential to broaden understanding and address the key challenge of designing photoactive classical polymer materials in the future.

A very attractive approach to using targeted material design for sustainable purposes is the fabrication of systems for performing chemical reactions in green solvents.[444] Water, in particular, is a cheap, safe, and environmentally friendly alternative to organic systems.[445] It is considered the preferred choice in practical applications concerning occupational safety, process safety, and environmental and regulatory aspects. Further, the applicability of materials in an aqueous medium opens several possibilities, such as water splitting,[94, 415, 446] antibacterial treatment,[262, 447] photodynamic therapy,[426] and water purification.[420-421] Conventional polymer photocatalysts are often unsuitable for applications in water due to their highly aromatic nature. Moreover, the rigid and high molecular weight conjugated networks hinder swelling by solvents and substrate diffusion. Previous modification strategies mainly included postsynthetic transformations,[401, 415, 448] surface functionalization,[420, 449-450] or protonation by acids.[451] However, such synthesis methods are complex to perform and cannot be precisely controlled.

In this work, we developed a novel concept for designing water-compatible photocatalysts by charged monomer copolymerization (**Figure 97**). The general effect of variable amounts of photoactive and water-mediating comonomers in the class of non-fully conjugated photocatalysts on structural, electrooptical, and photocatalytic properties was elucidated in detail. In practice, two series of crosslinked PMMA-based polymers were synthesized through radical polymerization. In the first series, the amount of photoactive moiety 4,7-diphenylbenzothiadiazole was gradually increased, and in the second series, the amount of solvent-mediating moiety 4-benzenesulfonate was gradually increased. The electronic, optical, and solubility properties of the PMMA photocatalysts could be tuned and showed direct dependence on the monomer composition. Mathematical as well as DFT calculations support the observed effects. Photocatalytic studies on the decomposition of organic pollutants show the high activity of the polymers in an aqueous medium. Kinetics of the 2,4-dichlorophenol degradation in water showed a polymer composition and solubility optimum for the photocatalytic reactivity. The reaction scope could be expanded to include the remediation of four contaminants detected in groundwater analyses.

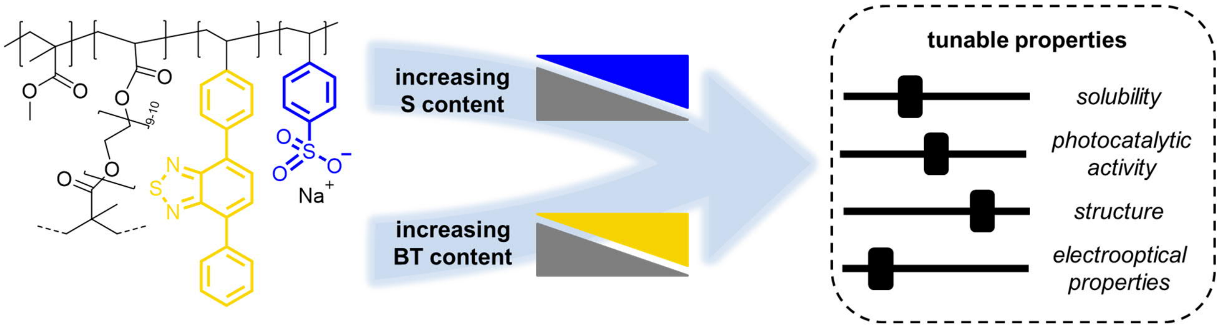

Figure 97. Schematic illustration of the copolymer molecular design and the tuning of properties by varying the amounts of benzothiadiazole (BT) and benzene sulfonate (S).

2.6.2 Synthesis and characterization

The polymers in this work were synthesized *via* free-radical polymerization from methyl methacrylate (MMA), poly(ethylene glycol dimethacrylate) (PEGDMA), 4-phenyl-7-(4-vinylphenyl)benzothiadiazole (BT), and sodium 4-vinylbenzenesulfonate (S). The synthesis was based on a previous literature report.[411] Details on synthetic procedures and comonomer ratios are given in the experimental part further below.

In the first series, the molar content of BT was gradually increased from 0% to 50% (0, 2.5, 5, 10, 20, 50). The amount of MMA was decreased accordingly, while PEGDMA (5%) and S (20%) were kept constant. The samples were denoted as cPMMA-BT_0-S_{20}, cPMMA-$BT_{2.5}$-S_{20}, cPMMA-BT_5-S_{20}, cPMMA-BT_{10}-S_{20}, cPMMA-BT_{20}-S_{20}, cPMMA-BT_{50}-S_{20}. In the second series, the molar content of S was gradually increased from 0% to 40% (0, 5, 10, 40). Again, the amount of MMA was decreased accordingly, while PEGDMA (5%) and BT (20%) were kept constant. The samples were denoted as cPMMA-BT_{20}-S_0, cPMMA-BT_{20}-S_5, cPMMA-BT_{20}-S_{10}, cPMMA-BT_{20}-S_{40}. Additionally, the sample cPMMA-BT_{20}-S_{20} was suitable to be compared within the second series (**Figure 98**).

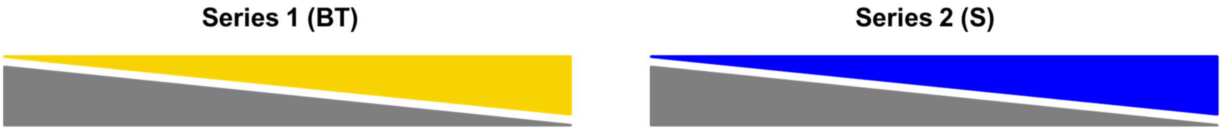

	PEGDMA	MMA	BT	S
cPMMA-BT$_{0}$-S$_{20}$	5	75	0	20
cPMMA-BT$_{2.5}$-S$_{20}$	5	72.5	2.5	20
cPMMA-BT$_{5}$-S$_{20}$	5	70	5	20
cPMMA-BT$_{10}$-S$_{20}$	5	65	10	20
cPMMA-BT$_{20}$-S$_{20}$	5	55	20	20
cPMMA-BT$_{50}$-S$_{20}$	5	25	50	20

	PEGDMA	MMA	BT	S
cPMMA-BT$_{20}$-S$_{0}$	5	75	20	0
cPMMA-BT$_{20}$-S$_{5}$	5	70	20	5
cPMMA-BT$_{20}$-S$_{10}$	5	65	20	10
cPMMA-BT$_{20}$-S$_{20}$	5	55	20	20
cPMMA-BT$_{20}$-S$_{40}$	5	35	20	40

Figure 98. Compositional overview of synthesized photocatalytic polymer series.

The synthesis of the polymers was confirmed by solid-state ^{13}C cross-polarization magic angle-spinning (CP-MAS) NMR spectroscopy. The signal intensities in the spectra can be used to estimate the ratios of the building blocks in the polymer. No double bond signals are apparent in either series of the cPMMAs. This indicates a high degree of polymerization and means that the reaction proceeded to completion. In case incompletely reacted vinyl monomers were present, purification by dialysis was successful. In the first series (**Figure 99a**), the signal of the keto group is observed at a chemical shift of 178 ppm. Further signals at 71, 52, 45, and 18 ppm can be assigned to MMA methyl and methoxy groups and the methylene backbone. All the signals of the MMA are in agreement with the literature values[411] and decrease within the series, which is in accordance with the decrease of the MMA content. The broad signal corresponding to the sulfonate unit (carbons in α- and δ-position concerning -SO$_3$H) around 145 ppm is comparably constant. It can be observed that in the series from cPMMA-BT$_0$S$_{20}$ to cPMMA-BT$_{50}$S$_{20}$, the BT signal at 154 ppm emerges. In sample cPMMA-BT$_0$S$_{20}$, the BT signal is entirely absent. The broad signal around 128 ppm corresponds to aromatic carbons at gets more pronounced when increasing the BT content. The number of aromatic carbons exceeds the number of MMA and backbone carbons to such an extent that the latter signals are strongly attenuated. The molar ratio trend can be confirmed in the first series with the ssNMR spectra.

In the second series, from cPMMA-BT$_{20}$S$_0$ to cPMMA-BT$_{20}$S$_{40}$, the BT signal intensity is constant. In comparison, the S signals at 145 ppm increase within the series. This corresponds to the increase in sulfonate units and confirms the expected trend. As in the first series, the MMA and backbone signals become less prominent while the intensity of the phenylic carbon atoms increases. These effects are less pronounced than in the first series due to the lower C-atom excess in the benzenesulfonate *versus* the backbone compared to the three-membered aromatic BT.

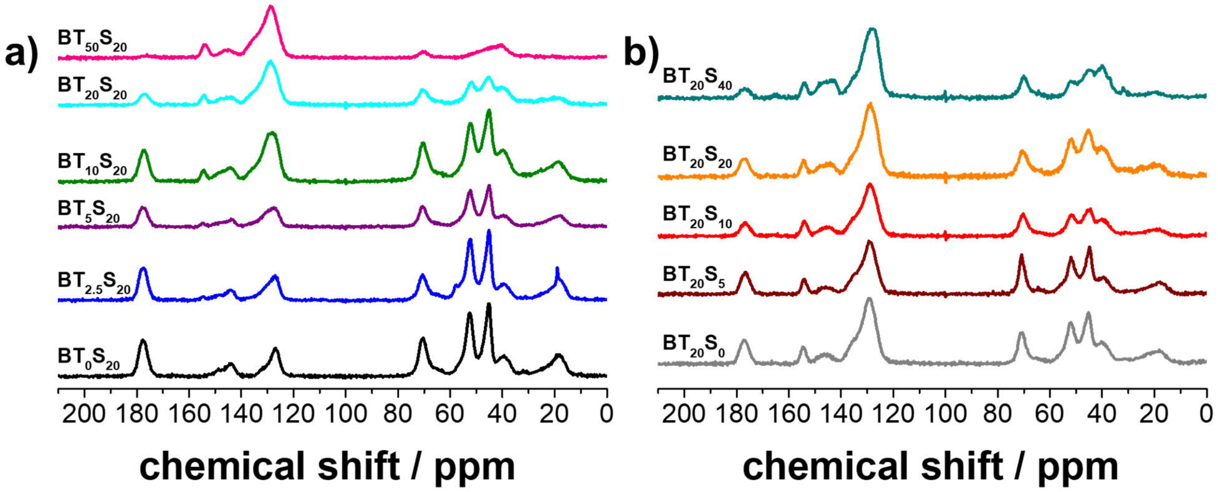

Figure 99. ^{13}C CP-MAS NMR spectra for the first series with increasing BT content (a) and the second series with increasing S content (b).

Fourier-transformed infrared (FTIR) spectra were measured to confirm the structural integrity of the polymers. Using the FTIR spectra of the vinyl monomers, bands were identified for normalization to a signal of the respective constant monomer (**Figure 100**).

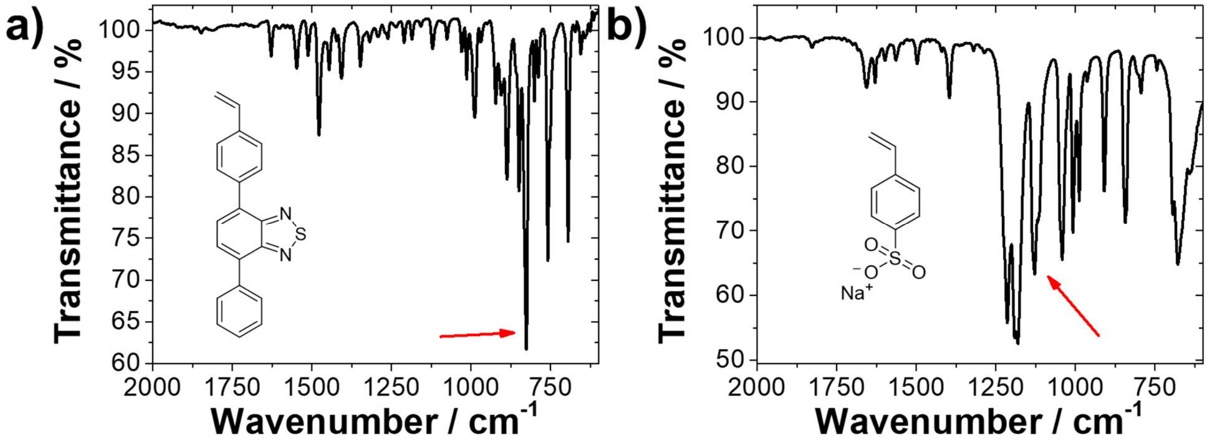

Figure 100. FTIR spectra of the benzothiadiazole (a) and the sulfonate monomer (b). The peaks used for the spectra normalization are marked with a red arrow.

Both series show no double bond signals, also indicating successful polymerization and purification. The increasing BT-content series was normalized to 1181 cm^{-1} (**Figure 101a**). The signal at 1750 cm^{-1}, which corresponds to the carboxyl group of the methyl methacrylate, becomes less pronounced from cPMMA-BT$_0$S$_{20}$ to cPMMA-BT$_{50}$S$_{20}$. The signal at 1500 cm^{-1} and the majority of peaks in the fingerprint region increase within the series since they are attributable to the BT unit. The region between 1000 and 1250 cm^{-1}, where concise signals from the sulfonate monomer can be expected, is comparatively unchanged over the samples of the first row. The second series was normalized to the peak at 827 cm^{-1} since the BT monomer content is expected to be constant. Again, the signal from the MMA decreases at 1750 cm^{-1} and signals corresponding to benzenesulfonate (1665 cm^{-1}, 1000-1250 cm^{-1}) increase in intensity. The FTIR spectra confirm the composition of the cPMMAs and the trends of increasing BT monomer in the first series and increasing S monomer in the second series.

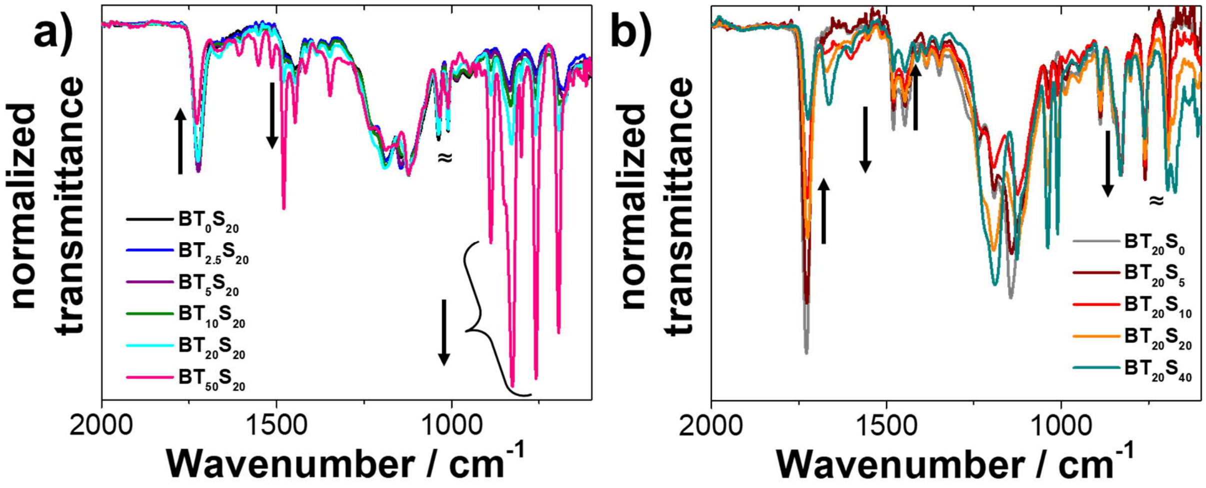

Figure 101. Normalized FTIR spectra of the increasing BT-series (a) and increasing S-series (b). The spectra were normalized to significant peaks of the respective constant monomer.

The structural and morphological characterization was extended by scanning electron microscopy (SEM) imaging and thermogravimetric analysis (TGA) of cPMMA-BT$_{20}$-S$_{20}$ as a representative polymer (**Figure 102**). SEM images showed the typical irregular appearance of a crosslinked polymer. No structured porosity or ordered features could be observed. TGA showed that the photocatalyst stayed intact up to 245 °C under air, comparable to previous data.[411]

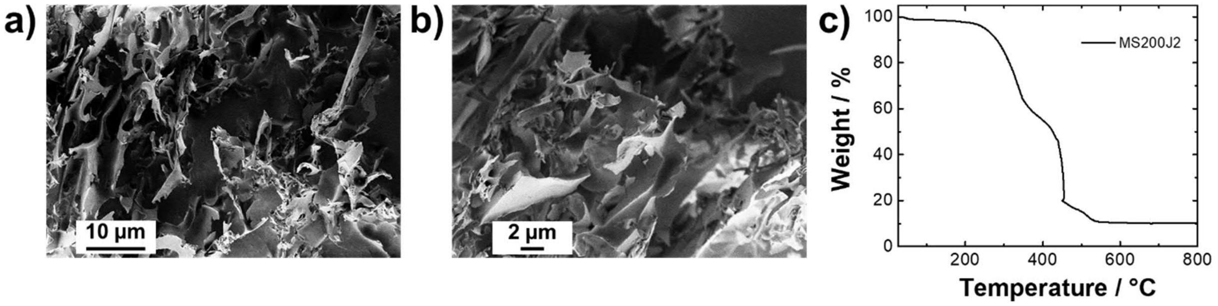

Figure 102. SEM imaging at two different magnifications (a,b) and TGA trace of cPMMA-BT_{20}-S_{20} (c).

In the following, the dispersibility and water compatibility of the polymers were assessed. In a simple experiment, all samples were dispersed in water using ultrasonication and examined after a rest period. In the first series, the $BT_{20}S_{20}$ and $BT_{50}S_{20}$ samples appeared to be the most dispersible. Even after the rest period, there are still noticeable particles distributed in the liquid. In the second row, with increasing S content, the dispersibility in water increases. In the samples $BT_{20}S_{20}$ and $BT_{20}S_{50}$, no material settles at the bottom of the vials.

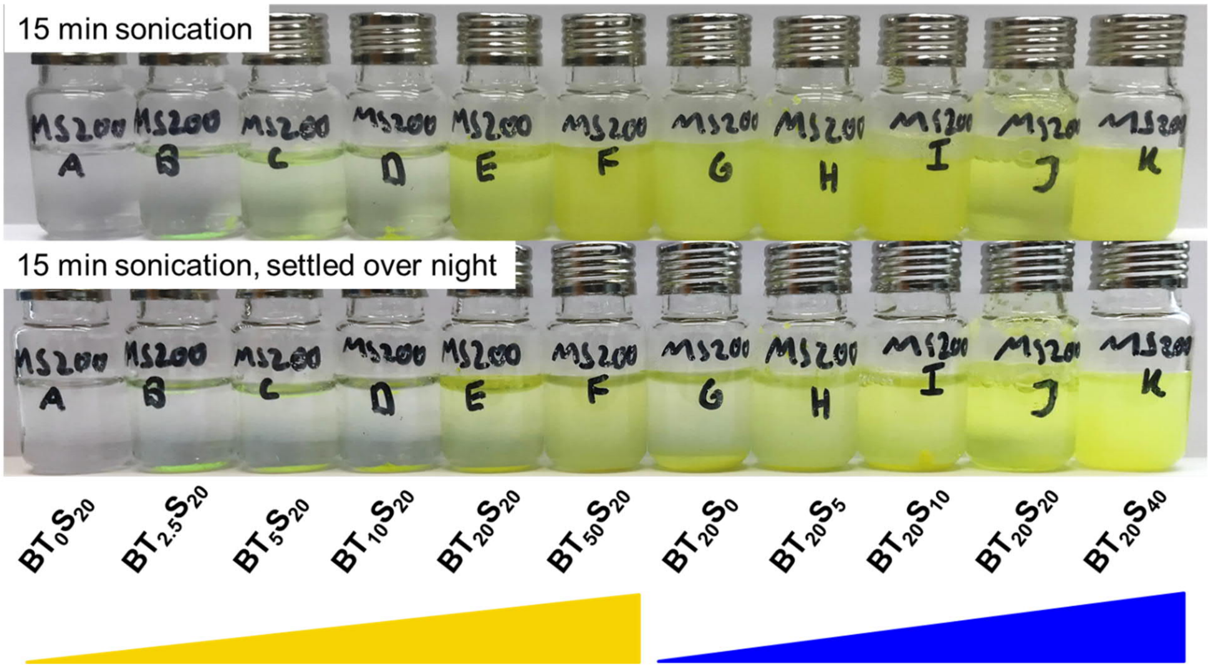

Figure 103. Qualitative dispersibility experiment. Catalyst (5 mg/mL) was dispersed in water through ultrasonication (15min) and left overnight for settling.

The observations made could be confirmed by a DFT-based estimation of hydration enthalpies. By subdividing the polymers into fragments, incremental hydration enthalpies can be calculated, and the tendency to dispersion and compatibility in the aqueous medium can be approximated (**Figure 113-SI**). Secondary entropic solubility effects resulting from the mobility of the chains, the polymer rigidity, and the structural organization of water around the solutes are neglected. In the series with increasing BT content, the enthalpy of hydration increases slightly (**Figure 104a**). The $BT_{40}S_{20}$ sample should have the highest enthalpy of hydration. This is consistent with the dispersion experiment, where a slight increase in solubility can be observed within the series. In the series with increasing S content, the enthalpy of hydration increases strongly. This is also consistent with the dispersion experiment, where an increase in solubility from almost insoluble ($BT_{20}S_{40}$) to fully dispersed over several hours ($BT_{20}S_{40}$) can be observed. The calculations emphasize that the solubility and dispersibility are primarily determined by the sulfonate content and modulated by the BT content.

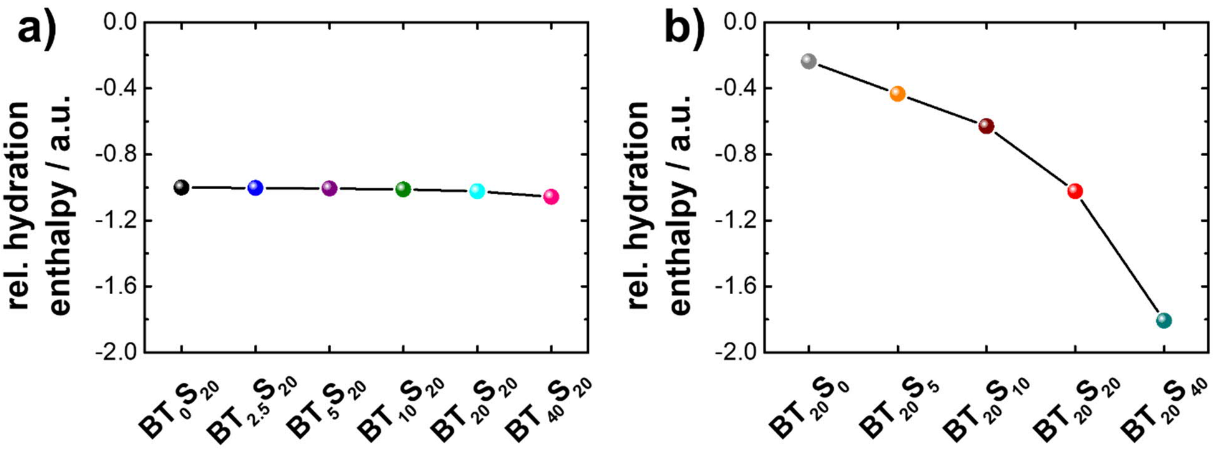

Figure 104. Calculated relative hydration enthalpies in the series of increasing BT content (a) and S content (b).

Zeta potential measurements were performed to draw further conclusions on water compatibility and electrostatic stabilization of the polymers in water. In both series, the magnitude of the electric potential grows with an increase in BT and S monomer, respectively (**Figure 105a-b**). The resulting increase in stabilization and water compatibility by surface charges is consistent with the previously observed trend. $BT_{20}S_0$ represents the only sample that, due to the absence of sulfonate comonomers, exhibits little electrokinetic potential in its dispersion.

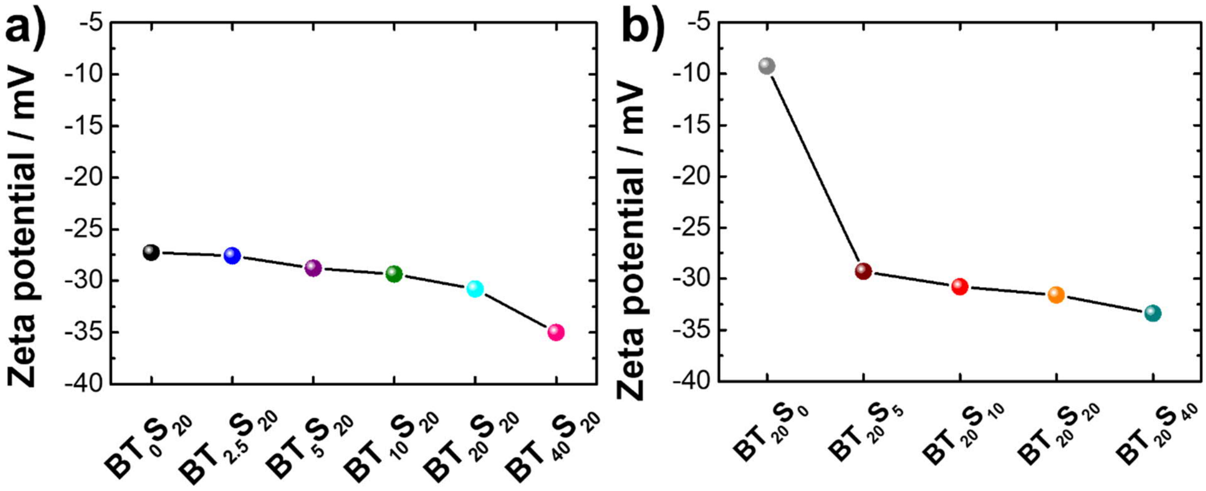

Figure 105. Zeta potential measurements with a concentration of 0.5 mg/mL performed in 10^{-3} M potassium chloride solution at pH 6.8 and 25 °C.

To characterize the electrooptic properties of the polymers, UV/Vis absorption spectroscopy, photoluminescence (PL), and time-resolved photoluminescence spectra (TRPL) were measured. For the PL spectra, the polymers were excited at their absorption maximum. For the TRPL measurements, the samples were exited at λ_{exc} = 380 nm and the decay was detected at the emission maximum. All copolymers were dispersed in water and measured in a glass cuvette.

The UV/Vis absorption spectra of the BT_0S_{20} to $BT_{50}S_{20}$ series are shown in **Figure 106a**. With increasing BT content, it can be observed that the absorption maximum remains comparatively constant (**Figure 106b**). However, the absorption maximum shifts noticeably to about 404 nm at particularly high BT contents in sample $BT_{50}S_{20}$. When observing the polymers’ PL behavior, a red shift of the emission maximum was observed as the BT content in the series increased (**Figure 106c-d)**. The lifetime of excited charge carriers was investigated by TRPL measurements (**Figure 106e-f**). With increasing BT content, the lifetime decreases from 5.6 ns for $BT_{2.5}S_{20}$ to 1.27 ns for $BT_{40}S_{20}$.

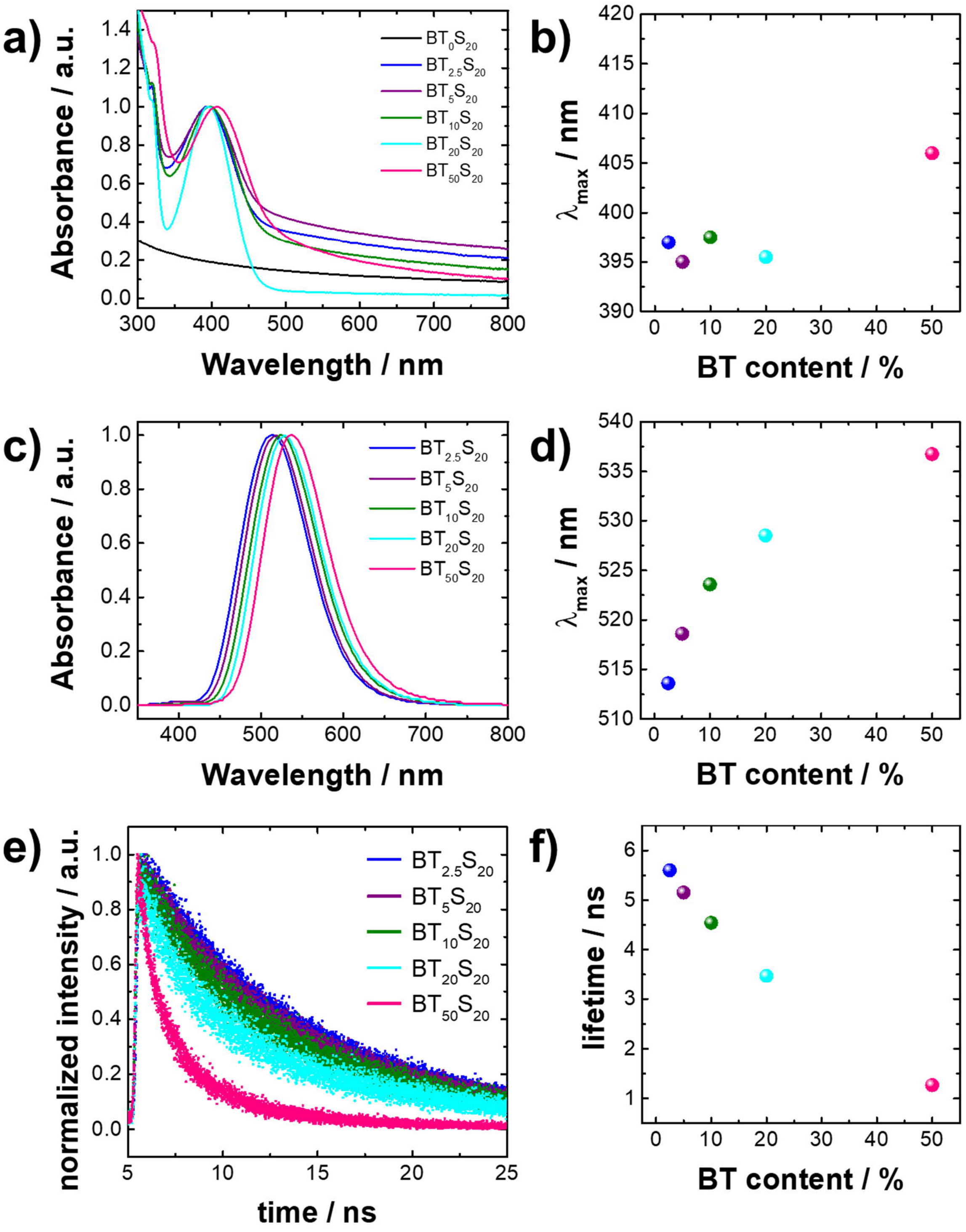

Figure 106. Comparison of UV/Vis (a), absorption maxima (b), PL spectra (c), emission maxima (d), TRPL measurements (e), and excited-state lifetimes (f) in the series from $BT_{2.5}S_{20}$ to $BT_{50}S_{20}$. As expected, BT_0S_{20} did not show relevant absorption behavior and was omitted from the comparison. Lifetimes were obtained from exponential fits and are given in the SI.

By increasing the BT content, the average distance between two photoactive units is reduced. However, the light absorption is independent of the ratio of the photoactive moiety to the other monomers since the electronic configuration in the ground state is not affected by changing the chemical composition of the polymers. Only at extremely high concentrations, where a large fraction of BT units is adjacent to BT units, an overlap of the π-systems occurs and results in a redshift of the absorption. In the excited state, energy transfers to neighboring BT units become more likely as BT content increases. In the case of direct proximity, electron transfers due to overlapping electron densities and the extension of delocalization are also conceivable. Both mechanisms lead to energy losses and shift the PL emission maximum to higher wavelengths. This effect is also evident when looking at the TRPL measurement results. The proximity of BT units and the associated transfer processes increases the number of possible decay mechanisms. With increasing BT content, the lifetime of charge carriers in the excited state decreases significantly.

The absorption spectra of the copolymers for the series cPMMA-$BT_{20}S_0$ to cPMMA-$BT_{20}S_{40}$ are plotted in **Figure 107a**. With increasing sulfonate content, a shift of the absorption maximum to smaller wavelengths can be observed (**Figure 107b**). A minimum is reached for sample $BT_{20}S_{20}$. Towards sample $BT_{20}S_{40}$, the absorption wavelength again assumes a slightly higher value of 399 nm. The PL emission spectra of the sulfonate series are almost identical, and all have their maximum at 533 nm (**Figure 107c-d**). The lifetime of excited charge carriers was investigated by TRPL measurements (**Figure 107e-f**). With increasing S content, the lifetime does not change drastically. At low sulfonate ratios, the lifetimes are slightly lower than for the higher content polymers.

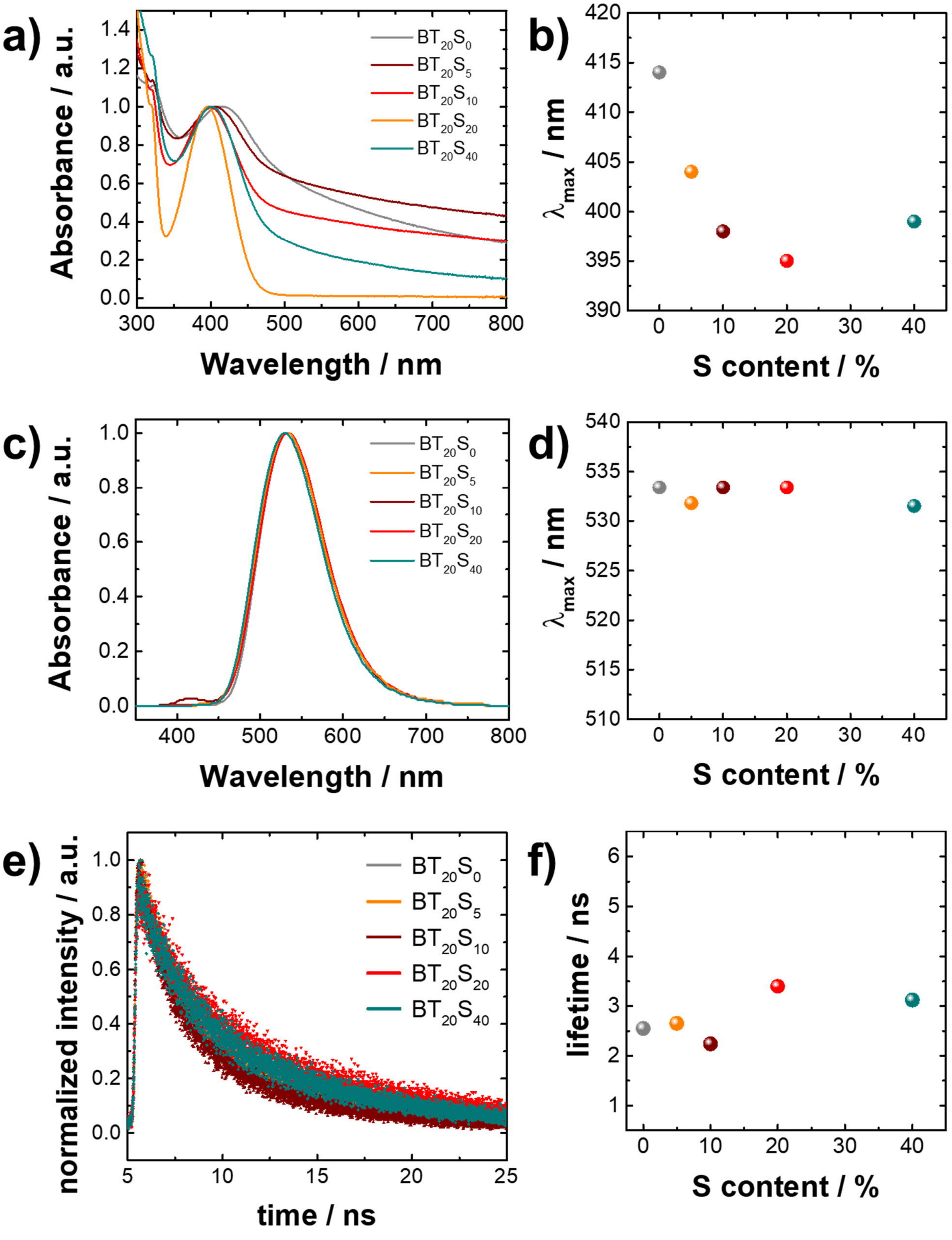

Figure 107. Comparison of UV/Vis (a), absorption maxima (b), PL spectra (c), emission maxima (d), TRPL measurements (e), and excited-state lifetimes (f) in the series from BT$_{20}$S$_0$ to BT$_{20}$S$_{40}$. Lifetimes were obtained from exponential fits and are given in the experimental part.

In the second series, the position of the absorption maximum depends on the sulfonate content. We hypothesize that increased concentrations of negatively charged monomers in close proximity stabilize polar mesomeric states and partial charges. The ground state energy levels of the photoactive moiety are lowered, similar to a negative solvatochromic effect. The absorption is blue-shifted. The emission spectra and the lifetimes of the excited charge carriers are independent of the sulfonate concentration. The BT concentration is sufficiently low so that interactions and transfer phenomena between the units play a minor role or are the same across all polymers. On closer consideration, the slightly red-shifted emission maxima and shorter lifetimes of $BT_{20}S_0$, $BT_{20}S_{10}$, and $BT_{20}S_{20}$ could be attributed to their solubility properties. Due to the lower sulfonate contents, the polymers are likely to be less swollen and the BT units are in closer spatial proximity. This could have similar quenching effects as in the first series but in an attenuated form.

The electro-optical characterization was extended by cyclovoltammetric (CV) measurements of cPMMA-BT_{20}-S_{20} as a representative polymer (**Figure 108a**). The data showed the lowest unoccupied molecular orbital (LUMO) to be -1.35 V vs. SCE. In combination with the Kubelka-Munk-transformed UV/Vis spectrum, which gives a bandgap of 2.83 eV, the highest occupied molecular orbital (HOMO) can be determined to be +1.48 V vs. SCE (**Figure 108b-c)**. The values correspond to literature examples and can be directly derived from the small molecular catalyst 4,7-diphenylbenzothiadiazole ($BTPh_2$).[224, 411, 430]

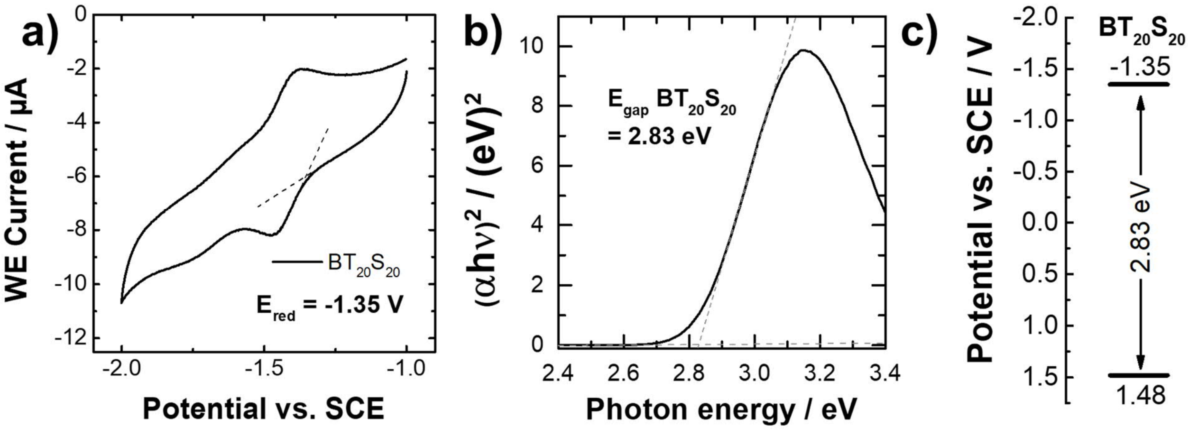

Figure 108. Kubelka-Munk-transformed UV/Vis spectrum (a), cyclic voltammogram (b), and HOMO-LUMO potentials versus the saturated calomel reference electrode (c).

2.6.3 Photocatalysis

Persistent organic pollutants are stable in natural waters and traceable in animal and plant organisms over long periods of time.[452] Although the contaminants pose a significant health risk and have been the subject of political action at the global level for decades, numerous toxins are detectable at high concentrations in groundwaters.[453-455] Therefore, the photocatalytic remediation of harmful organic compounds is of particular relevance.

For the kinetic comparison of the photocatalytic activity of the polymers, the degradation of 2,4-chlorotoluene was chosen. The concentrations were assessed by GC-MS using 4-*tert*-butyltoluene as an internal standard (**Figure 109**)

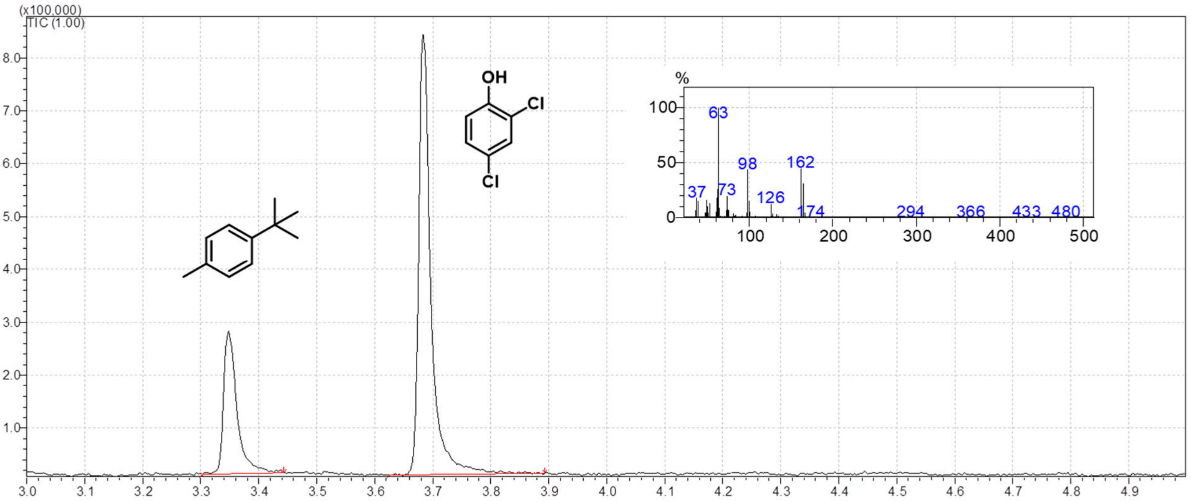

Figure 109. Exemplary chromatogram for the photocatalytic degradation of 2,4-dichlorophenol. The inset is the mass spectrum of the pollutant. 4-*tert*-butyltoluene is used as internal standard.

In the series from BT_0S_{20} to $BT_{40}S_{20}$, $BT_{20}S_{20}$ was the most efficient catalyst by reducing the initial concentration to 12% (**Figure 110a-b**). Without benzothiadiazole units, the polymer was not showing conversion of the target compound (BT_0S_{20}). The photocatalytic activity increases from BT_0S_{20} to $BT_{20}S_{20}$ and decreases again for $BT_{40}S_{20}$. Among the factors promoting higher conversion are the gradual increase in photoactive moiety and the improved water solubility within the series. Increasing the BT content to $BT_{40}S_{20}$ does not seem to have any other positive effect. As shown in the electro-optical characterization, high BT levels seem to contribute to charge carrier quenching and the fundamental change of the π-electronic constitution of the photoactive units.

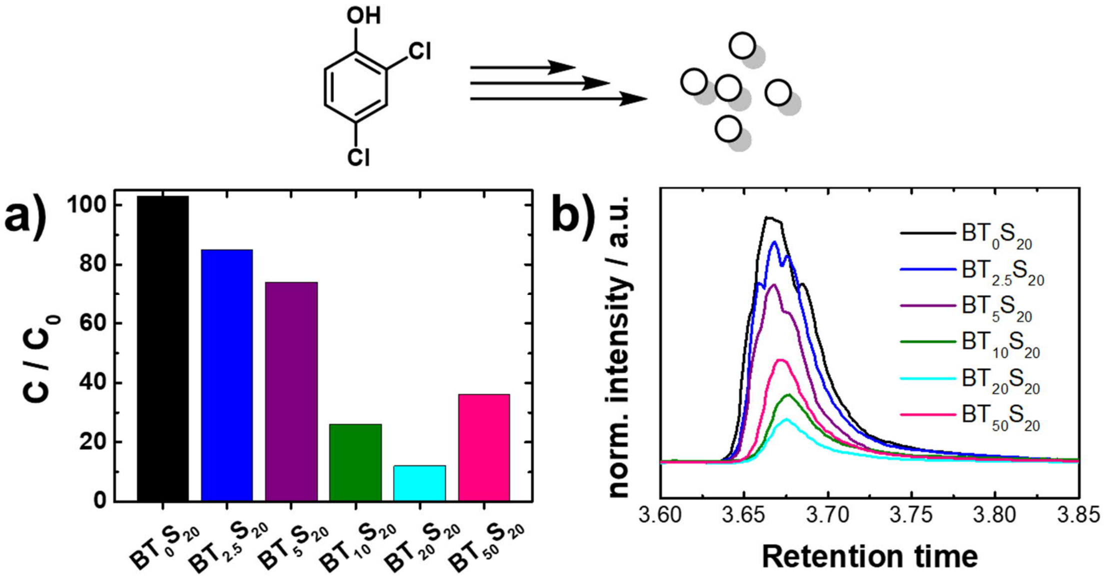

Figure 110. Bar diagram for the photocatalytic degradation of 2,4-dichlorophenol (a) and GCMS trace normalized to the standard 4-*tert*-butyltoluene (b).

In the second series, the photocatalytic activity increased from $BT_{20}S_0$ to $BT_{20}S_{40}$. $BT_{20}S_{40}$ was the most efficient catalyst by reducing the initial concentration to <1% (**Figure 111a-b**). As shown from sample $BT_{20}S_0$, the polarity and dispersibility without sulfonate unit are sufficient to catalyze the degradation reaction. The photocatalytic activity gradually increases from $BT_{20}S_0$ to $BT_{20}S_{40}$. Since PL and TRPL data do not indicate any significant change in photophysical properties within the series, the gradual increase in sulfonate content and water compatibility seems to be mainly responsible for the activity of the polymers. The changing optical absorption does not seem to significantly affect because the photocatalytic activity does not follow the absorption trend. Thus, the series emphasizes the concept of increasing activity in an aqueous medium by copolymerization of charged monomers.

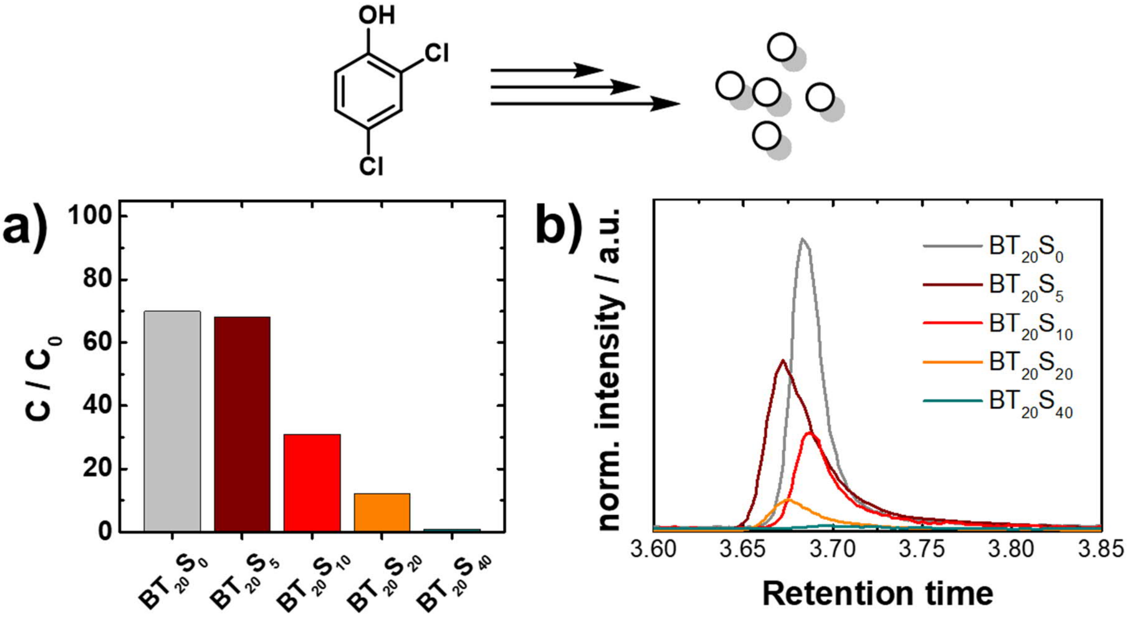

Figure 111. Bar diagram for the photocatalytic degradation of 2,4-dichlorophenol (a) and GCMS trace normalized to the standard 4-*tert*-butyltoluene (b).

The reaction scope could be extended by the degradation of further substances with the catalyst BT$_{20}$S$_{20}$. The plastic degradation products diethyl phthalate, acetophenone, and Bisphenol A could be degraded efficiently and underline the versatility of the system (**Figure 112**).

	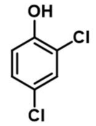	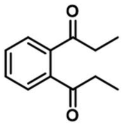	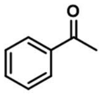	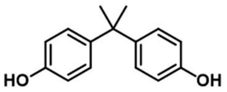
Initial concentration (n$_0$)	112 µmol	523 µmol	122 µmol	13 µmol
Concentration after 4h (n$_4$)	0 µmol	3.3 µmol	116 µmol	0 µmol
Degradation rate	28 µmol/h	122 µmol/h	1.5 µmol/h	3.3 µmol/h

Figure 112. Degradation rates of other organic pollutants. The photocatalytic reaction was performed using BT$_{20}$S$_{20}$.

2.6.4 Conclusion

In summary, we developed a new type of metal-free and redox-active polymers for efficient photocatalytic remediation of organic pollutants in aqueous media. The radical copolymerization of charged sulfonate comonomers with MMA and benzothiadiazole enabled the further development of PMMA-based photocatalysts towards highly increased water compatibility. Using two series of polymers, one with increasing BT content and one with increasing sulfonate content, key structure-property relationships were elucidated. While increasing proportions of photoactive units strongly influence the photophysical properties due to proximity effects, the latter characteristics remain comparatively unchanged when altering the levels of solvent-mediating monomers. Kinetic studies of the 2,4-dichlorophenol degradation in water showed a polymer composition and solubility optimum for the photocatalytic reactivity. The reaction scope could be expanded to include the remediation of different contaminants detected in groundwater analyses. The study contributes significantly to understanding future material design and balancing between monomer composition, catalyst properties, and photocatalytic efficiency.

2.6.5 Experimental details

Materials and methods

All chemicals and solvents were purchased from commercial sources and used as received unless otherwise noted. UV-Vis absorption and fluorescence spectra were recorded on an Agilent Cary 60 spectrophotometer and a J&M TIDAS spectrofluorometer at ambient temperature. Cyclic voltammetry measurements were carried out on a Metrohm Autolab PGSTAT204 potentiostat/galvanostat with a three-electrode-cell system: a glassy carbon electrode as the working electrode, a $Hg/HgCl_2$ electrode as the reference electrode, a platinum wire as a counter electrode, and Bu_4NPF_6 (0.1 M in acetonitrile) as electrolyte. The scan rate was 100 mV s^{-1} in the range of -1 eV to -2 eV. GC-MS measurements were performed on a Shimadzu GC-2010 plus gas chromatograph with a QP2010 ultra mass spectrometer. The system operates with a fused silica column (Phenomenex, Zebron 5-ms nonpolar) and a flame ionization detector. ^1H and ^{13}C NMR spectra for all compounds were measured using a Bruker Avance 300 MHz. Solid-state ^{13}C CP MAS NMR measurements were carried out using a Bruker Avance II solid-state NMR spectrometer operating at 300 MHz Larmor frequency. The system is equipped with a standard 4mm magic angle spinning (MAS) double resonance probe head. FTIR measurements were conducted with a Varian 1000 FTIR spectrometer. The morphology was investigated with a LEO Gemini 1530 scanning electron microscope (SEM). Thermogravimetric analysis (TGA) was conducted in an air atmosphere with temperature increasing from room temperature to 900 °C at a rate of 10 K/min. All DFT calculations were carried out with the Gaussian 09 package.[290] The structures were optimized at the B3LYP level of theory[331] with the basis set of 6-31G(d).[332-333] The hydration calculations were performed together with the PCM (Polarizable Continuum Model) model by employing water as the solvent.[294-296] Zeta potential measurements were performed in 10^{-3} M potassium chloride solution at pH 6.8 and 25 °C with a Malvern Zeta sizer (Malvern Instruments, UK). Time-resolved PL spectroscopy (TRPL) / time-correlated single-photon counting (TCSPC) measurements were conducted with a FluoTime200 time-correlated single-photon counting setup. Samples were excited with a laser at 380 nm, which was controlled by PicoQuant PDL 800-D. The signal was detected using a microchannel plate photomultiplier tube connected to a PicoHarp 300 time-correlated single-photon counting system. The instrument response function was measured using a dispersion of silica nanoparticles (LUDOX HS-40 colloidal silica) in water.

Monomer synthesis

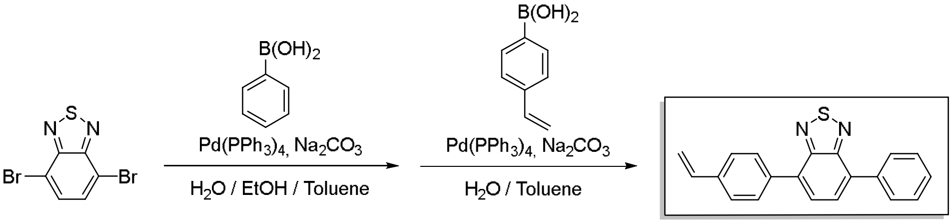

Step 1 (4-bromo-7-phenylbenzo[c][1,2,5]thiadiazole): Phenylboronic acid (899 mg, 7.37 mmol, 1.00 eq.), 4,7-dibromobenzo[c][1,2,5]thiadiazole (3.25 g, 11.06 mmol, 1.50 eq.), toluene (30 mL), aqueous Na_2CO_3 solution (2 M, 12.4 mL) and ethanol (12.4 mL) were placed in a 100 mL Schlenk flask. After degassing by Ar bubbling for 20min, $Pd(PPh_3)_4$ (254 mg, 220 µmol, 0.03 eq.) was added in an Ar counter stream. The solution was vigorously stirred at 90°C for 48h. After cooling to room temperature, the resulting mixture was extracted with dichloromethane (4 x 40 mL). The combined organic phases were washed with brine (100 mL) and dried over anhydrous $MgSO_4$. After filtration and rotary evaporation of solvents, the residue was purified by column chromatography on silica gel (petroleum ether/dichloromethane 3:1). The light green solid (2.4 g) was used as is in the next step.

Step 2 (4-phenyl-7-(4-vinylphenyl)benzo[c][1,2,5]thiadiazole): The crude product from step 1 (2.4 g), (4-vinylphenyl)boronic acid (1.59 g, 10.75 mmol, 1.3 eq.), toluene (22 mL) and aqueous Na_2CO_3 solution (2M, 12 mL) were combined in a 100 mL Schlenk tube. After degassing by Ar bubbling for 20min, $Pd(PPh_3)_4$ (190 mg, 165 µmol, 0.02 eq.) was added in an Ar counter stream. The solution was vigorously stirred at 90°C for 48h. After cooling to room temperature, water was added (55 mL), and the resulting mixture was extracted with dichloromethane (4 x 40 mL). The combined organic phases were washed with 1 M NaOH (70 mL) and brine (70 mL). After drying over anhydrous $MgSO_4$ and filtration, rotary evaporation yielded the crude product. The residue was purified by column chromatography on silica gel (petroleum ether / DCM 1:0 → 0:1). The product was obtained as a bright yellow powder (1.76 g). ^1H NMR (300 MHz, $CDCl_3$) δ 7.98 (d, 4H), 7.80 (s, 2H), 7.61-7.44 (m, 4H), 6.82 (q, 1H), 5.86 (d, 1H), 5.34 (d, 1H). ^{13}C NMR (75 MHz, $CDCl_3$) δ 154.27, 154.21, 137.78, 137.56, 136.91, 136.53, 133.50, 133.05, 129.52, 129.38, 128.77, 128.52, 128.27, 127.99, 126.61, 114.67.

Polymer synthesis

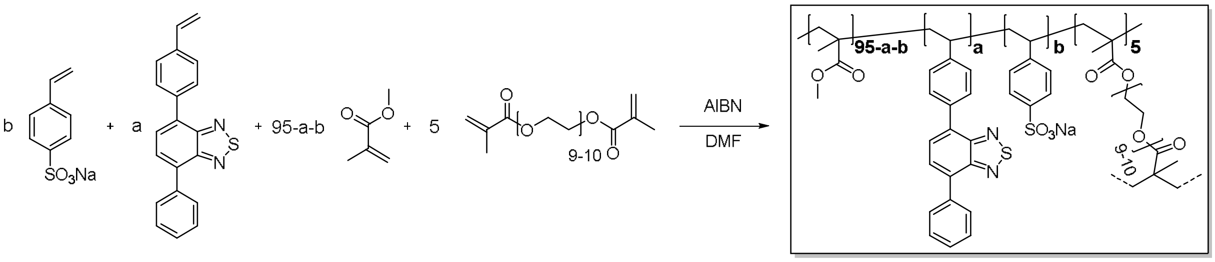

4-Phenyl-7-(4-vinylphenyl)benzo[c][1,2,5]thiadiazole (0-0.5 eq.), methyl methacrylate (0.25-0.75 eq.) and poly(ethylene glycol dimethacrylate) (0.05 eq.) were charged in a vial and dissolved in DMF (3.6 mL). The solution was degassed with Ar for 5min and azobisisobutyronitrile (0.008 eq.) was added. Then the vial was capped and the solution was purged with Ar while stirring for 5min. After heating to 70 °C overnight, the reaction was cooled to room temperature. The polymer was transferred with Mili Q water and dialyzed with THF/water (1:10) for 24h (SnakeSkin dialysis tubing, 3.5K MWCO, 2mm, ThermoFisher). After 12h, the solution was exchanged for fresh THF/water (1:10). The polymers were freeze-dried for 24h under high vacuum and appeared as dry colorless to bright yellow solids.

In **Table 11** and **Table 12**, the polymerization setups are described in detail.

Table 11. Overview of molar ratios and weights of the polymer series with increasing BT content.

		PEGDMA	MMA	BT	S	AIBN	DMF
MS200A	*eq.*	5	75	-	20	0.8	-
	n	223 µmol	3.35 mmol	-	891 µmol	35.6 µmol	-
	m or *V*	128.0 mg	335.0 mg	-	183.5 mg	5.85 mg	3.6 mL
MS200B	*eq.*	5	72.5	2.5	20	0.8	-
	n	223 µmol	3.23 mmol	111 µmol	891 µmol	35.6 µmol	-
	m or *V*	128.0 mg	322.5 mg	35 mg	183.5 mg	5.85 mg	3.6 mL
MS200C	*eq.*	5	70	5	20	0.8	-
	n	223 µmol	3.12 mmol	223 µmol	891 µmol	35.6 µmol	-
	m or *V*	128.0 mg	312.1 mg	70 mg	183.5 mg	5.85 mg	3.6 mL
MS200D	*eq.*	5	65	10	20	0.8	-
	n	223 µmol	2.90 mmol	445 µmol	891 µmol	35.6 µmol	
	m or *V*	128.0 mg	290.0 mg	140 mg	183.5 mg	5.85 mg	3.6 mL
MS200E	*eq.*	5	55	20	20	0.8	-
	n	111 µmol	1.22 mmol	445 µmol	445 µmol	17.8 µmol	-
	m or *V*	64.0 mg	122.6 mg	140 mg	91.8 mg	2.92 mg	3.6 mL
MS200F	*eq.*	5	25	50	20	0.8	-
	n	45 µmol	0.22 mmol	445 µmol	178 µmol	7.1 µmol	
	m or *V*	25.6 mg	22.3 mg	140 mg	36.7 mg	1.17 mg	3.6 mL

Table 12. Overview of molar ratios and weights of the polymer series with increasing S content.

		PEGDMA	MMA	BT	S	AIBN	DMF
MS200G	*eq.*	5	75	20	-	0.8	-
	n	111 µmol	1.67 mmol	445 µmol	-	17,8 µmol	-
	m or *V*	64,0 mg	169 mg	140 mg	-	2,92 mg	3,6 mL
MS200H	*eq.*	5	70	20	5	0.8	-
	n	111 µmol	1.55 mmol	445 µmol	111 µmol	17,8 µmol	-
	m or *V*	64,0 mg	158 mg	140 mg	22.9 mg	2,92 mg	3,6 mL
MS200I	*eq.*	5	65	20	10	0.8	-
	n	111 µmol	1.44 mmol	445 µmol	222 µmol	17.8 µmol	-
	m or *V*	64,0 mg	146 mg	140 mg	45.8 mg	2.92 mg	3.6 mL
MS200J	*eq.*	5	55	20	20	0.8	-
	n	111 µmol	1.22 mmol	445 µmol	445 µmol	17.8 µmol	-
	m or *V*	64,0 mg	124 mg	140 mg	91.5 mg	2.92 mg	3.6 mL
MS200K	*eq.*	5	35	20	40	0.8	-
	n	111 µmol	0.78 mmol	445 µmol	890 µmol	17.8 µmol	-
	m or *V*	64,0 mg	79 mg	140 mg	183.1 mg	2.92 mg	3.6 mL

Photocatalysis kinetics

To obtain a saturated solution, 2,4-dichlorophenol (1.0 g, 6.14 mmol) was added to Milli Q water (50 mL). The suspension was stirred for 24h at room temperature. After settling, the supernatant was collected and used as a stock solution for the kinetic experiments. In a 20 mL vial equipped with a magnetic stir bar, polymer (10 mg) and stock solution (5 mL) were combined. After passing air through the setup for 2min, the reaction was stirred for 30min in the dark to rule out the potential absorption of the small molecule on the organic polymer networks. A sample for GCMS analysis was taken and used as a starting point (0h). Next, the vial was placed under irradiation of blue LEDs (0.061 W/cm^2) and stirred at room temperature for 4h. Samples for GCMS analysis were taken after 1, 2, and 4h.

Every sample taken from the aqueous solution (200µL) was extracted with DCM (1000 µL). The organic phase was further used. 4-*tert*-butyltoluene (PTBT) was added as an internal standard (333 µL in 1000 µL DCM stock solution, 10 µL stock solution in every GCMS vial).

For diethyl phthalate, acetophenone and bisphenol-A saturated aqueous solutions were obtained similarly. The further procedure followed the one described above. The degradation rate was determined using a sample taken after a reaction time of 4h.

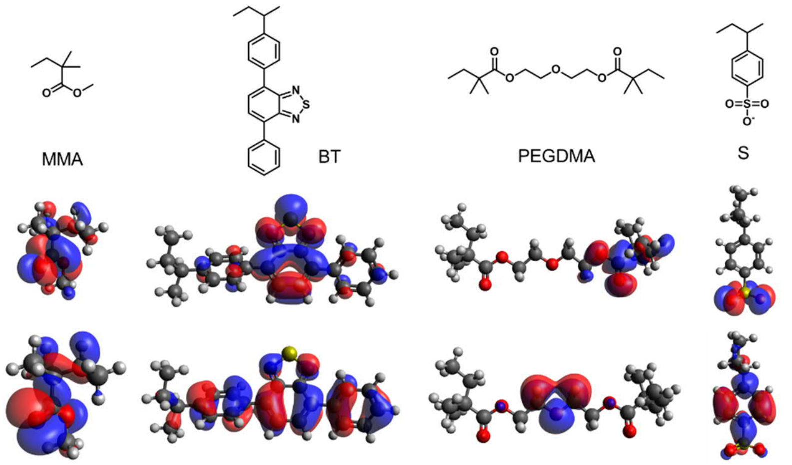

Total energy / H	-425,64225589	-1.358,0883455	-1.003,9167616	-1.012,77198575
Total energy hydrated / H	-425,64710568	-1.358,09579333	-1.003,9244714	-1.012,86815202
Difference = Hydration enthalpy / H	-0,00484979	-0,00744783	-0,00770989	-0,09616627
Hydration enthalpy / kJ	-2,11436E-23	-3,24702E-23	-3,36127E-23	-4,19255E-22
Hydration enthalpy / kJ mol^{-1}	-12,73267029	-19,55358145	-20,24159548	-252,4755524

	MMA	BT	S	PEGDMA	Rel. Hydration enthalpy
BT_0S_{20}	75	0	20	5	1
$BT_{2.5}S_{20}$	72,5	2,5	20	5	1,00279
BT_5S_{20}	70	5	20	5	1,00559
$BT_{10}S_{20}$	65	10	20	5	1,01117
$BT_{20}S_{20}$	55	20	20	5	1,02234
$BT_{50}S_{20}$	25	50	20	5	1,05586
$BT_{20}S_0$	75	20	0	5	0,23703
$BT_{20}S_5$	70	20	5	5	0,43336
$BT_{20}S_{10}$	65	20	10	5	0,62969
$BT_{20}S_{20}$	55	20	20	5	1,02234
$BT_{20}S_{40}$	35	20	40	5	1,80766

Figure 113. To estimate the hydration enthalpy, the total energy of four fragments in vacuum vs. in water was compared. By multiplying the obtained fragment hydration enthalpies with the respective monomer content, relative hydration enthalpies for every polymer were calculated. The relative hydration enthalpy compared to BT_0S_{20} was obtained and is displayed in the main text. All DFT calculations were carried at the B3LYP level of theory, with the basis set of 6-31G(d). The hydration calculations were performed together with the PCM (Polarizable Continuum Model) model by employing water as the solvent.

Table 13. Lifetimes of the polymers obtained from exponential fitting.

	A1	t1 / ns	y0	<τ> / ns	R^2
BT_0S_{20}	-	-	-	-	-
$BT_{2.5}S_{20}$	1.87	8.08	0.047	5.60	0.991
BT_5S_{20}	1.90	7.43	0.058	5.15	0.989
$BT_{10}S_{20}$	1.99	6.55	0.065	4.54	0.981
$BT_{20}S_{20}$	2.39	4.91	0.087	3.40	0.972
$BT_{40}S_{20}$	17.1	1.83	0.046	1.27	0.984
$BT_{20}S_0$	3.87	3.68	0.067	2.55	0.987
$BT_{20}S_5$	3.78	3.83	0.050	2.66	0.990
$BT_{20}S_{10}$	4.53	3.30	0.052	2.29	0.984
$BT_{20}S_{20}$	2.39	4.91	0.087	3.40	0.972
$BT_{20}S_{40}$	2.69	4.51	0.069	3.12	0.978

Fit results gave R^2(adjusted) of >0.97, which confirms good fits to the data points.

3 Supporting information

3.1 Visible-light-driven selective oxidation of hydrocarbons under ambient conditions over covalent triazine frameworks

^{1}H and ^{13}C NMR spectra

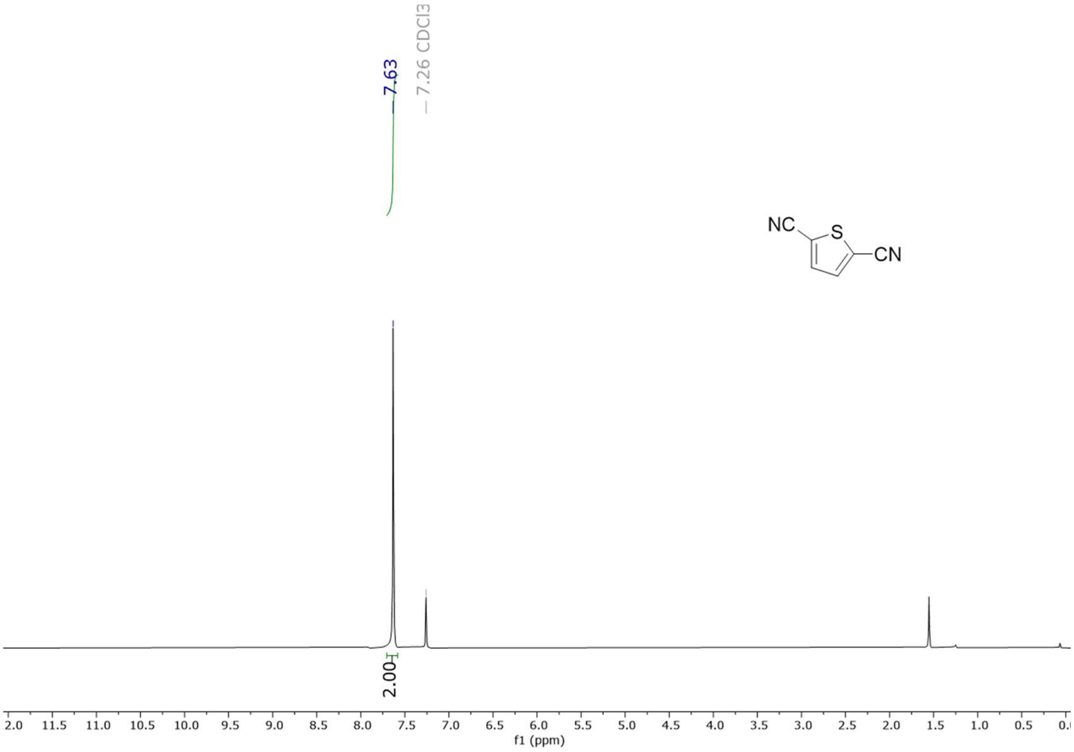

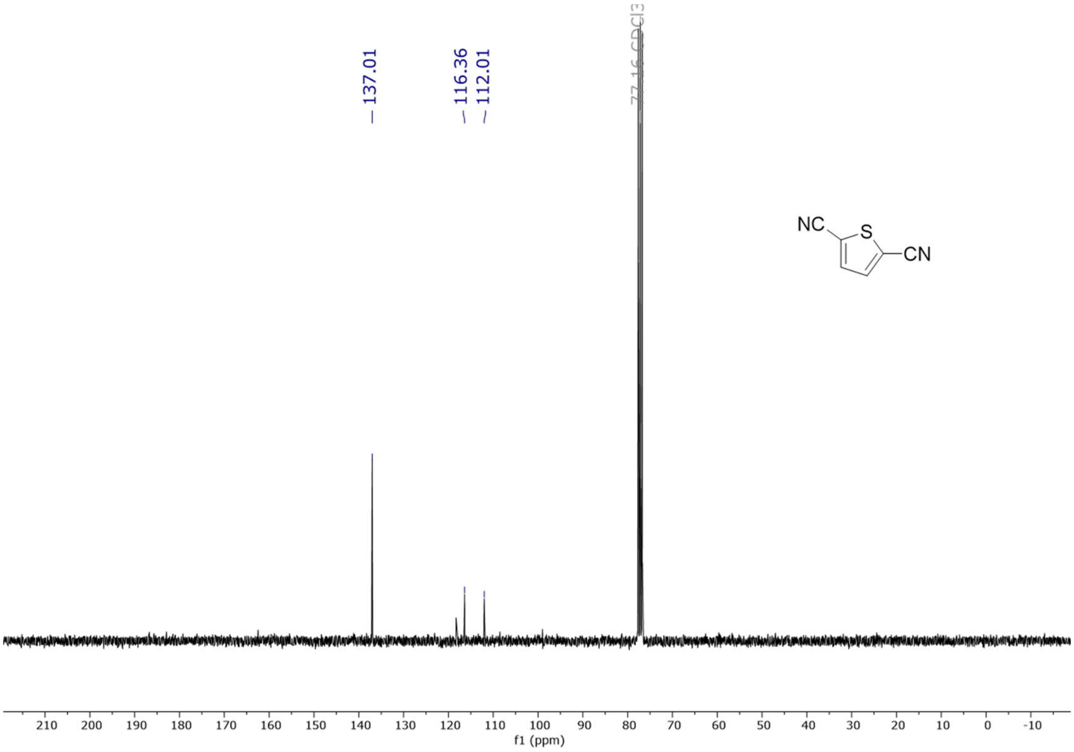

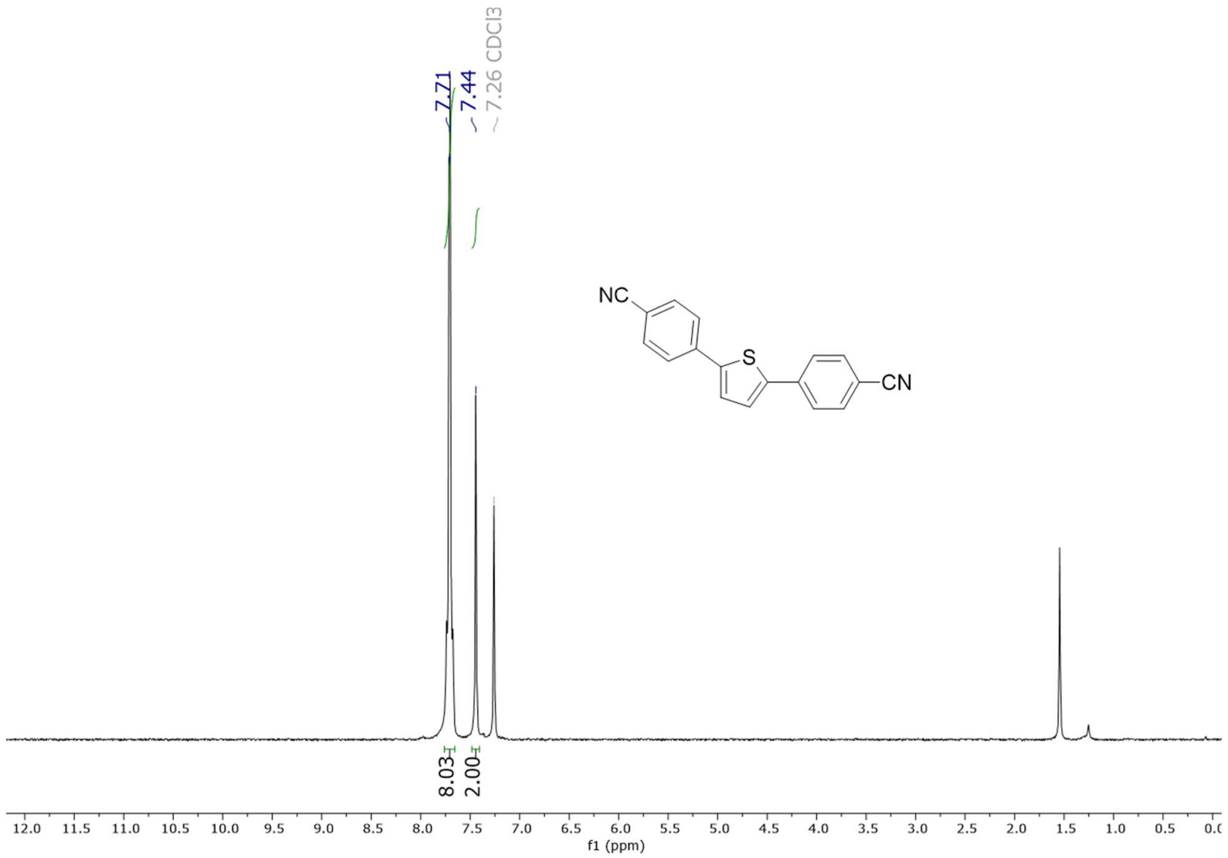
7.71
7.44
7.26 CDCl3
NC
S
CN
8.03
2.00
12.0 11.5 11.0 10.5 10.0 9.5 9.0 8.5 8.0 7.5 7.0 6.5 6.0 5.5 5.0 4.5 4.0 3.5 3.0 2.5 2.0 1.5 1.0 0.5 0.0
f1 (ppm)

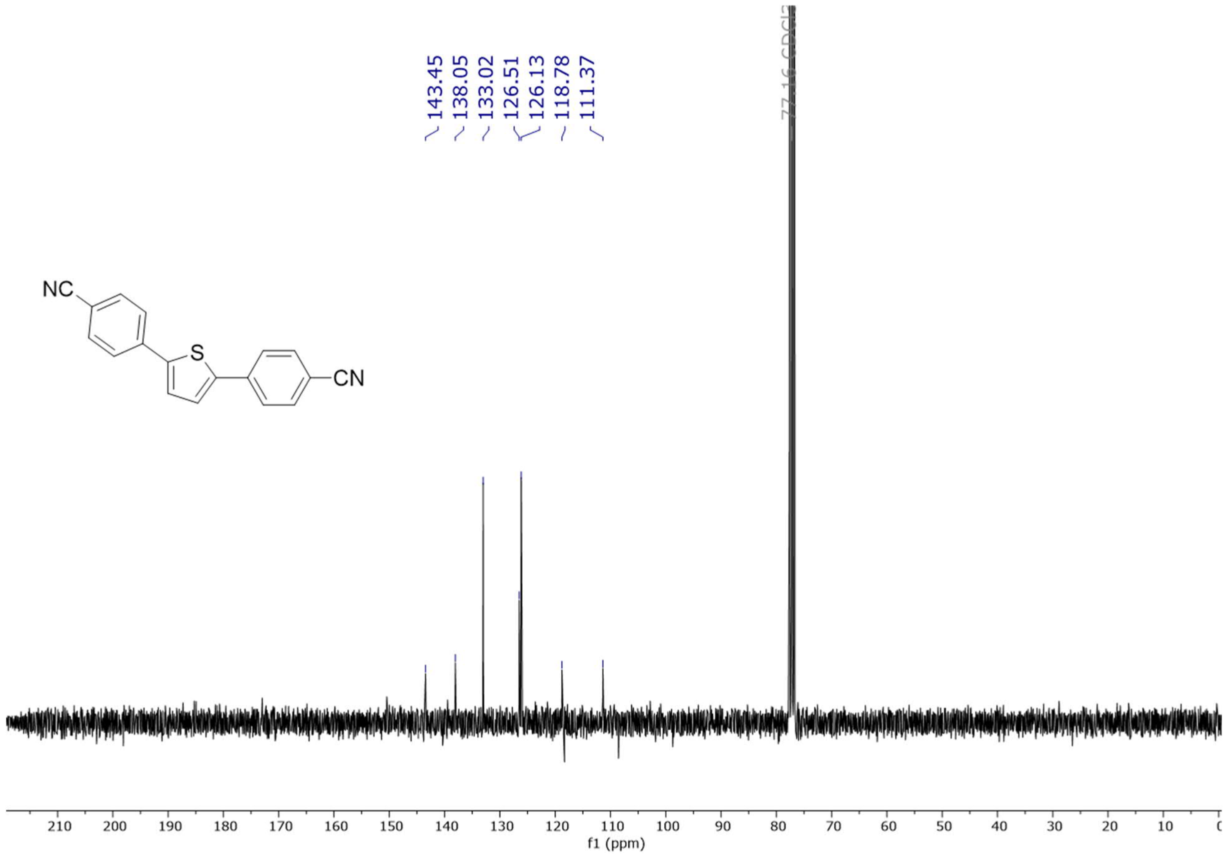
143.45
138.05
133.02
126.51
126.13
118.78
111.37
77.16 CDCl3
NC
S
CN
210 200 190 180 170 160 150 140 130 120 110 100 90 80 70 60 50 40 30 20 10 0
f1 (ppm)

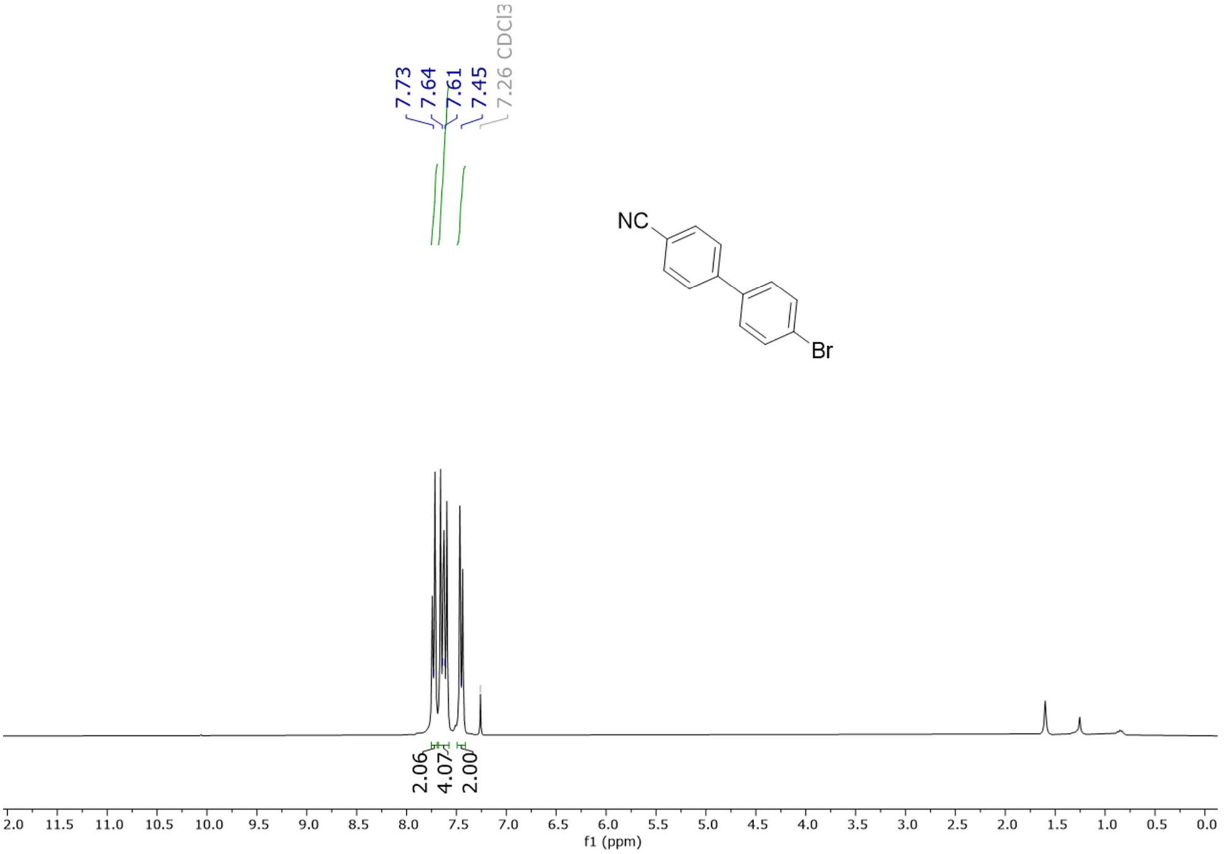
7.73
7.64
7.61
7.45
7.26 CDCl3
NC
Br
2.06
4.07
2.00
2.0
11.5
11.0
10.5
10.0
9.5
9.0
8.5
8.0
7.5
7.0
6.5
6.0
5.5
5.0
4.5
4.0
3.5
3.0
2.5
2.0
1.5
1.0
0.5
0.0
f1 (ppm)

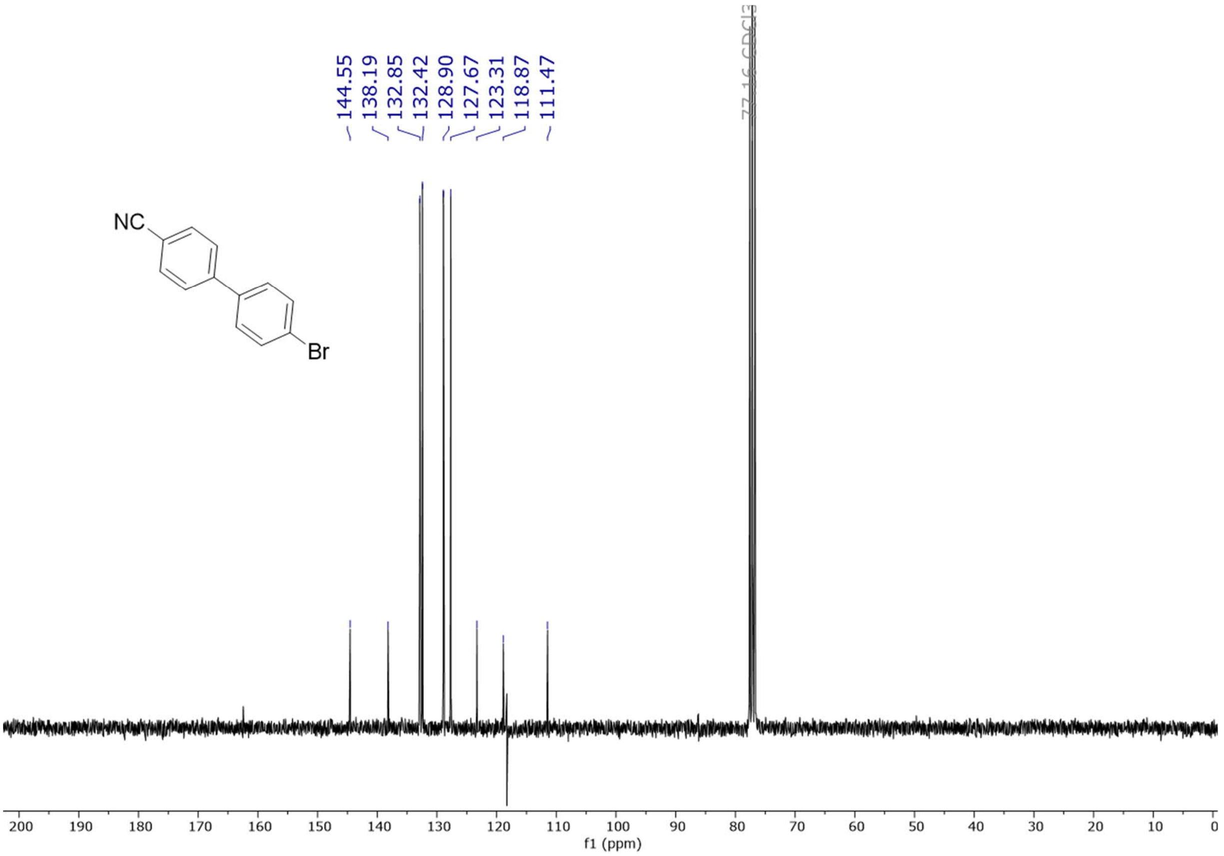
144.55
138.19
132.85
132.42
128.90
127.67
123.31
118.87
111.47
77.16 CDCl3
NC
Br
200
190
180
170
160
150
140
130
120
110
100
90
80
70
60
50
40
30
20
10
0
f1 (ppm)

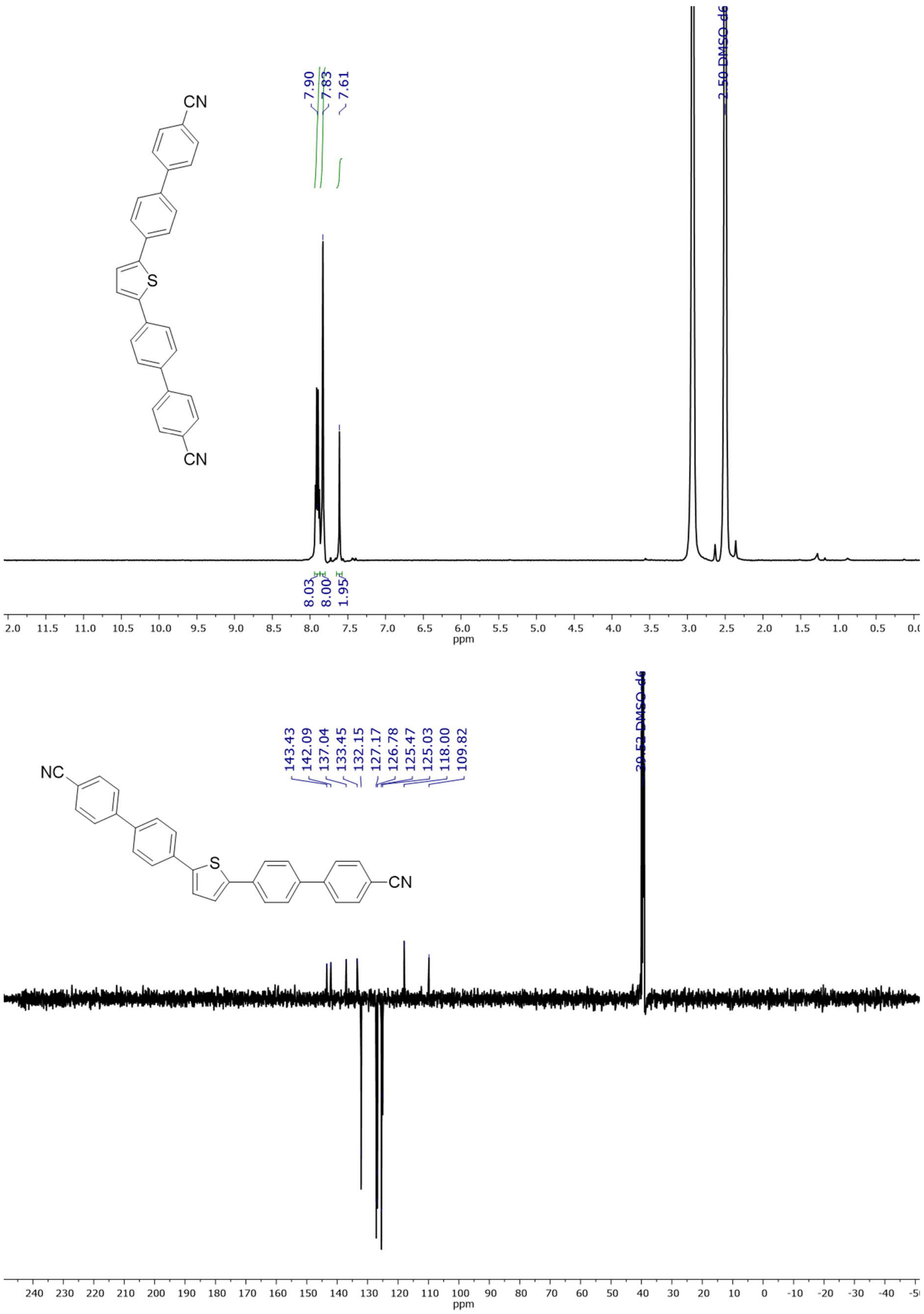

The ^1H and ^{13}C NMR spectra of monomer 4',4'''-(thiophene-2,5-diyl)bis(([1,1'-biphenyl]4-carbonitrile)) were taken in d_6-DMSO at 373 K.

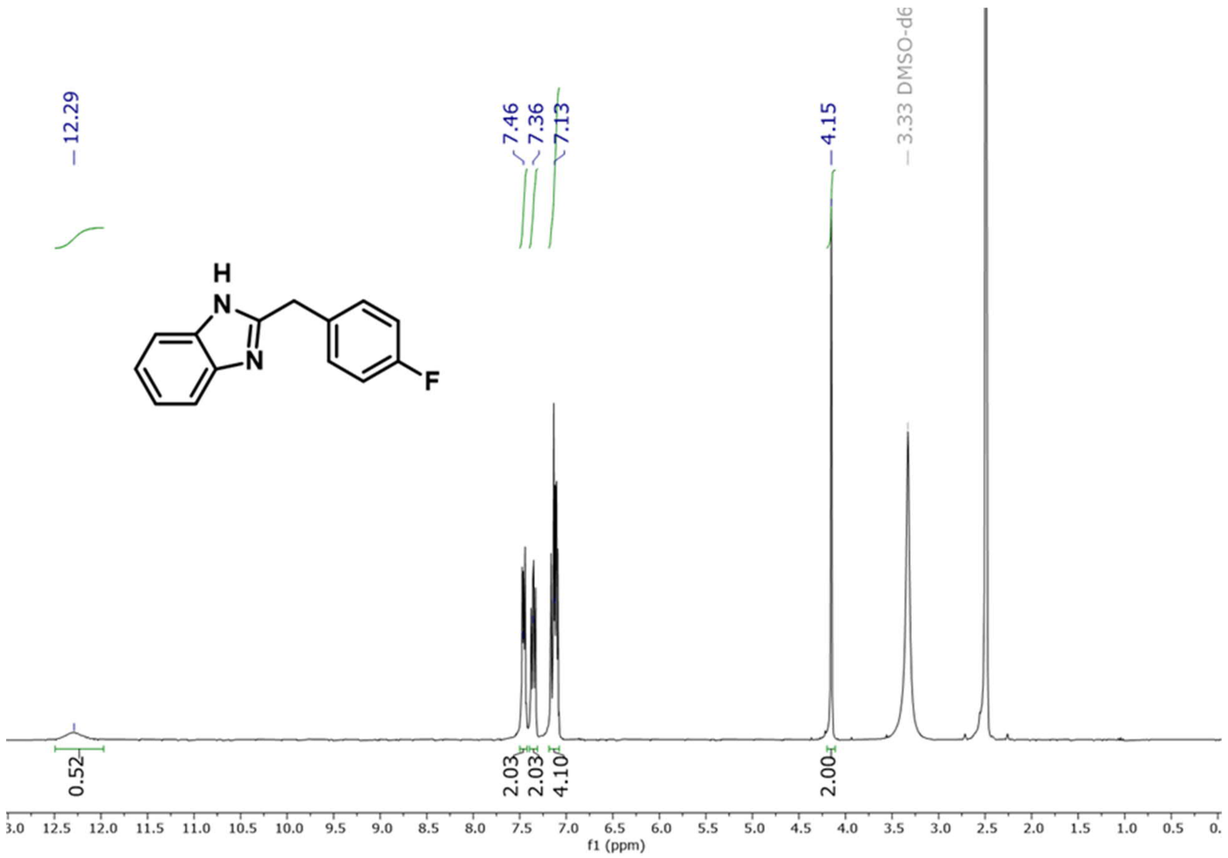
12.29
7.46
7.36
7.13
4.15
3.33 DMSO-d6
H
N
N
F
0.52
2.03
2.03
4.10
2.00
3.0
12.5
12.0
11.5
11.0
10.5
10.0
9.5
9.0
8.5
8.0
7.5
7.0
6.5
6.0
5.5
5.0
4.5
4.0
3.5
3.0
2.5
2.0
1.5
1.0
0.5
0.
f1 (ppm)

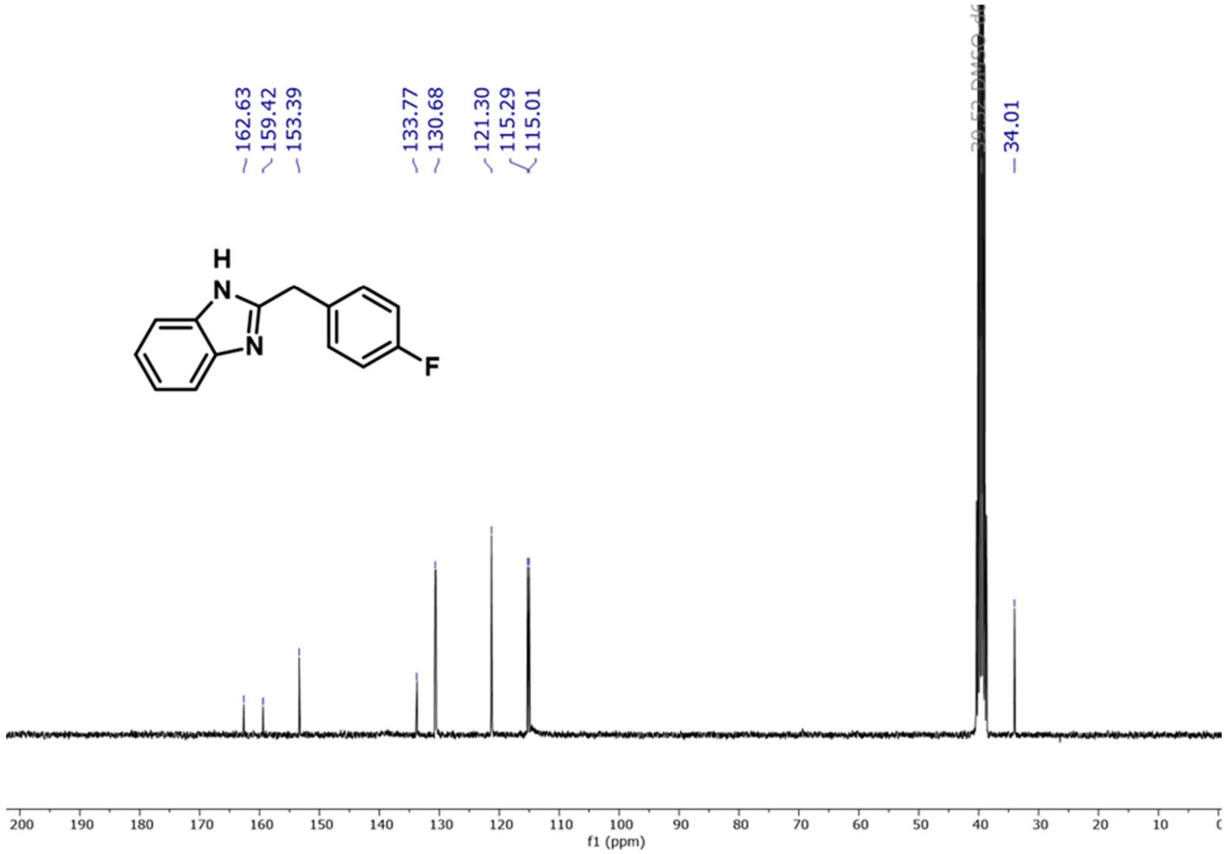
162.63
159.42
153.39
133.77
130.68
121.30
115.29
115.01
39.52 DMSO-d6
34.01
H
N
N
F
200
190
180
170
160
150
140
130
120
110
100
90
80
70
60
50
40
30
20
10
f1 (ppm)

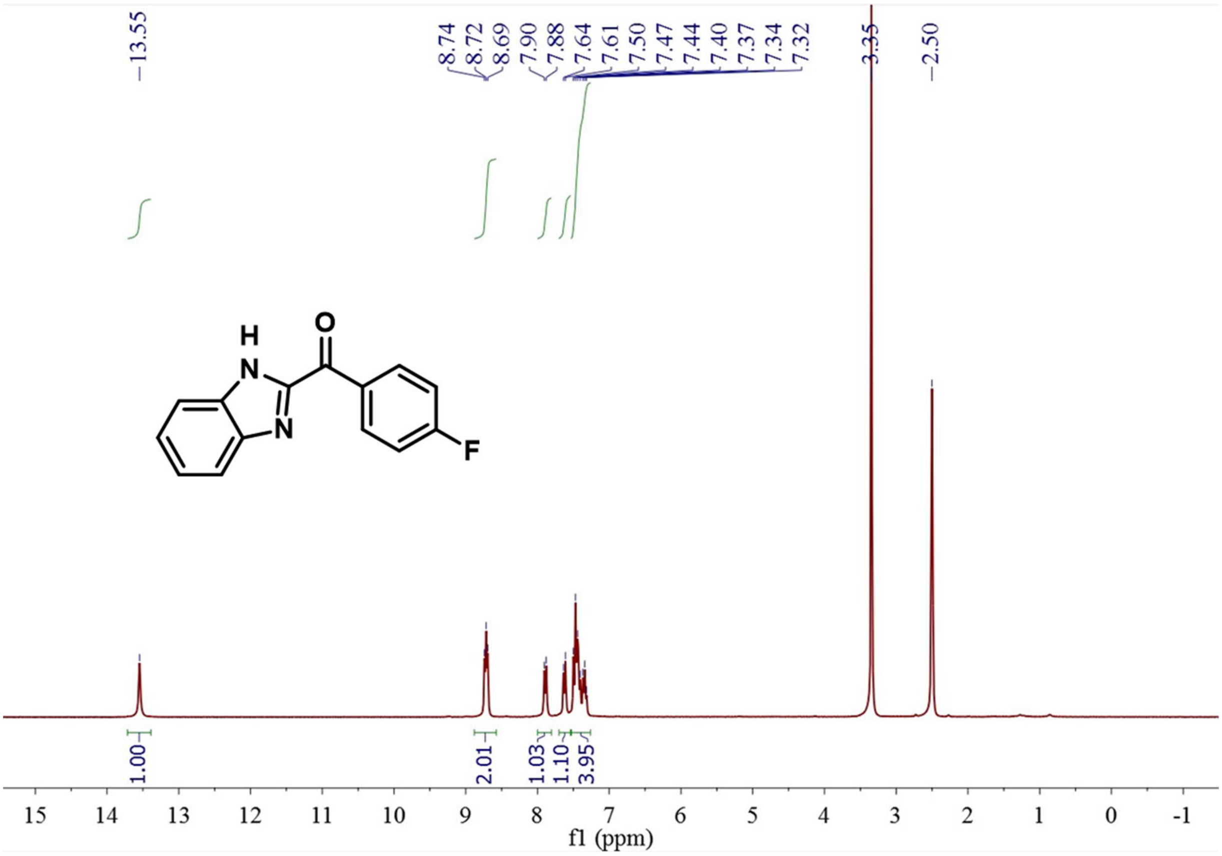
13.55
8.74
8.72
8.69
7.90
7.88
7.64
7.61
7.50
7.47
7.44
7.40
7.37
7.34
7.32
3.35
2.50
H
N
O
N
F
1.00
2.01
1.03
1.10
3.95
15
14
13
12
11
10
9
8
7
6
5
4
3
2
1
0
-1
f1 (ppm)

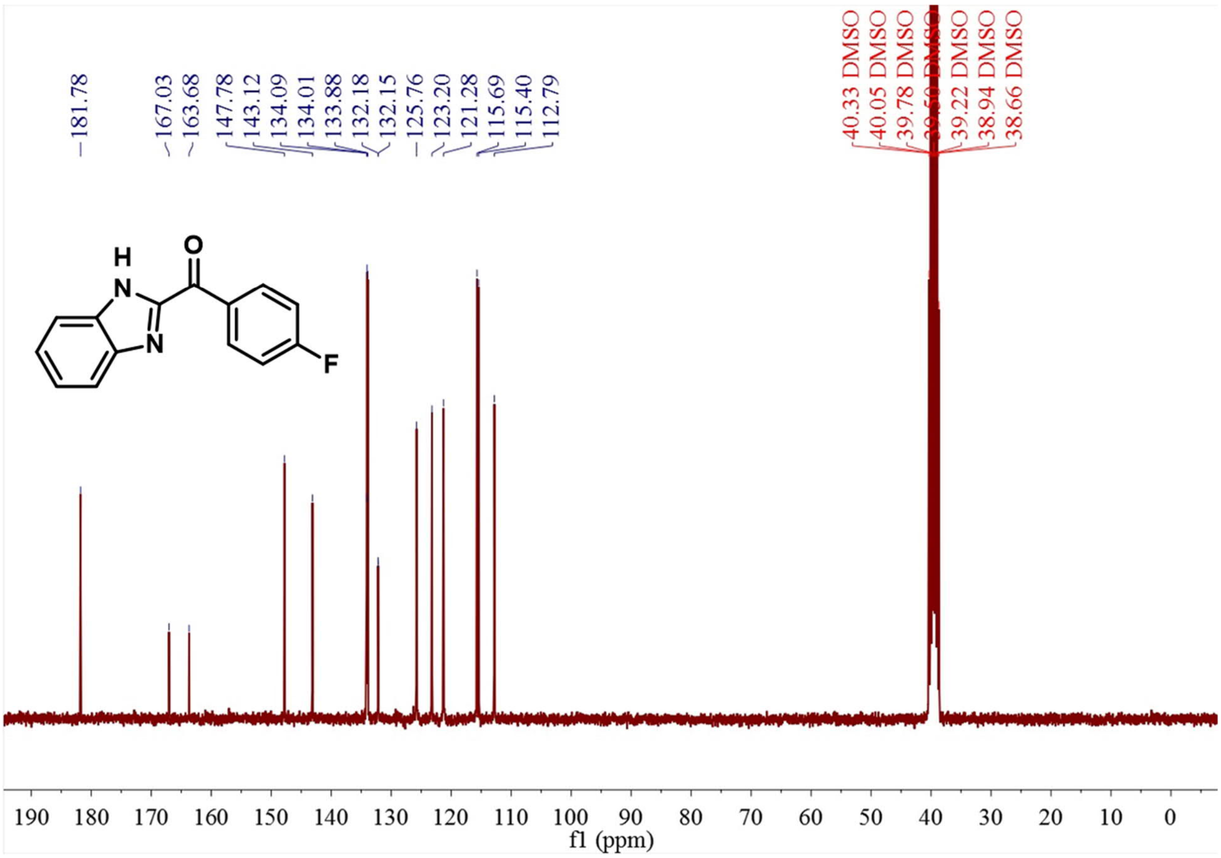
181.78
167.03
163.68
147.78
143.12
134.09
134.01
133.88
132.18
132.15
125.76
123.20
121.28
115.69
115.40
112.79
40.33 DMSO
40.05 DMSO
39.78 DMSO
39.50 DMSO
39.22 DMSO
38.94 DMSO
38.66 DMSO
H
N
O
N
F
190
180
170
160
150
140
130
120
110
100
90
80
70
60
50
40
30
20
10
0
f1 (ppm)

GCMS traces

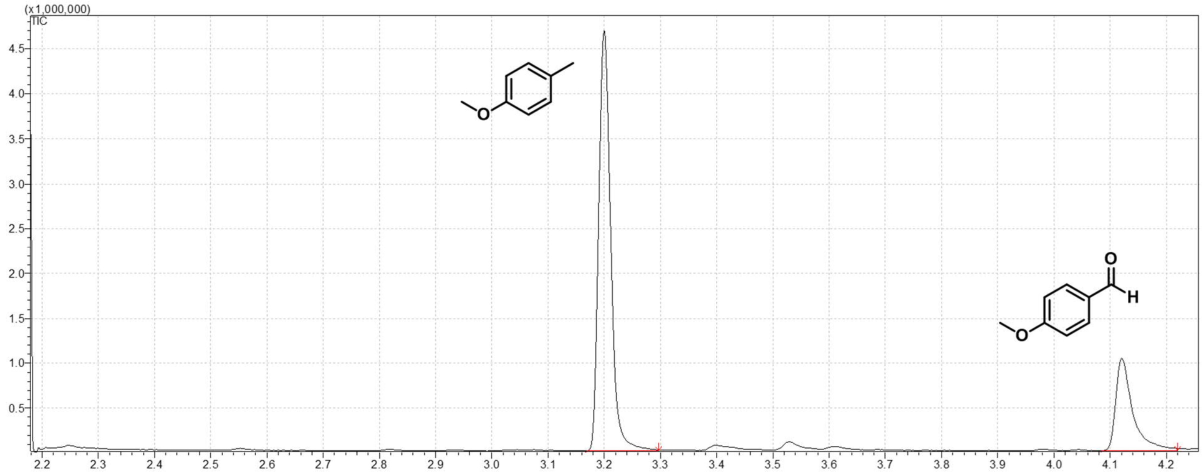
(x1,000,000)
TIC
4.5
4.0
3.5
3.0
2.5
2.0
1.5
1.0
0.5
O
O
H
O
2.2 2.3 2.4 2.5 2.6 2.7 2.8 2.9 3.0 3.1 3.2 3.3 3.4 3.5 3.6 3.7 3.8 3.9 4.0 4.1 4.2

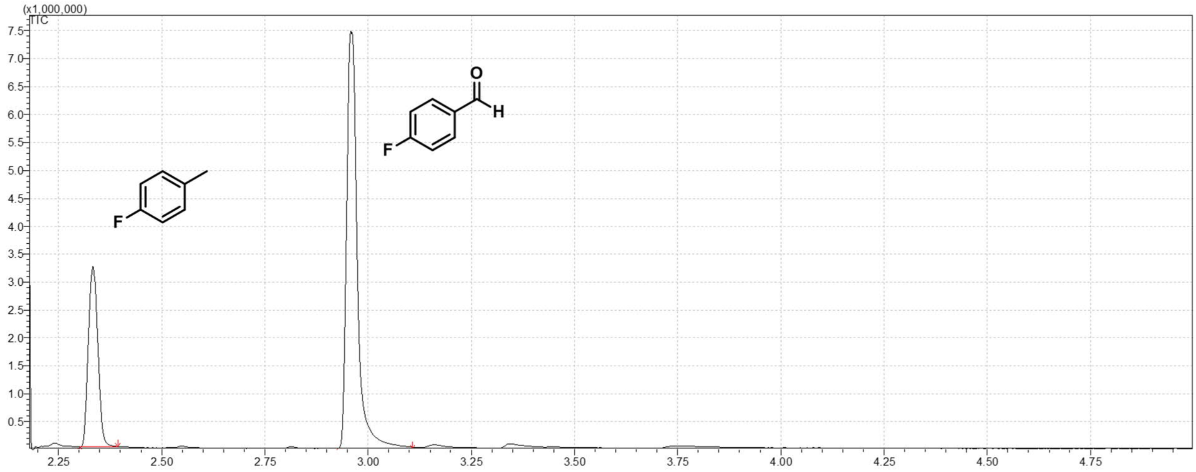
(x1,000,000)
TIC
7.5
7.0
6.5
6.0
5.5
5.0
4.5
4.0
3.5
3.0
2.5
2.0
1.5
1.0
0.5
O
H
F
F
2.25 2.50 2.75 3.00 3.25 3.50 3.75 4.00 4.25 4.50 4.75

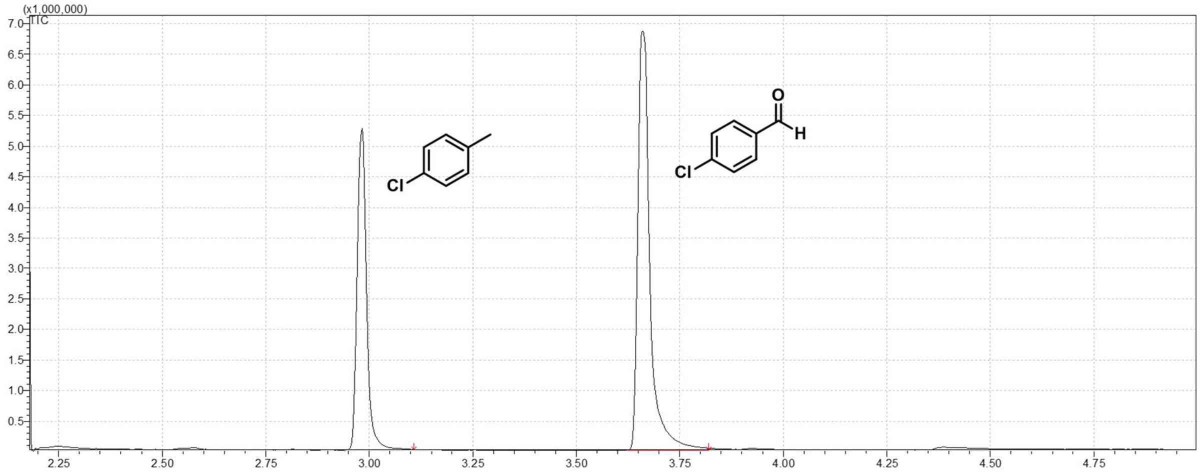
(x1,000,000)
TIC
7.0
6.5
6.0
5.5
5.0
4.5
4.0
3.5
3.0
2.5
2.0
1.5
1.0
0.5
O
H
Cl
Cl
2.25 2.50 2.75 3.00 3.25 3.50 3.75 4.00 4.25 4.50 4.75

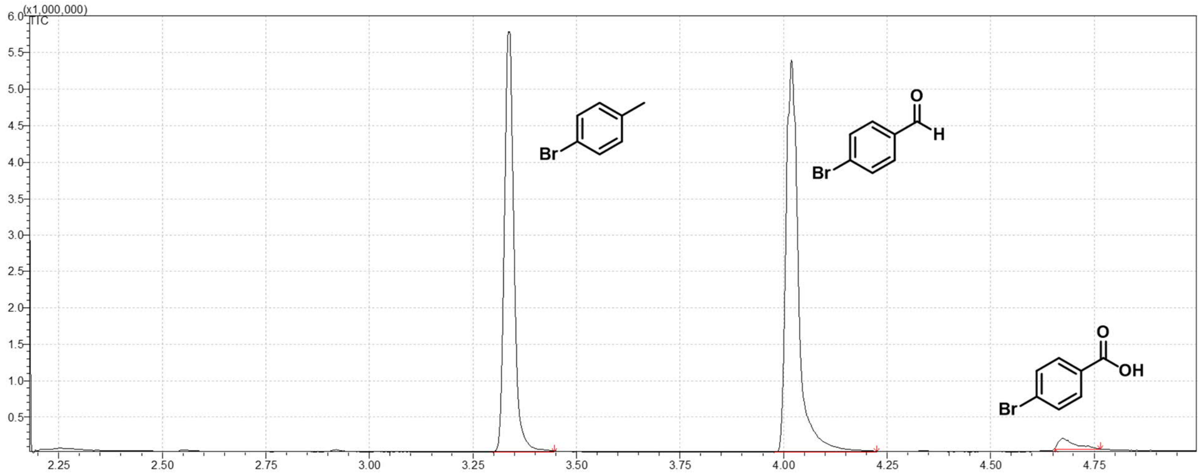
(x1,000,000)
TIC
6.0
5.5
5.0
4.5
4.0
3.5
3.0
2.5
2.0
1.5
1.0
0.5
2.25
2.50
2.75
3.00
3.25
3.50
3.75
4.00
4.25
4.50
4.75
Br
O
H
Br
O
OH
Br

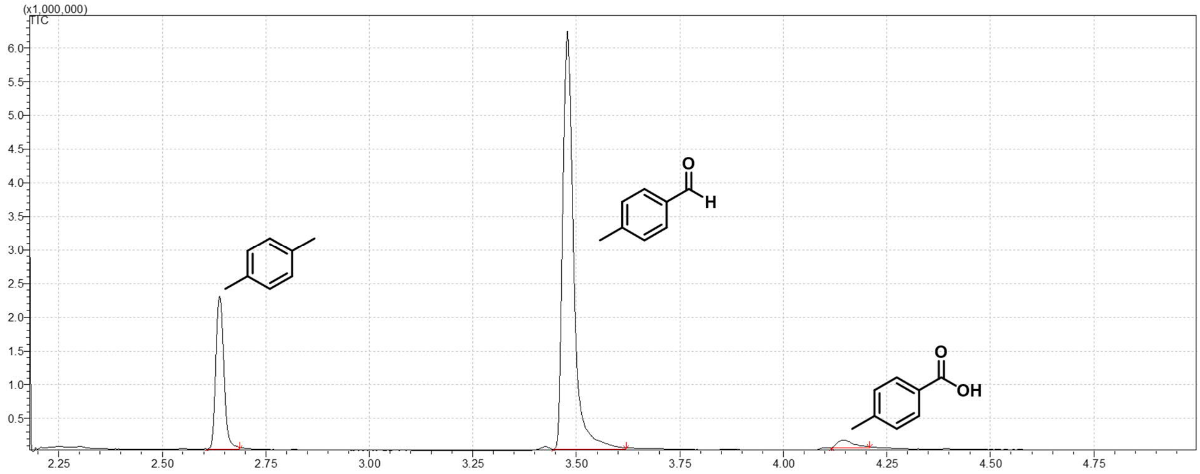
(x1,000,000)
TIC
6.0
5.5
5.0
4.5
4.0
3.5
3.0
2.5
2.0
1.5
1.0
0.5
2.25
2.50
2.75
3.00
3.25
3.50
3.75
4.00
4.25
4.50
4.75
O
H
O
OH

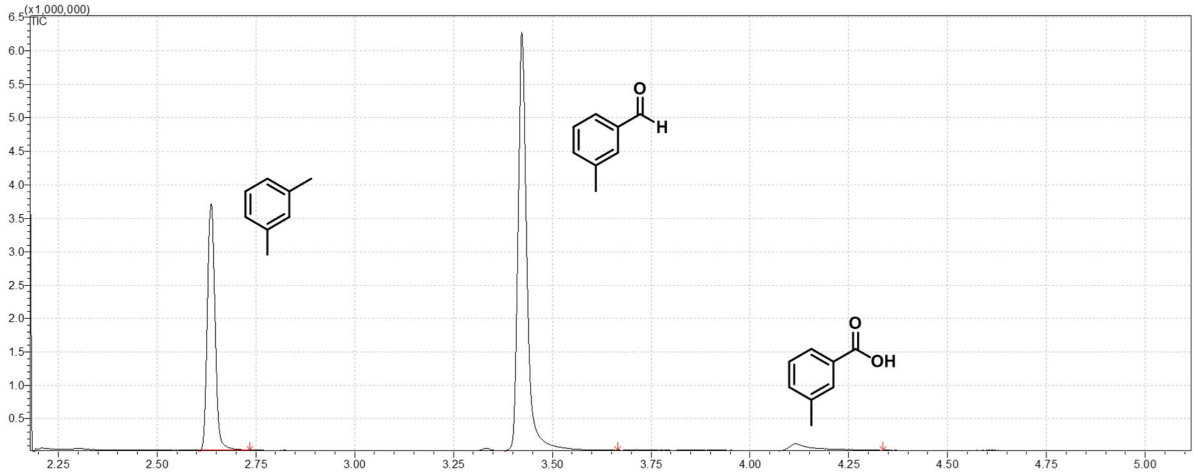
(x1,000,000)
TIC
6.5
6.0
5.5
5.0
4.5
4.0
3.5
3.0
2.5
2.0
1.5
1.0
0.5
2.25
2.50
2.75
3.00
3.25
3.50
3.75
4.00
4.25
4.50
4.75
5.00
O
H
O
OH

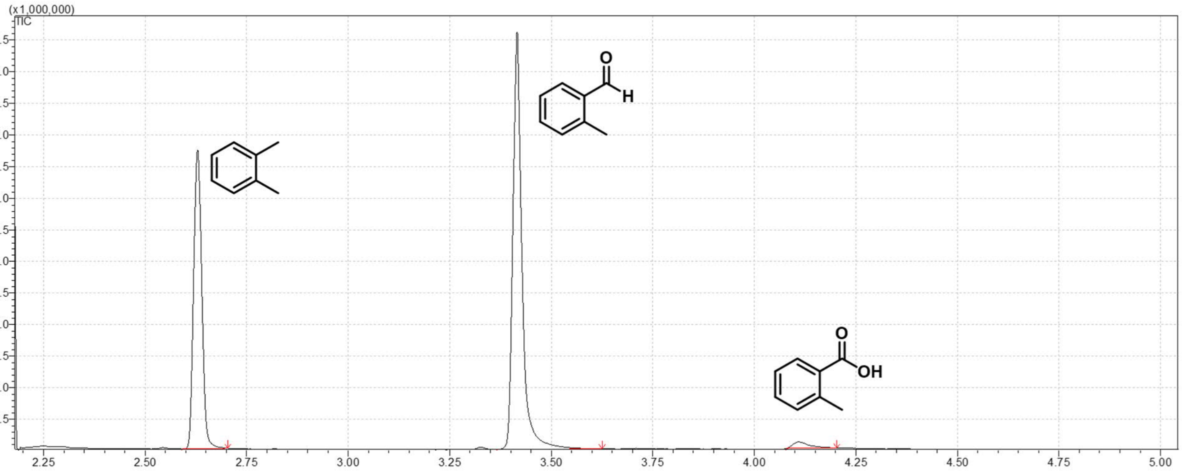
(x1,000,000)
TIC
6.5
6.0
5.5
5.0
4.5
4.0
3.5
3.0
2.5
2.0
1.5
1.0
0.5
2.25
2.50
2.75
3.00
3.25
3.50
3.75
4.00
4.25
4.50
4.75
5.00
O
H
O
OH

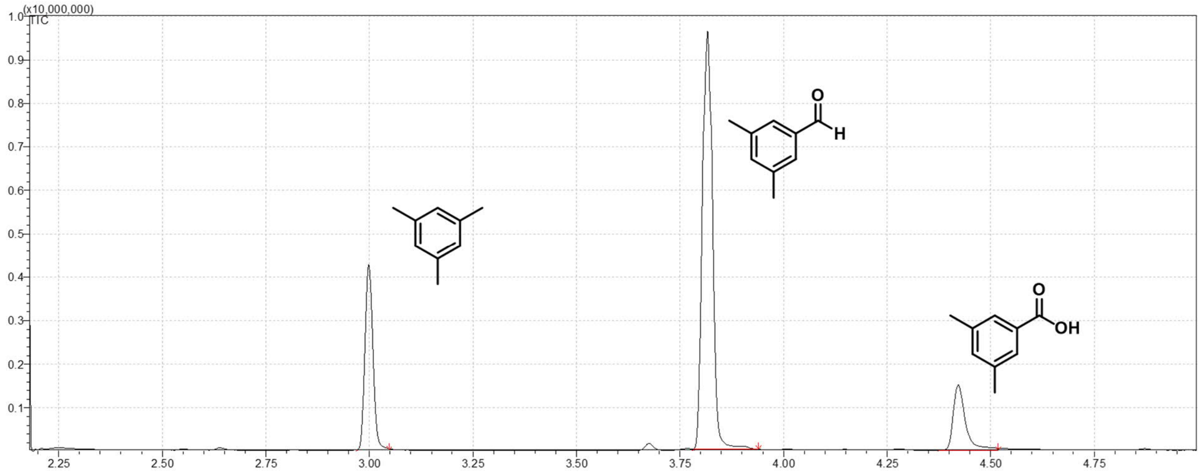
(x10,000,000)
TIC
1.0
0.9
0.8
0.7
0.6
0.5
0.4
0.3
0.2
0.1
2.25
2.50
2.75
3.00
3.25
3.50
3.75
4.00
4.25
4.50
4.75
O
H
O
OH

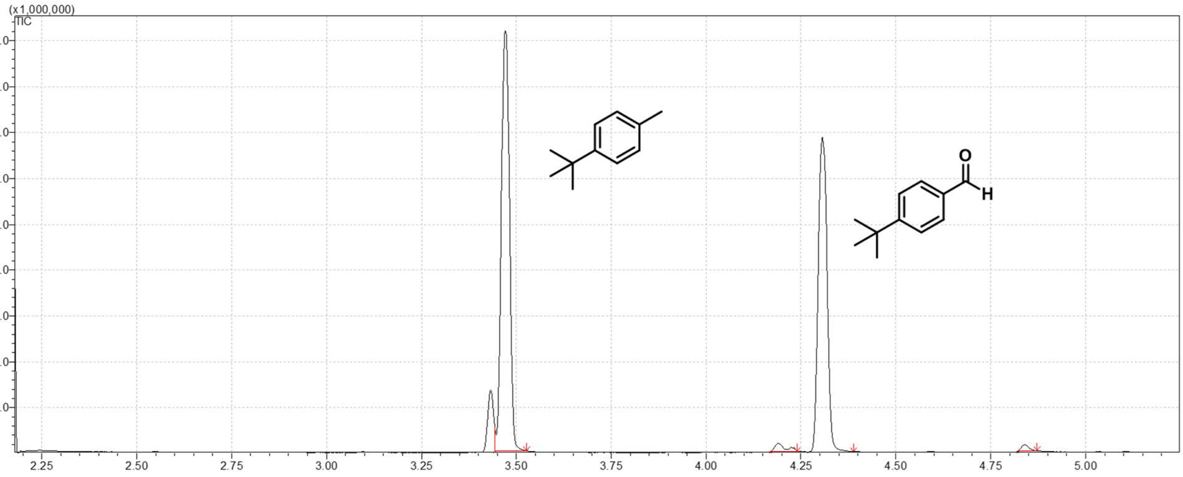
(x1,000,000)
TIC
9.0
8.0
7.0
6.0
5.0
4.0
3.0
2.0
1.0
2.25
2.50
2.75
3.00
3.25
3.50
3.75
4.00
4.25
4.50
4.75
5.00
O
H

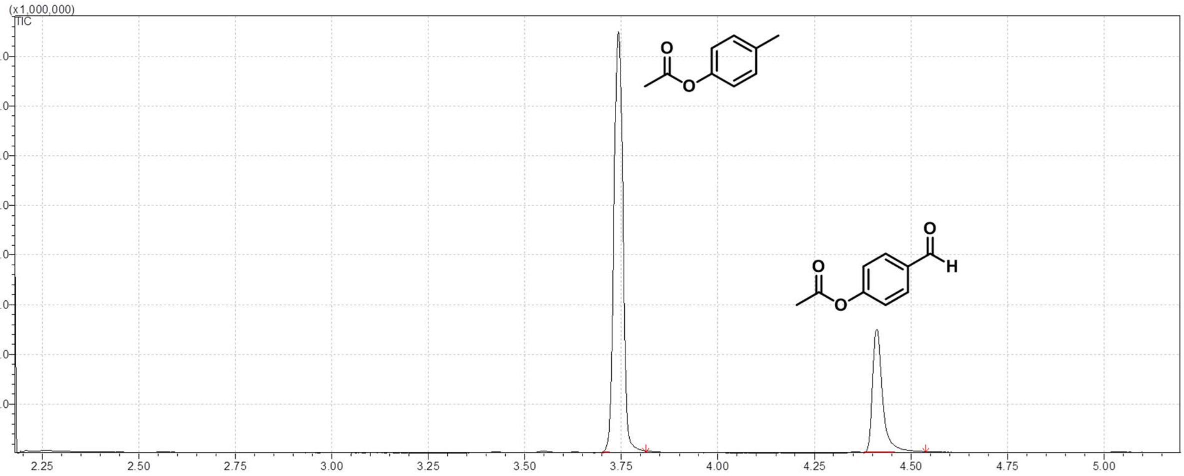
(x1,000,000)
TIC
8.0
7.0
6.0
5.0
4.0
3.0
2.0
1.0
2.25
2.50
2.75
3.00
3.25
3.50
3.75
4.00
4.25
4.50
4.75
5.00
O
O
O
O
H

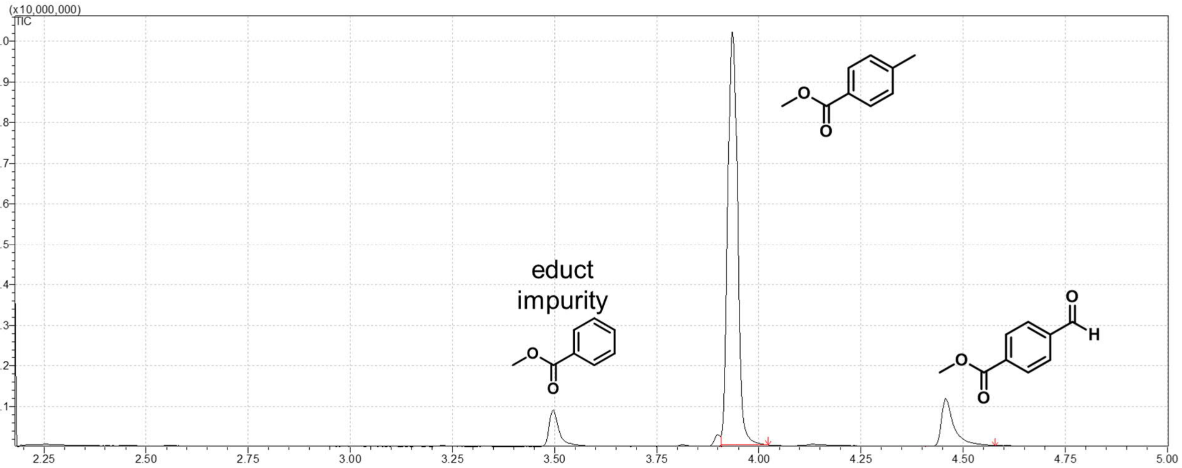
(x10,000,000)
TIC
1.0
0.9
0.8
0.7
0.6
0.5
0.4
0.3
0.2
0.1
2.25
2.50
2.75
3.00
3.25
3.50
3.75
4.00
4.25
4.50
4.75
5.00
educt
impurity
O
O
O
O
O
O
O
H

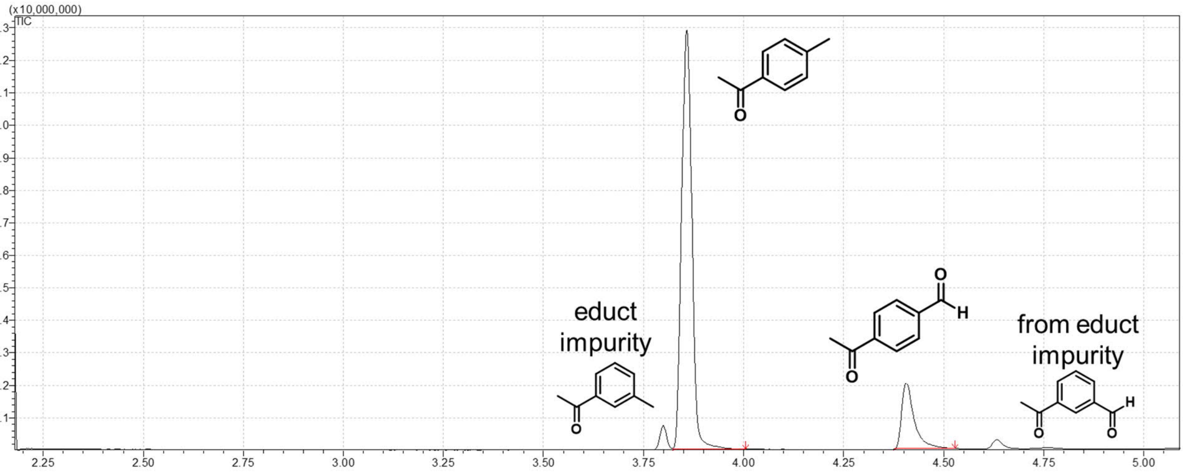
(x10,000,000)
TIC
1.3
1.2
1.1
1.0
0.9
0.8
0.7
0.6
0.5
0.4
0.3
0.2
0.1
2.25
2.50
2.75
3.00
3.25
3.50
3.75
4.00
4.25
4.50
4.75
5.00
educt
impurity
O
O
O
H
O
from educt
impurity
H
O
O

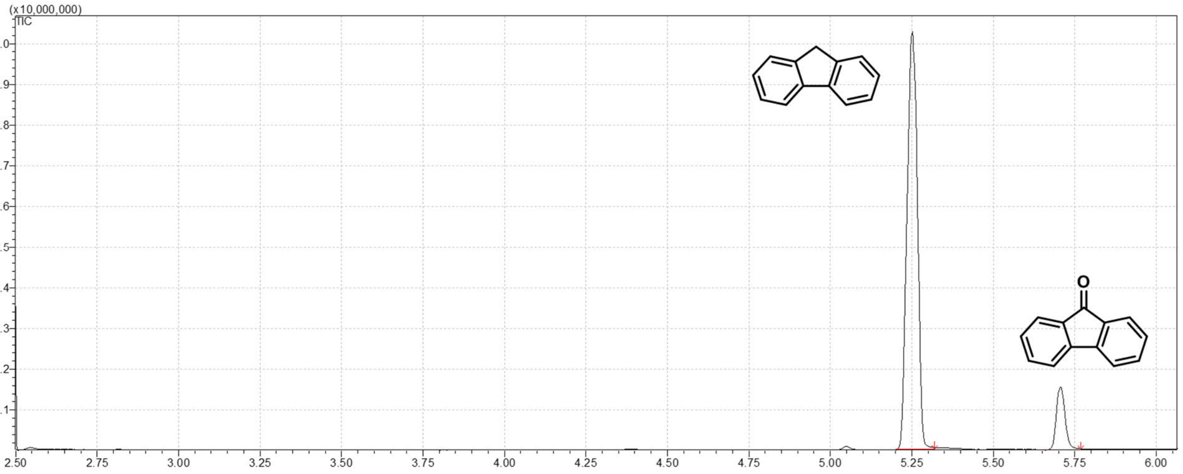
(x10,000,000)
TIC
1.0
0.9
0.8
0.7
0.6
0.5
0.4
0.3
0.2
0.1
2.50
2.75
3.00
3.25
3.50
3.75
4.00
4.25
4.50
4.75
5.00
5.25
5.50
5.75
6.00
O

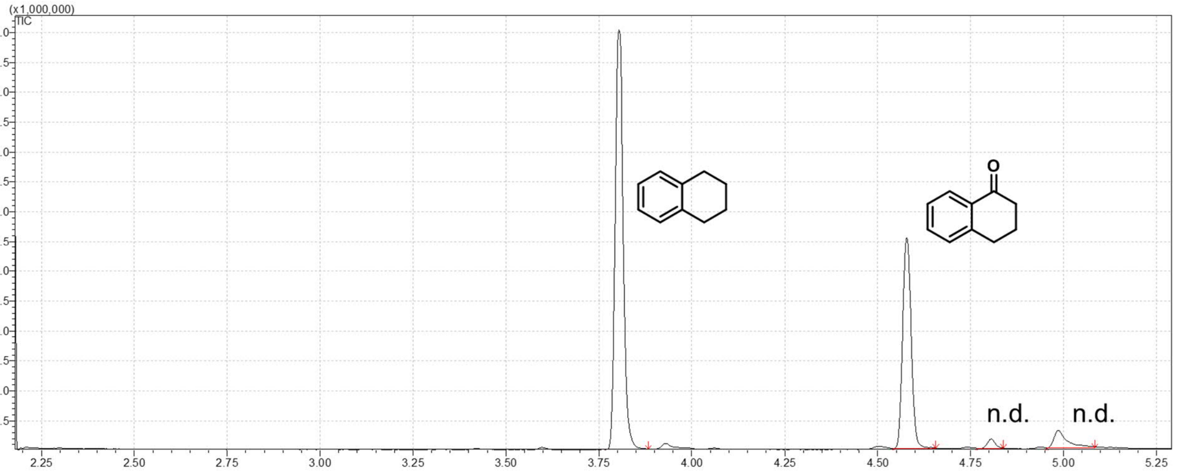
(x1,000,000)
TIC
7.0
6.5
6.0
5.5
5.0
4.5
4.0
3.5
3.0
2.5
2.0
1.5
1.0
0.5
2.25
2.50
2.75
3.00
3.25
3.50
3.75
4.00
4.25
4.50
4.75
5.00
5.25
O
n.d.
n.d.

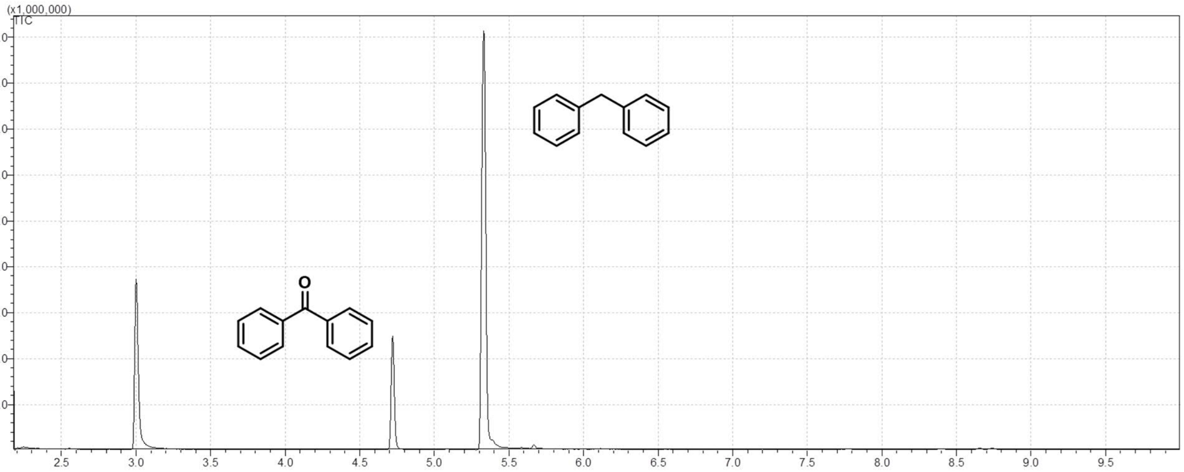
(x1,000,000)
TIC
9.0
8.0
7.0
6.0
5.0
4.0
3.0
2.0
1.0
2.5
3.0
3.5
4.0
4.5
5.0
5.5
6.0
6.5
7.0
7.5
8.0
8.5
9.0
9.5
O

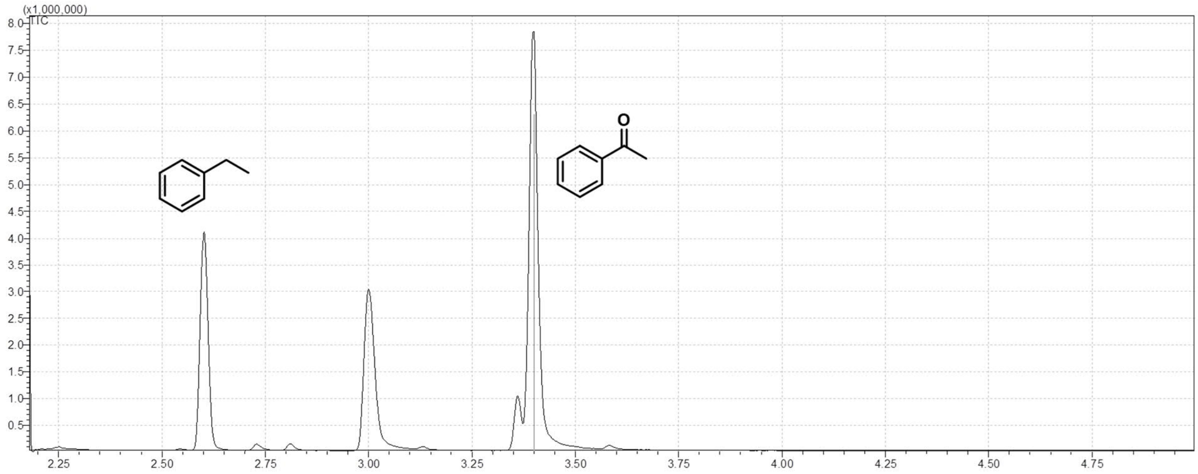
(x1,000,000)
TIC
8.0
7.5
7.0
6.5
6.0
5.5
5.0
4.5
4.0
3.5
3.0
2.5
2.0
1.5
1.0
0.5
O
2.25
2.50
2.75
3.00
3.25
3.50
3.75
4.00
4.25
4.50
4.75

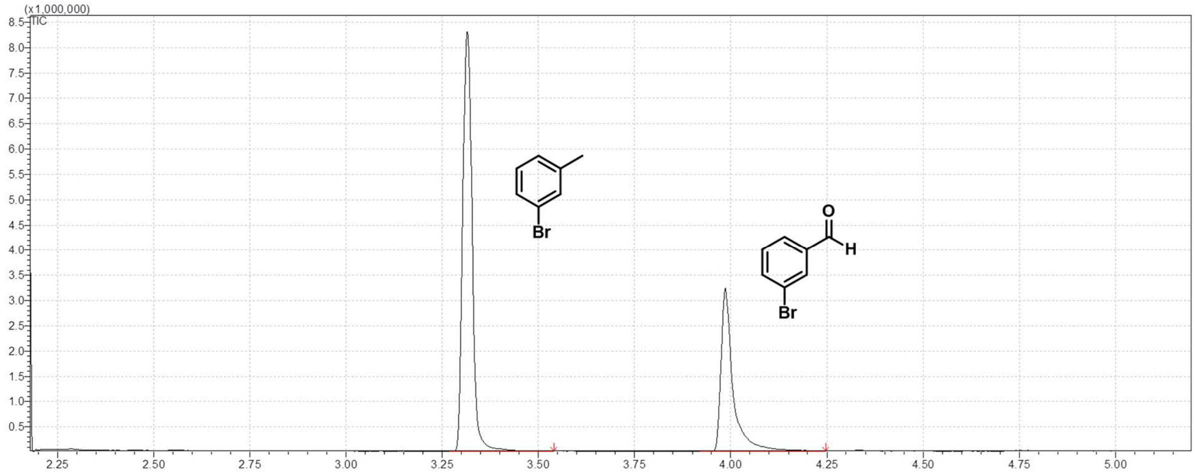
(x1,000,000)
TIC
8.5
8.0
7.5
7.0
6.5
6.0
5.5
5.0
4.5
4.0
3.5
3.0
2.5
2.0
1.5
1.0
0.5
Br
O
H
Br
2.25
2.50
2.75
3.00
3.25
3.50
3.75
4.00
4.25
4.50
4.75
5.00

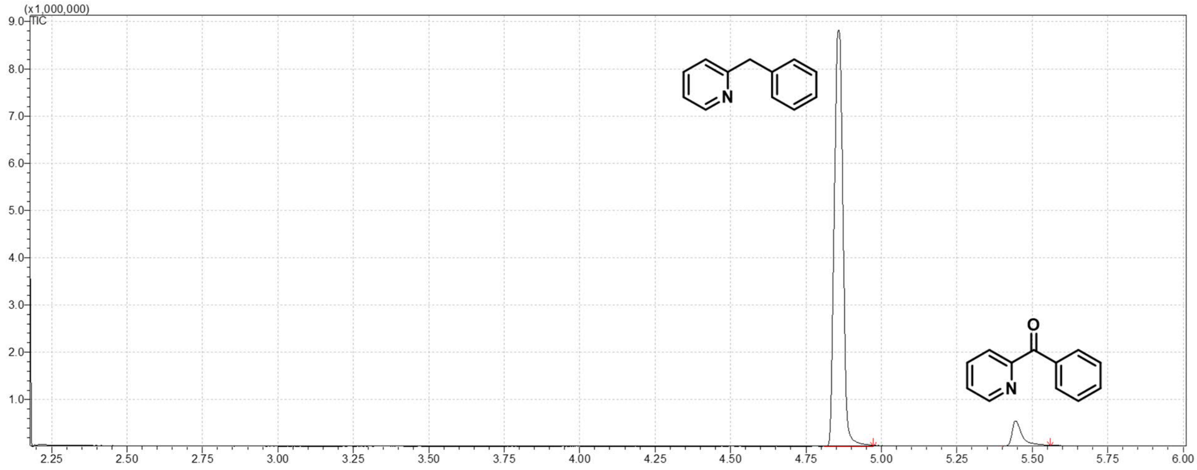
(x1,000,000)
TIC
9.0
8.0
7.0
6.0
5.0
4.0
3.0
2.0
1.0
N
O
N
2.25
2.50
2.75
3.00
3.25
3.50
3.75
4.00
4.25
4.50
4.75
5.00
5.25
5.50
5.75
6.00

3.2 Covalent triazine framework nanoparticles via size-controllable confinement synthesis for enhanced visible-light photoredox catalysis

^{1}H and ^{13}C NMR spectra

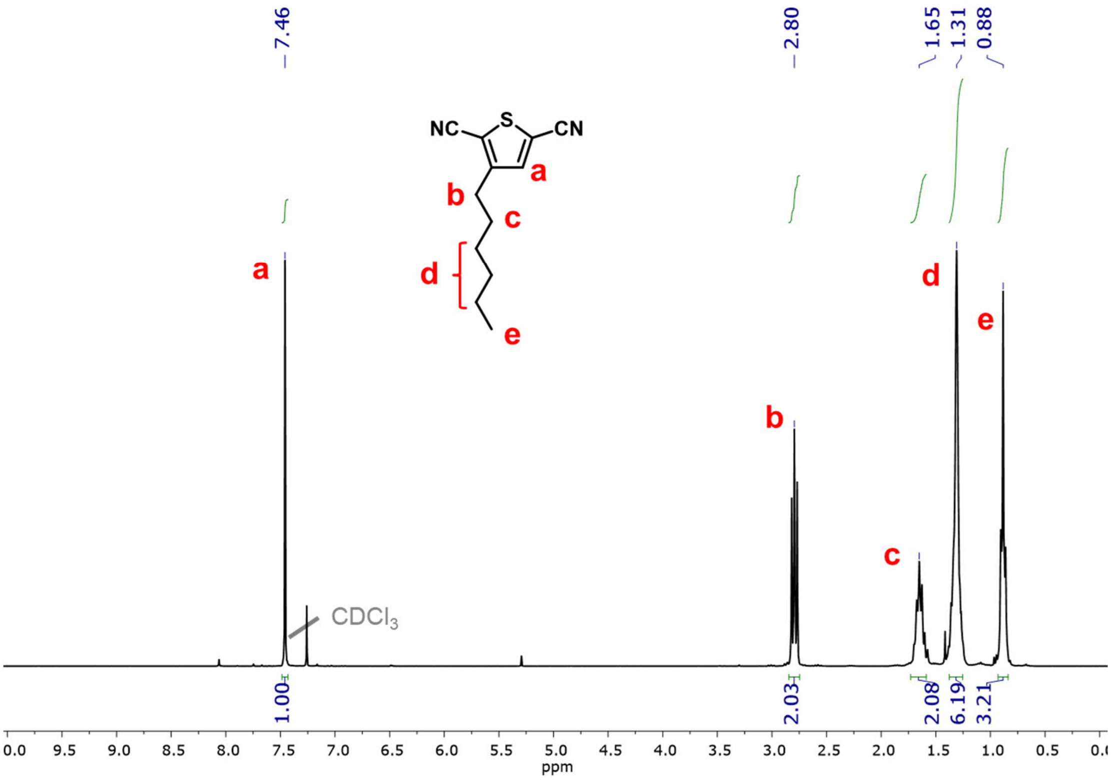

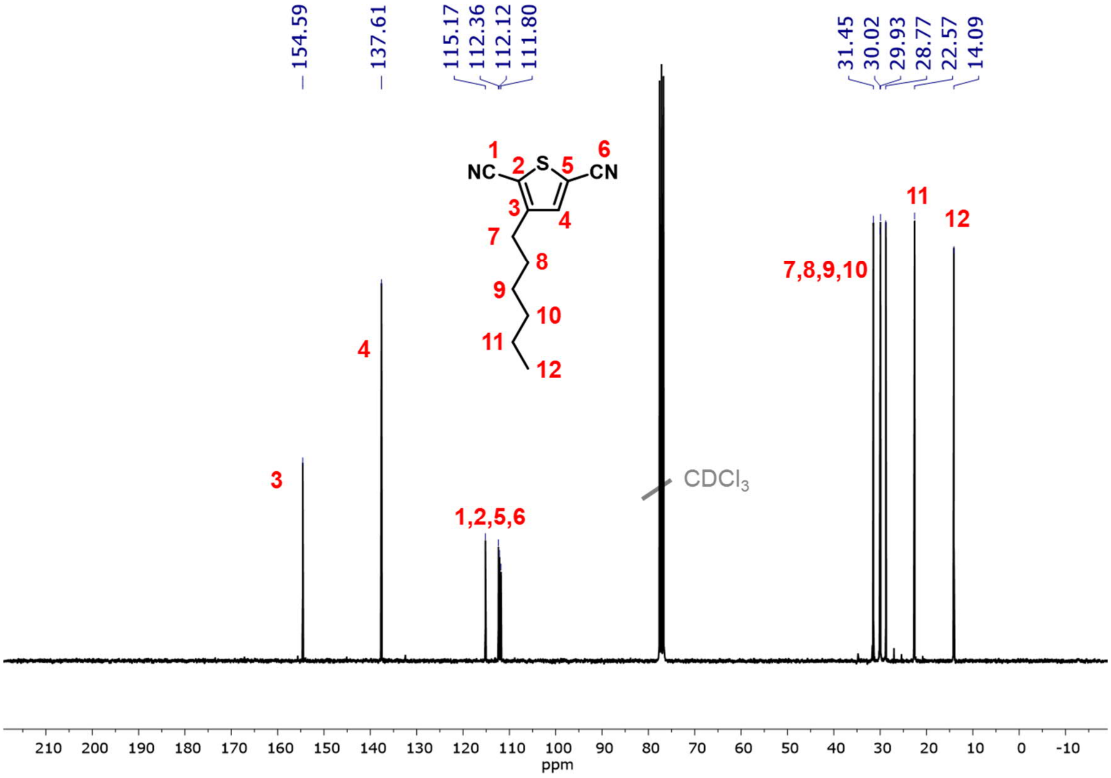

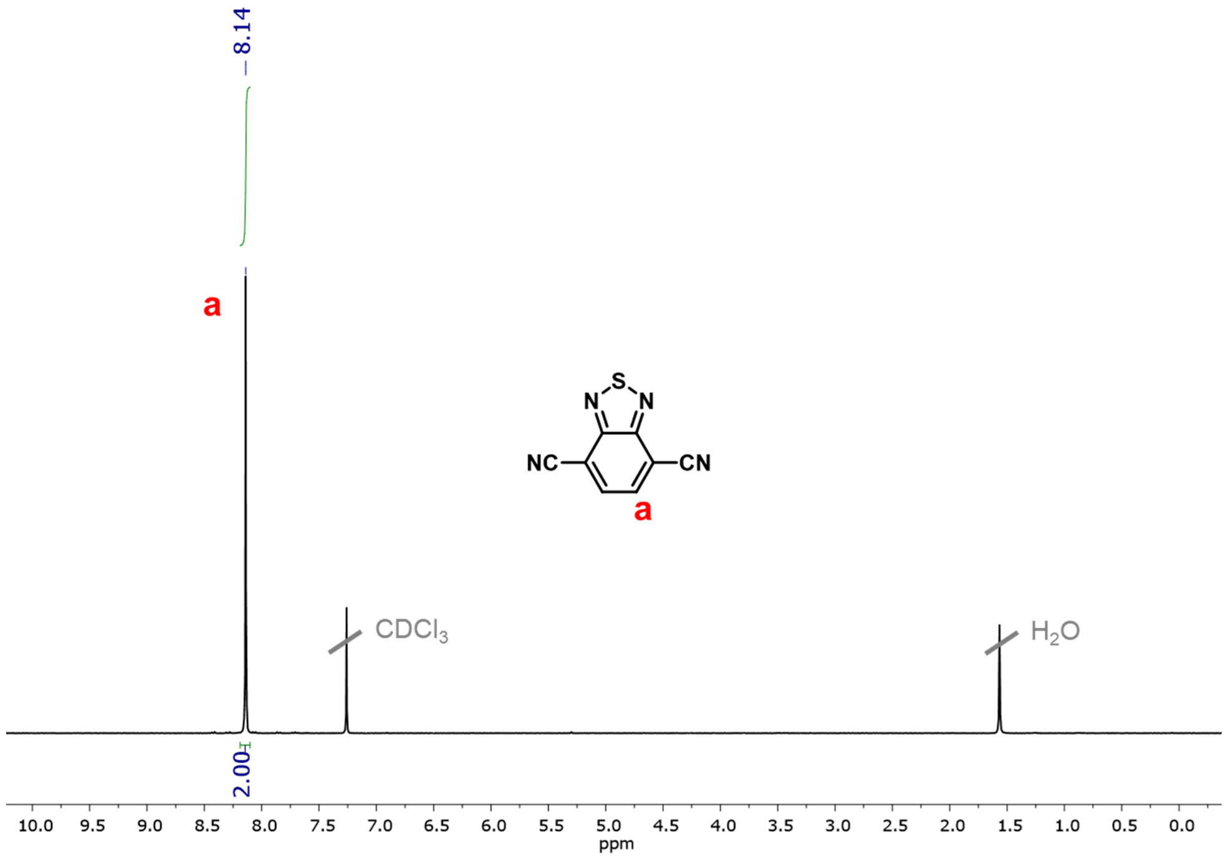
8.14
a
S
N
N
NC
CN
a
CDCl$_3$
H$_2$O
2.00
10.0 9.5 9.0 8.5 8.0 7.5 7.0 6.5 6.0 5.5 5.0 4.5 4.0 3.5 3.0 2.5 2.0 1.5 1.0 0.5 0.0
ppm

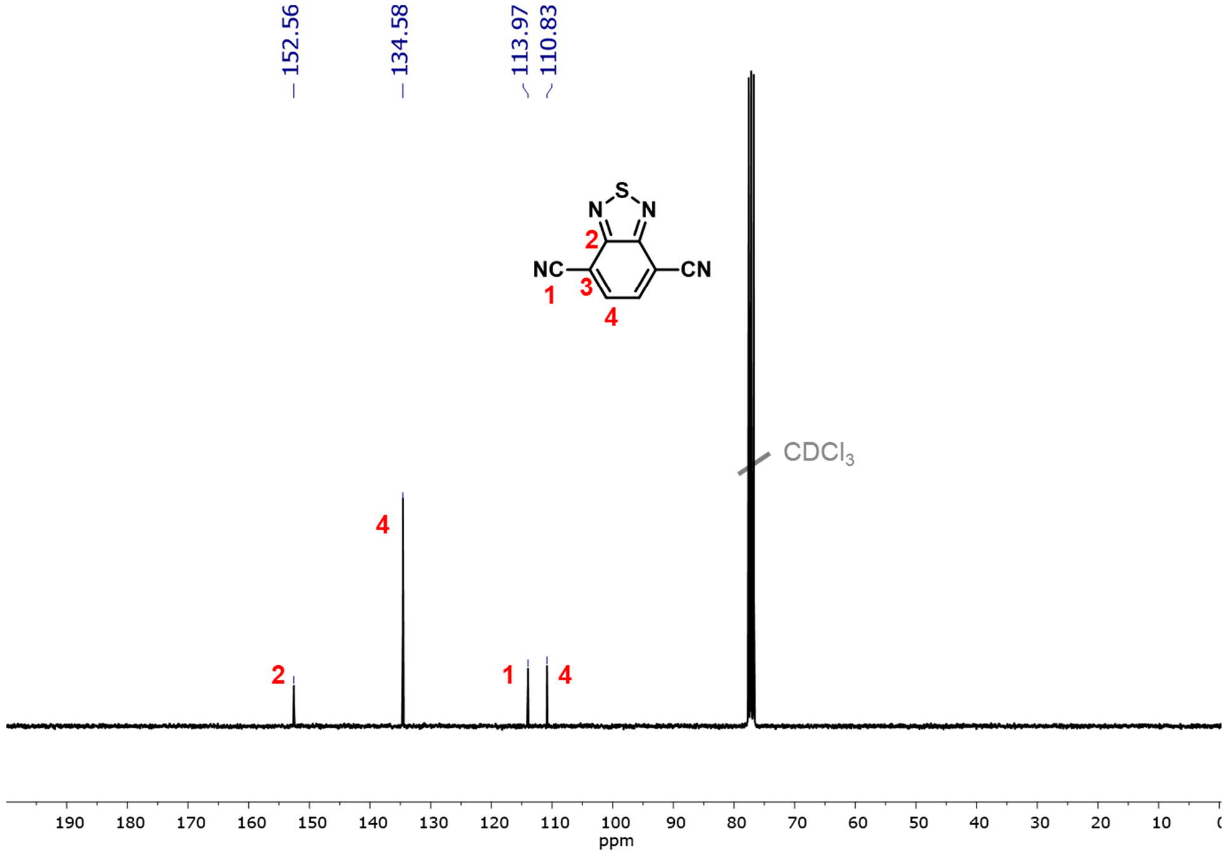
152.56
134.58
113.97
110.83
S
N
N
2
NC
CN
1
3
4
CDCl$_3$
4
2
1
4
190 180 170 160 150 140 130 120 110 100 90 80 70 60 50 40 30 20 10 0
ppm

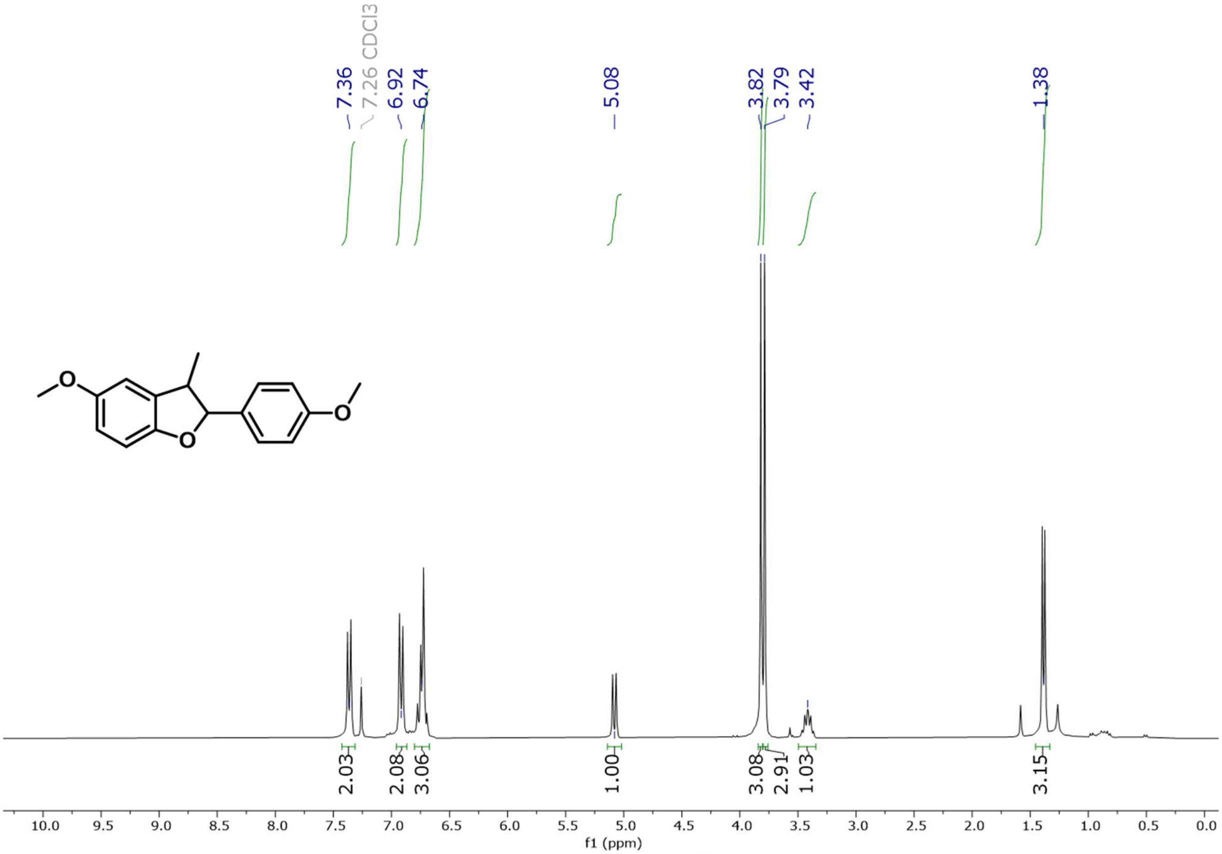
7.36
7.26 CDCl3
6.92
6.74
5.08
3.82
3.79
3.42
1.38
2.03
2.08
3.06
1.00
3.08
2.91
1.03
3.15
10.0
9.5
9.0
8.5
8.0
7.5
7.0
6.5
6.0
5.5
5.0
4.5
4.0
3.5
3.0
2.5
2.0
1.5
1.0
0.5
0.0
f1 (ppm)
O
O
O

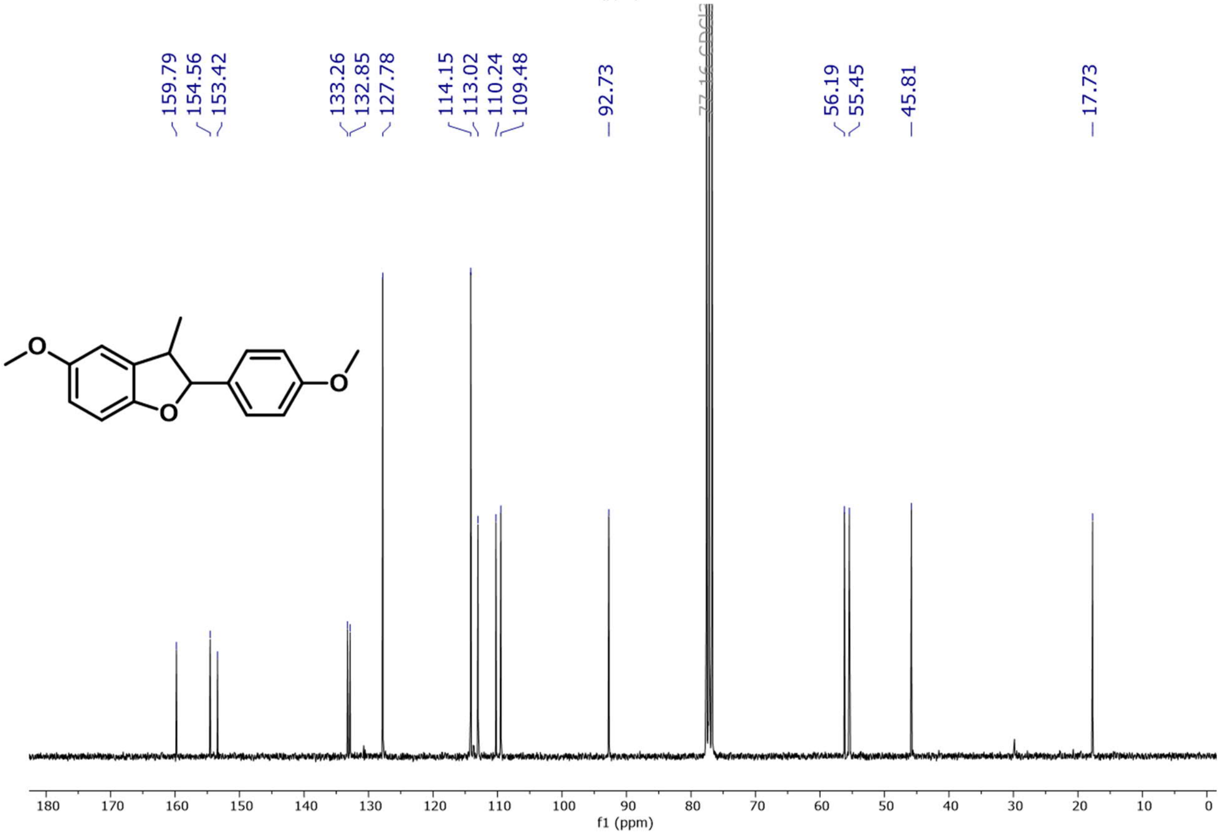
159.79
154.56
153.42
133.26
132.85
127.78
114.15
113.02
110.24
109.48
92.73
77.16 CDCl3
56.19
55.45
45.81
17.73
180
170
160
150
140
130
120
110
100
90
80
70
60
50
40
30
20
10
0
f1 (ppm)
O
O
O

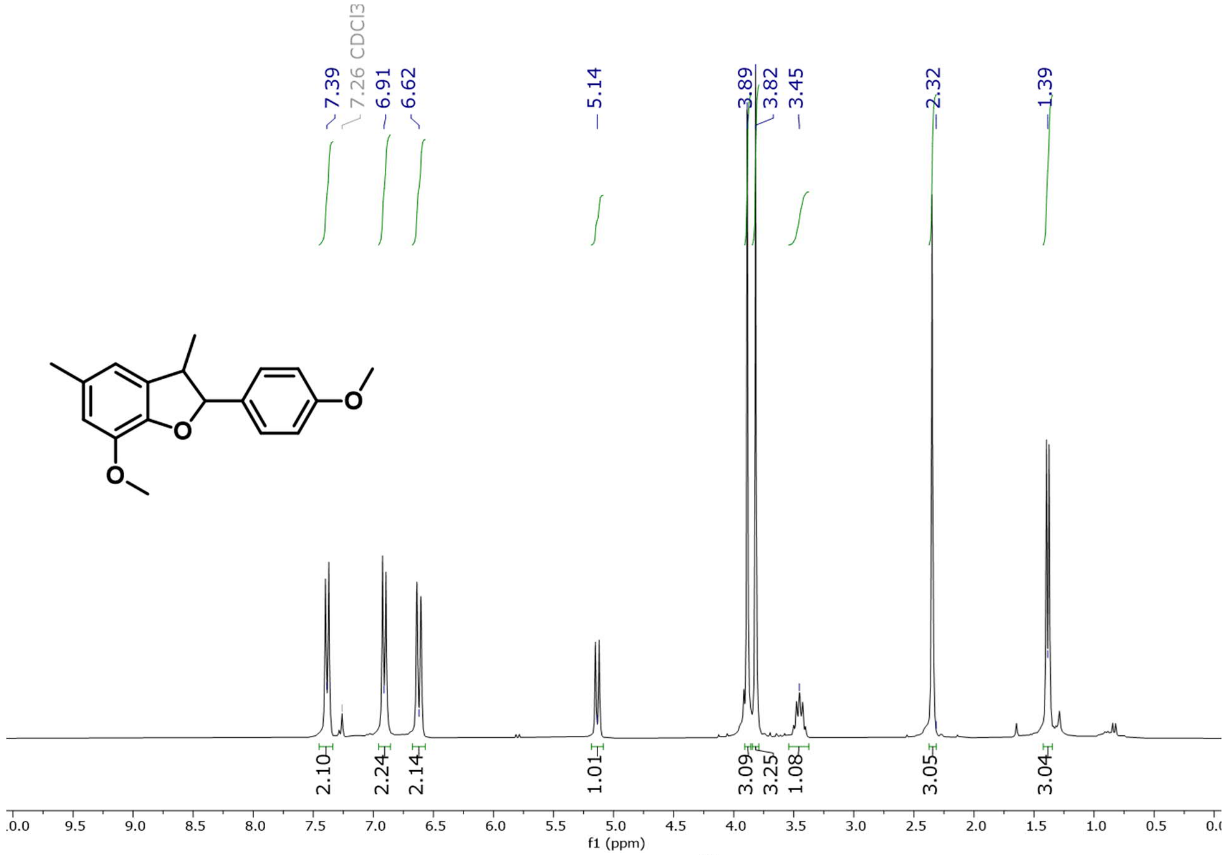
7.39
7.26 CDCl3
6.91
6.62
5.14
3.89
3.82
3.45
2.32
1.39
2.10
2.24
2.14
1.01
3.09
3.25
1.08
3.05
3.04
.0.0
9.5
9.0
8.5
8.0
7.5
7.0
6.5
6.0
5.5
5.0
4.5
4.0
3.5
3.0
2.5
2.0
1.5
1.0
0.5
0.(
f1 (ppm)
O
O
O

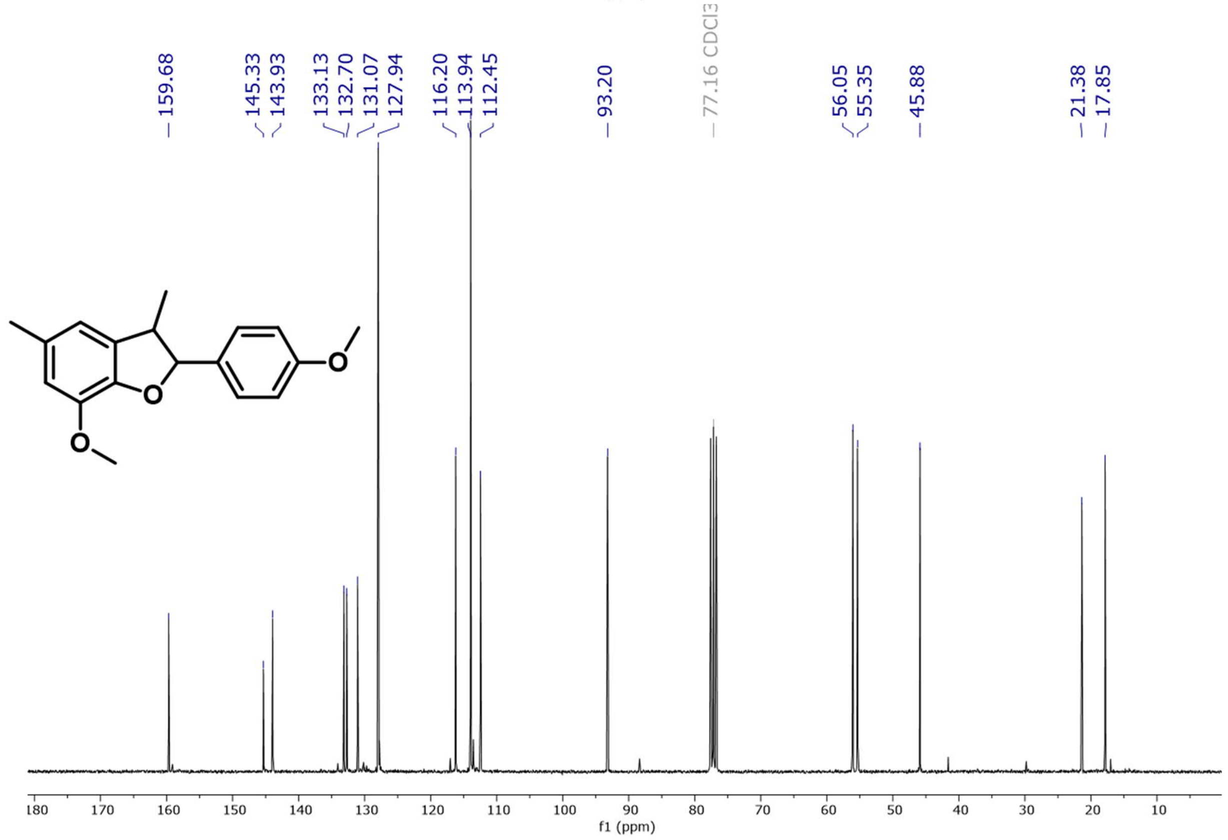
159.68
145.33
143.93
133.13
132.70
131.07
127.94
116.20
113.94
112.45
93.20
77.16 CDCl3
56.05
55.35
45.88
21.38
17.85
180
170
160
150
140
130
120
110
100
90
80
70
60
50
40
30
20
10
f1 (ppm)
O
O
O

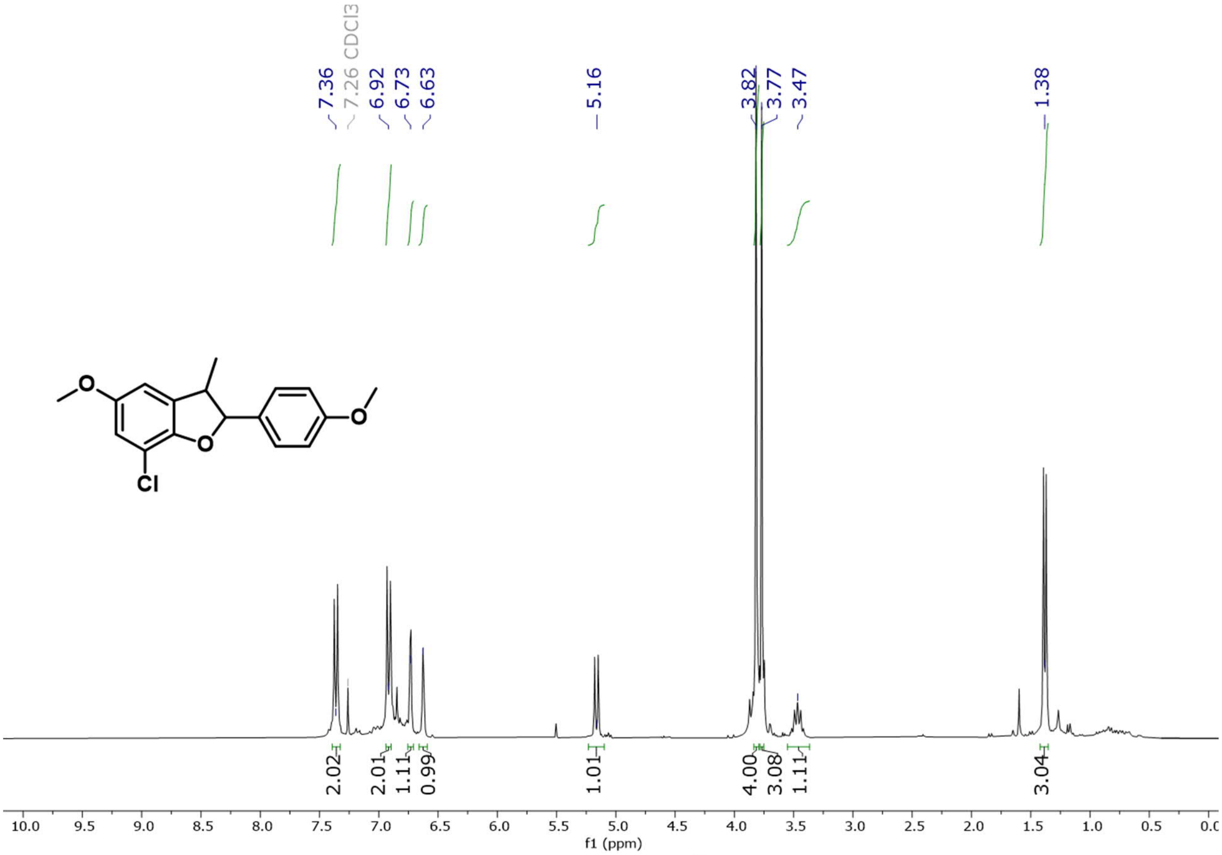

7.36
7.26 CDCl3
6.92
6.73
6.63
5.16
3.82
3.77
3.47
1.38
2.02
2.01
1.11
0.99
1.01
4.00
3.08
1.11
3.04
O
O
O
Cl
10.0
9.5
9.0
8.5
8.0
7.5
7.0
6.5
6.0
5.5
5.0
4.5
4.0
3.5
3.0
2.5
2.0
1.5
1.0
0.5
0.0
f1 (ppm)

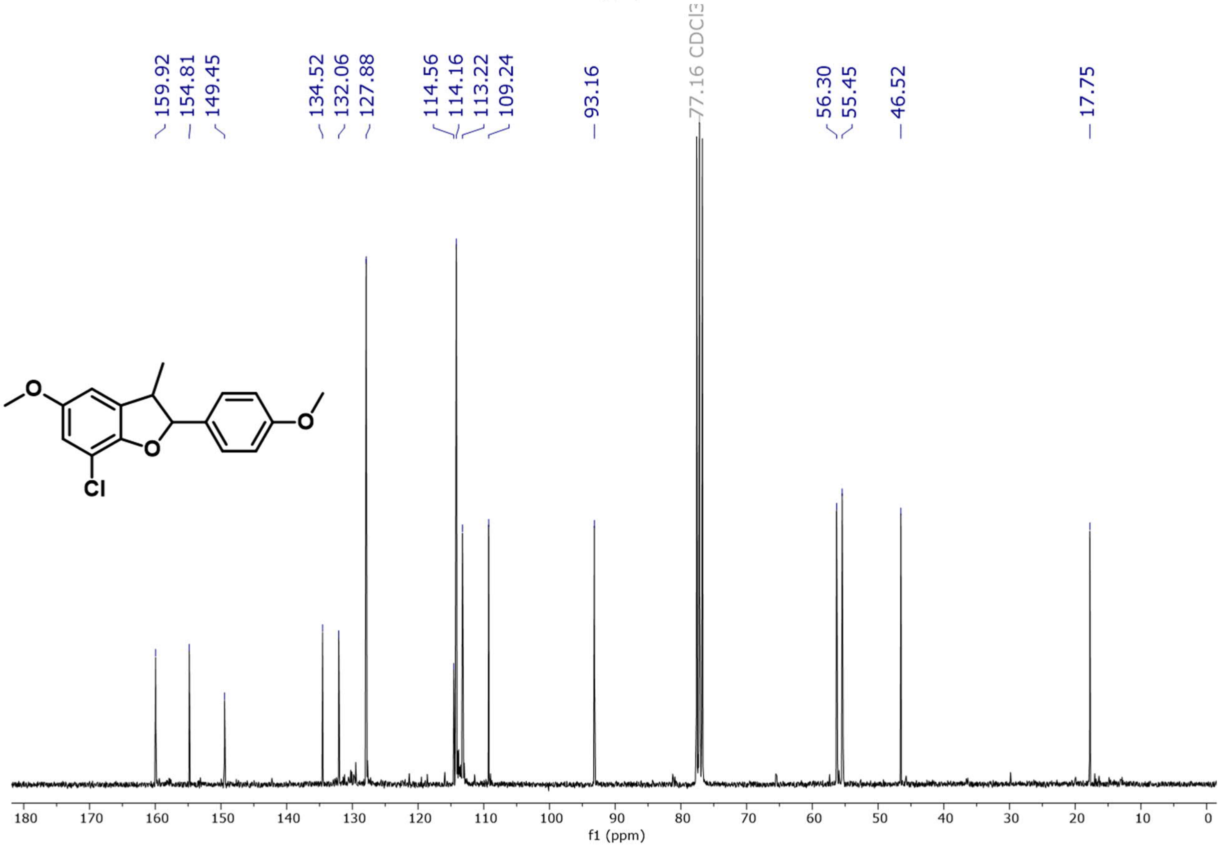

159.92
154.81
149.45
134.52
132.06
127.88
114.56
114.16
113.22
109.24
93.16
77.16 CDCl3
56.30
55.45
46.52
17.75
O
O
O
Cl
180
170
160
150
140
130
120
110
100
90
80
70
60
50
40
30
20
10
0
f1 (ppm)

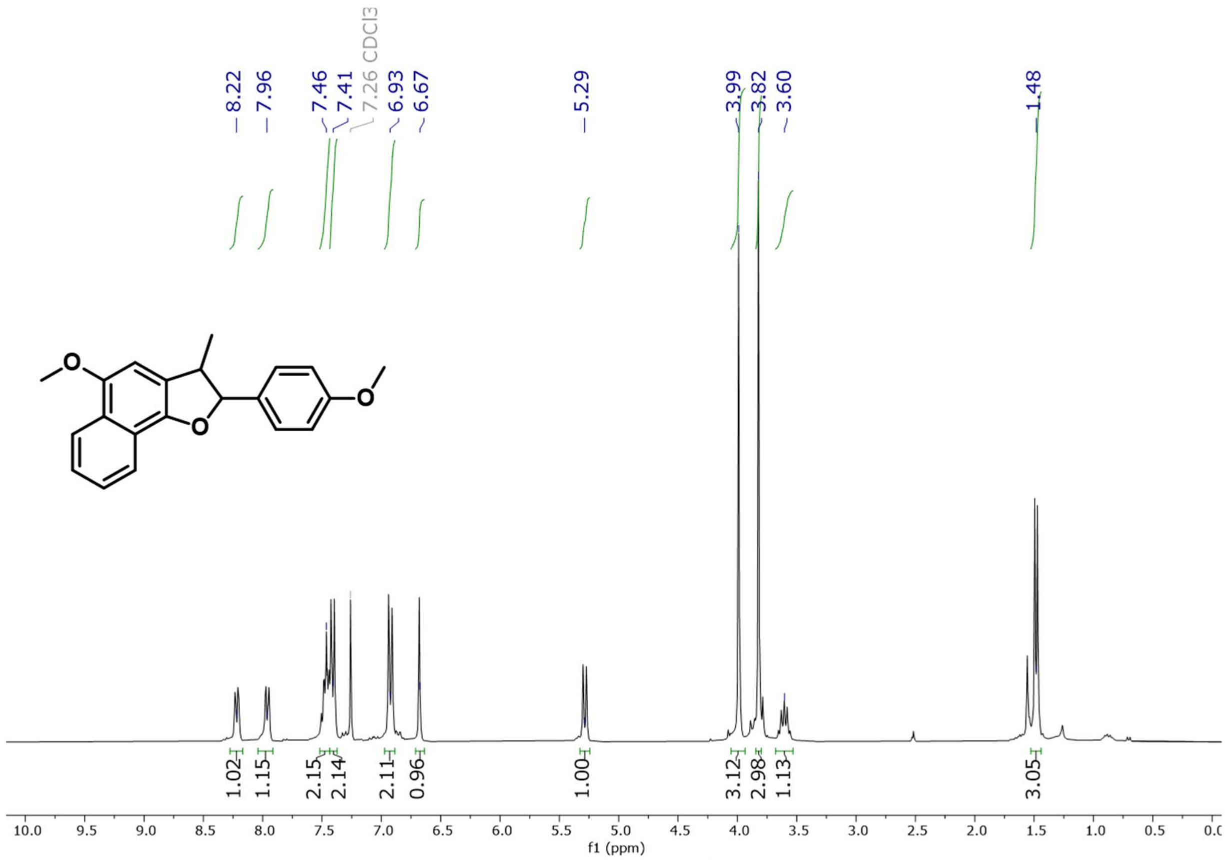
8.22
7.96
7.46
7.41
7.26 CDCl3
6.93
6.67
5.29
3.99
3.82
3.60
1.48
O
O
O
1.02
1.15
2.15
2.14
2.11
0.96
1.00
3.12
2.98
1.13
3.05
10.0
9.5
9.0
8.5
8.0
7.5
7.0
6.5
6.0
5.5
5.0
4.5
4.0
3.5
3.0
2.5
2.0
1.5
1.0
0.5
0.0
f1 (ppm)

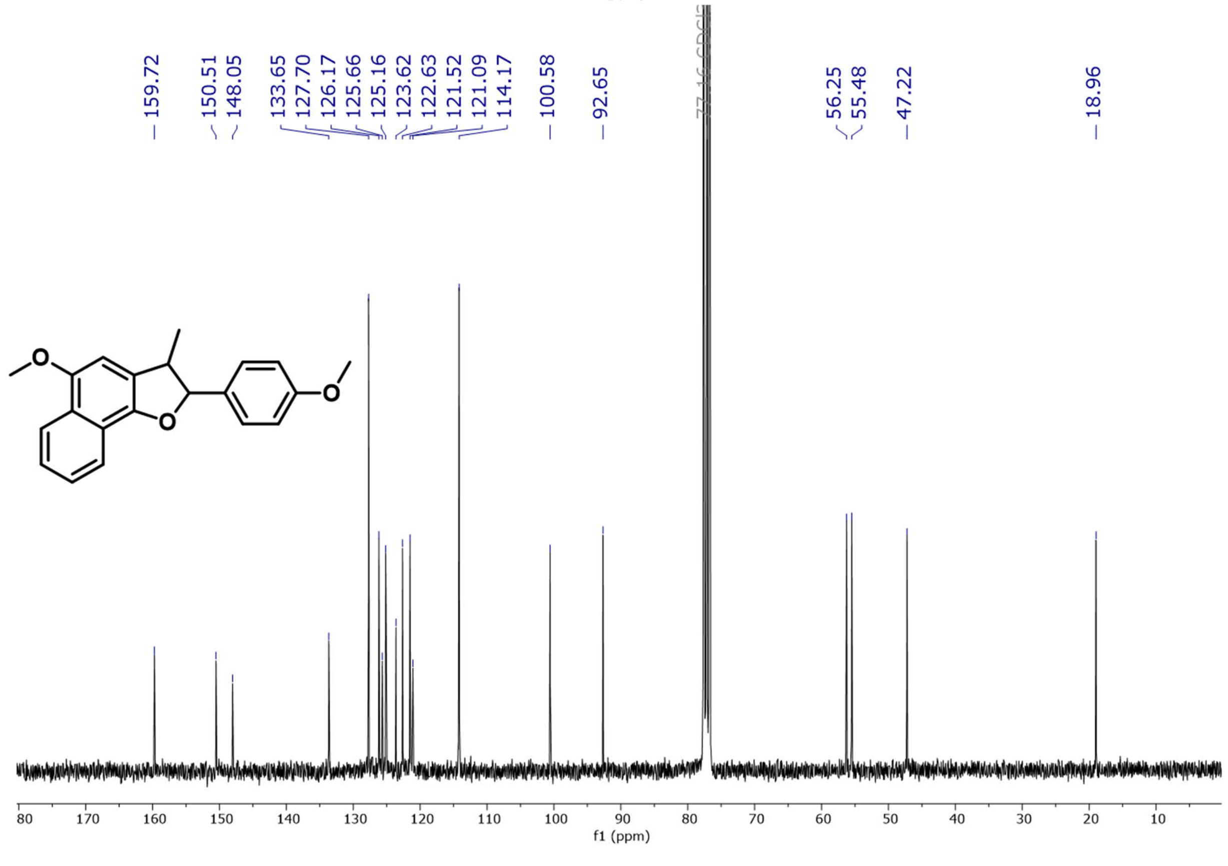
159.72
150.51
148.05
133.65
127.70
126.17
125.66
125.16
123.62
122.63
121.52
121.09
114.17
100.58
92.65
77.16 CDCl3
56.25
55.48
47.22
18.96
O
O
O
180
170
160
150
140
130
120
110
100
90
80
70
60
50
40
30
20
10
f1 (ppm)

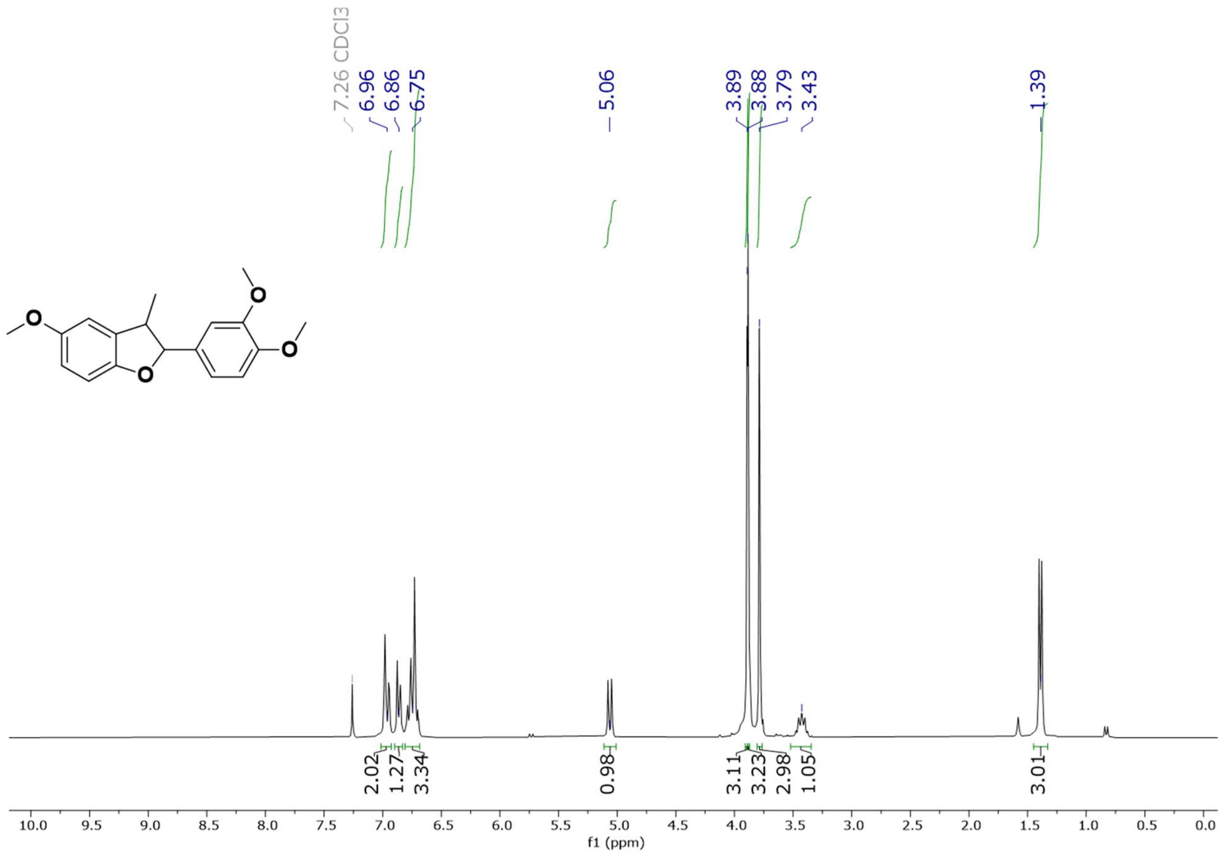
7.26 CDCl3
6.96
6.86
6.75
5.06
3.89
3.88
3.79
3.43
1.39
O
O
O
O
2.02
1.27
3.34
0.98
3.11
3.23
2.98
1.05
3.01
10.0
9.5
9.0
8.5
8.0
7.5
7.0
6.5
6.0
5.5
5.0
4.5
4.0
3.5
3.0
2.5
2.0
1.5
1.0
0.5
0.0
f1 (ppm)

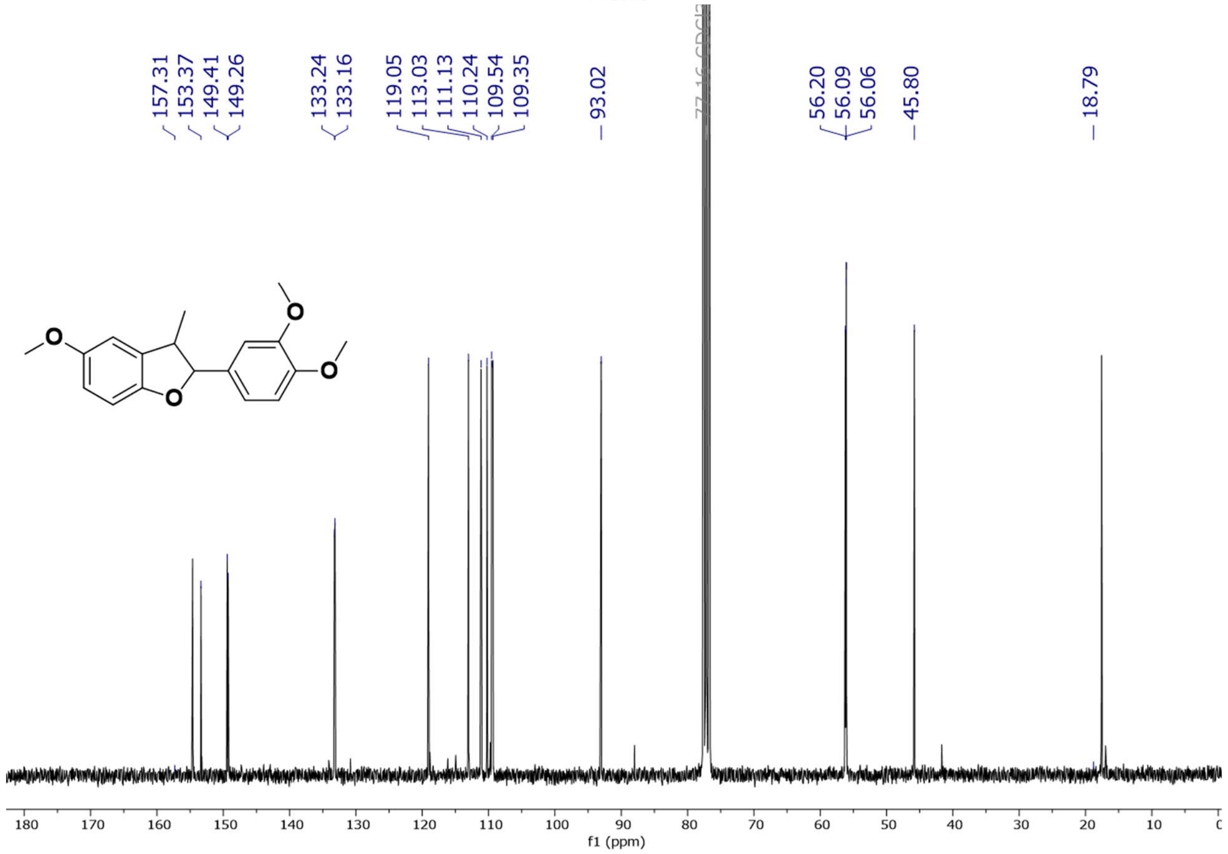
157.31
153.37
149.41
149.26
133.24
133.16
119.05
113.03
111.13
110.24
109.54
109.35
93.02
77.16 CDCl3
56.20
56.09
56.06
45.80
18.79
O
O
O
O
180
170
160
150
140
130
120
110
100
90
80
70
60
50
40
30
20
10
0
f1 (ppm)

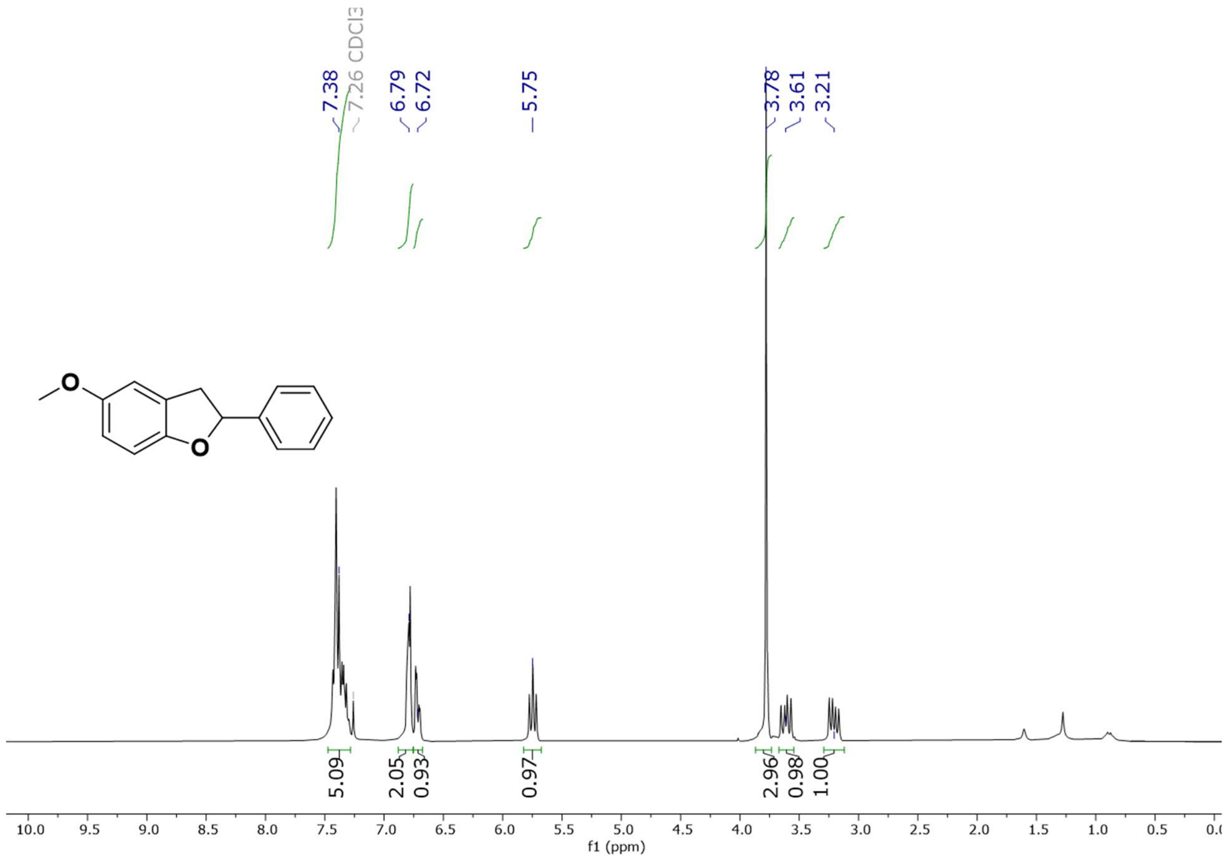
7.38
7.26 CDCl3
6.79
6.72
5.75
3.78
3.61
3.21
O
O
5.09
2.05
0.93
0.97
2.96
0.98
1.00
10.0 9.5 9.0 8.5 8.0 7.5 7.0 6.5 6.0 5.5 5.0 4.5 4.0 3.5 3.0 2.5 2.0 1.5 1.0 0.5 0.0
f1 (ppm)

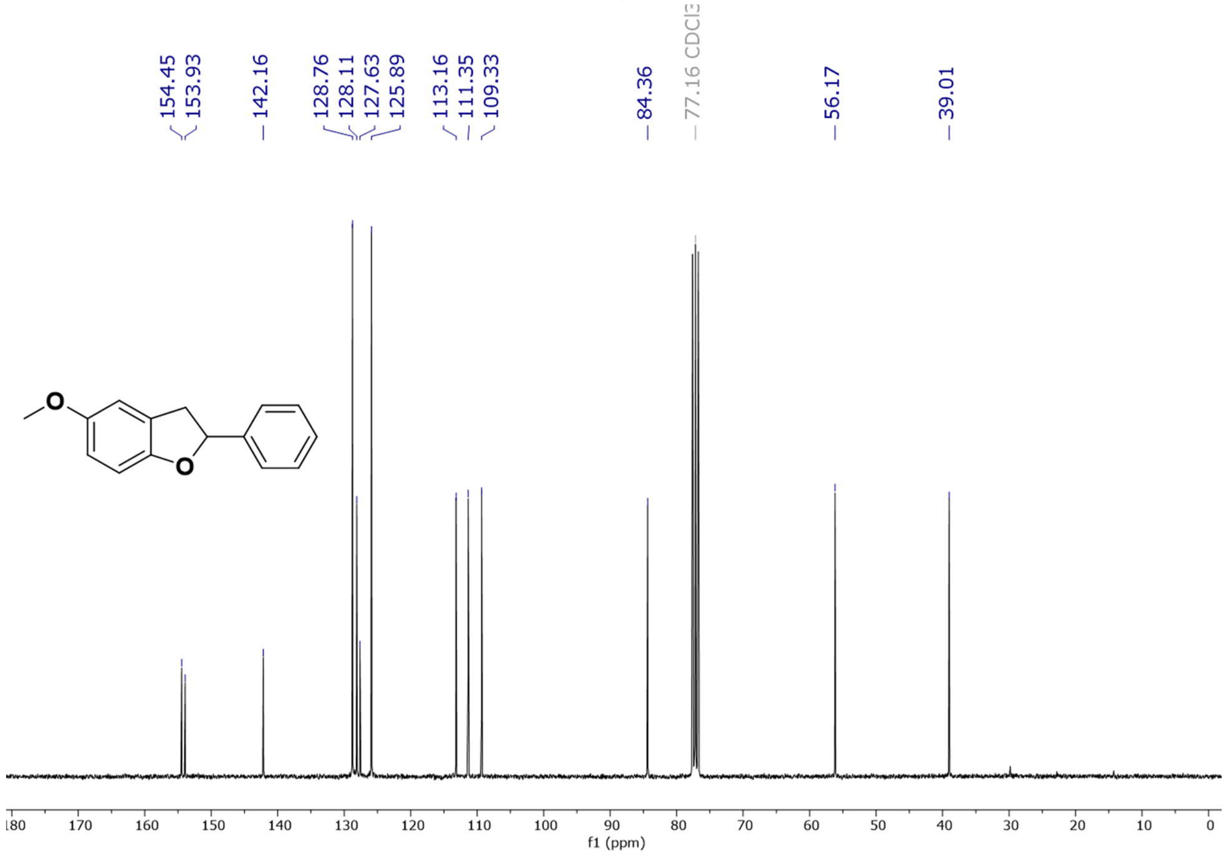
154.45
153.93
142.16
128.76
128.11
127.63
125.89
113.16
111.35
109.33
84.36
77.16 CDCl3
56.17
39.01
O
O
180 170 160 150 140 130 120 110 100 90 80 70 60 50 40 30 20 10 0
f1 (ppm)

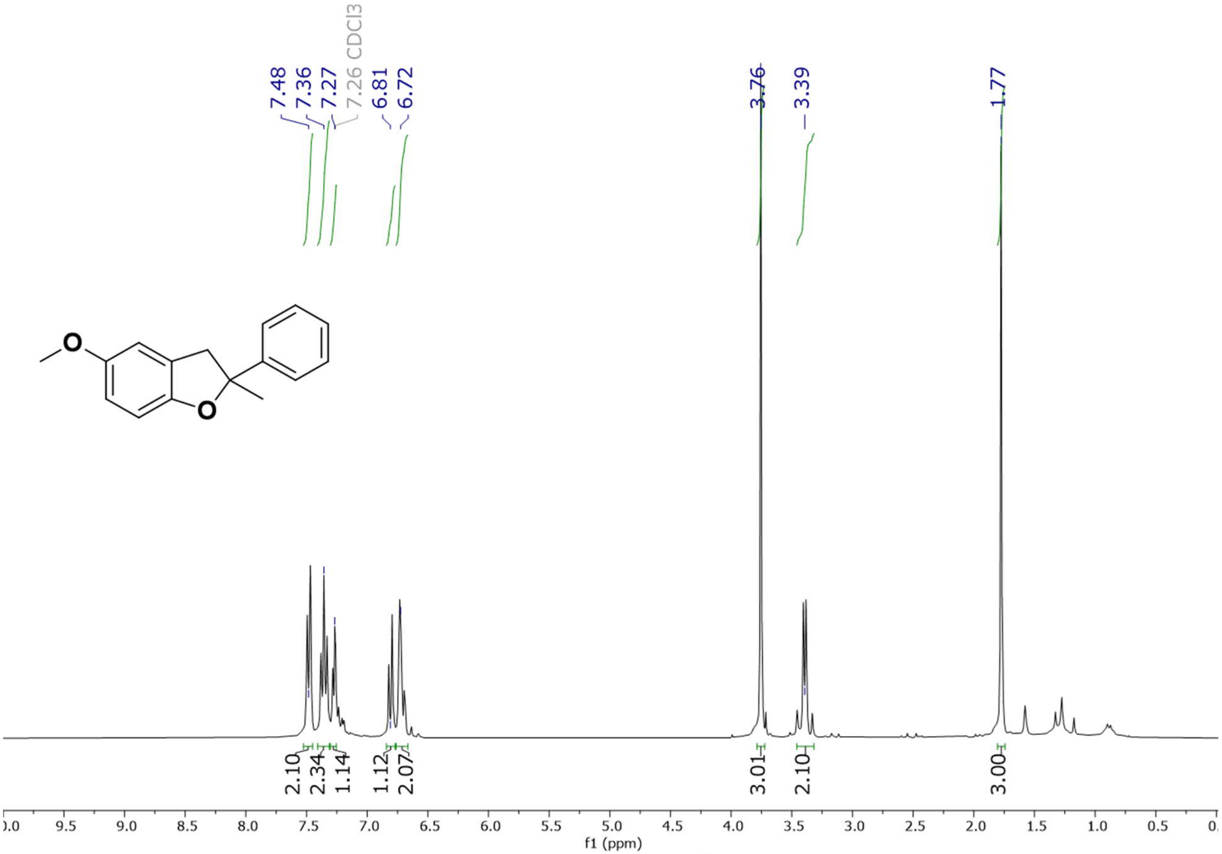
7.48
7.36
7.27
7.26 CDCl3
6.81
6.72
3.76
3.39
1.77
O
O
2.10
2.34
1.14
1.12
2.07
3.01
2.10
3.00
10.0
9.5
9.0
8.5
8.0
7.5
7.0
6.5
6.0
5.5
5.0
4.5
4.0
3.5
3.0
2.5
2.0
1.5
1.0
0.5
0.
f1 (ppm)

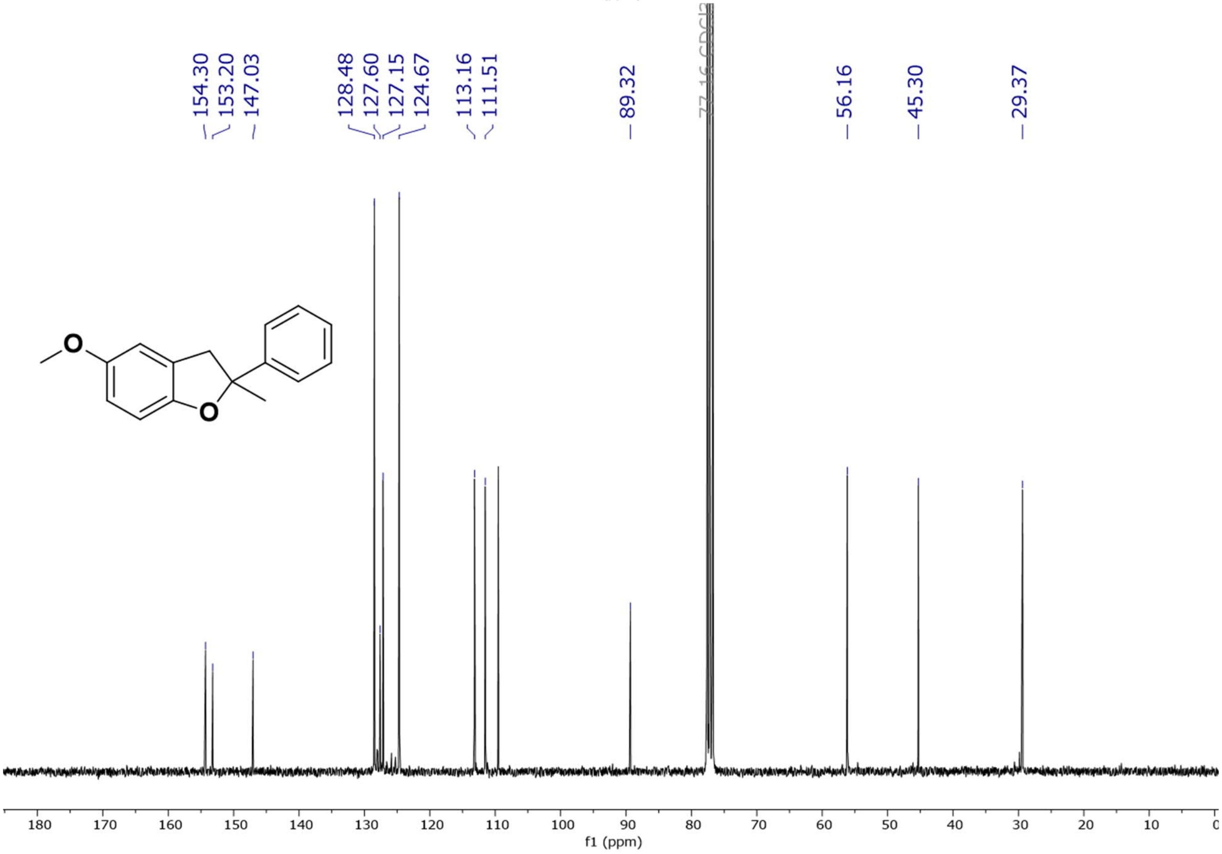
154.30
153.20
147.03
128.48
127.60
127.15
124.67
113.16
111.51
89.32
77.16 CDCl3
56.16
45.30
29.37
O
O
180
170
160
150
140
130
120
110
100
90
80
70
60
50
40
30
20
10
0
f1 (ppm)

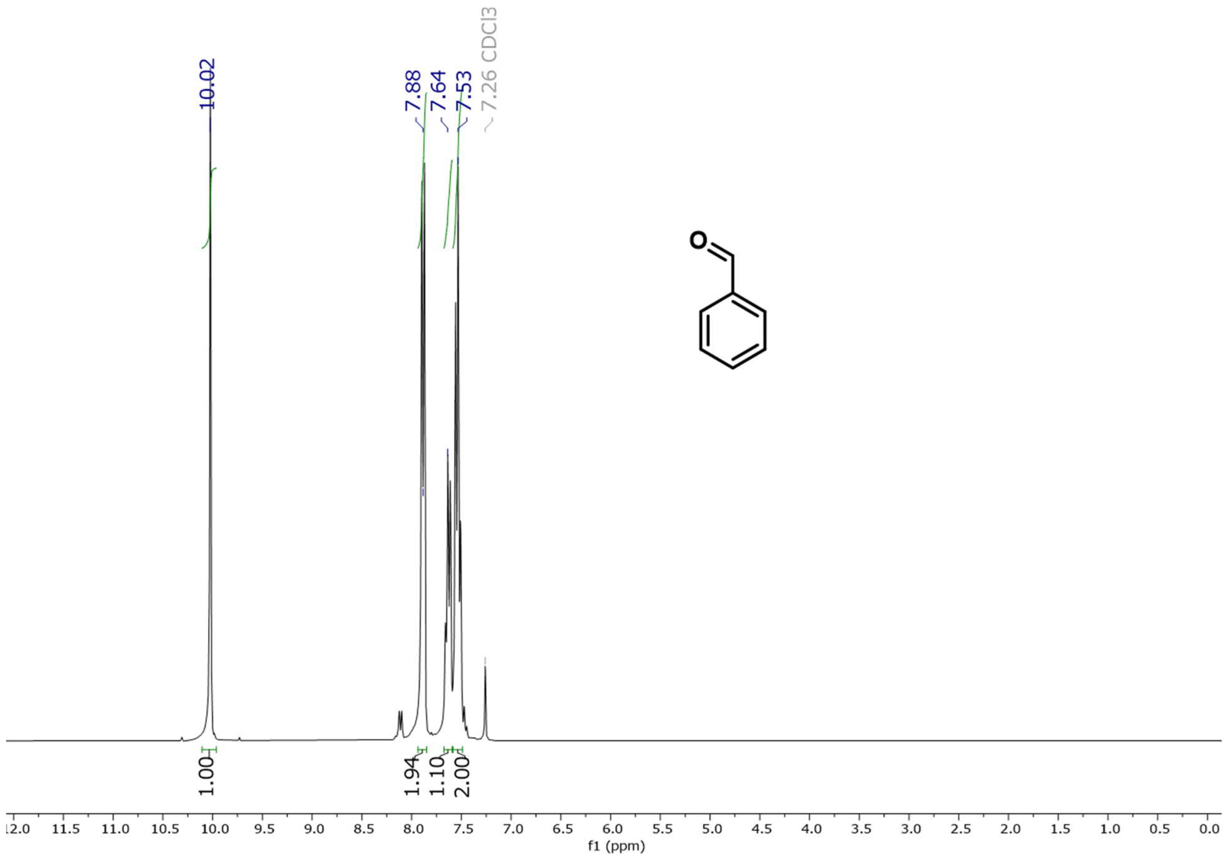
10.02
7.88
7.64
7.53
7.26 CDCl3
1.00
1.94
1.10
2.00
O
12.0 11.5 11.0 10.5 10.0 9.5 9.0 8.5 8.0 7.5 7.0 6.5 6.0 5.5 5.0 4.5 4.0 3.5 3.0 2.5 2.0 1.5 1.0 0.5 0.0
f1 (ppm)

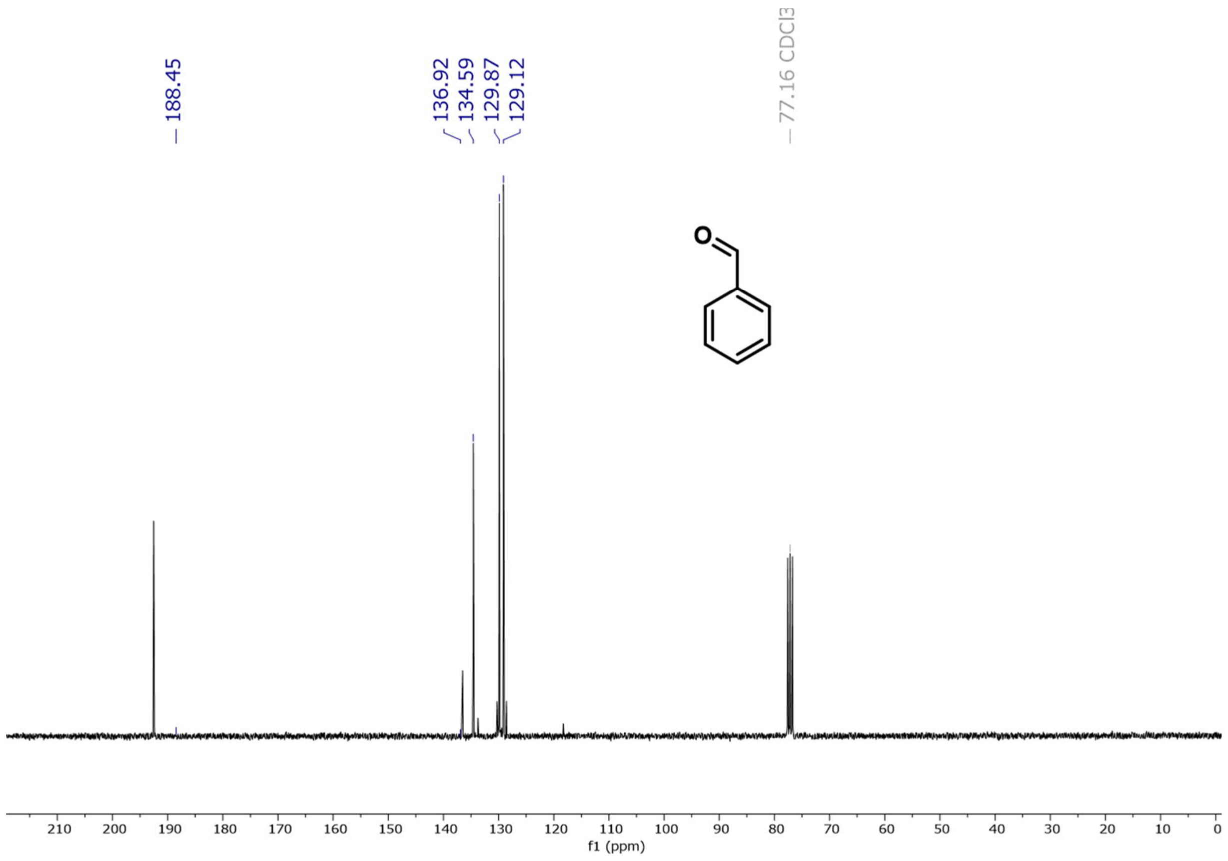
188.45
136.92
134.59
129.87
129.12
77.16 CDCl3
O
210 200 190 180 170 160 150 140 130 120 110 100 90 80 70 60 50 40 30 20 10 0
f1 (ppm)

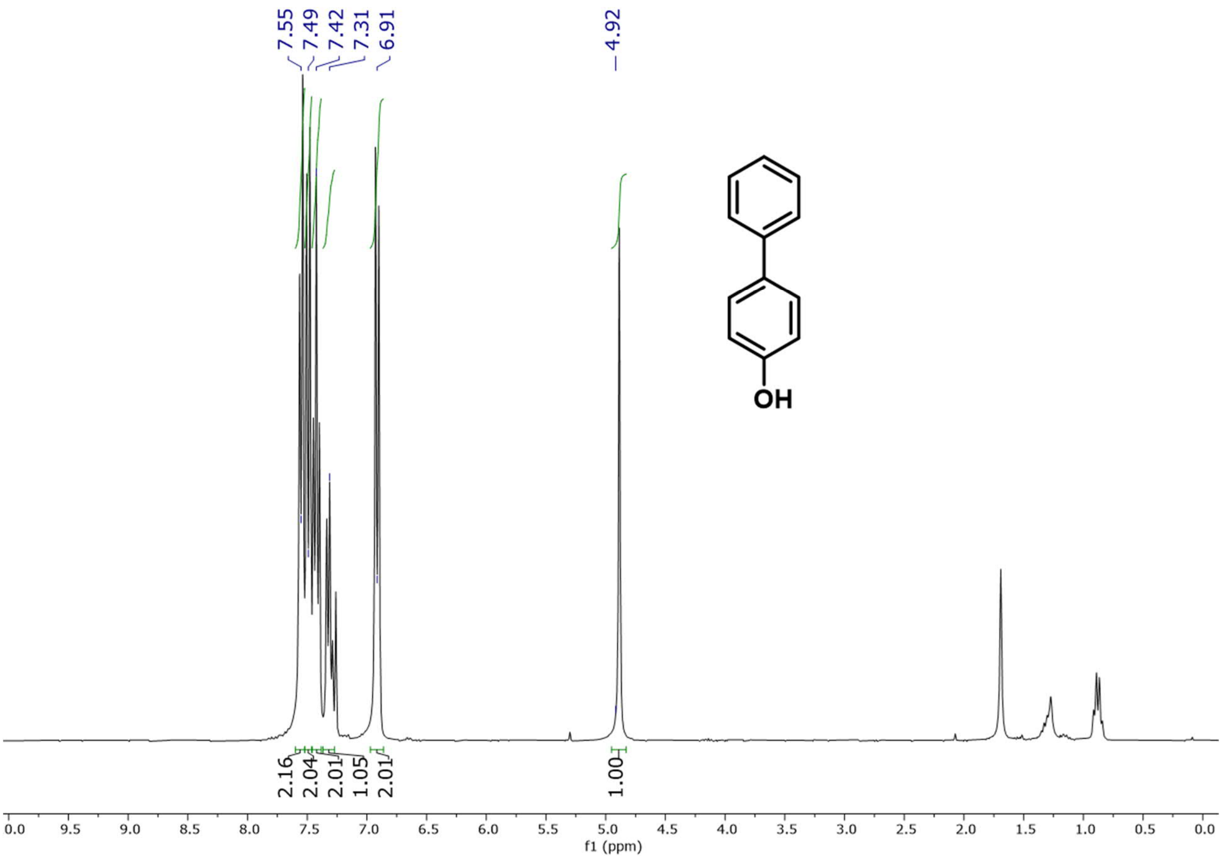
7.55
7.49
7.42
7.31
6.91
4.92
OH
2.16
2.04
2.01
1.05
2.01
1.00
10.0 9.5 9.0 8.5 8.0 7.5 7.0 6.5 6.0 5.5 5.0 4.5 4.0 3.5 3.0 2.5 2.0 1.5 1.0 0.5 0.0
f1 (ppm)

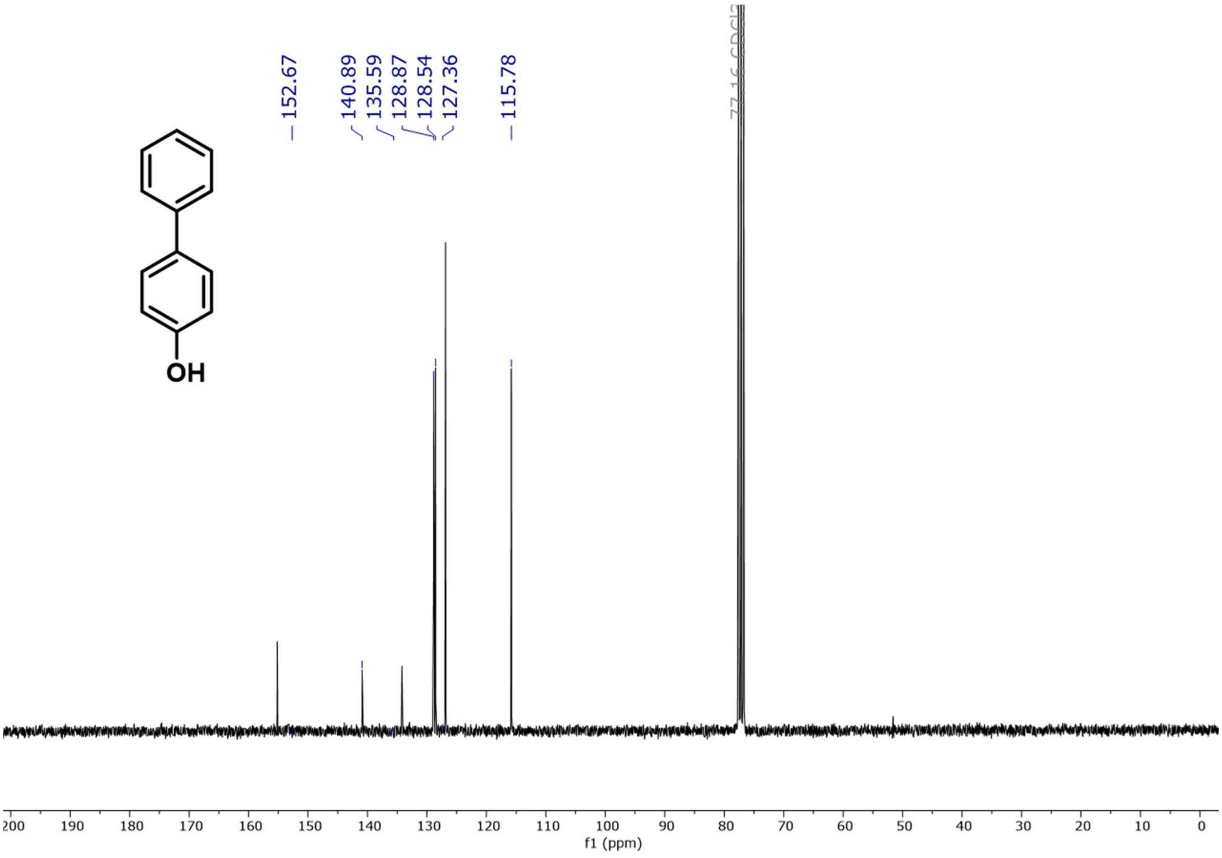
152.67
140.89
135.59
128.87
128.54
127.36
115.78
77.16 CDCl3
OH
200 190 180 170 160 150 140 130 120 110 100 90 80 70 60 50 40 30 20 10 0
f1 (ppm)

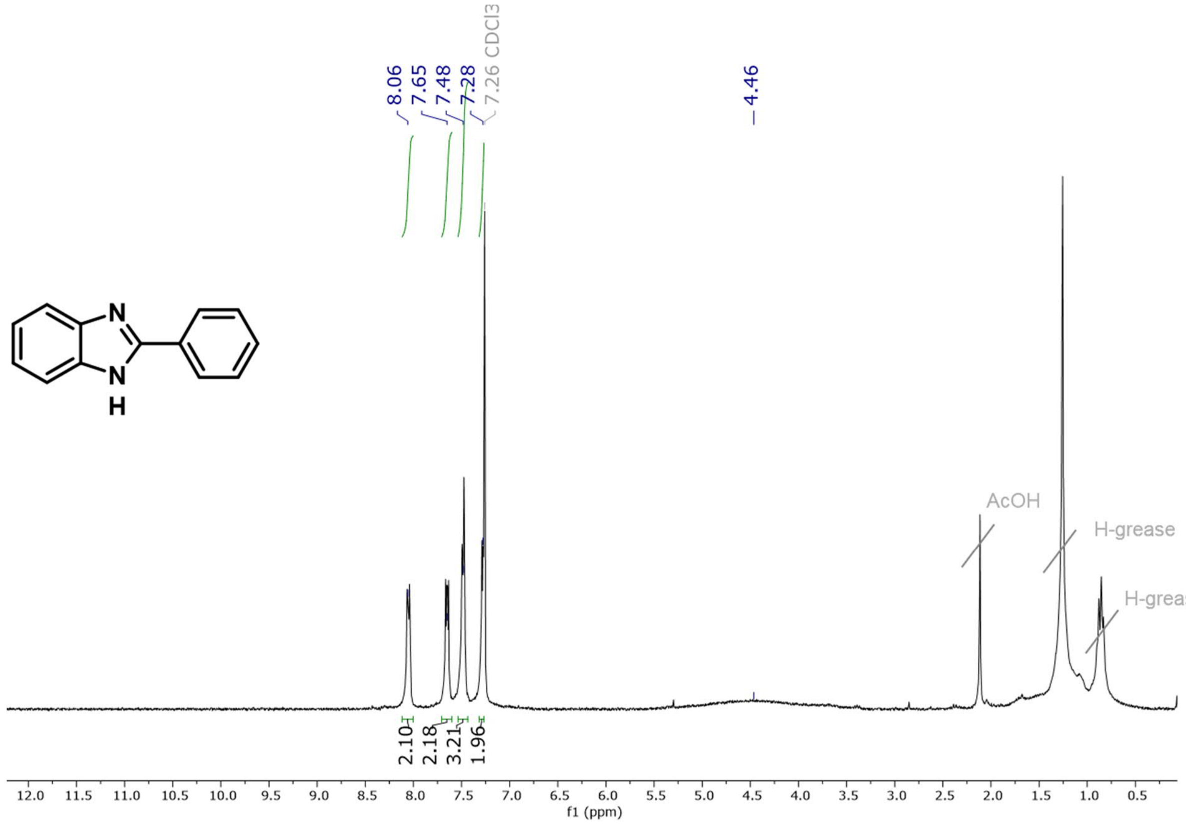
8.06
7.65
7.48
7.28
7.26 CDCl3
4.46
N
N
H
AcOH
H-grease
H-grease
2.10
2.18
3.21
1.96
12.0
11.5
11.0
10.5
10.0
9.5
9.0
8.5
8.0
7.5
7.0
6.5
6.0
5.5
5.0
4.5
4.0
3.5
3.0
2.5
2.0
1.5
1.0
0.5
f1 (ppm)

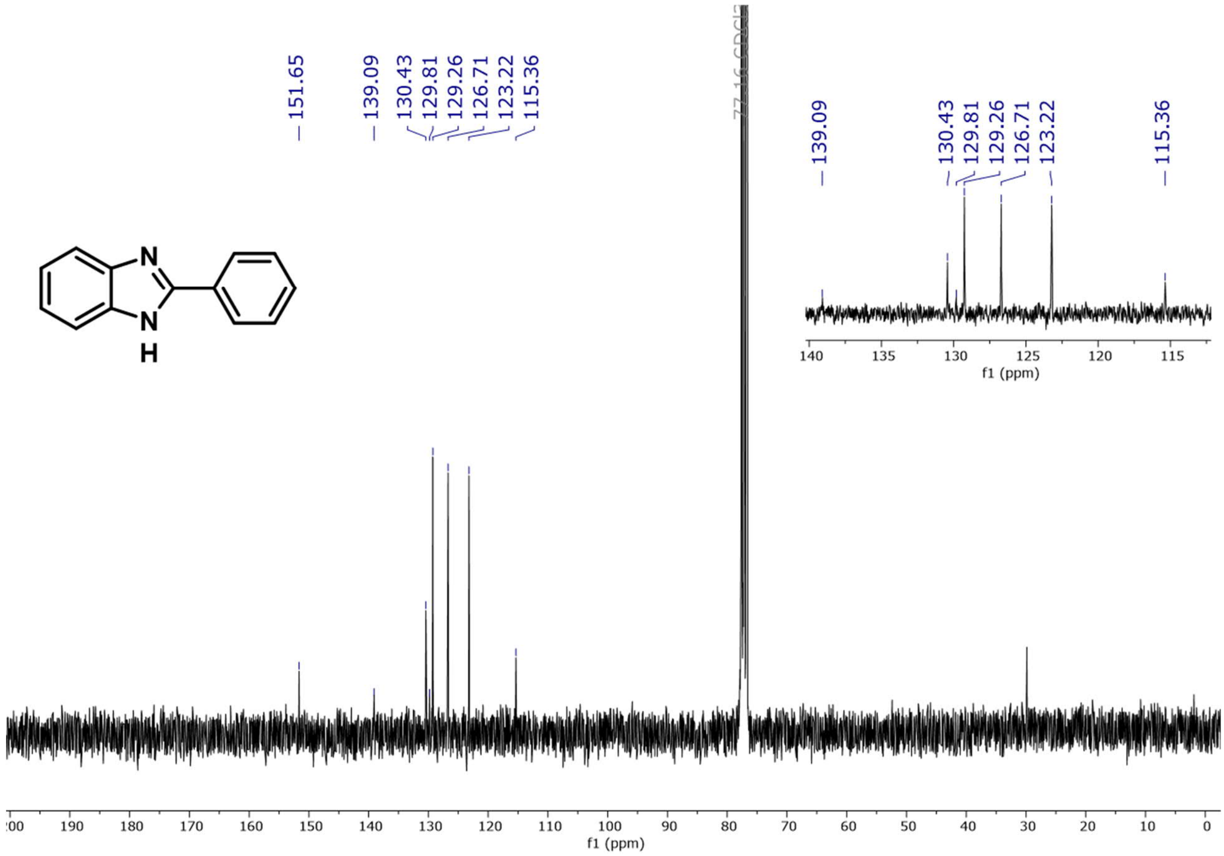
151.65
139.09
130.43
129.81
129.26
126.71
123.22
115.36
77.16 CDCl3
N
N
H
139.09
130.43
129.81
129.26
126.71
123.22
115.36
140
135
130
125
120
115
f1 (ppm)
200
190
180
170
160
150
140
130
120
110
100
90
80
70
60
50
40
30
20
10
0
f1 (ppm)

3.3 Semiconductor nanoplatelets with tunable photocatalytic activity for selective synthesis of azoxy aromatics

Scope GC traces

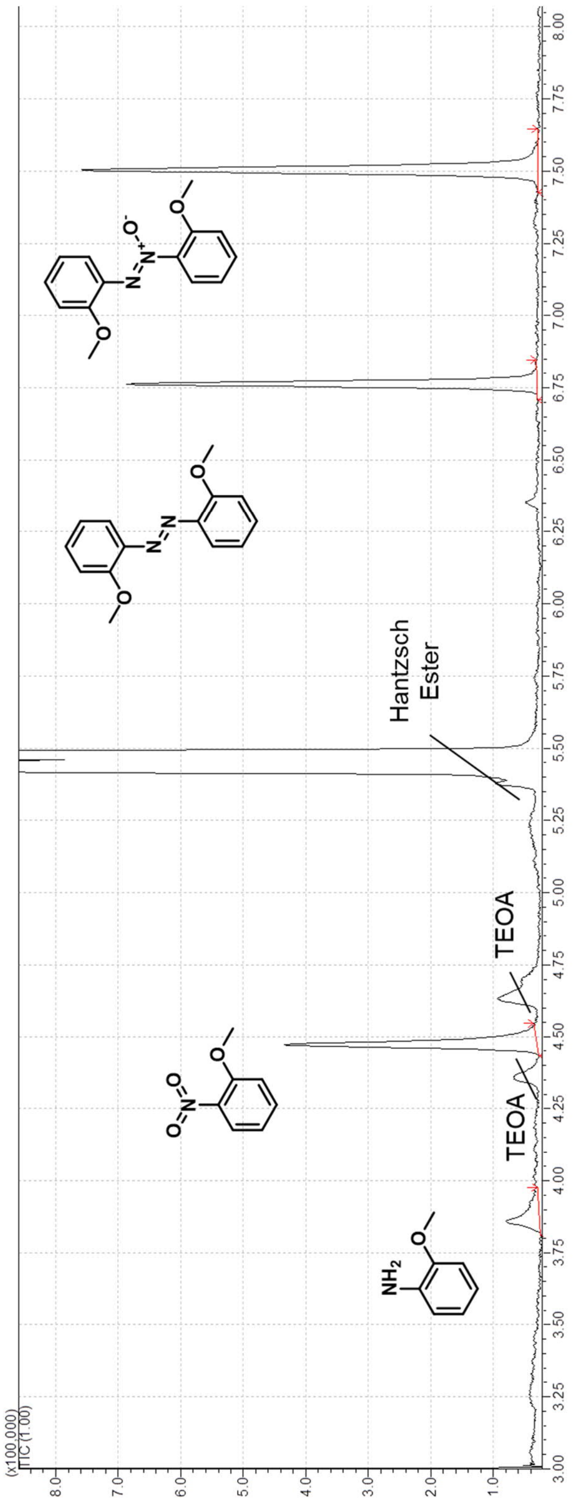

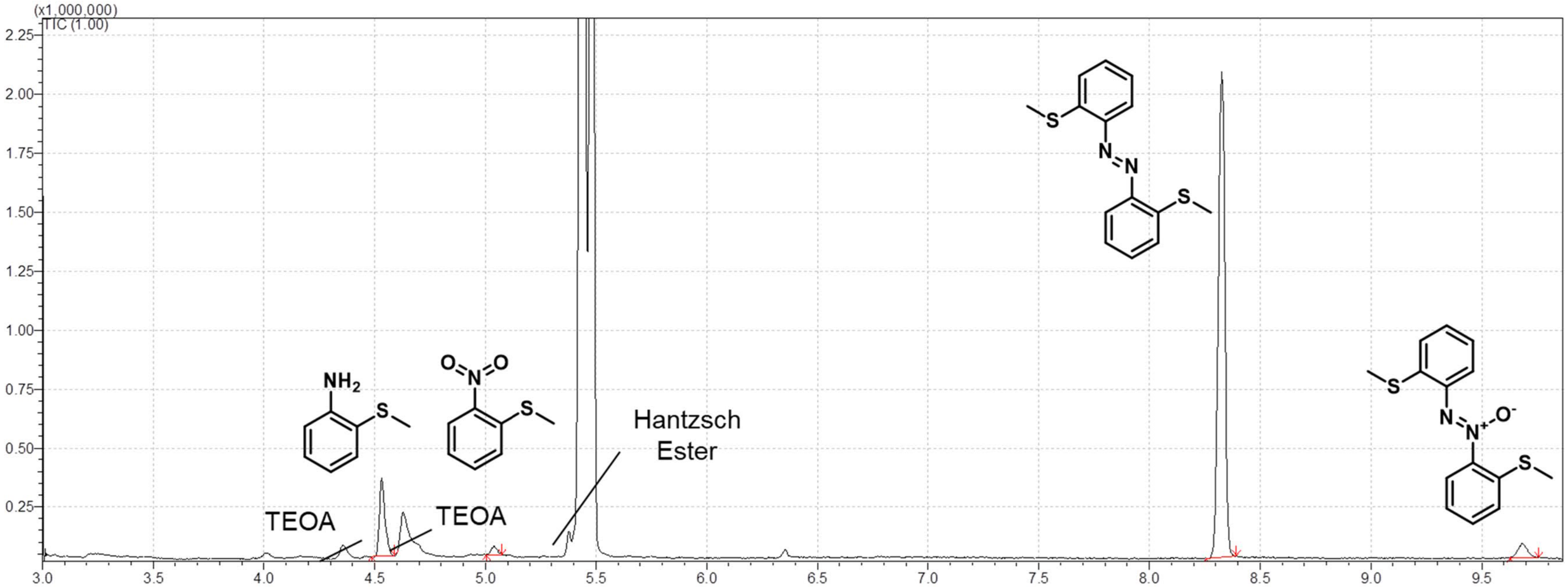
(x1,000,000)
TIC (1.00)
2.25
2.00
1.75
1.50
1.25
1.00
0.75
0.50
0.25
3.0
3.5
4.0
4.5
5.0
5.5
6.0
6.5
7.0
7.5
8.0
8.5
9.0
9.5
TEOA
TEOA
NH₂
S
O
N
O
S
Hantzsch
Ester
S
N
N
S
S
N
N⁺
O⁻
S

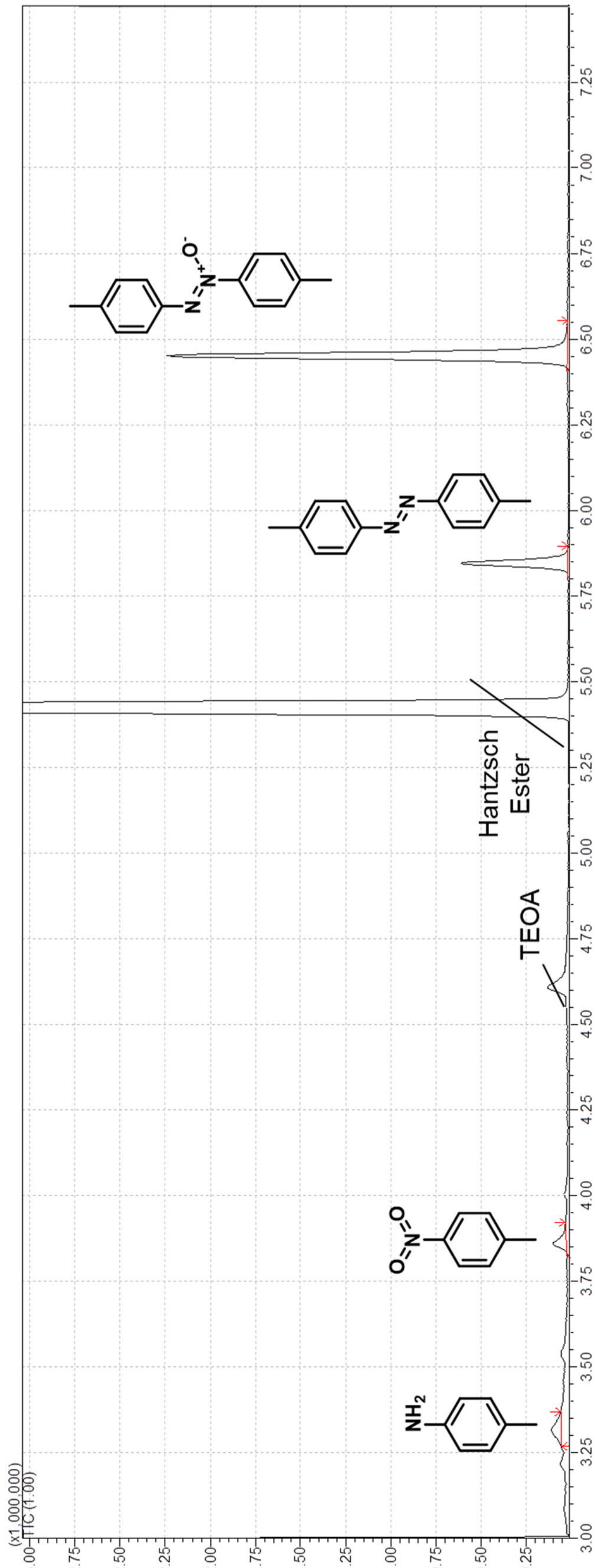
(x1,000,000)
TIC (1.00)
3.00
2.75
2.50
2.25
2.00
1.75
1.50
1.25
1.00
0.75
0.50
0.25
3.00
3.25
3.50
3.75
4.00
4.25
4.50
4.75
5.00
5.25
5.50
5.75
6.00
6.25
6.50
6.75
7.00
7.25
NH2
TEOA
Hantzsch Ester

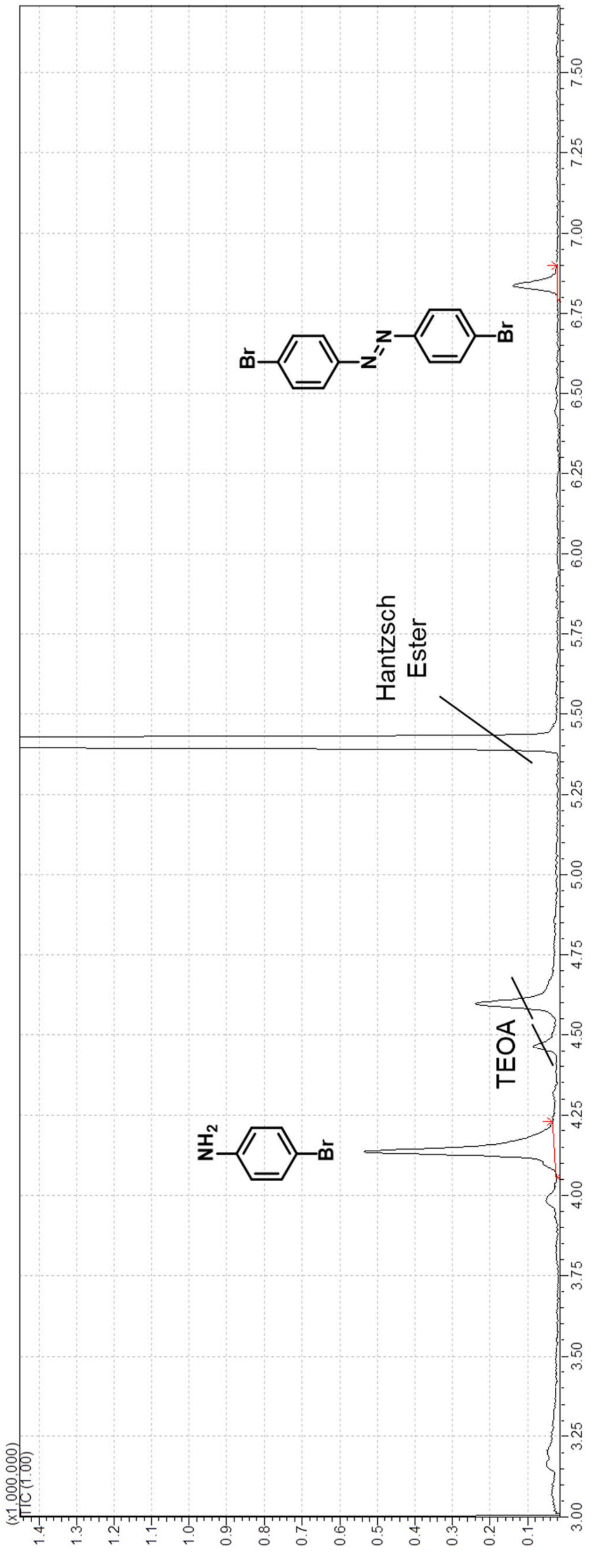
(x1,000,000)
TIC (1.00)
1.4
1.3
1.2
1.1
1.0
0.9
0.8
0.7
0.6
0.5
0.4
0.3
0.2
0.1
3.00
3.25
3.50
3.75
4.00
4.25
4.50
4.75
5.00
5.25
5.50
5.75
6.00
6.25
6.50
6.75
7.00
7.25
7.50
NH2
Br
TEOA
Hantzsch Ester
Br
N=N
Br

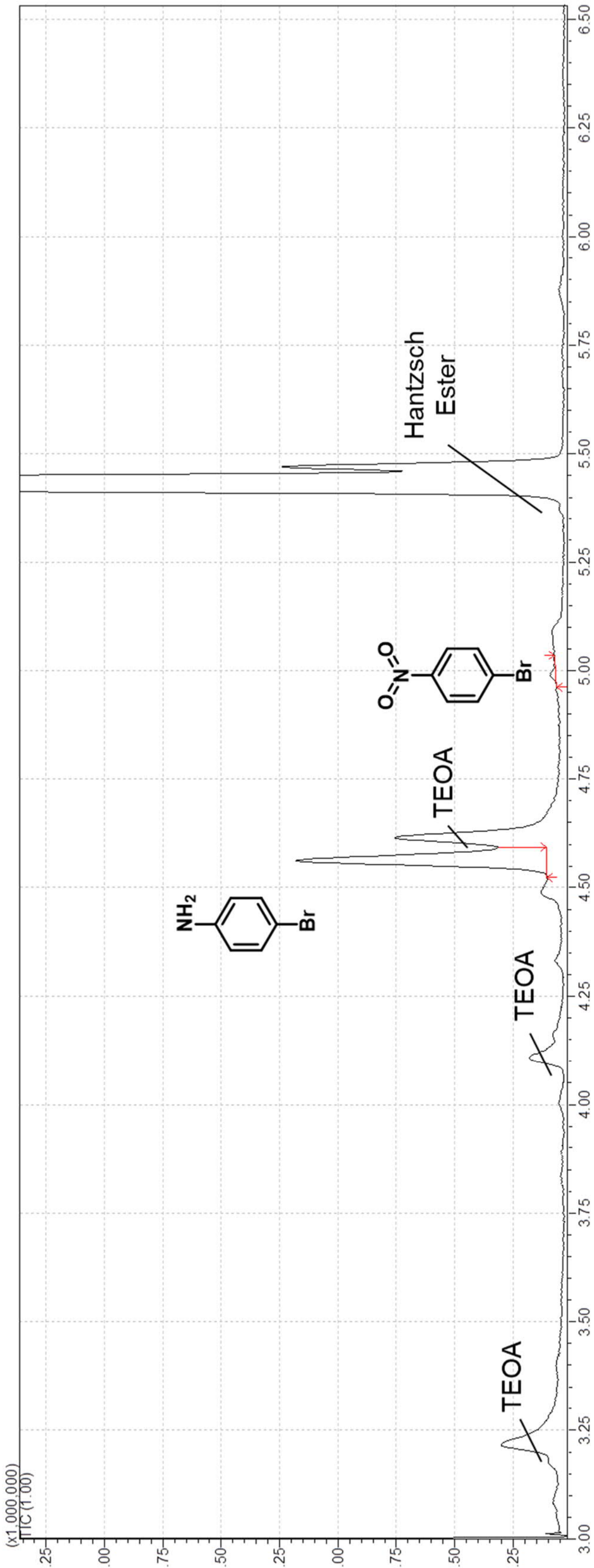
(x1,000,000)
TIC (1.00)
2.25
2.00
1.75
1.50
1.25
1.00
0.75
0.50
0.25
3.00
3.25
3.50
3.75
4.00
4.25
4.50
4.75
5.00
5.25
5.50
5.75
6.00
6.25
6.50
TEOA
TEOA
TEOA
NH2
Br
O
N
O
Br
Hantzsch Ester

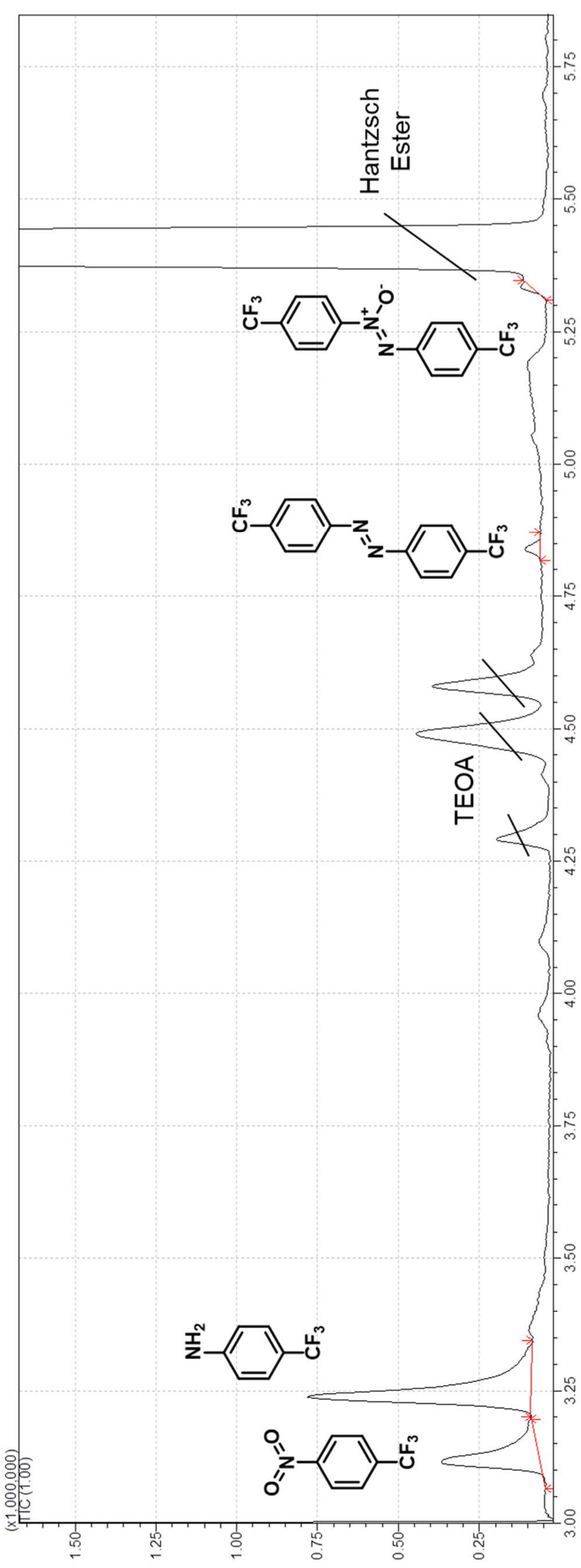
(x1,000,000)
TIC (1.00)
1.50
1.25
1.00
0.75
0.50
0.25
3.00
3.25
3.50
3.75
4.00
4.25
4.50
4.75
5.00
5.25
5.50
5.75
TEOA
Hantzsch Ester
NH2
CF3
O
N
N+
O-

3.4 Porous aromatic frameworks with precisely controllable conjugation lengths for visible-light-driven photocatalytic selective C-H activation reactions

^{1}H and ^{13}C NMR spectra

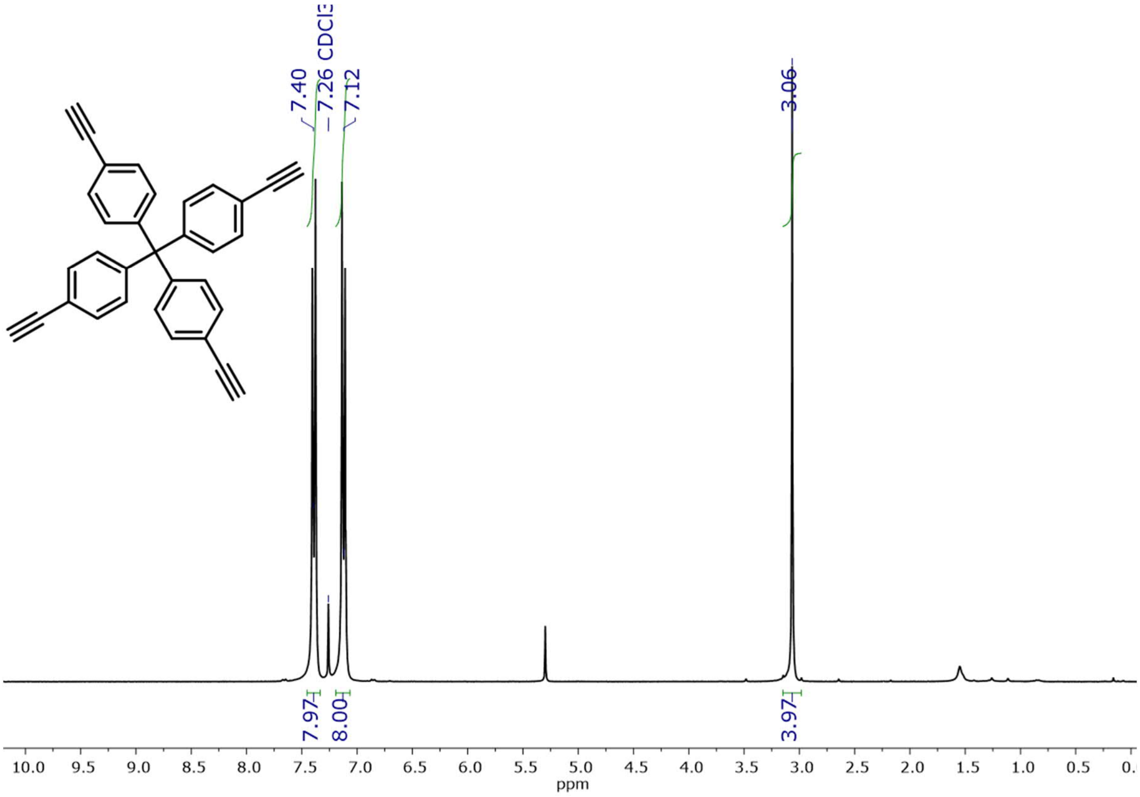

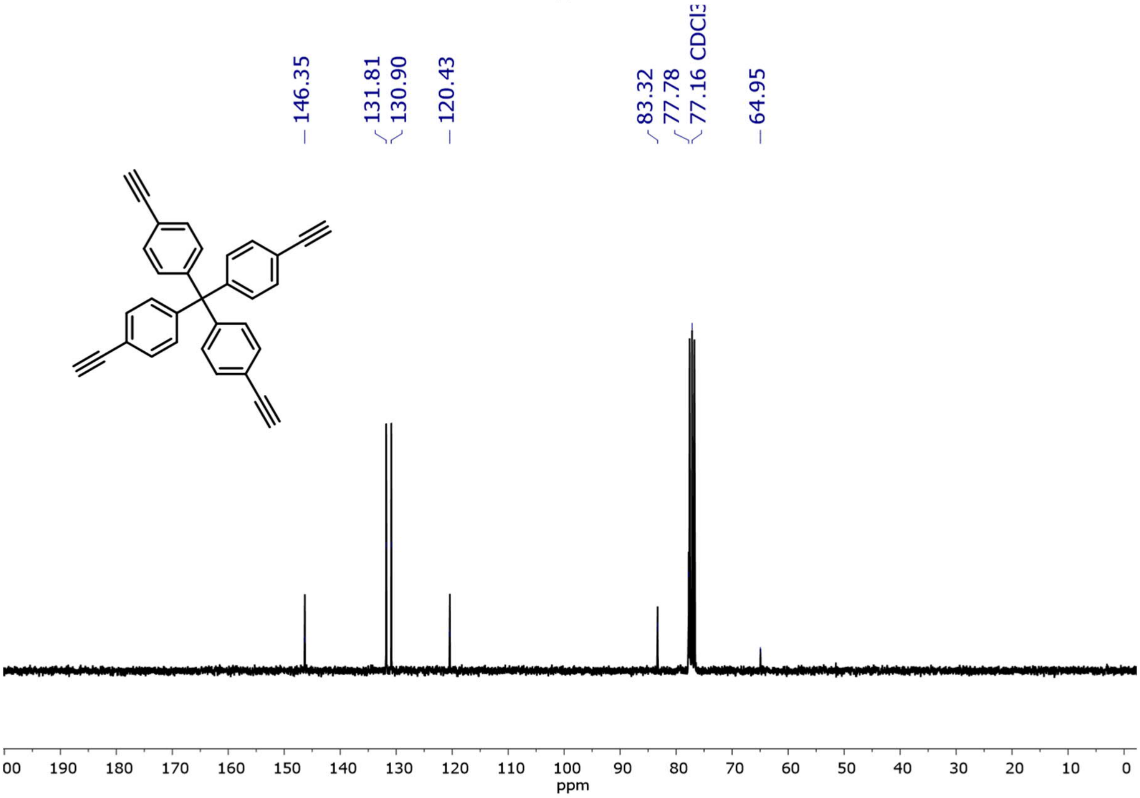

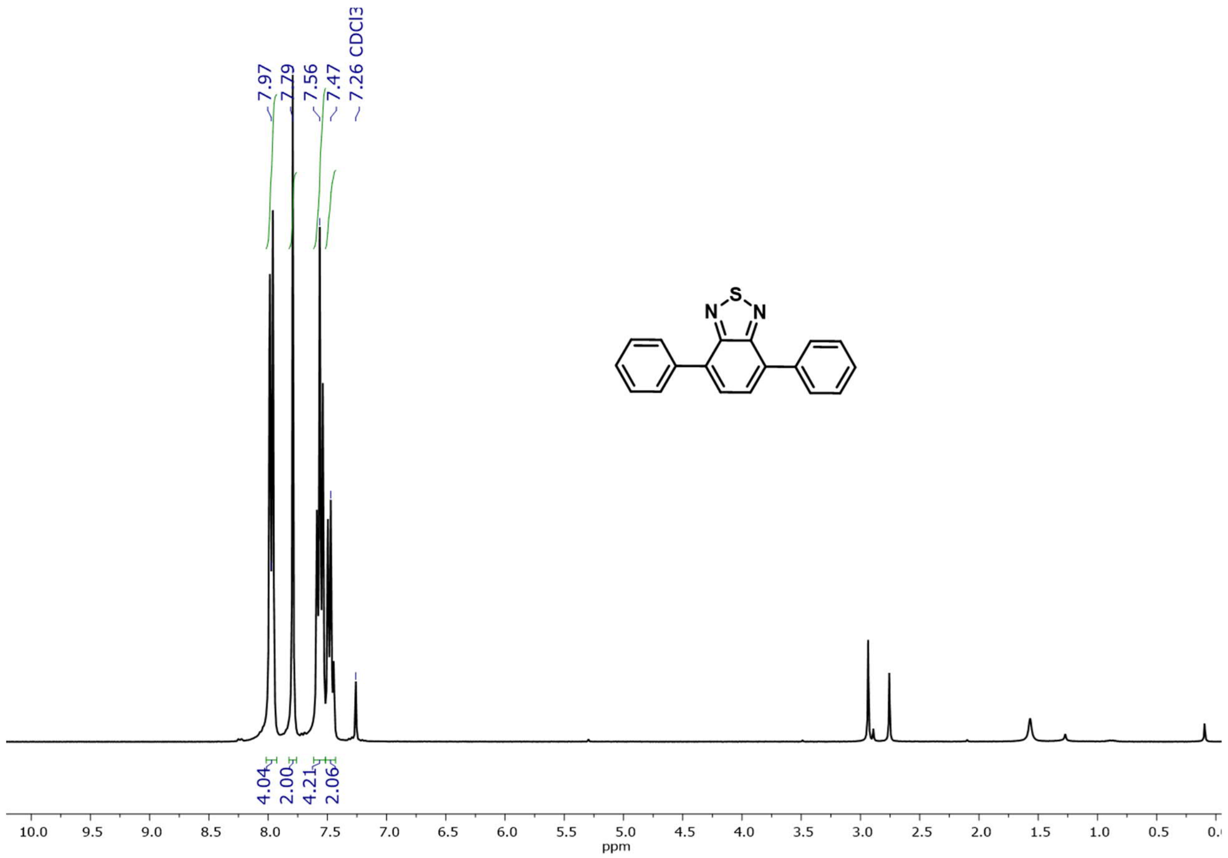
7.97
7.79
7.56
7.47
7.26 CDCl3
4.04
2.00
4.21
2.06
10.0 9.5 9.0 8.5 8.0 7.5 7.0 6.5 6.0 5.5 5.0 4.5 4.0 3.5 3.0 2.5 2.0 1.5 1.0 0.5 0.
ppm
S
N
N

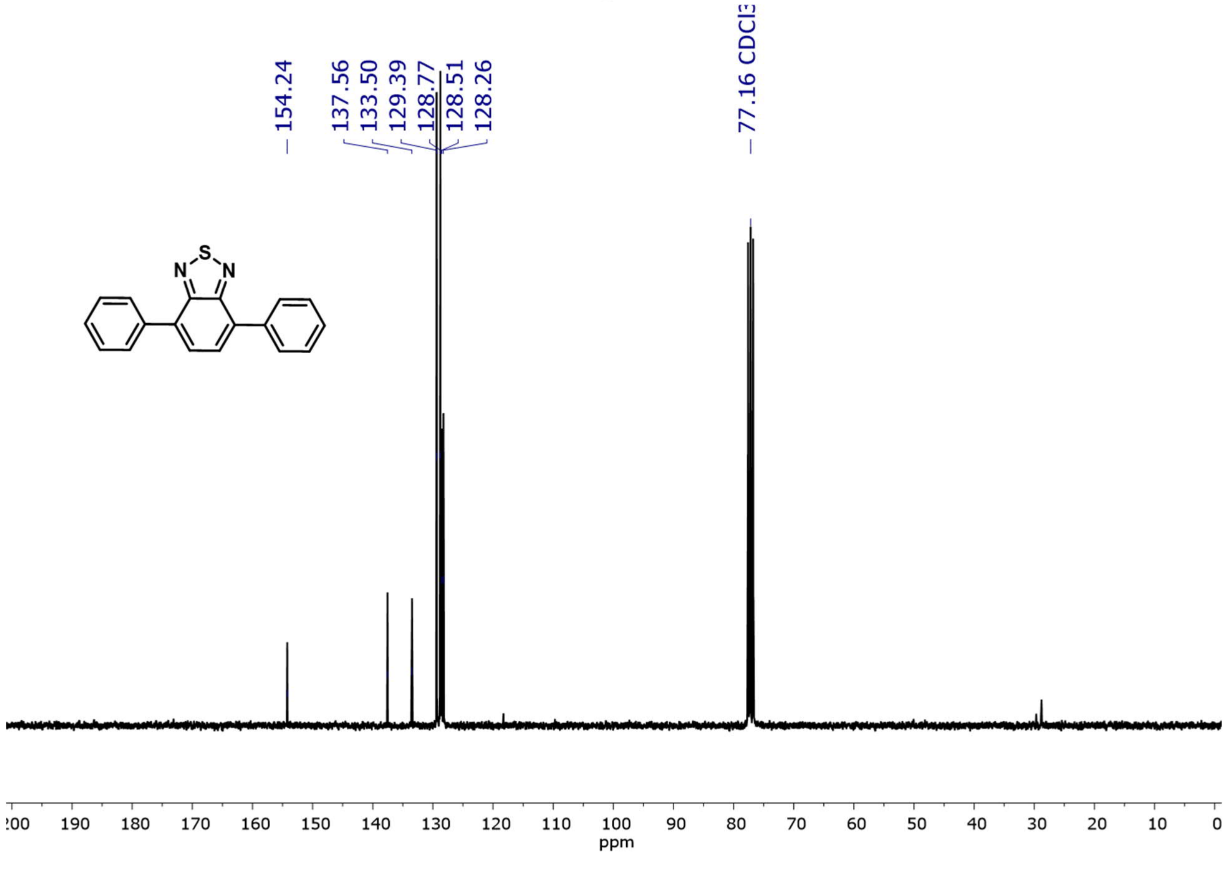
154.24
137.56
133.50
129.39
128.77
128.51
128.26
77.16 CDCl3
S
N
N
200 190 180 170 160 150 140 130 120 110 100 90 80 70 60 50 40 30 20 10 0
ppm

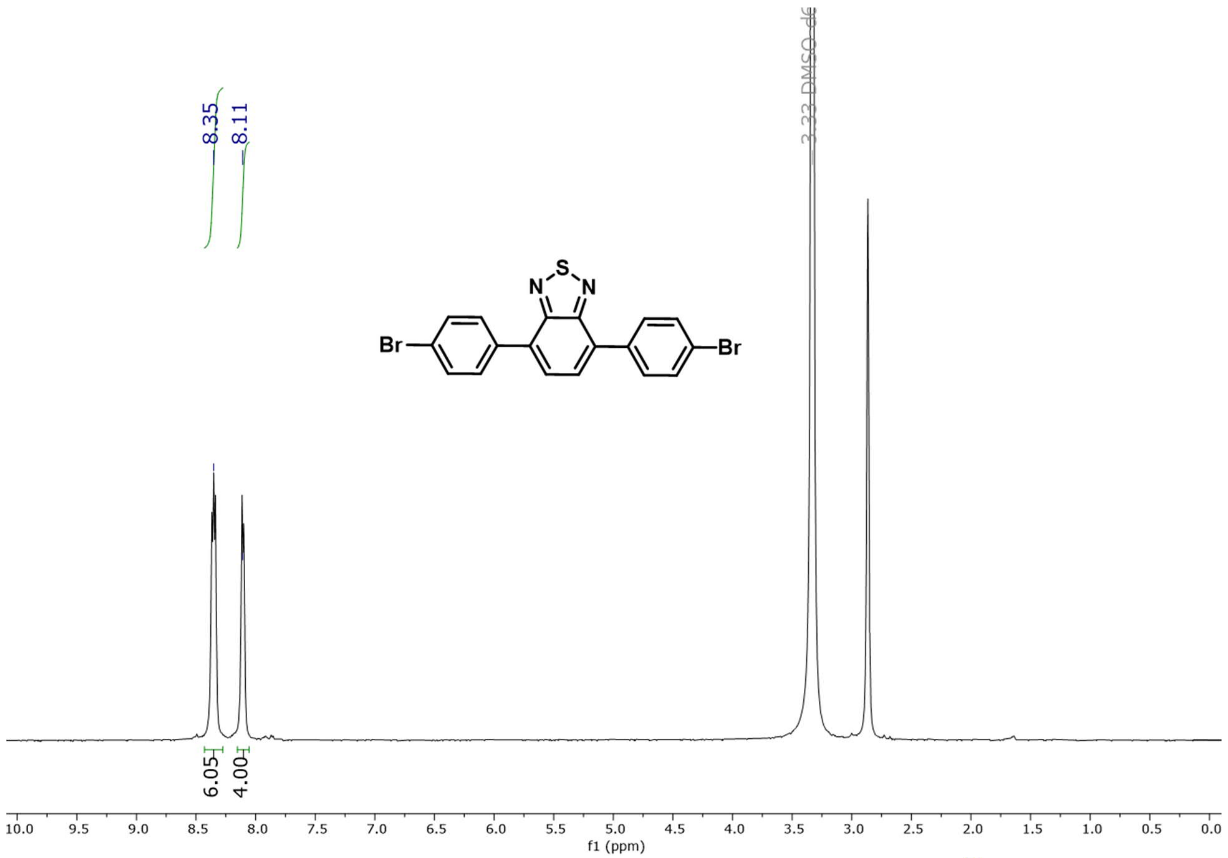
8.35
8.11
3.33 DMSO-d6
6.05
4.00
Br
N
S
N
Br
10.0
9.5
9.0
8.5
8.0
7.5
7.0
6.5
6.0
5.5
5.0
4.5
4.0
3.5
3.0
2.5
2.0
1.5
1.0
0.5
0.0
f1 (ppm)

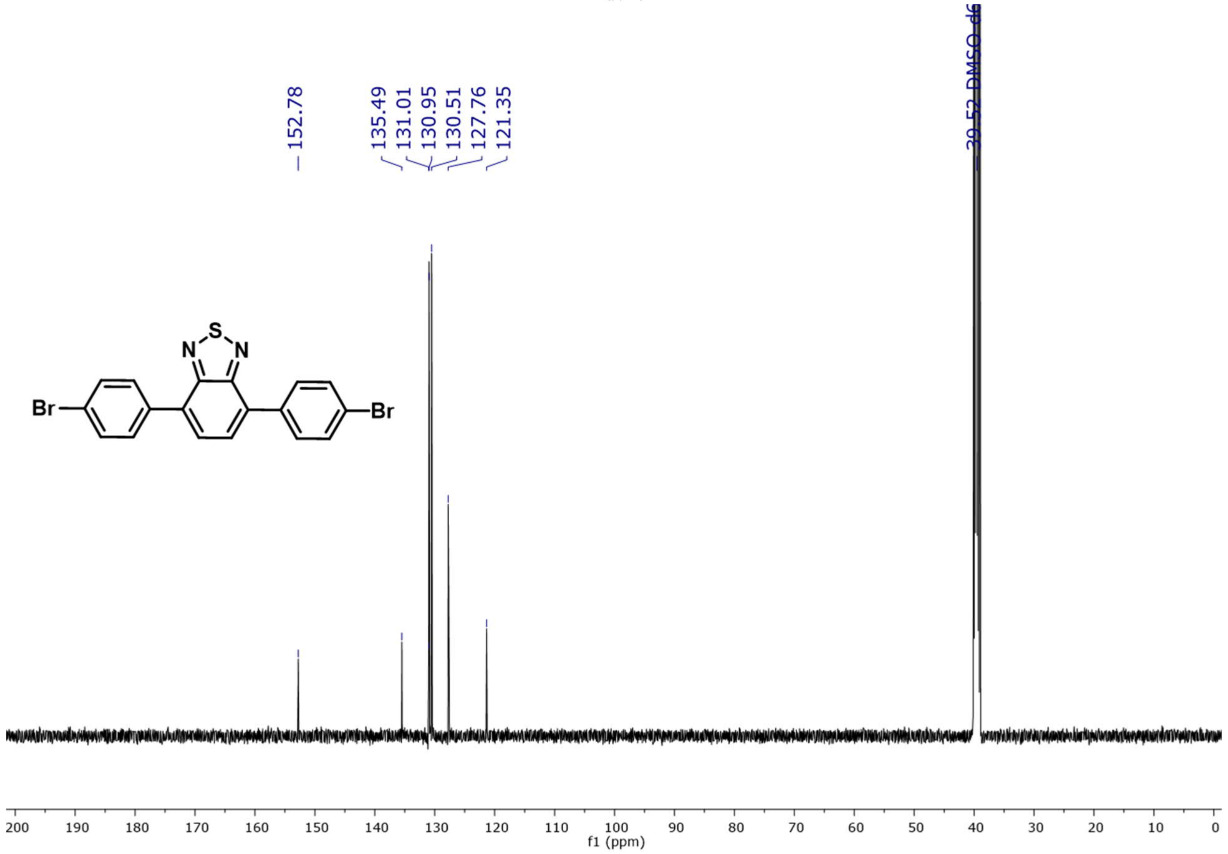
152.78
135.49
131.01
130.95
130.51
127.76
121.35
39.52 DMSO-d6
Br
N
S
N
Br
200
190
180
170
160
150
140
130
120
110
100
90
80
70
60
50
40
30
20
10
0
f1 (ppm)

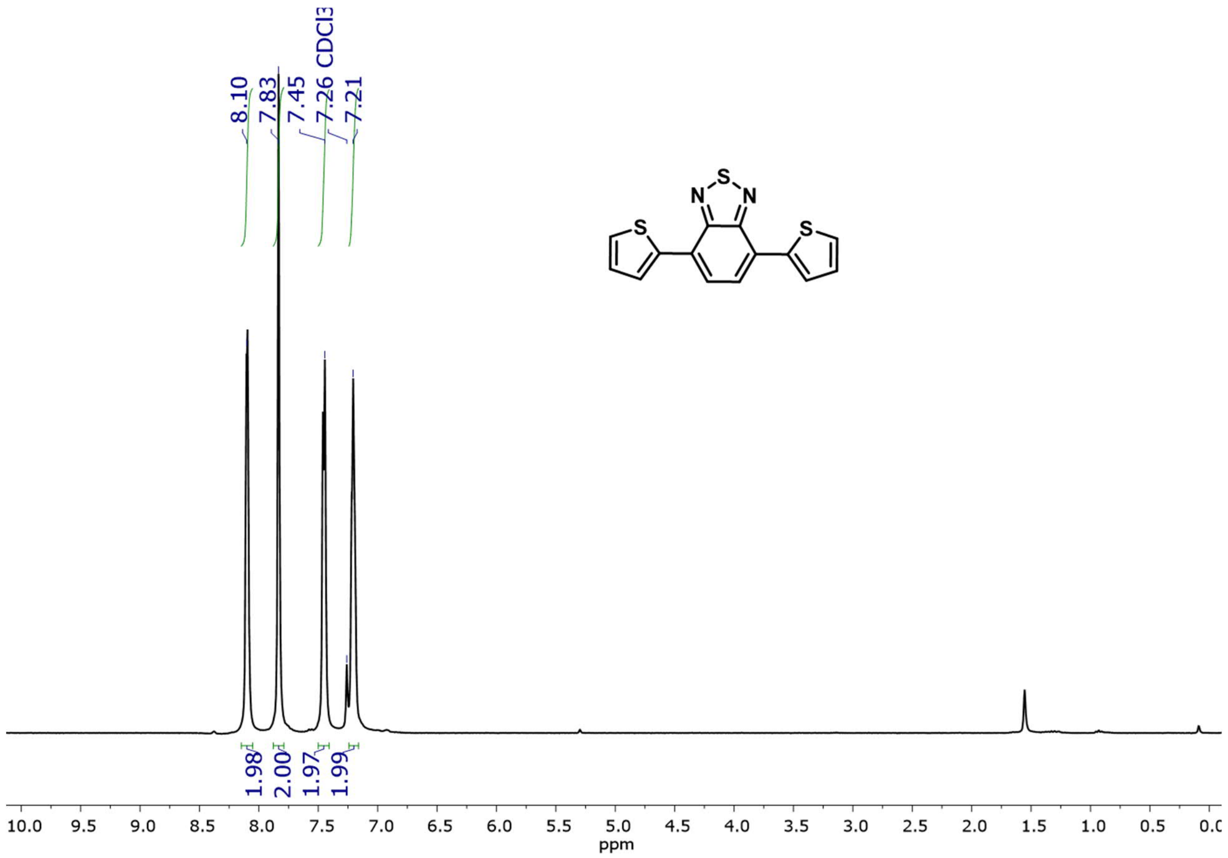
8.10
7.83
7.45
7.26 CDCl3
7.21
S
N
N
S
S
1.98
2.00
1.97
1.99
10.0
9.5
9.0
8.5
8.0
7.5
7.0
6.5
6.0
5.5
5.0
4.5
4.0
3.5
3.0
2.5
2.0
1.5
1.0
0.5
0.0
ppm

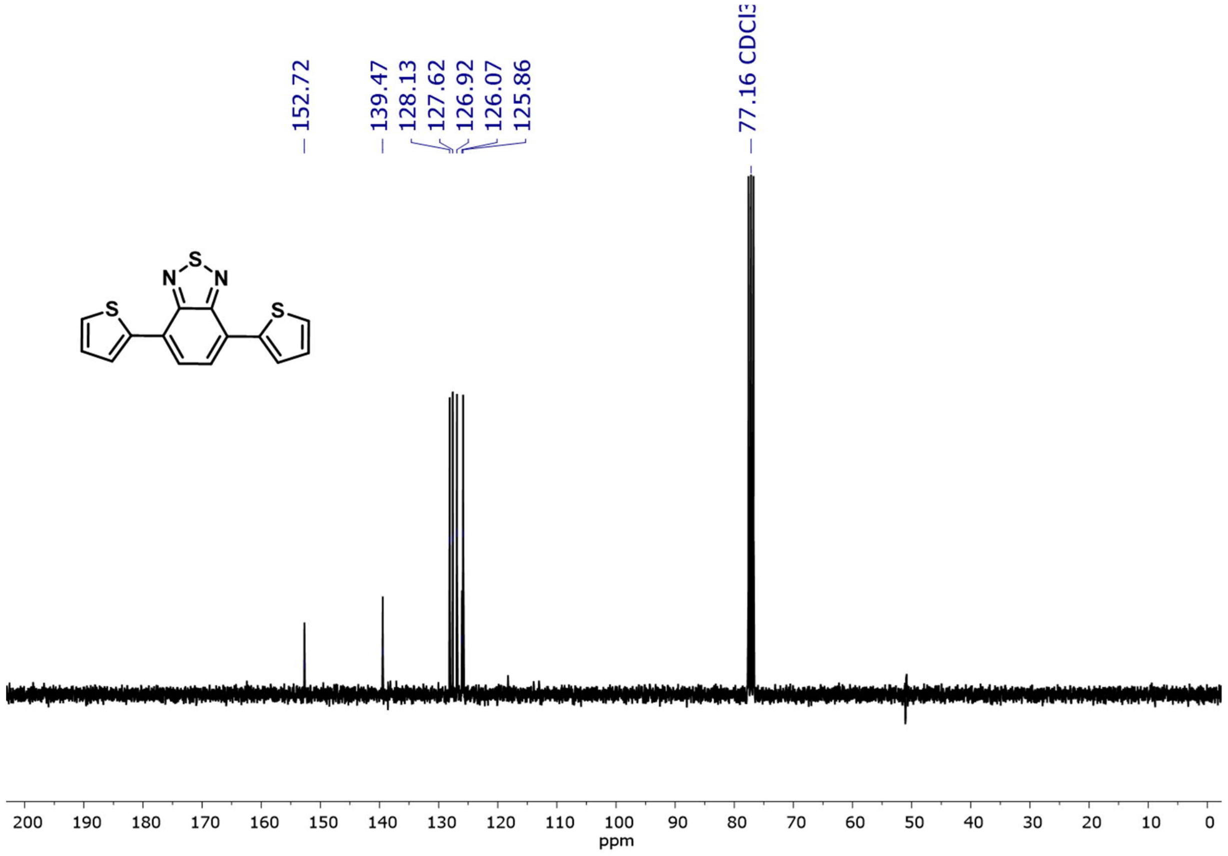
152.72
139.47
128.13
127.62
126.92
126.07
125.86
77.16 CDCl3
S
N
N
S
S
200
190
180
170
160
150
140
130
120
110
100
90
80
70
60
50
40
30
20
10
0
ppm

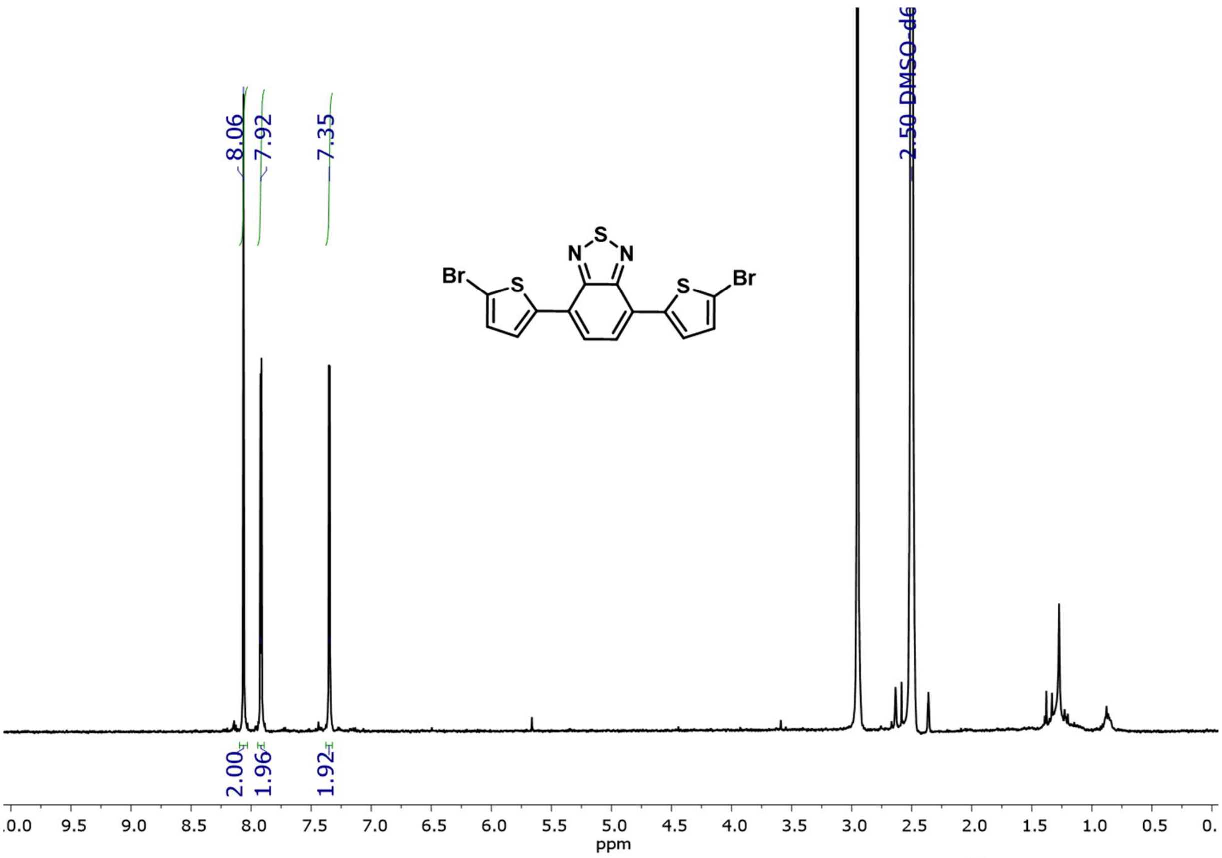
8.06
7.92
7.35
2.50 DMSO-d6
2.00
1.96
1.92
S
N
N
Br
S
S
Br
10.0
9.5
9.0
8.5
8.0
7.5
7.0
6.5
6.0
5.5
5.0
4.5
4.0
3.5
3.0
2.5
2.0
1.5
1.0
0.5
0.
ppm

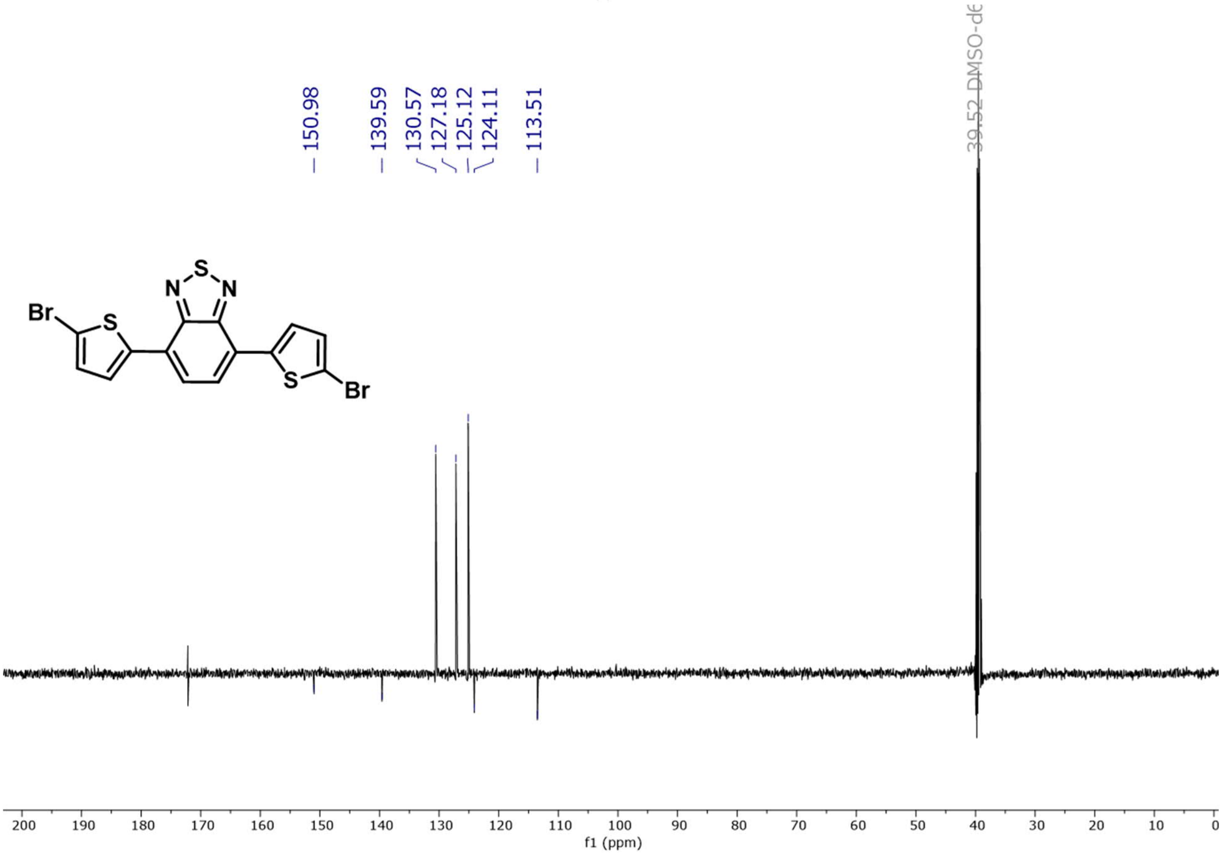
150.98
139.59
130.57
127.18
125.12
124.11
113.51
39.52 DMSO-d6
S
N
N
Br
S
S
Br
200
190
180
170
160
150
140
130
120
110
100
90
80
70
60
50
40
30
20
10
0
f1 (ppm)

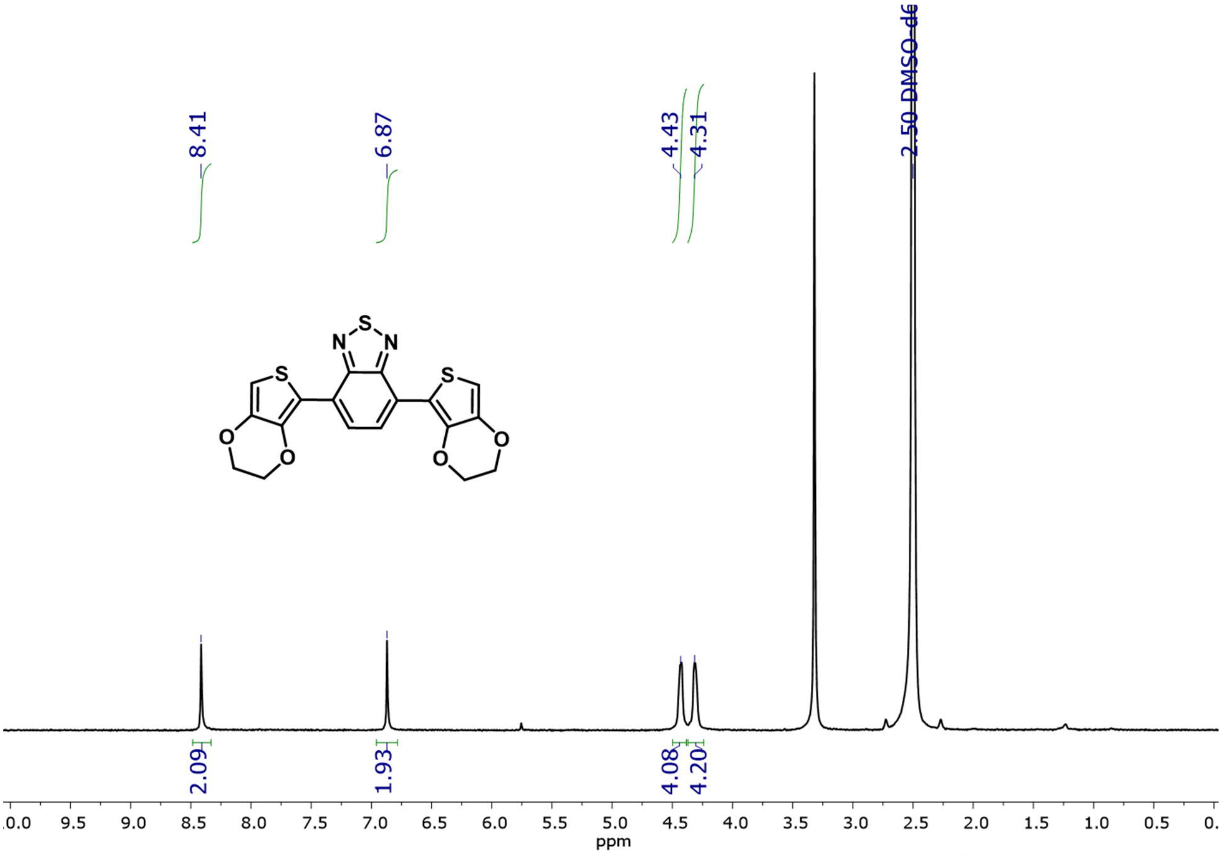
8.41
6.87
4.43
4.31
2.50 DMSO-d6
2.09
1.93
4.08
4.20
N S N
S
S
O
O
O
O
10.0 9.5 9.0 8.5 8.0 7.5 7.0 6.5 6.0 5.5 5.0 4.5 4.0 3.5 3.0 2.5 2.0 1.5 1.0 0.5 0.
ppm

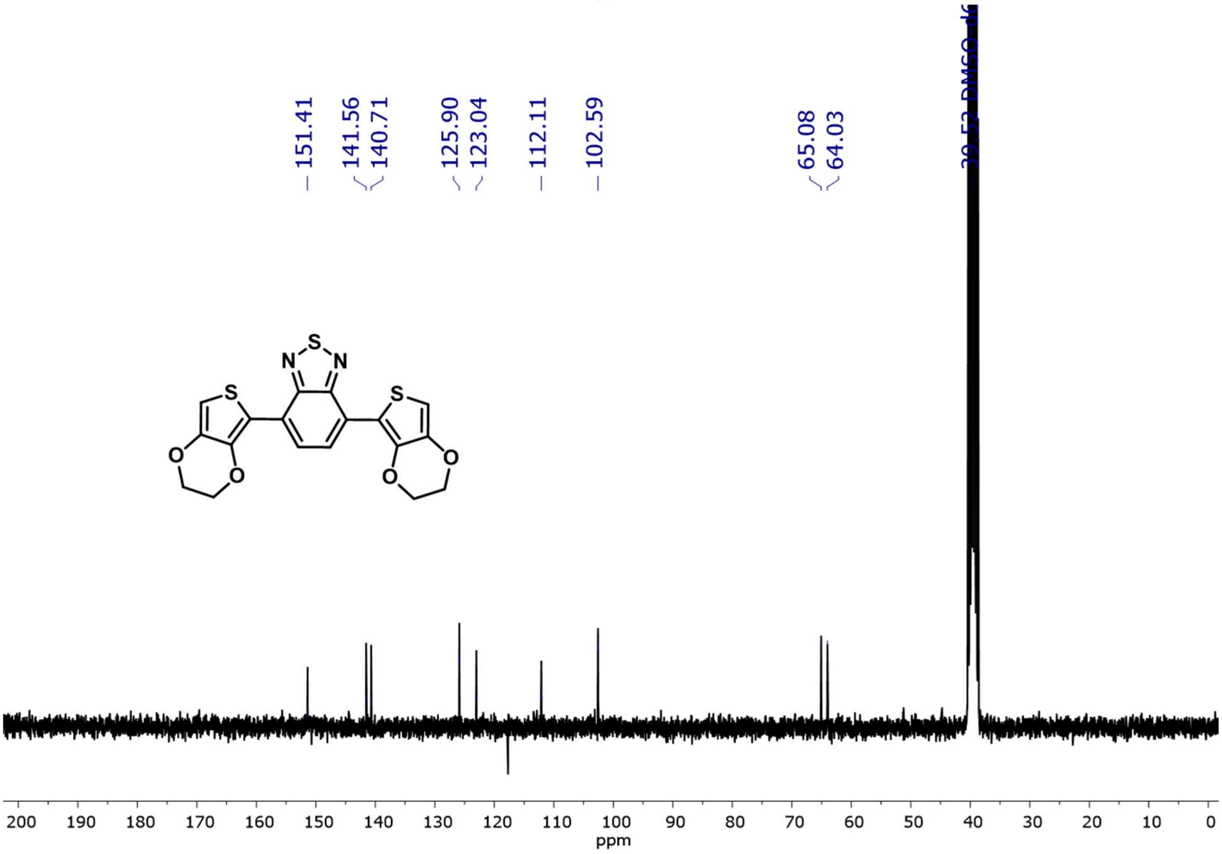
151.41
141.56
140.71
125.90
123.04
112.11
102.59
65.08
64.03
39.52 DMSO-d6
N S N
S
S
O
O
O
O
200 190 180 170 160 150 140 130 120 110 100 90 80 70 60 50 40 30 20 10 0
ppm

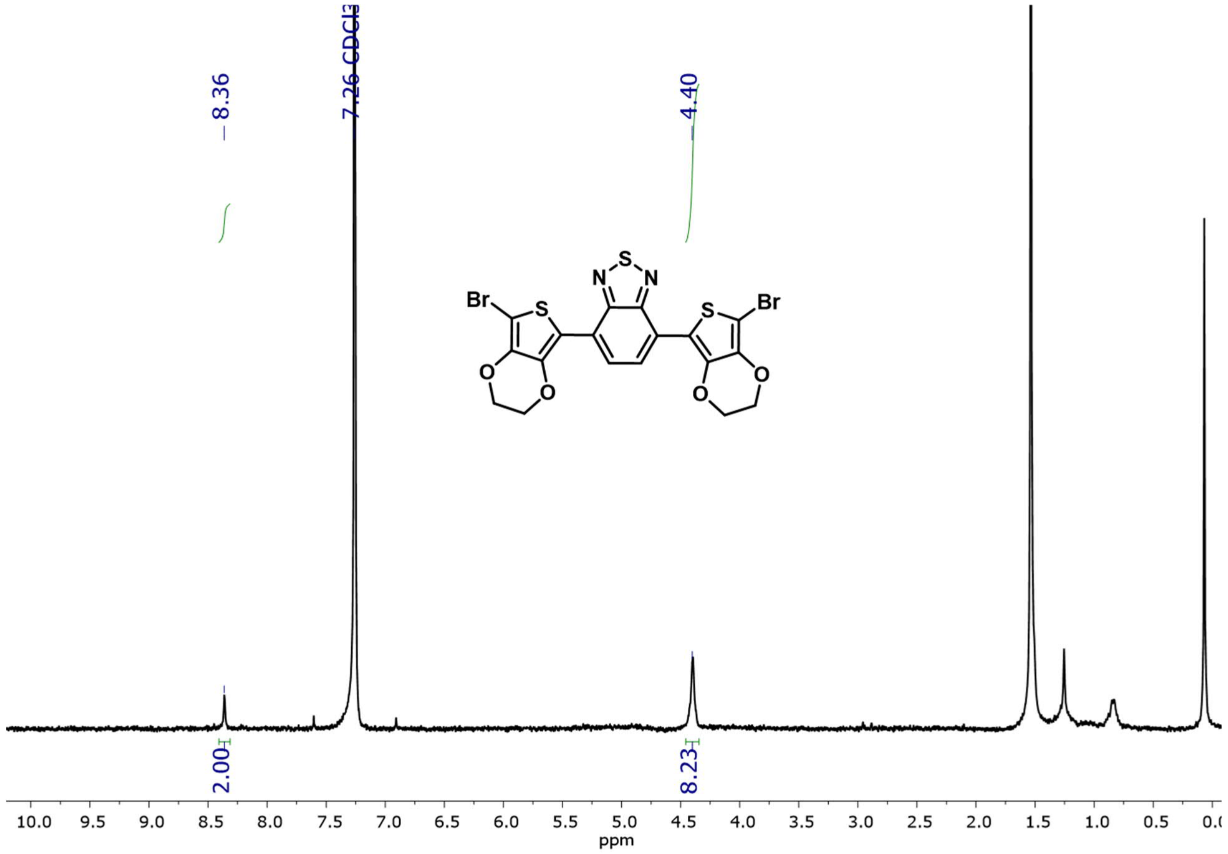
8.36
7.26 CDCl3
4.40
Br
S
N
N
S
Br
O
O
S
O
O
2.00
8.23
10.0
9.5
9.0
8.5
8.0
7.5
7.0
6.5
6.0
5.5
5.0
ppm
4.5
4.0
3.5
3.0
2.5
2.0
1.5
1.0
0.5

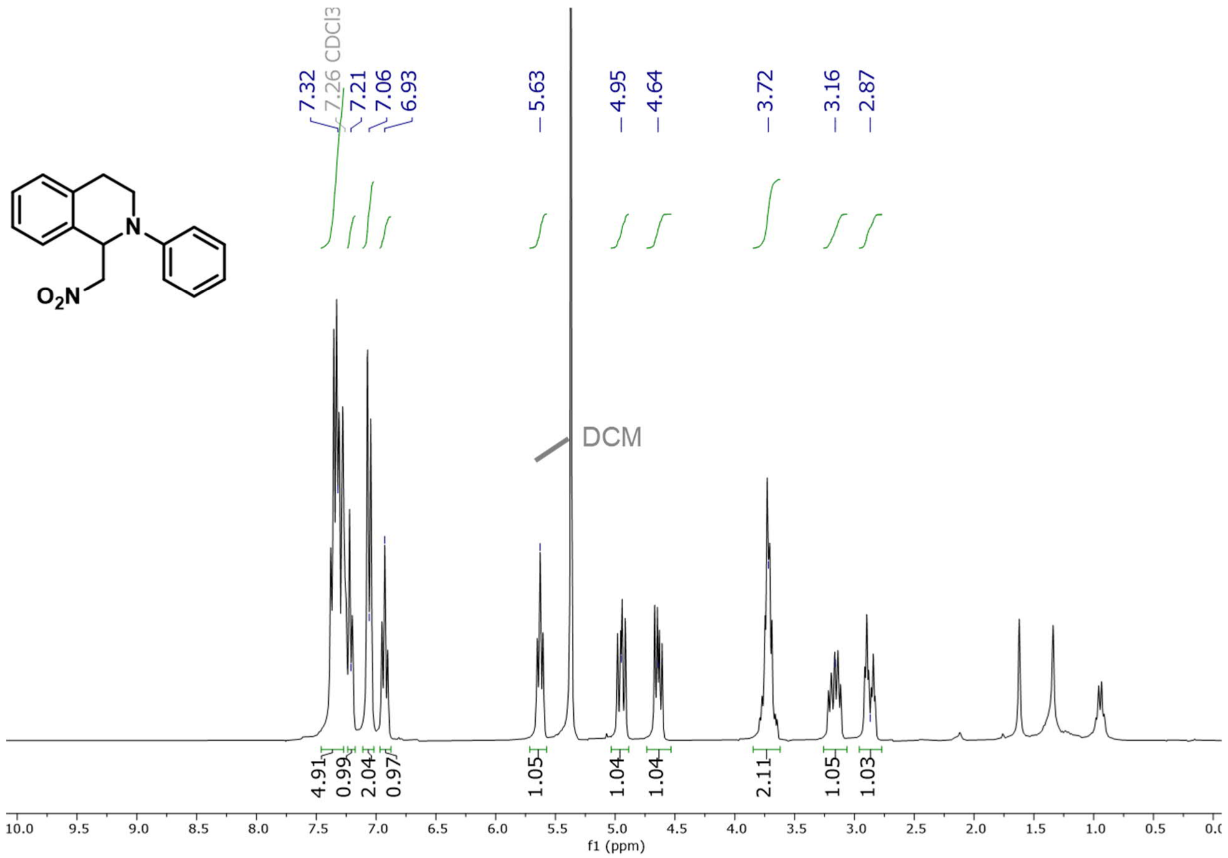
7.32
7.26 CDCl3
7.21
7.06
6.93
5.63
4.95
4.64
3.72
3.16
2.87
O2N
N
DCM
4.91
0.99
2.04
0.97
1.05
1.04
1.04
2.11
1.05
1.03
10.0
9.5
9.0
8.5
8.0
7.5
7.0
6.5
6.0
5.5
5.0
4.5
4.0
3.5
3.0
2.5
2.0
1.5
1.0
0.5
0.0
f1 (ppm)

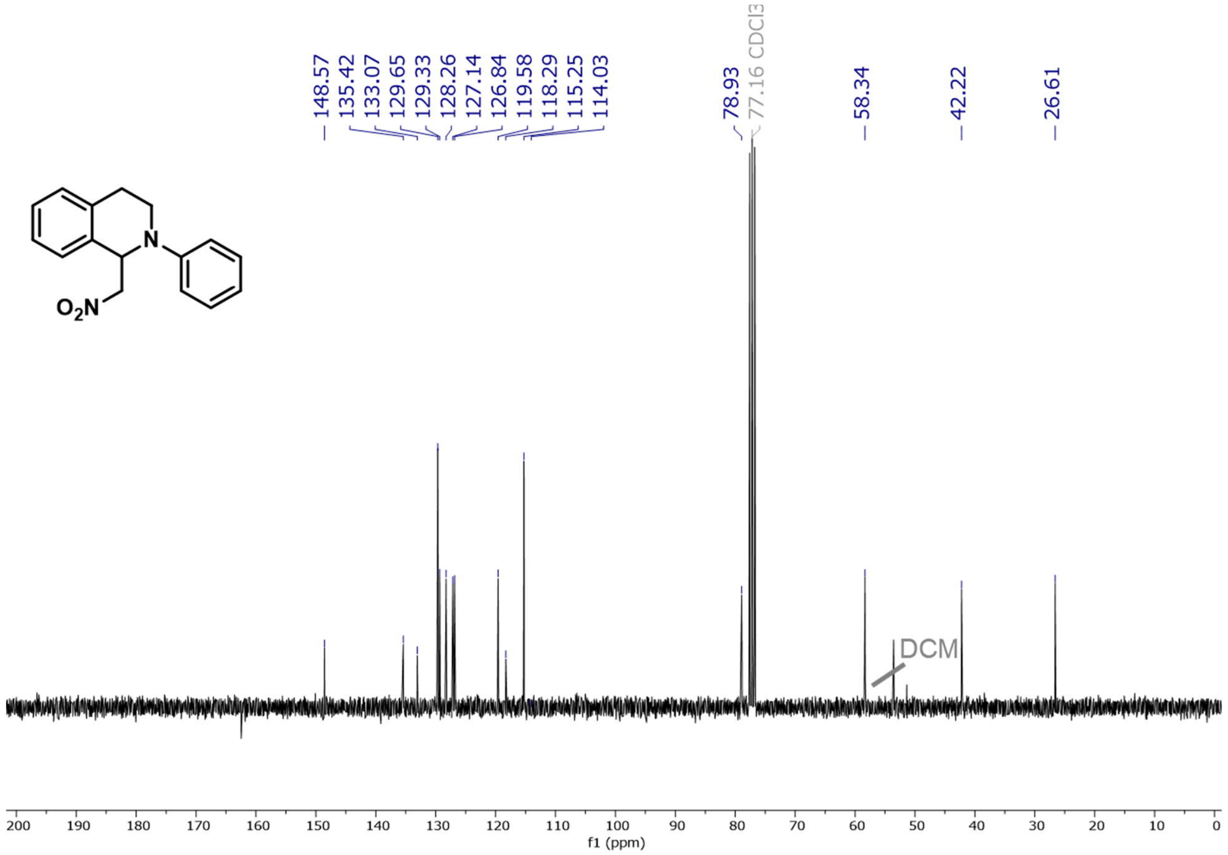
148.57
135.42
133.07
129.65
129.33
128.26
127.14
126.84
119.58
118.29
115.25
114.03
78.93
77.16 CDCl3
58.34
42.22
26.61
O2N
N
DCM
200
190
180
170
160
150
140
130
120
110
100
90
80
70
60
50
40
30
20
10
0
f1 (ppm)

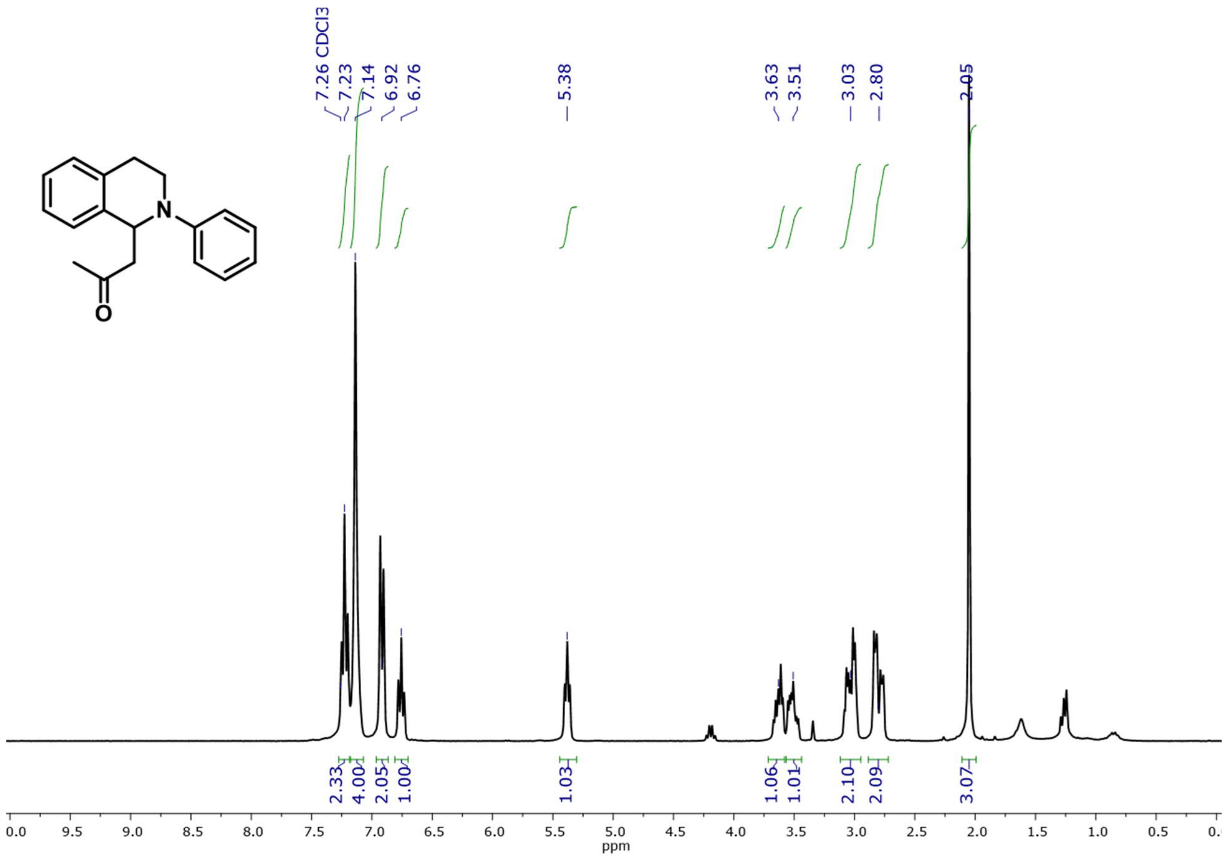
7.26 CDCl3
7.23
7.14
6.92
6.76
5.38
3.63
3.51
3.03
2.80
2.05
N
O
2.33
4.00
2.05
1.00
1.03
1.06
1.01
2.10
2.09
3.07
0.0
9.5
9.0
8.5
8.0
7.5
7.0
6.5
6.0
5.5
5.0
4.5
4.0
3.5
3.0
2.5
2.0
1.5
1.0
0.5
0.
ppm

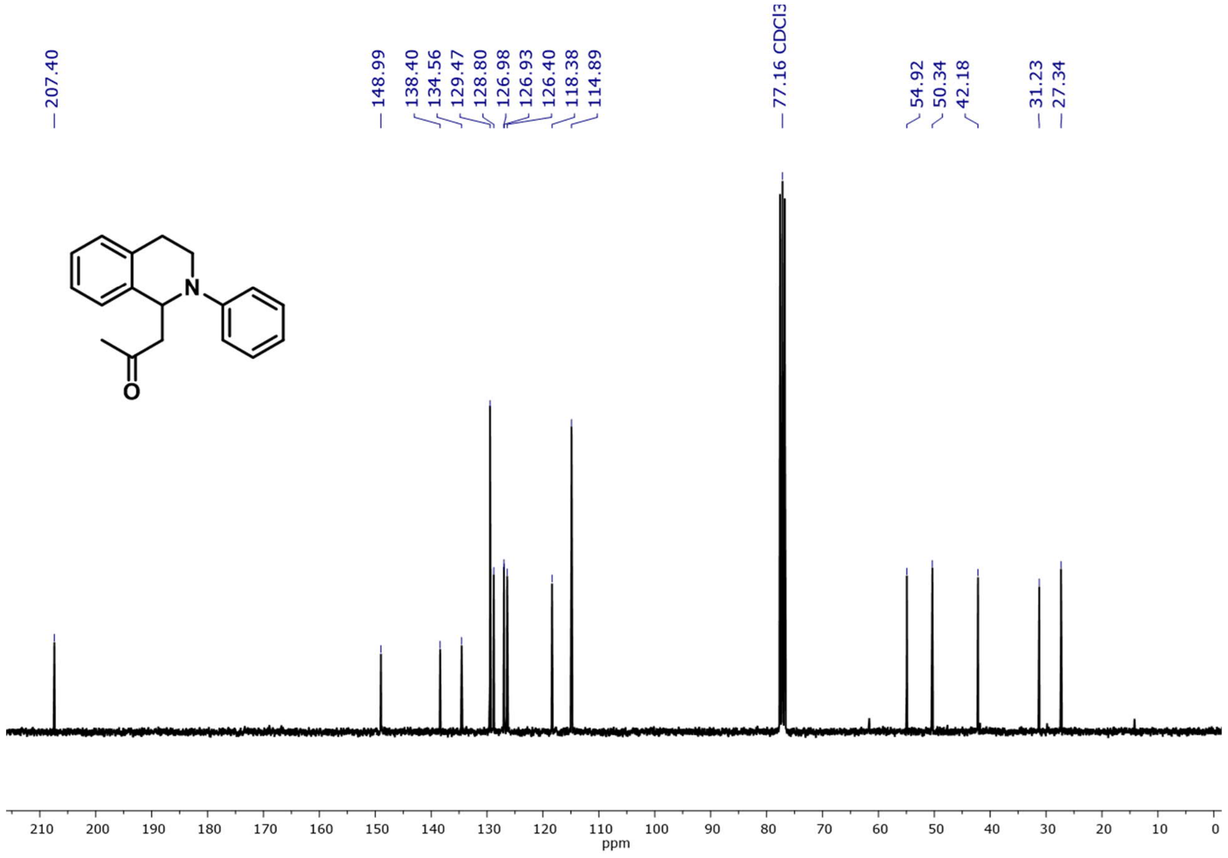
207.40
148.99
138.40
134.56
129.47
128.80
126.98
126.93
126.40
118.38
114.89
77.16 CDCl3
54.92
50.34
42.18
31.23
27.34
N
O
210
200
190
180
170
160
150
140
130
120
110
100
90
80
70
60
50
40
30
20
10
0
ppm

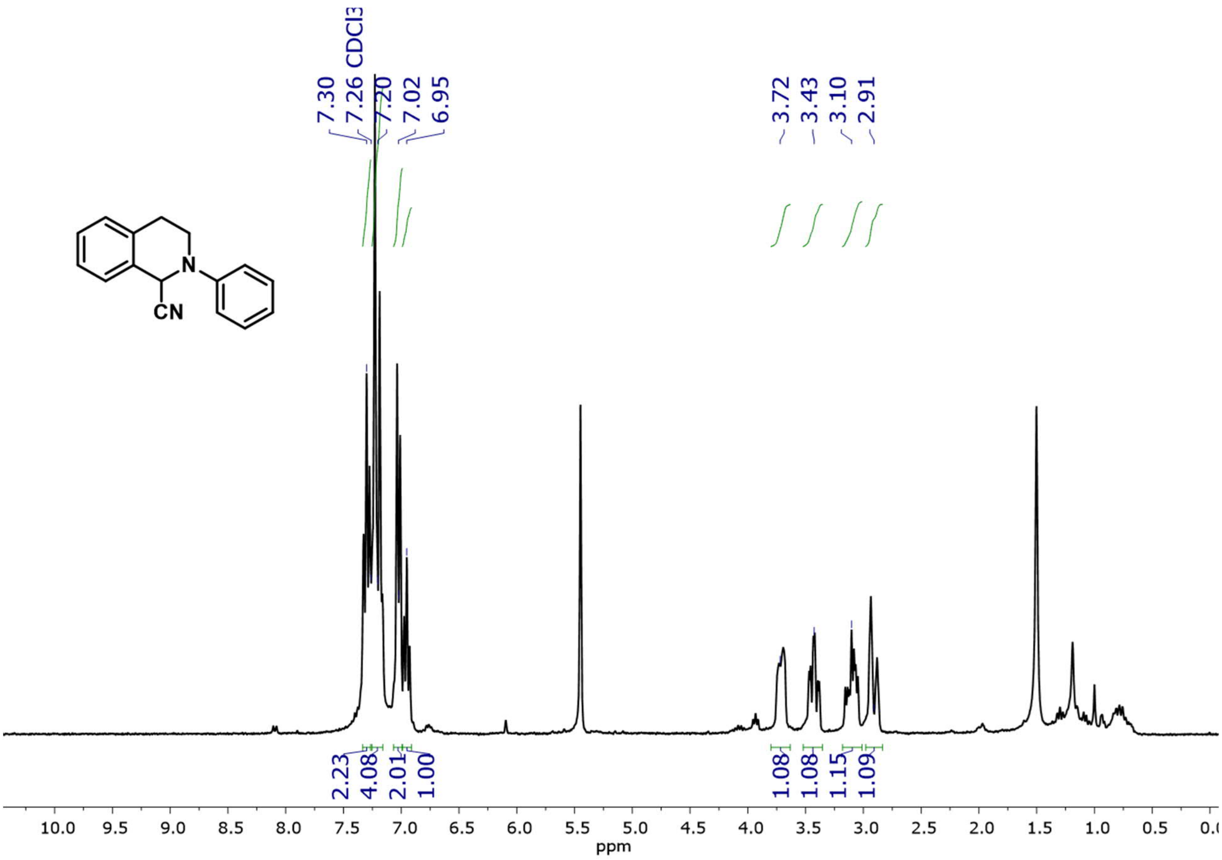
7.30
7.26 CDCl3
7.20
7.02
6.95
3.72
3.43
3.10
2.91
2.23
4.08
2.01
1.00
1.08
1.08
1.15
1.09
N
CN
10.0
9.5
9.0
8.5
8.0
7.5
7.0
6.5
6.0
5.5
5.0
4.5
4.0
3.5
3.0
2.5
2.0
1.5
1.0
0.5
ppm

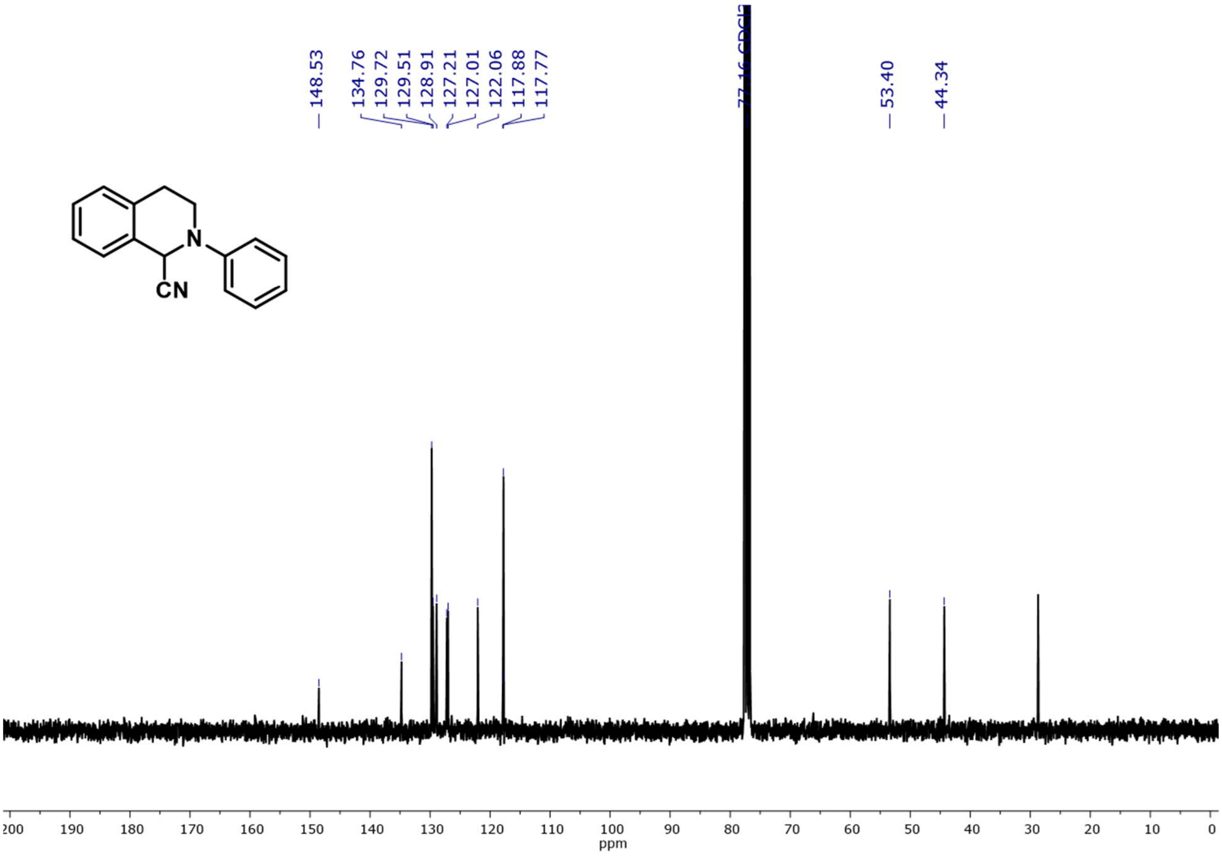
148.53
134.76
129.72
129.51
128.91
127.21
127.01
122.06
117.88
117.77
77.16 CDCl3
53.40
44.34
N
CN
190
180
170
160
150
140
130
120
110
100
90
80
70
60
50
40
30
20
10
0
ppm

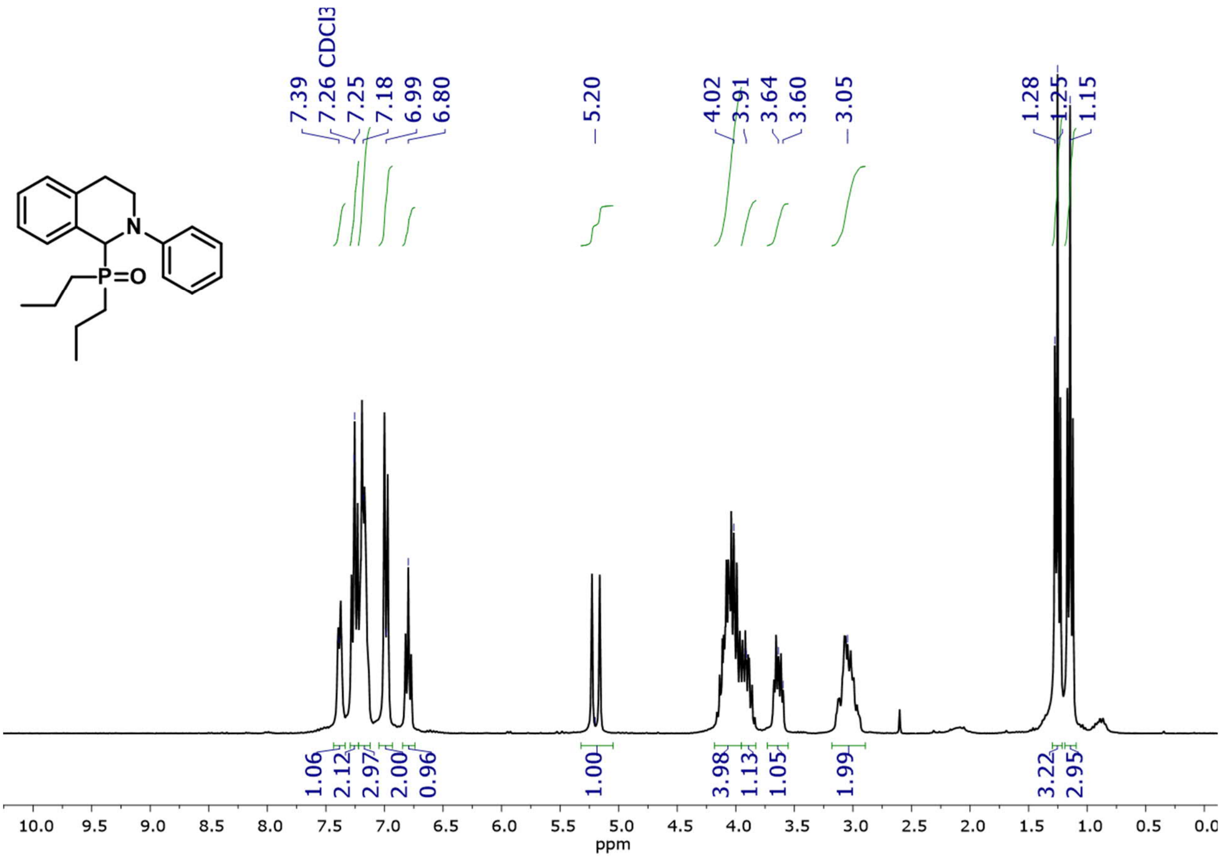
7.39
7.26 CDCl3
7.25
7.18
6.99
6.80
5.20
4.02
3.91
3.64
3.60
3.05
1.28
1.25
1.15
N
P
O
1.06
2.12
2.97
2.00
0.96
1.00
3.98
1.13
1.05
1.99
3.22
2.95
10.0
9.5
9.0
8.5
8.0
7.5
7.0
6.5
6.0
5.5
5.0
4.5
4.0
3.5
3.0
2.5
2.0
1.5
1.0
0.5
0.0
ppm

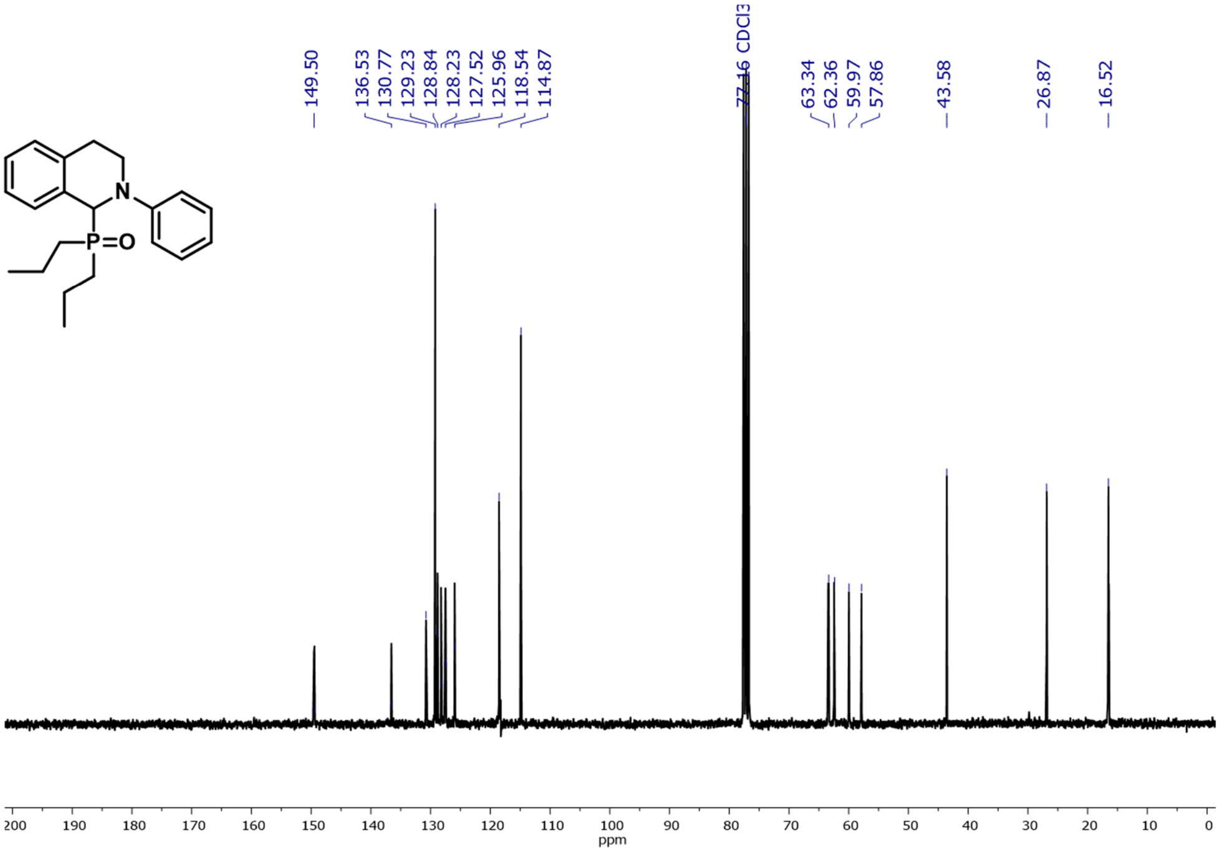
149.50
136.53
130.77
129.23
128.84
128.23
127.52
125.96
118.54
114.87
77.16 CDCl3
63.34
62.36
59.97
57.86
43.58
26.87
16.52
N
P
O
200
190
180
170
160
150
140
130
120
110
100
90
80
70
60
50
40
30
20
10
0
ppm

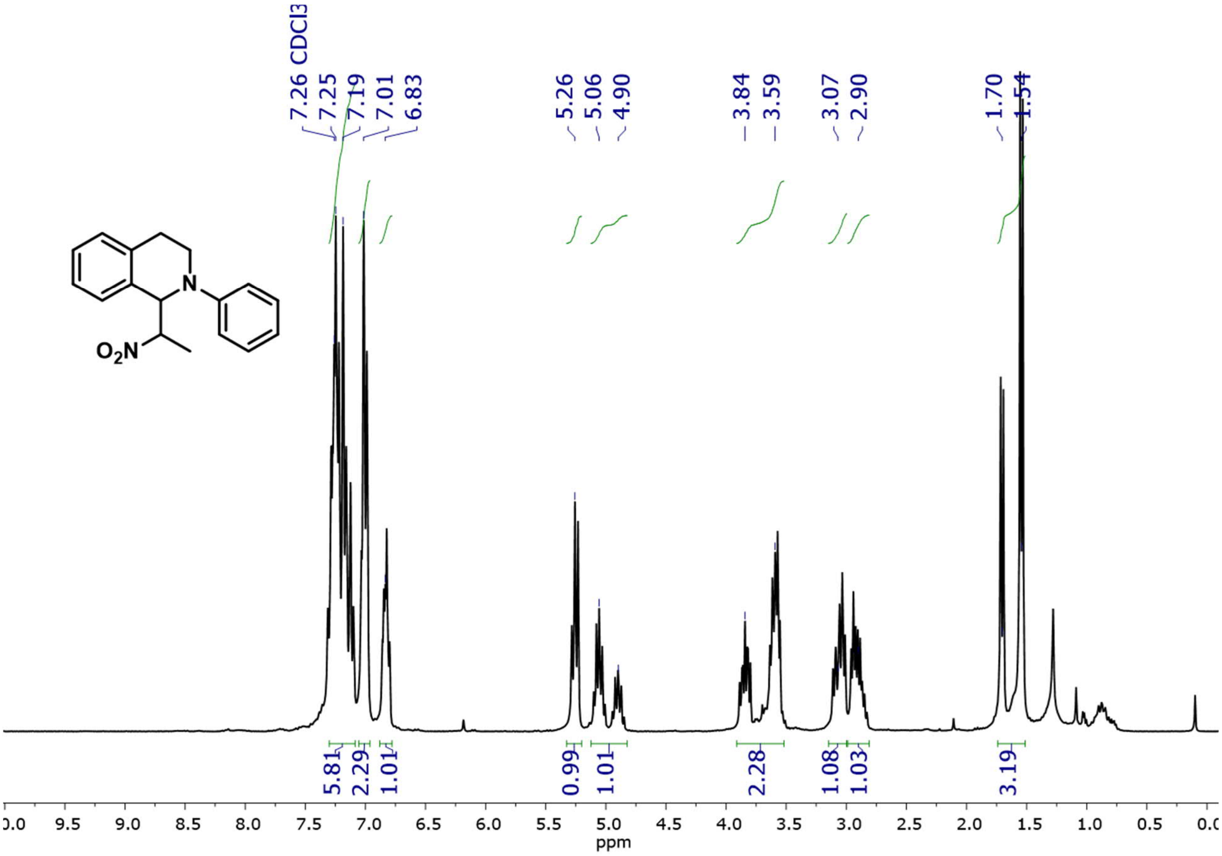
7.26 CDCl3
7.25
7.19
7.01
6.83
5.26
5.06
4.90
3.84
3.59
3.07
2.90
1.70
1.54
5.81
2.29
1.01
0.99
1.01
2.28
1.08
1.03
3.19
O_2N
N
9.5
9.0
8.5
8.0
7.5
7.0
6.5
6.0
5.5
5.0
4.5
4.0
3.5
3.0
2.5
2.0
1.5
1.0
0.5
ppm

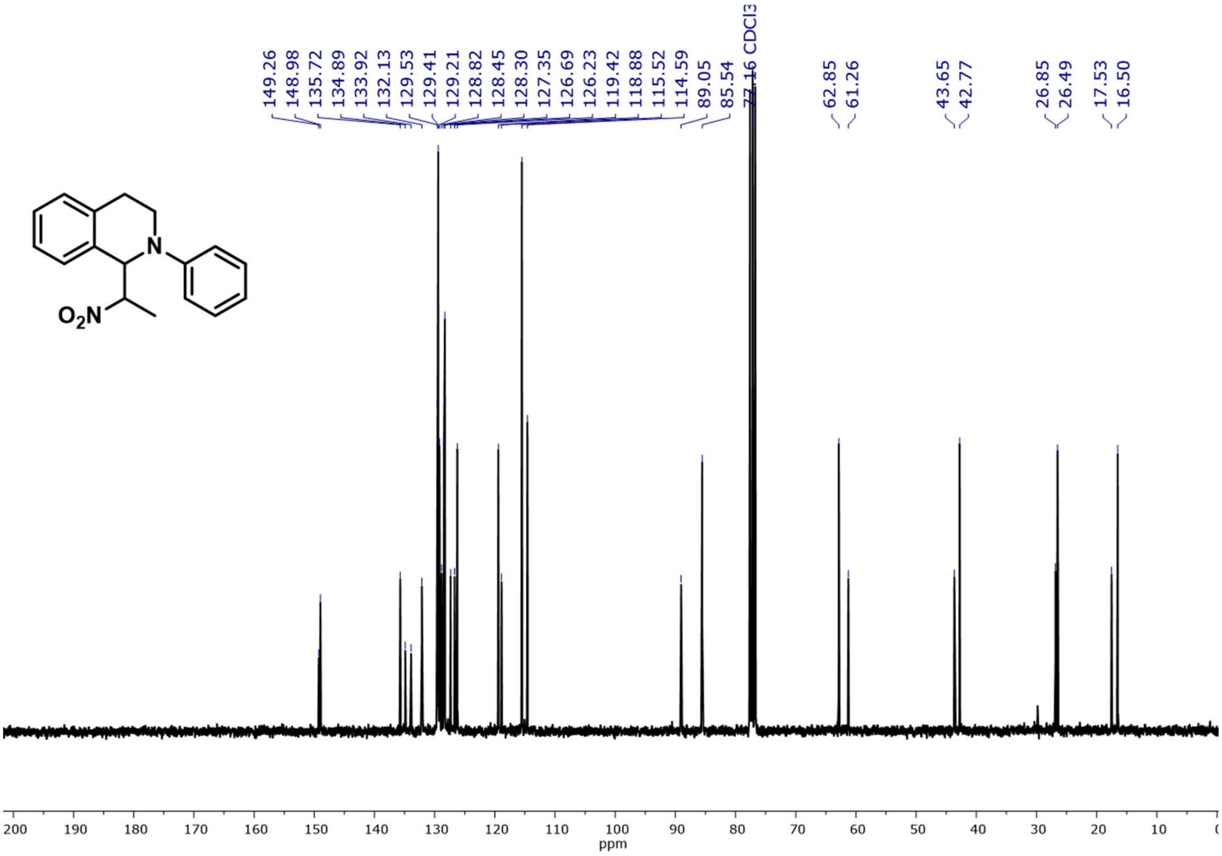
149.26
148.98
135.72
134.89
133.92
132.13
129.53
129.41
129.21
128.82
128.45
128.30
127.35
126.69
126.23
119.42
118.88
115.52
114.59
89.05
85.54
77.16 CDCl3
62.85
61.26
43.65
42.77
26.85
26.49
17.53
16.50
O_2N
N
200
190
180
170
160
150
140
130
120
110
100
90
80
70
60
50
40
30
20
10
ppm

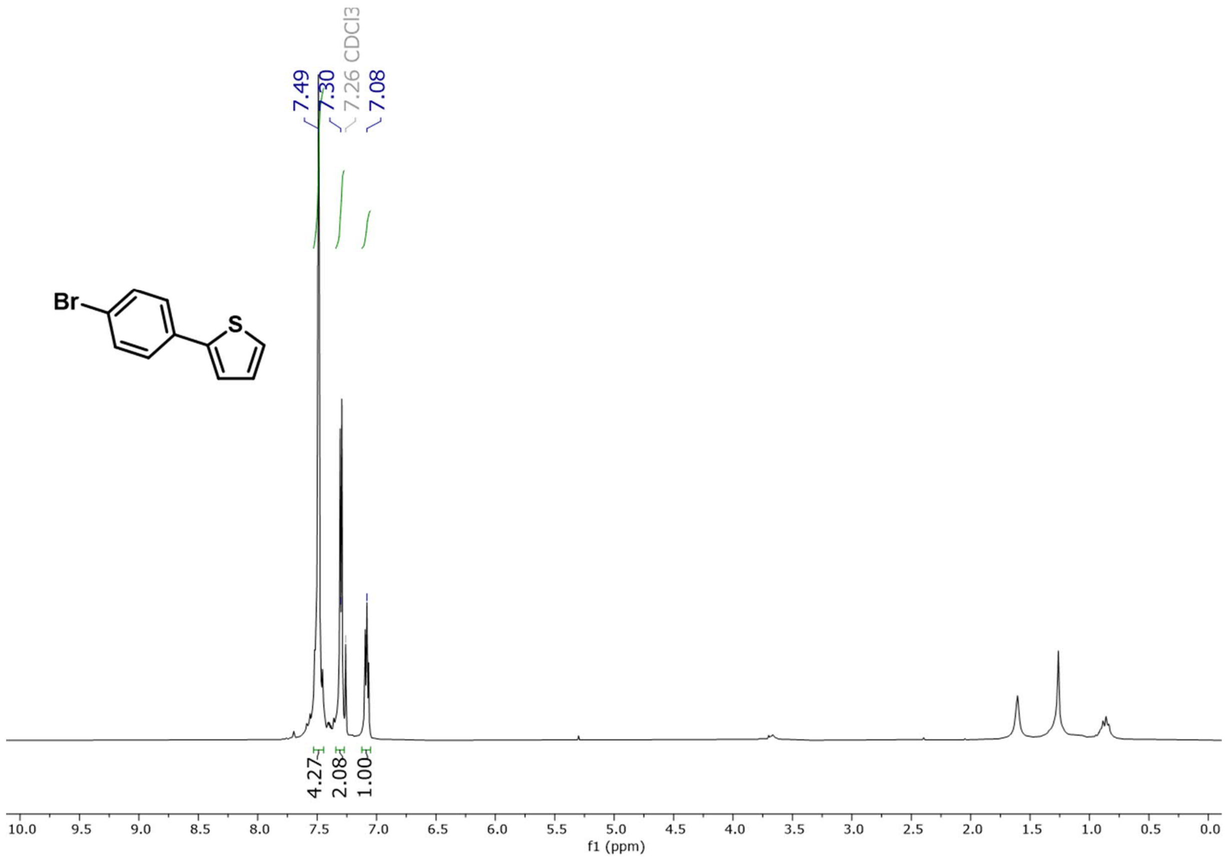
7.49
7.30
7.26 CDCl3
7.08
Br
S
4.27
2.08
1.00
10.0 9.5 9.0 8.5 8.0 7.5 7.0 6.5 6.0 5.5 5.0 4.5 4.0 3.5 3.0 2.5 2.0 1.5 1.0 0.5 0.0
f1 (ppm)

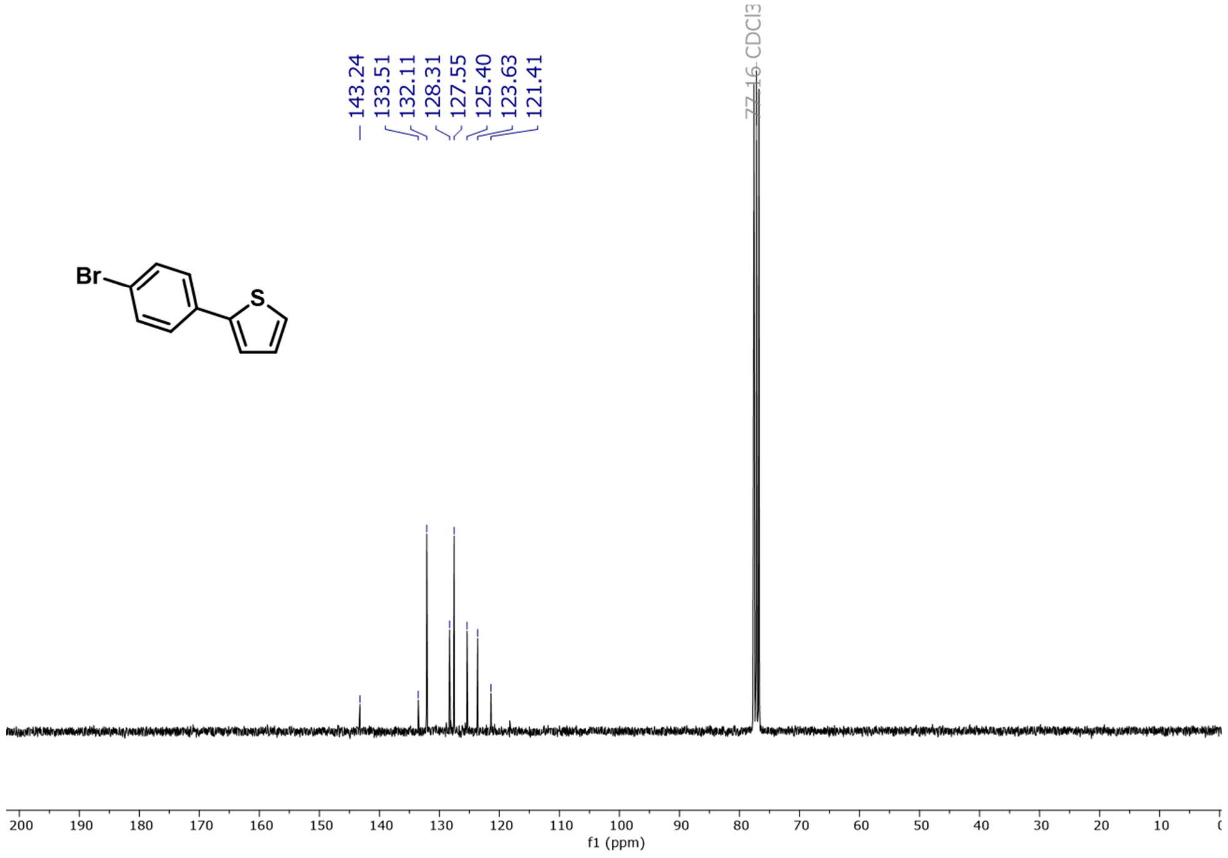
143.24
133.51
132.11
128.31
127.55
125.40
123.63
121.41
77.16 CDCl3
Br
S
200 190 180 170 160 150 140 130 120 110 100 90 80 70 60 50 40 30 20 10 0
f1 (ppm)

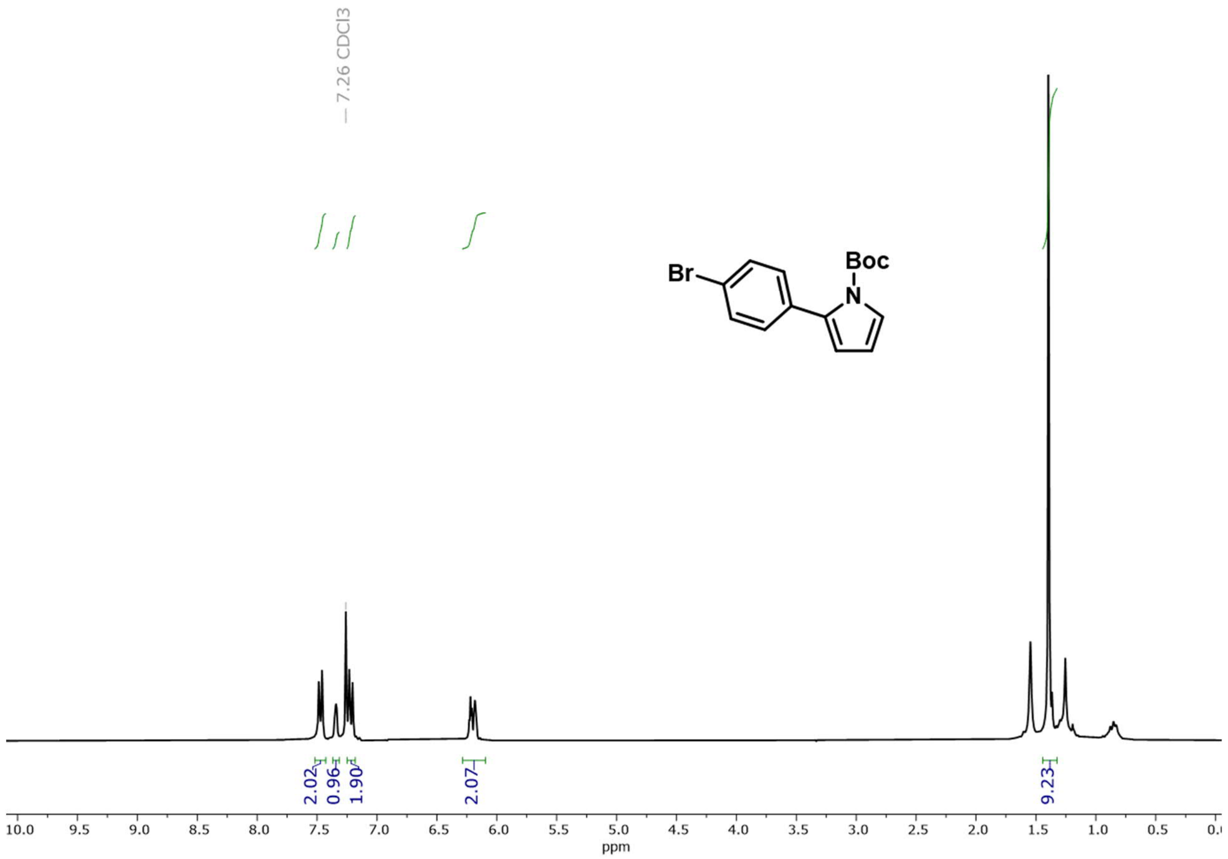
7.26 CDCl3
Br
Boc
N
2.02
0.96
1.90
2.07
9.23
10.0
9.5
9.0
8.5
8.0
7.5
7.0
6.5
6.0
5.5
5.0
4.5
4.0
3.5
3.0
2.5
2.0
1.5
1.0
0.5
0.0
ppm

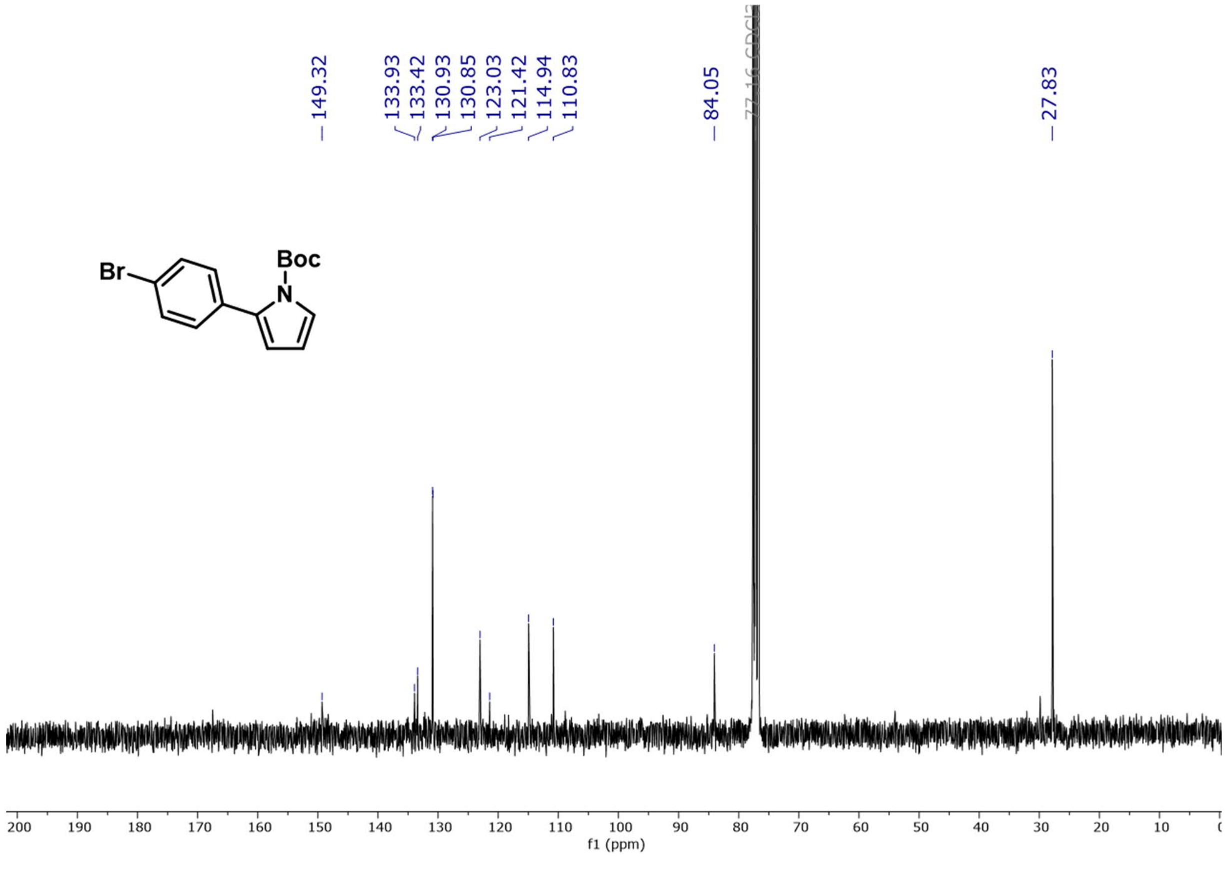
149.32
133.93
133.42
130.93
130.85
123.03
121.42
114.94
110.83
84.05
77.16 CDCl3
27.83
Br
Boc
N
200
190
180
170
160
150
140
130
120
110
100
90
80
70
60
50
40
30
20
10
0
f1 (ppm)

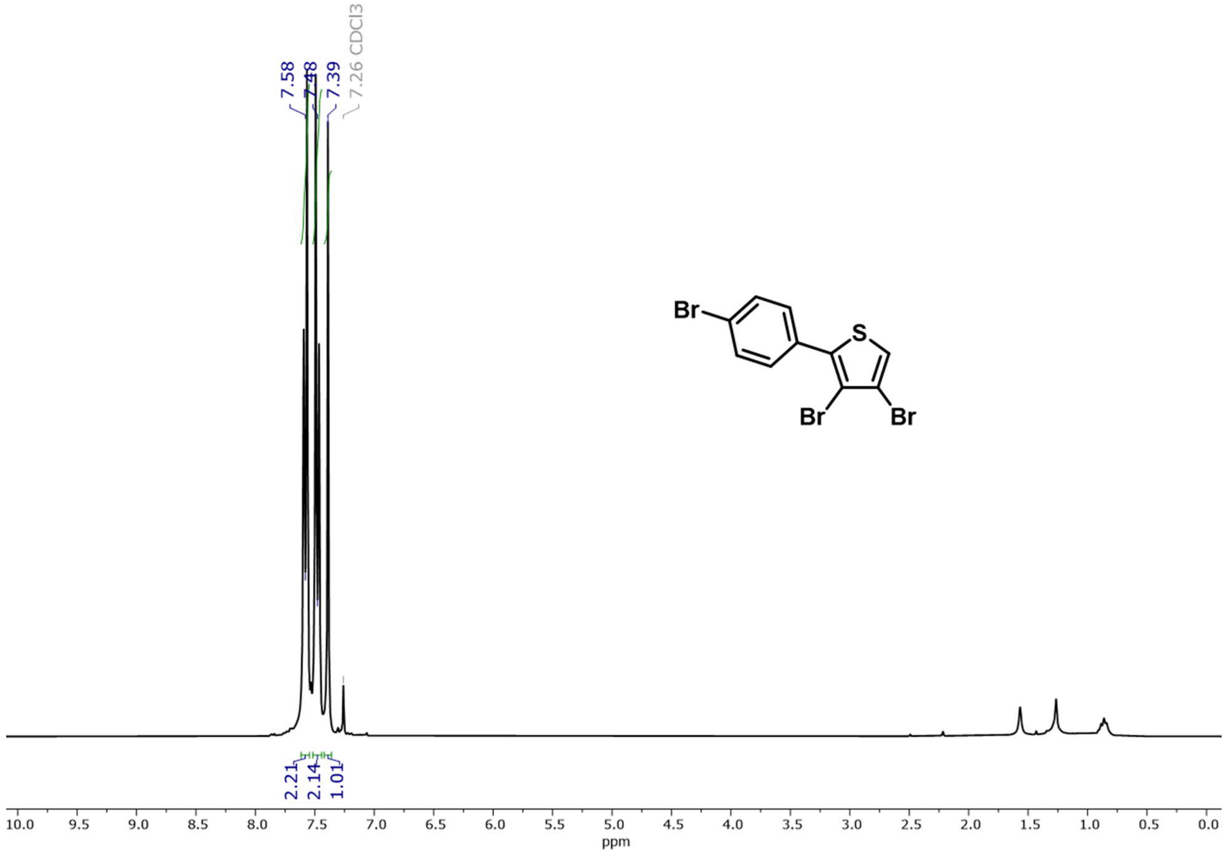
7.58
7.48
7.39
7.26 CDCl3
Br
S
Br
Br
2.21
2.14
1.01
10.0
9.5
9.0
8.5
8.0
7.5
7.0
6.5
6.0
5.5
5.0
4.5
4.0
3.5
3.0
2.5
2.0
1.5
1.0
0.5
0.0
ppm

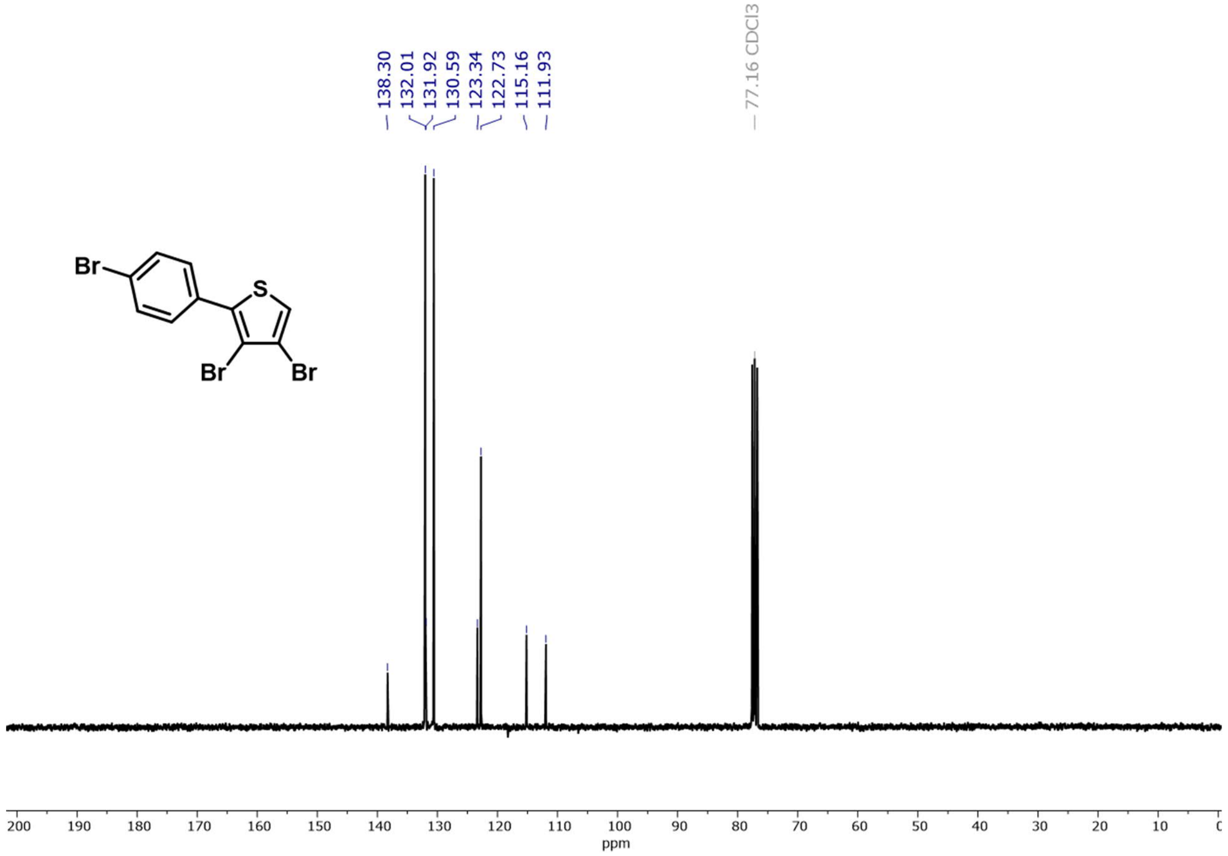
138.30
132.01
131.92
130.59
123.34
122.73
115.16
111.93
77.16 CDCl3
Br
S
Br
Br
200
190
180
170
160
150
140
130
120
110
100
90
80
70
60
50
40
30
20
10
0
ppm

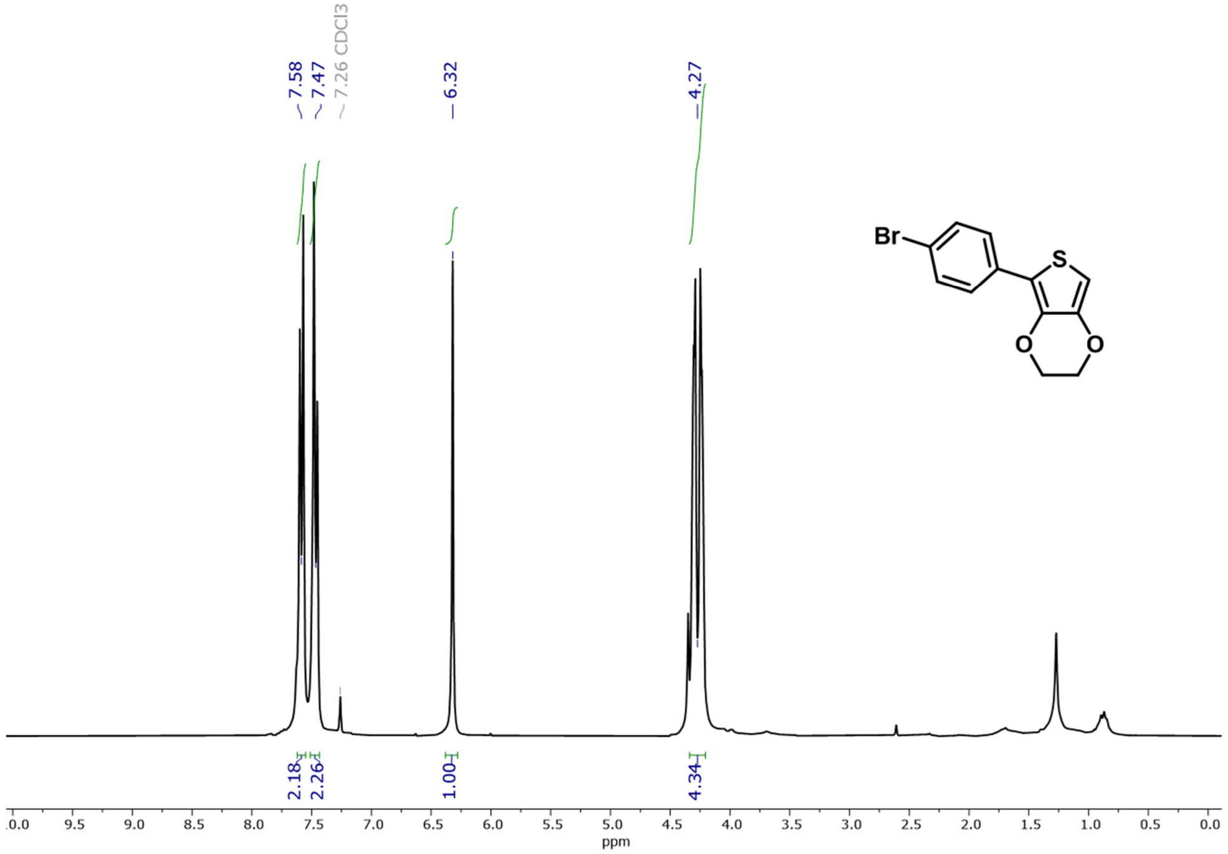
7.58
7.47
7.26 CDCl3
6.32
4.27
Br
S
O
O
2.18
2.26
1.00
4.34
10.0
9.5
9.0
8.5
8.0
7.5
7.0
6.5
6.0
5.5
5.0
4.5
4.0
3.5
3.0
2.5
2.0
1.5
1.0
0.5
0.0
ppm

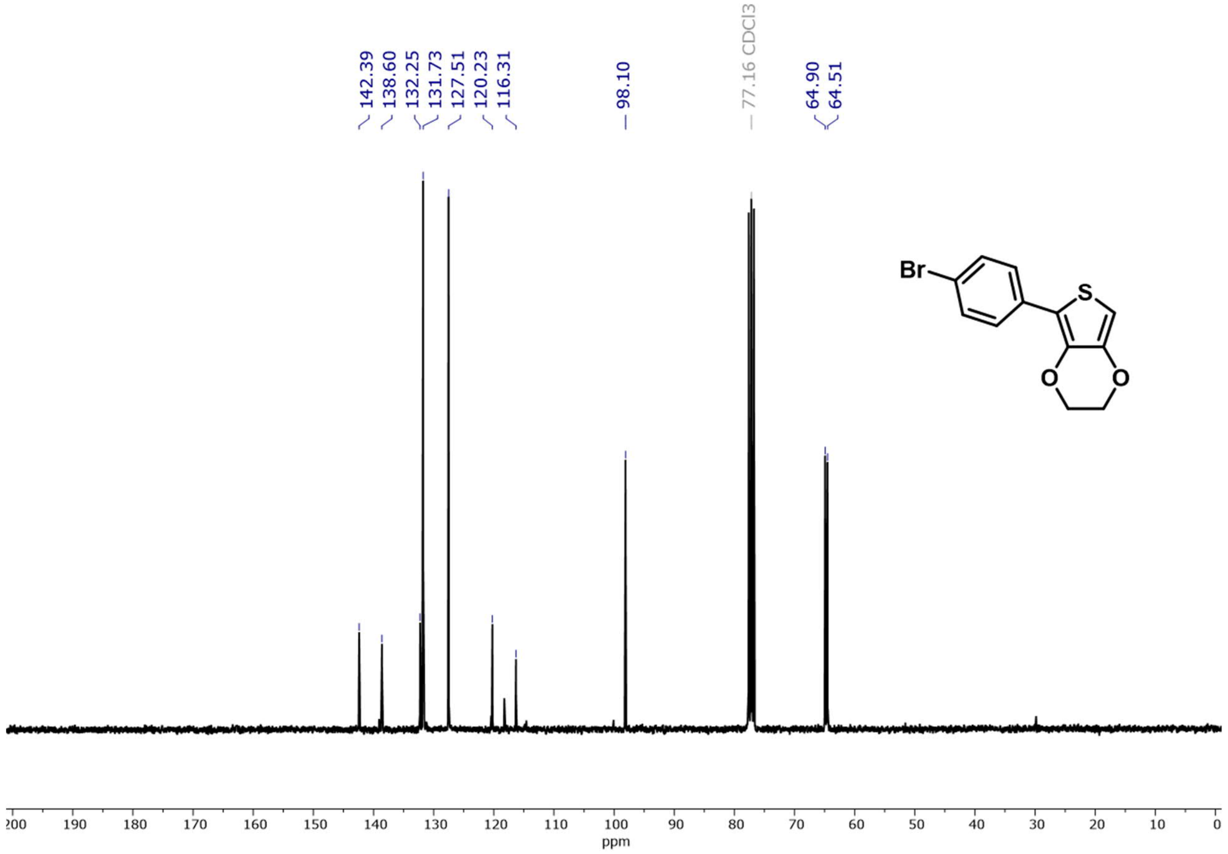
142.39
138.60
132.25
131.73
127.51
120.23
116.31
98.10
77.16 CDCl3
64.90
64.51
Br
S
O
O
200
190
180
170
160
150
140
130
120
110
100
90
80
70
60
50
40
30
20
10
0
ppm

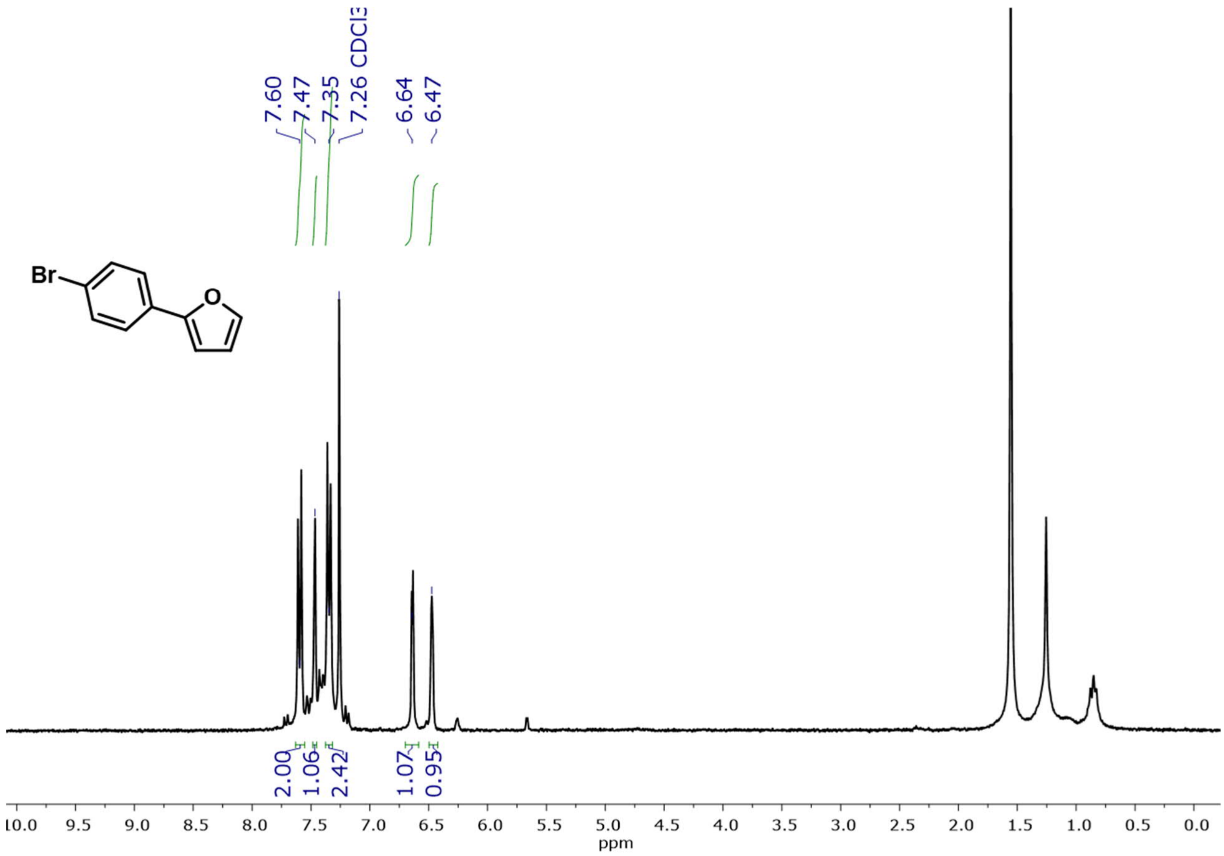
7.60
7.47
7.35
7.26 CDCl3
6.64
6.47
Br
O
2.00
1.06
2.42
1.07
0.95
10.0
9.5
9.0
8.5
8.0
7.5
7.0
6.5
6.0
5.5
5.0
4.5
4.0
3.5
3.0
2.5
2.0
1.5
1.0
0.5
0.0
ppm

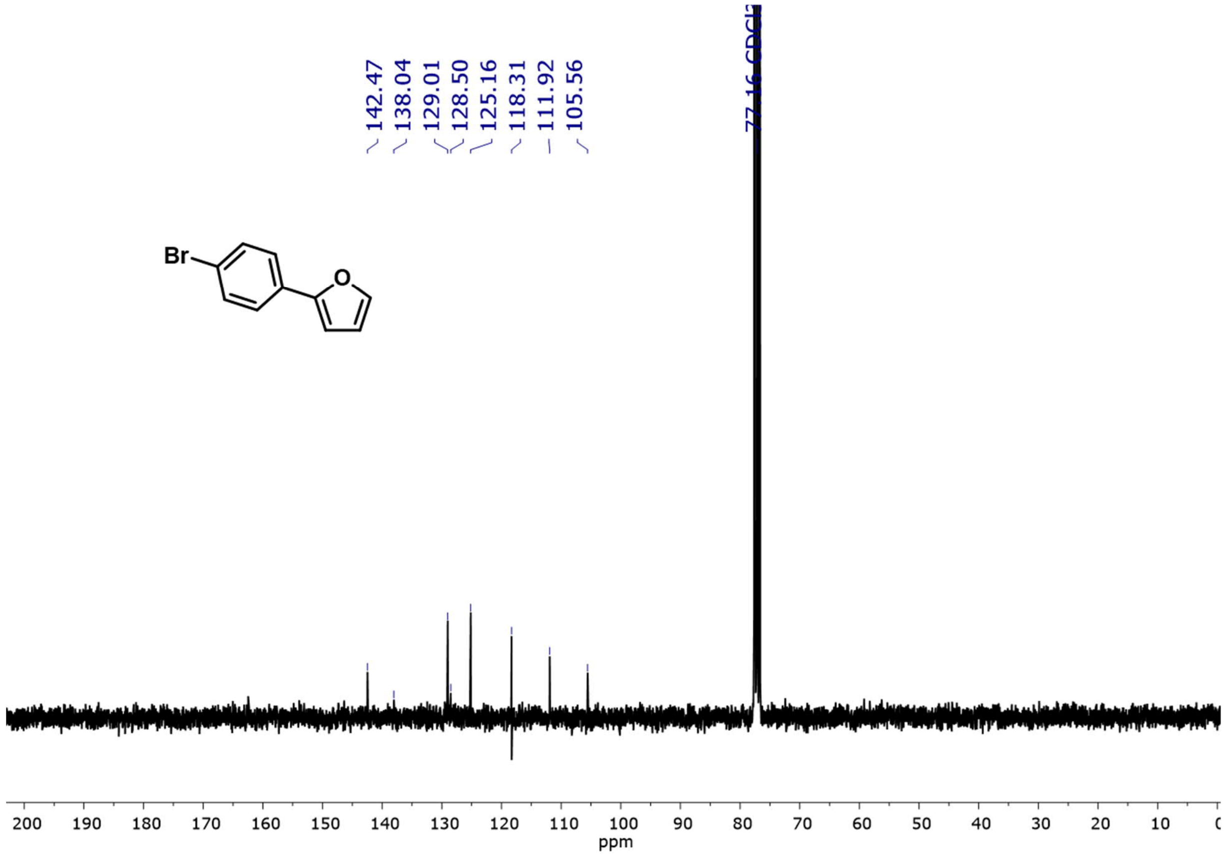
142.47
138.04
129.01
128.50
125.16
118.31
111.92
105.56
77.16 CDCl3
Br
O
200
190
180
170
160
150
140
130
120
110
100
90
80
70
60
50
40
30
20
10
0
ppm

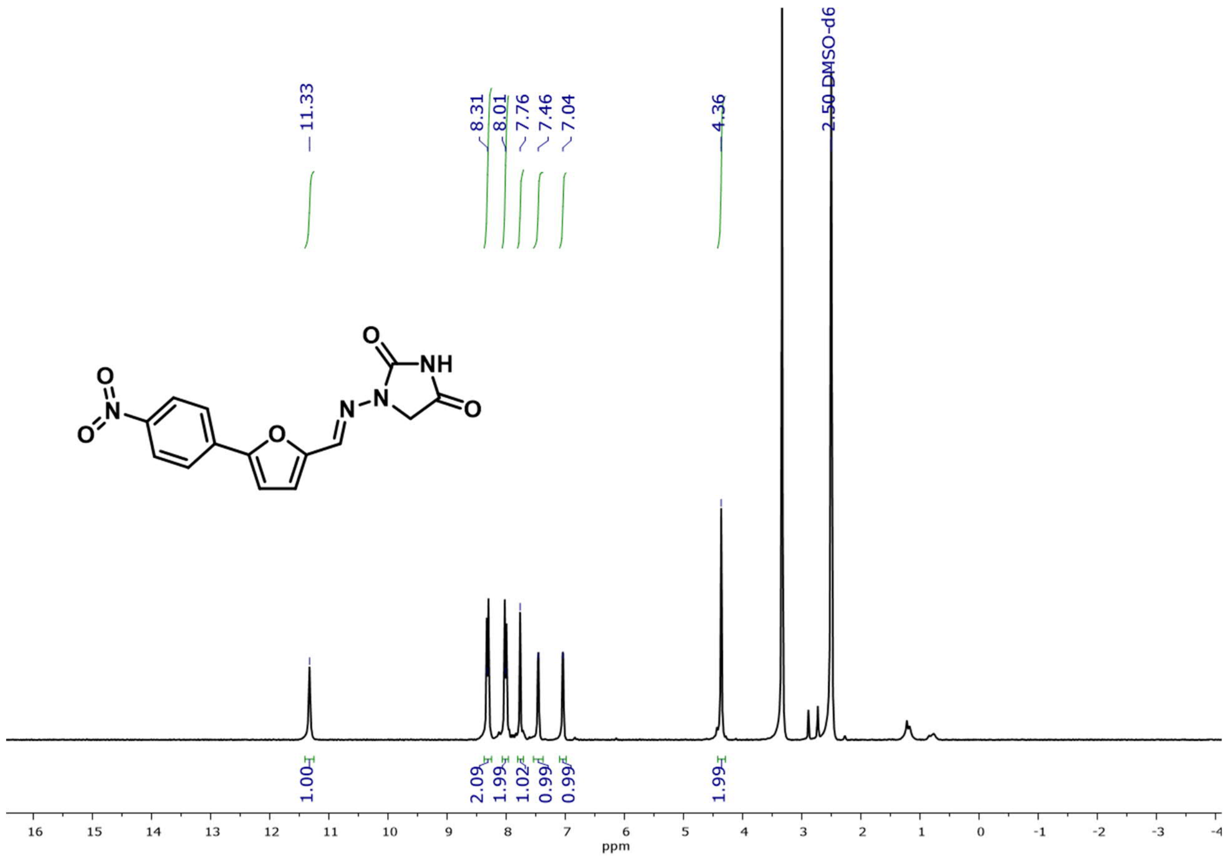
11.33
8.31
8.01
7.76
7.46
7.04
4.36
2.50 DMSO-d6
O
N
O
O
NH
N
N
O
O
1.00
2.09
1.99
1.02
0.99
0.99
1.99
16 15 14 13 12 11 10 9 8 7 6 5 4 3 2 1 0 -1 -2 -3 -4
ppm

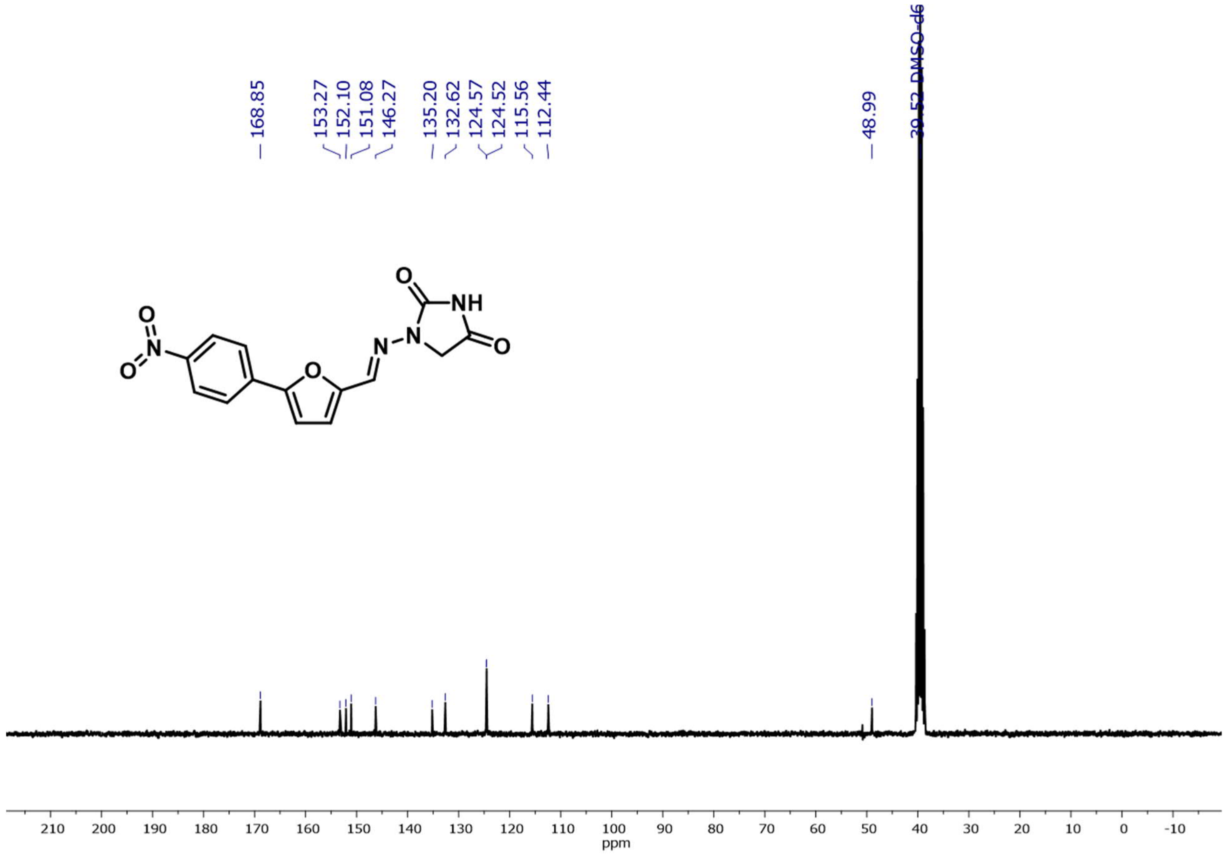
168.85
153.27
152.10
151.08
146.27
135.20
132.62
124.57
124.52
115.56
112.44
48.99
39.52 DMSO-d6
O
N
O
O
NH
N
N
O
O
210 200 190 180 170 160 150 140 130 120 110 100 90 80 70 60 50 40 30 20 10 0 -10
ppm

3.5 A PMMA-based heterogeneous photocatalyst for visible-light-promoted [4+2] cycloaddition

^{1}H and ^{13}C NMR spectra

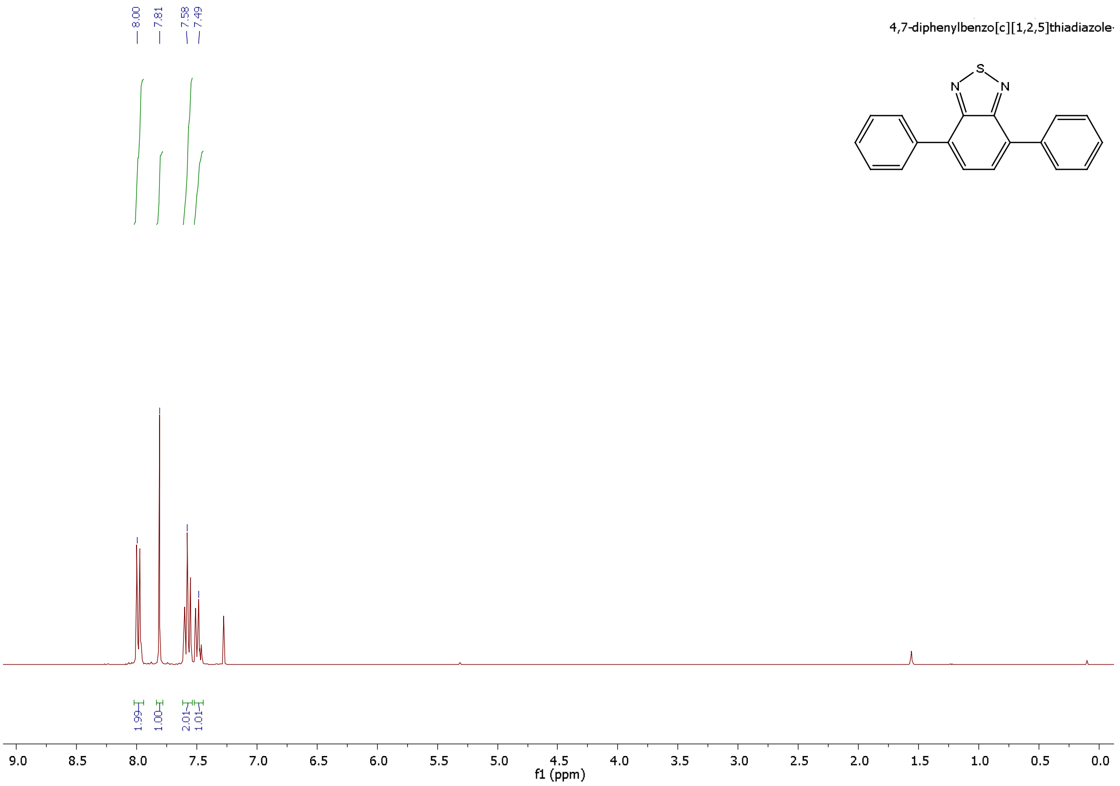

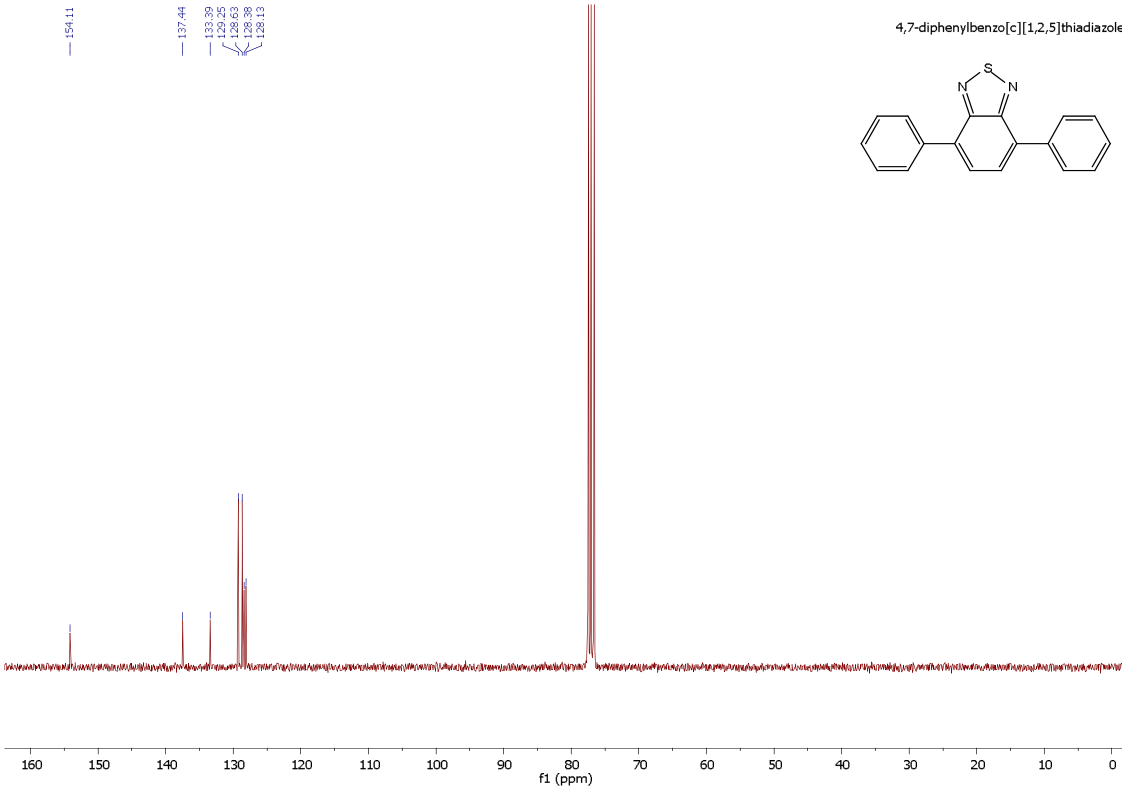

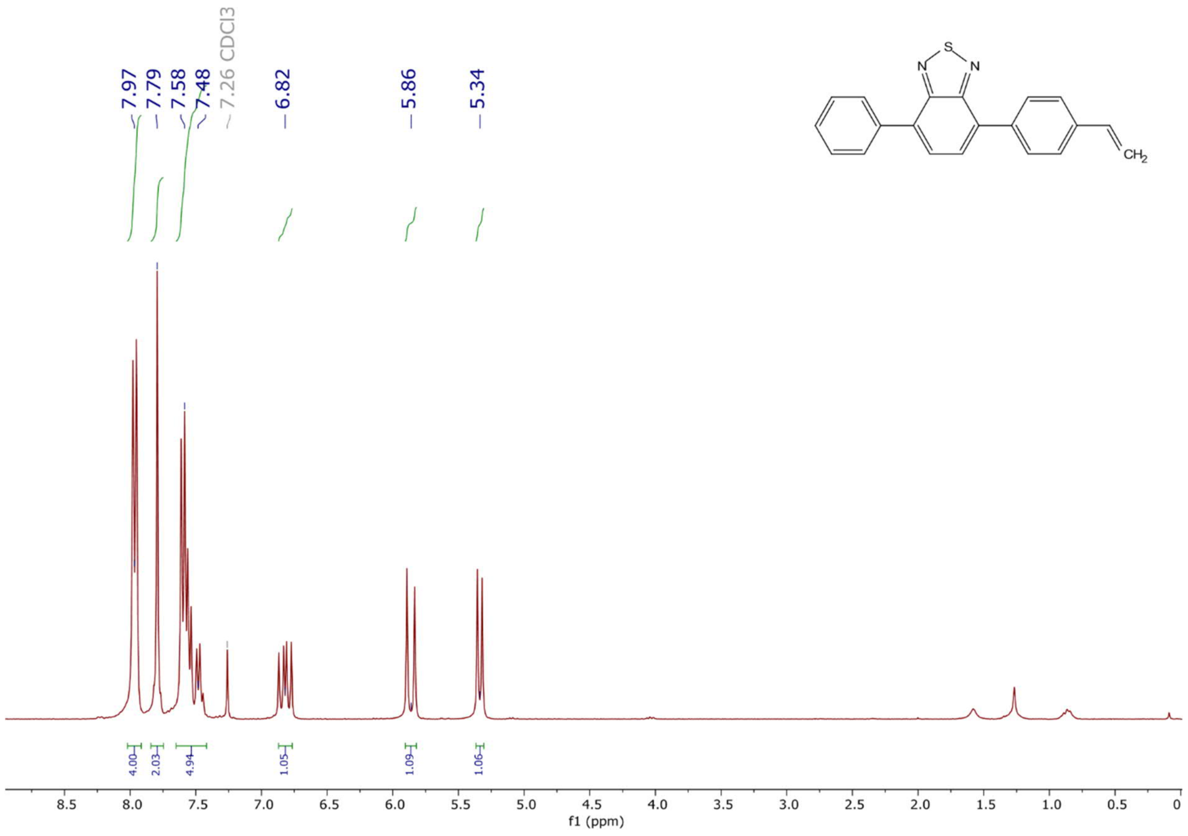
7.97
7.79
7.58
7.48
7.26 CDCl3
6.82
5.86
5.34
4.00
2.03
4.94
1.05
1.09
1.06
f1 (ppm)
S
N
N
CH2

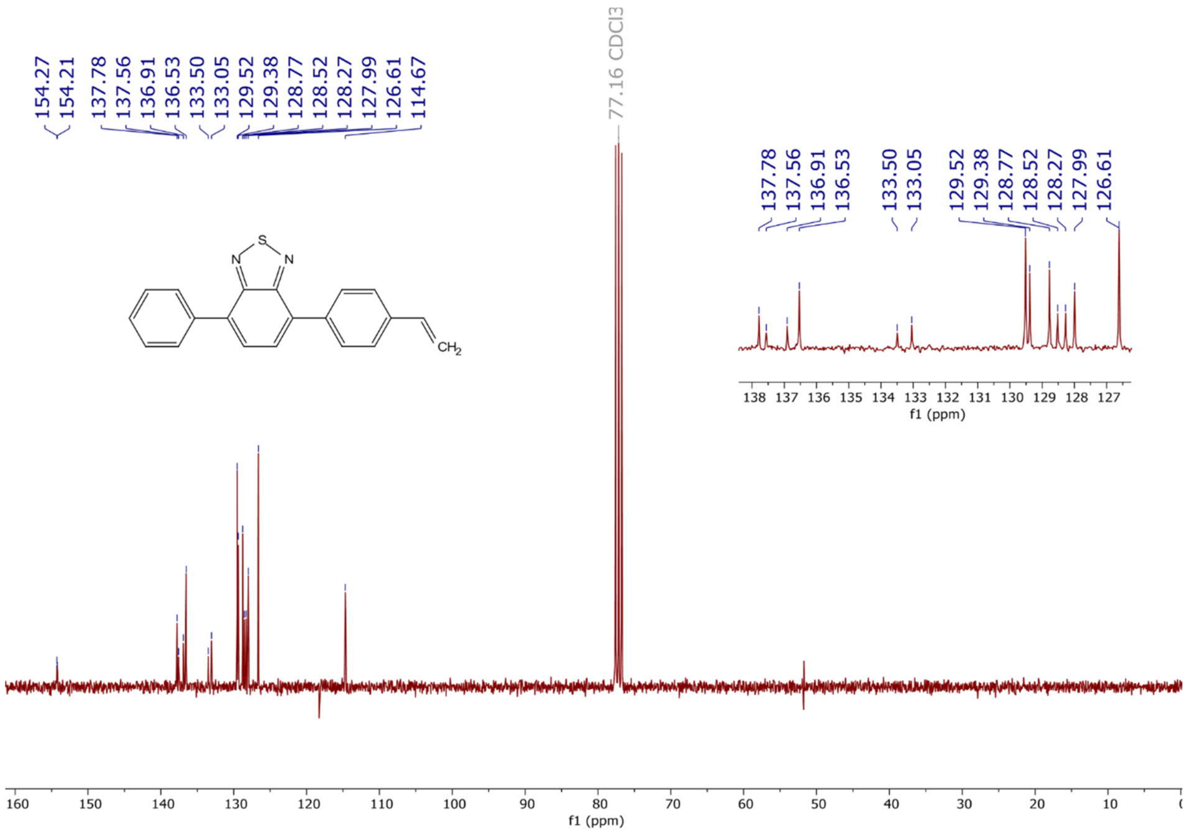
154.27
154.21
137.78
137.56
136.91
136.53
133.50
133.05
129.52
129.38
128.77
128.52
128.27
127.99
126.61
114.67
77.16 CDCl3
f1 (ppm)
S
N
N
CH2

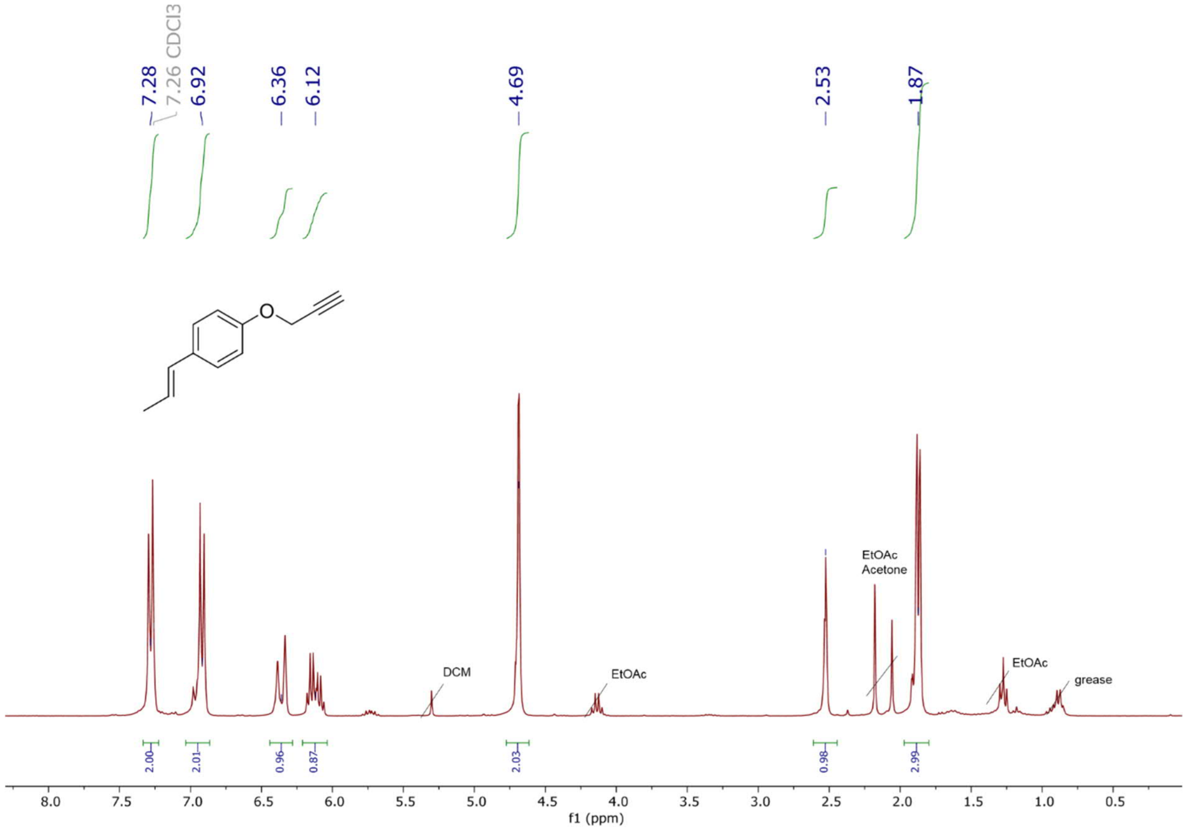
7.28
7.26 CDCl3
6.92
6.36
6.12
4.69
2.53
1.87
O
DCM
EtOAc
EtOAc
Acetone
EtOAc
grease
2.00
2.01
0.96
0.87
2.03
0.98
2.99
8.0
7.5
7.0
6.5
6.0
5.5
5.0
4.5
4.0
3.5
3.0
2.5
2.0
1.5
1.0
0.5
f1 (ppm)

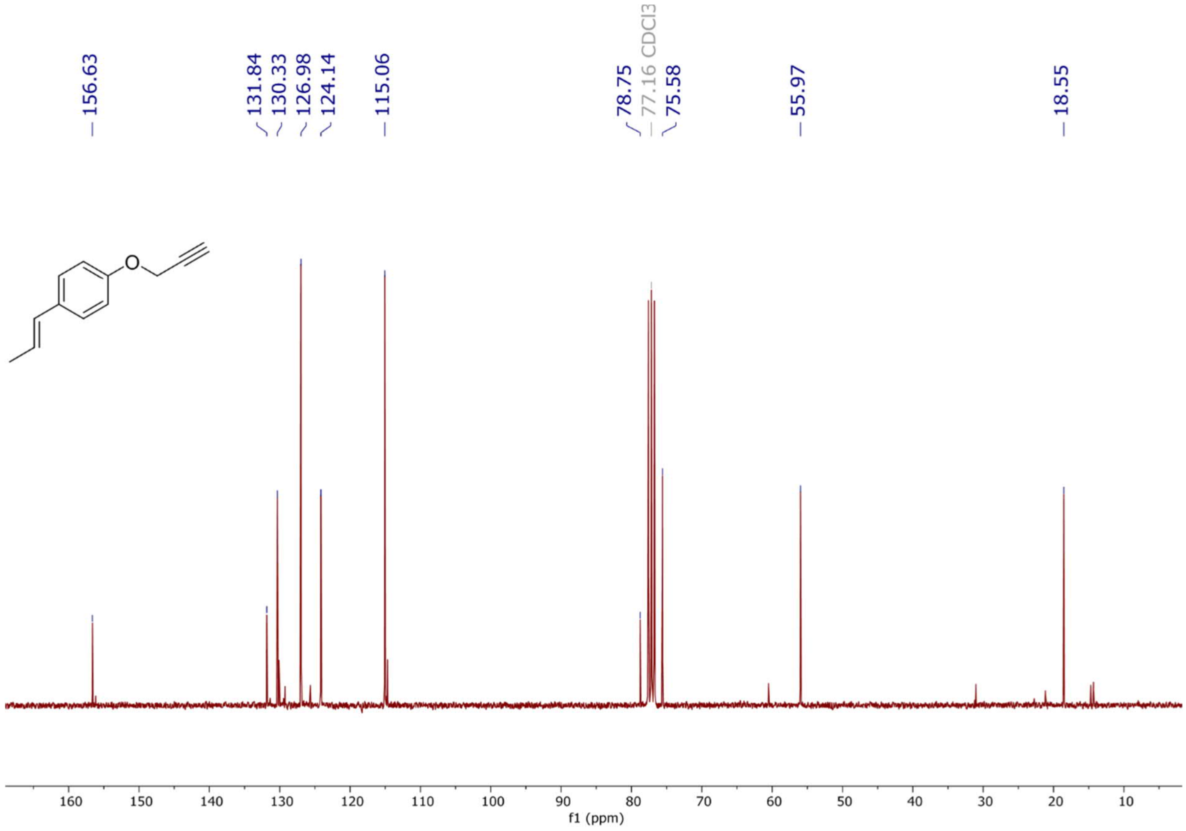
156.63
131.84
130.33
126.98
124.14
115.06
78.75
77.16 CDCl3
75.58
55.97
18.55
O
160
150
140
130
120
110
100
90
80
70
60
50
40
30
20
10
f1 (ppm)

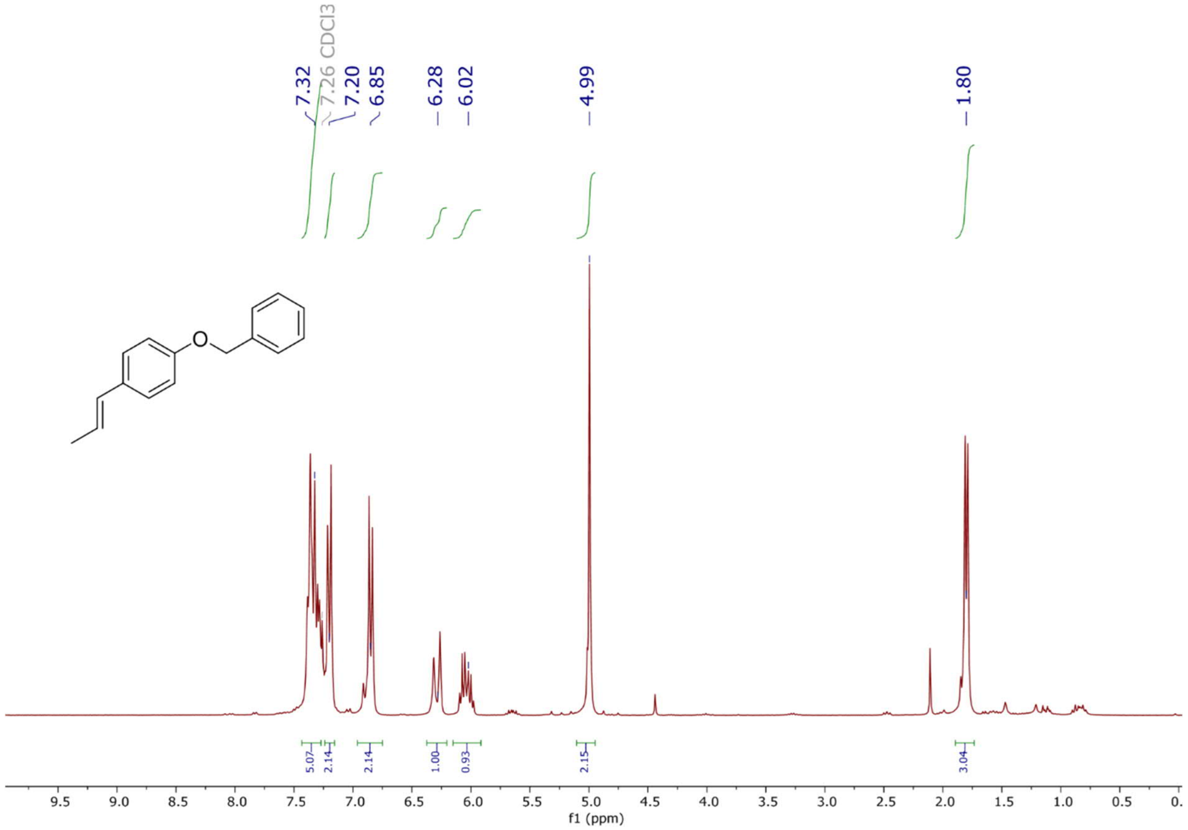
7.32
7.26 CDCl3
7.20
6.85
6.28
6.02
4.99
1.80
O
5.07
2.14
2.14
1.00
0.93
2.15
3.04
9.5
9.0
8.5
8.0
7.5
7.0
6.5
6.0
5.5
5.0
4.5
4.0
3.5
3.0
2.5
2.0
1.5
1.0
0.5
0.
f1 (ppm)

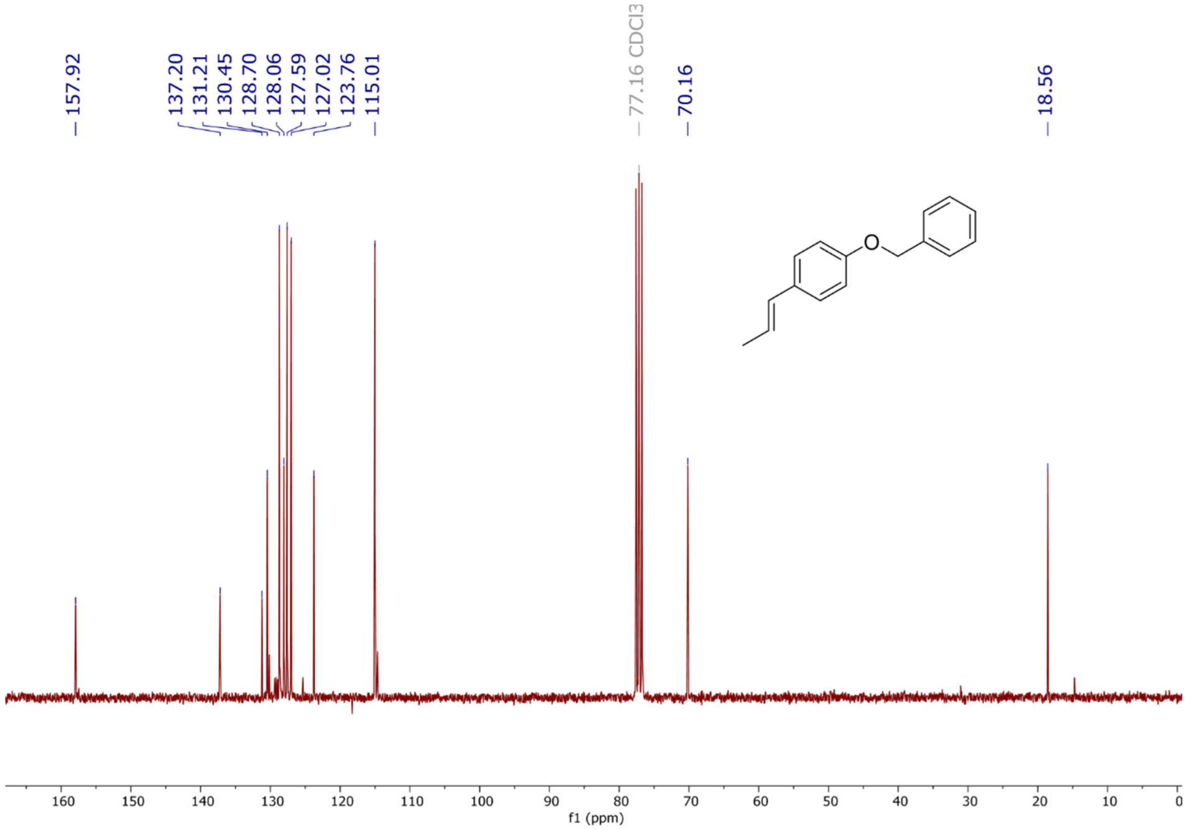
157.92
137.20
131.21
130.45
128.70
128.06
127.59
127.02
123.76
115.01
77.16 CDCl3
70.16
18.56
O
160
150
140
130
120
110
100
90
80
70
60
50
40
30
20
10
0
f1 (ppm)

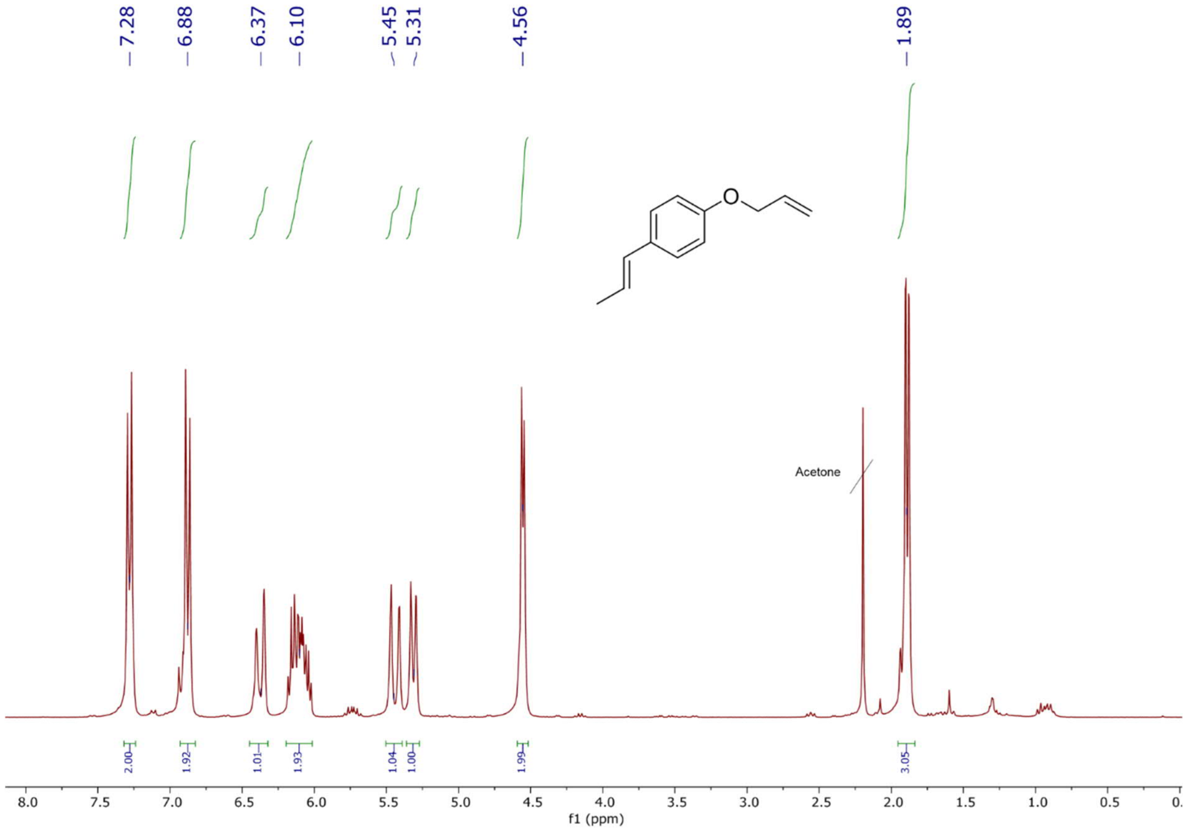
7.28
6.88
6.37
6.10
5.45
5.31
4.56
1.89
O
Acetone
2.00
1.92
1.01
1.93
1.04
1.00
1.99
3.05
8.0
7.5
7.0
6.5
6.0
5.5
5.0
4.5
4.0
3.5
3.0
2.5
2.0
1.5
1.0
0.5
0.
f1 (ppm)

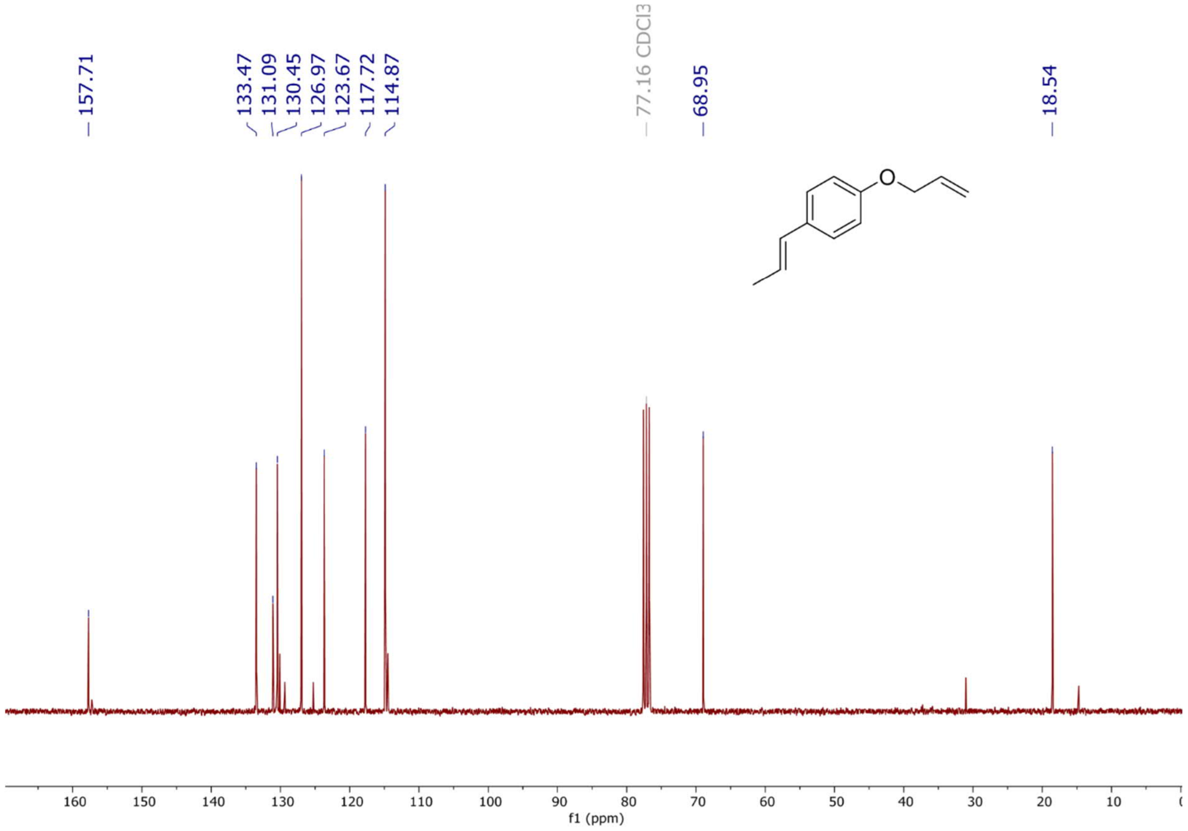
157.71
133.47
131.09
130.45
126.97
123.67
117.72
114.87
77.16 CDCl3
68.95
18.54
O
160
150
140
130
120
110
100
90
80
70
60
50
40
30
20
10
0
f1 (ppm)

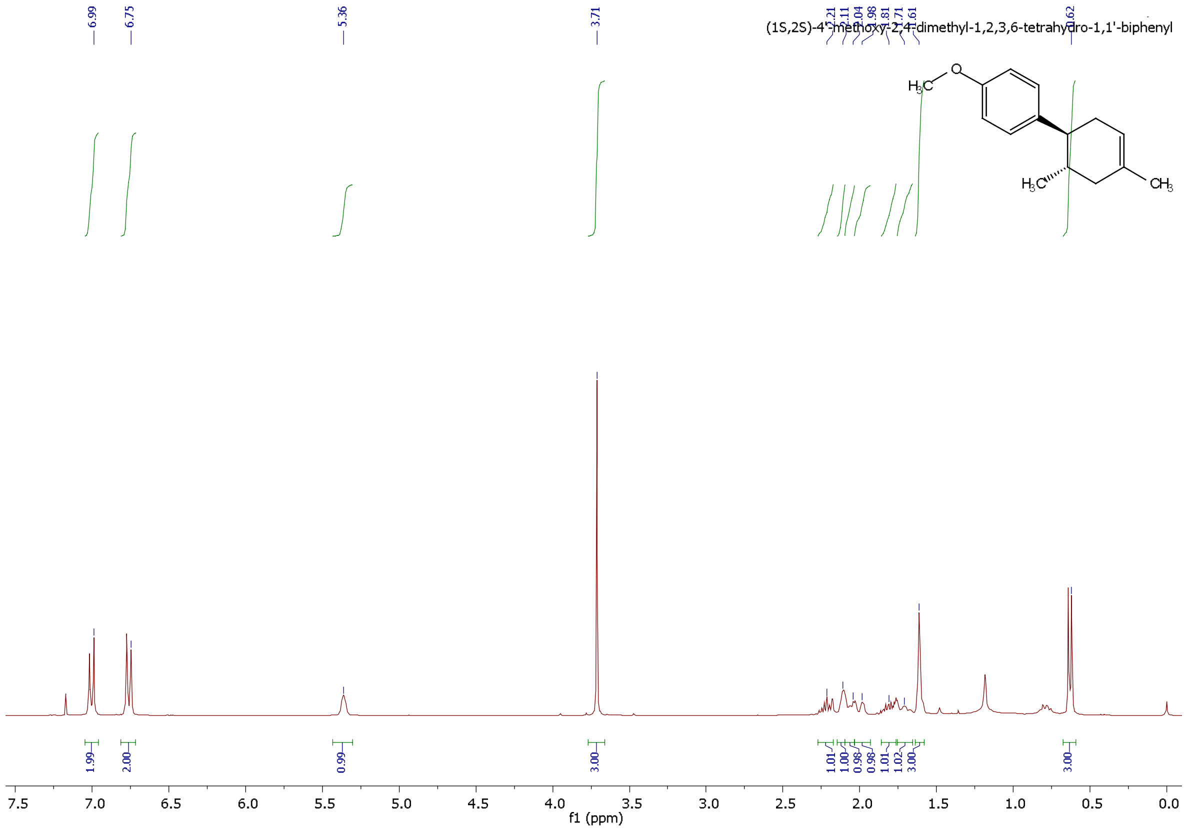
(1S,2S)-4'-methoxy-2,4-dimethyl-1,2,3,6-tetrahydro-1,1'-biphenyl
6.99
6.75
5.36
3.71
2.21
2.11
2.04
1.98
1.81
1.71
1.61
0.62
H3C
O
H3C
CH3
1.99
2.00
0.99
3.00
1.01
1.00
0.98
0.98
1.01
1.02
3.00
3.00
7.5
7.0
6.5
6.0
5.5
5.0
4.5
4.0
3.5
3.0
2.5
2.0
1.5
1.0
0.5
0.0
f1 (ppm)

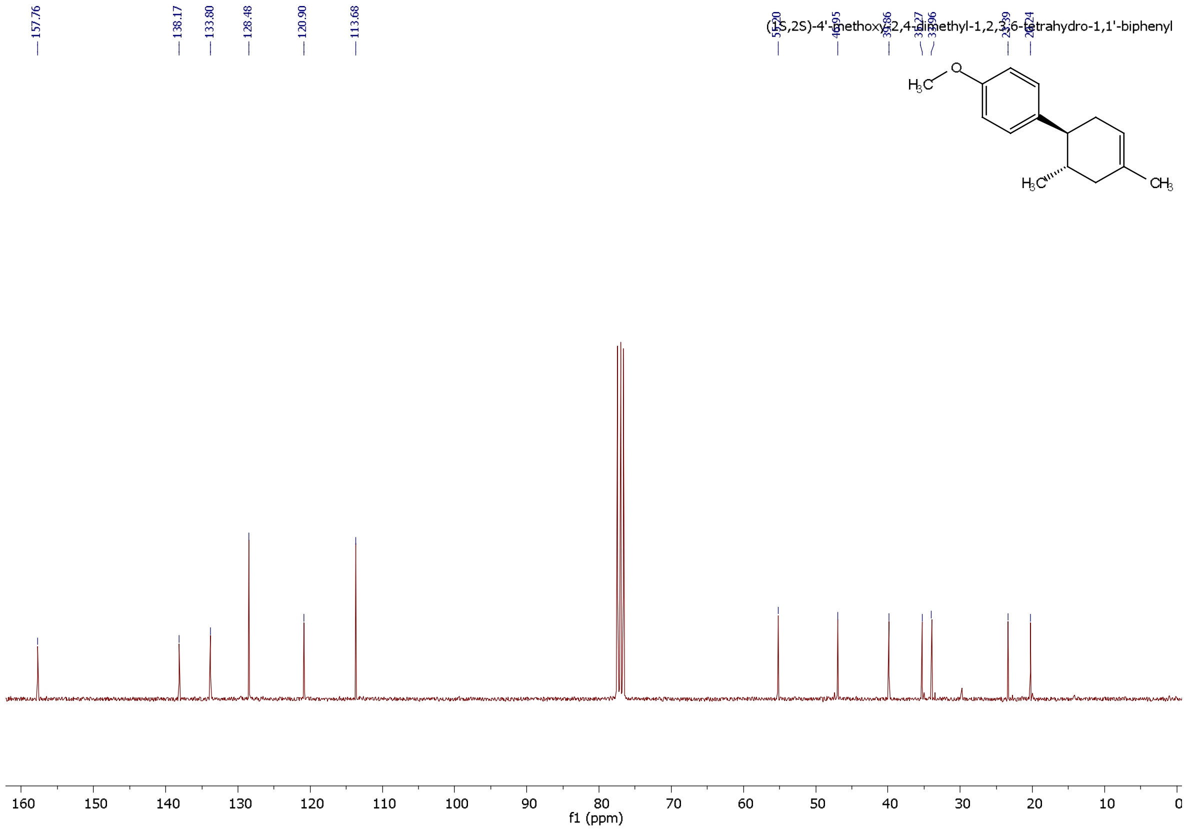
(1S,2S)-4'-methoxy-2,4-dimethyl-1,2,3,6-tetrahydro-1,1'-biphenyl
157.76
138.17
133.80
128.48
120.90
113.68
55.20
46.95
39.86
35.27
33.96
23.39
20.24
H3C
O
H3C
CH3
160
150
140
130
120
110
100
90
80
70
60
50
40
30
20
10
0
f1 (ppm)

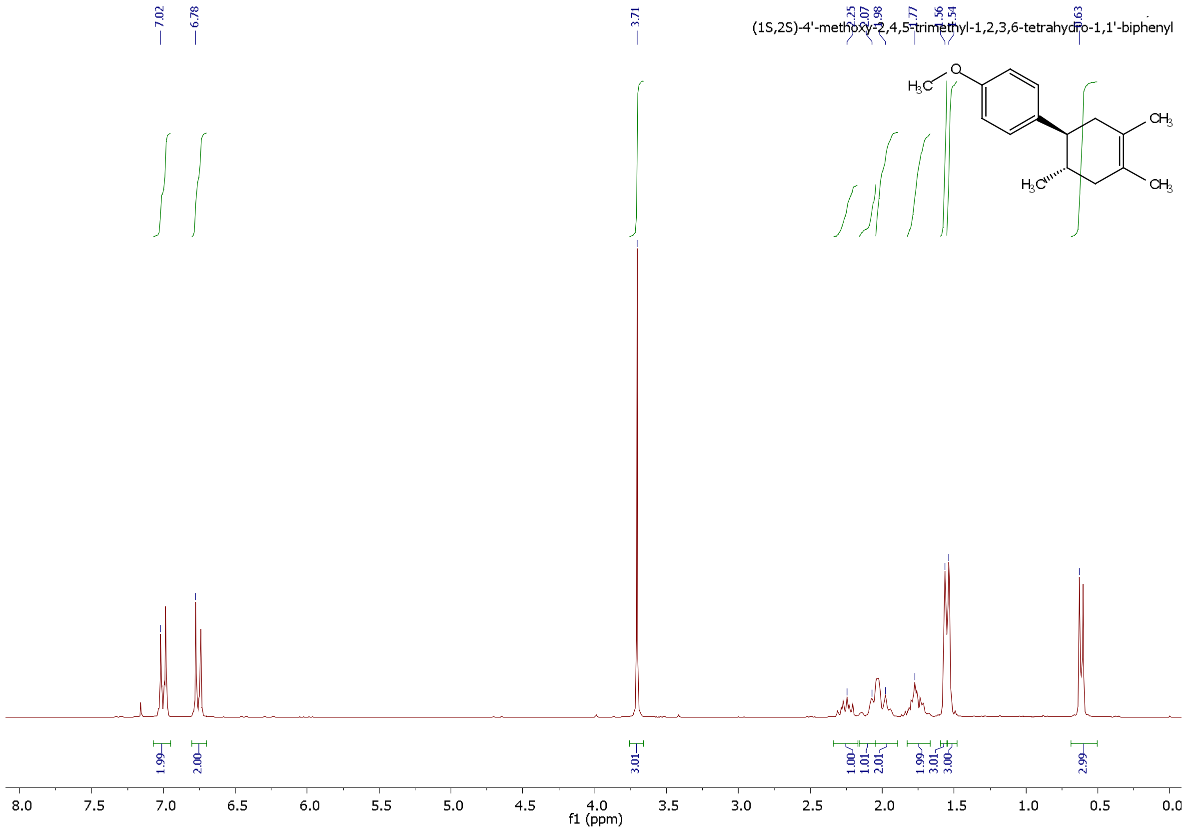
(1S,2S)-4'-methoxy-2,4,5-trimethyl-1,2,3,6-tetrahydro-1,1'-biphenyl
7.02
6.78
3.71
2.25
2.07
1.98
1.77
1.56
1.54
0.63
H_3C
O
CH_3
H_3C
CH_3
1.99
2.00
3.01
1.00
1.01
2.01
1.99
3.01
3.00
2.99
8.0
7.5
7.0
6.5
6.0
5.5
5.0
4.5
4.0
3.5
3.0
2.5
2.0
1.5
1.0
0.5
0.0
f1 (ppm)

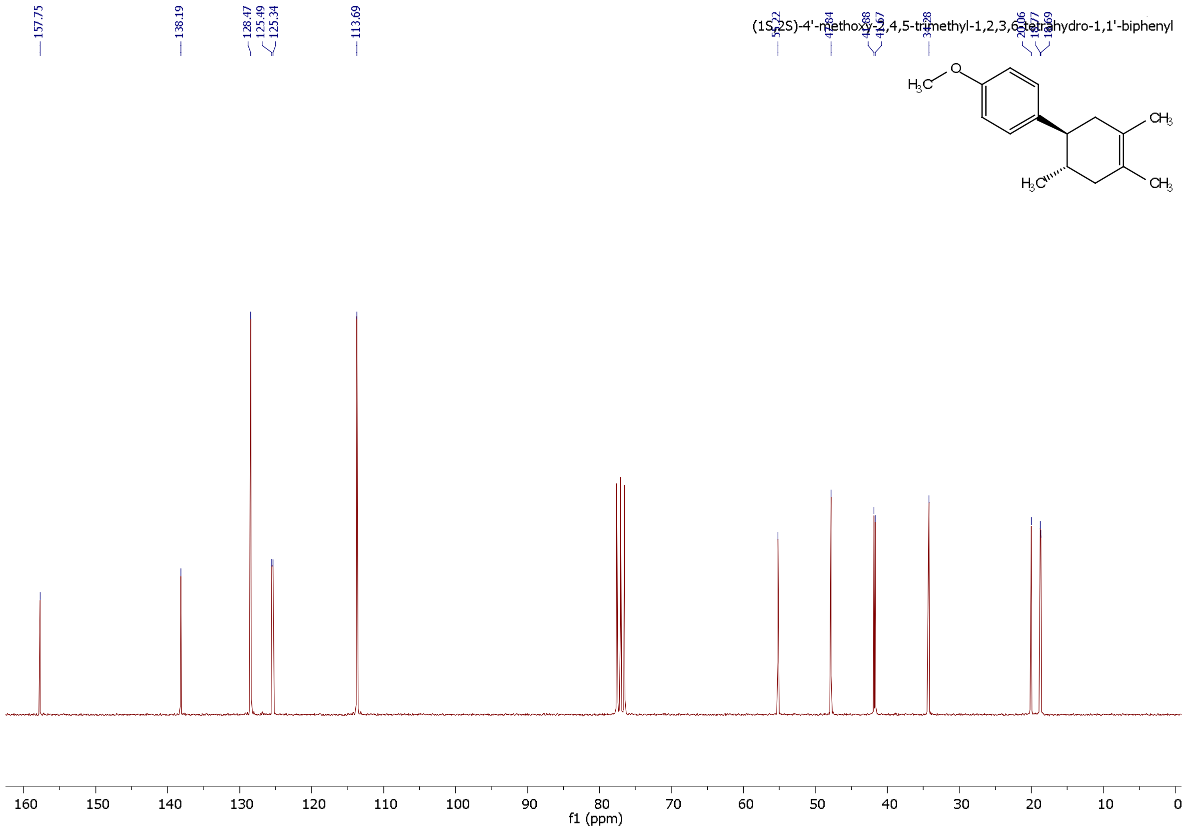
(1S,2S)-4'-methoxy-2,4,5-trimethyl-1,2,3,6-tetrahydro-1,1'-biphenyl
157.75
138.19
128.47
125.49
125.34
113.69
55.22
47.84
41.88
41.67
34.28
20.06
18.77
18.69
H_3C
O
CH_3
H_3C
CH_3
160
150
140
130
120
110
100
90
80
70
60
50
40
30
20
10
0
f1 (ppm)

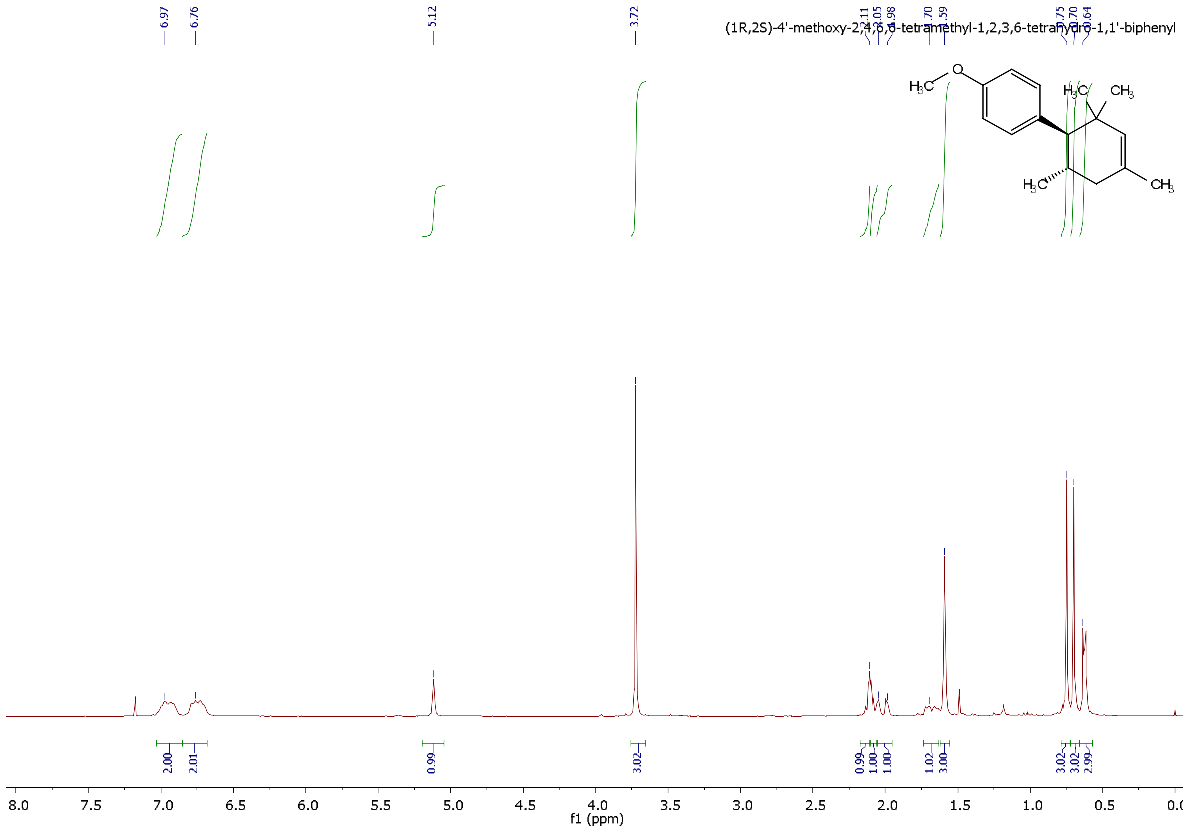
(1R,2S)-4'-methoxy-2,4,6,6-tetramethyl-1,2,3,6-tetrahydro-1,1'-biphenyl
6.97
6.76
5.12
3.72
2.11
2.05
1.98
1.70
1.59
0.75
0.70
0.64
H3C
O
H3C
CH3
H3C
CH3
2.00
2.01
0.99
3.02
0.99
1.00
1.00
1.02
3.00
3.02
3.02
2.99
8.0
7.5
7.0
6.5
6.0
5.5
5.0
4.5
4.0
3.5
3.0
2.5
2.0
1.5
1.0
0.5
0.0
f1 (ppm)

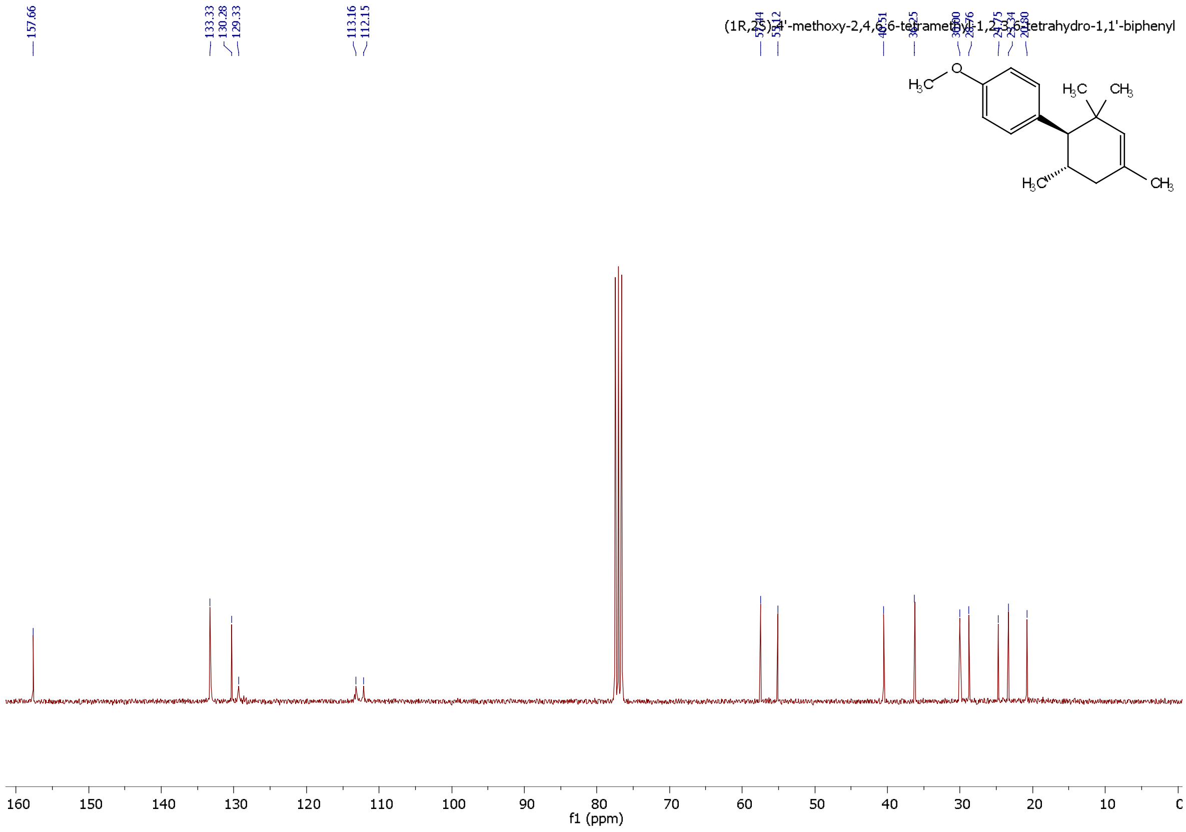
(1R,2S)-4'-methoxy-2,4,6,6-tetramethyl-1,2,3,6-tetrahydro-1,1'-biphenyl
157.66
133.33
130.28
129.33
113.16
112.15
57.44
55.12
40.51
36.25
30.00
28.76
24.75
23.34
20.80
H3C
O
H3C
CH3
H3C
CH3
160
150
140
130
120
110
100
90
80
70
60
50
40
30
20
10
0
f1 (ppm)

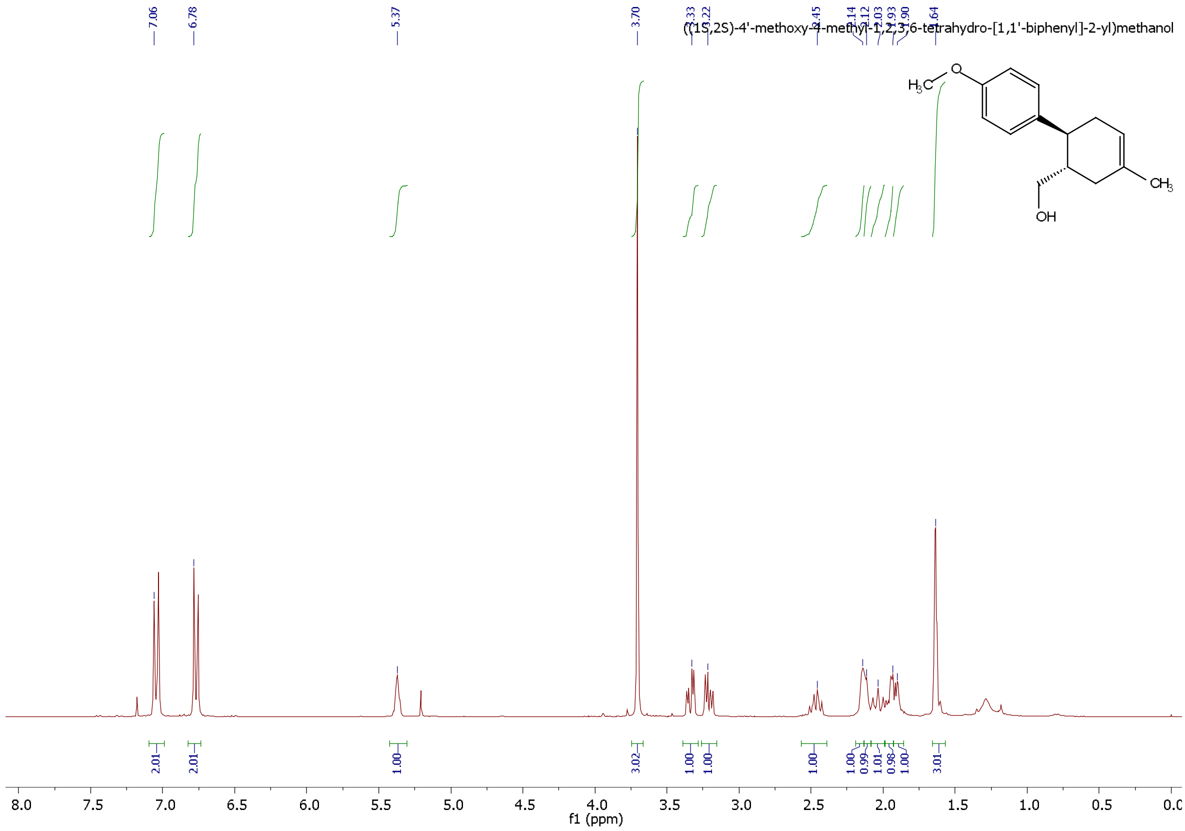
7.06
6.78
5.37
3.70
3.33
3.22
2.45
2.14
2.12
2.03
1.93
1.90
1.64
((1S,2S)-4'-methoxy-4-methyl-1,2,3,6-tetrahydro-[1,1'-biphenyl]-2-yl)methanol
H_3C
O
CH_3
OH
2.01
2.01
1.00
3.02
1.00
1.00
1.00
1.00
0.99
1.01
0.98
1.00
3.01
8.0
7.5
7.0
6.5
6.0
5.5
5.0
4.5
4.0
3.5
3.0
2.5
2.0
1.5
1.0
0.5
0.0
f1 (ppm)

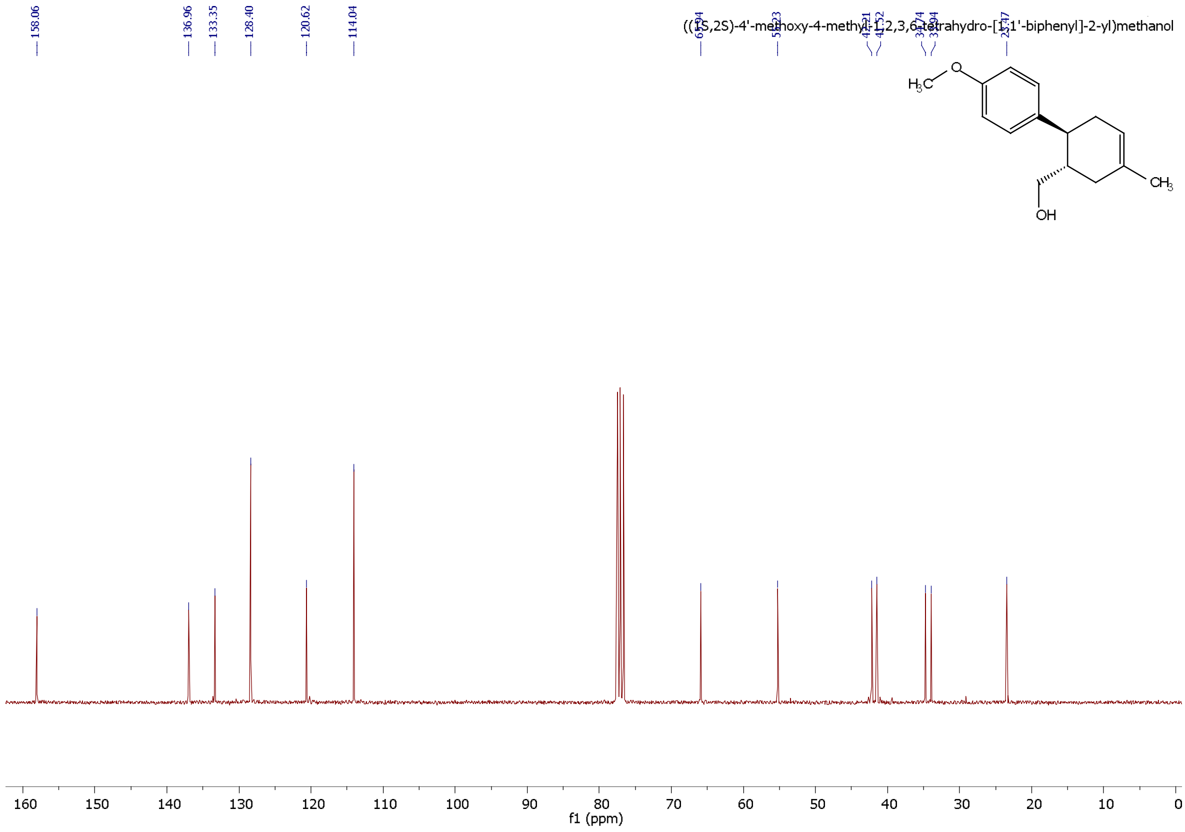
158.06
136.96
133.35
128.40
120.62
114.04
65.94
55.23
42.21
41.52
34.74
33.94
23.47
((1S,2S)-4'-methoxy-4-methyl-1,2,3,6-tetrahydro-[1,1'-biphenyl]-2-yl)methanol
H_3C
O
CH_3
OH
160
150
140
130
120
110
100
90
80
70
60
50
40
30
20
10
0
f1 (ppm)

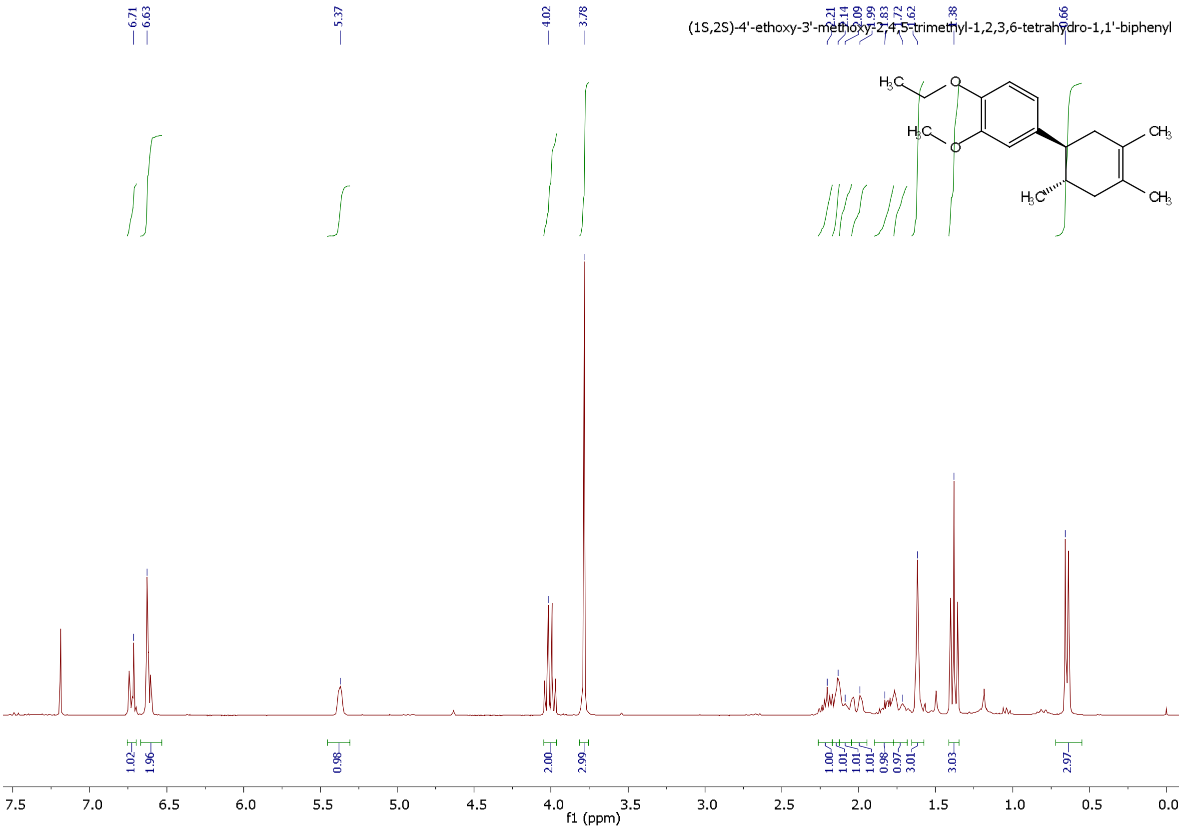
6.71
6.63
5.37
4.02
3.78
2.21
2.14
2.09
1.99
1.83
1.72
1.62
1.38
0.66
(1S,2S)-4'-ethoxy-3'-methoxy-2,4,5-trimethyl-1,2,3,6-tetrahydro-1,1'-biphenyl
H3C
O
H3C
O
CH3
H3C
CH3
1.02
1.96
0.98
2.00
2.99
1.00
1.01
1.01
1.01
0.98
0.97
3.01
3.03
2.97
7.5
7.0
6.5
6.0
5.5
5.0
4.5
4.0
3.5
3.0
2.5
2.0
1.5
1.0
0.5
0.0
f1 (ppm)

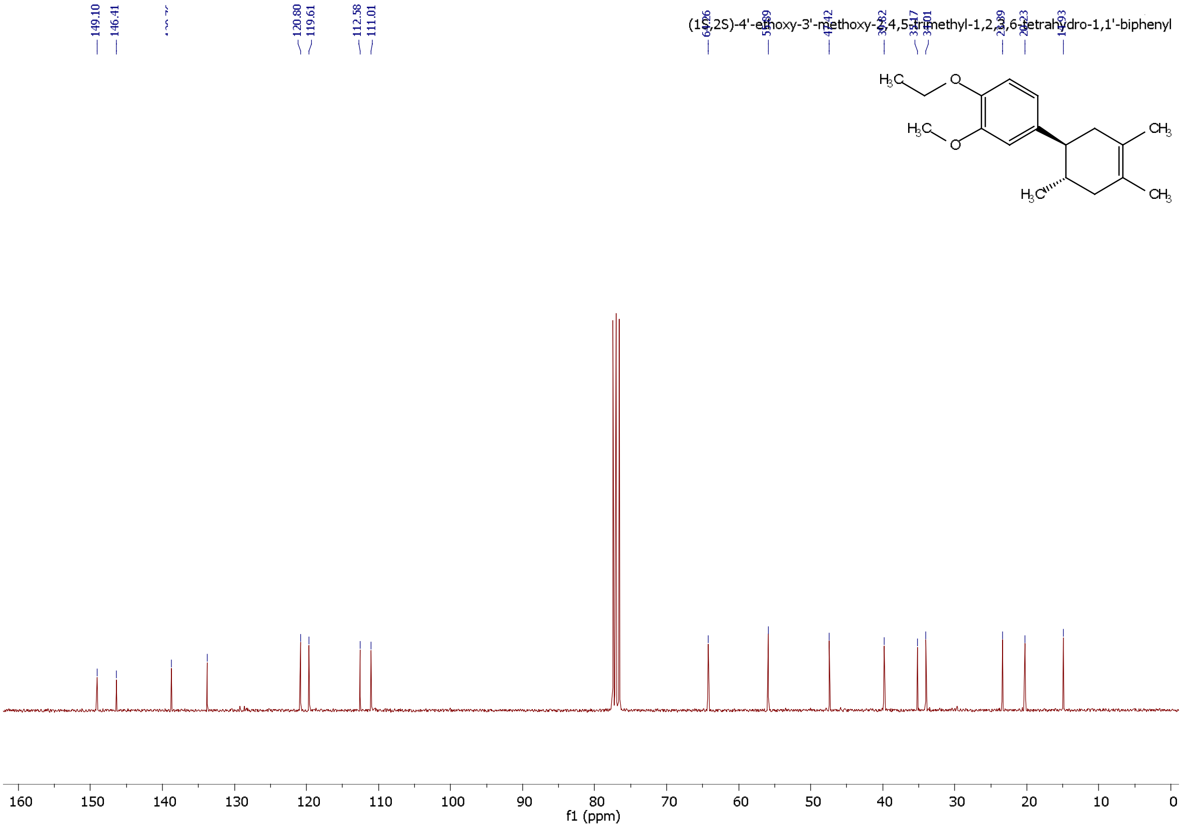
149.10
146.41
120.80
119.61
112.58
111.01
64.26
55.89
47.42
39.82
35.17
34.01
23.39
20.23
14.93
(1S,2S)-4'-ethoxy-3'-methoxy-2,4,5-trimethyl-1,2,3,6-tetrahydro-1,1'-biphenyl
H3C
O
H3C
O
CH3
H3C
CH3
160
150
140
130
120
110
100
90
80
70
60
50
40
30
20
10
0
f1 (ppm)

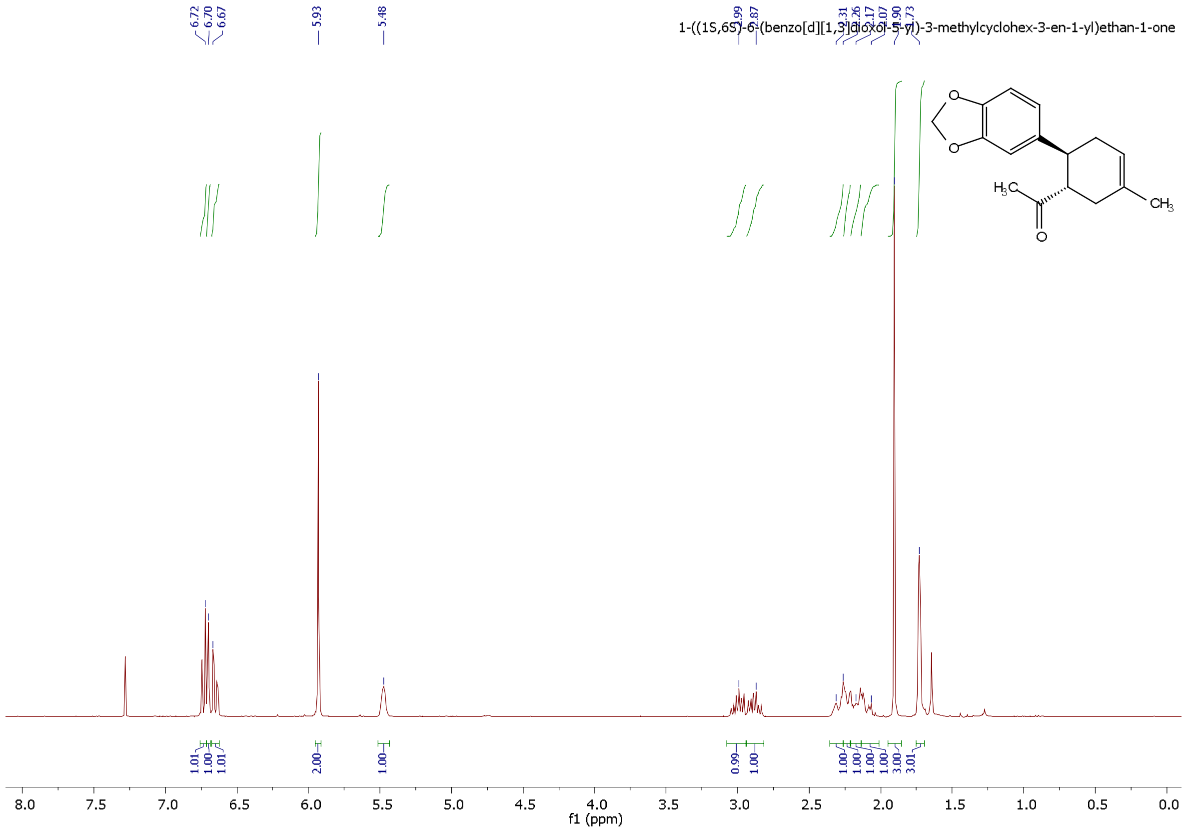

1-((1S,6S)-6-(benzo[d][1,3]dioxol-5-yl)-3-methylcyclohex-3-en-1-yl)ethan-1-one

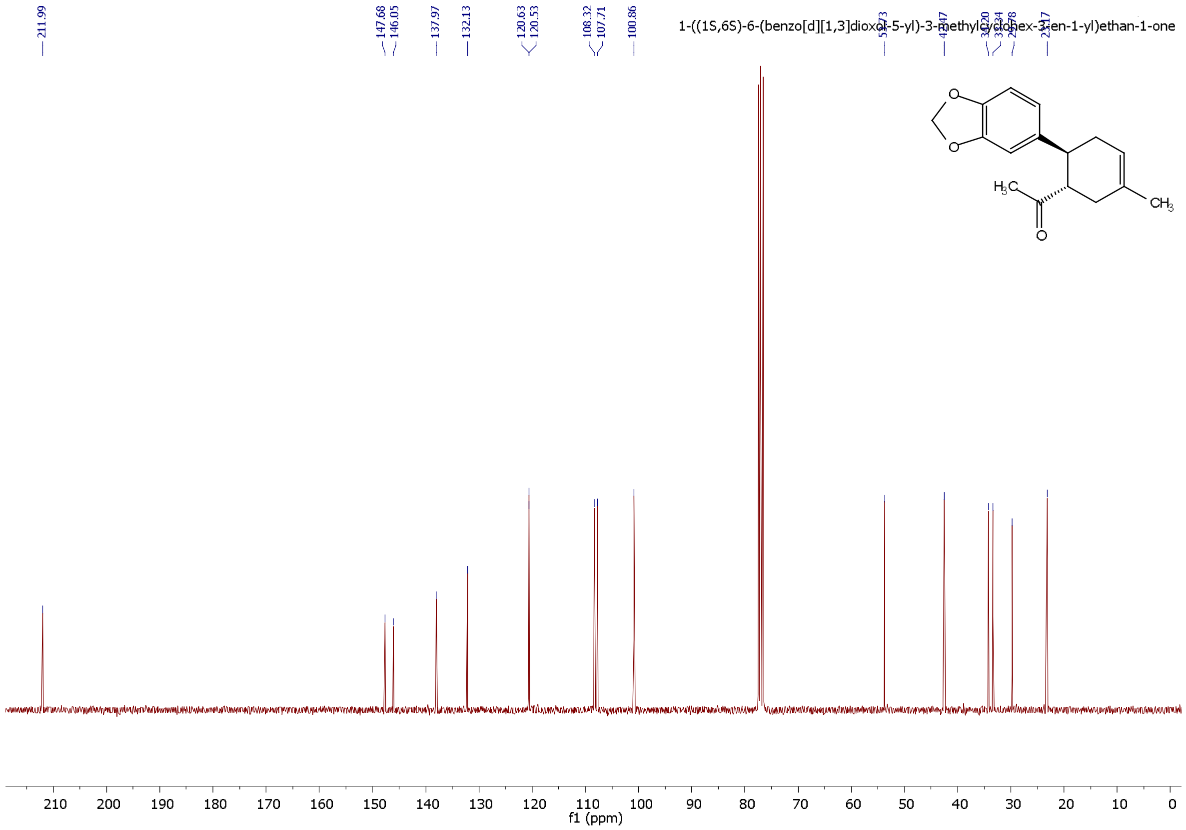

1-((1S,6S)-6-(benzo[d][1,3]dioxol-5-yl)-3-methylcyclohex-3-en-1-yl)ethan-1-one

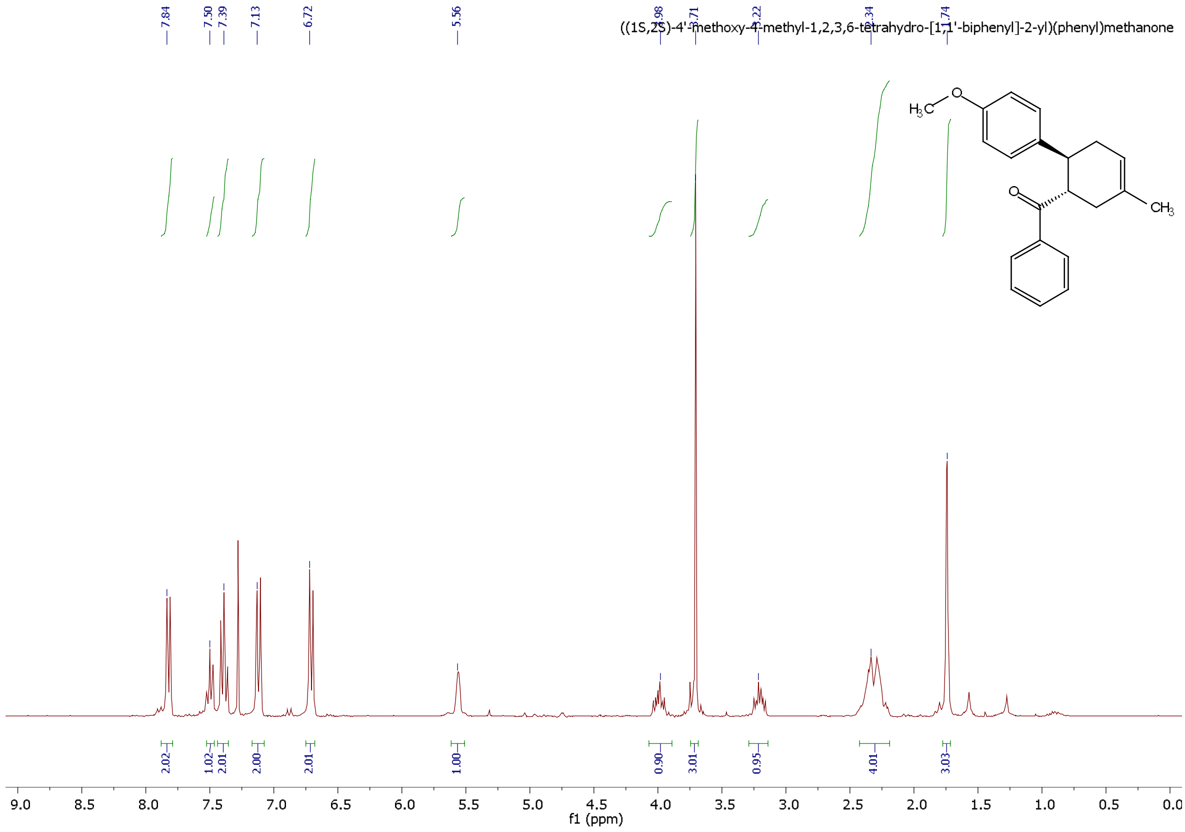

7.84
7.50
7.39
7.13
6.72
5.56
3.98
3.71
3.22
2.34
1.74
((1S,2S)-4'-methoxy-4-methyl-1,2,3,6-tetrahydro-[1,1'-biphenyl]-2-yl)(phenyl)methanone
H3C
O
CH3
2.02
1.02
2.01
2.00
2.01
1.00
0.90
3.01
0.95
4.01
3.03
9.0
8.5
8.0
7.5
7.0
6.5
6.0
5.5
5.0
4.5
4.0
3.5
3.0
2.5
2.0
1.5
1.0
0.5
0.0
f1 (ppm)

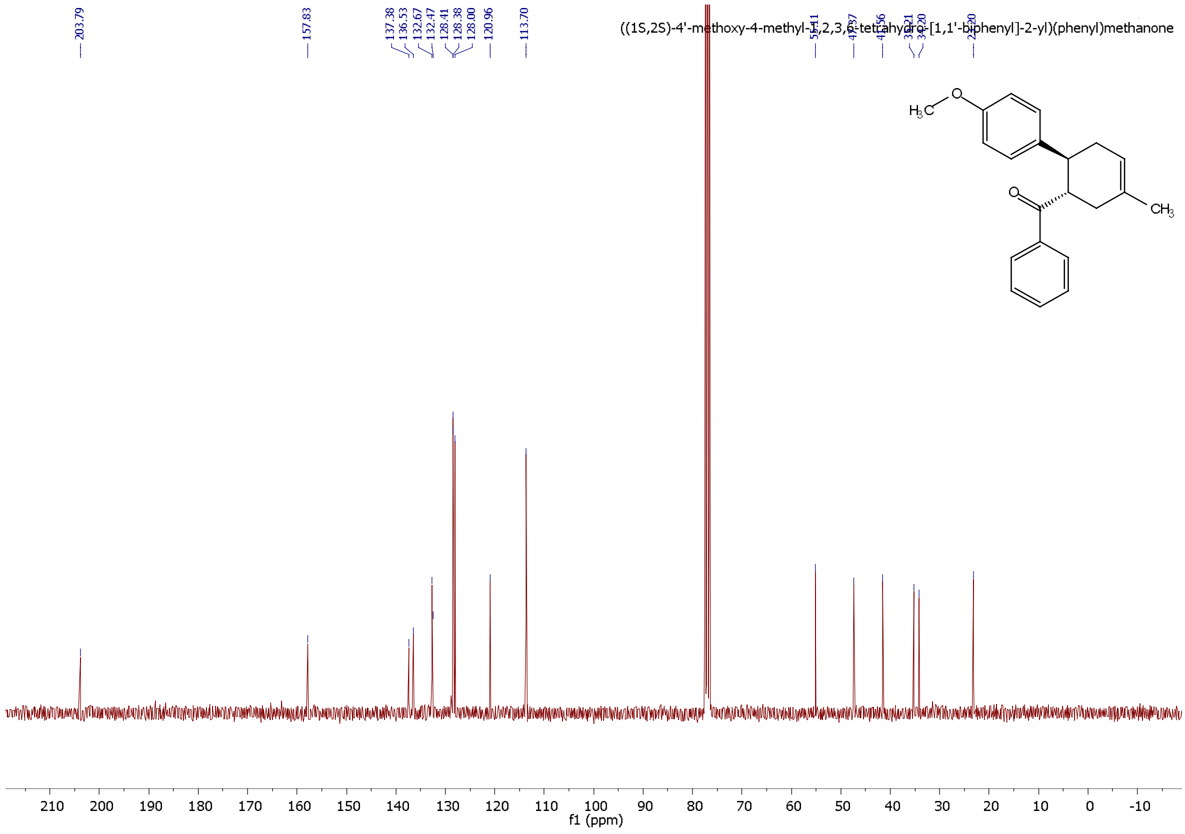

203.79
157.83
137.38
136.53
132.67
132.47
128.41
128.38
128.00
120.96
113.70
((1S,2S)-4'-methoxy-4-methyl-1,2,3,6-tetrahydro-[1,1'-biphenyl]-2-yl)(phenyl)methanone
55.11
47.37
41.56
35.21
34.20
23.20
H3C
O
CH3
210
200
190
180
170
160
150
140
130
120
110
100
90
80
70
60
50
40
30
20
10
0
-10
f1 (ppm)

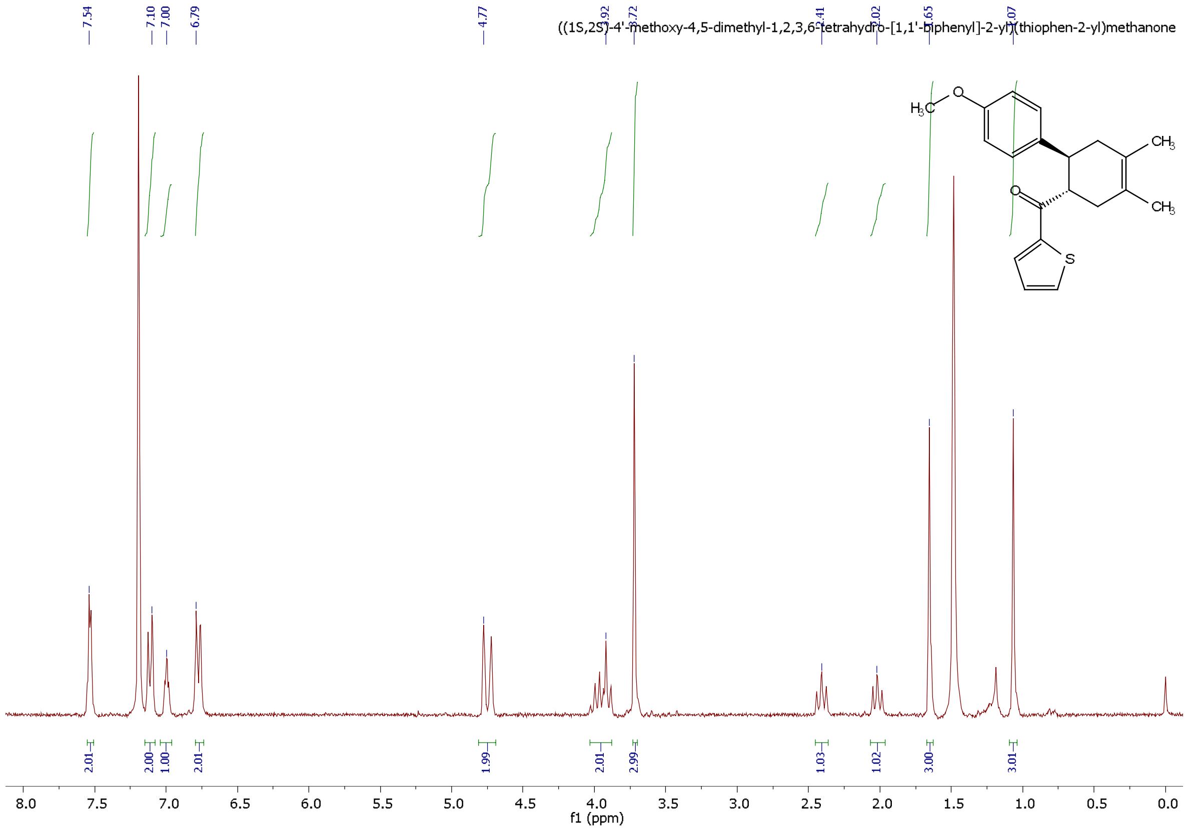
((1S,2S)-4'-methoxy-4,5-dimethyl-1,2,3,6-tetrahydro-[1,1'-biphenyl]-2-yl)(thiophen-2-yl)methanone
7.54
7.10
7.00
6.79
4.77
3.92
3.72
2.41
2.02
1.65
1.07
2.01
2.00
1.00
2.01
1.99
2.01
2.99
1.03
1.02
3.00
3.01
8.0
7.5
7.0
6.5
6.0
5.5
5.0
4.5
4.0
3.5
3.0
2.5
2.0
1.5
1.0
0.5
0.0
f1 (ppm)
H3C
O
CH3
CH3
O
S

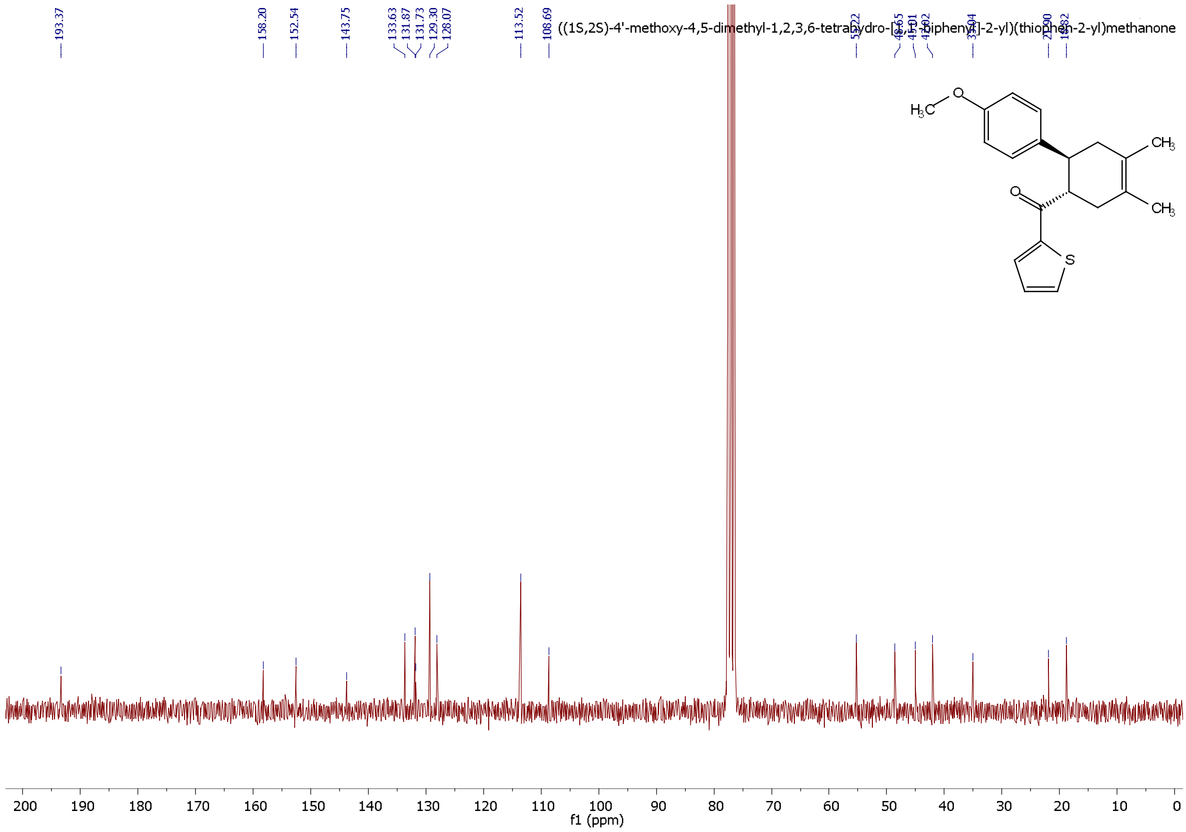
((1S,2S)-4'-methoxy-4,5-dimethyl-1,2,3,6-tetrahydro-[1,1'-biphenyl]-2-yl)(thiophen-2-yl)methanone
193.37
158.20
152.54
143.75
133.63
131.87
131.73
129.30
128.07
113.52
108.69
55.22
48.65
45.01
42.02
35.04
21.90
18.82
200
190
180
170
160
150
140
130
120
110
100
90
80
70
60
50
40
30
20
10
0
f1 (ppm)
H3C
O
CH3
CH3
O
S

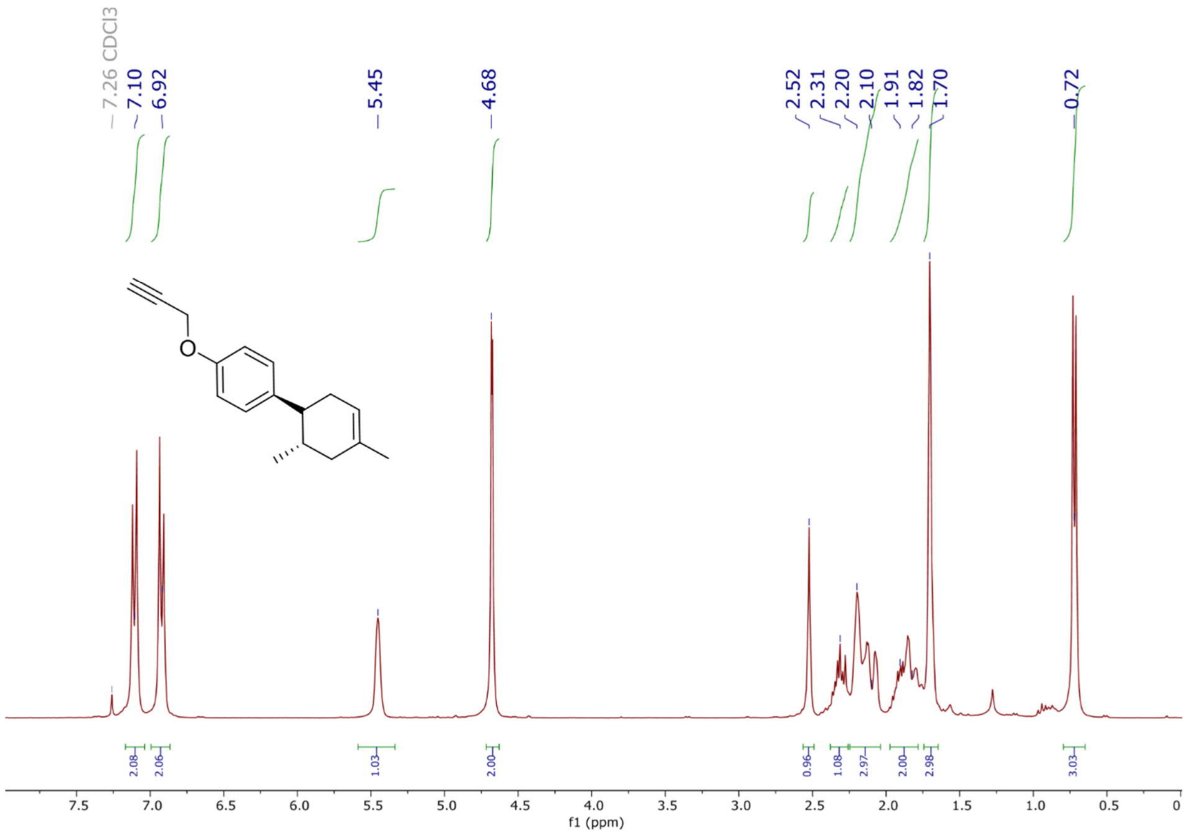
7.26 CDCl3
7.10
6.92
5.45
4.68
2.52
2.31
2.20
2.10
1.91
1.82
1.70
0.72
2.08
2.06
1.03
2.00
0.96
1.08
2.97
2.00
2.98
3.03
7.5
7.0
6.5
6.0
5.5
5.0
4.5
4.0
3.5
3.0
2.5
2.0
1.5
1.0
0.5
0
f1 (ppm)
O

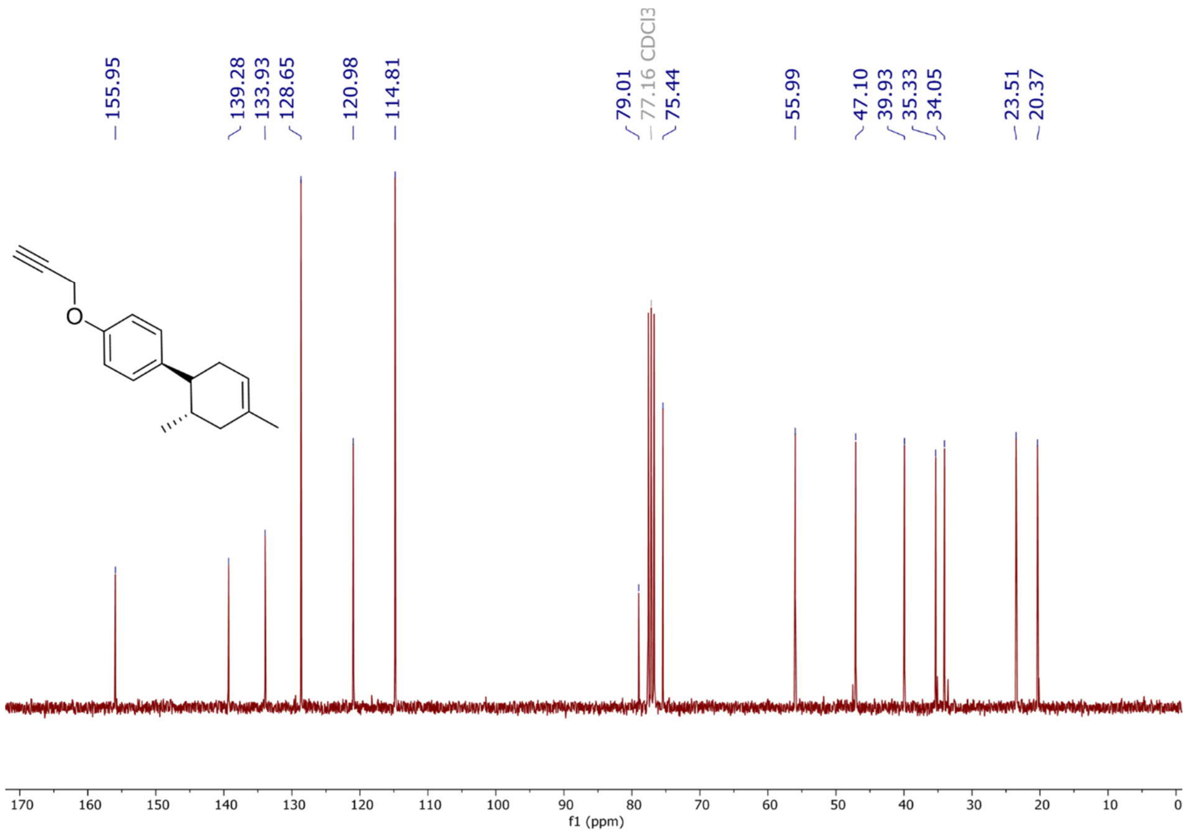
155.95
139.28
133.93
128.65
120.98
114.81
79.01
77.16 CDCl3
75.44
55.99
47.10
39.93
35.33
34.05
23.51
20.37
170
160
150
140
130
120
110
100
90
80
70
60
50
40
30
20
10
0
f1 (ppm)
O

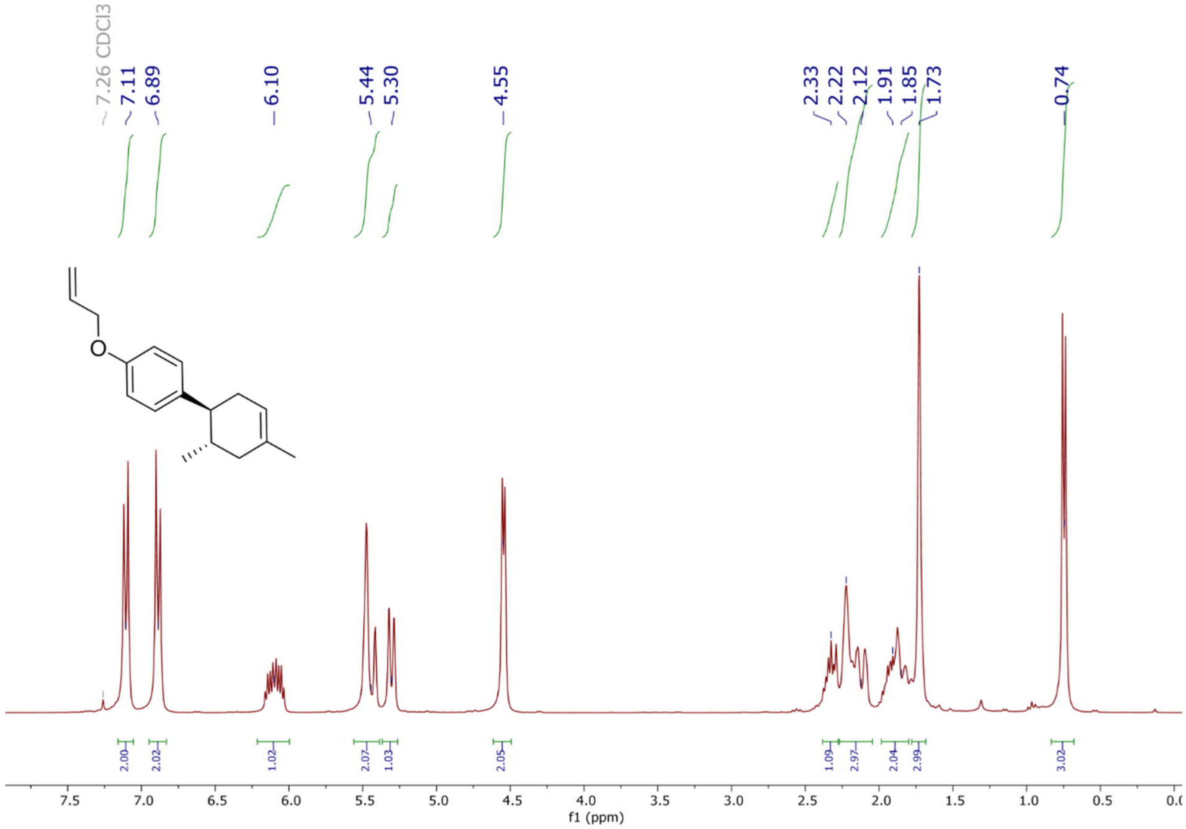
7.26 CDCl3
7.11
6.89
6.10
5.44
5.30
4.55
2.33
2.22
2.12
1.91
1.85
1.73
0.74
O
2.00
2.02
1.02
2.07
1.03
2.05
1.09
2.97
2.04
2.99
3.02
7.5
7.0
6.5
6.0
5.5
5.0
4.5
4.0
3.5
3.0
2.5
2.0
1.5
1.0
0.5
f1 (ppm)

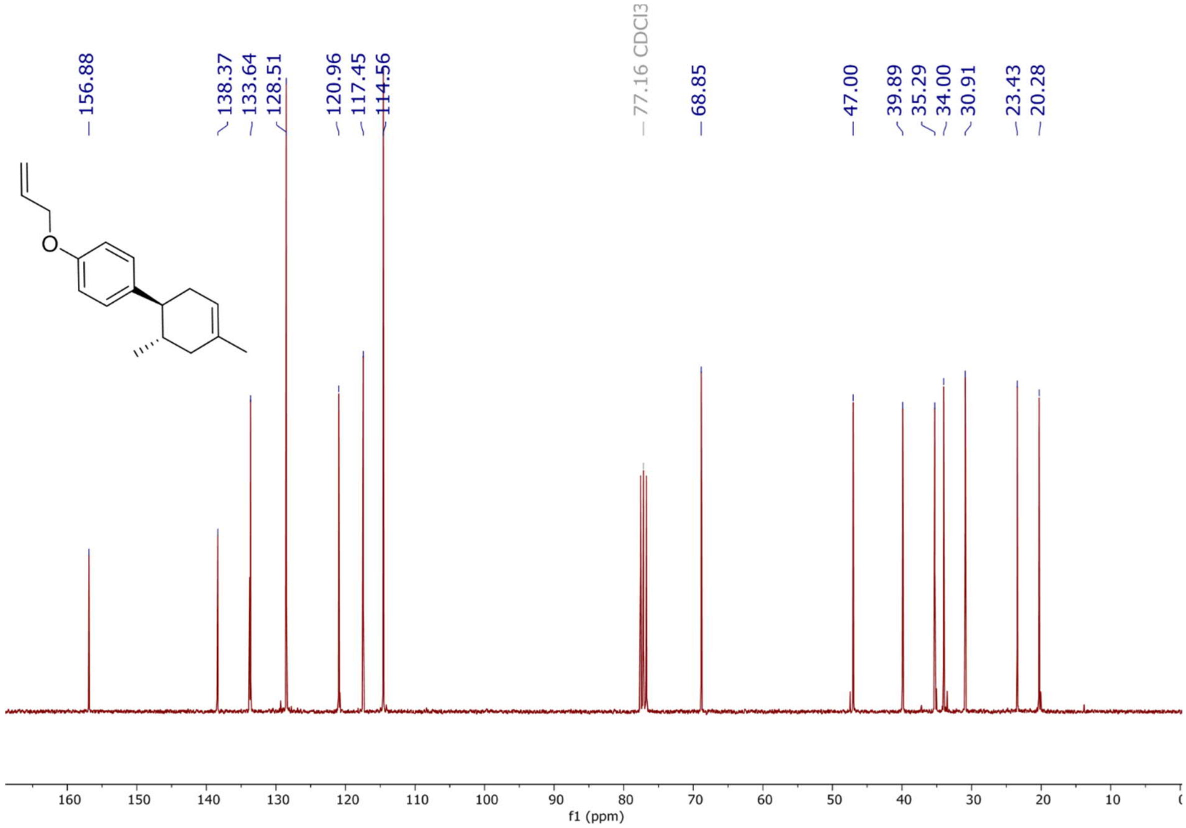
156.88
138.37
133.64
128.51
120.96
117.45
114.56
77.16 CDCl3
68.85
47.00
39.89
35.29
34.00
30.91
23.43
20.28
O
160
150
140
130
120
110
100
90
80
70
60
50
40
30
20
10
f1 (ppm)

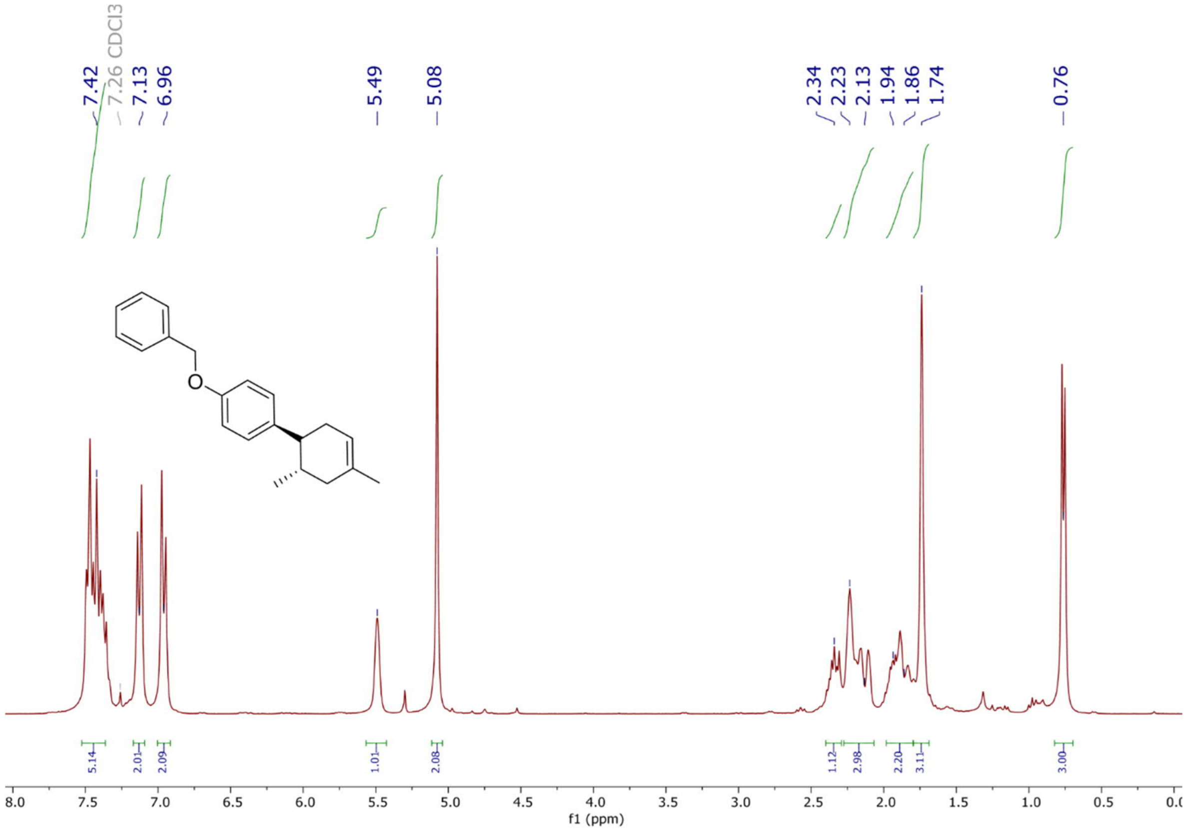
7.42
7.26 CDCl3
7.13
6.96
5.49
5.08
2.34
2.23
2.13
1.94
1.86
1.74
0.76
5.14
2.01
2.09
1.01
2.08
1.12
2.98
2.20
3.11
3.00
8.0
7.5
7.0
6.5
6.0
5.5
5.0
4.5
4.0
3.5
3.0
2.5
2.0
1.5
1.0
0.5
0.0
f1 (ppm)
O

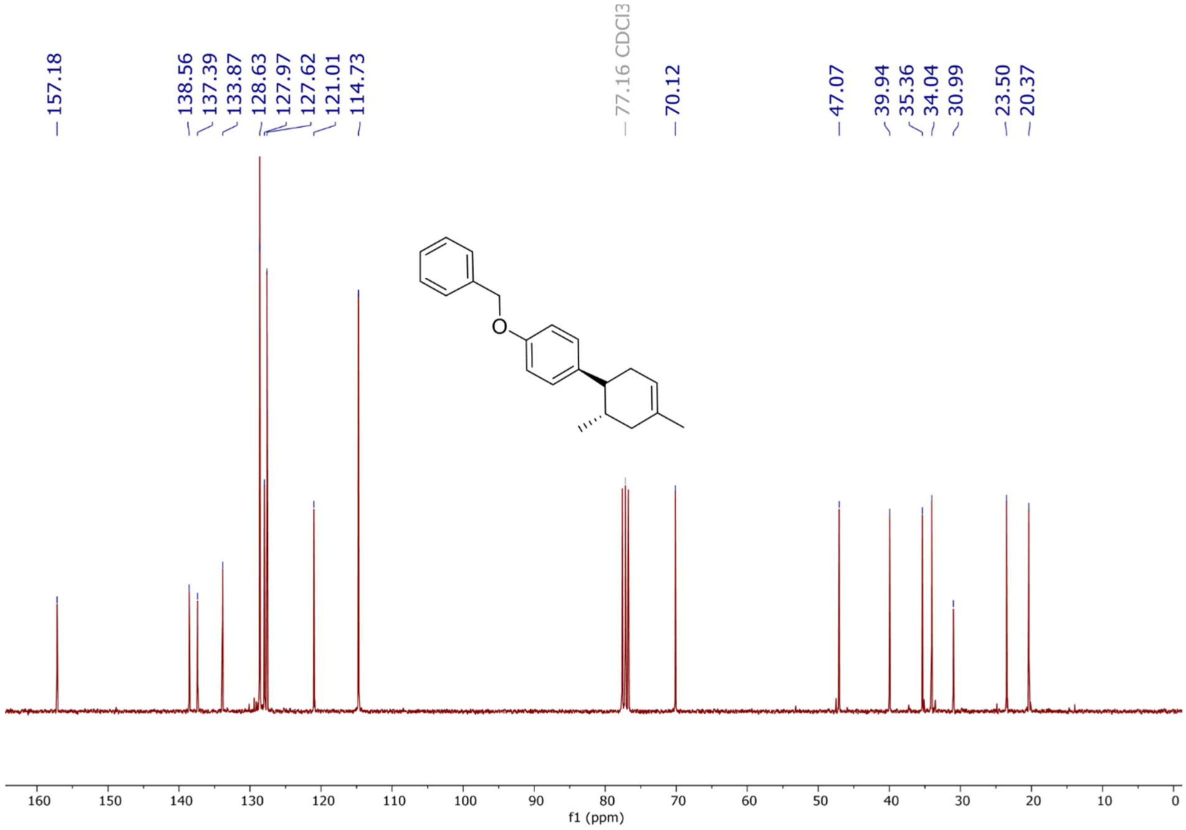
157.18
138.56
137.39
133.87
128.63
127.97
127.62
121.01
114.73
77.16 CDCl3
70.12
47.07
39.94
35.36
34.04
30.99
23.50
20.37
160
150
140
130
120
110
100
90
80
70
60
50
40
30
20
10
0
f1 (ppm)
O

3.6 A water-compatible PMMA-based polymer for photocatalytic pollutant remediation in aqueous media

<u>TRPL traces</u>

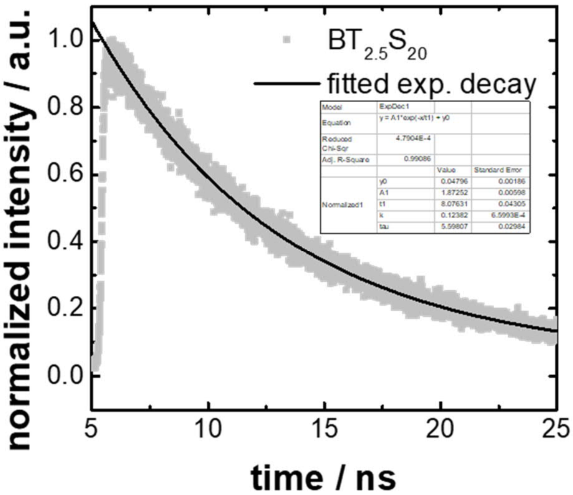

Model	ExpDec1		
Equation	y = A1*exp(-x/t1) + y0		
Reduced Chi-Sqr	4.7904E-4		
Adj. R-Square	0.99086		
		Value	Standard Error
Normalized1	y0	0.04796	0.00186
	A1	1.87252	0.00598
	t1	8.07631	0.04305
	k	0.12382	6.5993E-4
	tau	5.59807	0.02984

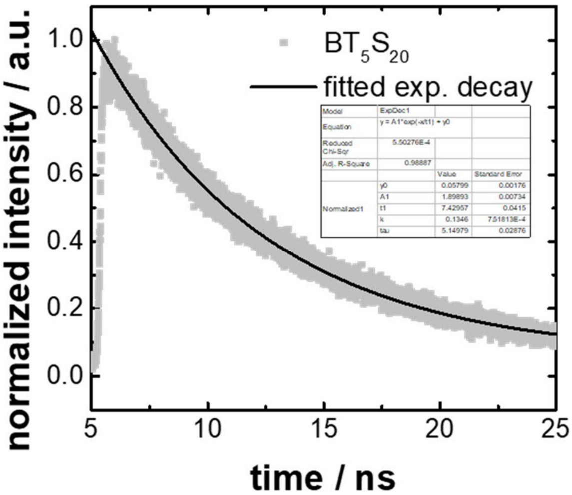

Model	ExpDec1		
Equation	y = A1*exp(-x/t1) + y0		
Reduced Chi-Sqr	5.50276E-4		
Adj. R-Square	0.98887		
		Value	Standard Error
Normalized1	y0	0.05799	0.00176
	A1	1.89893	0.00734
	t1	7.42957	0.0415
	k	0.1346	7.51813E-4
	tau	5.14979	0.02876

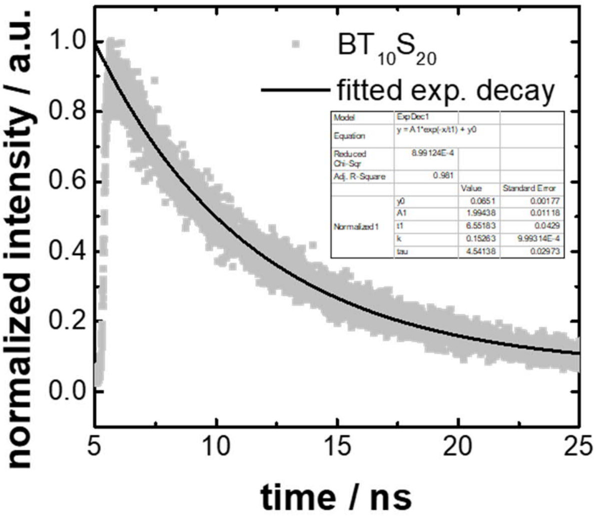

Model	ExpDec1		
Equation	y = A1*exp(-x/t1) + y0		
Reduced Chi-Sqr	8.99124E-4		
Adj. R-Square	0.981		
		Value	Standard Error
Normalized1	y0	0.0651	0.00177
	A1	1.99438	0.01118
	t1	6.55183	0.0429
	k	0.15263	9.99314E-4
	tau	4.54138	0.02973

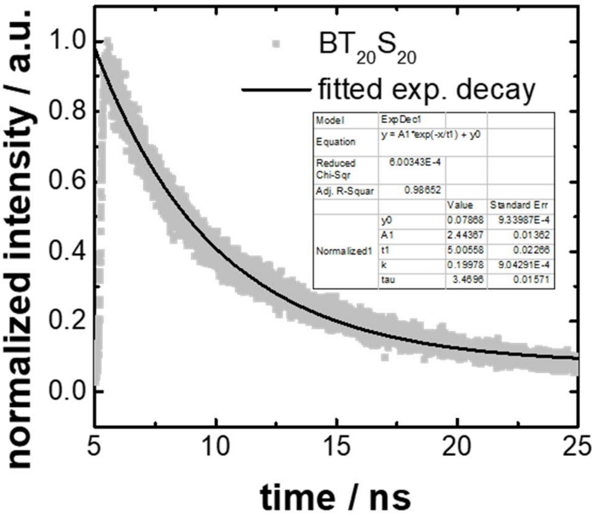

Model	ExpDec1		
Equation	y = A1*exp(-x/t1) + y0		
Reduced Chi-Sqr	6.00343E-4		
Adj. R-Squar	0.98652		
		Value	Standard Err
Normalized1	y0	0.07868	9.33987E-4
	A1	2.44367	0.01362
	t1	5.00558	0.02266
	k	0.19978	9.04291E-4
	tau	3.4696	0.01571

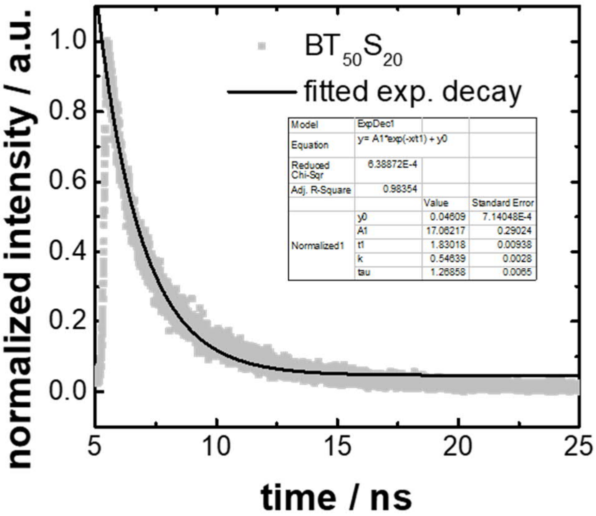

Model	ExpDec1		
Equation	y= A1*exp(-x/t1) + y0		
Reduced Chi-Sqr	6.38872E-4		
Adj. R-Square	0.98354		
		Value	Standard Error
Normalized1	y0	0.04609	7.14048E-4
	A1	17.06217	0.29024
	t1	1.83018	0.00938
	k	0.54639	0.0028
	tau	1.26858	0.0065

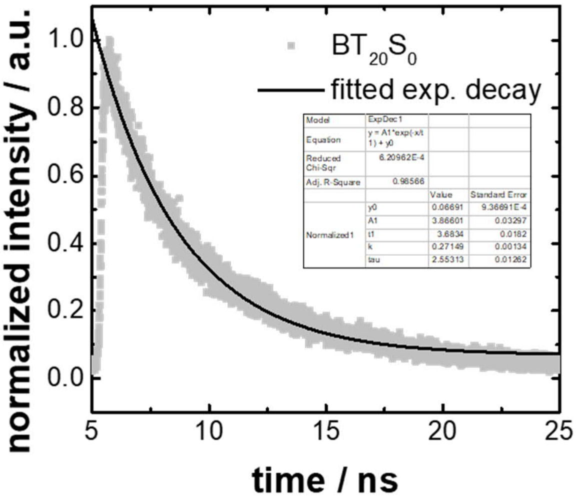

Model	ExpDec1		
Equation	y = A1*exp(-x/t1) + y0		
Reduced Chi-Sqr	6.20962E-4		
Adj. R-Square	0.98566		
		Value	Standard Error
Normalized1	y0	0.06691	9.36691E-4
	A1	3.86601	0.03297
	t1	3.6834	0.0182
	k	0.27149	0.00134
	tau	2.55313	0.01262

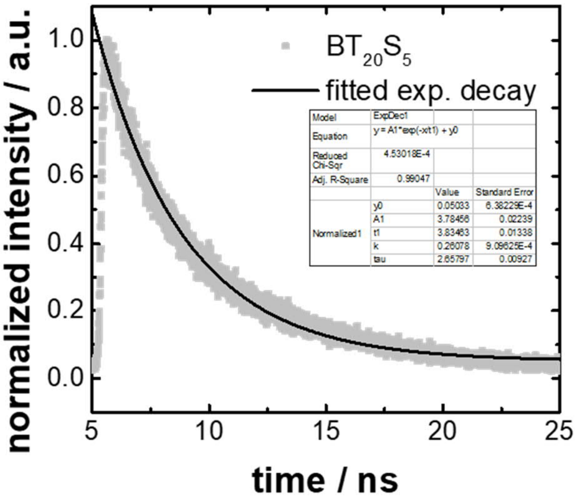

Model	ExpDec1		
Equation	y = A1*exp(-x/t1) + y0		
Reduced Chi-Sqr	4.53018E-4		
Adj. R-Square	0.99047		
		Value	Standard Error
Normalized1	y0	0.05033	6.38229E-4
	A1	3.78456	0.02239
	t1	3.83463	0.01338
	k	0.26078	9.09625E-4
	tau	2.65797	0.00927

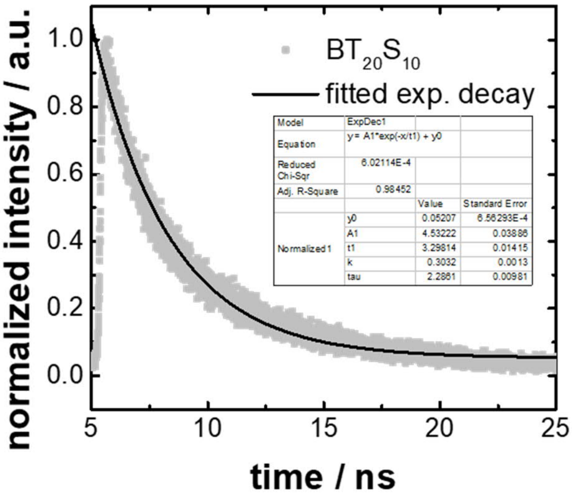

Model	ExpDec1		
Equation	y= A1*exp(-x/t1) + y0		
Reduced Chi-Sqr	6.02114E-4		
Adj. R-Square	0.98452		
		Value	Standard Error
Normalized1	y0	0.05207	6.56293E-4
	A1	4.53222	0.03886
	t1	3.29814	0.01415
	k	0.3032	0.0013
	tau	2.2861	0.00981

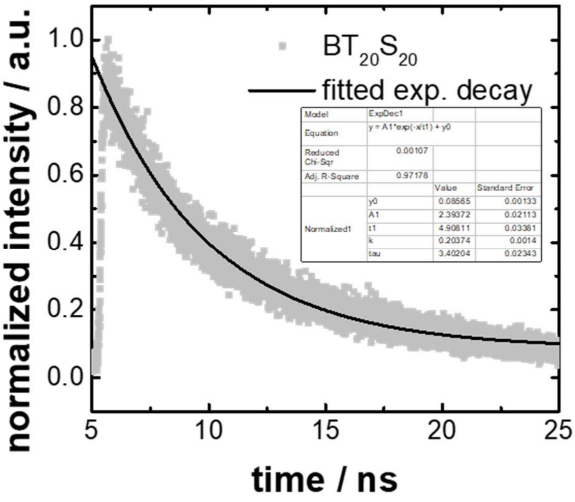

Model	ExpDec1		
Equation	y = A1*exp(-x/t1) + y0		
Reduced Chi-Sqr	0.00107		
Adj. R-Square	0.97178		
		Value	Standard Error
Normalized1	y0	0.08565	0.00133
	A1	2.39372	0.02113
	t1	4.90811	0.03381
	k	0.20374	0.0014
	tau	3.40204	0.02343

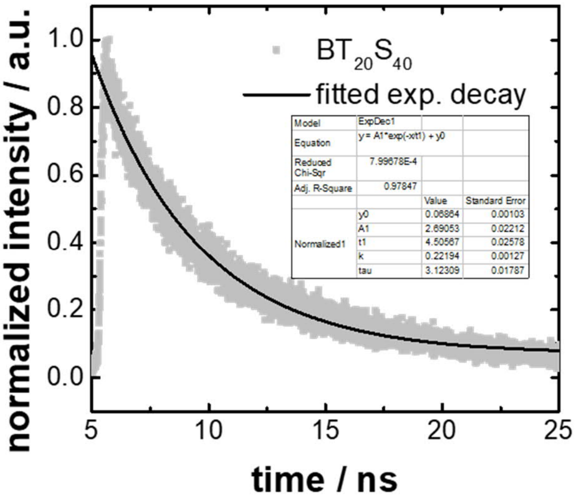

Model	ExpDec1		
Equation	y= A1*exp(-x/t1) + y0		
Reduced Chi-Sqr	7.99678E-4		
Adj. R-Square	0.97847		
		Value	Standard Error
Normalized1	y0	0.06864	0.00103
	A1	2.69053	0.02212
	t1	4.50567	0.02578
	k	0.22194	0.00127
	tau	3.12309	0.01787

4 Summary and outlook

In this thesis, new materials for efficient heterogeneous photocatalysis of organic redox reactions with visible light were explored in depth. The introduced novel catalyst concepts address the most critical challenges for large-scale and future practical applications.

First, thiophene-based covalent triazine frameworks (CTFs) with variable phenyl spacer lengths were prepared and used as efficient and tunable visible-light photocatalysts for the selective aerobic oxidation of inert hydrocarbons under ambient conditions. The photocatalytic activity of the thiophene-based CTF-Th without phenylic linkers exceeds the state-of-art literature examples of metal or non-metal catalysts. A series of alkyl aromatics can be oxidized to their aldehyde and ketone derivatives with excellent conversion and selectivity. To further elaborate on the potential of the high-value reaction, a precursor to the neurological drug AMG 579 was synthesized through direct oxidation of a benzimidazole derivative.

Given the importance of photocatalytic sp^3 carbon oxidation, a so-called dream reaction, future work could focus on performing the reaction in bulk, i.e., in toluene and without additional solvents. Further simplifications in CTF production, e.g., by microwave syntheses, are conceivable. In addition, scaling up this reaction by suitable reactor design or flow chemistry would be helpful.

In the second part, a confinement synthesis for size-controllable CTF nanoparticles was presented. Encapsulation of a thiophene-derived dinitrile monomer in a silica shell, superacid polymerization, and shell removal yields particles with uniform size distributions between 80 and 550 nm. Electronic and optical properties of the CTFs can be optimized through copolymerizing electron-withdrawing benzothiadiazole units. Kinetic studies of a photocatalytic dihydrobenzofuran synthesis proved that both nanoscaling and copolymerization significantly affected photocatalytic activity with an enhanced 18-fold efficiency compared to bulk CTF. The versatility of the CTF nanoparticles was emphasized by conducting three additional reactions.

Given the relevance of nanostructuring to practical applications, further efforts could be made in the size reduction of CTFs. The potential for enhanced catalyst activity or interesting physical effects at the nanoscale is highly interesting. Dispersive embedding in porous support materials for larger-scale applications could be promising.

Next, 2D cadmium selenide nanoplatelets (NPLs) were introduced as efficient heterogeneous photocatalysts for the highly challenging and selective reduction of nitrobenzene towards azoxybenzene. Facile and reproducible syntheses yielded platelet dispersions with 3, 4, or 5 monolayers thickness. The platelets' unique morphological and pure optophysical characteristics allowed the demonstration of direct correlations between their photocatalytic performance, bandgap, light absorption, and charge separation and generation. Particularly low catalyst concentrations of about 10^{-7} M CdSe and recyclability showcase the applicability and potential of CdSe NPLs as a new class of effective photocatalysts.

The property control of photocatalytic systems, which is enormously important for further practical understanding, could be extended in various ways with the continuation of the project. Synthesis of CdSe nanoplatelets with more than five monolayers could allow harvesting longer wavelength regions of the visible spectrum. The precise synthesizability of the platelets could allow more detailed studies of the surface chemistry of photocatalysis. The significance of certain crystal facets or edge regions for the catalytic activity could be interesting.

Furthermore, porous aromatic frameworks (PAFs) are established as a versatile and highly porous platform for heterogeneous photocatalysis. Based on benzothiadiazole, three PAFs were prepared in a building block approach and exhibited tunable optical and redox properties similar to the molecular analogs. The polymer architectures showed precise conjugation length control, high intrinsic porosity up to 1070 m^2/g, advantageous chemical robustness, and recyclability. Within two photocatalytic C-H activations, one hole-initiated aza-Henry reaction - one electron-initiated arylation, the PAFs allowed photocatalytic performance control in direct correlation with their respective band edge potentials. The practical relevance was underlined by the one-batch preparation of the muscle relaxant dantrolene.

PAFs provide a large, tunable platform of materials for photocatalysis. The accurate predictability of their redox potentials through theoretical calculations could be used to synthesize catalysts for any target application. Future work could address automated synthesis as well as screening experiments and thus elucidating the available structure-property space. Factors relevant to photocatalysis could be studied by correlation analyses.

In the fifth part, a low-cost photoactive copolymer based on PMMA was designed. This material exhibited optical and redox properties similar to the analogous molecular photocatalyst while demonstrating advantageous chemical robustness and recyclability attributed to its polymeric nature. The material could efficiently catalyze various Diels-Alder [4+2] cycloaddition reactions at particularly low catalyst loadings of 0.06 mol-%. Detailed photophysical time-resolved photoluminescence (TRPL), transient absorption (TA) studies, and successful recycling experiments complement the project.

The cost-efficient and economic viability of the catalyst make the polymer attractive for practical applications. For example, incorporating other photocatalytically active molecules, using the polymer architecture for biological compatibility and bioorthogonal reactions, or constructing reactors based on the PMMA polymer could be of interest.

In the last part, the previously introduced PMMA photocatalyst platform is further developed towards advanced water compatibility. Variable copolymerization of photoactive benzothiadiazole units as well as a vinylbenzene sulfonate monomer resulted in two series of polymers that could be compared concerning their electro-optical, water-compatible, and photocatalytic properties. Furthermore, the polymers are capable of efficiently removing organic pollutants commonly found in wastewater from aqueous solutions.

Solvent compatibility is an enormously important factor in practical applications. The extension of the project to water splitting experiments could be highly interesting. The polymer could further be used to design nanoreactors to mediate the challenging catalysis of organic reactions in water. Attaching highly polar or charged groups directly to the photoactive moiety could bring positive effects for photocatalytic efficiency. Incorporating responsive behavior, e.g., for metal ions, appears to be a promising direction.

In summary, the approaches investigated in this thesis highlight promising prospects for heterogeneous photocatalytic materials and their photocatalytic application. Overall, the findings make a significant contribution to the development of the scientific area. Moreover, the made observations and drawn conclusions lay a foundation for future research in the field of visible-light-induced photocatalysis.

Appendix

A.1 References

[1] UN Department of economic and social affairs, *World Population Prospects 2019: Highlights*, **2019**,

[2] World Bank, *Global Economic Prospects*, Washington DC, **2021**,

[3] K. von Grebmer, J. Bernstein, R. Alders, O. Dar, R. Kock, F. Rampa, M. Wiemers, K. Acheampong, A. Hanano, B. Higgins, Welthungerhilfe, *Global Hunger Index: One Decade to Zero Hunger - Linking Health and Sustainable Food Systems*, Bonn, Germany, **2020**,

[4] British Petroleum BP, *Statistical Review of World Energy*, **2020**,

[5] International Energy Agency (IEA), *Chemicals*, Paris, **2020**,

[6] D. Tonini, D. Schrijvers, S. Nessi, P. Garcia-Gutierrez, J. Giuntoli, *Int. J. Life Cycle Assess.* **2021**, 1-17.

[7] J. Tsao, N. Lewis, G. Crabtree, US Department of Energy, *Solar FAQs*, **2006**,

[8] K. J. Laidler, *Pure Appl. Chem.* **1996**, *68*, 149-192.

[9] W. Reschetilowski, *Einführung in die heterogene Katalyse*, Springer-Verlag, Berlin, **2015**.

[10] J. Hagen, *Industrial catalysis: a practical approach*, 3rd ed., Wiley-VCH, Weinheim, **2015**.

[11] S. E. Braslavsky, *Pure Appl. Chem.* **2007**, *79*, 293-465.

[12] G. Ciamician, *Science* **1912**, *36*, 385-394.

[13] I. S. Plotnikow, *Z. Phys. Chem.* **1911**, *77*, 472-481.

[14] A. Eibner, *Chem. Ztg.* **1911**, *35*, 753-755.

[15] L. Bruner, J. Kozak, *Z. Elektrochem. Angew. Phys. Chem.* **1911**, *17*, 354-360.

[16] M. A. Fox, *Acc. Chem. Res.* **1983**, *16*, 314-321.

[17] A. Fujishima, K. Honda, *Nature* **1972**, *238*, 37-38.

[18] A. Singh, *Solar Lasers: Another Dimension in Renewable Energy Applications*, **2016**,

[19] Newport Corporation, *Introduction to Solar Radiation*, *https://www.newport.com/t/introduction-to-solar-radiation*, 04.01.2020.

[20] A. L. Linsebigler, G. Q. Lu, J. T. Yates, *Chem. Rev.* **1995**, *95*, 735-758.

[21] N. Li, X. Lang, W. Ma, H. Ji, C. Chen, J. Zhao, *Chem. Commun.* **2013**, *49*, 5034-5036.

[22] S. Yurdakal, G. Palmisano, V. Loddo, V. Augugliaro, L. Palmisano, *J. Am. Chem. Soc.* **2008**, *130*, 1568-1569.

[23] K. Sayama, H. Arakawa, *J. Phys. Chem.* **1993**, *97*, 531-533.

[24] Z. R. Tian, J. A. Voigt, J. Liu, B. Mckenzie, M. J. Mcdermott, M. A. Rodriguez, H. Konishi, H. Xu, *Nat. Mater.* **2003**, *2*, 821-826.

[25] N. Daneshvar, D. Salari, A. Khataee, *J. Photochem. Photobiol. A* **2004**, *162*, 317-322.

[26] C. K. Prier, D. A. Rankic, D. W. C. MacMillan, *Chem. Rev.* **2013**, *113*, 5322-5363.

[27] T. P. Yoon, M. A. Ischay, J. Du, *Nat. Chem.* **2010**, *2*, 527-532.

[28] D. M. Schultz, T. P. Yoon, *Science* **2014**, *343*, 1239176.

[29] J. M. R. Narayanam, C. R. J. Stephenson, *Chem. Soc. Rev.* **2011**, *40*, 102-113.

[30] J. M. R. Narayanam, J. W. Tucker, C. R. J. Stephenson, *J. Am. Chem. Soc.* **2009**, *131*, 8756-8757.

[31] J. W. Tucker, J. M. R. Narayanam, S. W. Krabbe, C. R. J. Stephenson, *Org. Lett.* **2010**, *12*, 368-371.

[32] M. A. Ischay, M. E. Anzovino, J. Du, T. P. Yoon, *J. Am. Chem. Soc.* **2008**, *130*, 12886.

[33] M. A. Ischay, Z. Lu, T. P. Yoon, *J. Am. Chem. Soc.* **2010**, *132*, 8572.

[34] D. A. Nicewicz, D. W. C. MacMillan, *Science* **2008**, *322*, 77-80.

[35] D. A. Nicewicz, T. M. Nguyen, *ACS Catal.* **2014**, *4*, 355-360.

[36] D. Ravelli, M. Fagnoni, A. Albini, *Chem. Soc. Rev.* **2013**, *42*, 97-113.

[37] D. P. Hari, P. Schroll, B. König, *J. Am. Chem. Soc.* **2012**, *134*, 2958-2961.

[38] K. Ohkubo, T. Kobayashi, S. Fukuzumi, *Angew. Chem. Int. Ed.* **2011**, *123*, 8811-8814.

[39] K. Ohkubo, K. Mizushima, R. Iwata, S. Fukuzumi, *Chem. Sci.* **2011**, *2*, 715-722.

[40] D. P. Hari, B. König, *Org. Lett.* **2011**, *13*, 3852-3855.

[41] J. Deng, H. Li, S. Wang, D. Ding, M. Chen, C. Liu, Z. Tian, K. Novoselov, C. Ma, D. Deng, *Nat. Commun.* **2017**, *8*, 1-8.

[42] X.-B. Li, Y.-J. Gao, Y. Wang, F. Zhan, X.-Y. Zhang, Q.-Y. Kong, N.-J. Zhao, Q. Guo, H.-L. Wu, Z.-J. Li, *J. Am. Chem. Soc.* **2017**, *139*, 4789-4796.

[43] J. Zhang, Z. Zhu, X. Feng, *Chem. Eur. J.* **2014**, *20*, 10632-10635.

[44] V. Kumaravel, S. Mathew, J. Bartlett, S. C. Pillai, *Appl. Catal. B Environ.* **2019**, *244*, 1021-1064.

[45] X. Liu, J. Iocozzia, Y. Wang, X. Cui, Y. Chen, S. Zhao, Z. Li, Z. Lin, *Energy Environ. Sci.* **2017**, *10*, 402-434.

[46] X. Lang, X. Chen, J. Zhao, *Chem. Soc. Rev.* **2014**, *43*, 473-486.

[47] Y. Wang, Q. Wang, X. Zhan, F. Wang, M. Safdar, J. He, *Nanoscale* **2013**, *5*, 8326-8339.

[48] C. Karthikeyan, P. Arunachalam, K. Ramachandran, A. M. Al-Mayouf, S. Karuppuchamy, *J. Alloys Compd.* **2020**, *828*, 154281.

[49] F. P. Parrino, Leonardo, *Titanium Dioxide (TiO2) and its Applications*, 1st ed., Elsevier, Amsterdam, **2020**.

[50] M. Zhang, C. Chen, W. Ma, J. Zhao, *Angew. Chem. Int. Ed.* **2008**, *47*, 9730-9733.

[51] V. Jeena, R. S. Robinson, *Chem. Commun.* **2012**, *48*, 299-301.

[52] G. Kim, W. Choi, *Appl. Catal. B Environ.* **2010**, *100*, 77-83.

[53] Y. Park, N. J. Singh, K. S. Kim, T. Tachikawa, T. Majima, W. Choi, *Chem. Eur. J.* **2009**, *15*, 10843-10850.

[54] X. Li, J.-L. Shi, H. Hao, X. Lang, *Appl. Catal. B Environ.* **2018**, *232*, 260-267.

[55] R. Asahi, T. Morikawa, T. Ohwaki, K. Aoki, Y. Taga, *Science* **2001**, *293*, 269-271.

[56] W.-C. Lin, Y.-J. Lin, *Environ. Eng. Sci.* **2012**, *29*, 447-452.

[57] J. Zhu, W. Zheng, B. He, J. Zhang, M. Anpo, *J. Mol. Catal. Chem.* **2004**, *216*, 35-43.

[58] X. Chen, L. Liu, Y. Y. Peter, S. S. Mao, *Science* **2011**, *331*, 746-750.

[59] A. Naldoni, M. Altomare, G. Zoppellaro, N. Liu, Š. Kment, R. Zbořil, P. Schmuki, *ACS Catal.* **2019**, *9*, 345-364.

[60] A. Naldoni, M. Allieta, S. Santangelo, M. Marelli, F. Fabbri, S. Cappelli, C. L. Bianchi, R. Psaro, V. Dal Santo, *J. Am. Chem. Soc.* **2012**, *134*, 7600-7603.

[61] Y. Zhao, Y. Zhao, R. Shi, B. Wang, G. I. Waterhouse, L. Z. Wu, C. H. Tung, T. Zhang, *Adv. Mater.* **2019**, *31*, 1806482.

[62] S. Furukawa, Y. Ohno, T. Shishido, K. Teramura, T. Tanaka, *ACS Catal.* **2011**, *1*, 1150-1153.

[63] T. Shishido, T. Miyatake, K. Teramura, Y. Hitomi, H. Yamashita, T. Tanaka, *J. Phys. Chem. C* **2009**, *113*, 18713-18718.
[64] S. Sakthivel, B. Neppolian, M. V. Shankar, B. Arabindoo, M. Palanichamy, V. Murugesan, *Sol. Energy Mater. Sol. Cells* **2003**, *77*, 65-82.
[65] C. Hariharan, *Appl. Catal. A Gen.* **2006**, *304*, 55-61.
[66] C. Lops, A. Ancona, K. Di Cesare, B. Dumontel, N. Garino, G. Canavese, S. Hernandez, V. Cauda, *Appl. Catal. B Environ.* **2019**, *243*, 629-640.
[67] Y. Zhang, N. Zhang, Z.-R. Tang, Y.-J. Xu, *Chem. Sci.* **2012**, *3*, 2812-2822.
[68] J. Z. Chen, X. J. Wu, L. S. Yin, B. Li, X. Hong, Z. X. Fan, B. Chen, C. Xue, H. Zhang, *Angew. Chem. Int. Ed.* **2015**, *54*, 1210-1214.
[69] H. J. Yan, J. H. Yang, G. J. Ma, G. P. Wu, X. Zong, Z. B. Lei, J. Y. Shi, C. Li, *J. Catal.* **2009**, *266*, 165-168.
[70] M. F. Kuehnel, K. L. Orchard, K. E. Dalle, E. Reisner, *J. Am. Chem. Soc.* **2017**, *139*, 7217-7223.
[71] J. Wang, T. Xia, L. Wang, X. Zheng, Z. Qi, C. Gao, J. Zhu, Z. Li, H. Xu, Y. Xiong, *Angew. Chem. Int. Ed.* **2018**, *57*, 16447-16451.
[72] Y. Hou, A. B. Laursen, J. Zhang, G. Zhang, Y. Zhu, X. Wang, S. Dahl, I. Chorkendorff, *Angew. Chem. Int. Ed.* **2013**, *52*, 3621-3625.
[73] Y.-J. Yuan, Z. Shen, S. Wu, Y. Su, L. Pei, Z. Ji, M. Ding, W. Bai, Y. Chen, Z.-T. Yu, *Appl. Catal. B Environ.* **2019**, *246*, 120-128.
[74] Q. Xiang, F. Cheng, D. Lang, *ChemSusChem* **2016**, *9*, 996-1002.
[75] C. Liu, Z. Chen, C. Su, X. Zhao, Q. Gao, G.-H. Ning, H. Zhu, W. Tang, K. Leng, W. Fu, *Nat. Commun.* **2018**, *9*, 1-9.
[76] J. A. Caputo, L. C. Frenette, N. Zhao, K. L. Sowers, T. D. Krauss, D. J. Weix, *J. Am. Chem. Soc.* **2017**, *139*, 4250-4253.
[77] S. Linic, P. Christopher, D. B. Ingram, *Nat. Mater.* **2011**, *10*, 911-921.
[78] W. Hou, S. B. Cronin, *Adv. Funct. Mater.* **2013**, *23*, 1612-1619.
[79] H. J. Huang, J. C.-S. Wu, H.-P. Chiang, Y.-F. Chou Chau, Y.-S. Lin, Y. H. Wang, P.-J. Chen, *Catalysts* **2020**, *10*, 46.
[80] N. Wu, *Nanoscale* **2018**, *10*, 2679-2696.
[81] S. Mukherjee, F. Libisch, N. Large, O. Neumann, L. V. Brown, J. Cheng, J. B. Lassiter, E. A. Carter, P. Nordlander, N. J. Halas, *Nano Lett.* **2013**, *13*, 240-247.
[82] H. Robatjazi, H. Zhao, D. F. Swearer, N. J. Hogan, L. Zhou, A. Alabastri, M. J. McClain, P. Nordlander, N. J. Halas, *Nat. Commun.* **2017**, *8*, 27.
[83] A. Tanaka, K. Hashimoto, H. Kominami, *Chem. Commun.* **2011**, *47*, 10446-10448.
[84] A. Tanaka, K. Hashimoto, H. Kominami, *J. Am. Chem. Soc.* **2012**, *134*, 14526-14533.
[85] W. Feast, J. Tsibouklis, K. Pouwer, L. Groenendaal, E. Meijer, *Polymer* **1996**, *37*, 5017-5047.
[86] M. G. Kanatzidis, *Chem. Eng. News* **1990**, *68*.
[87] H. Shirakawa, E. J. Louis, A. G. MacDiarmid, C. K. Chiang, A. J. Heeger, *J. Chem. Soc. D* **1977**, 578-580.
[88] C. K. Chiang, C. Fincher Jr, Y. W. Park, A. J. Heeger, H. Shirakawa, E. J. Louis, S. C. Gau, A. G. MacDiarmid, *Phys. Rev. Lett.* **1977**, *39*, 1098.
[89] B. Nordén, E. Krutmeijer, The Royal Swedish Academy of Sciences, **2000**.
[90] J. Byun, K. A. I. Zhang, *Mater. Horiz.* **2020**, *7*, 15-31.
[91] Y. B. Zhou, Z. P. Zhan, *Chem.: Asian J.* **2018**, *13*, 9-19.
[92] C. H. Dai, B. Liu, *Energy Environ. Sci.* **2020**, *13*, 24-52.

[93] S. Yanagida, A. Kabumoto, K. Mizumoto, C. Pac, K. Yoshino, *J. Chem. Soc. D* **1985**, 474-475.
[94] X. C. Wang, K. Maeda, A. Thomas, K. Takanabe, G. Xin, J. M. Carlsson, K. Domen, M. Antonietti, *Nat. Mater.* **2009**, *8*, 76-80.
[95] Y. Wang, X. Wang, M. Antonietti, *Angew. Chem. Int. Ed.* **2012**, *51*, 68-89.
[96] T.-T. Pham, E. W. Shin, *Langmuir* **2018**, *34*, 13144-13154.
[97] W. J. Ong, L. L. Tan, Y. H. Ng, S. T. Yong, S. P. Chai, *Chem. Rev.* **2016**, *116*, 7159-7329.
[98] A. Thomas, A. Fischer, F. Goettmann, M. Antonietti, J.-O. Müller, R. Schlögl, J. M. Carlsson, *J. Mater. Chem.* **2008**, *18*, 4893-4908.
[99] C. Y. Zhou, C. Lai, D. L. Huang, G. M. Zeng, C. Zhang, M. Cheng, L. Hu, J. Wan, W. P. Xiong, M. Wen, X. F. Wen, L. Qin, *Appl. Catal. B Environ.* **2018**, *220*, 202-210.
[100] P. Niu, L. Zhang, G. Liu, H. M. Cheng, *Adv. Funct. Mater.* **2012**, *22*, 4763-4770.
[101] K. Schwinghammer, M. B. Mesch, V. Duppel, C. Ziegler, J. Senker, B. V. Lotsch, *J. Am. Chem. Soc.* **2014**, *136*, 1730-1733.
[102] Y. Kang, Y. Yang, L. C. Yin, X. Kang, G. Liu, H. M. Cheng, *Adv. Mater.* **2015**, *27*, 4572-4577.
[103] G. Liu, P. Niu, C. Sun, S. C. Smith, Z. Chen, G. Q. Lu, H.-M. Cheng, *J. Am. Chem. Soc.* **2010**, *132*, 11642-11648.
[104] P. Niu, L. C. Yin, Y. Q. Yang, G. Liu, H. M. Cheng, *Adv. Mater.* **2014**, *26*, 8046-8052.
[105] X. Ye, Y. Cui, X. Wang, *ChemSusChem* **2014**, *7*, 738-742.
[106] D. D. Zheng, C. J. Huang, X. C. Wang, *Nanoscale* **2015**, *7*, 465-470.
[107] C. K. Yao, A. L. Yuan, Z. S. Wang, H. Lei, L. Zhang, L. M. Guo, X. P. Dong, *J. Mater. Chem. A* **2019**, *7*, 13071-13079.
[108] G. Zhang, C. Huang, X. Wang, *Small* **2015**, *11*, 1215-1221.
[109] Y. Yang, C. Zhang, D. L. Huang, G. M. Zeng, J. H. Huang, C. Lai, C. Y. Zhou, W. J. Wang, H. Guo, W. J. Xue, R. Deng, M. Cheng, W. P. Xiong, *Appl. Catal. B Environ.* **2019**, *245*, 87-99.
[110] X. Chen, J. Zhang, X. Fu, M. Antonietti, X. Wang, *J. Am. Chem. Soc.* **2009**, *131*, 11658-11659.
[111] J.-S. M. Lee, A. I. Cooper, *Chem. Rev.* **2020**, *120*, 2171-2214.
[112] Y. Xu, S. Jin, H. Xu, A. Nagai, D. Jiang, *Chem. Soc. Rev.* **2013**, *42*, 8012-8031.
[113] J.-X. Jiang, F. Su, A. Trewin, C. D. Wood, N. L. Campbell, H. Niu, C. Dickinson, A. Y. Ganin, M. J. Rosseinsky, Y. Z. Khimyak, A. I. Cooper, *Angew. Chem. Int. Ed.* **2007**, *46*, 8574-8578.
[114] K. Zhang, D. Kopetzki, P. H. Seeberger, M. Antonietti, F. Vilela, *Angew. Chem. Int. Ed.* **2013**, *52*, 1432-1436.
[115] N. Kang, J. H. Park, K. C. Ko, J. Chun, E. Kim, H. W. Shin, S. M. Lee, H. J. Kim, T. K. Ahn, J. Y. Lee, *Angew. Chem. Int. Ed.* **2013**, *52*, 6228-6232.
[116] Z. J. Wang, S. Ghasimi, K. Landfester, K. A. I. Zhang, *Chem. Commun.* **2014**, *50*, 8177-8180.
[117] Z. J. Wang, S. Ghasimi, K. Landfester, K. A. I. Zhang, *Adv. Synth. Catal.* **2016**, *358*, 2576-2582.
[118] J.-X. Jiang, Y. Li, X. Wu, J. Xiao, D. J. Adams, A. I. Cooper, *Macromolecules* **2013**, *46*, 8779-8783.
[119] C.-A. Wang, Y.-W. Li, X.-L. Cheng, J.-P. Zhang, Y.-F. Han, *RSC Adv.* **2017**, *7*, 408-414.

[120] M. Liras, M. Iglesias, F. l. Sánchez, *Macromolecules* **2016**, *49*, 1666-1673.
[121] Y. Zhao, K. X. Yao, B. Teng, T. Zhang, Y. Han, *Energy Environ. Sci.* **2013**, *6*, 3684-3692.
[122] P. Lindemann, M. Tsotsalas, S. Shishatskiy, V. Abetz, P. Krolla-Sidenstein, C. Azucena, L. Monnereau, A. Beyer, A. Gölzhäuser, V. Mugnaini, *Chem. Mater.* **2014**, *26*, 7189-7193.
[123] S. N. Talapaneni, D. Kim, G. Barin, O. Buyukcakir, S. H. Je, A. Coskun, *Chem. Mater.* **2016**, *28*, 4460-4466.
[124] K. V. Rao, S. Mohapatra, T. K. Maji, S. J. George, *Chem. Eur. J.* **2012**, *18*, 4505.
[125] X.-S. Wang, J. Liu, J. M. Bonefont, D.-Q. Yuan, P. K. Thallapally, S. Ma, *Chem. Commun.* **2013**, *49*, 1533-1535.
[126] L. Chen, Y. Yang, D. Jiang, *J. Am. Chem. Soc.* **2010**, *132*, 9138-9143.
[127] Y. Xie, T.-T. Wang, X.-H. Liu, K. Zou, W.-Q. Deng, *Nat. Commun.* **2013**, *4*, 1-7.
[128] Y. He, D. Gehrig, F. Zhang, C. Lu, C. Zhang, M. Cai, Y. Wang, F. Laquai, X. Zhuang, X. Feng, *Adv. Funct. Mater.* **2016**, *26*, 8255-8265.
[129] Z. S. Wu, L. Chen, J. Liu, K. Parvez, H. Liang, J. Shu, H. Sachdev, R. Graf, X. Feng, K. Müllen, *Adv. Mater.* **2014**, *26*, 1450-1455.
[130] Y. Xu, L. Chen, Z. Guo, A. Nagai, D. Jiang, *J. Am. Chem. Soc.* **2011**, *133*, 17622-17625.
[131] J.-X. Jiang, A. Trewin, D. J. Adams, A. I. Cooper, *Chem. Sci.* **2011**, *2*, 1777-1781.
[132] Y. Xu, A. Nagai, D. Jiang, *Chem. Commun.* **2013**, *49*, 1591-1593.
[133] X. Liu, Y. Xu, D. Jiang, *J. Am. Chem. Soc.* **2012**, *134*, 8738-8741.
[134] J. L. Novotney, W. R. Dichtel, *ACS Macro Lett.* **2013**, *2*, 423-426.
[135] Z. Li, H. Li, H. Xia, X. Ding, X. Luo, X. Liu, Y. Mu, *Chem. Eur. J.* **2015**, *21*, 17355-17362.
[136] Y. Kou, Y. Xu, Z. Guo, D. Jiang, *Angew. Chem. Int. Ed.* **2011**, *50*, 8753-8757.
[137] Y. Liao, H. Wang, M. Zhu, A. Thomas, *Adv. Mater.* **2018**, *30*, 1705710.
[138] H. Zhang, Y. Zhang, C. Gu, Y. Ma, *Adv. Funct. Mater.* **2015**, *5*, 1402175.
[139] C. Zhang, Y. He, P. Mu, X. Wang, Q. He, Y. Chen, J. Zeng, F. Wang, Y. Xu, J. X. Jiang, *Adv. Funct. Mater.* **2018**, *28*, 1705432.
[140] J. Tan, J. Wan, J. Guo, C. Wang, *Chem. Commun.* **2015**, *51*, 17394-17397.
[141] Z. Li, X. Feng, S. Gao, Y. Jin, W. Zhao, H. Liu, X. Yang, S. Hu, K. Cheng, J. Zhang, *ACS Appl. Bio Mater.* **2019**, *2*, 613-618.
[142] C. Gu, N. Huang, J. Gao, F. Xu, Y. Xu, D. Jiang, *Angew. Chem. Int. Ed.* **2014**, *53*, 4850-4855.
[143] W. Toland, in *US Patent, Vol. 3060179*, **1962**.
[144] G. Miller, in *US Patent, Vol. 3775380*, **1973**.
[145] H. A. Vogel, in *US Patent, Vol. 3654192*, **1972**.
[146] P. Kuhn, M. Antonietti, A. Thomas, *Angew. Chem. Int. Ed.* **2008**, *47*, 3450-3453.
[147] Y. Shirota, *J. Mater. Chem.* **2000**, *10*, 1-25.
[148] H. Hoppe, N. S. Sariciftci, *J. Mater. Res.* **2004**, *19*, 1924-1945.
[149] Y. F. Xu, N. Mao, C. Zhang, X. Wang, J. H. Zeng, Y. Chen, F. Wang, J. X. Jiang, *Appl. Catal. B Environ.* **2018**, *228*, 1-9.
[150] M. Y. Liu, L. P. Guo, S. B. Jin, B. E. Tan, *J. Mater. Chem. A* **2019**, *7*, 5153-5172.
[151] P. Katekomol, J. Roeser, M. Bojdys, J. Weber, A. Thomas, *Chem. Mater.* **2013**, *25*, 1542-1548.
[152] M. J. Bojdys, J. Jeromenok, A. Thomas, M. Antonietti, *Adv. Mater.* **2010**, *22*, 2202-2205.

[153] K. Schwinghammer, S. Hug, M. B. Mesch, J. Senker, B. V. Lotsch, *Energy Environ. Sci.* **2015**, *8*, 3345-3353.
[154] D. Y. Osadchii, A. I. Olivos-Suarez, A. V. Bavykina, J. Gascon, *Langmuir* **2017**, *33*, 14278-14285.
[155] S. Kuecken, J. Schmidt, L. Zhi, A. Thomas, *J. Mater. Chem. A* **2015**, *3*, 24422-24427.
[156] S. Ren, M. J. Bojdys, R. Dawson, A. Laybourn, Y. Z. Khimyak, D. J. Adams, A. I. Cooper, *Adv. Mater.* **2012**, *24*, 2357-2361.
[157] X. Zhu, C. Tian, S. M. Mahurin, S.-H. Chai, C. Wang, S. Brown, G. M. Veith, H. Luo, H. Liu, S. Dai, *J. Am. Chem. Soc.* **2012**, *134*, 10478-10484.
[158] J. Liu, W. Zan, K. Li, Y. Yang, F. Bu, Y. Xu, *J. Am. Chem. Soc.* **2017**, *139*, 11666-11669.
[159] J. Liu, P. Lyu, Y. Zhang, P. Nachtigall, Y. Xu, *Adv. Mater.* **2018**, *30*, 1705401.
[160] W. Huang, B. C. Ma, H. Lu, R. Li, L. Wang, K. Landfester, K. A. I. Zhang, *ACS Catal.* **2017**, *7*, 5438-5442.
[161] W. Huang, Z. J. Wang, B. C. Ma, S. Ghasimi, D. Gehrig, F. Laquai, K. Landfester, K. A. Zhang, *J. Mater. Chem. A* **2016**, *4*, 7555-7559.
[162] K. Wang, L. M. Yang, X. Wang, L. Guo, G. Cheng, C. Zhang, S. Jin, B. Tan, A. Cooper, *Angew. Chem. Int. Ed.* **2017**, *56*, 14149-14153.
[163] M. Liu, Q. Huang, S. Wang, Z. Li, B. Li, S. Jin, B. Tan, *Angew. Chem. Int. Ed.* **2018**, *57*, 11968-11972.
[164] M. Liu, K. Jiang, X. Ding, S. Wang, C. Zhang, J. Liu, Z. Zhan, G. Cheng, B. Li, H. Chen, *Adv. Mater.* **2019**, *31*, 1807865.
[165] N. Wang, G. Cheng, L. P. Guo, B. E. Tan, S. B. Jin, *Adv. Funct. Mater.* **2019**, *29*, 1904781.
[166] X. Zhu, C. Tian, G. M. Veith, C. W. Abney, J. r. m. Dehaudt, S. Dai, *J. Am. Chem. Soc.* **2016**, *138*, 11497-11500.
[167] C. Krishnaraj, H. S. Jena, K. Leus, H. M. Freeman, L. G. Benning, P. Van Der Voort, *J. Mater. Chem. A* **2019**, *7*, 13188-13196.
[168] S. Hug, L. Stegbauer, H. Oh, M. Hirscher, B. V. Lotsch, *Chem. Mater.* **2015**, *27*, 8001-8010.
[169] A. Bhunia, S. Dey, M. Bous, C. Zhang, W. von Rybinski, C. Janiak, *Chem. Commun.* **2015**, *51*, 484-486.
[170] S. Mondal, S. Chatterjee, S. Mondal, A. Bhaumik, *ACS Sustain. Chem. Eng.* **2019**, *7*, 7353-7361.
[171] R. Palkovits, M. Antonietti, P. Kuhn, A. Thomas, F. Schüth, *Angew. Chem. Int. Ed.* **2009**, *48*, 6909-6912.
[172] C. E. Chan-Thaw, A. Villa, P. Katekomol, D. Su, A. Thomas, L. Prati, *Nano Lett.* **2010**, *10*, 537-541.
[173] C. Lu, J. Yang, S. Wei, S. Bi, Y. Xia, M. Chen, Y. Hou, M. Qiu, C. Yuan, Y. Su, *Adv. Funct. Mater.* **2019**, *29*, 1806884.
[174] J.-D. Yi, R. Xu, Q. Wu, T. Zhang, K.-T. Zang, J. Luo, Y.-L. Liang, Y.-B. Huang, R. Cao, *ACS Energy Lett.* **2018**, *3*, 883-889.
[175] S. H. Je, H. J. Kim, J. Kim, J. W. Choi, A. Coskun, *Adv. Funct. Mater.* **2017**, *27*, 1703947.
[176] L. Hao, J. Ning, B. Luo, B. Wang, Y. Zhang, Z. Tang, J. Yang, A. Thomas, L. Zhi, *J. Am. Chem. Soc.* **2015**, *137*, 219-225.
[177] Y. Li, S. Zheng, X. Liu, P. Li, L. Sun, R. Yang, S. Wang, Z.-S. Wu, X. Bao, W.-Q. Deng, *Angew. Chem. Int. Ed.* **2018**, *57*, 7992-7996.

[178] Z. A. Lan, Y. X. Fang, Y. F. Zhang, X. C. Wang, *Angew. Chem. Int. Ed.* **2018**, *57*, 470-474.
[179] S. Kuecken, A. Acharjya, L. J. Zhi, M. Schwarze, R. Schomacker, A. Thomas, *Chem. Commun.* **2017**, *53*, 5854-5857.
[180] L. Guo, Y. Niu, H. Xu, Q. Li, S. Razzaque, Q. Huang, S. Jin, B. Tan, *J. Mater. Chem. A* **2018**, *6*, 19775-19781.
[181] J. Xie, S. A. Shevlin, Q. Ruan, S. J. Moniz, Y. Liu, X. Liu, Y. Li, C. C. Lau, Z. X. Guo, J. Tang, *Energy Environ. Sci.* **2018**, *11*, 1617-1624.
[182] R. Xu, X.-S. Wang, H. Zhao, H. Lin, Y.-B. Huang, R. Cao, *Catal. Sci. Technol.* **2018**, *8*, 2224-2230.
[183] H. Zhong, Z. Hong, C. Yang, L. Li, Y. Xu, X. Wang, R. Wang, *ChemSusChem* **2019**, *12*, 4493-4499.
[184] W. Huang, J. Byun, I. Rörich, C. Ramanan, P. W. M. Blom, H. Lu, D. Wang, L. C. da Silva, R. Li, L. Wang, K. Landfester, K. A. I. Zhang, *Angew. Chem. Int. Ed.* **2018**, *57*, 8316-8320.
[185] T. Ben, H. Ren, S. Q. Ma, D. P. Cao, J. H. Lan, X. F. Jing, W. C. Wang, J. Xu, F. Deng, J. M. Simmons, S. L. Qiu, G. S. Zhu, *Angew. Chem. Int. Ed.* **2009**, *48*, 9457-9460.
[186] D. Yuan, W. Lu, D. Zhao, H. C. Zhou, *Adv. Mater.* **2011**, *23*, 3723-3725.
[187] Y. Tian, G. Zhu, *Chem. Rev.* **2020**, *120*, 8934-8986.
[188] T. Ben, C. Pei, D. Zhang, J. Xu, F. Deng, X. Jing, S. Qiu, *Energy Environ. Sci.* **2011**, *4*, 3991-3999.
[189] Y. Yuan, G. Zhu, *ACS Cent. Sci.* **2019**, *5*, 409-418.
[190] C. H. Lau, K. Konstas, A. W. Thornton, A. C. Y. Liu, S. Mudie, D. F. Kennedy, S. C. Howard, A. J. Hill, M. R. Hill, *Angew. Chem. Int. Ed.* **2015**, *54*, 2669-2673.
[191] B. Li, Y. Zhang, D. Ma, Z. Shi, S. Ma, *Nat. Commun.* **2014**, *5*, 1-7.
[192] B. Li, Q. Sun, Y. Zhang, C. W. Abney, B. Aguila, W. Lin, S. Ma, *ACS Appl. Mater. Interfaces* **2017**, *9*, 12511-12517.
[193] Y. Yuan, Y. Yang, M. Faheem, X. Zou, X. Ma, Z. Wang, Q. Meng, L. Wang, S. Zhao, G. Zhu, *Adv. Mater.* **2018**, *30*, 1800069.
[194] Y. Yuan, F. Sun, H. Ren, X. Jing, W. Wang, H. Ma, H. Zhao, G. Zhu, *J. Mater. Chem.* **2011**, *21*, 13498-13502.
[195] J. R. Holst, E. Stöckel, D. J. Adams, A. I. Cooper, *Macromolecules* **2010**, *43*, 8531-8538.
[196] Z. Yan, Y. Yuan, Y. Tian, D. Zhang, G. Zhu, *Angew. Chem. Int. Ed.* **2015**, *54*, 12733-12737.
[197] N. Miyaura, A. Suzuki, *J. Chem. Soc. D* **1979**, 866-867.
[198] N. Miyaura, K. Yamada, A. Suzuki, *Tet. Lett.* **1979**, *20*, 3437-3440.
[199] A. Suzuki, *J. Organomet. Chem.* **1999**, *576*, 147-168.
[200] C. Seechurn, M. O. Kitching, T. J. Colacot, V. Snieckus, *Angew. Chem. Int. Ed.* **2012**, *51*, 5062-5085.
[201] B. P. Carrow, J. F. Hartwig, *J. Am. Chem. Soc.* **2011**, *133*, 2116-2119.
[202] A. A. Thomas, S. E. Denmark, *Science* **2016**, *352*, 329-332.
[203] K. Sonogashira, Y. Tohda, N. Hagihara, *Tet. Lett.* **1975**, 4467-4470.
[204] R. Chinchilla, C. Najera, *Chem. Soc. Rev.* **2011**, *40*, 5084-5121.
[205] M. Gazvoda, M. Virant, B. Pinter, J. Košmrlj, *Nat. Commun.* **2018**, *9*, 4814.
[206] M. García-Melchor, M. C. Pacheco, C. Nájera, A. Lledós, G. Ujaque, *ACS Catal.* **2012**, *2*, 135-144.

[207] L. H. Zou, A. J. Johansson, E. Zuidema, C. Bolm, *Chem. Eur. J.* **2013**, *19*, 8144-8152.

[208] R. Mülhaupt, *Angew. Chem. Int. Ed.* **2004**, *43*, 1054-1063.

[209] Grand View Research Inc., Plastic Market Size Share & Trends Analysis Report 2020-2027, *Plastic Market Size, Share & Trends Analysis Report 2020-2027*, **2020**,

[210] M. Gallei, B. V. Schmidt, *Nachr. Chem.* **2020**, *68*, 56-64.

[211] A. P. Schaap, A. L. Thayer, E. C. Blossey, D. C. Neckers, *J. Am. Chem. Soc.* **1975**, *97*, 3741-3745.

[212] B. Paczkowska, J. Paczkowski, D. Neckers, *Macromolecules* **1986**, *19*, 863-870.

[213] J. Paczkowski, D. Neckers, *Macromolecules* **1985**, *18*, 1245-1253.

[214] M. I. Burguete, R. Gavara, F. Galindo, S. V. Luis, *Catal. Commun.* **2010**, *11*, 1081-1084.

[215] W. Li, L. Li, G. Cui, Y. Bai, X. Xiao, Y. Li, L. Yan, *Chem.: Asian J.* **2017**, *12*, 392-396.

[216] J. Guerra, D. Cantillo, C. O. Kappe, *Catal. Sci. Technol.* **2016**, *6*, 4695-4699.

[217] N. Priyadarshani, Y. Liang, J. Suriboot, H. S. Bazzi, D. E. Bergbreiter, *ACS Macro Lett.* **2013**, *2*, 571-574.

[218] D. Rackl, P. Kreitmeier, O. Reiser, *Green Chem.* **2016**, *18*, 214-219.

[219] H. Shimakoshi, M. Nishi, A. Tanaka, K. Chikama, Y. Hisaeda, *Chem. Commun.* **2011**, *47*, 6548-6550.

[220] W. Lü, C. Sun, Q. Lu, N. Li, D. Wu, Y. Yao, W. Chen, *Sci. China Chem.* **2012**, *55*, 1108-1114.

[221] W.-J. Yoo, S. Kobayashi, *Green Chem.* **2014**, *16*, 2438-2442.

[222] C. Boussiron, M. Le Bechec, L. Petrizza, J. Sabalot, S. Lacombe, M. Save, *Macromol. Rapid Commun.* **2019**, *40*.

[223] J. M. Tobin, T. J. McCabe, A. W. Prentice, S. Holzer, G. O. Lloyd, M. J. Paterson, V. Arrighi, P. A. Cormack, F. Vilela, *ACS Catal.* **2017**, *7*, 4602-4612.

[224] L. Wang, J. Byun, R. Li, W. Huang, K. A. I. Zhang, *Adv. Synth. Catal.* **2018**, *360*, 4312-4318.

[225] M. Hesse, H. Meier, B. Zeeh, *Spektroskopische Methoden in der organischen Chemie, Vol. 8*, Georg Thieme Verlag, Stuttgart, **2012**.

[226] L. Reimer, *Transmission electron microscopy: physics of image formation and microanalysis, Vol. 36*, Springer, Berlin/Heidelberg, **2013**.

[227] L. Reimer, *Scanning Electron Microscopy: Physics of Image Formation and Microanalysis, Vol. 45*, Springer, Berlin/Heidelberg, **2013**.

[228] J. B. Condon, *Surface Area and Porosity Determinations by Physisorption: Measurement, Classical Theories and Quantum Theory'*, 1st ed., Elsevier, Amsterdam, **2006**.

[229] S. Brunauer, P. H. Emmett, *J. Am. Chem. Soc.* **1937**, *59*, 2682-2689.

[230] J. Rouquerol, D. Avnir, C. Fairbridge, D. Everett, J. Haynes, N. Pernicone, J. Ramsay, K. Sing, K. Unger, *Pure Appl. Chem* **1994**, *66*, 1739.

[231] K. S. E. Sing, D H; Haul, R A W; Moscou, L; Pierotti, R A; Rouquérol, J; Siemieniewska, T, *Pure Appl. Chem.* **1985**, *57*, 603-619.

[232] M. J. Duer, *Solid state NMR spectroscopy*, 1st ed., Blackwell Science London, **2002**.

[233] C. S. Kumar, *UV-VIS and photoluminescence spectroscopy for nanomaterials characterization*, Springer, Berlin / Heidelberg, **2013**.

[234] P. T. Kissinger, W. R. Heineman, *J. Chem. Educ.* **1983**, *60*, 702.

[235] N. Elgrishi, K. J. Rountree, B. D. McCarthy, E. S. Rountree, T. T. Eisenhart, J. L. Dempsey, *J. Chem. Educ.* **2018**, *95*, 197-206.
[236] R. A. Sheldon, H. Van Bekkum, *Fine chemicals through heterogeneous catalysis*, John Wiley & Sons, **2008**.
[237] A. A. Amin, J. K. Beattie, *Org. Process Res. Dev.* **2003**, *7*, 879-882.
[238] D. P. Hruszkewycz, K. C. Miles, O. R. Thiel, S. S. Stahl, *Chem. Sci.* **2017**, *8*, 1282-1287.
[239] H. Sterckx, B. Morel, B. U. Maes, *Angew. Chem. Int. Ed.* **2019**, *58*, 7946-7970.
[240] P. Zhang, Y. Gong, H. Li, Z. Chen, Y. Wang, *Nat. Commun.* **2013**, *4*, 1593.
[241] L. Kesavan, R. Tiruvalam, M. H. Ab Rahim, M. I. bin Saiman, D. I. Enache, R. L. Jenkins, N. Dimitratos, J. A. Lopez-Sanchez, S. H. Taylor, D. W. Knight, *Science* **2011**, *331*, 195-199.
[242] Y. Mao, A. Bakac, *J. Phys. Chem.* **1996**, *100*, 4219-4223.
[243] S. S. Stahl, P. L. Alsters, *Liquid Phase Aerobic Oxidation Catalysis: Industrial Applications and Academic Perspectives*, Wiley-VCH, Weinheim, **2016**.
[244] B. M. Trost, *Angew. Chem. Int. Ed.* **1995**, *34*, 259-281.
[245] R. A. Sheldon, *Pure Appl. Chem.* **2000**, *72*, 1233-1246.
[246] P. Wu, C. He, J. Wang, X. Peng, X. Li, Y. An, C. Duan, *J. Am. Chem. Soc.* **2012**, *134*, 14991-14999.
[247] M. Cherevatskaya, M. Neumann, S. Füldner, C. Harlander, S. Kümmel, S. Dankesreiter, A. Pfitzner, K. Zeitler, B. König, *Angew. Chem. Int. Ed.* **2012**, *51*, 4062-4066.
[248] F.-L. Cao, J.-G. Wang, F.-J. Lv, D.-Q. Zhang, Y.-N. Huo, G.-S. Li, H.-X. Li, J. Zhu, *Catal. Commun.* **2011**, *12*, 946-950.
[249] M.-Q. Yang, Y. Zhang, N. Zhang, Z.-R. Tang, Y.-J. Xu, *Sci. Rep.* **2013**, *3*.
[250] K. Teramura, T. Ohuchi, T. Shishido, T. Tanaka, *J. Phys. Chem. C* **2009**, *113*, 17018-17024.
[251] S. Sarina, H. Zhu, Z. Zheng, S. Bottle, J. Chang, X. Ke, J.-C. Zhao, Y. Huang, A. Sutrisno, M. Willans, *Chem. Sci.* **2012**, *3*, 2138-2146.
[252] S. Furukawa, T. Shishido, K. Teramura, T. Tanaka, *J. Phys. Chem. C* **2011**, *115*, 19320-19327.
[253] K. Tamai, K. Murakami, S. Hosokawa, H. Asakura, K. Teramura, T. Tanaka, *J. Phys. Chem. C* **2017**, *121*, 22854-22861.
[254] Y. Liu, L. Chen, Q. Yuan, J. He, C.-T. Au, S.-F. Yin, *ChemComm* **2016**, *52*, 1274-1277.
[255] J. Luo, X. Zhang, J. Lu, J. Zhang, *ACS Catal.* **2017**, *7*, 5062-5070.
[256] G. Zhang, Z. A. Lan, X. Wang, *Angew. Chem. Int. Ed.* **2016**, *55*, 15712-15727.
[257] A. Casey, S. D. Dimitrov, P. Shakya-Tuladhar, Z. P. Fei, M. Nguyen, Y. Han, T. D. Anthopoulos, J. R. Durrant, M. Heeney, *Chem. Mater.* **2016**, *28*, 5110-5120.
[258] J. Luo, X. Zhang, J. Zhang, *ACS Catal.* **2015**, *5*, 2250-2254.
[259] W. J. Zhang, J. T. Tang, W. G. Yu, Q. Huang, Y. Fu, G. C. Kuang, C. Y. Pan, G. P. Yu, *ACS Catal.* **2018**, *8*, 8084-8091.
[260] L. Y. Li, W. Fang, P. Zhang, J. H. Bi, Y. H. He, J. Y. Wang, W. Y. Su, *J. Mater. Chem. A* **2016**, *4*, 12402-12406.
[261] C. C. Wang, Y. Guo, Y. Yang, S. Chu, C. K. Zhou, Y. Wang, Z. G. Zou, *ACS Appl. Mater. Interfaces* **2014**, *6*, 4321-4328.
[262] B. C. Ma, S. Ghasimi, K. Landfester, K. A. Zhang, *J. Mater. Chem. B* **2016**, *4*, 5112-5118.
[263] N. Wang, G. Cheng, L. Guo, B. Tan, S. Jin, *Adv. Funct. Mater.* **2019**, *29*, 1904781.

[264] J. H. Ko, N. Kang, N. Park, H.-W. Shin, S. Kang, S. M. Lee, H. J. Kim, T. K. Ahn, S. U. Son, *ACS Macro Lett.* **2015**, *4*, 669-672.
[265] M. G. Schwab, M. Hamburger, X. Feng, J. Shu, H. W. Spiess, X. Wang, M. Antonietti, K. Müllen, *Chem. Commun.* **2010**, *46*, 8932-8934.
[266] V. S. Vyas, F. Haase, L. Stegbauer, G. Savasci, F. Podjaski, C. Ochsenfeld, B. V. Lotsch, *Nat. Commun.* **2015**, *6*, 8508.
[267] L. Li, Z. Cai, *Polym. Chem.* **2016**, *7*, 4937-4943.
[268] L. W. Li, Z. X. Cai, Q. H. Wu, W. Y. Lo, N. Zhang, L. X. Chen, L. P. Yu, *J. Am. Chem. Soc.* **2016**, *138*, 7681-7686.
[269] C. B. Meier, R. S. Sprick, A. Monti, P. Guiglion, J.-S. M. Lee, M. A. Zwijnenburg, A. I. Cooper, *Polymer* **2017**.
[270] M. Watanabe, H. Hagiwara, A. Iribe, Y. Ogata, K. Shiomi, A. Staykov, S. Ida, K. Tanaka, T. Ishihara, *J. Mater. Chem. A* **2014**, *2*, 12952-12961.
[271] R. S. Sprick, C. M. Aitchison, E. Berardo, L. Turcani, L. Wilbraham, B. M. Alston, K. E. Jelfs, M. A. Zwijnenburg, A. I. Cooper, *J. Mater. Chem. A* **2018**, *6*, 11994-12003.
[272] Z.-A. Lan, Y. Fang, Y. Zhang, X. Wang, *Angew. Chem. Int. Ed.* **2017**.
[273] S. Kuecken, A. Acharjya, L. Zhi, M. Schwarze, R. Schomäcker, A. Thomas, *ChemComm* **2017**, *53*, 5854-5857.
[274] J. Bi, W. Fang, L. Li, J. Wang, S. Liang, Y. He, M. Liu, L. Wu, *Macromol. Rapid Commun.* **2015**, *36*, 1799-1805.
[275] Y. Sun, S. Gao, F. Lei, Y. Xie, *Chem. Soc. Rev.* **2015**, *44*, 623-636.
[276] W. Huang, N. Huber, S. Jiang, K. Landfester, K. A. Zhang, *Angew. Chem. Int. Ed.* **2020**, *59*, 18368-18373.
[277] T. Lu, F. Chen, *J. Comput. Chem.* **2012**, *33*, 580-592.
[278] J. P. Losada, I. Heckl, B. Bertok, F. Friedler, J. C. Garcia-Ojeda, A. Argoti, *Chem. Eng. Trans.* **2015**, *45*, 1369-1374.
[279] F. Brühne, E. Wright, *Benzaldehyde - Ullmann's Encyclopedia of Industrial Chemistry, Vol. 6*, Wiley-VCH, Weinheim, **2011**.
[280] B. E. Obgrande J.L., Hesser M., Andrews J., *Benzaldehyde - Kirk-Othmer Encyclopedia of Chemical Technology*, John Wiley and Sons Inc., Hoboken, New Jersey, **1987**.
[281] S. Verma, R. Nasir Baig, M. N. Nadagouda, R. S. Varma, *ACS Sustain. Chem. Eng.* **2016**, *4*, 2333-2336.
[282] R. Yuan, S. Fan, H. Zhou, Z. Ding, S. Lin, Z. Li, Z. Zhang, C. Xu, L. Wu, X. Wang, *Angew. Chem. Int. Ed.* **2013**, *125*, 1069-1073.
[283] B. Mühldorf, R. Wolf, *Angew. Chem. Int. Ed.* **2016**, *55*, 427-430.
[284] X. Ding, B. H. Han, *Angew. Chem. Int. Ed.* **2015**, *54*, 6536-6539.
[285] H. Wang, S. Jiang, S. Chen, D. Li, X. Zhang, W. Shao, X. Sun, J. Xie, Z. Zhao, Q. Zhang, *Adv. Mater.* **2016**, *28*, 6940-6945.
[286] M. Sleiman, P. Conchon, C. Ferronato, J.-M. Chovelon, *Appl. Catal. B Environ.* **2009**, *86*, 159-165.
[287] O. d'Hennezel, P. Pichat, D. F. Ollis, *J. Photochem. Photobiol. A* **1998**, *118*, 197-204.
[288] E. Hu, N. Chen, M. P. Bourbeau, P. E. Harrington, K. Biswas, R. K. Kunz, K. L. Andrews, S. Chmait, X. Zhao, C. Davis, *J. Med. Chem.* **2014**, *57*, 6632-6641.
[289] O. R. Thiel, J. R. Huckins, D. B. Brown, E. A. Bercot, J. T. Colyer, B. Riahi, R. R. Milburn, S. M. Shaw, J. Tomaskevitch, in *Managing Hazardous Reactions and Compounds in Process Chemistry*, ACS Symp. Ser., **2014**, pp. 1181, 1269-1282.

[290] M. Frisch, G. Trucks, H. B. Schlegel, G. E. Scuseria, M. A. Robb, J. R. Cheeseman, G. Scalmani, V. Barone, B. Mennucci, G. Petersson, Gaussian, Inc., Wallingford CT, **2009**.
[291] C. Adamo, V. Barone, *J. Chem. Phys.* **1999**, *110*, 6158-6170.
[292] F. Weigend, R. Ahlrichs, *Phys. Chem. Chem. Phys.* **2005**, *7*, 3297-3305.
[293] F. Weigend, *Phys. Chem. Chem. Phys.* **2006**, *8*, 1057-1065.
[294] S. Miertuš, E. Scrocco, J. Tomasi, *Chem. Phys.* **1981**, *55*, 117-129.
[295] S. Miertus, J. Tomasi, *Chem. Phys.* **1982**, *65*, 239-245.
[296] J.-L. Pascual-ahuir, E. Silla, I. Tunon, *J. Comput. Chem.* **1994**, *15*, 1127-1138.
[297] W. Stöber, A. Fink, E. Bohn, *J. Colloid Interface Sci.* **1968**, *26*, 62-69.
[298] D. Astruc, F. Lu, J. R. Aranzaes, *Angew. Chem. Int. Ed.* **2005**, *44*, 7852-7872.
[299] D. Astruc, *Nanoparticles and catalysis*, John Wiley & Sons, Weinheim, **2008**.
[300] J. Grunes, A. Zhu, G. A. Somorjai, *Chem. Commun.* **2003**, 2257-2260.
[301] R. J. White, R. Luque, V. L. Budarin, J. H. Clark, D. J. Macquarrie, *Chem. Soc. Rev.* **2009**, *38*, 481-494.
[302] B. H. Wu, N. F. Zheng, *Nano Today* **2013**, *8*, 168-197.
[303] A. T. Bell, *Science* **2003**, *299*, 1688-1691.
[304] P. V. Kamat, *J. Phys. Chem. B* **2002**, *106*, 7729-7744.
[305] L. D. Li, J. Q. Yan, T. Wang, Z. J. Zhao, J. Zhang, J. L. Gong, N. J. Guan, *Nat. Commun.* **2015**, *6*.
[306] H. S. Jung, Y. J. Hong, Y. Li, J. Cho, Y. J. Kim, G. C. Yi, *ACS Nano* **2008**, *2*, 637-642.
[307] H. B. Wu, H. H. Hng, X. W. Lou, *Adv. Mater.* **2012**, *24*, 2567-2571.
[308] J. H. Sun, J. S. Zhang, M. W. Zhang, M. Antonietti, X. Z. Fu, X. C. Wang, *Nat. Commun.* **2012**, *3*.
[309] J. S. Zhang, M. W. Zhang, C. Yang, X. C. Wang, *Adv. Mater.* **2014**, *26*, 4121-4126.
[310] H. Q. Zheng, H. Syengren, Z. H. Huang, Z. Y. Yang, X. D. Zou, M. Johnsson, *Micropor. Mesopor. Mat.* **2018**, *264*, 147-150.
[311] X. J. Wang, J. Feng, Y. C. Bai, Q. Zhang, Y. D. Yin, *Chem. Rev.* **2016**, *116*, 10983-11060.
[312] X. L. Yu, A. Shavel, X. Q. An, Z. S. Luo, M. Ibanez, A. Cabot, *J. Am. Chem. Soc.* **2014**, *136*, 9236-9239.
[313] R. Ullah, J. Dutta, *J. Hazard. Mater.* **2008**, *156*, 194-200.
[314] B. C. Ma, S. Ghasimi, K. Landfester, F. Vilela, K. A. I. Zhang, *J. Mater. Chem. A* **2015**, *3*, 16064-16071.
[315] C. B. Meier, R. Clowes, E. Berardo, K. E. Jelfs, M. A. Zwijnenburg, R. S. Sprick, A. I. Cooper, *Chem. Mater.* **2019**, *31*, 8830-8838.
[316] F. Niu, L. M. Tao, Y. C. Deng, H. Gao, J. G. Liu, W. G. Song, *New J. Chem.* **2014**, *38*, 5695-5699.
[317] X. Jiang, P. Wang, J. J. Zhao, *J. Mater. Chem. A* **2015**, *3*, 7750-7758.
[318] C. Yang, W. Huang, L. C. da Silva, K. A. I. Zhang, X. C. Wang, *Chem.: Eur. J.* **2018**, *24*, 17454-17458.
[319] L. Guo, Y. Niu, S. Razzaque, B. Tan, S. Jin, *ACS Catal.* **2019**, *9*, 9438-9445.
[320] C. B. Meier, R. S. Sprick, A. Monti, P. Guiglion, J. S. M. Lee, M. A. Zwijnenburg, A. I. Cooper, *Polymer* **2017**, *126*, 283-290.
[321] S. Gu, J. Guo, Q. Huang, J. Q. He, Y. Fu, G. C. Kuang, C. Y. Pan, G. P. Yu, *Macromolecules* **2017**, *50*, 8512-8520.
[322] S. Jiang, B. C. Ma, J. Reinholz, Q. F. Li, J. W. Wang, K. A. I. Zhang, K. Landfester, D. Crespy, *ACS Appl. Mater. Interfaces* **2016**, *8*, 29915-29922.

[323] J. Fickert, P. Rupper, R. Graf, K. Landfester, D. Crespy, *J. Mater. Chem.* **2012**, *22*, 2286-2291.
[324] D. Hashemi, X. Ma, R. Ansari, J. Kim, J. Kieffer, *Phys. Chem. Chem. Phys.* **2019**, *21*, 789-799.
[325] T. R. Blum, Y. Zhu, S. A. Nordeen, T. P. Yoon, *Angew. Chem. Int. Ed.* **2014**, *53*, 11056-11059.
[326] E. D. C. Barrera, L. E. C. Suarez, *Chem. Pharm. Bull.* **2009**, *57*, 639-642.
[327] E. D. Coy, L. E. Cuca, M. Sefkow, *Bioorg. Med. Chem. Lett.* **2009**, *19*, 6922-6925.
[328] M. Lachia, C. J. Moody, *Nat. Prod. Rep.* **2008**, *25*, 227-253.
[329] T. Shen, X. N. Wang, H. X. Lou, *Nat. Prod. Rep.* **2009**, *26*, 916-935.
[330] H. J. Zhang, S. X. Qiu, P. Tamez, G. T. Tan, Z. Aydogmus, N. Van Hung, N. M. Cuong, C. Angerhofer, D. D. Soejarto, J. M. Pezzuto, H. H. S. Fong, *Pharm. Biol.* **2002**, *40*, 221-224.
[331] A. D. Becke, *J. Chem. Phys.* **1993**, *98*, 5648-5652.
[332] T. Clark, J. Chandrasekhar, G. W. Spitznagel, P. V. Schleyer, *J. Comput. Chem.* **1983**, *4*, 294-301.
[333] A. D. McLean, G. S. Chandler, *J. Chem. Phys.* **1980**, *72*, 5639-5648.
[334] M. Ahmed, G. Xinxin, *Inorg. Chem. Front.* **2016**, *3*, 578-590.
[335] R. Daghrir, P. Drogui, D. Robert, *Ind. Eng. Chem. Res.* **2013**, *52*, 3581-3599.
[336] C. B. Ong, L. Y. Ng, A. W. Mohammad, *Renew. Sustain. Energy Rev.* **2018**, *81*, 536-551.
[337] J. Xing, W. Q. Fang, H. J. Zhao, H. G. Yang, *Chem.: Asian J.* **2012**, *7*, 642-657.
[338] Z. Wang, Y. Liu, B. Huang, Y. Dai, Z. Lou, G. Wang, X. Zhang, X. Qin, *Phys. Chem. Chem. Phys.* **2014**, *16*, 2758-2774.
[339] R. Chen, S. Pang, H. An, J. Zhu, S. Ye, Y. Gao, F. Fan, C. Li, *Nat. Energy* **2018**, *3*, 655-663.
[340] Y. Bai, Y. Zhou, J. Zhang, X. Chen, Y. Zhang, J. Liu, J. Wang, F. Wang, C. Chen, C. Li, R. Li, C. Li, *ACS Catal.* **2019**, *9*, 3242-3252.
[341] C. Yang, Z. Wang, T. Lin, H. Yin, X. Lü, D. Wan, T. Xu, C. Zheng, J. Lin, F. Huang, *J. Am. Chem. Soc.* **2013**, *135*, 17831-17838.
[342] Y. Huang, H. Li, W. Fan, F. Zhao, W. Qiu, H. Ji, Y. Tong, *ACS Appl. Mater. Interfaces* **2016**, *8*, 27859-27867.
[343] H. H. Mohamed, D. W. Bahnemann, *Appl. Catal. B Environ.* **2012**, *128*, 91-104.
[344] X. Qiu, L. Li, J. Zheng, J. Liu, X. Sun, G. Li, *J. Phys. Chem. C* **2008**, *112*, 12242-12248.
[345] Z. Li, Y. Zhang, *Nanotechnology* **2008**, *19*, 345606.
[346] J. Bandara, K. Tennakone, P. Jayatilaka, *Chemosphere* **2002**, *49*, 439-445.
[347] J. Liqiang, W. Baiqi, X. Baifu, L. Shudan, S. Keying, C. Weimin, F. Honggang, *J. Solid State Chem.* **2004**, *177*, 4221-4227.
[348] M. Zhukovskyi, P. Tongying, H. Yashan, Y. Wang, M. Kuno, *ACS Catal.* **2015**, *5*, 6615-6623.
[349] Q. Li, F. Zhao, C. Qu, Q. Shang, Z. Xu, L. Yu, J. R. McBride, T. Lian, *J. Am. Chem. Soc.* **2018**, *140*, 11726-11734.
[350] M. Zhang, T. An, X. Hu, C. Wang, G. Sheng, J. Fu, *Appl. Catal. A Gen.* **2004**, *260*, 215-222.
[351] R. S. Mane, W. J. Lee, H. M. Pathan, S.-H. Han, *J. Phys. Chem. B* **2005**, *109*, 24254-24259.
[352] M. Xiao, Z. Wang, M. Lyu, B. Luo, S. Wang, G. Liu, H. M. Cheng, L. Wang, *Adv. Mater.* **2019**, *31*, 1801369.

[353] C. Xu, P. R. Anusuyadevi, C. Aymonier, R. Luque, S. Marre, *Chem. Soc. Rev.* **2019**, *48*, 3868-3902.
[354] B. Weng, S. Liu, Z.-R. Tang, Y.-J. Xu, *RSC Adv.* **2014**, *4*, 12685-12700.
[355] J. Joo, J. S. Son, S. G. Kwon, J. H. Yu, T. Hyeon, *J. Am. Chem. Soc.* **2006**, *128*, 5632-5633.
[356] Y.-H. Liu, F. Wang, Y. Wang, P. C. Gibbons, W. E. Buhro, *J. Am. Chem. Soc.* **2011**, *133*, 17005-17013.
[357] S. Ithurria, B. Dubertret, *J. Am. Chem. Soc.* **2008**, *130*, 16504-16505.
[358] M. Nasilowski, B. Mahler, E. Lhuillier, S. Ithurria, B. Dubertret, *Chem. Rev.* **2016**, *116*, 10934-10982.
[359] M. D. Tessier, C. Javaux, I. Maksimovic, V. Loriette, B. Dubertret, *ACS Nano* **2012**, *6*, 6751-6758.
[360] S. Ithurria, M. Tessier, B. Mahler, R. Lobo, B. Dubertret, A. L. Efros, *Nat. Mater.* **2011**, *10*, 936-941.
[361] M. Olutas, B. Guzelturk, Y. Kelestemur, A. Yeltik, S. Delikanli, H. V. Demir, *ACS Nano* **2015**, *9*, 5041-5050.
[362] A. Yeltik, S. Delikanli, M. Olutas, Y. Kelestemur, B. Guzelturk, H. V. Demir, *J. Phys. Chem. C* **2015**, *119*, 26768-26775.
[363] C. E. Rowland, I. Fedin, H. Zhang, S. K. Gray, A. O. Govorov, D. V. Talapin, R. D. Schaller, *Nat. Mater.* **2015**, *14*, 484-489.
[364] C. She, I. Fedin, D. S. Dolzhnikov, A. Demortière, R. D. Schaller, M. Pelton, D. V. Talapin, *Nano Lett.* **2014**, *14*, 2772-2777.
[365] A. Riedinger, F. D. Ott, A. Mule, S. Mazzotti, P. N. Knüsel, S. J. Kress, F. Prins, S. C. Erwin, D. J. Norris, *Nat. Mater.* **2017**, *16*, 743-748.
[366] Z. Chen, B. Nadal, B. Mahler, H. Aubin, B. Dubertret, *Adv. Funct. Mater.* **2014**, *24*, 295-302.
[367] E. Lhuillier, S. Pedetti, S. Ithurria, H. Heuclin, B. Nadal, A. Robin, G. Patriarche, N. Lequeux, B. Dubertret, *ACS Nano* **2014**, *8*, 3813-3820.
[368] D. O. Sigle, L. Zhang, S. Ithurria, B. Dubertret, J. J. Baumberg, *J. Phys. Chem. Lett.* **2015**, *6*, 1099-1103.
[369] H. Chauhan, Y. Kumar, J. Dana, B. Satpati, H. N. Ghosh, S. Deka, *Nanoscale* **2016**, *8*, 15802-15812.
[370] R. Momper, H. Zhang, S. Chen, H. Halim, E. Johannes, S. Yordanov, D. Braga, B. Blülle, D. Doblas, T. Kraus, *Nano Lett.* **2020**, *20*, 4102-4110.
[371] S. N. Inamdar, P. P. Ingole, S. K. Haram, *ChemPhysChem* **2008**, *9*, 2574-2579.
[372] E. Kucur, J. Riegler, G. A. Urban, T. Nann, *J. Chem. Phys.* **2003**, *119*, 2333-2337.
[373] D. Spittel, J. Poppe, C. Meerbach, C. Ziegler, S. G. Hickey, A. Eychmüller, *ACS Nano* **2017**, *11*, 12174-12184.
[374] R. Egli, A. Peter, H. Freeman, *Colour chemistry: the design and synthesis of organic dyes and pigments*, Elsevier, London, **1991**.
[375] W.-Z. Gao, Y. Xu, Y. Chen, W.-F. Fu, *Chem. Commun.* **2015**, *51*, 13217-13220.
[376] Y. Dai, C. Li, Y. Shen, T. Lim, J. Xu, Y. Li, H. Niemantsverdriet, F. Besenbacher, N. Lock, R. Su, *Nat. Commun.* **2018**, *9*, 60.
[377] X. Guo, C. Hao, G. Jin, H. Y. Zhu, X. Y. Guo, *Angew. Chem. Int. Ed.* **2014**, *53*, 1973-1977.
[378] L. Han, D. Qin, X. Jiang, Y. Liu, L. Wang, J. Chen, Y. Cao, *Nanotechnology* **2006**, *17*, 4736-4742.
[379] G. H. V. Bertrand, A. Polovitsyn, S. Christodoulou, A. H. Khan, I. Moreels, *Chem. Commun.* **2016**, *52*, 11975-11978.

[380] Y. Jiang, W.-S. Ojo, B. Mahler, X. Xu, B. Abécassis, B. Dubertret, *ACS Omega* **2018**, *3*, 6199-6205.

[381] M. Koketsu, F. Nada, S. Hiramatsu, H. Ishihara, *Perkin Trans.* **2002**, 737-740.

[382] A. Riedinger, A. S. Mule, P. N. Knüsel, F. D. Ott, A. A. Rossinelli, D. J. Norris, *Chem. Commun.* **2018**, *54*, 11789-11792.

[383] M. D. Tessier, L. Biadala, C. Bouet, S. Ithurria, B. Abecassis, B. Dubertret, *ACS Nano* **2013**, *7*, 3332-3340.

[384] N. Huber, K. A. Zhang, *Eur. Polym. J* **2020**, *140*, 110060.

[385] D. J. Woods, R. S. Sprick, C. L. Smith, A. J. Cowan, A. I. Cooper, *Adv. Energy Mater.* **2017**, *7*.

[386] J. L. Lin, Z. M. Pan, X. C. Wang, *ACS Sustain. Chem. Eng.* **2014**, *2*, 353-358.

[387] Y. T. Dai, C. Li, Y. B. Shen, T. B. Lim, J. Xu, Y. W. Li, H. Niemantsverdriet, F. Besenbacher, N. Lock, R. Su, *Nat. Commun.* **2018**, *9*.

[388] N. Chaoui, M. Trunk, R. Dawson, J. Schmidt, A. Thomas, *Chem. Soc. Rev.* **2017**, *46*, 3302-3321.

[389] R. S. Sprick, J. X. Jiang, B. Bonillo, S. J. Ren, T. Ratvijitvech, P. Guiglion, M. A. Zwijnenburg, D. J. Adams, A. I. Cooper, *J. Am. Chem. Soc.* **2015**, *137*, 3265-3270.

[390] Y. Bai, L. Wilbraham, B. J. Slater, M. A. Zwijnenburg, R. S. Sprick, A. I. Cooper, *J. Am. Chem. Soc.* **2019**, *141*, 9063-9071.

[391] S. B. Rawal, S. Bera, D. Lee, D. J. Jang, W. I. Lee, *Catal. Sci. Technol.* **2013**, *3*, 1822-1830.

[392] Z. J. Wang, K. Garth, S. Ghasimi, K. Landfester, K. A. I. Zhang, *ChemSusChem* **2015**, *8*, 3459-3464.

[393] M. Heeney, W. Zhang, D. J. Crouch, M. L. Chabinyc, S. Gordeyev, R. Hamilton, S. J. Higgins, I. McCulloch, P. J. Skabara, D. Sparrowe, S. Tierney, *Chem. Commun.* **2007**, 5061-5063.

[394] L. Wang, W. Huang, R. Li, D. Gehrig, P. W. M. Blom, K. Landfester, K. A. I. Zhang, *Angew. Chem. Int. Ed.* **2016**, *55*, 9783-9787.

[395] T. Ben, S. Qiu, *CrystEngComm* **2013**, *15*, 17-26.

[396] W. Lu, D. Yuan, J. Sculley, D. Zhao, R. Krishna, H. C. Zhou, *J. Am. Chem. Soc.* **2011**, *133*, 18126-18129.

[397] H. Zhao, Z. Jin, H. Su, X. Jing, F. Sun, G. Zhu, *Chem. Commun.* **2011**, *47*, 6389-6391.

[398] H. Ren, T. Ben, F. Sun, M. Guo, X. Jing, H. Ma, K. Cai, S. Qiu, G. Zhu, *J. Mater. Chem.* **2011**, *21*, 10348-10353.

[399] Z. Xie, C. Wang, K. E. deKrafft, W. Lin, *J. Am. Chem. Soc.* **2011**, *133*, 2056-2059.

[400] C. Wang, Z. Xie, K. E. deKrafft, W. Lin, *ACS Appl. Mater. Interfaces* **2012**, *4*, 2288-2294.

[401] B. C. Ma, S. Ghasimi, K. Landfester, K. A. I. Zhang, *J. Mater. Chem. B* **2016**, *4*, 5112-5118.

[402] J. Mei, Z. Bao, *Chem. Mater.* **2014**, *26*, 604-615.

[403] J.-Q. Yu, Z. Shi, *CH activation, Vol. 292*, Springer, **2010**.

[404] R. H. Crabtree, A. W. Lei, *Chem. Rev.* **2017**, *117*, 8481-+.

[405] J. B. Xia, C. Zhu, C. Chen, *J. Am. Chem. Soc.* **2013**, *135*, 17494-17500.

[406] J. Rouquerol, P. Llewellyn, F. Rouquerol, *Stud. Surf. Sci. Catal.* **2007**, *160*, 1016.

[407] Z.-Z. Yang, Y. Zhao, H. Zhang, B. Yu, Z. Ma, G. Ji, Z. Liu, *Chem. Commun.* **2014**, *50*, 13910-13913.

[408] J. Liu, L. Bu, J. Dong, Q. Zhou, Y. Geng, D. Ma, L. Wang, X. Jing, F. Wang, *J. Mater. Chem.* **2007**, *17*, 2832-2838.

[409] Y. Jeon, T.-M. Kim, J.-J. Kim, J.-I. Hong, *New J. Chem.* **2015**, *39*, 9591-9595.

[410] P. Giannopoulos, D. Raptis, K. Theodosiou, A. K. Andreopoulou, C. Anastasopoulos, A. Dokouzis, G. Leftheriotis, P. Lianos, J. K. Kallitsis, *Dyes Pigm.* **2018**, *148*, 167-179.

[411] N. Huber, R. Li, C. T. Ferguson, D. W. Gehrig, C. Ramanan, P. W. Blom, K. Landfester, K. A. Zhang, *Cat. Sci. Tech.* **2020**, *10*, 2092-2099.

[412] J. Liu, Y. Liu, N. Y. Liu, Y. Z. Han, X. Zhang, H. Huang, Y. Lifshitz, S. T. Lee, J. Zhong, Z. H. Kang, *Science* **2015**, *347*, 970-974.

[413] Y. H. Xu, S. B. Jin, H. Xu, A. Nagai, D. L. Jiang, *Chem. Soc. Rev.* **2013**, *42*, 8012-8031.

[414] R. S. Sprick, B. Bonillo, R. Clowes, P. Guiglion, N. J. Brownbill, B. J. Slater, F. Blanc, M. A. Zwijnenburg, D. J. Adams, A. I. Cooper, *Angew. Chem. Int. Ed.* **2016**, *55*, 1792-1796.

[415] L. Wang, R. Fernandez-Teran, L. Zhang, D. L. Fernandes, L. Tian, H. Chen, H. Tian, *Angew. Chem. Int. Ed.* **2016**, *55*, 12306-12310.

[416] C. Yang, B. C. Ma, L. Zhang, S. Lin, S. Ghasimi, K. Landfester, K. A. I. Zhang, X. Wang, *Angew. Chem. Int. Ed.* **2016**, *55*, 9202-9206.

[417] C. L. Su, R. Tandiana, B. B. Tian, A. Sengupta, W. Tang, J. Su, K. P. Loh, *ACS Catal.* **2016**, *6*, 3594-3599.

[418] Y. Chen, J. S. Zhang, M. W. Zhang, X. C. Wang, *Chem. Sci.* **2013**, *4*, 3244-3248.

[419] Z. J. Wang, S. Ghasimi, K. Landfester, K. A. I. Zhang, *Chem. Mater.* **2015**, *27*, 1921-1924.

[420] S. Ghasimi, S. Prescher, Z. J. Wang, K. Landfester, J. Yuan, K. A. I. Zhang, *Angew. Chem. Int. Ed.* **2015**, *54*, 14549-14553.

[421] S. Ghosh, N. A. Kouamé, L. Ramos, S. Remita, A. Dazzi, A. Deniset-Besseau, P. Beaunier, F. Goubard, P.-H. Aubert, H. Remita, *Nat. Mater.* **2015**, *14*, 505-511.

[422] C. Lu, P. Zhang, S. Jiang, X. Wu, S. Song, M. Zhu, Z. Lou, Z. Li, F. Liu, Y. Liu, Y. Wang, Z. Le, *Appl. Catal. B Environ.* **2017**, *200*, 378-385.

[423] J. Geng, C. Sun, J. Liu, L.-D. Liao, Y. Yuan, N. Thakor, J. Wang, B. Liu, *Small* **2015**, *11*, 1603-1610.

[424] L. Xu, L. Cheng, C. Wang, R. Peng, Z. Liu, *Polym. Chem.* **2014**, *5*, 1573-1580.

[425] K. Yang, H. Xu, L. Cheng, C. Sun, J. Wang, Z. Liu, *Adv. Mater.* **2012**, *24*, 5586-5592.

[426] C. Zhu, L. Liu, Q. Yang, F. Lv, S. Wang, *Chem. Rev.* **2012**, *112*, 4687-4735.

[427] J. Liu, M. Antonietti, *Energy Environ. Sci.* **2013**, *6*, 1486-1493.

[428] J. Liu, R. Cazelles, Z. P. Chen, H. Zhou, A. Galarneau, M. Antonietti, *Phys. Chem. Chem. Phys.* **2014**, *16*, 14699-14705.

[429] K. T. Oppelt, J. Gasiorowski, D. A. M. Egbe, J. P. Kollender, M. Himmelsbach, A. W. Hassel, N. S. Sariciftci, G. Knör, *J. Am. Chem. Soc.* **2014**, *136*, 12721-12729.

[430] C. T. J. Ferguson, N. Huber, K. Landfester, K. A. I. Zhang, *Angew. Chem. Int. Ed.* **2019**, *58*, 10567-10571.

[431] F. S. Mancilha, B. A. DaSilveira Neto, A. S. Lopes, P. F. Moreira, F. H. Quina, R. S. Gonçalves, J. Dupont, *Eur. J. Org. Chem.* **2006**, *2006*, 4924-4933.

[432] D. Aldakov, M. A. Palacios, P. Anzenbacher, *Chem. Mater.* **2005**, *17*, 5238-5241.

[433] M. S. Lowry, J. I. Goldsmith, J. D. Slinker, R. Rohl, R. A. Pascal, G. G. Malliaras, S. Bernhard, *Chem. Mater.* **2005**, *17*, 5712-5719.

[434] M. A. Cismesia, T. P. Yoon, *Chem. Sci.* **2015**, *6*, 5426-5434.

[435] S. M. Stevenson, M. P. Shores, E. M. Ferreira, *Angew. Chem. Int. Ed.* **2015**, *54*, 6506-6510.

[436] S. S. Lin, M. A. Ischay, C. G. Fry, T. P. Yoon, *J. Am. Chem. Soc.* **2011**, *133*, 19350-19353.
[437] Y. B. Zhao, M. Antonietti, *Angew. Chem. Int. Ed.* **2017**, *56*, 9336-9340.
[438] A. U. Meyer, T. Slanina, C. J. Yao, B. Konig, *ACS Catal.* **2016**, *6*, 369-375.
[439] S. Tojo, S. Toki, S. Takamuku, *J. Org. Chem.* **1991**, *56*, 6240-6243.
[440] M. Frisch, G. Trucks, H. B. Schlegel, G. E. Scuseria, M. A. Robb, J. R. Cheeseman, G. Scalmani, V. Barone, B. Mennucci, G. Petersson, *Gaussian 09, revision D. 01*, Gaussian Inc., Wallingford CT, **2009**.
[441] C. D. Dzierba, R. A. Hartz, Y. Bi, V. T. Ahuja, J. J. Bronson, K. Carson, G. Cianchetta, M. Green, D. Kimball, S. R. Kimura, U.S. Patent and Trademark Office, **2012**, pp. 63-64.
[442] B. König, *Eur. J. Org. Chem.* **2017**, *2017*, 1979-1981.
[443] L. Marzo, S. K. Pagire, O. Reiser, B. König, *Angew. Chem. Int. Ed.* **2018**, *57*, 10034-10072.
[444] K. Alfonsi, J. Colberg, P. J. Dunn, T. Fevig, S. Jennings, T. A. Johnson, H. P. Kleine, C. Knight, M. A. Nagy, D. A. Perry, *Green Chem.* **2008**, *10*, 31-36.
[445] G.-J. t. Brink, I. W. C. E. Arends, R. A. Sheldon, *Science* **2000**, *287*, 1636-1639.
[446] P. B. Pati, G. Damas, L. Tian, D. L. Fernandes, L. Zhang, I. B. Pehlivan, T. Edvinsson, C. M. Araujo, H. Tian, *Energy Environ. Sci.* **2017**, *10*, 1372-1376.
[447] S. Jiang, B. C. Ma, W. Huang, A. Kaltbeitzel, G. Kizisavas, D. Crespy, K. A. Zhang, K. Landfester, *Nanoscale horiz.* **2018**, *3*, 439-446.
[448] J. Byun, W. Huang, D. Wang, R. Li, K. A. Zhang, *Angew. Chem. Int. Ed.* **2018**, *57*, 2967-2971.
[449] R. Dawson, A. Laybourn, R. Clowes, Y. Z. Khimyak, D. J. Adams, A. I. Cooper, *Macromolecules* **2009**, *42*, 8809-8816.
[450] H. Urakami, K. Zhang, F. Vilela, *Chem. Commun.* **2013**, *49*, 2353-2355.
[451] S. Ghasimi, K. Landfester, K. A. Zhang, *ChemCatChem* **2016**, *8*, 694-698.
[452] V.-H. Nguyen, S. M. Smith, K. Wantala, P. Kajitvichyanukul, *Arab. J. Chem.* **2020**.
[453] J. Buccini, in *Persistent organic pollutants*, Springer, Berlin Heidelberg, **2003**, pp. 13-30.
[454] R. Weber, A. Watson, M. Forter, F. Oliaei, *Waste Manag. Res.* **2011**, *29*, 107-121.
[455] T. Eggen, M. Moeder, A. Arukwe, *Sci. Total Environ.* **2010**, *408*, 5147-5157.

A.2 List of Figures

Figure 1. Simplified energy diagram of a monomolecular exothermic reaction with and without the use of a catalyst.[9] 14

Figure 2. Photocatalytic reaction using semiconducting materials as photocatalysts. The process can be divided into light absorption and excitation (1), charge separation and transport (2), electron transfer between photocatalyst and substrates (3). 17

Figure 3. The solar spectrum at the top of the atmosphere and sea level compared to an ideal 5800 K emitter. The data is based on the American Society for Testing and Materials (ASTM) terrestrial reference spectra.[18-19] 18

Figure 4. Selection of important photocatalytic transition metal complexes and small-molecular organic dyes (a). Simplified orbital illustration of the functional principle of Rubpy32+ photocatalysis (b). 20

Figure 5. Types of energy transfers in plasmonic photocatalysts with 1) Plasmonic light scattering, 2) PIRET, 3) hot electron injection, and 4) thermal energy dissipation.[79-80] 23

Figure 6. Thermal synthesis of graphitic carbon nitride *g*-C_3N_4 and selected precursors cyanamide, dicyanamide, melamine, urea, and thiourea.[96-97] The structure shown represents the thermodynamically most stable tri-s-triazine phase 25

Figure 7. Exemplary ionothermal synthesis of a covalent triazine framework by Kuhn *et al.*[146] 27

Figure 8. Selected literature examples of superacid-catalyzed CTF syntheses. First TfOH-based CTF preparation (a),[156] CTF membrane (b),[157] few-layer CTF through interfacial polymerization (c),[158] and nanoporous thiophene-based CTF through SBA-15 templating (d).[160] 29

Figure 9. Exemplary amidine-based syntheses of covalent triazine frameworks. Mechanism of the triazine ring formation[162] (a) and slowdown synthesis strategies (b).[163-164] 30

Figure 10. One-step Ullmann polycondensation of the tetrahedral precursors gave PAF-1 and PPN-3 to 5.[185-186] 32

Figure 11. General scheme of the Suzuki-Miyaura cross-coupling reaction. Y is typically O-alkyl or OH, R^1 and R^2 are aryl residues, and X is an organohalide. Commonly used bases are carbonates. Further, more special cases are known from the literature.[199-200] 33

Figure 12. General scheme of the Sonogashira-Hagihara cross-coupling. R^1 and R^2 are typically aryl residues and X is an organohalide. A frequently used base is triethylamine. Further, more special cases are known from the literature.[204] 34

Figure 13. Reaction mechanisms for the Suzuki-type (a) and Sonogashira-type (b) cross-couplings 35

Figure 14. Literature examples for photocatalytic units with vinyl groups for radical copolymerization to photoactive classical polymers.[222-224] 37

Figure 15. Types of physisorption isotherms.[231] 40

Figure 16. Schematic illustration of the CTF molecular design and their application for visible-light-driven selective aerobic oxidation of hydrocarbons..49

Figure 17. SEM imaging of CTFs (a-c) and synthesized silica nanoparticles (d-e). Dynamic light scattering (DLS) data on SiNPs. 50

Figure 18. Regular (a) and magnified (b) FTIR spectra. The signals originating from triazine vibrations are highlighted. 51

Figure 19. ^{13}C CP/MAS NMR spectra (a), nitrogen sorption isotherms (b), PXRD patterns (c), and thermogravimetric analysis (d, in air, 10 K/min) of CTF-Th-0, CTF-Th-1, and CTF-Th-2. 52

Figure 20. Regular (a) and Kubelka-Munk transformed UV/Vis reflectance spectra (b) of CTFs with different phenyl spacer lengths. Photograph of the CTFs (c)...................................53

Figure 21. Cyclic voltammetry with a scan rate of 100 mV/s in CH3CN (a) and derived HOMO and LUMO potentials (b). DFT calculations on the PBE0 level using def2svp as a basis set for triazine structures analogous to the CTFs in this study (c). The systems were reduced to smaller units to limit the complexity of the theoretical calculations and were conducted to prove the general trend on frontier orbital energies upon spacer elongation. 54

Figure 22. DFT calculations on the influence of conversion on the HOMO and LUMO potentials. The calculations were performed on three different levels of complexity to obtain representative trends (a). Cyanides or triazine rings were placed at position X depending on the conversion tested. At level 1, for example three conversions (0%, 50%, 100%) result. Ground state HOMO and LUMO potentials vs. vacuum (b) and the magnified HOMO potentials vs. vacuum (c). 55

Figure 23. Steady-state photoluminescence spectra with λ_{exc} = 380 nm (a). Normalized PL lifetimes of CTFs with different spacer lengths (b). PL signals were read at the respective emission maximum. Lifetimes of the NPLs were fitted with an exponential function. The samples were excited with λ_{exc} = 380 nm. Excited state electron and hole distributions calculated on the PBE0 level using def2svp as basis set (c). The color code indicates the percentage distribution of electrons and holes (red = 100%, black = 0% localization on respective fragment). For the visualization, the multifunctional wave function analyzer Multiwfn was used.[277]...56

Figure 24. Representative GC trace and MS information for the photocatalytic oxidation of toluene to benzaldehyde with the used CTFs. The conditions of the experiment are listed in the experimental details. 57

Figure 25. Visible-light-induced selective oxidation of toluene in different solvents performed with CTFs with different phenyl spacer lengths. 58

Figure 26. Solvent optimization (a) and control experiments (b) of the photocatalytic oxidation of toluene with CTF-Th-0. 60

Figure 27. EPR spectra of superoxide radical (a) and singlet oxygen (b) trapping by DMPO and TEMP, respectively. 60

Figure 28. Proposed mechanism of the photocatalytic oxidation of toluene towards benzaldehyde...61

Figure 29. Substrate scope for visible-light-induced aerobic oxidation of C-H bonds in hydrocarbons. The values in the bracket represent the selectivity. Reaction conditions: substrate (0.1 mmol), photocatalyst (10 mg), nitromethane (1.5 mL), O_2 bubbling for 5min, blue LED irradiation (λ = 460 nm, 0.16 W/cm^2), 5h, room temperature. The conversion and selectivity were determined by GC-MS analysis...62

Figure 30. Possible retrosynthesis of AMG 549 (inhibitor of phosphodiesterase 10A for the treatment of schizophrenia) via a photocatalytic synthesized intermediate...............................63

Figure 31. Bar diagram of conversion and selectivity after 5h of reaction using CTF-Th-0 in the benchmark reaction (a). UV/Vis and IR spectra before and after the application (b,c) 64

Figure 32. GCMS traces from the solvent-free experiment. The reaction setup is given in the experimental details. 65

Figure 33. Synthetic route for covalent triazine framework nanoparticles in confinement. In a combined sol-gel emulsion and TfOH vapor-assisted polymerization approach, CTF nanoparticles are formed. The resulting material can be used for visible-light-promoted organic redox photocatalysis..77

Figure 34. TEM image of monomer (a) and CTF-NPs (b) confined in silica capsules. Elemental mapping shows enriched contents of silicon and oxygen in the shell and carbon and sulfur in the core (c). 78

Figure 35. Different CTF-NP sizes of 80, 180, and 550 nm on average could be obtained (a-c). Size histogram of counted nanoparticles (N=50 each) from transmission electron microscopy images (d). The inset in (d) shows the Tyndall effect of CTF_{80} in THF (0.01 mg/mL)..79

Figure 36. TEM images of silica capsules synthesized without DCHT (a, b) and silica capsules with DCHT (c, d)...80

Figure 37. Comparison of Fourier-transform infrared (FTIR) spectra of CTF_{80} NPs with the monomer 2,5-dibromo-3-hexylhiophene (a). 13C CP-MAS NMR spectrum of CTF_{80} NPs (b). Powder XRD pattern comparison of CTF_{80}, CTF-1BT, CTF-2BT and CTF-4BT (c). TGA of

CTF_{80} NPs under N_2 with temperature increasing from room temperature to 800°C at a rate of 10 K/min (d). 81

Figure 38. Transmission electron microscopy of CTF-NPs with different BT contents in silica capsules (a-c) and after removing silica (d-f)....................82

Figure 39. Comparison of FTIR spectra (a) and ^{13}C CP-MAS NMR spectra (b) of CTF-NPs with different BT content. 83

Figure 40. Diffuse reflectance spectra (a), Kubelka-Munk transformed UV/Vis spectra (b), and photograph (c) of CTF nanoparticles with different BT contents. 84

Figure 41. Cyclic voltammetry of CTF-NPs with different BT contents with a scan rate of 100 mV/s in CH_3CN (a) and CV HOMO/LUMO potentials vs. SCE (b). LUMO values result from the CV onset potentials; HOMO levels are derived by combining CV values and bandgaps from the Kubelka-Munk-transformed diffuse reflectance UV/Vis spectra....................84

Figure 42. DFT Calculations on the B3LYP/6-31G(d) level for triazine structures analogous to the CTFs in this study. The structures were reduced to smaller units to limit the complexity of the theoretical calculations and were conducted to prove the general trend on frontier orbital energies upon benzothiadiazole incorporation....................85

Figure 43. Steady state photoluminescence spectra with λ_{exc}=380 nm (a) and photocurrent measurement under visible-light irradiation for CTF-xBT NPs (b)....................86

Figure 44. EPR spectra at room temperature with integrated blue light irradiation (a) Time-resolved photoluminescence (TRPL) spectra of the CTF-xBT NPs at an excitation wavelength of 400 nm (b). TRPL) spectra of the different sizes of pristine CTF NPs using the same excitation wavelength. 87

Figure 45. (a) Benchmark [3+2] cycloaddition reaction of *trans*-anethole and mequinol. (b) Kinetic study using different CTF nanoparticles as photocatalysts over the course of 24h and (c) at the specific time point of 10h reaction time....................88

Figure 46. Nitrogen sorption isotherms for CTF NPs. The nitrogen sorption isotherms are typical for non-porous materials. It is supposed that porosity, if present, would not be detectable due to the long alkyl chains of DCHT blocking N_2 from accessing pores....................89

Figure 47. Proposed mechanism of the oxidative [3+2] cycloaddition on CTF NPs. 91

Figure 48. Apparent quantum yield (AQY) for CTF-2BT when irradiated at four different wavelengths....................91

Figure 49. Bar diagram of yields after 24h of reaction using CTF_{80} as photocatalyst in the benchmark reaction. The error bar represents two independent measurements. UV/Vis and IR spectra before and after (b,c) and TEM image after the application (d)....................92

Figure 50. Overview of the substrate scope for different 2,3-dibenzofurans (a) and three further redox reactions (b) catalyzed using CTF-2BT NPs. Detail on synthetic procedures is given in the experimental subchapter. 93

Figure 51. Synthetic route for covalent triazine framework nanoparticles in confinement.........96

Figure 52. Illustration of the thickness variation concept of the CdSe nanoplatelets and their application in the photocatalytic azoxybenzene synthesis. 107

Figure 53. TEM imaging of 3, 4, and 5 ML CdSe nanoplatelets. 108

Figure 54. Combined UV/Vis absorption and PL (a) and Kubelka-Munk transformed UV/Vis spectra of nanoplatelets with different thicknesses in n-hexane (b). Normalized PL lifetimes of NPLs with different ML thicknesses. The signals were read at 462 nm, 510 nm, and 550 nm for 3ML, 4ML, and 5ML NPLs. Lifetimes of the NPLs were fitted with a double exponential function. 109

Figure 55. Cyclic voltammetry of nanoplatelets with different ML thickness with a scan rate of 100 mV/s in CH_3CN. CV conduction band potentials vs. SCE were deducted from the onset potential (a). CB and VB positioning derived from cyclovoltammetry and optical absorption (b). 110

Figure 56. Proposed reaction mechanism and intermediate products of the photocatalytic reduction of nitrobenzene (a). Catalytic cycle involving conduction band and valence band of the photocatalytic CdSe nanoplatelets (b). 111

Figure 57. Conversion of nitrobenzene to azoxybenzene at different time points, using NPL photocatalyst of different ML thicknesses and white LED excitation. Reaction conditions: [Nitrobenzene] = 75 mM, [TEOA] = 100 mM, [Hantzsch ester] = 45 mM, toluene/acetonitrile 1.7 mL (70:30), [CdSe NPL] = 1 x 10^{-7} M, white LED lamp (0.16 W/cm^2), room temperature, Argon atmosphere. Conversion determined by GC-MS........112

Figure 58. Relative integral covered from the white LED based on the absorption range of the NPLs. 113

Figure 59. Intermediates nitrosobenzene and *N*-phenylhydroxylamine in the concentrated reaction setup. 114

Figure 60. Photocatalytic conversions for recycling 5 ML NPLs in the reduction of nitrobenzene. 116

Figure 61. Scope of the photocatalytic reduction of nitrobenzene derivatives using 5 ML NPLs (a). The reactions were irradiated with a white LED lamp (0.16 W/cm^2). PBE0/def2svp DFT study on vertical electron affinities of the reaction intermediates (b). While the absolute values are prone to systematic errors, the general trend between intermediates and between substrates should suffice for analysis........117

Figure 62. Exemplary GC trace and mass spectra at the peak maxima for the kinetic study obtained from the 3ML series after 24h. Depending on the amount injected, signals for TEOA and its interaction products with the column material appear for other samples............124

Figure 63. GCMS traces for recycling experiments. The signal around 3.3min elution time can be assigned to the starting material. Other signals include TEOA (4.6min), azobenzene (5.2min), Hantzsch ester (5.5min) and azoxybenzene (5.8min)...125

Figure 64. Illustration of the design concept of the PAF-based photocatalysts and their dual-functional application in the selective photocatalytic activation of C-H bonds either by the photogenerated electron on LUMO or hole on HOMO...129

Figure 65. The synthetic route towards PAF-BT(Ph)$_2$, PAF-BT(Th)$_2$, and PAF-BT(EDOT)$_2$.....130

Figure 66. Comparison of ^{13}C solid-state NMR (a), Fourier-transformed infrared (FTIR) spectra (b) and thermogravimetric analysis from 25 to 1000°C (10 K/min) in N_2 atmosphere (c) for PAF-BT(Ph)$_2$, PAF-BT(Th)$_2$ and PAF-BT(EDOT)$_2$. 131

Figure 67. Nitrogen adsorption isotherms at 77K (a) and pore size distributions of PAF-BT(Ph)$_2$, PAF-BT(Th)$_2$, and PAF-BT(EDOT)$_2$ (b). 132

Figure 68. Scanning electron microscopy (SEM) images of PAF-BT(Ph)$_2$, PAF-BT(Th)$_2$, and PAF-BT(EDOT)$_2$...133

Figure 69. DR UV/Vis absorption (a) and photoluminescence spectra of PAF-BT(Ph)$_2$, PAF-BT(Th)$_2$, and PAF-BT(EDOT)$_2$ (b). The excitation wavelengths were 450 nm, 525 nm, and 575 nm, respectively. Kubelka-Munk transformed UV/Vis spectra for deduction of bandgap potentials (c). 134

Figure 70. Cyclic voltammetry of the PAF photocatalysts at a scan rate of 100 mV/s. A Pt wire was used as the counter electrode; a saturated calomel electrode as the reference electrode. Bu4NPF6 (0.1 M in acetonitrile) was used as the electrolyte (a). HOMO and LUMO frontier orbital potentials derived from cyclovoltammetry and optical absorption (b). 135

Figure 71. Determination of frontier orbital potentials for BT(Ph)$_2$, BT(Th)$_2$, and BT(EDOT)$_2$, from CV and UV/Vis studies...136

Figure 72. Frontier orbital comparison between the molecular analogs BT(X)$_2$ and the PAF photocatalysts in this study. In the center, the average of the deviations (both Ph systems compared, both Th systems compared, both EDOT systems compared) and the standard deviation of the value comparison are given. 136

Figure 73. Kinetic study of the (a) aza-Henry reaction of 2-phenyl-1,2,3,4-tetrahydroisoquinoline and nitromethane, and (b) direct arylation of thiophene with 4-bromobenzenediazonium tetrafluoroborate using different PAFs as photocatalysts. 140

Figure 74. Proposed reaction mechanisms of the investigated electron- and hole-initiated reactions. 141

Figure 75. (a) Photocatalytic conversions for recycling PAF-BT(Ph)$_2$ in the aza-Henry reaction and PAF-BT(EDOT)$_2$ in the direct arylation. (b) UV/Vis DR spectra before and after recycling the catalysts five times. 142

Figure 76. Reaction scopes for the reaction of 2-phenyl-1,2,3,4-tetrahydroisoquinoline (a) and 4-bromobenzenediazonium tetrafluoroborate (b) with different substrates. PAF-BT(Ph)$_2$ and PAF-BT(EDOT)$_2$ were used as photocatalysts. 143

Figure 77. Synthesis of dantrolene in two steps and one batch as a practical example for applying the PAF-based photocatalysts. 143

Figure 78. HOMO and LUMO levels of simplified PAF structures at the B3LYP/6-31G(d) level. 153

Figure 79. Logarithmic plot of the concentration of N-Phenyltetrahydroisoquinoline and 4-Bromobenzodiazonium tetrafluoroborate during the reaction with PAF-BT(Ph)$_2$ and PAF-BT(EDOT)$_2$, respectively. The initial concentrations were 0.125 M of PTHI and 0.09 M of BBDT. 154

Figure 80. Illustration of the PMMA-based photocatalyst copolymer design concept and its application in the photocatalytic [4+2] cycloaddition. 159

Figure 81. ^{13}C CP-MAS NMR spectra at different contact times (0.3 ms, 1 ms, 3 ms) of cPMMA-BTPh$_2$ (a) and cPMMA (b). 160

Figure 82. Photoluminescence and UV/Vis comparison of BTPh$_2$ units and the polymer cPMMA-BTPh$_2$ in the solid state. 160

Figure 83. Cyclic voltammetry of cPMMA-BTPh$_2$ and BTPh$_2$ with a scan rate of 100 mV/s in CH_3CN (a). DFT/B3LYP 6-31G(d) calculated electronic structures for HOMO and LUMO of a simplified cPMMA-BTPh$_2$. Potentials result from the CV measurement on cPMMA-BTPh$_2$ (b). 161

Figure 84. Optical microscopy images of cPMMA-BTPh$_2$ swelling after exposure to CH_3NO_2. 163

Figure 85. FTIR comparison of cPMMA-BTPh$_2$ and the blank cPMMA sample (a). Detailed FTIR comparison of cPMMA-BTPh$_2$, cPMMA and BTPh$_2$ (b). cPMMA and cPMMA-BTPh$_2$ differ only slightly at 696 cm^{-1}, the major resonance of BTPh$_2$. TGA comparison of cPMMA-BTPh$_2$ and the blank cPMMA sample (c) 164

Figure 86. Material cost estimation for the synthesis of 1g of cPMMA-BTPh$_2$. 165

Figure 87. Monitoring experiment of the photocatalytic Diels-Alder reaction. Reaction conversion (a) and logarithmic plot of the concentration of *trans*-anethole during the reaction (b). The initial concentration of *trans*-anethole was 0.1 M 166

Figure 88. Reaction conversion change during the light-on-and-off experiment 167

Figure 89. Repeating experiment of the photocatalytic Diels-Alder reaction with cPMMA-$BTPh_2$ (a) and with $BTPh_2$ (b). UV-Vis spectra of cPMMA-$BTPh_2$ before and after the photocatalytic Diels-Alder reaction (c). The maximum intensities on both peaks show a similar decrease indicating this to be a concentration-related effect. 170

Figure 90. Proposed reaction mechanism of the photocatalytic [4+2] cycloaddition using cPMMA-$BTPh_2$ as photocatalyst. 171

Figure 91. (a) EPR spectra of DMPO-$O_2^{\bullet-}$ adducts with cPMMA-$BTPh_2$ as photocatalyst in darkness or under blue light irradiation (λ = 460 nm, 1.2 W/cm^2). (b) Time-resolved photoluminescence spectra of $BTPh_2$ under N_2 (black), O_2 (red), with *trans*-anethole under N_2 (green) or in air (blue) with 20 mg/mL of $BTPh_2$ and 2 mM *trans*-anethole in acetonitrile....172

Figure 92. TA spectra of $BTPh_2$ (20 mg/L in CH_3CN) under N_2 at different times (a). TA spectra of $BTPh_2$ (20 mg/L in CH_3CN) under O_2 at different times (b). TA spectra of $BTPh_2$ (20 mg/L) and *trans*-anethole with lower concentration (2 mM, c) and higher concentration (20 mM, d) under N_2 atmosphere in CH_3CN at different times. Time profiles of the absorbance decay at 675 nm of $BTPh_2$ with 0, 10, and 20 mM *trans*-anethole in CH_3CN (e). Transient absorption spectra of $BTPh_2$ (20 mg/L) and *trans*-anethole (2 mM) under O_2 atmosphere in CH_3CN at different times (f). For all measurements, an excitation wavelength of 355 nm was used...173

Figure 93. Comparison of decay profiles of transient absorption (TA) at 660 – 690 nm and time-resolved photoluminescence (TRPL) at 480-520 nm for the Diels-Alder reaction. Pure $BTPh_2$ (20 mg/L in CH_3CN) under N_2 (a), pure $BTPh_2$ (20 mg/L in CH_3CN) under O_2 (b), $BTPh_2$ (20 mg/L) and *trans*-anethole (2 mM) under N_2 atmosphere in CH_3CN (c), $BTPh_2$ (20 mg/L) and *trans*-anethole (2 mM) under O_2 atmosphere in CH_3CN (d)..................................174

Figure 94. Scope of the photocatalytic Diels-Alder reaction using cPMMA-$BTPh_2$ as photocatalyst. The reactions were irradiated with a blue LED lamp (460 nm, 0.16 W/cm^2)......175

Figure 95. Apparent quantum yield calculation..189

Figure 96. ^{1}H-NMR spectra of a) experiment I (CH_3NO_2), b) experiment II ($CDCl_3$), and c) experiment III (d_8-THF)..190

Figure 97. Schematic illustration of the copolymer molecular design and the tuning of properties by varying the amounts of benzothiadiazole (BT) and benzene sulfonate (S).........195

Figure 98. Compositional overview of synthesized photocatalytic polymer series..................196

Figure 99. ^{13}C CP-MAS NMR spectra for the first series with increasing BT content (a) and the second series with increasing S content (b). 197

Figure 100. FTIR spectra of the benzothiadiazole (a) and the sulfonate monomer (b). The peaks used for the spectra normalization are marked with a red arrow. 197

Figure 101. Normalized FTIR spectra of the increasing BT-series (a) and increasing S-series (b). The spectra were normalized to significant peaks of the respective constant monomer....198

Figure 102. SEM imaging at two different magnifications (a,b) and TGA trace of cPMMA-BT_{20}-S_{20} (c). 199

Figure 103. Qualitative dispersibility experiment. Catalyst (5 mg/mL) was dispersed in water through ultrasonication (15min) and left overnight for settling....199

Figure 104. Calculated relative hydration enthalpies in the series of increasing BT content (a) and S content (b). 200

Figure 105. Zeta potential measurements with a concentration of 0.5 mg/mL performed in 10^{-3} M potassium chloride solution at pH 6.8 and 25 °C....201

Figure 106. Comparison of UV/Vis (a), absorption maxima (b), PL spectra (c), emission maxima (d), TRPL measurements (e), and excited-state lifetimes (f) in the series from $BT_{2.5}S_{20}$ to $BT_{50}S_{20}$. As expected, BT_0S_{20} did not show relevant absorption behavior and was omitted from the comparison. Lifetimes were obtained from exponential fits and are given in the SI. 202

Figure 107. Comparison of UV/Vis (a), absorption maxima (b), PL spectra (c), emission maxima (d), TRPL measurements (e), and excited-state lifetimes (f) in the series from $BT_{20}S_0$ to $BT_{20}S_{40}$. Lifetimes were obtained from exponential fits and are given in the experimental part. 204

Figure 108. Kubelka-Munk-transformed UV/Vis spectrum (a), cyclic voltammogram (b), and HOMO-LUMO potentials versus the saturated calomel reference electrode (c)....205

Figure 109. Exemplary chromatogram for the photocatalytic degradation of 2,4-dichlorophenol. The inset is the mass spectrum of the pollutant. 4-*tert*-butyltoluene is used as internal standard....206

Figure 110. Bar diagram for the photocatalytic degradation of 2,4-dichlorophenol (a) and GCMS trace normalized to the standard 4-*tert*-butyltoluene (b)....207

Figure 111. Bar diagram for the photocatalytic degradation of 2,4-dichlorophenol (a) and GCMS trace normalized to the standard 4-*tert*-butyltoluene (b)....208

Figure 112. Degradation rates of other organic pollutants. The photocatalytic reaction was performed using $BT_{20}S_{20}$. 208

Figure 113. To estimate the hydration enthalpy, the total energy of four fragments in vacuum vs. in water was compared. By multiplying the obtained fragment hydration enthalpies with the respective monomer content, relative hydration enthalpies for every polymer were calculated. The relative hydration enthalpy compared to BT_0S_{20} was obtained and is displayed in the main text. All DFT calculations were carried at the B3LYP level of

theory, with the basis set of 6-31G(d). The hydration calculations were performed together with the PCM (Polarizable Continuum Model) model by employing water as the solvent.........214

A.3 List of Tables

Table 1. Selected large-scale industrial processes using heterogeneous catalysts..................15

Table 2. Benchmark of the present study to literature examples of photocatalytic oxidation of sp^3-hydrocarbons. a) Under UV light (310 nm); b) 4-chlorotoluene as the substrate 58

Table 3. Control reactions of the benchmark reaction. 4-Methoxyphenol (0.1 mmol), anethole (0.15 mmol), $(NH_4)_2S_2O_8$ (0.2 mmol) and photocatalyst (2 mg) were added into solvent (2 mL). The mixture was irradiated with a blue LED lamp (λ = 460 nm) for 22h. The yield was determined by GC-MS with trimethylsilican as an internal standard. ***** In reaction 1 with O_2 as oxidant, multiple products (>4) can be detected by GC-MS. The desired compound is among the products but could not be synthesized selectively. 90

Table 4. Screening and control experiments of the photocatalytic reduction of nitrobenzene. [a] Reaction conditions: [Nitrobenzene] = 75 mM, [TEOA] = 100 mM, [Hantzsch ester] = 45 mM, toluene/acetonitrile 1.7 mL (70:30), [CdSe 5 ML NPL] = 5x 10^{-8} M (300µL stock solution), white LED lamp (0.16 W/cm^2), room temperature, Argon atmosphere. [b] Conversion determined by GC-MS. [c] [Aniline] = 75 mM, [d] $[CuCl_2]$ = 200 mM [e] toluene 1.7 mL..114

Table 5. Lifetimes of the components obtained from double exponential fitting.......................122

Table 6. Conversion and selectivity overview of the kinetic study. Data points with low conversions do not have robust values for selectivity (*). 123

Table 7. Control experiments of the photocatalytic aza-Henry reaction with *N*-phenyltetrahydroisoquinoline and nitromethane (left) and the direct arylation of thiophene and 4-bromobenzenediazonium tetrafluoroborate (right). Reaction conditions for the aza-Henry reaction: *N*-phenyltetrahydroisoquinoline (52 mg, 0.25 mmol), nitromethane (40µL, 0.75 mmol), DMF (2 mL), catalyst (2 mg), 23W lamp, room temperature, air. Reaction conditions direct arylation 4-bromobenzenediazonium tetrafluoroborate (40 mg, 0.15 mmol), thiophene (118 µL, 1.5 mmol), DMSO (2 mL), catalyst (2 mg), 23W lamp, room temperature, argon atmosphere. [a] Conversion determined by NMR. [b] Conversion determined by GC-MS. 138

Table 8. DFT and TDDFT-calculated electrooptical parameters of the catalysts (rB3LYP, 6-31+g(d)). 162

Table 9. Screening and control experiments of the photocatalytic [4+2] cycloaddition of *trans*-anethole and isoprene. Reaction conditions: [*trans*-anethole] = 0.1 M, [isoprene] = 1 M, nitromethane 1.5 mL, $[cPMMA\text{-}BTPh_2]$ = 4 mg/mL (effective concentration of photocatalytic unit = 0.6 mM), blue LED lamp (460 nm, 0.16 W/cm^2), room temperature, air. [a] Conversion determined by GC-MS. [b] $[CuCl_2]$ = 1.5 M, [c] [KI] = 1.5 M, [d] $[BTPh_2]$ = 0.6 mM. 169

Table 10. Excited-state lifetime of the measured mixtures. 174

Table 11. Overview of molar ratios and weights of the polymer series with increasing BT content. 212
Table 12. Overview of molar ratios and weights of the polymer series with increasing S content. 213
Table 13. Lifetimes of the polymers obtained from exponential fitting. 215

A.4 List of publications

1. **N. Huber**, R. Li, C. T. J. Ferguson, D. W. Gehrig, C. Ramanan, P. W. M. Blom, K. Landfester, K. A. I. Zhang, A PMMA-based heterogeneous photocatalyst for visible-light-promoted [4+ 2] cycloaddition, *Catalysis Science & Technology* 2020, *10*(7), 2092-2099.
2. **N. Huber**, K. A. I. Zhang, Porous aromatic frameworks with precisely controllable conjugation lengths for visible-light-driven photocatalytic selective CH activation reactions, *European Polymer Journal* 2020, *140*, 110060.
3. W. Huang‡, **N. Huber‡**, S. Jiang‡, K. Landfester, K. A. I. Zhang, Covalent triazine framework nanoparticles *via* size-controllable confinement synthesis for enhanced visible-light photoredox catalysis, *Angewandte Chemie International Edition* 2020, *59*(42), 18368-18373.
4. **N. Huber**, H. Halim, A. Riedinger, K. A. I. Zhang, Semiconductor nanoplatelets with tunable photocatalytic activity for selective synthesis of azoxy aromatics, in preparation.
5. **N. Huber**, W. Huang, K. Landfester, K. A. I. Zhang, Visible-light-driven selective oxidation of hydrocarbons under ambient conditions over covalent triazine frameworks, in preparation.
6. **N. Huber**, M. Sirim, Z. Qian, K. Landfester, K. A. I. Zhang, A water-compatible PMMA-based polymer for photocatalytic pollutant remediation in aqueous media, in preparation.
7. C. T. J. Ferguson, **N. Huber**, K. Landfester, K. A. I. Zhang, Dual-responsive photocatalytic polymer nanogels, *Angewandte Chemie International Edition* 2019, *58*(31), 10567-10571.
8. C. T. J. Ferguson**,** **N. Huber**, T. Kuckhoff, K. A. I. Zhang, K. Landfester, Dispersible porous classical polymer photocatalysts for visible-light-mediated production of pharmaceutically relevant compounds in multiple solvents, *Journal of Materials Chemistry A* 2020, *8*(3), 1072-1076.

9. T. Gleede, J. C. Markwart, **N. Huber**, E. Rieger, F. R. Wurm, Competitive Copolymerization: Access to Aziridine Copolymers with Adjustable Gradient Strengths, *Macromolecules* 2019, *52*(24), 9703-9714.
10. H. Halim, D. Trieb, **N. Huber**, M. Martínez-Negro, L. A. Meyer, T. Basché, S. Morsbach, K. A. I. Zhang, A. Riedinger, Lateral Size Dependence in FRET between Semiconductor Nanoplatelets and Conjugated Fluorophores, *The Journal of Physical Chemistry C* 2020, *124*(45), 25028-25037.
11. W. Wei, R. Li, **N. Huber**, G. Kizilsavas, C. T. J. Ferguson, K. Landfester, K. A. I. Zhang, Visible-light-promoted aryl azoline formation over mesoporous organosilica as heterogeneous photocatalyst, submitted.